materials

Special Issue Reprint

Cutting Processes for Materials in Manufacturing

Edited by
Jian Weng, Kejia Zhuang, Dongdong Xu, Benkai Li, Hongguang Liu
and Gang Wang

mdpi.com/journal/materials

MDPI

Cutting Processes for Materials in Manufacturing

Cutting Processes for Materials in Manufacturing

Guest Editors

Jian Weng
Kejia Zhuang
Dongdong Xu
Benkai Li
Hongguang Liu
Gang Wang

MDPI

Basel • Beijing • Wuhan • Barcelona • Belgrade • Novi Sad • Cluj • Manchester

Guest Editors
Jian Weng
Department of Industrial and Systems Engineering
The Hong Kong Polytechnic University
Hong Kong
Hong Kong

Kejia Zhuang
School of Mechanical and Electronic Engineering
Wuhan University of Technology
Wuhan
China

Dongdong Xu
School of Mechanical Engineering
Tongji University
Shanghai
China

Benkai Li
School of Mechanical and Automotive Engineering
Qingdao University of Technology
Qingdao
China

Hongguang Liu
School of Mechanical Engineering
Xi'an Jiaotong University
Xi'an
China

Gang Wang
College of Mechanical and Vehicle Engineering
Chongqing University
Chongqing
China

Editorial Office
MDPI AG
Grosspeteranlage 5
4052 Basel, Switzerland

This is a reprint of the Special Issue, published open access by the journal *Materials* (ISSN 1996-1944), freely accessible at: https://www.mdpi.com/journal/materials/special_issues/R2N83013KX.

For citation purposes, cite each article independently as indicated on the article page online and as indicated below:

Lastname, A.A.; Lastname, B.B. Article Title. *Journal Name* **Year**, *Volume Number*, Page Range.

ISBN 978-3-7258-4078-6 (Hbk)
ISBN 978-3-7258-4077-9 (PDF)
https://doi.org/10.3390/books978-3-7258-4077-9

Contents

Preface

Dear Colleagues,

This Special Issue collected recent progresses regarding material-cutting techniques in manufacturing. This does not only include cutting techniques for metals, but also for composites, optic glass, or any other key engineering material. High-efficiency and high-performance cutting of difficult-to-cut materials has been an important topic for over one hundred years. As there is an increasing emergence of new machining techniques and materials, there is an increasing need to undate the current pool of knowledge in order to gain a deeper understanding of various cutting techniques. The topics covered in this Special Issue include material removal mechanisms, chip formation, cutting force, temperature, surface integrity, etc.

For this Special Issue, 15 diverse articles were collected. These studies have broadened our collective knowledge in the field of material processing and we appreciate the contributions from the authors.

Jian Weng, Kejia Zhuang, Dongdong Xu, Benkai Li, Hongguang Liu, and Gang Wang
Guest Editors

materials

MDPI

Article

Transient Temperature at Tool–Chip Interface during Initial Period of Chip Formation in Orthogonal Cutting of Inconel 718

Youssef Alammari [1], Jian Weng [2,*], Jannis Saelzer [2] and Dirk Biermann [2]

[1] Department of Mechanical Engineering, College of Engineering, Qassim University, Buraydah 51452, Saudi Arabia; y.alammari@qu.edu.sa

[2] Institute of Machining Technology, TU Dortmund University, Baroper Str. 303, 44227 Dortmund, Germany; jannis.saelzer@tu-dortmund.de (J.S.); dirk.biermann@tu-dortmund.de (D.B.)

* Correspondence: jian.weng@tu-dortmund.de

Abstract: Machining nickel-based super alloys such as Inconel 718 generates a high thermal load induced via friction and plastic deformation, causing these alloys to be among most difficult-to-cut materials. Localized heat generation occurring in machining induces high temperature gradients. Experimental techniques for determining cutting tool temperature are challenging due to the small dimensions of the heat source and the chips produced, making it difficult to observe the tool–chip interface. Therefore, theoretical analysis of cutting temperatures is crucial for understanding heat generation and temperature distribution during cutting operations. Periodic heating and cooling occurring during cutting and interruption, respectively, are modeled using a hybrid analytical and finite element (FE) transient thermal model. In addition to identifying a transition distance associated with initial period of chip formation (IPCF) from apparent coefficient of friction results using a sigmoid function, the transition temperature is also identified using the thermal model. The model is validated experimentally by measuring the tool–chip interface temperature using a two-color pyrometer at a specific cutting distance. Due to the cyclic behavior in interrupted cutting, where a steady-state condition may or may not be achieved, transient thermal modeling is required in this case. Input parameters required to identify the heat flux for the transient thermal model are obtained experimentally and the definitions of heat-flux-reducing factors along the cutting path are associated with interruptions and the repeating IPCF. The thermal model consists of two main parts: one is related to identifying the heat flux, and the other part involves the determination of the temperature field within the tool using a partial differential equation (PDE) solved numerically via a 2D finite element method.

Keywords: machining; transient thermal modeling; initial period of chip formation; Inconel 718; FEM; metals; modeling

1. Introduction

Machining difficult-to-cut materials like Inconel 718 presents significant challenges due to the material's mechanical and thermal properties, resulting in high mechanical and thermal loads. De Bartolomeis et al. [1] extensively reviewed the machinability of Inconel 718. Typically, machining this alloy involves flood cooling with metalworking fluids (MWF), but sustainable practices suggest minimizing or eliminating MWF use. Recent contributions to the literature [2,3] have explored sustainable machining methods across various materials and processes. The observed low tool–chip contact in the initial period of chip formation (IPCF), where reduced tool–chip friction is observed at the beginning of cutting [4], indicates promising potential for sustainable machining. Figure 1 illustrates the main characteristics of IPCF chips: small chip thickness, large shear angle, minimal secondary shear zone, and small chip curl radius. These characteristics, in addition to reduced passive force, are all indicators of reduced tool–chip contact friction. However, additional process adaptation may be necessary to enable and sustain the effect of the IPCF in continuous machining operations. For example, interruption can be induced using intermittent vibration-assisted machining to influence MWF delivery to the tool–chip interface. To adopt sustainable lubrication like MQL for Inconel 718, it is crucial to fundamentally investigate chip formation and the related thermal effects to understand the tribological aspects involved.

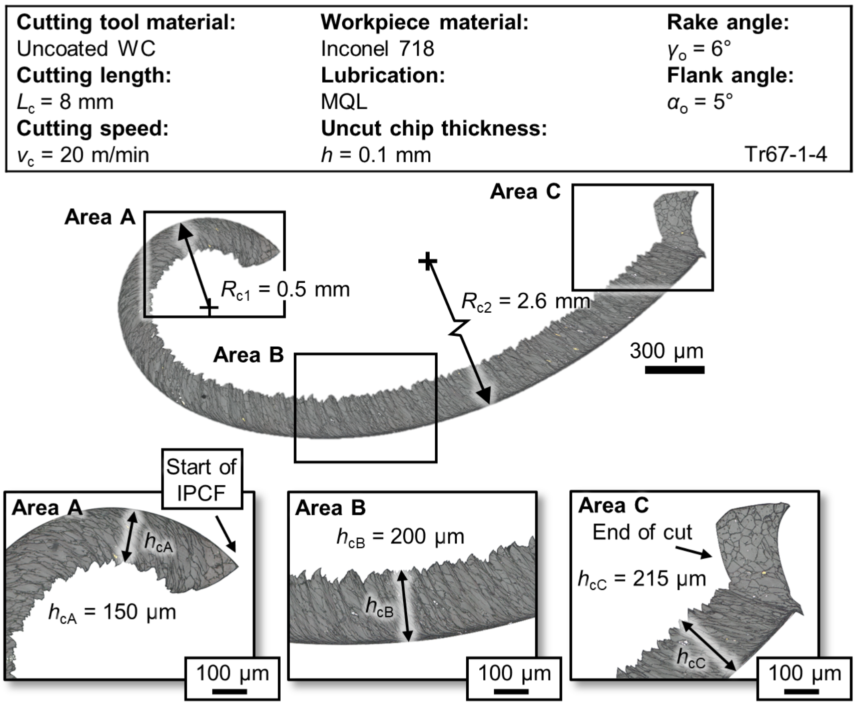

Figure 1. Main characteristics of an IPCF chip—obtained experimentally. Chip thickness h_c was measured using a calibrated optical microscope. Curl radius R_c was calculated through fitting an arc of 3 points to the contact side of the chip.

Measuring temperature in machining can be quite challenging, especially within the tool–chip interface, as the temperature distribution changes considerably along the rake face with a steep temperature field. Additionally, the transient behavior occurring in interrupted machining, which lasts for a very short time, poses an additional challenge for experimental temperature investigations. Researchers have experimentally investigated temperature measurement using different techniques, as reviewed in a CIRP keynote paper by Davies et al. [5]. In addition to experimental temperature measurement, analytical and numerical models provide detailed insights into the transient temperature behavior, both spatially and temporally.

Trigger and Chao [6] conducted pioneering research on determining cutting temperatures in continuous cutting. The heat source in the shear plane was accounted for in the model and the average temperature of the chip in the shear zone was evaluated. Other researchers have built upon Trigger and Chao's model for continuous cutting. Komanduri and Hou [7] investigated the orthogonal continuous cutting process regarding shear plane heat sources. The frictional heat source within the tool–chip interface was incorporated first [8]. Later, the heat from two sources, friction and shearing, was incorporated [9]. Chenwei et al. [10] proposed an enhanced model based on the Komanduri–Hou and Huang–Liang models. To validate their model, they incorporated a thermocouple into the cutting tool during the cutting of a titanium alloy. Weng et al. [11] introduced an enhanced analytical thermal model, building upon the Komanduri–Hou framework, to predict the steady-state temperature of the rake face. Their method incorporated temperature-dependent thermal properties and was validated through direct in situ temperature measurements using a two-color pyrometer. Salame and Malakizadi [12] investigated an improved semi-analytical thermal model, which employed physics-based estimation to account for variable heat flux at the tool–chip interface. Ning and Linag [13] performed a comparative study of three widely recognized analytical thermal models to forecast the orthogonal cutting temperature of AISI 1045. Zhao et al. [14] carried out a thorough review of analytical and numerical methods developed to explore the effects of coatings on cutting temperature. Barzegar and Ozlu [15] employed the finite difference method to investigate the steady-state influence of including the cutting edge radius and the third deformation zone. While most research on cutting temperature has focused on continuous cutting operations, several studies have also been conducted on interrupted cutting operations.

In interrupted machining, transient temperature modeling is highly relevant. Only a few researchers have addressed this problem and developed complete analytical or numerical models with experimental validation. Interrupted cutting is characterized by the production of discontinuous chips and cyclic mechanical and thermal loading. The tool and the workpiece are influenced by this type of loading.

Stephenson and Ali [16] utilized an approach where they approximated the tool's geometry by employing a semi-infinite rectangular corner. This method was employed to simulate the transient temperatures at specific points within the tool during interrupted cutting. They investigated the effects of various heat source distributions across the rake face, along with time-dependent variations in heat source intensities. Their model suggested that interrupted cutting leads to lower tool temperatures compared to continuous cutting due to the cooling effect during non-cutting periods. They explained how the Green's function can be implemented to solve for temperature within the tool. Identifying the input heat flux can pose challenges, as it requires determining the spatial and temporal distribution of heat flux. Stephenson and Ali utilized the steady-state cutting temperature model developed by Loewen and Shaw [17], which involves calculating the total amount of frictional energy dissipated at the tool–chip interface, based on parameters related to machining process parameters, the mechanical load, and chip-related parameters such as chip velocity, chip thickness, and contact length. The analytical model by Stephenson and Ali [16] is a fundamental approach in transient temperature modeling that has been accepted and implemented by many researchers, such as Karaguzel et al. [18] and Augspurger et al. [19].

Non-uniform heat flux distribution was investigated by Jen and Anagonye [20]. They investigated the influence of initial transient behavior on tool temperature, extending the model of Stephenson and Ali [16]. Jen et al. [21] developed conduction equations in three-dimensional space to represent nonlinear transient heat sources. The equations were numerically solved to study their effect on transient temperature. Potdar and Zehnder [22] developed a finite element model for investigating transient temperature behavior based on a friction model with critical stress criteria. A numerical model was developed by Lazoglu and Altintas [23] to investigate transient temperature fields based on finite difference. Islam et al. [24] developed their work further to include three-dimensional effects. Islam and Altintas [25] used the finite difference method in 2D to investigate the transient conditions related to thermal modelling of coated tools.

Jiang et al. [26] used an analytical model for contact length to determine the time-dependent spatial heat source distribution on the rake face during the milling process. They validated their approach by integrating thermocouples into the tool and used a least square optimization algorithm proposed by Beck et al. [27] to solve the inverse heat conduction problems and determine the heat flux in the tool and workpiece. Liu et al. [28] investigated a three-dimensional analytical model that incorporates transient behavior, including convective cooling, by employing the transient Green's function method to solve the energy equation. They applied initial and boundary conditions with a defined heat source within the tool–chip interface. To validate the results, a ratio pyrometer was embedded in the cutting tool and positioned at 0.4 mm from the tool tip.

To accurately model cutting temperatures, it is important to consider the contact properties between the cutting tool and chip, particularly the complex frictional interactions at the tool–chip interface. Previous studies have used simplified friction models, such as Coulomb friction. However, Zorev [29] showed that the tool–chip interface has two distinguishable regions: the sticking region and the sliding region. Nevertheless, this distinction is not quite accurate for precise modeling since friction properties also depend on temperature, pressure, and sliding velocity.

Recently, Karaguzel [30] proposed a hybrid model that combines analytical and numerical methods, taking into consideration zonal contact as described by Zorev [29]. The model determines heat flux analytically and uses a numerical transient heat conduction model to calculate temperature within the tool. The MATLAB PDE Toolbox was used to develop the numerical model. A similar approach is utilized in this research for thermal modeling related to IPCF, but with variations in how the heat flux is defined spatially and temporally based on experimental data.

A transition temperature related to the end of the IPCF is obtained by correlating the transition distance with the calculated temperature from the model at the transition distance. Identifying the transition temperature, using the proposed model, enables better understanding of the IPCF, where low friction at the tool–chip interface is observed up to the transition distance. Being able to identify the transition temperature and transition distance facilitates identifying key parameters such as interruption/cutting periods to sustain the favorable effects of the IPCF through interrupted machining.

2. Materials and Methods

This section details the experimental work, and a description of the model is provided. Input parameters required in the model are determined experimentally and model results are validated using two-color pyrometer in orthogonal cutting. The model is described in detail, highlighting how interruptions and the effect of the initial period of chip formation are incorporated into it.

2.1. Experimental Setup

A custom-made machine tool was used to conduct orthogonal experiments in the context of this research. The machine used for chip formation analysis was a special machine based on the model PFS 5558/1 from the company Heinz Berger Maschinenfabrik GmbH & Co. KG, Wuppertal, Germany. It has three axes that are utilized for positioning and feed movement. The machine, along with its specifications, is shown in Figure 2.

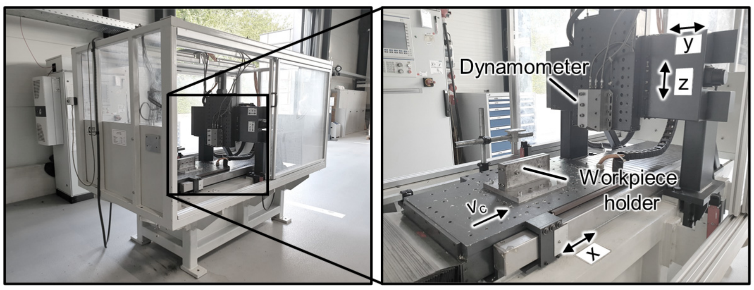

Machine type: Chip formation analysis machine, **Model:** Berger PFS 5558/1

Axis	Range of travel	Max. acceleration	Max. speed
x-axis	900 mm	30 m/s^2	180 m/min
y-axis	200 mm	10 m/s^2	15 m/min
z-axis	95 mm	10 m/s^2	15 m/min

Figure 2. Machine tool used in orthogonal cutting.

For the recording of the mechanical tool load, a piezoelectric dynamometer from Kistler Instrumente AG, Winterthur, Switzerland, was used. The force measuring platform, type 9263, offers the possibility to measure mechanical loads of up to 10 kN in the *y*- and *z*-directions and 20 kN in the x-direction. It was attached to a platform sliding on the cross rail of a Berger machine. According to the manufacturer of the dynamometer, its lowest natural frequency is $f_n > 2.5$ kHz and stiffness $k_c \approx 2$ kN/µm, with a response threshold of less than 0.1 N. For signal conditioning, Kistler KIAG SWISS, Winterthur, Switzerland, type 5001 charge amplifiers were used to convert the charge signals to proportional voltage signals. The charge amplifiers amplify the signal using calibrated gain factors to within ±10 V. Multi-channel data acquisition from a TEAK Corporation KK, Tokyo, Japan, type GX1 integrated recorder was used to collect the data at a sampling frequency $f_s = 50$ kHz upon manual trigger before the beginning of cutting.

To determine the temperature, a two-color pyrometer, Fire III, manufactured by Energy Engineering Aachen (en2AIX) GmbH, Achen, Germany, was used. The pyrometer operates at wavelengths $\lambda_1 = 1.675$ µm and $\lambda_2 = 1.945$ µm. It has a maximum sampling rate of $f_s = 500$ kHz and a temperature range of $T = 250\ldots1200$ °C. To collect the thermal radiation, the pyrometer system utilized a fiber optic cable with a diameter of $d_{fo} = 330$ µm. This fiber optic technology enables measurements in confined spaces.

While it is possible to estimate tool temperature using a thermographic camera, as demonstrated by Saez-de-Buruaga et al. [31], this method is subject to fundamental limitations concerning calibration and accuracy, particularly related to emissivity. Additionally, the location from which temperature measurements are typically taken, usually from the tool side, poses challenges [32]. In this study, temperature evaluation utilized a ratio pyrometer to mitigate uncertainties associated with emissivity. The fiber optic of the pyrometer was positioned to directly measure the temperature of the chip-free side. Access to the rake face was facilitated via a small slot along the cutting path, as described by Saelzer et al. [33]. Figure 3 provides an overview of the temperature measurement procedure.

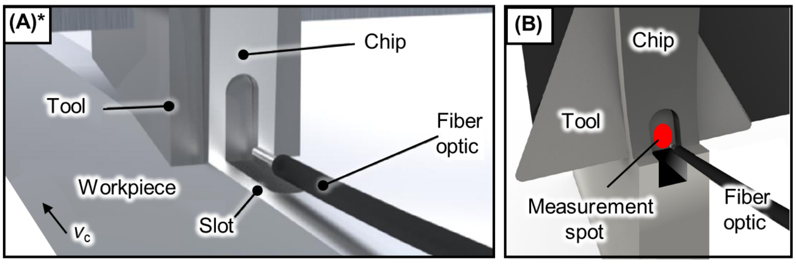

Figure 3. Temperature measurement during orthogonal cutting: (**A**) concept according to Saelzer et al. [33]; (**B**) measurement at the end of the workpiece.

An uncoated tungsten carbide (WC) insert (TPGN160308 H13A) with a cutting edge radius of $r_\beta = 8$ µm and a triangular shape was attached to the tool holder (CTFPL2525M16), both manufactured by Sandvik. The resulting rake angle was $\gamma_o = 6°$, and the clearance angle was $\alpha_o = 5°$. Inconel 718, which is the commercial name of the nickel-based superalloy NiCr19Fe19Nb5Mo3 (material number: 2.4886) [34], was used as the workpiece material. It is also known as UNS N07718 according to [35]. The alloy offers high corrosion and creep resistance at elevated temperatures. Due to its desirable thermomechanical properties, it is applied where high temperatures and high mechanical loads occur [1]. For instance, it is used in the hot segments of aero engines and power generation turbines, rocket engine nozzles, nuclear reactors, and in the exhaust systems of high-performance automotive vehicles.

Cuboid workpieces, in the annealed and aged condition with a hardness measured at 470 HV30, were prepared. The workpieces had a width of $b = 2$ mm. The individual cutting lengths $L_{ci} = 8$ mm. All experiments were repeated at least twice.

The MQL technique was used to supply lubricants to the cutting zones. The MQL aerosol was prepared remotely using a special aerosol generation device and supplied through a nozzle directed at the cutting zone. The MQL oil employed was Vascomill MMS HD1, a synthetic Ester oil from Blasser Swisslube AG, Rüegsau, Switzerland, consisting of 80% Ester and containing 10% sulfur. This oil has a viscosity of η = 40 mm^2/s at 40 °C and a flash point of T_{flash} = 200 °C. The oil was supplied at a flow rate of approximately $Q_{\text{oil}} \approx$ 50 mL/h.

2.2. Determination of Heat Flux at Tool–Chip Interface

In the IPCF, the friction within the tool–chip interface varies over a finite cutting distance, resulting in a corresponding influence on the heat flux. Additionally, the distribution of heat flux within the tool–chip interface is influenced by a dual zone model, namely sticking and sliding. Figure 4 provides an overview of the heat flux within the tool–chip interface in the IPCF.

The primary mechanism in the thermomechanical modeling of the secondary deformation zone is the friction between the tool and the chip. This friction arises from the contact between the two surfaces and is modeled using a dual zone approach [29]. The rake face contact is divided into two distinct regions: a sticking region and a sliding region. In the sticking region, high normal stress occurs, whereas the sliding region exhibits comparatively lower normal stress levels and the Coulomb friction law applies.

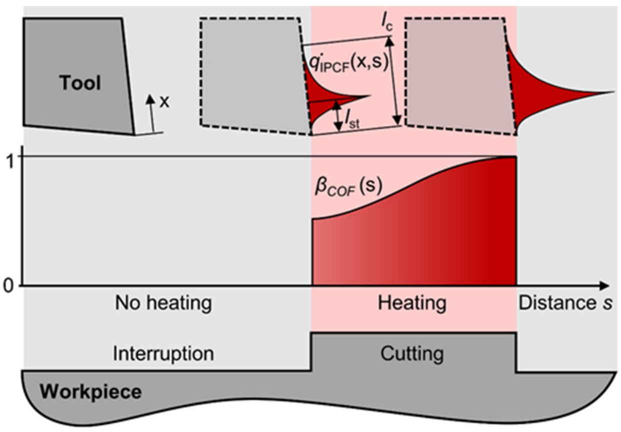

Figure 4. Schematic of heat flux in the IPCF.

Coulomb's friction law states that the shear stress is directly correlated with the normal stress, governed by sliding friction coefficient μ and normal stress p. If the friction coefficient remains constant, as the normal stress increases towards the tool tip, the shear stress also increases. Nevertheless, the shear stress cannot surpass the material's shear flow stress τ_1; thus, it is presumed to be equivalent to τ_1 within the sticking zone. Consequently, the allocation of shear stress across the rake face contact is determined in accordance with Childs [36]:

$$\tau = \begin{cases} \tau_1, & x \leq l_{\text{st}} \\ \mu p(x), & l_{\text{st}} < x \leq l_{\text{c}} \end{cases} \tag{1}$$

Karaguzel [30] provides the expression for the heat flux within the tool–chip interface, represented as $\dot{q}(x)$, which varies with the distance x from the cutting edge on the rake face.

$$\dot{q}(x) = \begin{cases} \tau_1 v_{\text{ch}}, & 0 \leq x \leq l_{\text{st}} \\ \mu v_{\text{ch}} p(x), & l_{\text{st}} < x \leq l_{\text{c}} \\ 0, & x > l_{\text{c}} \end{cases} \tag{2}$$

where l_c represents the total tool–chip contact length, which is measured at the end of adhesion marks appearing on the rake face. l_{st} denotes the sticking zone length and is calculated using the formula proposed by Budak and Ozlu [37]:

$$l_{st} = l_c\left(-\left(\frac{\tau_1}{p_0\mu}\right)^{\frac{1}{\zeta}} + 1\right) \tag{3}$$

where μ represents the tool–workpiece sliding friction coefficient, which is determined experimentally. τ_1 represents the shear flow stress of the material, assumed to be equivalent to the shear flow stress in the primary shear zone. This stress is influenced by material properties under conditions of high strain rates and elevated temperatures. It is calculated at as a steady state from measured forces and geometrical parameters, which identifies the primary shearing area, as follows, according to Childs [36]:

$$\tau_1 = \frac{(F_c\cos\phi - F_p\sin\phi)\cdot\sin(\phi)}{hb} \tag{4}$$

where F_c represents the cutting force and F_p denotes the passive force. The angle ϕ represents the shear angle, while the uncut chip thickness and width of cut are denoted as h and b, respectively. v_{ch} denotes the chip velocity calculated along the tool–chip contact, following the method proposed by Li et al. [38]:

$$v_{ch}(x) = \begin{cases} v_{ch0}\left(\frac{x}{l_{st}}\right)^{\omega_c}, & 0 \le x \le l_{st} \\ v_{ch0}, & l_{st} < x \le l_c \\ 0, & x > l_c \end{cases} \tag{5}$$

where ω_c represents the chip velocity distribution exponent, which is assumed to have a constant value of $\omega_c = 2$ in this investigation. v_{ch0} denotes the average chip velocity and can be determined using the following equation:

$$v_{ch0} = v_c\frac{\sin\phi}{\cos(\phi - \gamma_o)} \tag{6}$$

where v_c represents the cutting speed, γ_o is the rake angle, and ϕ denotes the shear angle, which can be determined geometrically by knowing the chip thickness ratio $r_c = h/h_c$, where h_c represents the average chip thickness. The relationship is as follows:

$$\phi = \tan^{-1}\left(\frac{r_c\cos\gamma_o}{1 - r_c\sin\gamma_o}\right) \tag{7}$$

$p(x)$ represents the normal pressure on the rake face and is given by Budak and Ozlu [37]:

$$p(x) = p_0\left(1 - \frac{x}{l_c}\right)^{\zeta} \tag{8}$$

Here, ζ indicates the stress distribution exponent, usually assumed to range between 2 and 3, and its value can be established via split tool experiments. In the current investigation, it was assumed to be $\zeta = 2$. p_0 is calculated according to Budak and Ozlu [37]:

$$p_0 = \tau_1\frac{h(\zeta + 1)}{l_c\sin\phi}\frac{\cos\lambda_f}{\cos(\phi + \lambda_f - \gamma_o)} \tag{9}$$

where λ_f represents the apparent friction angle, which is calculated as $\lambda_f = \tan^{-1}(COF)$, and *COF* denotes the apparent coefficient of friction obtained from the cutting forces F_c and passive forces F_p, as well as the rake angle, using the following equation:

$$COF = \frac{F_p + F_c \tan\gamma_o}{F_c - F_p \tan\gamma_o} \tag{10}$$

The partition ratio R_2 for the secondary shear zone heat flux is employed to determine how much of the overall heat flux $\dot{q}$ is allocated between the tool and the chip. In this investigation, R_2 was found iteratively by comparing the steady-state temperature obtained from the temperature analysis of Loewen and Shaw [17] with the steady-state tool temperature obtained from the proposed model. The tool heat flux was then determined as follows:

$$\dot{q}_{tool}(x) = (1 - R_2)\dot{q}(x) \tag{11}$$

Here, $\dot{q}_{tool}$ represents the steady-state heat flux at the tool. The cutting-distance-dependent heat flux in the IPCF was determined both during interruption and cutting as follows:

$$\dot{q}_{IPCF}(x,s) = \begin{cases} \beta_{COF}(s)\cdot\dot{q}_{tool}(x), & i(L_{ci} + L_{int}) \le s \le i(L_{ci} + L_{int}) + L_{ci} \\ 0, & i(L_{ci} + L_{int}) + L_{ci} \le s \le (i+1)(L_{ci} + L_{int}) \end{cases} \tag{12}$$

where i = 0, 1, 2, . . ., L_{ci} represents the length of each individual cutting interval, and L_{int} denotes the length of the interruption. The distance is related to time by $s = v_c\ t$. β_{COF} (s) is a factor that represents the reduction of steady-state heat flux due to a decrease in friction in the IPCF. It is obtained by fitting a sigmoid function to the average *COF* data of subsequent cutting segments. The sigmoid function for the IPCF is defined as follows:

$$COF_{fit}(s) = COF_{min} + \frac{COF_{max}}{1 + e^{-k_1(s-s_0)}}, \tag{13}$$

$$\beta_{COF}(s) = COF_{fit}(s)/COF_{max} \tag{14}$$

where COF_{min} and COF_{max} represent the minimum and maximum *COF* values in the IPCF, respectively. k_1 denotes the evolution rate, and s_0 represents the transition distance at the transition midpoint. If s_0 becomes negative, it indicates that the transition in the *COF* data has not been detected.

2.3. Determination of Tool Temperature Due to Heat Flux Occurring at Tool–Chip Interface

Once the heat flux is determined temporally and spatially, as discussed in the previous section, the temperature can be estimated using the heat equation. The partial differential equation for the temperature field in the tool is given as follows:

$$\rho c \frac{\partial T}{\partial t} = \nabla\cdot(k\nabla T) \tag{15}$$

where T represents the tool rake temperature, ρ is the density, k is the thermal conductivity, and c is the specific heat. Equation (15) is solved numerically using the MATLAB 2023a Partial Differential Equations (PDE) toolbox. The two-dimensional tool geometry is specified, and boundary conditions are defined on the edges of the tool as follows:

- Heat flux is applied only within tool–chip contact;
- Heat convection is implemented on both the flank face and the remaining portion of the rake face. The heat convection coefficient is assumed to be h_{conv} = 10 W/m^2, and the ambient temperature is T_∞ = T_{room} = 23 °C;
- The outermost edges of the tool are set to a constant temperature of T_{room} = 23 °C.

Figure 5 provides a summary of the tool geometry, mesh, and boundary conditions of the setup as applied in the MATLAB PDE toolbox. The "generateMesh" command in the MATLAB PDE toolbox was used with $H_{\max}$ and H_{edge} properties.

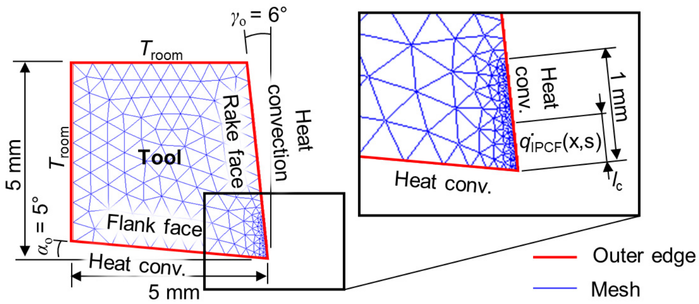

Figure 5. Tool geometry, mesh, and boundary conditions applied in MATLAB PDE toolbox.

A refined mesh size with an element length smaller than L_{elem} = 0.02 mm was used along the tool–chip contact, extending up to 1 mm from the cutting edge. The maximum element size was $L_{\text{elem\_max}}$ = 0.5 mm throughout the tool, except for the tool–chip contact. The total simulation time was set according to the desired number of heat cycles. The step size was defined by dividing the time of a single heat cycle by 1000.

The partial differential equation was solved using temperature-dependent values of thermal conductivity and specific heat for the tool. They were implemented in the MATLAB PDE toolbox as user defined functions using function handles. In order to determine the heat partition ratio, R_2, temperature-dependent thermal properties for both the tool and workpiece were employed in the model proposed by Loewen and Shaw [17]. Table 1 presents a summary of the temperature-dependent thermal properties for both the tool and the workpieces.

Table 1. Temperature-dependent thermal properties and density of tool and workpiece materials.

Material	Property	Equation or Value
Tool WC/6Co adapted from Spriggs et al. [39]	Thermal cond. in W/mK	$k(T°C) = 3 \times 10^{-5}\, T^2 - 0.0715\, T + 100.25$
	Specific heat in J/kgK	$c(T°C) = -6 \times 10^{-5}\, T^2 + 0.125\, T + 213.07$
	Density in kg/m^3	15,160 *
Inconel 718 adapted from Sweet et al. [40]	Thermal cond. in W/mK	$k(T°C) = 0.017\, T + 10.73$
	Specific heat in J/kgK	$c(T°C) = -2.9 \times 10^{-4}\, T^2 + 0.44\, T + 330$
	Ther. diffusivity in m^2/s	$K(T°C) = 2.83 \times 10^{-9}\, T + 2.82 \times 10^{-6}$
	Density in kg/m^3	8221

* Measured.

3. Results

3.1. Input Parameters

The model requires certain parameters as inputs. These parameters consist of the apparent coefficient of friction (*COF*), tool–chip contact length at different cutting speeds, mean chip thickness, and the sliding friction coefficient in both dry and lubricated conditions. The sliding friction coefficient was experimentally measured using an open tribometer, as described by Puls et al. [41]. Figure 6 presents a summary of these experimental results. Furthermore, the heat partition ratio R_2, obtained through iterative calculations, is also illustrated in Figure 6.

The parameters shown in Figure 6 are obtained under steady-state conditions. The apparent coefficient of friction influences the heat flux as it defines the maximum normal stress on the rake face, as shown in Equation (8). The contact length is an important factor that determines the spatial extent of the heat flux and is used to obtain the heat partition ratio in the steady state. The contact length impacts the heat partition [42]. The chip thickness and uncut chip thickness are used to calculate the shear angle, considering the rake angle, as shown in Equation (7). The experimentally obtained sliding friction values are used to define the sliding friction in the sliding zone. As expected, the apparent coefficient of friction, tool–chip contact length, and chip thickness decrease as the cutting speed increases. Furthermore, the use of MQL slightly reduces their values. As the cutting speed rises, the heat partition ratio R_2, representing the fraction of heat transferred into the chip, also increases. An interesting observation is the minimal influence of lubrication on the sliding friction for Inconel 718, as shown in Figure 6E.

Workpiece mat.	Inconel 718	**Cutting tool**	TPGN160308 H13A
Lubrication	Dry, MQL, Lub.	**Tool coating**	Uncoated
Uncut chip thick. *h*	0.1 mm	**Rake angle γ_o**	6°
Width of cut *b*	2 mm	**Flank angle α_o**	5°
Cutting speed v_c	10 … 50 m/min	**Friction tool angle**	5°
Relative speed v_r	10 … 90 m/min		

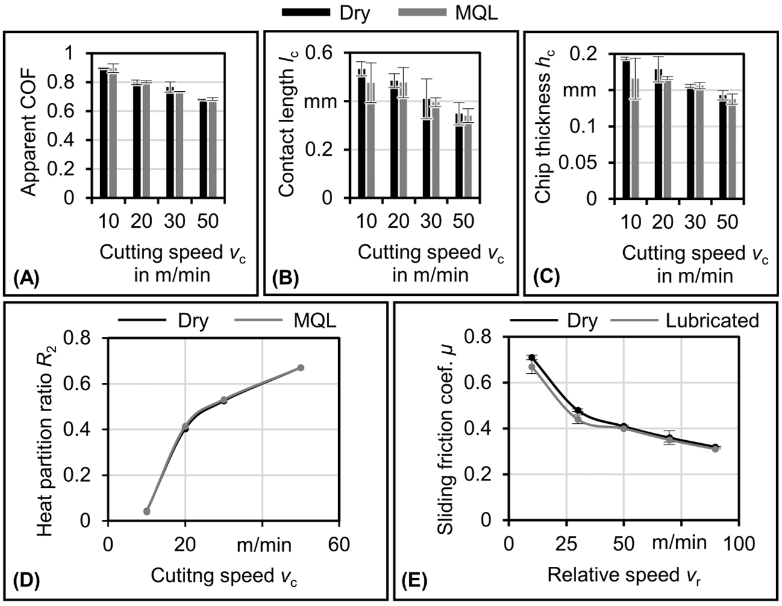

Figure 6. Input parameters of the IPCF transient temperature model for dry and lubricated cases for Inconel 718. (**A**) Apparent friction coefficient (*COF*). (**B**) Tool–chip contact length l_c. (**C**) Chip thickness h_c. (**D**) Heat partition ratio R_2. (**E**) Sliding friction coefficient μ.

3.2. Validation at Steady State

The reliability of the proposed model in estimating the steady-state temperature is examined by comparing these results with the results of steady-state temperature model of Loewen and Shaw [17]. Figure 7A provides a summary of the steady-state results. Additionally, a comparison with experimental temperature measurements at a finite distance using a two-color ratio pyrometer on the rake face, as described by Saelzer et al. [33], is shown in Figure 7B.

The results presented in Figure 7 demonstrate the validity of the model. As shown in Figure 7A, the transient behavior exists up to certain distances for different cutting speeds and eventually reaches a steady state. As shown in Figure 7B, the model predicts the average rake temperature, which is the average temperature along the tool chip contact length, with reasonable accuracy. The estimated mean rake temperature error is approximately ±10% within the cutting speed range of v_c = 10 to 50 m/min for Inconel 718. It is expected that the temperature increases when the cutting speed increases. The model can represent this fundamental phenomenon, which indicates its validity. This error could be attributed to measurement accuracy issues related to the measuring spot size and its exact position on the rake face, as well as inherent limitations of the model resulting from the calculated sticking zone length using Equation (3).

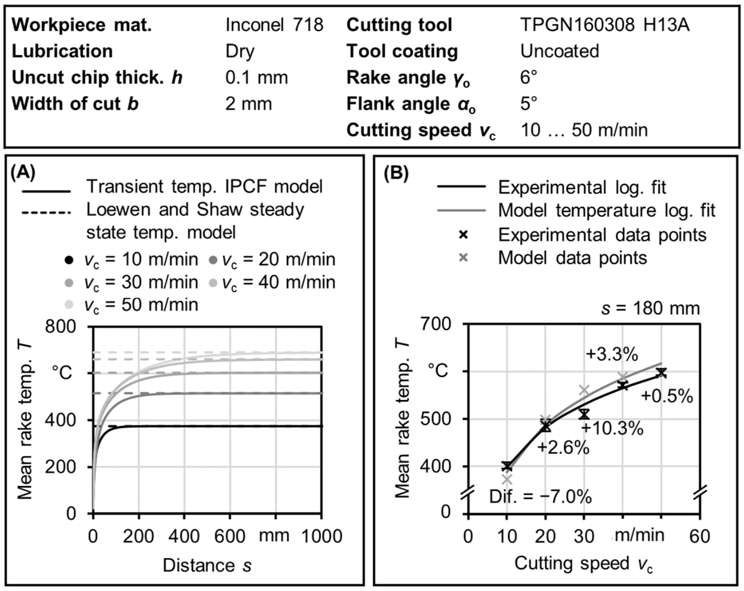

Figure 7. (**A**) Comparison with Loewen and Shaw analytical steady-state model. (**B**) Model results in comparison with experimental average rake temperatures obtained using ratio pyrometer at cutting distance s = 180 mm.

3.3. Determination of Heat Flux Reduction Factor within the IPCF

The steady-state heat flux is reduced within the IPCF by utilizing the IPCF heat flux reduction factor β_{COF}, as shown in Figure 8. This reduction factor accounts for distance-related events such as interruptions where no heat input occurs, as well as the reduction observed in the IPCF, which exhibits a decrease in the *COF*.

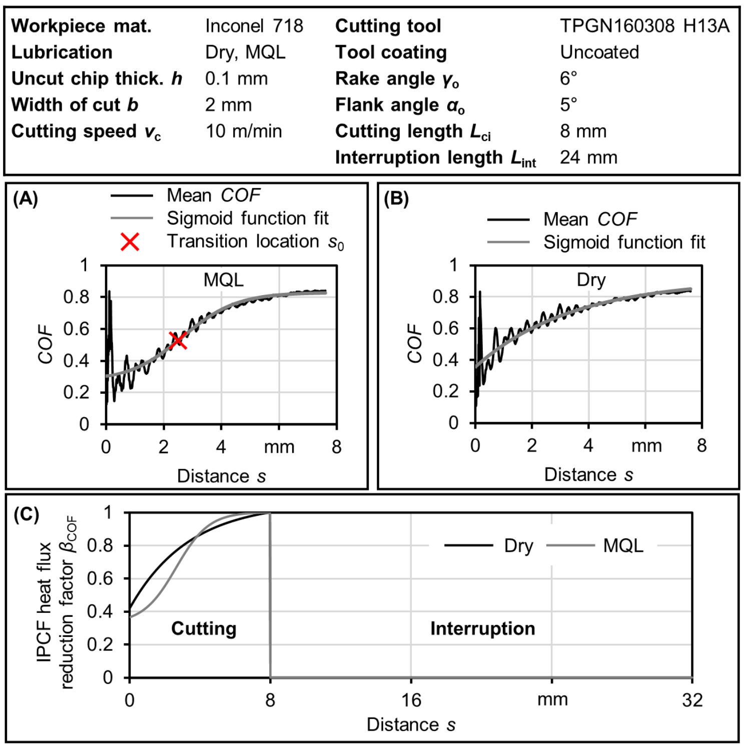

Figure 8. Example of the influence of the IPCF on the heat flux. (**A**) An MQL case showing mean *COF* fitted with sigmoid function with identified transition location s_0. (**B**) Corresponding dry case showing mean *COF* fitted with sigmoid function and no transition in *COF* was identified. (**C**) The resulting IPCF heat flux reduction factor for a single heating cycle of cases shown in (**A**,**B**).

The sigmoid function fit, as shown in Figure 8A,B, provides a close approximation that describes the reduction in *COF* observed in the IPCF. Whether a transition between low and high friction occurs or not, the sigmoid function fits the data. In cases where no transition is detected, a negative transition value is assigned directly by the fitting function. The fitted data are then divided by the maximum *COF* value, which approximates the steady-state condition. The IPCF heat flux reduction factor β_{COF} can be determined for both cutting and interruption segments. The steady-state heat flux within the tool–chip interface is multiplied by the reduction factor along the tool movement pathway, accounting for multiple heat cycles. The difference between dry and MQL in Figure 8C is caused by low friction within the IPCF when MQL is applied and appears as low *COF*. This effect is reflected in the heat flux reduction factor that is used later to calculate the transition temperature of the IPCF.

3.4. Heat Flux and Temperature Results

This section presents the temperature within the tool, resulting from the determined heat flux. Figure 9 displays selected temperature results obtained from the model, specifically showing the maximum temperature on the rake face.

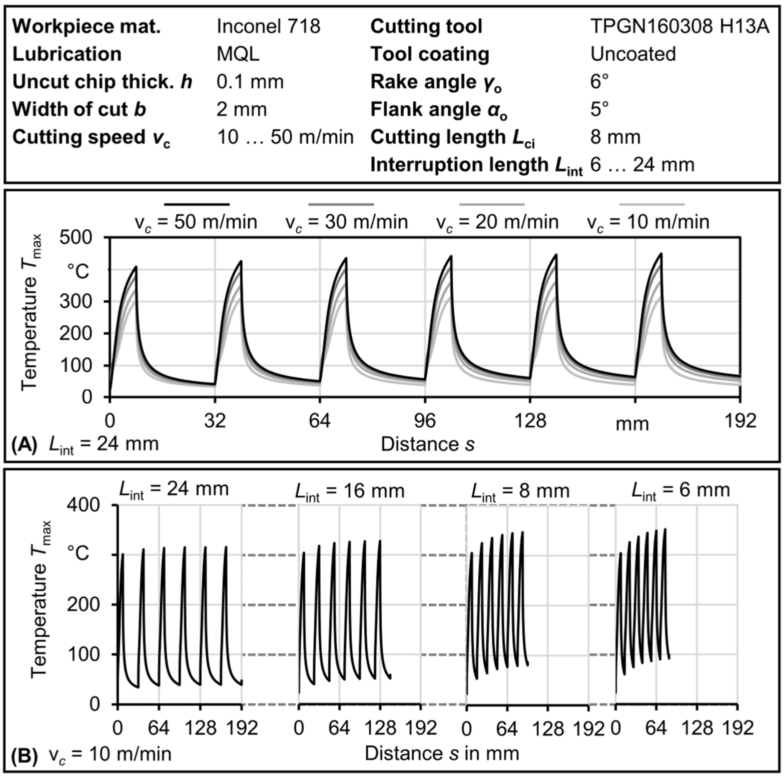

Figure 9. Maximum rake temperature at the rake face obtained from the model in interrupted cutting for Inconel 718: (**A**) at different speeds for L_{int} = 24 mm; (**B**) at different interruption lengths at v_{c} = 10 m/min.

Figure 9A demonstrates that higher cutting speeds result in higher maximum temperatures at the tool–chip contact, as expected, due to the increased heat flux. However, the heat partition ratio may limit its influence on the tool temperature, as only a small amount of heat enters the tool at high speeds. During cutting, the temperature gradually rises due to the heat supplied by the cutting process, resulting from shearing and friction. When cutting is interrupted, the temperature increase halts and a reduction in temperature occurs. Figure 9B shows that shorter interruption lengths lead to higher minimum and maximum temperatures, as the time available for cooling the tool becomes shorter. The temperature change associated with different interruption lengths suggests a potential impact of temperature on the reduced tool–chip contact in the lubricated IPCF, where temperature and interruption time become crucial factors. At low speeds and longer interruption lengths, the reduced contact in the IPCF becomes more noticeable between the dry and MQL cases. Figure 9 reveals that the reduced tool–chip contact friction in the IPCF appears to slow down the temperature increase during cutting.

Figure 10 illustrates a single heating cycle, emphasizing the impact of MQL on the maximum temperature at the tool–chip interface. The heat flux reduction factor, β_{COF}, plays an important role in reducing the rate of temperature increase at the beginning of the cutting process. This factor reflects the impact of the low apparent coefficient of friction within the IPCF and determines the extent to which a reduction in steady-state heat flux can be achieved. The decrease in heat flux at the start of the cut affects the final temperature before interruption, resulting in a lower maximum temperature achieved using MQL compared to the dry condition.

Workpiece mat.	Inconel 718	**Cutting tool**	TPGN160308 H13A
Lubrication	Dry, MQL	**Tool coating**	Uncoated
Uncut chip thick. *h*	0.1 mm	**Rake angle γ_o**	6°
Width of cut *b*	2 mm	**Flank angle α_o**	5°
Cutting speed v_c	20 m/min	**Cutting length L_{ci}**	8 mm
		Interruption length L_{int}	24 mm

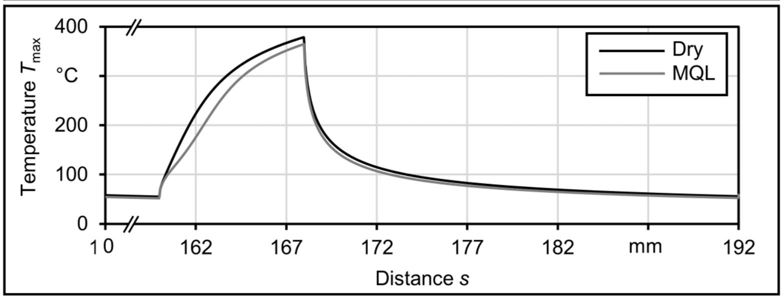

Figure 10. Effect of MQL on maximum rake temperature for Inconel 718.

Figure 11A illustrates the total heat flux along the tool–chip contact length in the steady-state condition, $\dot{q}(x)$, for different cutting speeds and lubrication conditions. The heat flux, denoted as $\dot{q}(x)$, undergoes reduction via the heat partition ratio, R_2. A fraction of this flux passes through the chip, while the remaining part $(1 - R_2)$ is transferred into the tool. Additionally, the heat reducing factor, β_{COF}, allows for a non-uniform heat flux that depends on the tool's position within the IPCF. The non-uniform distribution of heat flux across the tool–chip contact length results in a non-uniform temperature distribution along the contact area. The highest temperature occurs at a specific distance from the cutting edge, as illustrated in Figure 11B. The temperature field within the tool at these maximum values is shown in Figure 11C for different cutting speeds using MQL.

The heat flux illustrated in Figure 11A spans a finite length along the tool–chip contact surface. The end point of this flux and the position of its peak value (found at the end of the sticking zone) impact both the temperature distribution along the contact and within the tool, as demonstrated in Figure 11B. High temperatures are reached at high cutting speeds, although the temperature field within the tool may vary, as seen in Figure 11C. At low cutting speeds, a lower maximum temperature is observed, but with an extended temperature field due to the longer tool–chip contact length.

The temperature analysis discussed so far raises an important question regarding the existence of a transition temperature for the IPCF and its quantification. Figure 12 attempts to provide more detail on this aspect.

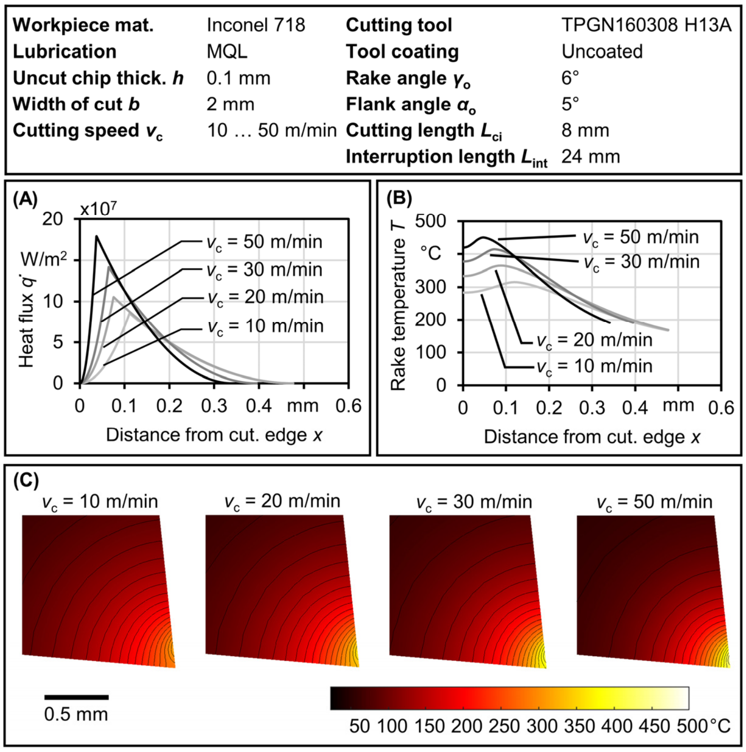

Figure 11. Heat flux and tool temperature for Inconel 718. (**A**) Heat flux along tool–chip contact length at steady state. (**B**) Temperature along tool–chip contact length before interruption. (**C**) Temperature field within the tool at different cutting speeds occurring before interruption.

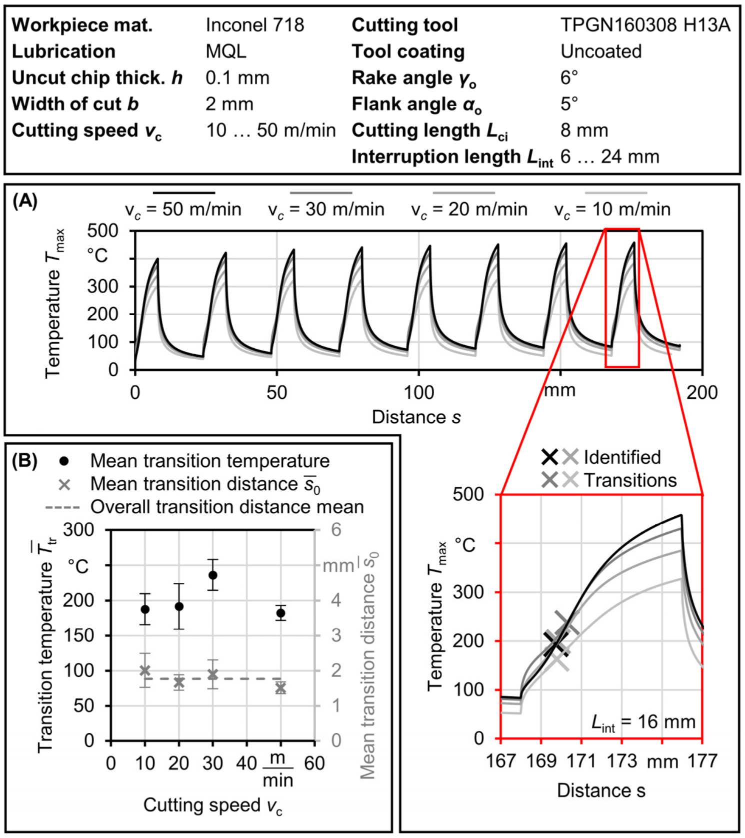

Figure 12. Identification of transition temperatures. (**A**) Example of transition temperature identification. (**B**) Transition temperature and distance results.

As previously shown in Figure 8A,B, a sigmoid function was utilized to fit the data of the apparent coefficient of friction (*COF*). The transition distance, denoted as s_0, was determined as the value at the sigmoid's midpoint. In Figure 12, the identified transition distance was employed to find the transition temperature at different cutting speeds. It should be noted that the transition distance is only valid for cases with MQL; the dry cases either exhibit negative values or very small values that were not considered to be transition points. An example illustrating how the transition temperature is identified is presented in Figure 12A. A summary of the transition results is provided in Figure 12B. The transition distance, s_0, appears to remain constant across different cutting speeds at an average value of $\overline{s_0}$ = 1.8 mm, and the corresponding transition temperature, T_{tr}, falls within a limited range with an average of $\overline{T_{\mathrm{tr}}}$ = 200 °C. The relationship between transition distance and transition temperature and the minimal effect of cutting speed characterizes the transition of the IPCF into the steady state.

4. Discussion and Conclusions

Transient thermal modeling of the IPCF in interrupted machining enables a deeper understanding of the working mechanism of the IPCF. The heat flux in interrupted machining is cyclic, reaching zero during interruption and having a reduced value at the IPCF. Consequently, the temperature becomes cyclic with transient behavior that is always present, regardless of the contact condition. In the IPCF, the transient temperature rise can be delayed, resulting in a reduced maximum temperature before the next interruption interval. However, for this additional reduction in temperature to be observed, the transition associated with the IPCF between low and high friction must occur. This transition was only observed when effective application of a lubricant was achieved.

An important observation is that the transition distance, as obtained from fitting a sigmoid function, lies within a very narrow range. A similar observation holds true for the corresponding transition temperature. It was found that the transition distance was less than a couple of millimeters, and the corresponding mean transition temperature was about 200 °C.

Uncertainties related to the accuracy of heat flux determination might also affect the model results. In particular, the calculation of sticking length and the assumption that the pressure distribution exponent ζ and chip velocity distribution exponent ω are constants at variable cutting conditions might contribute to increased uncertainty in accurately determining tool temperature. Further experimental investigations are still required to validate the transient temperature rise on the rake face in real-time, which is still one of the major limitations in machining research.

Author Contributions: Conceptualization, Y.A.; methodology, Y.A and J.S.; software, Y.A.; formal analysis, Y.A.; investigation, Y.A.; resources, J.W., J.S. and D.B.; writing—original draft preparation, Y.A.; writing—review and editing, Y.A., J.W, J.S. and D.B.; supervision, D.B. All authors have read and agreed to the published version of the manuscript.

Funding: This research received no external funding.

Institutional Review Board Statement: Not applicable.

Informed Consent Statement: Not applicable.

Data Availability Statement: Dataset available on request from the authors.

Acknowledgments: The authors would like to acknowledge the support from Qassim University in Saudi Arabia via the provision of a doctoral scholarship to Y.A.

Conflicts of Interest: The authors declare no conflicts of interest.

References

1. De Bartolomeis, A.; Newman, S.T.; Jawahir, I.S.; Biermann, D.; Shokrani, A. Future research directions in the machining of Inconel 718. *J. Mater. Process. Technol.* **2021**, *297*, 117260. [CrossRef]
2. Mallick, R.; Kumar, R.; Panda, A.; Sahoo, A.K. Current status of hard turning in manufacturing: Aspects of cooling strategy and sustainability. *Lubricants* **2023**, *11*, 108. [CrossRef]
3. Lee, Y.J.; Wang, H. Sustainability of Methods for Augmented Ultra-Precision Machining. *Int. J. Precis. Eng. Manuf. Green Technol.* **2023**, *11*, 585–624. [CrossRef]
4. Alammari, Y.; Saelzer, J.; Berger, S.; Iovkov, I.; Biermann, D. Initial Period of Chip Formation: Observations towards Enhancing Machining Sustainability. In *Manufacturing Driving Circular Economy*; Kohl, H., Seliger, G., Dietrich, F., Eds.; GCSM 2022; Lecture Notes in Mechanical Engineering; Springer: Cham, Switzerland, 2023; pp. 193–201.
5. Davies, M.A.; Ueda, T.; M'saoubi, R.; Mullany, B.; Cooke, A.L. On the measurement of temperature in material removal processes. *CIRP Ann.* **2007**, *56*, 581–604. [CrossRef]
6. Trigger, K.J.; Chao, B.T. An analytical evaluation of metal-cutting temperatures. *Trans. Am. Soc. Mech. Eng.* **1951**, *73*, 57–66. [CrossRef]
7. Komanduri, R.; Hou, Z.B. Thermal modeling of the metal cutting process: Part I—Temperature rise distribution due to shear plane heat source. *Int. J. Mech. Sci.* **2000**, *42*, 1715–1752. [CrossRef]
8. Komanduri, R.; Hou, Z.B. Thermal modeling of the metal cutting process—Part II: Temperature rise distribution due to frictional heat source at the tool–chip interface. *Int. J. Mech. Sci.* **2001**, *43*, 57–88. [CrossRef]
9. Komanduri, R.; Hou, Z.B. Thermal modeling of the metal cutting process—Part III: Temperature rise distribution due to the combined effects of shear plane heat source and the tool–chip interface frictional heat source. *Int. J. Mech. Sci.* **2001**, *43*, 89–107. [CrossRef]
10. Chenwei, S.H.A.N.; Zhang, X.; Bin, S.H.E.N.; Zhang, D. An improved analytical model of cutting temperature in orthogonal cutting of Ti6Al4V. *Chin. J. Aeronaut.* **2019**, *32*, 759–769.
11. Weng, J.; Saelzer, J.; Berger, S.; Zhuang, K.; Bagherzadeh, A.; Budak, E.; Biermann, D. Analytical and experimental investigations of rake face temperature considering temperature-dependent thermal properties. *J. Mater. Process. Technol.* **2023**, *314*, 117905. [CrossRef]
12. Salame, C.; Malakizadi, A. An enhanced semi-analytical estimation of tool-chip interface temperature in metal cutting. *J. Manuf. Process.* **2023**, *105*, 407–430. [CrossRef]
13. Ning, J.; Liang, S.Y. A comparative study of analytical thermal models to predict the orthogonal cutting temperature of AISI 1045 steel. *Int. J. Adv. Manuf. Technol.* **2019**, *102*, 3109–3119. [CrossRef]
14. Zhao, J.; Liu, Z.; Wang, B.; Hu, J.; Wan, Y. Tool coating effects on cutting temperature during metal cutting processes: Comprehensive review and future research directions. *Mech. Syst. Signal Process.* **2021**, *150*, 107302. [CrossRef]
15. Barzegar, Z.; Ozlu, E. Analytical prediction of cutting tool temperature distribution in orthogonal cutting including third deformation zone. *J. Manuf. Process.* **2021**, *67*, 325–344. [CrossRef]
16. Stephenson, D.A.; Ali, A. Tool temperatures in interrupted metal cutting. *ASME J. Eng. Ind.* **1992**, *114*, 127–136. [CrossRef]
17. Loewen, E.G.; Shaw, M.C. On the analysis of cutting-tool temperatures. *Trans. Am. Soc. Mech. Eng.* **1954**, *76*, 217–225. [CrossRef]
18. Karaguzel, U.; Bakkal, M.; Budak, E. Modeling and measurement of cutting temperatures in milling. *Procedia CIRP* **2016**, *46*, 173–176. [CrossRef]
19. Augspurger, T.; Da Silva, G.; Schraknepper, D.; Mattfeld, P.; Bergs, T. Model-based monitoring of temperatures and heat flows in the milling cutter. *Int. J. Adv. Manuf. Technol.* **2020**, *107*, 4231–4238. [CrossRef]
20. Jen, T.-C.; Anagonye, A.U. An improved transient model of tool temperatures in metal cutting. *J. Manuf. Sci. Eng.* **2001**, *123*, 30–37. [CrossRef]
21. Jen, T.-C.; Eapen, S.; Gutierrez, G. Nonlinear numerical analysis in transient cutting tool temperatures. *J. Manuf. Sci. Eng.* **2003**, *125*, 48–56. [CrossRef]
22. Potdar, Y.K.; Zehnder, A.T. Measurements and simulations of temperature and deformation fields in transient metal cutting. *J. Manuf. Sci. Eng.* **2003**, *125*, 645–655. [CrossRef]
23. Lazoglu, I.; Altintas, Y. Prediction of tool and chip temperature in continuous and interrupted machining. *Int. J. Mach. Tools Manuf.* **2002**, *42*, 1011–1022. [CrossRef]
24. Islam, C.; Lazoglu, I.; Altintas, Y. A three-dimensional transient thermal model for machining. *J. Manuf. Sci. Eng.* **2016**, *138*, 021003. [CrossRef]
25. Islam, C.; Altintas, Y. A two-dimensional transient thermal model for coated cutting tools. *J. Manuf. Sci. Eng.* **2019**, *141*, 071003. [CrossRef]
26. Jiang, F.; Liu, Z.; Wan, Y.; Shi, Z. Analytical modeling and experimental investigation of tool and workpiece temperatures for interrupted cutting 1045 steel by inverse heat conduction method. *J. Mater. Process. Technol.* **2013**, *213*, 887–894. [CrossRef]
27. Beck, J.V.; Blackwell, B.; Clair, C.R., Jr. *Inverse Heat Conduction: Ill-Posed Problems*; John Wiley & Sons, Inc.: New York, NY, USA, 1985.
28. Liu, H.; Rodrigues, L.; Meurer, M.; Bergs, T. A three-dimensional analytical model for transient tool temperature in cutting processes considering convection. *CIRP J. Manuf. Sci. Technol.* **2023**, *43*, 1–14. [CrossRef]

29. Zorev, N.N. Inter-relationship between shear processes occurring along tool face and shear plane in metal cutting. *Int. Res. Prod. Eng.* **1963**, *49*, 143–152.
30. Karaguzel, U. Transient multi-domain thermal modeling of interrupted cutting with coated tools. *Int. J. Adv. Manuf. Technol.* **2021**, *116*, 345–361. [CrossRef]
31. Saez-de-Buruaga, M.; Soler, D.; Aristimuño, P.X.; Esnaola, J.A.; Arrazola, P.J. Determining tool/chip temperatures from thermography measurements in metal cutting. *Appl. Therm. Eng.* **2018**, *145*, 305–314. [CrossRef]
32. Soler, D.; Childs, T.H.; Arrazola, P.J. A note on interpreting tool temperature measurements from thermography. *Mach. Sci. Technol.* **2015**, *19*, 174–181. [CrossRef]
33. Saelzer, J.; Berger, S.; Iovkov, I.; Zabel, A.; Biermann, D. In-Situ measurement of rake face temperatures in orthogonal cutting. *CIRP Ann.* **2020**, *69*, 61–64. [CrossRef]
34. *DIN EN 10302*; Creep Resisting Steels, Nickel and Cobalt Alloys. European Committee for Standardization: Brussels, Belgium, 2008.
35. *ASTM B637–18*; Standard Specification for Precipitation-Hardening and Cold Worked Nickel Alloy Bars, Forgings, and Forging Stock for Moderate or High Temperature Service. ASTM International: West Conshohocken, PA, USA, 2018.
36. Childs, T.H. Friction modelling in metal cutting. *Wear* **2006**, *260*, 310–318. [CrossRef]
37. Budak, E.; Ozlu, E. Development of a thermomechanical cutting process model for machining process simulations. *CIRP Ann.* **2008**, *57*, 97–100. [CrossRef]
38. Li, L.; Li, B.; Ehmann, K.F.; Li, X. A thermo-mechanical model of dry orthogonal cutting and its experimental validation through embedded micro-scale thin film thermocouple arrays in PCBN tooling. *Int. J. Mach. Tools Manuf.* **2013**, *70*, 70–87. [CrossRef]
39. Spriggs, G.E. 13.4 Properties of hardmetals and cermets. In *Hard Materials. Powder Metallurgy Data. Refractory, Hard and Intermetallic Materials*; Beiss, P., Ruthardt, R., Warlimont, H., Eds.; Springer: Berlin/Heidelberg, Germany; Gmbh & Co. Kg: Velbert, Germany, 2002; pp. 86–117.
40. Sweet, J.N.; Roth, E.P.; Moss, M. Thermal conductivity of Inconel 718 and 304 stainless steel. *Int. J. Thermophys.* **1987**, *8*, 593–606. [CrossRef]
41. Puls, H.; Klocke, F.; Lung, D. A new experimental methodology to analyse the friction behaviour at the tool-chip interface in metal cutting. *Prod. Eng.* **2012**, *6*, 349–354. [CrossRef]
42. Hao, G.; Liu, Z. The heat partition into cutting tool at tool-chip contact interface during cutting process: A review. *Int. J. Adv. Manuf. Technol.* **2020**, *108*, 393–411. [CrossRef]

materials

Article

Effect of Spray Characteristic Parameters on Friction Coefficient of Ultra-High-Strength Steel against Cemented Carbide

Bangfu Wu [1], Minxiu Zhang [1], Biao Zhao [1], Benkai Li [2,*] and Wenfeng Ding [1,*]

[1] National Key Laboratory of Science and Technology on Helicopter Transmission, College of Mechanical and Electrical Engineering, Nanjing University of Aeronautics and Astronautics, Nanjing 210016, China; wubangfu@nuaa.edu.cn (B.W.); zhangmx2000@nuaa.edu.cn (M.Z.); zhaobiao@nuaa.edu.cn (B.Z.)

[2] School of Mechanical and Automotive Engineering, Qingdao University of Technology, Qingdao 266520, China

* Correspondence: lbk17082@163.com (B.L.); dingwf2000@vip.163.com (W.D.)

Abstract: Ultra-high-strength steels have been considered an essential material for aviation components owing to their excellent mechanical properties and superior fatigue resistance. When machining these steels, severe tool wear frequently results in poor surface quality and low machining efficiency, which is intimately linked to the friction behavior at the tool–workpiece interface. To enhance the service life of tools, the adoption of efficient cooling methods is paramount. However, the understanding of friction behavior at the tool–workpiece interface under varying cooling conditions remains limited. In this work, both air atomization of cutting fluid (AACF) and ultrasonic atomization of cutting fluid (UACF) were employed, and their spray characteristic parameters, including droplet size distribution, droplet number density, and droplet velocity, were evaluated under different air pressures. Discontinuous sliding tests were conducted on the ultra-high-strength steel against cemented carbide and the effect of spray characteristic parameters on the adhesion friction coefficient was studied. The results reveal that ultrasonic atomization significantly improved the uniformity of droplet size distribution. An increase in air pressure resulted in an increase in both droplet number density and droplet velocity under both AACF and UACF conditions. Furthermore, the thickness of the liquid film was strongly dependent on the spray characteristic parameters. Additionally, UACF exhibited a reduction of 4.7% to 9.8% in adhesion friction coefficient compared to AACF. UACF provided the appropriate combination of spray characteristic parameters, causing an increased thickness of the liquid film, which subsequently exerted a positive impact on reducing the adhesion friction coefficient.

Keywords: ultra-high-strength steel; spray characteristic parameters; cooling condition; liquid film; friction coefficient

1. Introduction

Ultra-high-strength steels, renowned for their high strength, high toughness, and superior fatigue resistance, have been widely utilized in aviation transmission gears and aircraft landing gear [1–3]. Currently, mechanical cutting is the primary method for machining ultra-high-strength steel parts. However, the excellent physical and mechanical properties of these steels lead to the rapid wear of tools, significantly affecting the surface quality, machining efficiency, and costs [4,5]. Tool wear is primarily influenced by the friction and wear behaviors in the cutting zone [6–8]. Therefore, it is meaningful to investigate the tribological behavior between workpiece material and tool material under different cooling conditions, with the aim of inhibiting rapid tool wear.

The reciprocating ball–disc sliding tests have been chosen by many researchers for evaluating the tribological behavior between the workpiece and the tool [9,10]. Li et al. [11] investigated the tribological behavior of 7050 aluminum alloy against YG8 cemented carbide under different sliding velocities and loads. They found that the friction coefficient exhibited a decreasing trend as the sliding velocity and load increased. Li et al. [12] carried out the reciprocating sliding tests using TiAlN-coated and AlTiN-coated cutting tools and found that the TiAlN coating exhibited a better wear resistance than the AlTiN coating. Jamil et al. [13] studied the effect of different cooling media (e.g., ethanol, ester oil, and dry ice) on the tribological behavior between Ti-6Al-4V alloy and WC cemented carbide. They demonstrated that the mixtures of ethanol, ester oil, and dry ice could achieve a lower friction coefficient and wear rate compared to single cooling media. García-Martínez et al. [14] compared the tribological behavior of copper–nickel alloy against a coated tool under three cooling conditions including dry, flood, and low initial lubrication. The results indicated that the low initial lubrication condition could reduce the friction coefficient due to the existence of a lubrication layer formed by the mixture of oil and debris. El-Tayeb et al. [15] investigated the wear behavior of Ti54 alloy against the cemented carbide under cryogenic conditions and reported that abrasion and delamination were the predominant wear modes. However, it was noted that the reciprocating sliding test can't reflect the real contact conditions of the workpiece tool during the cutting process due to the repeated contact between the ball surface and the workpiece surface.

To solve this problem, scholars have developed the open ball–disc tribo-system to achieve the single sliding of a ball on the fresh surface of the workpiece [16–19]. Bonnet et al. [20] developed a new friction model to calculate the friction coefficient between 316L stainless steel and TiN-coated carbide during the dry sliding process. They concluded that the friction coefficient was strongly affected by the sliding velocity. Klinkova et al. [21] carried out the sliding tests of carbon fiber reinforced plastics (CFRP) with cemented carbide under dry conditions and revealed that the friction coefficient experienced a remarkable reduction from 0.25 to 0.1 as the sliding velocity varied from 10 m/min to 120 m/min. On the contrary, Mondelin et al. [22] insisted that the friction coefficient remained largely unaffected by variations in both sliding velocity and contact pressure during the sliding process of the CFRP with monocrystalline diamond. Abdelali et al. [23] pointed out that varying sliding velocities led to distinct tribological behaviors, which can be distinguished by examining the friction coefficient, heat partition coefficient, and material adhesion. Xu et al. [24,25] performed friction experiments on CFRP material and concluded that the elastic recovery of CFRP material affected the friction coefficient and the generation of friction heat.

Many efforts have been undertaken to eliminate the adverse effect of severe friction during the sliding process. Claudin et al. [26] conducted an investigation into the tribological behavior of AISI4140 steel sliding against TiN-coated carbide under dry and straight oil conditions. Their finding indicated that the straight oil can effectively penetrate the contact interface, reducing the friction coefficient. Fersi et al. [27] conducted a friction test of Ti-6Al-4V alloy with WC cemented carbide under various cooling conditions, including dry, emulsion, and cryogenic conditions. They discovered that the application of cryogenic conditions led to a notable reduction in the friction coefficient compared to the dry and emulsion conditions. The authors further explained that superior cooling ability under cryogenic conditions lowered the temperature, subsequently reducing the material adhesion of the Ti-6Al-4V alloy, resulting in a low friction coefficient. However, different results were reported by Courbon et al. [28], who investigated the influence of cryogenic conditions on the friction behavior of Ti-6Al-4V alloy against WC cemented carbide. They demonstrated that the cryogenic condition did not affect the friction coefficient and material adhesion. Etri et al. [29] carried out tribological tests on Ti-6Al-4V alloy against WC cemented carbide using minimal quantity lubrication (MQL) with different nanoparticles (i.e., graphene and hBN). Their research indicated that hybrid nanofluid (graphene + hBN + vegetable oil) attained a low friction coefficient and wear rate due to its superior heat conductivity and lubrication capability. Demirsoz et al. [30] studied the effect of different cooling conditions (i.e., dry, MQL, cryogenic, and cryo-MQL) on the tribological performance of 316L stainless steel against 100 Cr6 alloy. They concluded that the synergistic effect of cooling and lubrication in cryo-MQL significantly contributed to lowering the friction coefficient and enhancing the wear resistance of 316L stainless steel. Furthermore, Behera et al. [31] and Chetan et al. [32] applied MQL to the friction tests and found that the friction coefficient was strongly influenced by the air pressure and flow rate.

In summary, previous studies have mainly focused on the continuous contact situation, which was suitable for describing the friction behavior during the continuous cutting processes, such as turning. However, for the intermittent cutting behavior in a milling operation, the continuous contact condition was not applicable. Therefore, the tribological behavior under the discontinuous contact condition needs to be further studied. In addition, the implementation of effective cooling and lubrication conditions significantly contributed to the reduction of the friction coefficient at the contact interface and the enhancement of the lubrication state. Especially, during the milling process of ultra-high-strength steel, atomization modes of cutting fluid have exhibited excellent cooling and lubrication performance [33]. The liquid film generated by droplets is the main factor determining the lubrication state, and the film's characteristics are primarily affected by the spray characteristic parameters. Therefore, the novelty of this work lies in studying the effect of spray characteristic parameters on the tribological behavior of ultra-high-strength steel against cemented carbide during the discontinuous sliding process.

In this study, air atomization of cutting fluid (AACF) and ultrasonic atomization of cutting fluid (UACF) were applied to obtain the different spray characteristic parameters. The effect of different spray characteristic parameters on the liquid film thickness was investigated. Subsequently, the relationship between liquid film thickness and adhesion friction coefficient was discussed. The remainder of this paper is organized as follows. Section 2 presents the cooling system and the characterization method for spray characteristic parameters (i.e., droplet size distribution, droplet velocity, and droplet number density). Section 3 introduces the experimental setup and materials used for the discontinuous sliding test. Additionally, a calculation model of the adhesion friction coefficient during the discontinuous sliding process was developed. Section 4 analyzes the influence of air pressure on the spray characteristic parameters, the thickness of the liquid film, and the adhesion friction coefficient.

2. Cooling Methods

2.1. Cooling System

A self-developed cooling system was utilized to implement these two cooling conditions, namely AACF and UACF. This system consisted of an ultrasonic atomization nozzle, an air compressor, a cutting fluid tank, and an ultrasonic generator, as depicted in Figure 1. Further details regarding the cooling system can be found in the previous study [33]. The air compressor can provide high-pressure air for the ultrasonic atomization nozzle. Additionally, a small amount of compressed air forced the cutting fluid from the cutting fluid tank to the inside of the nozzle. The ultrasonic atomization nozzle played two crucial roles. Firstly, it dispersed the cutting fluid into fine droplets through the capillary wave effect [34]. Secondly, these droplets were subsequently mixed with a high-velocity airflow at the nozzle outlet, forming a uniform spray. The ultrasonic atomization process operated at a frequency of 50.5 kHz. The AACF condition could be achieved by stopping the ultrasonic generator. In this case, the cutting fluid was dispersed into small droplets by the shearing effect of airflow [35]. It was noted that different atomization methods affected the spray characteristic parameters, resulting in different liquid film characteristics.

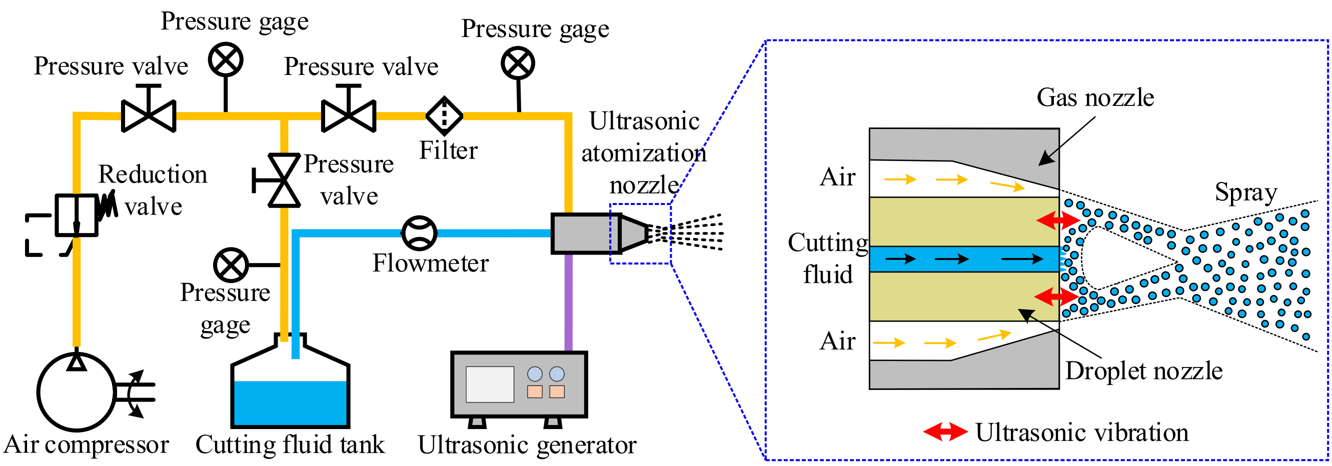

Figure 1. Schematic diagram of the cooling system for AACF and UACF conditions.

2.2. Characterization of Spray Characteristic Parameters

In the machining process, the droplet forms a liquid film, which serves to enhance both cooling and lubrication capabilities. The spray characteristic parameters, including droplet size distribution, droplet velocity, and droplet number density, are crucial factors influencing the formation of the liquid film. Consequently, the impact of air pressure on these parameters was investigated. The droplet deposition method was employed to obtain the droplet size distribution and density number density. The droplet number density is defined as the number of droplets per unit area. Subsequently, the droplet velocity was calculated based on the force balance equation.

Figure 2 illustrates the setup for droplet measurement. A polished silicon wafer was utilized to collect the droplets. The spray distance between the nozzle outlet and the silicon wafer was maintained at 55 mm. Moreover, a screening plate featuring a hole was positioned between the nozzle outlet and the silicon wafer to avoid droplet overlap (Figure 2a). The droplets discharged from the nozzle outlet passed through the screening plate and were then deposited on the silicon wafer. Subsequently, high-resolution droplet images were captured using an optical microscope (Figure 2b). The original droplet image was identified using Image J fiji software, as shown in Figure 3. The recognition procedure included image binarization, droplet boundary detection and filling, image filtering, image scale conversion, and statistical analysis of the droplet sizes. Based on the statistical results gathered from 10 distinct droplet images, the droplet size distribution and droplet number density were derived.

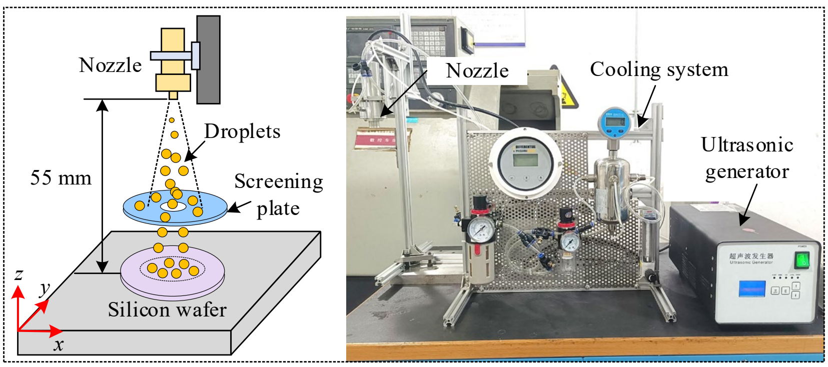

(a)

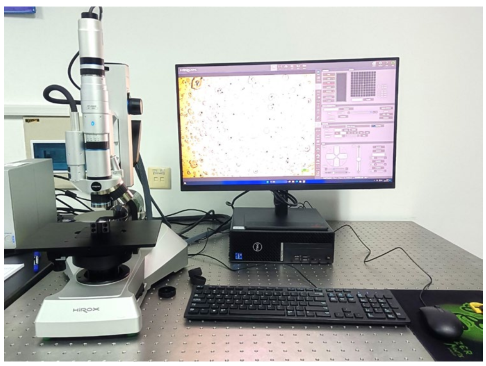

(b)

Figure 2. Experimental setup for droplet measurement: (**a**) droplet deposition device and (**b**) optical microscope.

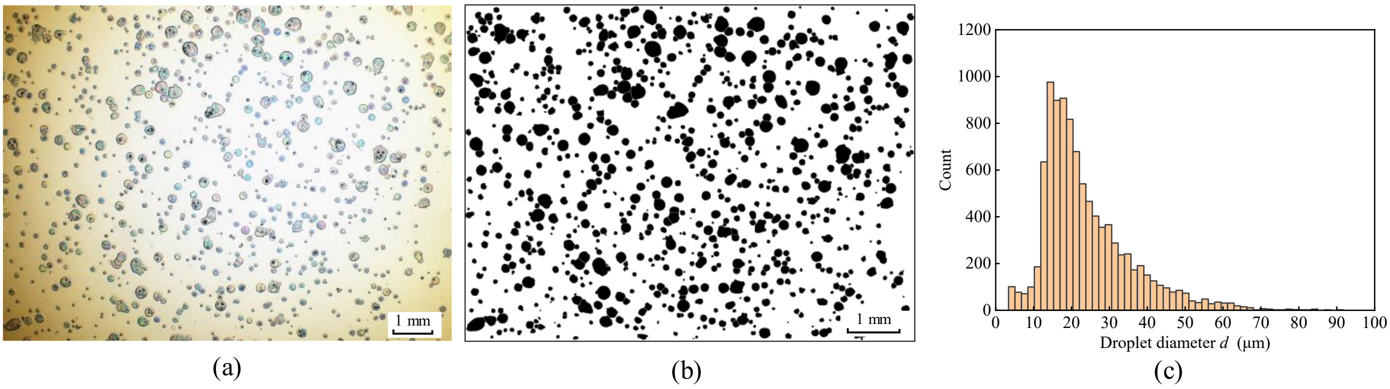

Figure 3. The recognition process of droplet image: (**a**) original image, (**b**) binary image, and (**c**) statistics results of droplet size distribution.

During the formation of the spray under AACF and UACF, the airflow provided the driving force for the droplet movement. To obtain the droplet velocity, the force situation of an individual droplet within the airflow was analyzed. The force balance equation governing the droplet dynamics can be formulated as follows [36]:

$$\rho_d V_d \frac{dv_d}{dt} = V_d(\rho_d - \rho_g)g - \frac{1}{2}\rho_g A_s C_d (v_d - v_g)|v_d - v_g| \tag{1}$$

where ρ_d and ρ_g denote the densities of the droplet and air, respectively. v_d and v_g represent the velocities of the droplet and air, respectively. V_d is the volume of the droplet, g stands for the gravitational acceleration, and A_s is the cross-sectional area of the droplet. The drag coefficient C_d for a spherical droplet can be estimated by Equation (2) [37]:

$$C_d = 0.28 + \frac{6\sqrt{Re_r} + 21}{Re_r} \tag{2}$$

where Re_r represents the relative Reynolds number, which is defined as follows:

$$Re_r = \frac{\rho_g d |v_g - v_d|}{\mu_g} \tag{3}$$

where μ_g signifies the dynamic viscosity of the air.

Table 1 lists the detailed cooling parameters for the AACF and UACF processes. A 12% concentration of cutting fluid was obtained by mixing a water-soluble synthetic (Castrol 9954) with water. The measured cutting fluid density is 995 kg/m^3. The air has a density of 1.29 kg/m^3 and a dynamic viscosity of 1.82×10^{-5} Pa·s, respectively. The effect of different air pressures on air velocity has been studied in previous work [33]. Based on the aforementioned parameters, the droplet velocities under different air pressures were determined by solving Equation (1).

Table 1. Cooling parameters under AACF and UACF.

Contents	Value
Air pressure P (kPa)	140, 180, 220, 260, 300
Flow rate of cutting fluid Q (mL/min)	15
Concentration of cutting fluid W (%)	12

3. Experimental Setup and Method

3.1. Discontinuous Sliding Test

The discontinuous sliding tests under various cooling conditions were carried out on a precision machining center (DMG) equipped with a developed open ball–disc tribometer system (Figure 4). Figure 4b depicts the specific configuration of the open ball–disc tribometer system, comprising a ball, a holder, a tool handle, a workpiece, and a piezoelectric dynamometer. The ball was securely fastened to the side of the holder via a jackscrew and bolt (Figure 4c). This holder was then mounted onto the tool handle, which has the capability to rotate synchronously with the spindle of the machine tool. During the test, the ball made a single contact with the workpiece as the spindle completed a full rotation cycle. Furthermore, the feed motion of the workpiece ensured that the ball only slid on a fresh surface of the workpiece. The workpiece was placed on the piezoelectric dynamometer, and the force acting upon it was measured by the force measurement system (Kistler, Winterthur, Switzerland), featuring a three-component dynamometer, charge amplifier, and data acquisition card, as shown in Figure 4d. Additionally, the ultrasonic atomization nozzle was mounted on the machine spindle to provide different cooling conditions for the contact interface between the ball and the workpiece.

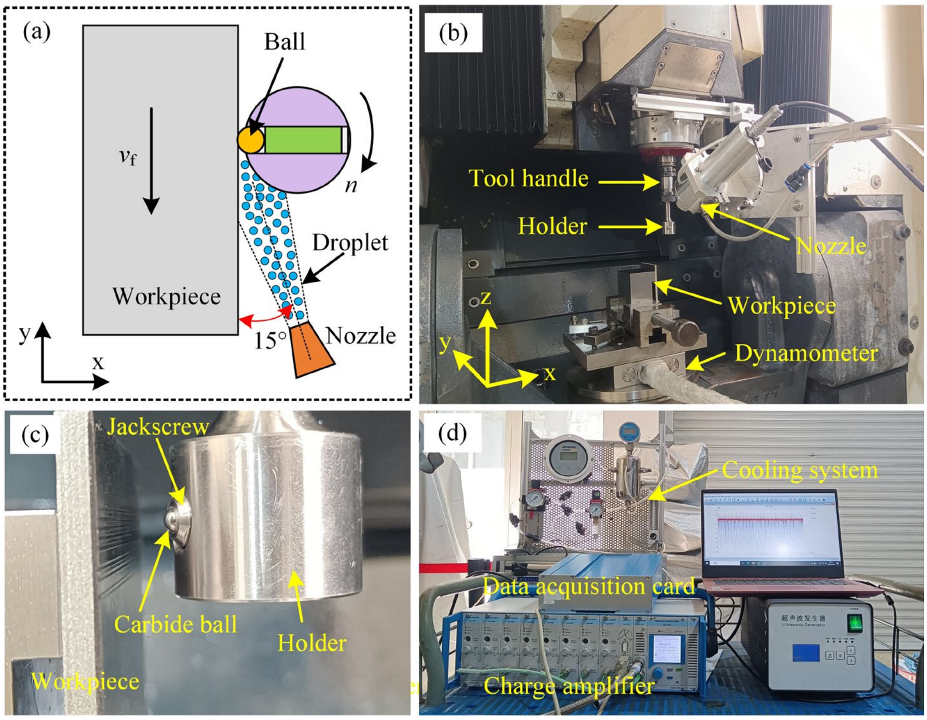

Figure 4. Experimental setup for the discontinuous sliding test under different cooling conditions: (**a**) schematic diagram of the discontinuous sliding process, (**b**) open ball–disc tribometer system, (**c**) holder, and (**d**) force measurement system and cooling system.

The ball employed in this work was a commercial WC-Co cemented carbide ball with a diameter of 3.17 mm. Figure 5 displays the microstructure and chemical composition of the cemented carbide ball. The measured surface roughness S_a was 0.45 ± 0.02 μm and the hardness was 76 ± 2 HRC. The tested workpiece was 15Cr14Co12Mo5Ni2 ultra-high-strength steel with dimensions of 60 mm × 60 mm × 5 mm. The workpiece surface was polished to eliminate the effect of surface roughness on the sliding process. The surface roughness S_a of the polished surface has reached 0.17 ± 0.04 μm. Figure 6 presents the microstructure of the polished surface and the chemical composition of the workpiece. Table 2 lists the mechanical properties of 15Cr14Co12Mo5Ni2 ultra-high-strength steel [38].

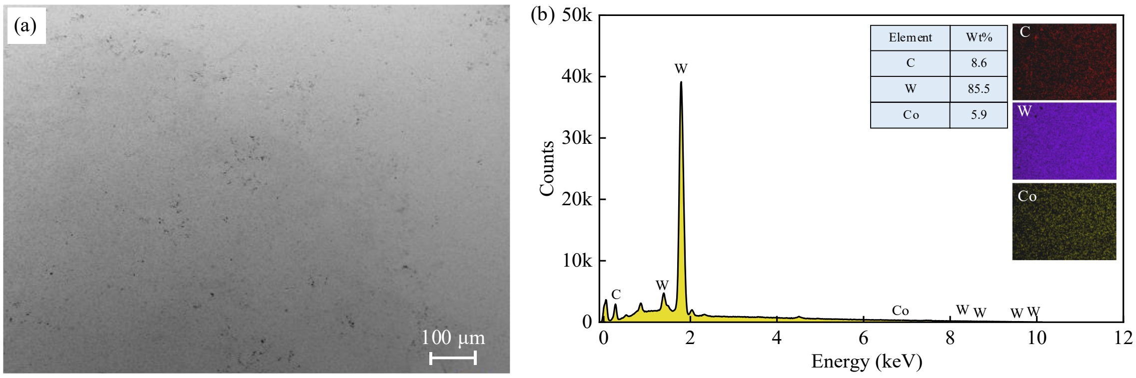

Figure 5. WC cemented carbide ball: (**a**) SEM image of microstructure and (**b**) EDS mapping.

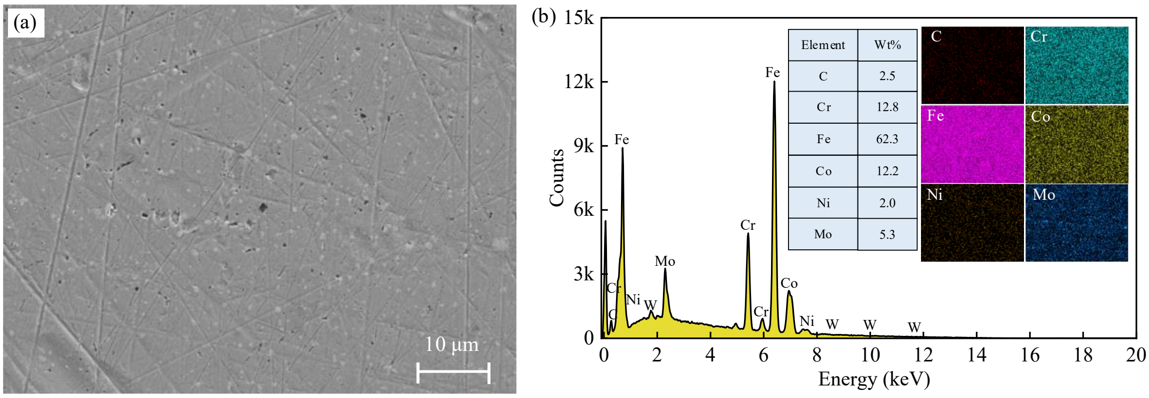

Figure 6. Ultra-high-strength steel: (**a**) SEM image of microstructure and (**b**) EDS mapping.

Table 2. Mechanical properties of the 15Cr14Co12Mo5Ni2 ultra-high-strength steel.

Contents	Value
Tensile strength σ_b (MPa)	1780
Yield strength σ_s (MPa)	1380
Density ρ (kg/m^3)	7960
Hardness (HRC)	35
Fracture toughness K_{IC} (MPa$\cdot^{1/2}$)	75

The sliding test was performed with a sliding velocity of 50 m/min and a feed rate of 0.01 mm/z. Additionally, to ensure that the cemented carbide ball experienced a constant load from the workpiece, the initial indentation depth was maintained at 0.1 mm. The spray distance between the ball surface and the nozzle outlet was fixed at 55 mm. The angle between the nozzle and the workpiece was 15°. Each sliding test lasted for a duration of 10 min. Three repeated experiments for each cooling parameter were conducted. After the sliding experiment, the pollutants on the workpiece surface were removed using ultrasonic cleaning with an alcohol solution. A 3D optical profilometer (Sensofar, Barcelona, Spain) was employed to detect the 3D surface morphology of the wear mark on the workpiece. Additionally, the worn surfaces of the balls were detected using the scanning electron microscope (Zeiss sigma300, Carl Zeiss AG, Oberkochen, Germany).

3.2. Analysis of Adhesion Friction Coefficient

The friction coefficient is commonly used to evaluate the friction behavior of frictional pairs. In the sliding process, the contact zone of frictional pairs is subjected to the tangential force and normal force. It is noted that the high contact pressure results in the plastic deformation of the workpiece material. In this case, the measured macroscopic tangential force can be comprised of an adhesion component and a ploughing component [39,40]. Therefore, the tangential force can be expressed as follows:

$$F_{\mathrm{t}} = F_{\mathrm{a}} + F_{\mathrm{p}} \tag{4}$$

where F_{a} is the adhesion force between the ball and the workpiece, and F_{p} is the ploughing force caused by the plastic deformation of the workpiece material.

Similarly, the apparent friction coefficient can be written as follows:

$$\mu = \frac{F_{\mathrm{a}}}{F_{\mathrm{n}}} + \frac{F_{\mathrm{p}}}{F_{\mathrm{n}}} = \mu_{\mathrm{a}} + \mu_{\mathrm{p}} \tag{5}$$

where F_{n} is the normal force, μ_{a} is the adhesion friction coefficient, and μ_{p} is the ploughing friction coefficient.

Based on the above analysis, the adhesion friction coefficient μ_{a} can represent the real friction coefficient of the contact surface between frictional pairs. The adhesion friction coefficient can be calculated by Equation (6) [26].

$$\mu_{\mathrm{a}} = \frac{S_1\mu - S_2}{S_2\mu + S_1} \tag{6}$$

where S_1 and S_2 are the projection areas of the contact surfaces along the tangential and normal directions, respectively.

It should be noted that the plastic deformation of the workpiece material resulted in the formation of the pile-up, directly affecting the projection area of the contact surface. Specifically, the pile-up of material resulting from the previous sliding process can increase the area of the contact surface in the subsequent sliding process. Therefore, the influence of material pile-up on the adhesion friction coefficient needs to be considered during the discontinuous sliding process.

Since the discontinuous sliding process is similar to the milling process, the sliding depth of the ball varies with the rotation angle of the holder, as shown in Figure 7. The situation that the contact surface at the maximum sliding depth was analyzed in this study. The maximum sliding depth h_{c} can be approximately written as [41]:

$$h_{\mathrm{c}} = v_{\mathrm{f}} \sin \alpha \tag{7}$$

where v_{f} stands for the feed rate of the workpiece, and α denotes the rotation angle of the holder when the sliding depth varies from zero to its maximum value.

Based on the force transformation relationships depicted in Figure 7a, the tangential force and normal force acting on the contact surface at the maximum sliding depth can be given as follows:

$$F_{\mathrm{t}} = F_{\mathrm{y}} \cos \alpha - F_{\mathrm{x}} \sin \alpha \tag{8}$$

$$F_{\mathrm{n}} = F_{\mathrm{y}} \sin \alpha + F_{\mathrm{x}} \cos \alpha \tag{9}$$

where F_{x} and F_{y} represent the forces measured by the dynamometer in the x and y directions, respectively.

Additionally, the rotation angle of the ball under maximum sliding depth can be calculated as follows:

$$\alpha = \arctan \frac{\sqrt{R^2 - (R - h_{\mathrm{a}} - h_{\mathrm{p}})^2} - v_{\mathrm{f}}}{R - h_{\mathrm{a}} - h_{\mathrm{p}}} \tag{10}$$

where R represents the rotation radius of the cemented carbide ball, h_{a} denotes the depth of wear mark, and h_{p} signifies the height of pile-up of the material.

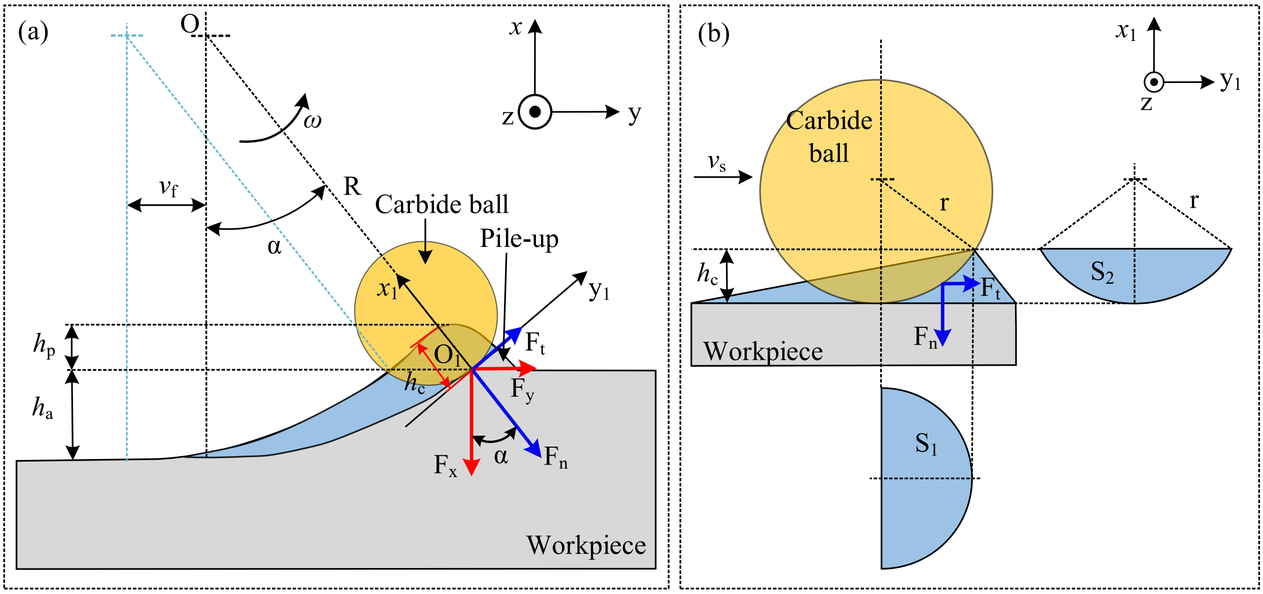

Figure 7. Discontinuous sliding process: (**a**) force transformation relationship under maximum sliding depth and (**b**) projection area of the contact surface in a local coordinate system.

Since the rotation angle of the ball is small, the maximum sliding depth h_c can also be written as follows:

$$h_c = v_f \sin\alpha = v_f \tan\alpha = \frac{v_f\sqrt{R^2-(R-h_a-h_p)^2-v_f^2}}{R-h_a-h_p} \tag{11}$$

Moreover, the projection areas of contact surfaces S_1 and S_2 in Figure 7b can be calculated as follows:

$$S_1 = \frac{\pi}{2}\left(r^2-(r-h_c)^2\right) \tag{12}$$

$$S_2 = r^2\arccos\frac{r-h_c}{r} - (r-h_c)\sqrt{r^2-(r-h_c)^2} \tag{13}$$

where r is the radius of the cemented carbide ball.

Substituting Equations (8), (9), (12) and (13) into Equation (6), the adhesion friction coefficient in the discontinuous sliding process can be expressed as follows:

$$\mu_a = \frac{\frac{\pi}{2}\left(r^2-(r-h_c)^2\right)\left(\frac{F_y\cos\alpha-F_x\sin\alpha}{F_y\sin\alpha+F_x\cos\alpha}\right)-\left(r^2\arccos\frac{r-h_c}{r}-(r-h_c)\sqrt{r^2-(r-h_c)^2}\right)}{\left(r^2\arccos\frac{r-h_c}{r}-(r-h_c)\sqrt{r^2-(r-h_c)^2}\right)\left(\frac{F_y\cos\alpha-F_x\sin\alpha}{F_y\sin\alpha+F_x\cos\alpha}\right)+\frac{\pi}{2}\left(r^2-(r-h_c)^2\right)} \tag{14}$$

Equation (14) demonstrates that the adhesion friction coefficient relies on specific parameters, including the depth of the wear mark h_a, the height of material pile-up h_p, and the measured forces F_x and F_y. These parameters can be acquired from the sliding experiment. Figure 8 illustrates the calculation process of the adhesion friction coefficient. Initially, the wear mark depth h_a and pile-up height h_p were measured through the cross-section of the wear mark. Then, the parameters of rotation angle α, maximum sliding depth hc, and projection areas S_1 and S_2 were calculated sequentially. To simplify the processing of measured force signal data and reduce the computational complexity, the force signal was extracted every second. Furthermore, the peak force was determined, and the tangential force F_t and normal force F_n were subsequently calculated. Finally, the adhesion friction coefficient curve was obtained, and the average adhesion friction coefficient in the steady stage was analyzed.

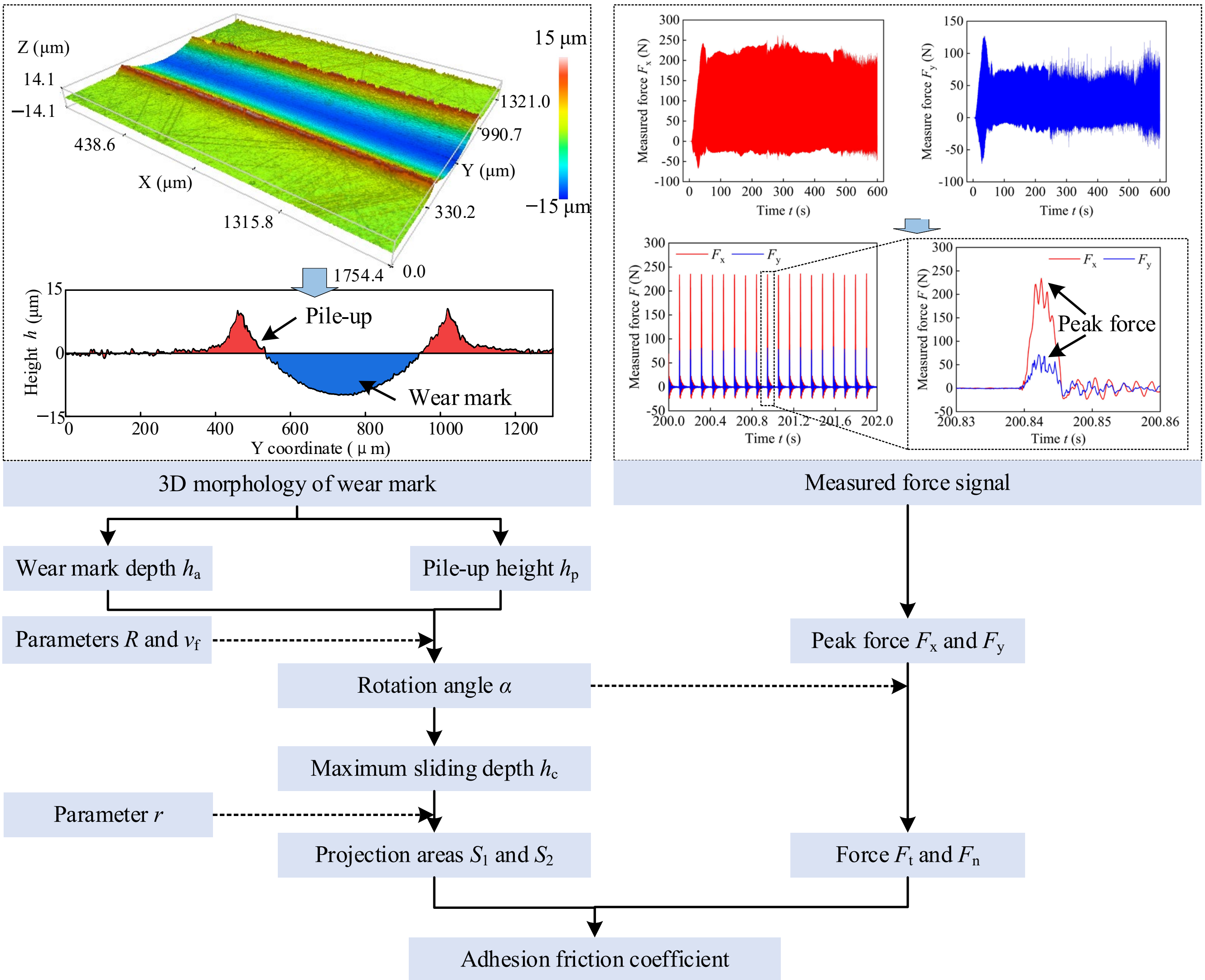

Figure 8. Calculation process of adhesion friction coefficient.

4. Results and Discussion

4.1. Effect of Air Pressure on Spray Characteristic Parameters

The histogram plots in Figure 9 clearly present the droplet size distribution at different air pressures for AACF and UACF. These histograms illustrate the correlation between the droplet count and the droplet diameter. Notably, it was observed that the majority of droplet diameters lie within the range of 0 μm to 60 μm. To quantitatively assess this droplet size distribution, both the average value and the standard deviation of the droplet diameters were employed. Furthermore, Figure 10 comprehensively depicts the effect of different air pressures on the three key parameters: the average droplet diameter, standard deviation of droplet diameter, and droplet number density.

As shown in Figure 10a, under AACF conditions, the average droplet diameter decreased linearly from 35.5 μm to 16.8 μm as the air pressure varied from 140 kPa to 300 kPa. This was because the enhanced air velocity in higher air pressure exerted a stronger shear force on the liquid surface, thereby facilitating the breakup of the liquid into smaller droplets [42]. In contrast, despite the increase in air pressure, the average droplet diameter remained virtually unchanged under UACF conditions. This was attributed to the fact that the droplet diameter generated by the ultrasonic atomization method was inherently dependent on the ultrasonic frequency and the physical properties of the liquid [43]. In this study, neither the ultrasonic frequency nor the physical properties of the cutting fluid were influenced by variations in air pressure, thus ensuring that the droplet diameter remained essentially stable. Similarly, the standard deviation of droplet diameter followed a comparable trend of variation as the air pressure varied, as depicted in Figure 10b. Specifically, under AACF conditions, the standard deviation of droplet diameter decreased from 29.1 μm to 9 μm as the air pressure increased from 140 kPa to 300 kPa. Conversely, under UACF conditions, there was little variation in the standard deviation with increasing air pressure. Notably, UACF exhibited a lower standard deviation than AACF, indicating that the UACF can enhance the uniformity of droplet size distribution compared to the AACF process.

Additionally, the statistical results of droplet number density are presented in Figure 10c. At an air pressure of 140 kPa, the droplet number densities under AACF and UACF conditions were 5 mm^{-2} and 10 mm^{-2}, respectively. When the air pressure reached 300 kPa, the droplet number densities under AACF and UACF conditions increased to 23 mm^{-2} and 26 mm^{-2}, respectively. The droplet velocity was mainly responsible for this phenomenon, where high air pressure resulted in an increase in droplet velocity, thus increasing the number of droplets reaching the deposition surface per unit time. In addition, high air pressure also reduced the droplet diameter, leading to an increase in droplet number density under AACF conditions. It was also observed that the droplet number density of UACF was higher than that of AACF, which was attributed to the improved uniformity of droplet size.

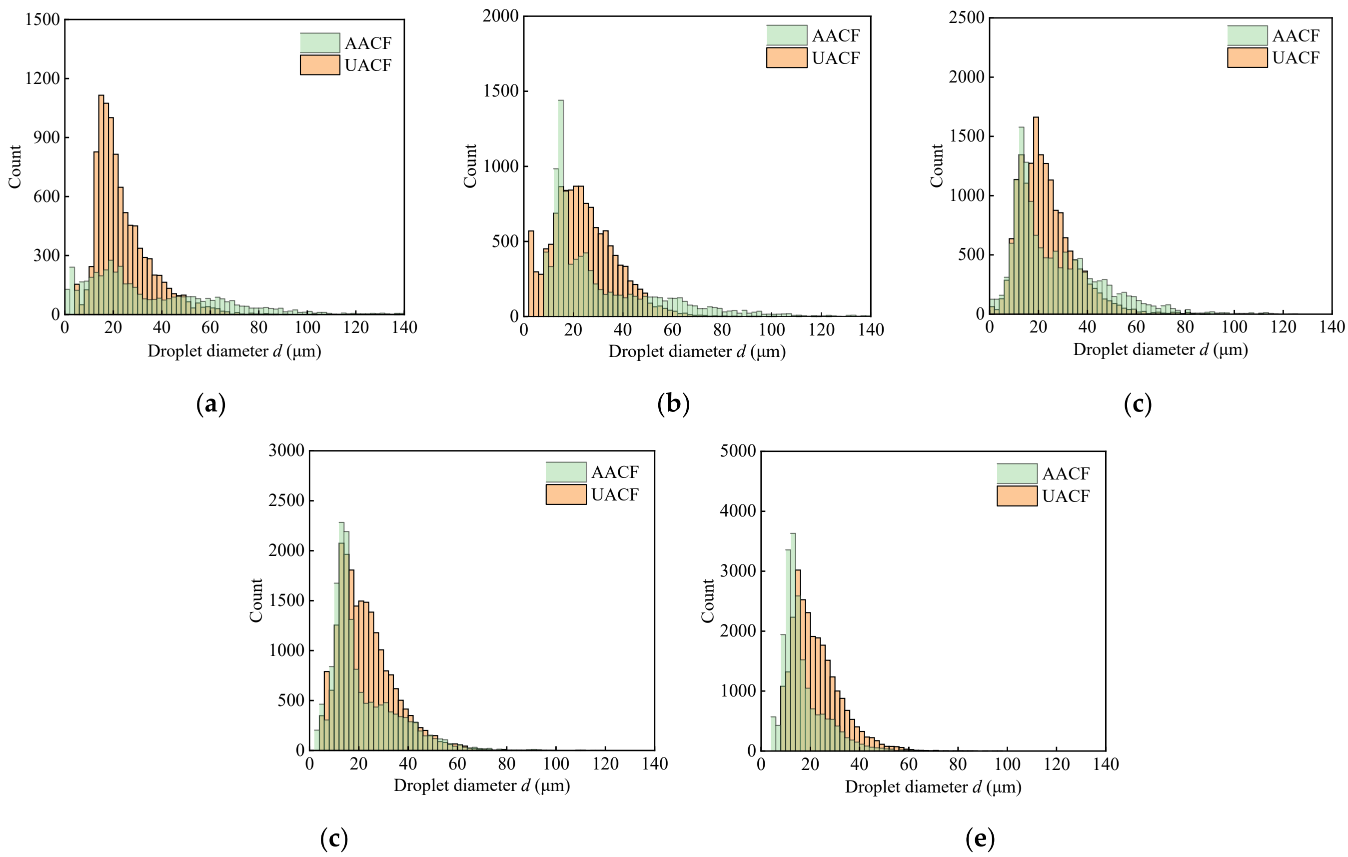

Figure 9. Histogram of droplet size distribution under different air pressures: (**a**) P = 140 kPa, (**b**) P = 180 kPa, (**c**) P = 220 kPa, (**d**) P = 260 kPa, and (**e**) P = 300 kPa.

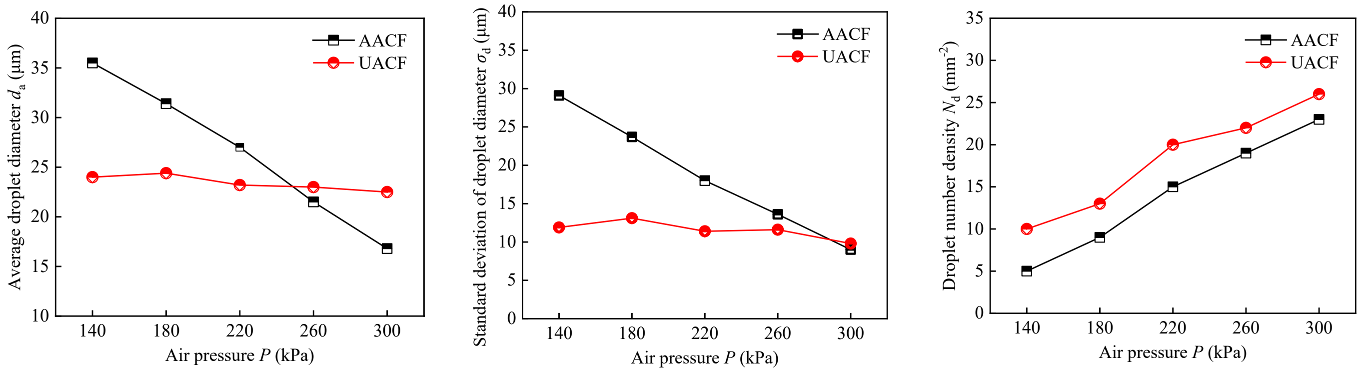

(**a**) (**b**) (**c**)

Figure 10. Statistical results of droplet size distribution and number density under different air pressures: (**a**) average droplet diameter d_a, (**b**) standard deviation of droplet diameter σ_d, and (**c**) droplet number density N_d.

The influence of varying air pressures and spray distances on the droplet velocity under AACF and UACF is illustrated in Figure 11. Specifically, Figure 11a displays the variation in droplet velocity as a function of spray distance at five levels of air pressure under AACF conditions. At a constant air pressure, the droplet velocity rapidly attained its peak and subsequently underwent a gradual decrease with further increases in spray distance. Similarly, the droplet velocity exhibits the same pattern of variation under UACF conditions (Figure 11b). Subsequently, the droplet velocities at a spray distance of 55 mm under different air pressures for AACF and UACF were compared in Figure 11c. It was observed that the droplet velocity in AACF increased from 16.7 m/s to 42.4 m/s as the air pressure varied from 140 kPa to 300 kPa. Furthermore, there was negligible variation in droplet velocity between AACF and UACF at a fixed level of air pressure. This situation allows for a good comparison of the effect of different atomization methods (i.e., air atomization and ultrasonic atomization) on cooling and lubrication performance.

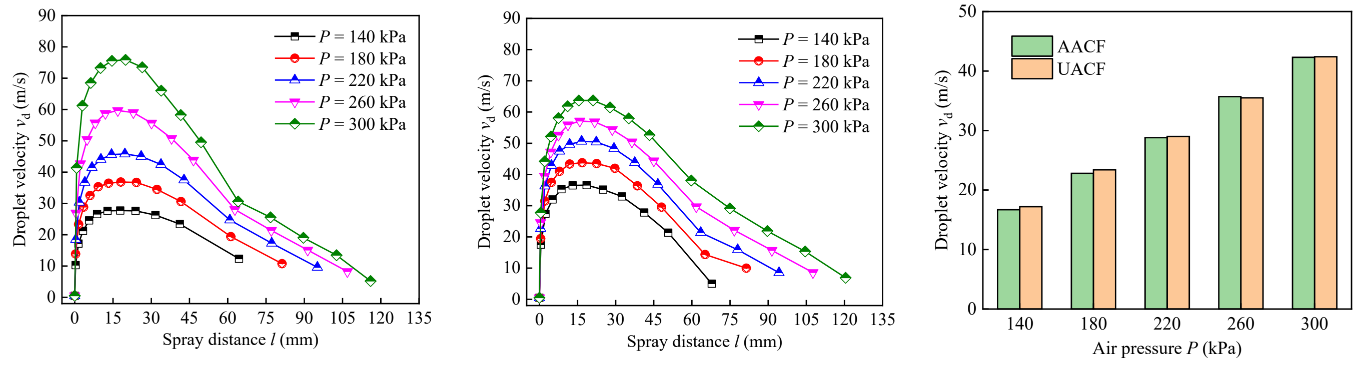

(**a**) (**b**) (**c**)

Figure 11. Droplet velocity under different air pressures: (**a**) variation of droplet velocity with spray distance under AACF, (**b**) variation of droplet velocity with spray distance under UACF, and (**c**) droplet velocity at a spray distance of 55 mm.

4.2. Effect of Air Pressure on Thickness of Liquid Film

As previously stated in reference [44], the spray characteristic parameters significantly affected the thickness of the liquid film, which provided effective cooling and lubrication for the cutting process. Therefore, the thickness of the liquid film for different combinations of spray characteristic parameters was evaluated. It was assumed that the volume loss of droplets resulting from evaporation was negligible.

For the droplet deposition region, the total droplet volume can be expressed as follows:

$$V = \frac{4}{3}\pi\left(\frac{d_a}{2}\right)^3 N_d s \tag{15}$$

where d_a represents the average droplet diameter, N_d is the droplet number density, and s stands for the area of droplet deposition region.

The standard deviation of droplet diameter also affected the thickness of the liquid film. That is, the larger the standard deviation of droplet diameter, the thinner the resulting liquid film becomes. Additionally, the increased droplet velocity promoted the spreading of the droplets, causing a decrease in the thickness of the liquid film. Therefore, the thickness of liquid film on the region of droplet deposition can be mathematically expressed as follows:

$$h_d = \frac{CV}{s\sigma_d v_d} = \frac{C\pi d_a^3 N_d}{6\sigma_d v_d} \tag{16}$$

where C is a constant, and σ_d is the standard deviation of droplet diameter.

Since C is an unknown constant, a dimensionless number was utilized to characterize the thickness of the liquid film. The dimensionless number λ was defined by Equation (17).

$$\lambda = \frac{h_d}{h_0} \tag{17}$$

where h_0 is the thickness of the liquid film at an air pressure of 140 kPa under AACF.

Figure 12 displays the effect of air pressure on the dimensionless number under AACF and UACF conditions. For the AACF condition, the dimensionless number initially showed an increasing trend, then followed by a decreasing trend. The dimensionless number in the UACF process presented a fluctuating variation trend, ranging between 1.3 and 1.7. Notably, under both AACF and UACF conditions, a higher dimensionless number can be achieved at an air pressure of 220 kPa. According to Equation (17), the thickness of the liquid film varies directly with the dimensionless number. This implied that an air pressure of 220 kPa can result in a higher thickness of the liquid film. In other words, the appropriate range of spray characteristic parameters contributed to the formation of liquid film. Furthermore, the UACF process exhibited a higher thickness of liquid film than AACF, suggesting that the ultrasonic atomization method can effectively control the spray characteristic parameters and enhance the formation of liquid film.

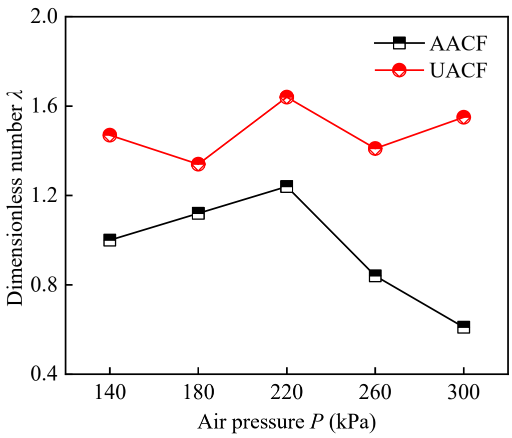

Figure 12. Effect of air pressure on the dimensionless number under AACF and UACF.

4.3. Effect of Air Pressure on Adhesion Friction Coefficient and Worn Surface

Figure 13 demonstrates the influence of air pressure on the adhesion friction coefficient under AACF and UACF conditions. Figure 10a,b plot the curves of adhesion friction coefficient for AACF and UACF conditions, respectively. Obviously, the adhesion friction coefficient curve can be divided into two stages: the running-in stage and the stable stage. After the initial running-in stage of the sliding process, the adhesion friction coefficient curves exhibited slight fluctuation and entered the stable stage from about 5 s. Subsequently, the average adhesion friction coefficient in the stable stage at different air pressures is summarized in Figure 10c. In the AACF condition, when the air pressure increased from 140 kPa to 220 kPa, the average adhesion friction coefficient decreased from 0.275 to 0.259. Then, it gradually rose again to reach a value of 0.284 when the air pressure reached 300 kPa. The UACF condition exhibited the same pattern of variation in average adhesion friction coefficient. Compared to AACF, UACF can reduce the adhesion friction coefficient by 4.7% to 9.8%. According to the results in Figure 12, it can be found that the higher the dimensionless number, the lower the average adhesion friction coefficient. This result indicated that an increase in the thickness of liquid film contributed to reducing the adhesion friction coefficient.

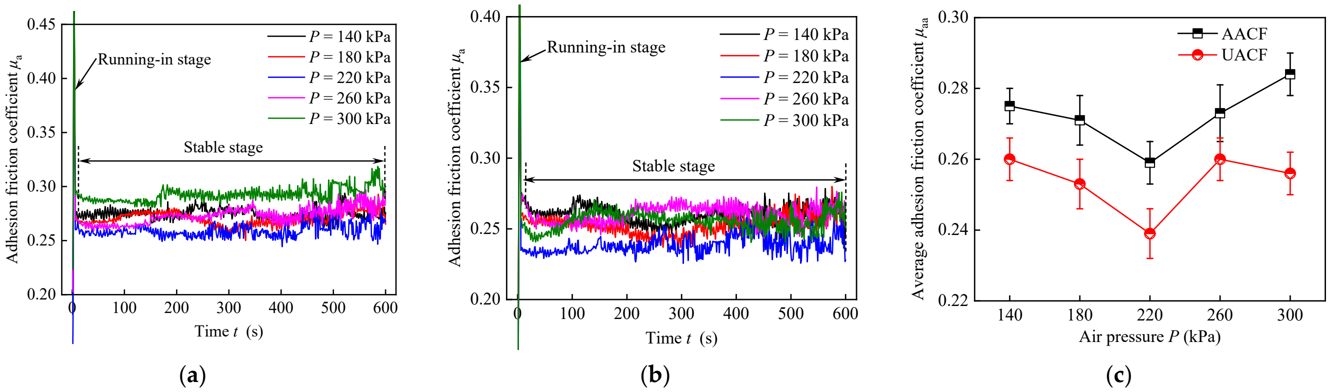

Figure 13. Effect of air pressure on the adhesion friction coefficient under different cooling conditions: (**a**) adhesion friction coefficient curve under AACF, (**b**) adhesion friction coefficient curve under UACF, and (**c**) variation of average adhesion friction coefficient with air pressure in the stable stage.

Additionally, the worn surfaces of WC balls were detected, as shown in Figure 14. It was noted that the surfaces of the WC balls exhibited small wear scars under AACF and UACF conditions, regardless of the air pressure level. However, there was no significant difference in the wear scars. This phenomenon was attributed to the fact that the 10-min duration was not enough to cause serious wear on the surface of the WC ball. In the future, discontinuous sliding tests will be conducted with a longer duration to further study the wear process of the WC balls.

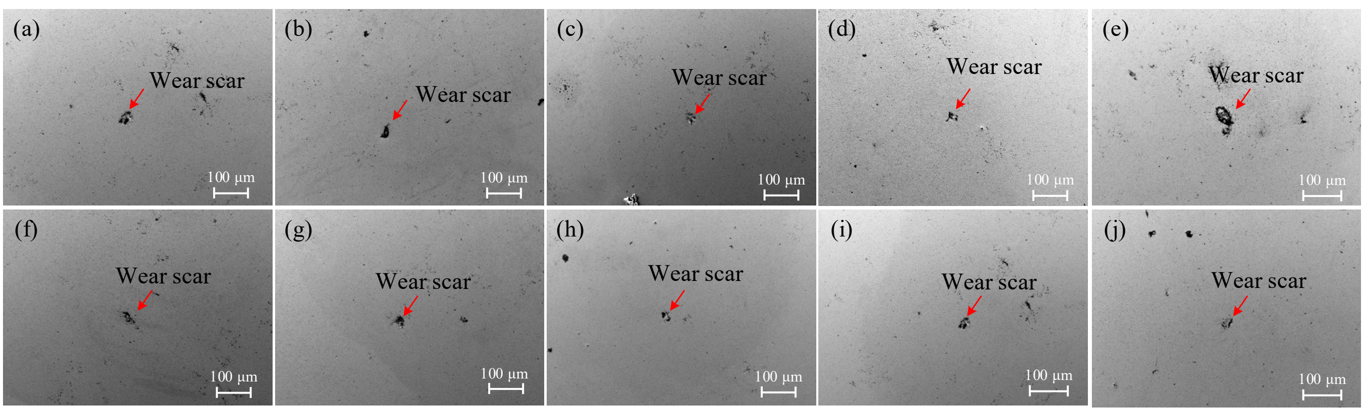

Figure 14. Effect of air pressure on the worn surface of the WC ball under (**a**–**e**) 140 kPa, 180 kPa, 220 kPa, 260 kPa, and 300 kPa for AACF, (**f**–**j**) 140 kPa, 180 kPa, 220 kPa, 260 kPa, and 300 kPa for UACF.

5. Conclusions

In this work, the spray characteristic parameters under AACF and UACF with different air pressures were evaluated in terms of droplet size distribution, droplet velocity, and droplet number density. Furthermore, the impact of spray characteristic parameters on the thickness of the liquid film and adhesion friction coefficient was investigated. The following conclusions have been drawn:

(1) The average value and standard deviation of droplet diameters were used to describe the size distribution of droplets. Under AACF conditions, an increase in air pressure reduced the average droplet diameter by 52.6% and the standard deviation of droplet diameter by 69%, respectively. However, under the UACF process, only a reduction of 6% and 17.6% was found in the average droplet diameter and standard deviation of droplet diameter, respectively. The air pressure in the UACF process has minimal effect on the size distribution of droplets compared to AACF condition.

(2) When the air pressure increased from 140 kPa to 300 kPa, the droplet number density in the AACF condition increased from 5 mm^{-2} to 23 mm^{-2}, and the droplet number density in the UACF condition increased from 10 mm^{-2} to 26 mm^{-2}. UACF exhibited a higher droplet number density than AACF due to the improved uniformity of droplet size distribution produced by the ultrasonic atomization method. Additionally, with the increase in air pressure, the droplet velocity exhibited an increasing trend, regardless of cooling conditions.

(3) Both AACF and UACF conditions yielded a higher thickness of liquid film at an air pressure of 220 kPa. The average droplet diameter, standard deviation of droplet diameter, droplet number density, and droplet velocity are the important parameters affecting the thickness of the liquid film.

(4) Compared to AACF, UACF could reduce the adhesion friction coefficient by 4.7–9.8%. The appropriate combination of spray characteristic parameters in UACF facilitates the formation of liquid film, thereby reducing the adhesion friction coefficient and improving friction conditions.

Author Contributions: Writing-original draft, B.W.; writing-review and editing, B.W. and B.L.; methodology, B.W.; visualization, B.W.; formal analysis, B.W. and B.L.; software, M.Z.; data curation, M.Z.; Supervision, B.Z. and B.L.; project administration, W.D. All authors have read and agreed to the published version of the manuscript.

Funding: This research was funded by the Postgraduate Research & Practice Innovation Program of Jiangsu Province (No. KYCX21_0189), and Funding for Outstanding Doctoral Dissertation in NUAA (No. BCXJ22-07).

Institutional Review Board Statement: Not applicable.

Informed Consent Statement: Not applicable.

Data Availability Statement: Dataset available on request from the authors.

Acknowledgments: We sincerely thank the Institute of Precision Machining Technology at Nanjing University of Aeronautics and Astronautics.

Conflicts of Interest: The authors declare no conflicts of interest.

References

1. Li, J.; Zhan, D.; Jiang, Z.; Zhang, H.; Yang, Y.; Zhang, Y. Progress on improving strength-toughness of ultra-high strength martensitic steels for aerospace applications: A review. *J. Mater. Res. Technol.* **2023**, *23*, 172–190. [CrossRef]
2. Li, K.; Yang, T.; Gong, N.; Wu, J.; Wu, X.; Zhang, D.; Murr, L. Additive manufacturing of ultra-high strength steels: A review. *J. Alloys Compd.* **2023**, *965*, 171390. [CrossRef]
3. Han, X.; Chen, L.; Hu, X.; Hua, L.; Chai, F. Microstructure and mechanical property evolution mechanisms of 15Cr14Co12Mo5Ni2WA aviation gear steel during cold rotary forging. *J. Mater. Res. Technol.* **2023**, *24*, 3005–3022. [CrossRef]
4. Coelho, R.; Ng, E.; Elbestawi, M. Tool wear when turning hardened AISI 4340 with coated PCBN tools using finishing cutting conditions. *Int. J. Mach. Tools Manuf.* **2007**, *47*, 263–272. [CrossRef]

5. Zeng, H.; Yan, R.; Du, P.; Zhang, M.; Peng, F. Notch wear prediction model in high speed milling of AerMet100 steel with bullnose tool considering the influence of stress concentration. *Wear* **2018**, *408*, 228–237. [CrossRef]
6. Liang, X.; Liu, Z.; Wang, B.; Wang, C.; Cheung, C. Friction behaviors in the metal cutting process: State of the art and future perspectives. *Int. J. Extrem. Manuf.* **2022**, *5*, 012002. [CrossRef]
7. Zhuang, K.; Zhu, K.; Wei, X.; Hu, C.; Liu, Z.; Gao, Z. A dual-stage wear rate model based on wear mechanisms analysis during cutting Inconel 718 with TiAlN coated tools. *J. Manuf. Process.* **2024**, *126*, 24–34. [CrossRef]
8. Zhuang, K.; Wu, Z.; Wan, L.; Weng, J.; Yang, Y.; Tian, C.; Li, Y.; Liu, Z. Investigation of different abrasive jet machining methods applied to milling tool coatings for post-treatment. *Surf. Coat. Technol.* **2024**, *491*, 131156. [CrossRef]
9. Kohutiar, M.; Krbata, M.; Escherova, J.; Eckert, M.; Mikus, P.; Jus, M.; Polášek, M.; Janík, R.; Dubec, A. The Influence of the Geometry of Movement during the Friction Process on the Change in the Tribological Properties of 30CrNiMo8 Steel in Contact with a G40 Steel Ball. *Materials* **2024**, *17*, 127. [CrossRef]
10. Krbata, M.; Ciger, R.; Kohutiar, M.; Sozańska, M.; Eckert, M.; Barenyi, I.; Kianicova, M.; Jus, M.; Beronská, N.; Mendala, B.; et al. Effect of Supercritical Bending on the Mechanical & Tribological Properties of Inconel 625 Welded Using the Cold Metal Transfer Method on a 16Mo3 Steel Pipe. *Materials* **2023**, *16*, 5014. [CrossRef]
11. Li, G.; Li, J.; Sun, J.; Jiang, F. Study on the tribological properties between the aluminum alloy 7050-T7451 and the YG8 cemented carbide. *J. Mater. Sci.* **2011**, *46*, 723–726. [CrossRef]
12. Li, D.; Zhang, T.; Zhao, N.; Dong, L.; Wu, M.; Li, G. Investigation on the tribological properties of different coatings of cutting tool with reciprocating friction test. *J. Braz. Soc. Mech. Sci. Eng.* **2023**, *11*, 45. [CrossRef]
13. Jamil, M.; He, N.; Zhao, W.; Khan, A.; Gupta, M.; Meng, L. Tribological behavior of WC-6Co against Ti–6Al–4V alloy under novel cryogenic ethanol-ester oil dry-ice hybrid lubri-cooling. *Tribol. Int.* **2021**, *156*, 106812. [CrossRef]
14. García-Martínez, E.; Miguel, V.; Martínez-Martínez, A.; Manjabacas, M.; Coello, J. Surface integrity and tool wear analysis on turning of copper-nickel 70/30 ASTM B122 alloy under low initial lubrication. *Materials* **2021**, *14*, 4868. [CrossRef]
15. El-Tayeb, N.; Yap, T.; Brevern, P. Wear characteristics of titanium alloy Ti54 for cryogenic sliding applications. *Tribol. Int.* **2010**, *43*, 2345–2354. [CrossRef]
16. Zemzemi, F.; Rech, J.; Salem, W.; Dogui, A.; Kapsa, P. Identification of a friction model at tool/chip/workpiece interfaces in dry machining of AISI4142 treated steels. *J. Mater. Process. Technol.* **2009**, *209*, 3978–3990. [CrossRef]
17. Smolenicki, D.; Boos, J.; Kuster, F.; Roelofs, H.; Wyen, C. In-process measurement of friction coefficient in orthogonal cutting. *CIRP Ann.* **2014**, *63*, 97–100. [CrossRef]
18. Sterle, L.; Pušavec, F.; Kalin, M. Determination of friction coefficient in cutting processes: Comparison between open and closed tribometers. *Procedia CIRP* **2019**, *82*, 101–106. [CrossRef]
19. Voss, R.; Seeholzer, L.; Kuster, F.; Wegener, K. Cutting process tribometer experiments for evaluation of friction coefficient close to a CFRP machining operation. *Procedia CIRP* **2017**, *66*, 204–209. [CrossRef]
20. Bonnet, C.; Valiorgue, F.; Rech, J.; Claudin, C.; Hamdi, H.; Bergheau, J.; Gilles, P. Identification of a friction model—Application to the context of dry cutting of an AISI 316L austenitic stainless steel with a TiN coated carbide tool. *Int. J. Mach. Tools Manuf.* **2008**, *48*, 1211–1223. [CrossRef]
21. Klinkova, O.; Rech, J.; Drapier, S.; Bergheau, J. Characterization of friction properties at the workmaterial/cutting tool interface during the machining of randomly structured carbon fibers reinforced polymer with carbide tools under dry conditions. *Tribol. Int.* **2011**, *44*, 2050–2058. [CrossRef]
22. Mondelin, A.; Furet, B.; Rech, J. Characterisation of friction properties between a laminated carbon fibres reinforced polymer and a monocrystalline diamond under dry or lubricated conditions. *Tribol. Int.* **2010**, *43*, 1665–1673. [CrossRef]
23. Abdelali, H.; Claudin, C.; Rech, J.; Salem, W.; Kapsa, P.; Dogui, A. Experimental characterization of friction coefficient at the tool–chip–workpiece interface during dry cutting of AISI 1045. *Wear* **2012**, *286*, 108–115. [CrossRef]
24. Xu, J.; Li, C.; Mansori, M.; Liu, G.; Chen, M. Study on the frictional heat at tool-work interface when drilling CFRP composites. *Procedia Manuf.* **2018**, *26*, 415–423. [CrossRef]
25. Xu, J.; Li, C.; Dang, J.; Mansori, M.; Ren, F. A study on drilling high-strength CFRP laminates: Frictional heat and cutting temperature. *Materials* **2018**, *11*, 2366. [CrossRef]
26. Claudin, C.; Mondelin, A.; Rech, J.; Fromentin, G. Effects of a straight oil on friction at the tool–workmaterial interface in machining. *Int. J. Mach. Tools Manuf.* **2010**, *50*, 681–688. [CrossRef]
27. Fersi, A.; Ayed, Y.; Lavisse, B.; Germain, G. Characterization of friction behavior under cryogenic conditions: Ti–6Al–4V. *Tribol. Int.* **2024**, *195*, 109588. [CrossRef]
28. Courbon, C.; Pusavec, F.; Dumont, F.; Rech, J.; Kopac, J. Tribological behaviour of Ti6Al4V and Inconel718 under dry and cryogenic conditions—Application to the context of machining with carbide tools. *Tribol. Int.* **2013**, *66*, 72–82. [CrossRef]
29. Etri, H.; Singla, A.; Özdemir, M.; Korkmaz, M.; Demirsöz, R.; Gupta, M.; Krolczyk, J.; Ross, N. Wear performance of Ti-6Al-4V titanium alloy through nano-doped lubricants. *Arch. Civ. Mech. Eng.* **2023**, *23*, 147. [CrossRef]
30. Demirsöz, R.; Korkmaz, M.; Gupta, M. A novel use of hybrid Cryo-MQL system in improving the tribological characteristics of additively manufactured 316 stainless steel against 100 Cr6 alloy. *Tribol. Int.* **2022**, *173*, 107613. [CrossRef]
31. Behera, B.; Ghosh, S.; Rao, P. Modeling of cutting force in MQL machining environment considering chip tool contact friction. *Tribol. Int.* **2018**, *117*, 283–295. [CrossRef]

32. Chetan; Ghosh, S.; Rao, P. Specific cutting energy modeling for turning nickel-based Nimonic 90 alloy under MQL condition. *Int. J. Mech. Sci.* **2018**, *146*, 25–38. [CrossRef]
33. Wu, B.; Zhang, M.; Zhao, B.; Ding, W.; Liu, G. Developing a novel ultrasonic atomization-based cutting fluid spray system and evaluating its performance during milling processes. *J. Manuf. Process.* **2023**, *104*, 334–347. [CrossRef]
34. Zhang, Y.; Yuan, S.; Wang, L. Investigation of capillary wave, cavitation and droplet diameter distribution during ultrasonic atomization. *Exp. Therm. Fluid Sci.* **2021**, *120*, 110219. [CrossRef]
35. Chen, B.; Gao, D.; Li, Y.; Chen, C.; Wang, Z.; Zhong, Q.; Sun, P.; Wu, S.; Wang, Z.; Liang, Y. Influence of atomizing core on droplet dynamic behavior and machining characteristics under synergistically enhanced twin-fluid spray. *Int. J. Adv. Manuf. Technol.* **2020**, *110*, 2269–2282. [CrossRef]
36. Emami, M.; Sadeghi, M.; Sarhan, A. Investigating the effects of liquid atomization and delivery parameters of minimum quantity lubrication on the grinding process of Al_2O_3 engineering ceramics. *J. Manuf. Process.* **2013**, *15*, 374–388. [CrossRef]
37. Zheng, B.; Lin, Y.; Zhou, Y.; Lavernia, E. Gas atomization of amorphous aluminum: Part I. Thermal behavior calculations. *Metall. Mater. Trans. B* **2009**, *40*, 768–778. [CrossRef]
38. Wu, B.; Zhang, M.; Zhao, B.; Ding, W.; Yu, W. Effect of different cooling and lubrication strategies on milling performance of ultra-high strength steel. *Int. J. Adv. Manuf. Technol.* **2024**, *131*, 2869–2880. [CrossRef]
39. Xiao, J.; Zhang, L.; Zhou, K.; Wang, X. Microscratch behavior of copper–graphite composites. *Tribol. Int.* **2013**, *57*, 38–45. [CrossRef]
40. Zhu, P.; Hu, Y.; Ma, T.; Wang, H. Molecular dynamics study on friction due to ploughing and adhesion in nanometric scratching process. *Tribol. Lett.* **2011**, *41*, 41–46. [CrossRef]
41. Duan, Z.; Li, C.; Zhang, Y.; Yang, M.; Gao, T.; Liu, X.; Li, R.; Said, Z.; Debnath, S.; Sharma, S. Mechanical behavior and semiempirical force model of aerospace aluminum alloy milling using nano biological lubricant. *Front. Mech. Eng.* **2023**, *18*, 4. [CrossRef]
42. Khan, W.; Hoang, N.; Tai, B.; Hung, W. Through-tool minimum quantity lubrication and effect on machinability. *J. Manuf. Process.* **2018**, *34*, 750–757. [CrossRef]
43. Kudo, T.; Sekiguchi, K.; Sankoda, K.; Namiki, N.; Nii, S. Effect of ultrasonic frequency on size distributions of nanosized mist generated by ultrasonic atomization. *Ultrason. Sonochem.* **2017**, *37*, 16–22. [CrossRef] [PubMed]
44. Ganguli, S.; Kapoor, S. Improving the performance of milling of titanium alloys using the atomization-based cutting fluid application system. *J. Manuf. Process.* **2016**, *23*, 29–36. [CrossRef]

materials

Article

Simulation Study on Residual Stress Distribution of Machined Surface Layer in Two-Step Cutting of Titanium Alloy

Jingyi Wang [1], Bo Kong [1,2], Shulei Wei [2], Jian Zang [1] and Anhai Li [1,*]

[1] Key Laboratory of High Efficiency and Clean Mechanical Manufacture of MOE, School of Mechanical Engineering, Shandong University, Jinan 250061, China; wjy6660820@163.com (J.W.); kongbo.sripe@sinopec.com (B.K.); jianzang0824@163.com (J.Z.)

[2] Shandong Engineering Research Center for Downhole Cementing and Completion Tools in Petroleum Engineering, Shelfoil Petroleum Equipment & Services Co., Ltd., Dezhou 253034, China; weishl.sripe@sinopec.com

* Correspondence: anhaili@sdu.edu.cn

Abstract: Ti-6Al-4V titanium alloy is known as one of the most difficult metallic materials to machine, and the machined surface residual stress distribution significantly affects properties such as static strength, fatigue strength, corrosion resistance, etc. This study utilized finite element software Abaqus 2020 to simulate the two-step cutting process of titanium alloy, incorporating stages of cooling, unloading, and de-constraining of the workpiece. The chip morphology and cutting force obtained from orthogonal cutting tests were used to validate the finite element model. Results from the orthogonal cutting simulations revealed that with increasing cutting speed and the tool rake angle, the residual stress undergoes a transition from compressive to tensile stress. To achieve greater residual compressive stress during machining, it is advisable to opt for a negative rake angle coupled with a lower cutting speed. Additionally, in two-step machining of titanium alloy, the initial cutting step exerts a profound influence on the subsequent cutting step, thereby shortening the evolution time of the Mises stress, equivalent plastic strain, and stiffness damage equivalent in the subsequent cutting step. These results contribute to optimizing titanium alloy machining processes by providing insights into controlling residual stress, ultimately enhancing product quality and performance of structural part of titanium alloy.

Keywords: finite element analysis; titanium alloy; two-step cutting; high-speed cutting; residual stress

1. Introduction

Titanium alloys, recognized for their significant application potential, boast high specific strength, excellent heat resistance, and superb corrosion resistance. Since the mid-20th century, these alloys have been extensively used in various industries, including aerospace, shipbuilding, medical, metallurgy, and chemical sectors [1]. Despite their numerous advantageous properties, titanium alloys pose challenges in machining due to low thermal conductivity, high chemical activity, and a small deformation coefficient. These characteristics often result in chip serration, increased cutting force, and accelerated tool wear during machining, hindering the broader application of titanium alloys. Machining titanium alloys involves complex phenomena such as tribology, elastic-plastic mechanics, and fracture mechanics. The process is characterized by high temperatures, high strain, high strain rate, and the presence of thermal-force coupling, all occurring over short time periods [2]. Consequently, machining surfaces inevitably develop residual stress, which significantly impacts the mechanical properties of titanium alloys, including strength, hardness, and toughness. These stresses can also increase surface roughness and reduce the fatigue life of parts. Therefore, studying the magnitude of residual stress and the factors influencing it is crucial for improving the machining processes of titanium alloys.

Measuring and studying the influencing factors of residual stress using experimental methods is both time-consuming and labor-intensive, increasing research costs and complicating the acquisition of local stresses and strains during the machining process. Consequently, simulation models are predominantly used to study the variation of residual stresses. Wang et al. [3] established a three-dimensional numerical model to predict surface residual stress in multi-axis milling of Ti-6Al-4V titanium alloy and conducted experimental validation, finding average absolute errors of 11.6% for σ_x and 15.2% for σ_y. Wu et al. [4] created a three-dimensional finite element model using ABAQUS to analyze chip formation, stress distribution, cutting forces, and milling temperatures during the complex milling process of Ti-6Al-4V. Dong et al. [5] applied a bimodal Gaussian function to fit the residual stress distribution obtained from a finite element model for Inconel 718 alloy, investigating the impact of cutting parameters on residual stress distribution and identifying cutting speed as the most influential factor. Ren et al. [6] utilized a three-dimensional finite element model based on the Johnson-Cook ontological model of Ti-6Al-4V, combined with a modified Coulomb friction stress model, to analyze defects in laser additive manufacturing metal parts with large residual stresses. Li et al. [7] used the FEM to characterize the kinematics of three-dimensional elliptical vibratory cutting, demonstrating that this method facilitates the acquisition of compressive stress near the machined surface, thereby improving performance.

Typically, residual tensile stress causes cracks on the machined surface, which in turn reduces the fatigue strength, while residual compressive stress can offset some of the tensile stress exerted by the working load, which in turn improves the fatigue life. The magnitude of residual stress is usually influenced by cutting parameters, tool geometry, workpiece shape, and material properties. Outeiro et al. [8] predicted residual stresses under different cutting conditions using a machine learning method based on mathematical regression analysis. Their results indicated that to increase compressive residual stress on the machined surface by 40%, the rake angle should be increased from $-6°$ to $5°$, and cutting speed should be reduced by 67% (from 60 m/min to 20 m/min). Yao et al. [9] found that surface residual compressive stress increases with the rake angle of the cutting tool during high-speed milling of titanium alloy TC11. Dehmani [10] et al. developed a numerical model of orthogonal cutting and investigated the effect of tool edge radius and heat generated by friction on the flank face on residual stress. It was shown that the impact of heat on residual stress could not be overlooked. Sun et al. [11] experimentally demonstrated that as cutting speed increases, the compressive residual stress in both the cutting and feed directions intensifies, with the residual compressive stress in the feed direction being approximately 30% greater than that in the cutting direction. Matuszak et al. [12] observed that the maximum residual compressive stress and its thickness peaked at a cutting speed of 190 m/min.

In practical machining, multistep cutting has garnered significant attention due to its impact on surface residual stress. Zhang et al. [13] demonstrated that cutting force and residual compressive stress decrease with increasing roughing cutting speed in two-step milling tests on Ti-6Al-4V titanium alloy. Song et al. [14] simulated and analyzed various cutting processes using a finite element simulation model and found that multistage cutting can increase compressive residual stress and alter the location of minimum residual stress along the depth direction. They also discovered that pre-stressing multistage cutting maximizes the compressive residual stress value. Liu and Guo [15] used finite element software to simulate multistage cutting and employed thermo-viscoelastic finite element simulations to study the effects of cutting force unloading and clamping forces on residual stress distribution. Aassif et al. [16] studied the influence of temperature and strain accumulation on the residual stress distribution of the subsequent machining process.

Currently, both domestic and international scholars primarily use a combination of experimental and simulation methods to study residual stress in titanium alloy machining. However, most simulation models for a single step do not account for the significant heat generated in the first high-speed cutting step or the impact of residual stress on the second cutting step, while the actual machining is usually a multi-step process. In this paper, we establish a two-dimensional cutting simulation model using the finite element method and set up key technologies such as cooling stage and workpiece material unloading and de-constraint, which solves the effects of residual heat and stress of the previous process on the newly machined surface and is more in line with the actual machining. We explore the effects of different tool angles and cutting speeds on residual stress and the reasons for changes in residual stress under various conditions. Additionally, we innovatively analyze the effects of the first cutting step on the evolution of stress, strain, and stiffness damage over time in the second cutting step, demonstrating the complex interactions between the steps in multistep machining. The study's findings can be used to evaluate the effects of tool rake angle, cutting speed, and different working steps on residual stress in the cutting process, providing practical insights for controlling residual stress and enhancing process optimization in actual machining.

2. Materials and Methods

This section will describe the materials and equipment used for simulation and experiments, and Figure 1 shows the flowchart of the simulation design and validation experiments.

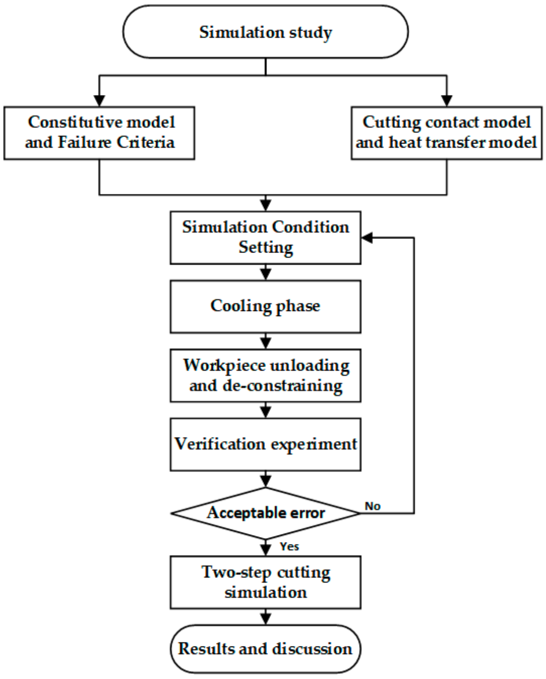

Figure 1. The flowchart of the simulation study.

2.1. Simulation Condition Setting

In the simulation test, a Ti-6Al-4V multistep cutting model was established using simulation software Abaqus 2020. The finite element model was configured as a two-dimensional orthogonal cutting model [17], as illustrated in Figure 2a. A simplified integral four-node bilinear thermodynamic coupling unit [18] was used for the workpiece. During the simulation, the tool was modeled as a rigid body due to its minimal deformation. The degrees of freedom at the bottom edge of the workpiece in both horizontal and vertical directions, as well as the horizontal direction of the side edges, were constrained to prevent displacement caused by the tool's motion (the green arrowheads in Figure 2a). The boundary temperature was set to room temperature, and a reference point was selected on the right side of the tool to which the cutting speed was applied. The tool angle and cutting parameters in the model are detailed in Table 1. Simulation trials No.1–No.4 are used to compare the results with those of the validation experiments, No.5–No.11 are used to study the effect of tool rake angle on the machined residual stress, No. 9 and No.12–14 are used to study the effect of cutting speed on the residual stress and the machined surfaces, and No.15–No.18 are used to study the effect of two-step cutting on the evolution of the machined surface layer state. To improve the efficiency of the cutting simulation, Figure 2b depicts the grid cell division of the workpiece. The mesh size of the layer to be cut was set to 5 × 5 µm, while the material matrix part was configured with a dimensionally gradual mesh.

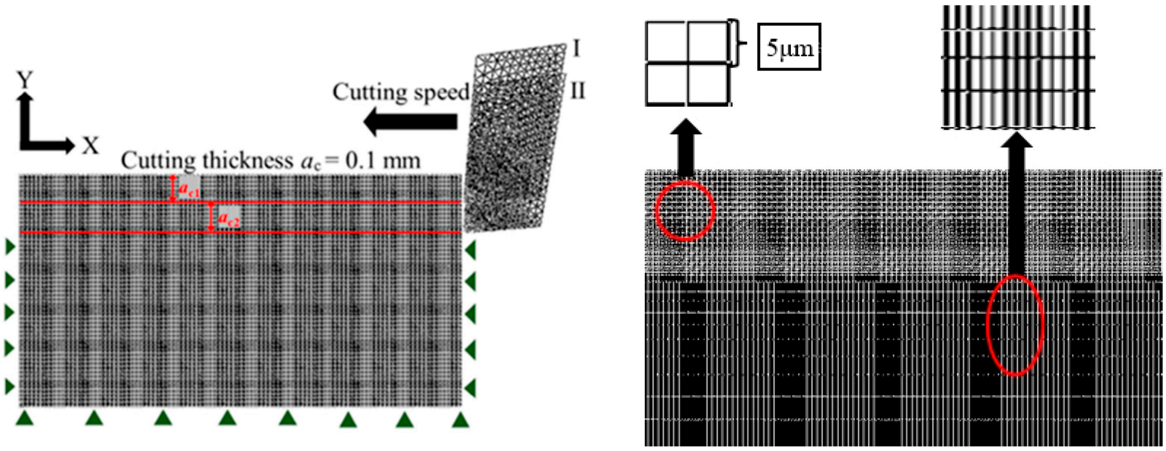

(**a**) (**b**)

Figure 2. Multi-step cutting finite element simulation model. (**a**) Multi-step cutting model; (**b**) Workpiece meshing model.

Table 1. Simulation parameters for multi-step cutting of titanium alloys.

Sim. No.	Tool Rake Angle γ (°)	Cutting Speed of the First Step v_1 (m/min)	Cutting Speed of the Second Step v_2 (m/min)	Cutting Thickness a_c (mm)
1	0	40		
2	0	80		
3	0	120		
4	0	160		
5	−15	200		
6	−10	200		
7	−5	200		
8	0	200	/	
9	5	200		
10	10	200		0.1
11	15	200		
12	5	100		
13	5	300		
14	5	400		
15	5	100	200	
16	5	200	200	
17	5	300	200	
18	5	400	200	

2.2. Constitutive Model and Failure Criteria

The ontological relationships of materials are fundamental for describing their dynamic mechanical behavior. During machining, the deformation of workpiece materials typically involves high strains, high strain rates, and elevated temperatures. The Johnson–Cook material model, which integrates the effects of strain, strain rate, and temperature on flow stress, accommodates high strain rates ranging from 10^2 to 10^6 [19]. Consequently, it is frequently used in finite element cutting simulation models. The expression of the Johnson-Cook material model is as follows [20].

$$\sigma = (A + B\varepsilon^n)\left(1 + Cln\frac{\dot{\bar{\varepsilon}}}{\dot{\bar{\varepsilon}}_0}\right)\left[1 - \left(\frac{T - T_r}{T_m - T_r}\right)^m\right] \tag{1}$$

where σ is the flow stress of the workpiece material; ε is the equivalent plastic strain of the workpiece material; ε is the equivalent plastic strain of the workpiece material; $\frac{\dot{\bar{\varepsilon}}}{\dot{\bar{\varepsilon}}_0}$ is the dimensionless plastic strain rate; $\dot{\bar{\varepsilon}}_0$ is the reference strain rate; T_r is the room temperature (20 °C); T_m is the melting temperature of the material.

Table 2 shows the specific values of the parameters of the Johnson-Cook material model for titanium alloys. Tables 3 and 4 show the performance parameters and main chemical composition of titanium alloys.

Table 2. Parameters of the Johnson-Cook constitutive model for Ti-6Al-4V titanium alloy [18].

A **(MPa)**	***B*** **(MPa)**	***n***	***C***	***m***
782	498	0.28	0.028	1

Table 3. Physical and chemical properties of Ti-6Al-4V titanium alloy [21].

Density ρ **(kg/m^3)**	**Elastic Modulus** E **(GPa)**	**Poisson Ratio** μ	**Thermal Conductivity** λ **(W/m·K)**	**Specific Heat** C_p **(J/kg·K)**
4430	109 (50 °C) 91 (250 °C) 75 (750 °C)	0.34	6.8 (20 °C) 7.4 (100 °C) 9.8 (300 °C) 11.8 (500 °C)	611 (20 °C) 624 (100 °C) 674 (300 °C) 703 (500 °C)

Table 4. Chemical composition of Ti-6Al-4V titanium alloy [22].

Elements	**Ti**	**Al**	**V**	**Fe**	**Si**	**C**	**N**	**H**	**O**
wt. %	Base	5.6	3.86	0.18	<0.01	0.02	0.023	<0.01	0.17

In this paper, the Johnson-Cook failure model [23] is used to define the damage parameters based on the equivalent plastic strain at the integration point of the unit, expressed as Equation (2).

$$w = \sum \frac{\Delta\bar{\varepsilon}}{\bar{\varepsilon}_f} \tag{2}$$

where w is workpiece material damage parameter; $\Delta\bar{\varepsilon}$ is increment of equivalent strain of workpiece material; $\bar{\varepsilon}_f$ is equivalent strain of workpiece material. Equivalent strain $\bar{\varepsilon}_f$ is expressed as Equation (3).

$$\bar{\varepsilon}_f = \left[D_1 + D_2 exp\left(D_3\frac{P}{\bar{\sigma}}\right)\right]\left[1 + D_4 ln\frac{\dot{\bar{\varepsilon}}}{\dot{\bar{\varepsilon}}_0}\right]\left[1 + D_5\frac{T - T_r}{T_m - T_r}\right] \tag{3}$$

where P is the average value of the three principal stress. $\bar{\sigma}$ is the equivalent stress. D_1~D_5 is material failure parameters. For titanium alloy materials, the specific values of these failure parameters are provided in Table 5. During the simulation, the finite element software accumulates the failure parameters at the end of each analysis step. If the damage parameter w exceeds 1, the mesh element is considered to have failed and is removed from the overall mesh.

Table 5. Johnson-Cook Failure Parameters for Ti-6Al-4V Titanium Alloy [24].

D_1	D_2	D_3	D_4	D_5
−0.09	0.25	−0.5	0.014	3.87

The stress-strain process of deformation damage in materials during cutting can be divided into three stages [25]. The first stage is elastic deformation, where stress gradually increases. Once the stress exceeds the yield stress σ_0, the material enters the stable plastic deformation stage, during which strain hardening is more significant than thermal softening. When the damage parameter w reaches 1, damage begins to appear, and the damage variable D starts to increase from 0, marking the onset of the damage evolution stage. At this point, thermal softening becomes dominant, strain increases, and stress decreases until the material completely fails (D = 1) and the stress drops to 0.

2.3. Cutting Contact Model and Heat Transfer Model

When machining titanium alloys, friction in the tool-workpiece contact zone significantly affects tool life, cutting heat, and the quality of the machined surface. In the cutting simulation model, it is crucial to accurately represent material deformation and the friction between the tool and the chip. Friction in the cutting process primarily occurs between the tool's rake face and the chip, as well as between the flank face and the machined surface. The modified Coulomb friction model [26] is used to define the friction properties. The friction region between the chip and the tool's rake face is divided into two segments: the bonding zone, where the material experiences shear stress τ_f approximately equal to its shear yield strength τ_γ, and the sliding zone, where the friction stress is proportional to the normal stress σ_n, with the proportionality coefficient being the friction factor. In the model, the friction factor μ is set to 0.3 [27].

$$\tau_f = \begin{cases} \tau_\gamma, \tau_\gamma \leq \mu\sigma_n \\ \mu\sigma_n, \tau_\gamma > \mu\sigma_n \end{cases} \tag{4}$$

During the cutting process, a large amount of cutting heat is generated due to the friction in the tool-chip and tool-workpiece contact zones as well as the deformation of the material, and it is mainly concentrated in the shear zone and the tool-chip contact zone. Its heat transfer control equation is [28].

$$\lambda\left(\frac{\partial^2 T}{\partial^2 x} + \frac{\partial^2 T}{\partial^2 y}\right) + \dot{Q} = \rho C_p\left(u_x\frac{\partial T}{\partial x} + u_y\frac{\partial T}{\partial y}\right) \tag{5}$$

T is the temperature as a function of x and y in a two-dimensional plane. λ represents thermal conductivity, and $\dot{Q}$ denotes heat flow per unit volume. The transfer velocity of the moving heat source is u_x in the x direction and u_y in the y direction.

Calculation of heat due to plastic deformation of materials

$$\dot{Q}_p = \eta_p\bar{\sigma} \cdot \bar{\varepsilon}/J \tag{6}$$

where $\dot{Q}_p$ is volumetric heat flow rate from plastic deformation; η_p is plastic deformation work conversion coefficient, set to 0.9 [29]; J is thermal work equivalence coefficient; $\bar{\sigma}$ is equivalent force of the material in the cutting process; $\bar{\varepsilon}$ is equivalent strain of the material in the cutting process.

Calculation of heat generated due to tool-chip friction

$$\dot{Q}_f = \eta_f\tau_f v_{chip}/J \tag{7}$$

where $\dot{Q}_f$ is volumetric heat flow rate from friction; v_{chip} is tool-chip relative rate; η_f is friction work conversion coefficient.

The frictional work conversion factor in the model is set to 0.5 [30], which indicates that the heat carried away by the tool and chip each accounts for 50% of the heat generated by friction.

2.4. Cooling Phase

Due to the tool-workpiece interaction, the surface temperature of the workpiece increases after each machining pass, causing some material softening. This softening can affect cutting results and the extraction of cutting process data if the next step in the cutting simulation is carried out immediately. Figure 3 illustrates the temperature distribution nephogram of the material after machining. Figure 3a shows that the substantial heat generated during machining raises the surface temperature of the workpiece, making it unsuitable for immediate subsequent cutting. Conversely, Figure 3b demonstrates a significant decrease in workpiece temperature after the cooling stage, which is crucial for ensuring the accuracy of subsequent cutting and machining results. Figure 4 depicts the temperature change curve of the machined surface post-machining. It is evident that the surface temperature reaches its peak during machining; upon completion, the boundary condition of room temperature is set in the model. The surface temperature gradually decreases to room temperature, with a time interval of 1.75 ms between each data point. Proceeding with subsequent machining at this stage will significantly reduce the impact of the first step on the second.

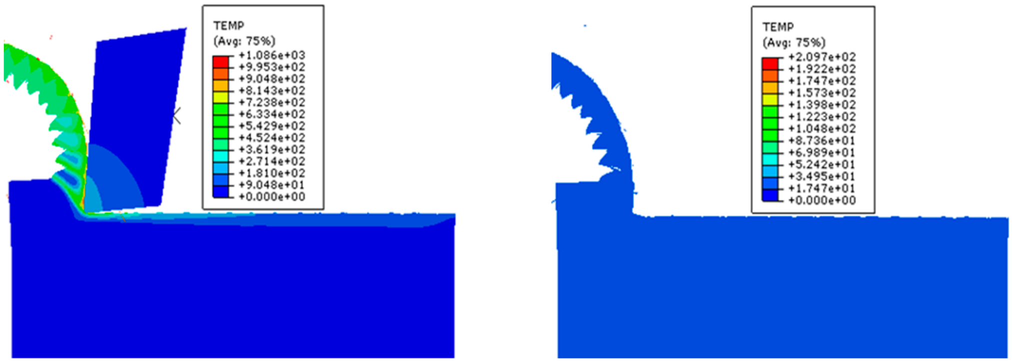

(**a**) (**b**)

Figure 3. Temperature distribution nephogram (**a**) workpiece before cooling; (**b**) workpiece after cooling.

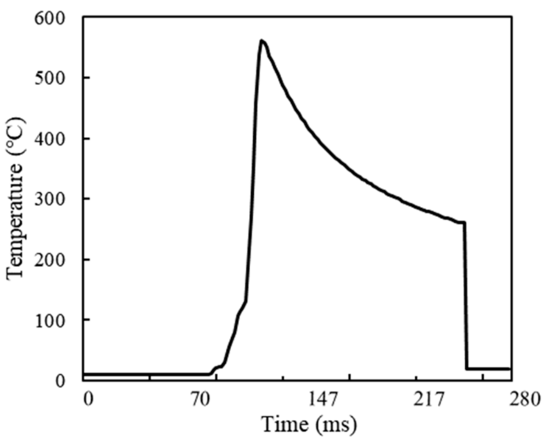

Figure 4. Temperature change of machined surface material.

2.5. Workpiece Unloading and De-Constraining

As can be seen in Figure 5a, there is a large amount of stress on the surface after machining is complete, and eliminating stress is critical for subsequent machining. In the simulation model, the unloading process is primarily divided into tool action unloading and workpiece constraint removal. After each machining process, the tool retracts away from the workpiece. From the start to the end of the tool-workpiece contact, the boundary conditions remain unchanged. The workpiece is de-constrained to eliminate the influence of boundary conditions on its free deformation. Figure 5b displays the stress distribution in the S_{11} direction (x direction) before and after unloading the tool action and removing workpiece constraints following the completion of cutting. The stress is released after de-constraining the workpiece, resulting in a more uniform stress distribution.

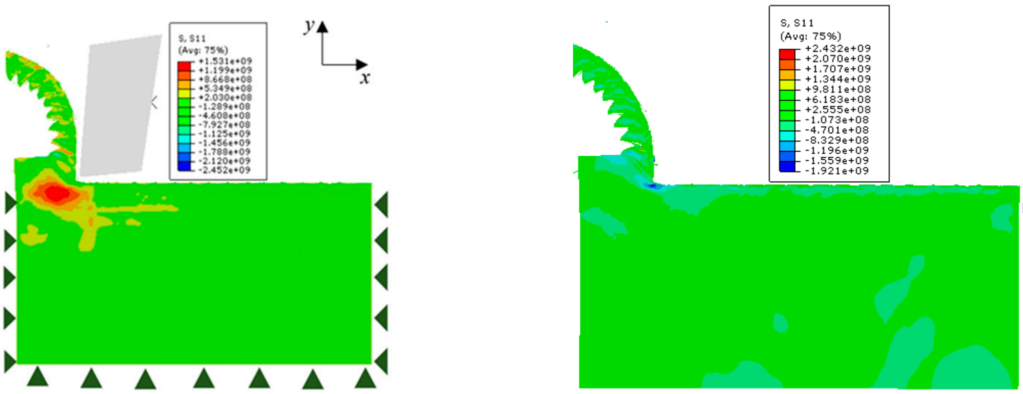

(**a**) (**b**)

Figure 5. Stress distribution of workpiece (**a**) before de-constraining; (**b**) after de-constraining.

2.6. Verification of the Simulation Model

2.6.1. Setting of Verification Experiment

The orthogonal cutting test of titanium alloy was conducted on a CKD6143H CNC lathe (made by Shandong University, Jinan, China), using a NG3156R KC5025 TiAlN coated carbide tool (made by Kennametal Inc., Latrobe, PA, USA). The tool featured a rake angle of 0°, a flank angle of 7°, and a cutting-edge width of 3.96 mm. The workpiece material was Ti-6Al-4V titanium alloy, with its main chemical composition listed in Table 4. The material diameter was 100 mm. The titanium alloy bar was machined into a ring-shaped groove with a width of 2 mm and a spacing of 3 mm by wire-cutting. The experimental equipment and measurement system in cutting tests are shown in Figure 6, and the cutting parameters are detailed in Table 6. Cutting forces during orthogonal turning were measured using a Kistler 9257B dynamometer (made by Kistler Group, Winterthur, Switzerland). Each set of tests was carried out three times, all with new tools to eliminate the errors introduced by tool wear on the cutting results.

Table 6. Orthogonal cutting parameters of Ti-6Al-4V titanium alloy.

Cutting Parameters	Value
Cutting width (mm)	2
Cutting speed v (m/min)	40, 80, 120, 160
Feed f (mm/r)	0.05, 0.10, 0.15, 0.20

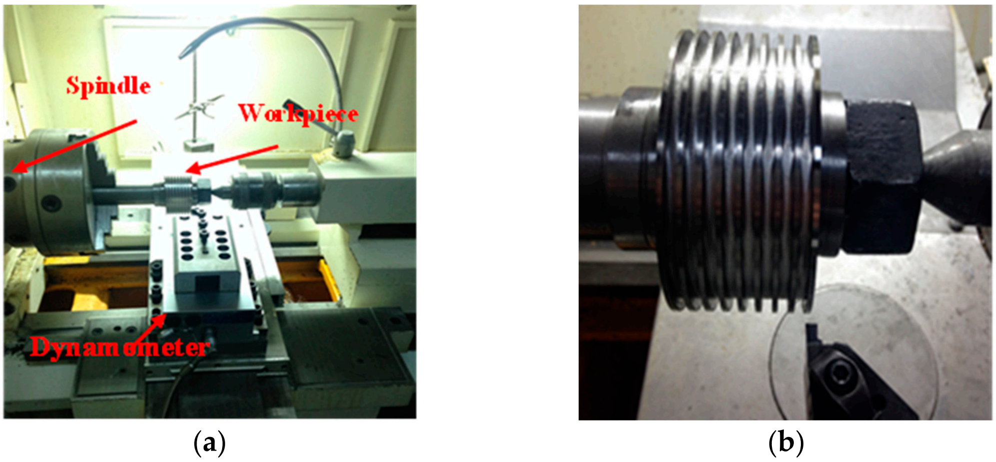

Figure 6. Experimental equipment in orthogonal cutting of Ti-6Al-4V titanium alloy (**a**) experimental equipment; (**b**) workpiece.

Upon completion of each test, the chips were collected and labeled according to the cutting parameters. The chips were set, ground, polished, and etched using a corrosive solution composed of 3 ml hydrofluoric acid, 5 ml nitric acid, and 100 ml water, with a typical corrosion time of 30 to 60 s. A scanning electron microscope was used to observe the chip morphology, with the degree of serration in the serrated chips denoted as G_s [16]

$$G_s = \frac{H - C}{H}, \tag{8}$$

where H is the height of top of tooth and C is the height of tooth valley.

2.6.2. Comparison of Cutting Forces

Using the established two-dimensional simulation model, cutting simulations were performed with a feed rate of 0.1 mm/rev, a depth of cut of 0.1 mm, and cutting speeds of 40 m/min, 80 m/min, 120 m/min, and 160 m/min. Figure 7 shows the cutting force obtained from the simulation and those measured during the tests. It can be observed that due to the wear of the turning test tool and the measurement error of the instrument, the cutting forces measured at cutting speeds of 80 m/min, 120 m/min, and 160 m/min are slightly higher than those in the simulation. At a cutting speed of 40 m/min, the measured cutting force is lower than the simulated cutting force. The relative errors are within 15%, demonstrating that the established simulation model has high prediction accuracy.

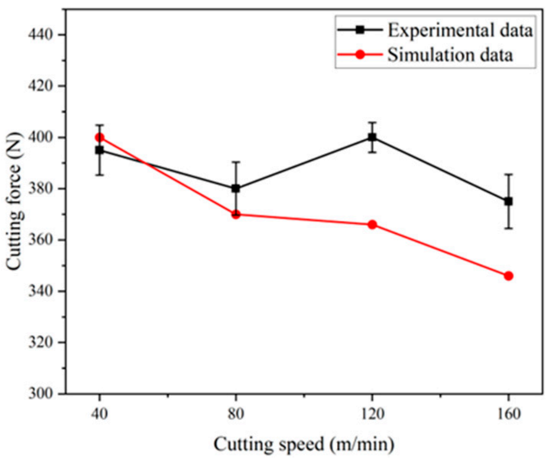

Figure 7. Comparison of cutting forces between test and simulation.

2.6.3. Comparison of Chip Morphology

Figure 8 compares the chip morphology obtained from the cutting simulation and the test, while Figure 9 illustrates the trend of chip serration degree from both the simulation and the test at various cutting speeds, along with the relative error between the two methods. It is evident that the chip morphology in both the simulation and the test shows consistent trends under different cutting parameters. At a cutting thickness of 0.1 mm and a cutting speed of 40 m/min, both the simulation and the test produce band-shaped chips. As the cutting speed increases to 80 m/min, 120 m/min, and 160 m/min, the chip morphology transitions from band-shaped to sawtooth-shaped, with the degree of serration increasing with the cutting speed. Errors in the degree of serration ranged from −2.63% to −10.94%. The similarity in chip shape between the simulation and the test directly reflects the accuracy and effectiveness of the simulation model.

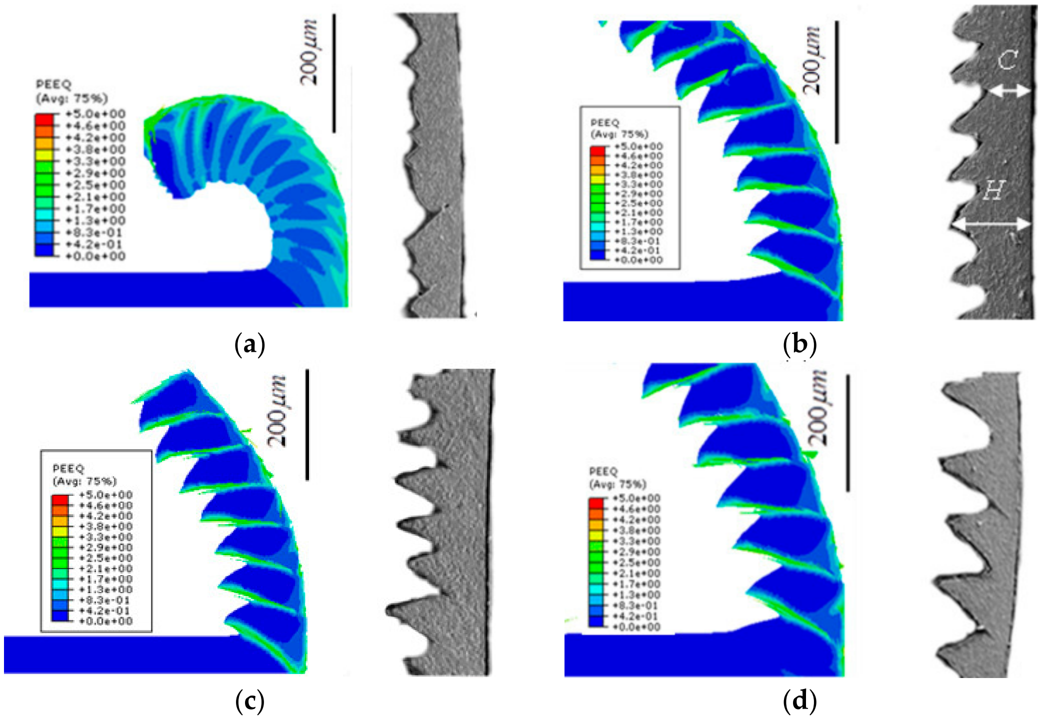

Figure 8. Comparison of chip morphology obtained from simulation and experiment (**a**) v = 40 m/min; (**b**) v = 80 m/min; (**c**) v = 120 m/min; (**d**) v = 160 m/min.

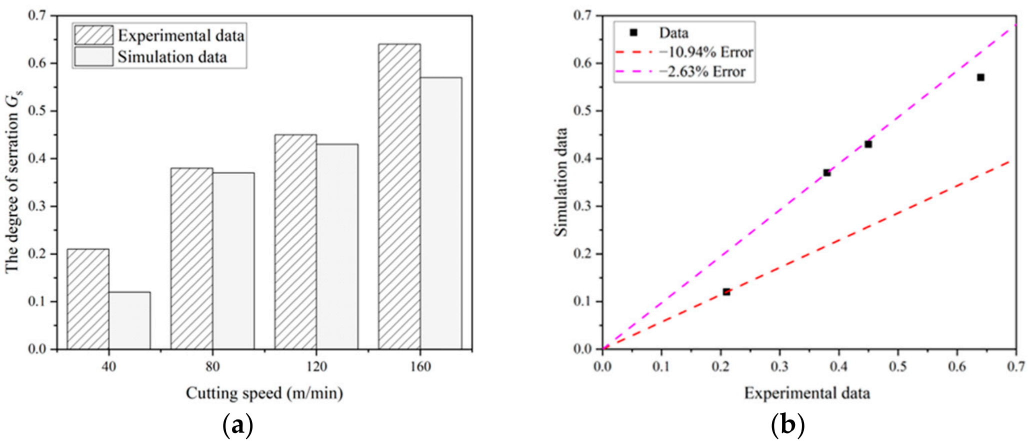

Figure 9. Degree of chip serration G_s obtained from simulation and experiment (**a**) trend of chip serration degree with cutting speed; (**b**) simulated and experimental chip serration degree error.

3. Results and Discussion

3.1. Selection of Residual Stress Direction

To extract residual stress data from the cutting model in all directions along the depth, the data extraction path is shown in Figure 10. The depth for residual stress extraction is 100 µm. At a cutting speed v of 400 m/min, a tool rake angle γ of 5°, and a cutting thickness a_c of 0.1 mm, the variation of residual stress in each direction with the depth of the workpiece surface layer is illustrated in Figure 11. In this figure, S_{11}, S_{22}, and S_{33} represent the stress along the X, Y, and Z axes, respectively, while S_{12} represents the shear stress along the Y direction on the XY plane. Positive values indicate tensile stress, and negative values indicate compressive stress. As shown in Figure 11, with increasing depth from the machined surface, the fluctuation range of S_{11} and S_{33} is larger and more evidently discernible. Therefore, the residual stress in the S_{11} and S_{33} directions are selected as the focus to study the influence of tool rake angle and cutting speed on their behavior.

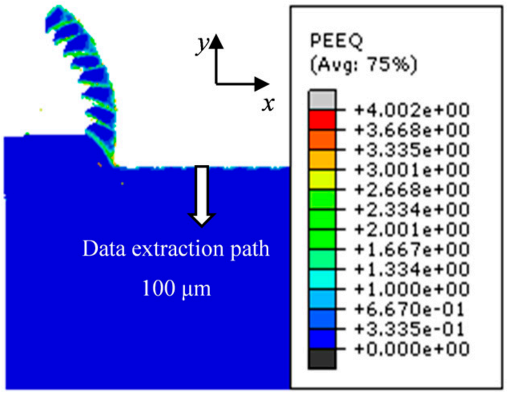

Figure 10. Residual stress data extraction path.

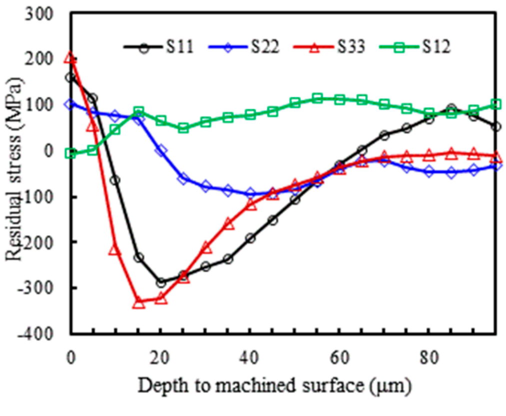

Figure 11. Variation of residual stress in all directions along the depth to the machined surface.

3.2. Effect of Tool Rake Angle on Machining Residual Stress

In the machining of titanium alloy, the distribution of residual stress in the depth direction from the machined surface is shown in Figure 12 when the tool rake angle is varied in the simulation model at a cutting speed of 200 m/min. From Figure 12a, it is evident that the distribution pattern of residual stress in the depth direction changes significantly with increasing tool rake angle. When the rake angles are −15°, −10°, −5°, 0°, and 5°, the surface material exhibits residual compressive stress in the S_{11} direction, and decreases with the increase in tool rake angle; when the tool rake angle is 10° and 15°, it presents surface residual tensile stress and increases gradually. At a tool rake angle of 15°, the tensile stress reaches 137 MPa. In Figure 12b, for the S_{33} direction, the machined surface is under compressive stress when the tool rake angle is −15°. As the tool rake angle increases, the machined surface residual stress shifts to tensile stress and gradually increases; when the tool rake angle is 15°, the tensile stress is the largest, at 535 MPa. The total peak residual compressive stress decreases with the increase in the rake angle. At the same time, it can be seen from Figure 12 that in the case of different tool rake angles, the distribution pattern of residual stress with the depth of the machined surface shows consistency, and the compressive stress increases first and then decreases.

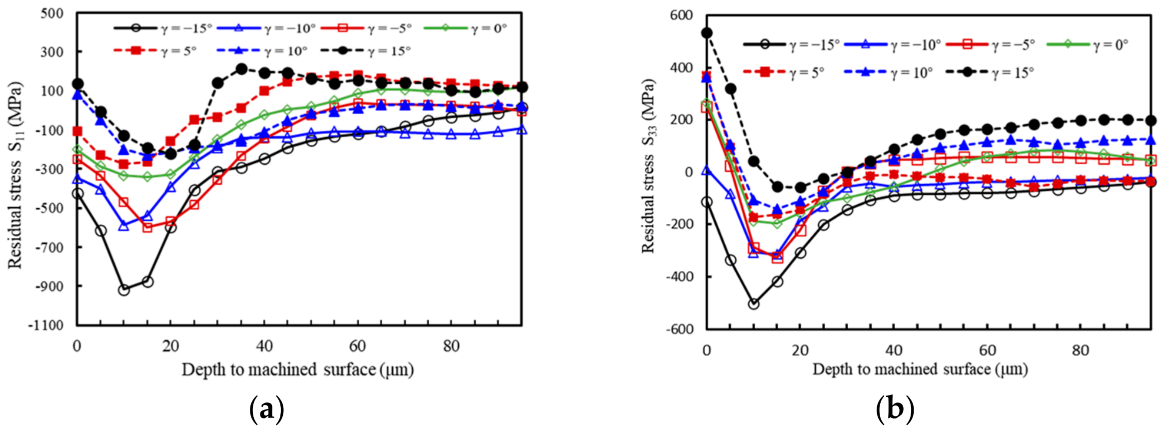

Figure 12. Variation of machining residual stress along the depth to the machined surface at different tool rake angles (**a**) S_{11} direction; (**b**) S_{33} direction.

The reason for this phenomenon is that during the cutting process, when the tool rake angle is small, the cutting edge radius is larger, and the extrusion and friction of the tool on the machined surface is greater. The machined surface is primarily influenced by mechanical load, resulting in residual compressive stress [31]. As the tool rake angle increases, the influence of thermal load on the machined surface becomes stronger than that of the mechanical load, leading to residual tensile stress. Additionally, as shown in Figure 12, the distribution of residual stress with the depth of the machined surface exhibits a consistent pattern across different tool rake angles. In practice, a negative rake angle can be selected to obtain residual compressive stress and thus reduce chipping.

3.3. Effect of Cutting Speed on Machining Residual Stress and Machined Surface

With other cutting parameters held constant, the residual stress in the depth direction were investigated using the finite element model at different cutting speeds. In this study, the tool rake angle was 5°, the cutting thickness was 0.1 mm, and the cutting speeds were 100 m/min, 200 m/min, 300 m/min, and 400 m/min.

The residual stress distribution on the machined surface is shown in Figure 13, revealing that the surface material presents a compressive stress state in the direction of S_{11}, when the cutting speed is small. Within a certain range of cutting speeds, the surface tensile stress increases as the cutting speed increases, and the maximum tensile stress is 161 MPa when the cutting speed is 400 m/min. While in the direction of S_{33}, the surface residual stress presents a tensile stress state, and it also increases with the increase in speed. The total peak residual compressive stress decreases with the increase in cutting speed. This trend is consistent with the results in the study by Yang et al. [32] and proves the accuracy of the model. This trend is primarily due to the increased thermal load on the machined surface at higher speeds, which gradually outweighs the mechanical load effect [33], resulting in residual tensile stress.

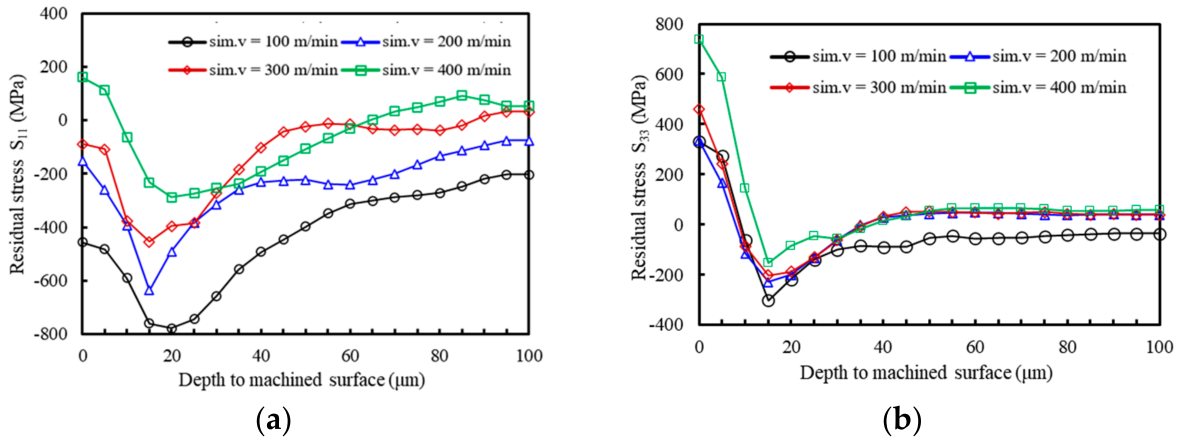

Figure 13. Variation of machining residual stress along the depth to the machined surface at different cutting speed (**a**) S_{11} direction; (**b**) S_{33} direction.

As the surface depth increases, the tensile stress decreases within the 0~15 μm range, and the slope of the corresponding curve increases sequentially with cutting speed. The primary reason for this behavior is that higher cutting speeds lead to increased strain rates in the processed surface material, thus increasing the compressive stress. However, as the depth of the surface layer increases, heat conduction diminishes, reducing the thermal load effect and enhancing the mechanical load effect. Plastic deformation of the material becomes dominant, and the stress state transitions to compressive stress [34]. The minimum values of residual tensile stress at different cutting speeds occur at nearly the same depth, indicating that mechanical and thermal loads have a minimal impact on the depth distribution of residual stress during the cutting process. Beyond a certain depth, the residual stress values tend to zero, primarily because the effects of mechanical and thermal loads diminish with increasing depth.

Figure 14 shows the changes in stress, strain, and stiffness damage equivalent with varying cutting speeds during the first cutting step, revealing the effect of cutting speed on surface machining performance. It can be seen that as the cutting speed in the first cutting step increases, the Mises stress gradually increases, while the equivalent plastic strain and stiffness damage equivalent gradually decrease.

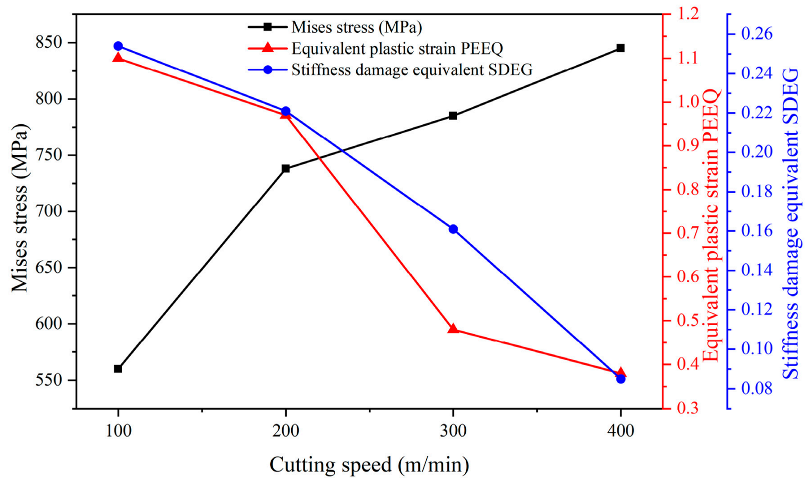

Figure 14. Variation of stress, strain, and stiffness damage equivalent with cutting speed on machined surfaces in the first cutting step.

3.4. Effect of Two-Step Cutting on the Evolution of the Machined Surface Layer State

Due to the interaction between the tool and the workpiece, the stress, strain, and stiffness damage equivalent of the machined surface change after the first cutting step of machining, subsequently affecting the surface quality of the second step. Figure 15 shows the nephogram of the stress and strain distribution on the workpiece surface after the first machining step. It can be observed that there are residual stress and plastic strains on the machined surface of the workpiece material.

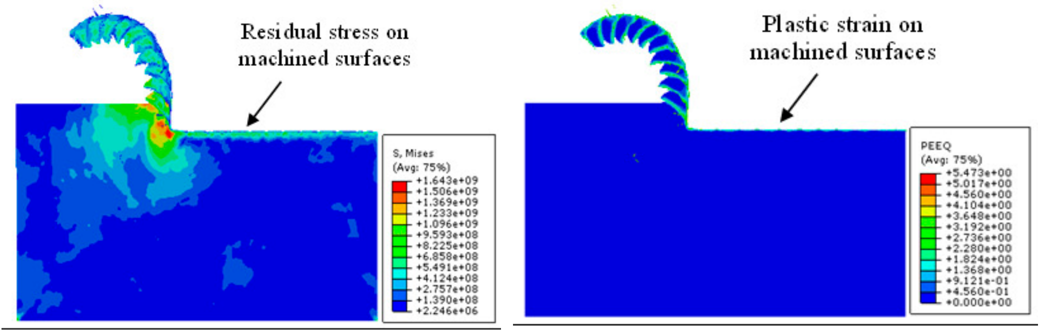

(**a**) (**b**)

Figure 15. Multi-step cutting simulation results (**a**) Mises stress distribution; (**b**) equivalent plastic strain distribution.

The stress-strain curves indicate that the stress, strain, and damage evolution of the material can describe the deformation process in greater detail. To investigate the effects of stress, strain, and stiffness damage equivalent on the machined surface of the first cutting step on the machined surface of the second cutting step, O points in the adiabatic shear band were marked before both the first and second cutting steps of machining, as shown in Figure 16. Data extraction for Mises stress, equivalent plastic strain, and stiffness damage equivalent was performed during the formation of the adiabatic shear zone, with a time interval of 1.75 ms between each data point.

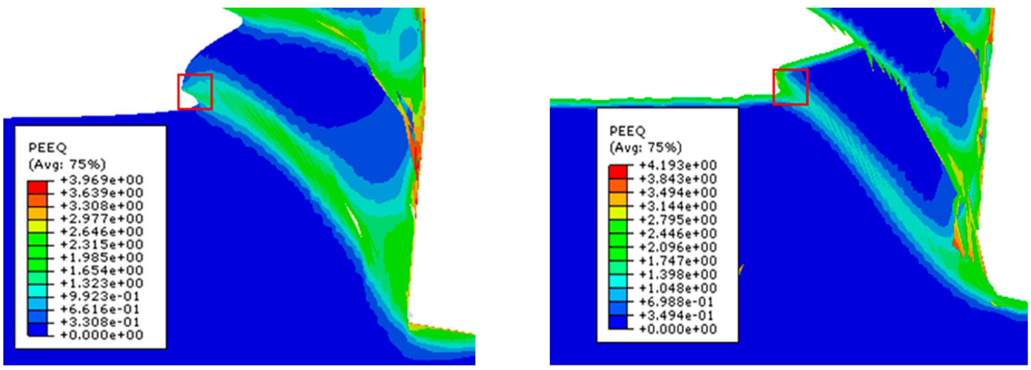

(**a**) (**b**)

Figure 16. Workpiece surface reference unit (**a**) surface reference unit for the first cutting step; (**b**) surface reference unit for the second cutting step.

Figure 17 shows the evolution of plastic strain, stress, and stiffness damage equivalent of the reference unit over time during the first cutting step. The cutting speed for both the first and second cutting steps is 200 m/min, and the cutting thickness is 0.1 mm. It can be seen that in the AB stage, the material is in the elastic deformation phase. Under the action of the cutting tool, the internal stress of the reference unit gradually rises, while the plastic strain and stiffness damage equivalent remain at 0. In the BC stage, as the stress within the unit increases, the material enters the plastic deformation phase. The stress gradually increases to the yield stress, and the reference unit plastic strain begins to increase, reaching 0.245 at point C. When the unit stress reaches its peak at the yield stress, it begins to decrease in the CD section, while the reference unit strain continues to increase. When the unit stress decreases to zero, the strain reaches a maximum value of 3.768. At point C, when the stress reaches its maximum value, the stiffness damage equivalent begins to rise. As the stiffness damage equivalent rapidly increases to 1, the reference unit fails, and the stress becomes 0, calling the CD stage as the damage evolution phase.

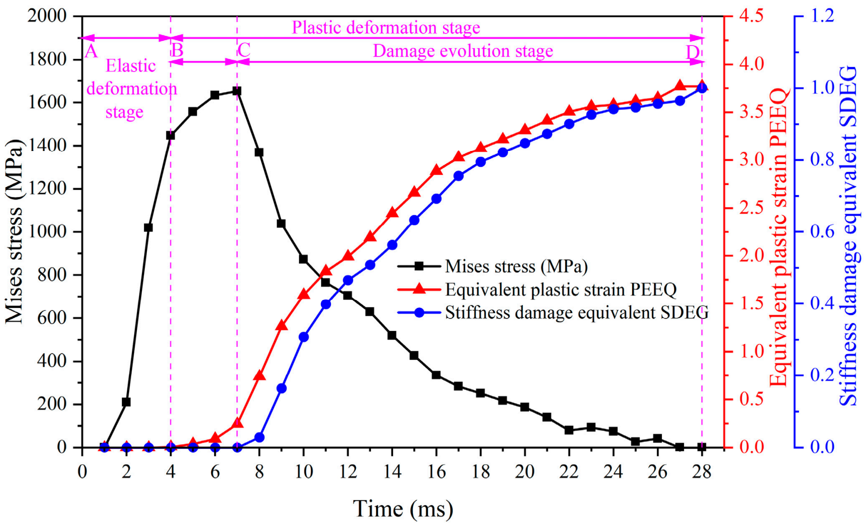

Figure 17. Evolution of stress, strain, and stiffness damage equivalent with time for the reference unit of the first cutting step.

Figure 18 shows the evolution of stress, strain, and stiffness damage equivalent over time in the reference cell of the chip's free surface obtained in the second cutting step. The evolution patterns in the second cutting step, including stress, plastic strain, and stiffness damage equivalent, are similar to those in the first cutting step, encompassing elastic deformation, plastic deformation, and damage evolution stages. The figure indicates that, due to the influence of the first cutting step, the initial values of stress, strain, and stiffness damage equivalent in the reference unit of the second cutting step differ from those in the first cutting step. The initial stress is 738 MPa, the strain is 0.97, and the stiffness damage is 0.221. At the end of the damage evolution stage, the strain reaches 3.914. This variation is primarily due to the friction and extrusion effects of the tool flank face and cutting edge on the machined surface during the first cutting step, which induce residual stress and generate substantial cutting heat. The heat-force coupling effect leads to stiffness damage on the machined surface. From the stiffness damage equivalent change curve over time, it is evident that the stiffness damage rate in the reference unit during the second cutting step is significantly higher than in the first cutting step. The stiffness damage equivalent reaches 1 in a much shorter time, resulting in the failure of the reference unit.

By comparing Figure 17 with Figure 18, it can be seen that under the same machining parameters in both the first and second cutting steps, the evolution time to failure of the workpiece surface unit in the second cutting step is substantially shorter than in the first cutting step. The time taken for the stress in the reference unit of the first cutting step to reach its maximum point is longer than the evolution time in the second cutting step. Additionally, during the damage evolution stage, the rate of stress decrease in the reference unit of the second cutting step is significantly greater than that in the first cutting step.

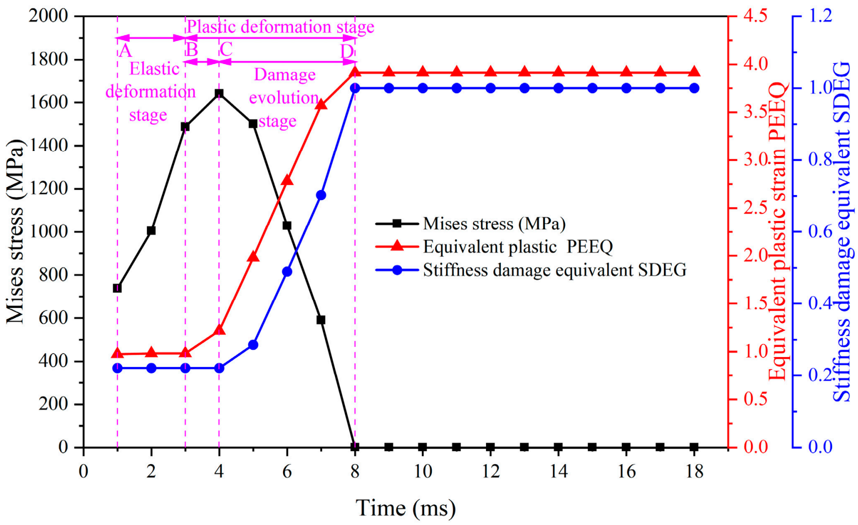

Figure 18. Evolution of stress, strain, and stiffness damage equivalent with time for the reference unit of the second cutting step.

3.5. Limitations and Outlook

Despite the progress made in this study, there are some limitations. In the cutting simulation, only the effects of different machining speeds and rake angles on residual stress were discussed, while no further analysis was performed on the effects of other tool geometry parameters and cutting parameters such as cutting thickness. And there is no research on systematic optimization parameters based on the simulation results. To address these limitations, future research should broaden the experimental scope to encompass the influence of multiple factors and devise optimization algorithms tailored for multi-step titanium alloy cutting parameters. In addition, for the multi-step simulation model, we should attempt to directly simulate the second step of machining by changing the properties of stress, strain and stiffness damage equivalent to the material to be cut, so as to improve the simulation efficiency and reduce the modeling workload.

4. Conclusions

This paper utilizes FEM to simulate the effect of cutting speed and tool rake angle on the residual stress on the machined surface. Additionally, the simulation analyzes the impact of the first cutting step on the second cutting step.

(1) The two-dimensional orthogonal cutting model of titanium alloy was carried out using Abaqus. The material cooling phase, unloading, and de-constraints were included to enhance the accuracy of multi-step cutting simulation. The correctness of the simulation model was verified by an orthogonal cutting test on the titanium alloy, and the relative error of cutting force was within 15%. The errors of the degree of serration ranged from −2.63 to −10.94%.

(2) The effect of different cutting parameters on residual stress was analyzed using simulation models. The results show that the residual compressive stress decreases and the residual tensile stress increases gradually with the increase in tool rake angle. When the tool rake angle is 15°, the tensile stress grows to 137 Mpa. The residual stress with the increase in cutting speed shows a similar trend with the rake angle. With the increase in surface depth, the residual compressive stress first increases and then decreases and gradually disappears beyond a certain depth.

(3) By extracting data from the reference unit of the simulation model, the change in Mises stress, equivalent plastic strain, and stiffness damage equivalent was analyzed during two cutting steps. The initial values of Mises stress, PEEQ, and SDEG for the first cutting step are 0, while for the second cutting step, the initial Mises stress is 738 MPa, the PEEQ is 0.97, and the SDEG is 0.221. Under the same conditions, the first

cutting step affects the initial values of indicators of the second cutting step, as well as the evolution time of them. As the cutting speed of the first cutting step increases, the Mises stress gradually increases, while the PEEQ and SDEG of the machined surface unit gradually decrease.

Author Contributions: Conceptualization, J.W. and A.L.; methodology, A.L.; software, J.Z.; validation, J.W., B.K. and S.W.; formal analysis, J.W.; investigation, B.K., S.W. and J.Z.; resources, B.K. and S.W.; data curation, J.Z. and A.L.; writing—original draft preparation, J.W.; writing—review and editing, B.K. and A.L.; visualization, S.W.; supervision, A.L. and B.K.; project administration, A.L.; funding acquisition, A.L. All authors have read and agreed to the published version of the manuscript.

Funding: This research was funded by the Natural Science Foundation of Shandong Province (ZR2021ME043), and the National Natural Science Foundation of China (51605260).

Institutional Review Board Statement: Not applicable.

Informed Consent Statement: Not applicable.

Data Availability Statement: The dataset used in this paper is available from the corresponding author upon request.

Conflicts of Interest: Authors Bo Kong and Shulei Wei were employed by the company Shelfoil Petroleum Equipment & Services Co., Ltd. The remaining authors declare that the research was conducted in the absence of any commercial or financial relationships that could be construed as a potential conflict of interest.

Nomenclature

The following parameters and abbreviations are used in this manuscript.

γ	Tool rake angle
v_1	Cutting speed of the first step
v_2	Cutting speed of the second step
a_c	Cutting thickness
σ	Flow stress of the workpiece material
ε	Equivalent plastic strain of the workpiece material
$\frac{\dot{\bar{\varepsilon}}}{\dot{\bar{\varepsilon}}_0}$	Plastic strain rate
$\dot{\bar{\varepsilon}}_0$	Reference strain rate
T_r	Room temperature (20 °C)
T_m	Melting temperature of the material
A	Yield strength
B	Hardening modulus
n	Strain hardening exponent
C	Strain rate sensitivity coefficient
m	Thermal softening coefficient
ρ	Density
E	Elastic Modulus
μ	Poisson Ratio
λ	Thermal conductivity
C_p	Specific Heat
w	Workpiece material damage parameter
$\Delta\bar{\varepsilon}$	Increment of equivalent strain of workpiece material
$\bar{\varepsilon}_f$	Equivalent strain of workpiece material
P	Average value of the three principal stress
$\bar{\sigma}$	Equivalent stress
D_1~D_5	Material failure parameters
σ_0	Yield stress
τ_f	Material experiences shear stress
τ_γ	Material shear yield strength

σ_n	Normal stress
μ	Friction factor
T	Temperature
$\dot{Q}$	Heat flow per unit volume
u_x	Transfer velocity of the moving heat source in the x direction
u_y	Transfer velocity of the moving heat sourcein the y direction
$\dot{Q}_p$	Volumetric heat flow rate from plastic deformation
η_p	Plastic deformation work conversion coefficient
J	Thermal work equivalence coefficient
$\bar{\varepsilon}$	Equivalent strain of the material in the cutting process
$\dot{Q}_f$	Volumetric heat flow rate from friction
v_{chip}	Tool-chip relative rate
η_f	Friction work conversion coefficient
f	Feed
G_s	The degree of serration
H	Height of top of tooth
C	Height of tooth valley
S_{11}	Stress along the X direction
S_{22}	Stress along the Y direction
S_{33}	Stress along the Z direction
S_{12}	Shear stress along the Y direction on the XY plane
FEM	Finite element method
PEEQ	Equivalent plastic strain
SDEG	Stiffness damage equivalent

References

1. Hai, N.A.N.; Cheng-mu, X.I.E.; Jia-qi, Z. Development and application of titanium alloy casting technology in China. *China Foundry* **2005**, *2*, 239–245.
2. Venkata Sivareddy, D.; Krishna, P.V.; Venu Gopal, A. Effect of Thermo-Mechanical Loading on Machining Induced Residual Stresses in Ultrasonic Vibration Assisted Turning of Ti6Al4V Alloy. *Proc. Inst. Mech. Eng. Part B J. Eng. Manuf.* **2022**, *236*, 1793–1806. [CrossRef]
3. Wang, Z.; Zhou, J.; Ren, J.; Shu, A. Predicting Surface Residual Stress for Multi-Axis Milling of Ti-6Al-4V Titanium Alloy in Combined Simulation and Experiments. *Materials* **2022**, *15*, 6471. [CrossRef] [PubMed]
4. Wu, H.B.; Zhang, S.J. 3D FEM Simulation of Milling Process for Titanium Alloy Ti6Al4V. *Int. J. Adv. Manuf. Technol.* **2014**, *71*, 1319–1326. [CrossRef]
5. Dong, P.; Peng, H.; Cheng, X.; Xing, Y.; Tang, W.; Zhou, X. Semi-Empirical Prediction of Residual Stress Profiles in Machining IN718 Alloy Using Bimodal Gaussian Curve. *Materials* **2019**, *12*, 3864. [CrossRef]
6. Ren, Z.; Zhang, X.; Wang, Y.; Li, Z.; Liu, Z. Finite Element Analysis of the Milling of Ti6Al4V Titanium Alloy Laser Additive Manufacturing Parts. *Appl. Sci.* **2021**, *11*, 4813. [CrossRef]
7. Li, S.; Han, J.; Yu, H.; Wang, J.; Lu, M.; Tian, Y.; Lin, J. Finite Element Investigation on Cutting Force and Residual Stress in 3D Elliptical Vibration Cutting Ti6Al4V. *Micromachines* **2022**, *13*, 1278. [CrossRef]
8. Outeiro, J.; Cheng, W.; Chinesta, F.; Ammar, A. Modelling and Optimization of Machining of Ti-6Al-4V Titanium Alloy Using Machine Learning and Design of Experiments Methods. *JMMP* **2022**, *6*, 58. [CrossRef]
9. Yao, C.F.; Yang, Z.C.; Huang, X.C.; Ren, J.X.; Zhang, D.H. The Study of Residual Stresses in High-Speed Milling of Titanium Alloy TC11. *AMR* **2012**, *443–444*, 160–165. [CrossRef]
10. Dehmani, H.; Salvatore, F.; Hamdi, H. Numerical Study of Residual Stress Induced by Multi-Steps Orthogonal Cutting. *Procedia CIRP* **2013**, *8*, 299–304. [CrossRef]
11. Sun, J.; Guo, Y. A comprehensive experimental study on surface integrity by end milling Ti–6Al–4V. *J. Mech. Work. Technol.* **2008**, *209*, 4036–4042. [CrossRef]
12. Matuszak, J.; Zaleski, K.; Zyśko, A. Investigation of the Impact of High-Speed Machining in the Milling Process of Titanium Alloy on Tool Wear, Surface Layer Properties, and Fatigue Life of the Machined Object. *Materials* **2023**, *16*, 5361. [CrossRef] [PubMed]
13. Zhang, R.; Li, A.; Song, X. Surface Quality Adjustment and Controlling Mechanism of Machined Surface Layer in Two-Step Milling of Titanium Alloy. *Int. J. Adv. Manuf. Technol.* **2022**, *119*, 2691–2707. [CrossRef]
14. Song, X.; Li, A.; Lv, M.; Lv, H.; Zhao, J. Finite Element Simulation Study on Pre-Stress Multi-Step Cutting of Ti-6Al-4V Titanium Alloy. *Int. J. Adv. Manuf. Technol.* **2019**, *104*, 2761–2771. [CrossRef]
15. Liu, C.R.; Guo, Y.B. Finite Element Analysis of the Effect of Sequential Cuts and Tool–Chip Friction on Residual Stresses in a Machined Layer. *Int. J. Mech. Sci.* **2000**, *42*, 1069–1086. [CrossRef]

16. Aassif, E.; Salvatore, F.; Hamdi, H. Multistep Hybrid Approach Applied to Material Removal Operation Using Cutting Tool. In Proceedings of the 21st French Congress of Mechanics, Bordeaux, France, 26–30 August 2013.
17. Wu, H.; To, S. Serrated Chip Formation and Their Adiabatic Analysis by Using the Constitutive Model of Titanium Alloy in High Speed Cutting. *J. Alloys Compd.* **2015**, *629*, 368–373. [CrossRef]
18. Zhang, Y.; Mabrouki, T.; Nelias, D.; Gong, Y. FE-Model for Titanium Alloy (Ti-6Al-4V) Cutting Based on the Identification of Limiting Shear Stress at Tool-Chip Interface. *Int. J. Mater. Form.* **2011**, *4*, 11–23. [CrossRef]
19. Meng, L.; Zhang, X.; Srivastava, A.K. Rapid Finite Element Prediction on Machining Process. In Proceedings of the ASME 2013 International Manufacturing Science and Engineering Conference collocated with the 41st North American Manufacturing Research Conference, Madison, WI, USA, 10–14 June 2013; Volume 1, p. V001T01A020.
20. Johnson, G.R.; Cook, W.H. A Constitutive Model and Data for Metals Subjected to Large Strains, High Strain Rates and High Temperatures. *Eng. Fract. Mech.* **1983**, *21*, 541–548.
21. Lee, W.-S.; Lin, C.-F. High-Temperature Deformation Behaviour of Ti6Al4V Alloy Evaluated by High Strain-Rate Compression Tests. *J. Mater. Process. Technol.* **1998**, *75*, 127–136. [CrossRef]
22. Schulz, H.; Abele, E.; Sahm, A. Material aspects of chip formation in HSC machining. *CIRP Ann.* **2001**, *50*, 45–48. [CrossRef]
23. Wang, Q.; Liu, Z.; Wang, B.; Song, Q.; Wan, Y. Evolutions of Grain Size and Micro-Hardness during Chip Formation and Machined Surface Generation for Ti-6Al-4V in High-Speed Machining. *Int. J. Adv. Manuf. Technol.* **2016**, *82*, 1725–1736. [CrossRef]
24. Zorev, N.N. Inter-Relationship between Shear Processes Occurring along Tool Face and Shear Plane in Metal Cutting. In Proceedings of the International Production Engineering Research Conference, Pittsburgh, PA, USA, 9–12 September 1963; Volume 49.
25. Wang, B.; Liu, Z. Shear Localization Sensitivity Analysis for Johnson–Cook Constitutive Parameters on Serrated Chips in High Speed Machining of Ti6Al4V. *Simul. Model. Pract. Theory* **2015**, *55*, 63–76. [CrossRef]
26. Wang, F.; Liu, Y.; Zhang, Y.; Tang, Z.; Ji, R.; Zheng, C. Compound Machining of Titanium Alloy by Super High Speed EDM Milling and Arc Machining. *J. Mater. Process. Technol.* **2014**, *214*, 531–538. [CrossRef]
27. Wang, F.; Zhao, J.; Li, A.; Zhu, N.; Zhao, J. Three-Dimensional Finite Element Modeling of High-Speed End Milling Operations of Ti-6Al-4V. *Proc. Inst. Mech. Eng. Part B J. Eng. Manuf.* **2014**, *228*, 893–902. [CrossRef]
28. Trent, E.M.; Wright, P.K. *Metal Cutting*, 4th ed.; Butterworth-Heinemann: Woburn, MA, USA, 2000.
29. Soo, S.L.; Dewes, R.C.; Aspinwall, D.K. 3D FE Modelling of High-Speed Ball Nose End Milling. *Int. J. Adv. Manuf. Technol.* **2010**, *50*, 871–882. [CrossRef]
30. Wang, F. *Research on Cutting Mechanism and Numerical Analysis of Micro-Structured Functional Surface Driven by Information Storage*; Shandong University: Jinan, China, 2013.
31. Meng-Yang, Q.; Bang-Yan, Y.; Xiong, J.; Ai-Dong, H. Experimental investigation of residual stress distribution in pre-stress cutting. *Int. J. Adv. Manuf. Technol.* **2012**, *65*, 355–361. [CrossRef]
32. Yang, D.; Liu, Z.; Ren, X.; Zhuang, P. Hybrid Modeling with Finite Element and Statistical Methods for Residual Stress Pre-diction in Peripheral Milling of Titanium Alloy Ti-6Al-4V. *Int. J. Mech. Sci.* **2016**, *108–109*, 29–38. [CrossRef]
33. Wang, S.; Ai, X.; Zhao, J.; Li, Z.; Meng, H. Effect of Cutting Speed on Residual Stress of Workpiece by Using FEM. *Tool Eng.* **2005**, *9*, 33–36. [CrossRef]
34. Guo, P.; Wang, S.; Li, M.; Zhang, Z. Finite Element Solution for Residual Stress in Machined Layerafter Cutting Process. *Manuf. Technol. Mach. Tool* **2007**, *1*, 38–40. [CrossRef]

materials

Article

Controllable Preparation of Fused Silica Micro Lens Array through Femtosecond Laser Penetration-Induced Modification Assisted Wet Etching

Kaijie Cheng [1,2], Ji Wang [1,2,*], Guolong Wang [2,3], Kun Yang [1,2] and Wenwu Zhang [2,*]

[1] Center of Materials Science and Optoelectronics Engineering, University of Chinese Academy of Sciences, Beijing 100049, China; chengkaijie@nimte.ac.cn (K.C.)
[2] Research Center for Laser Extreme Manufacturing, Ningbo Institute of Materials Technology & Engineering, Chinese Academy of Sciences, Ningbo 315201, China; wangguolong@nimte.ac.cn
[3] College of Mechanical Engineering, Zhejiang University of Technology, Hangzhou 310014, China
* Correspondence: wji@nimte.ac.cn (J.W.); zhangwenwu@nimte.ac.cn (W.Z.)

Abstract: As an integrable micro-optical device, micro lens arrays (MLAs) have significant applications in modern optical imaging, new energy technology, and advanced displays. In order to reduce the impact of laser modification on wet etching, we propose a technique of femtosecond laser penetration-induced modification-assisted wet etching (FLIPM-WE), which avoids the influence of previous modification layers on subsequent laser pulses and effectively improves the controllability of lens array preparation. We conducted a detailed study on the effects of the laser single pulse energy, pulse number, and hydrofluoric acid etching duration on the morphology of micro lenses and obtained the optimal process parameters. Ultimately, two types of fused silica micro lens arrays with different focal lengths but the same numerical aperture (NA = 0.458) were fabricated using the FLPIM-WE technology. Both arrays exhibited excellent geometric consistency and surface quality (Ra~30 nm). Moreover, they achieved clear imaging at various magnifications with an adjustment range of 1.3×~3.0×. This provides potential technical support for special micro-optical systems.

Keywords: micro lens array; femtosecond-laser-induced modification; wet etching; imaging; fused silica

1. Introduction

With the continuous development of modern optoelectronic technology, the demand for device integration, miniaturization, and multifunctionality in professional micro optical systems (MOSs) is becoming increasingly urgent. Among them, the micro lens arrays (MLAs), as a key optical component, can provide benefits, such as compact and lightweight designs, multifunctionality, and exceptional integration capability [1–3], for MOS systems, thus receiving increasing attention. The MLAs find applications across various domains, including optical imaging [4–6], emerging energy technologies [7,8], and cutting-edge display systems [9,10].

In the field of advanced technological applications, the fabrication techniques for MLAs have faced increasingly stringent demands. Traditional methods for MLA fabrication include photolithography [11–13], thermal reflow [14], electron beam lithography [15], and self-assembly [16]. However, photolithography and electron beam lithography are costly, complex in the process, and inefficient in production. Thermal reflow exhibits poor flexibility, low processing precision, and complex procedures, and is primarily applicable to polymers [17,18]. Fused silica is a typical hard and brittle material, which has excellent chemical stability, mechanical properties, and an extremely low coefficient of thermal expansion compared with materials like polydimethylsiloxane (PDMS) and polymethyl methacrylate (PMMA). Moreover, it boasts high transparency in the ultraviolet-to-near-infrared spectrum and an exceptionally stable refractive index, making it an ideal material for MLAs used in MOSs. Nevertheless, its high stability and fragility pose challenges for achieving high-precision processing.

With the development of laser technology, ultrafast lasers have emerged as an effective method for micro/nano fabrication [19–22]. Femtosecond (Fs) lasers have the advantages of extremely short pulses (~10^{-15} s), high peak power (10^{22} W/cm^2), and strong controllability, which allows them to direct writing and modify materials within transparent materials [23]. However, it is difficult to avoid thermal effects during the direct etching of quartz using a femtosecond laser, which will affect the quality and surface characteristics of the processing, hindering the creation of high-quality MLAs. For a long time, how to further improve the surface quality and preparation controllability of MLAs has been a challenge faced by researchers. Therefore, this limits the application of femtosecond laser processing as a single technological means in the manufacturing of micro lens arrays.

In recent years, researchers have improved many new processes based on femtosecond lasers. Liu et al. [19] successfully prepared uniformly arranged MLAs on a silicon surface using femtosecond laser-assisted plasma-etching technology (FLPE). However, this method exhibits extremely high sensitivity to experimental conditions and is costly, which poses great challenges for industrial applications. Femtosecond-laser-induced modification-assisted wet etching (FLIM-WE) has high processing efficiency, a low cost, and relatively relaxed environmental requirements [24–26], making it a more ideal method. This method is based on the deposition of femtosecond laser energy inside the material, which leads to a phase transition of the material. Due to the extremely high peak power of femtosecond lasers, atoms or molecules in materials absorb light energy and undergo nonlinear optical effects, such as photoionization and thermalization [27,28]. These effects can cause local high temperatures and pressures in materials, resulting in phenomena, such as densification, defect formation, and changes in the absorption rate [29,30]. The modified area can achieve rapid and high-quality structural etching through corrosion of the corresponding solvent. Currently, the FLIM-WE method has been widely used by researchers for the preparation of MLAs with a high surface quality [31–33]. Feng Chen et al. [34] fabricated a sub-millimeter-sized MLA on a silicon dioxide substrate with a variable NA, using femtosecond laser linear scanning modification-assisted wet etching. Generally speaking, the size of micro lenses is closely related to the area of the laser-modified region. Nevertheless, the majority of existing research employs a top-down femtosecond laser processing approach. In the process, the preceding laser pulse induces modifications to the material's surface, creating a previously modified layer. Defects, such as voids within this modified layer, can affect the absorption and scattering of subsequent laser pulses on the material's surface, thereby impacting the controllability of the interaction between subsequent pulses and the material significantly. Therefore, challenges persist in achieving size controllability, and there is a lack of foundational process explorations.

In this paper, we proposed a method based on femtosecond laser back-facing penetrating single-point exposure for material modification. Specifically, we adopted a bottom-up approach to achieve back-facing penetration-induced modification. Subsequent pulses directly interact with the material without passing through the modified layer, which is induced by the initial pulse. This approach significantly enhanced the controllability of MLA fabrication. By analyzing the influence of laser parameters on inducing modified pores, we have identified the optimal process parameters. By changing the area of the modified region, the geometric morphology of the micro lens was altered to achieve the goal of controlling the NA. Then, combined with hydrofluoric acid (HF) etching, we have realized the controllable fabrication of fused silica MLAs with a fixed NA (0.458) and variable focal length efficiently, by optimizing the laser parameters and etching time. And both types of the MLAs with a size of around 40 microns demonstrated excellent imaging capabilities, highlighting the potential applications of this method in the preparation of special MOSs.

2. Experiment

2.1. Method and Material

The FLIM-WE preparation method for a micro lens array (MLA) mainly includes the following three steps, as shown in Figure 1a: femtosecond laser penetration-induced modification (FLPIM) of fused silica (step 1), wet etching assisted by a ultrasonic water bath to remove the modified surface layer (step 2), and subsequent surface cleaning (step 3).

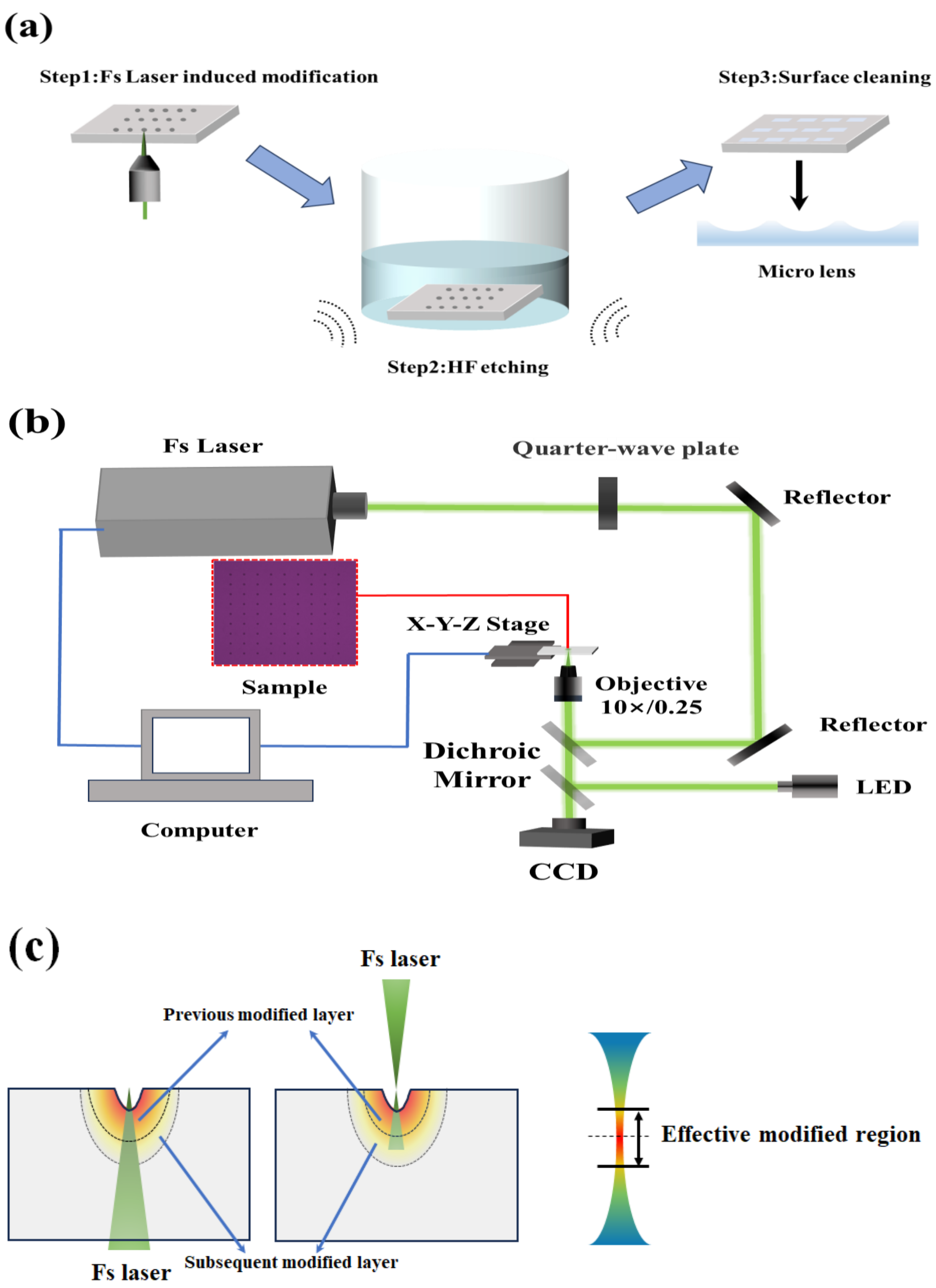

Figure 1. Experimental setup and method. (**a**) Steps in the fabrication of micro lens array. Step 1: using femtosecond laser-induced modification, step 2: place the modified sample in HF acid solution for ultrasonic-assisted wet etching, step 3: surface cleaning of MLA, the illustration pointed to by the black arrow shows a vertical-sectional schematic of the morphology of the microlens array; (**b**) schematic diagram of device femtosecond laser-induced modification of fused silica; (**c**) comparison between penetration FLPIM method and traditional top-down modification method.

Initially, the back facing of the fused silica sample underwent induced modification using femtosecond laser single-point exposure, which generated micro lens structures with each exposure. Then, HF acid solution was used to wet etch the modified micro lens structure. The concentration of etching solution used in the experiment was 20%. We mixed 15 mL of a hydrogen fluoride (40% concentration, analytical grade) solution and 15 mL of deionized water with a ratio of 1:1 in a polytetrafluoroethylene container. The modified samples were then immersed in the etching solution within a polytetrafluoroethylene container and subjected to wet etching under ultrasonic water bath conditions to form the final micro lens. In the experiment, the power of the ultrasonic equipment (JM-03D-80, Skymen, China) was set at 80 W, the ultrasonic frequency was 40 kHz, and the water bath temperature was 20 °C. Finally, the processed samples were subjected to ultrasonic cleaning to remove residual etching residues. During the whole experiment, the ambient temperature was controlled within 25 ± 2 °C, and the humidity was controlled within 50 ± 5%. In addition, the material used to prepare MLAs in this experiment was an ultraviolet fused silica glass thin plate (0.3 mm thickness, JGS1 brand).

2.2. Experimental Setup

The experimental setup for FLPIM is depicted in Figure 1b. The laser beam from the femtosecond laser (FemtoYL-Green, YSL Photonics, Wuhan, China, laser wavelength of 515 nm, pulse frequency of 25 kHz, pulse width of ~373 fs) passed through a quarter-wave plate, then through a reflection mirror group and a dichroic mirror, and entered into the microscope objective (10×, NA 0.25). The polarization state of the laser beam emitted by the laser was vertical polarization. We rotated the angle of the optical axis of the quarter wave plate to modulate linearly polarized light into circularly polarized light. The light beam focused by the microscope objective traveled from bottom to top, penetrating the interior of the sample. Then, the focus shifted to the back-facing surface of the sample. A CCD sensor was used for monitoring the laser exposure process and finding the focal plane. The sample moved downwards along the Z-axis. If the CCD observed two focal points, then the plane where the second focal point located is the back-facing upper surface to be induced for modification. This penetration-induced modification method will effectively avoid the absorption and scattering effects of the modified layer generated by the previous pulse on the subsequent pulse.

As shown in Figure 1c, we designed a bottom-up penetration-induced modification processing method. Firstly, the back surface of the sample is modified by a focused femtosecond laser to form induced modification holes. The material under the hole undergoes phase transition and defects, forming the previous modified layer. Next, the subsequent laser pulses continue to penetrate the material, forming a new layer of a modified area within it. However, in the traditional top-down surface treatment method, the following laser pulses inevitably need to pass through the previous modified layer and modified hole. Only then can the subsequent modified layer be formed inside the material. Obviously, this improved method effectively avoids the nonlinear effects of the previously modified layer on the subsequent pulses (including light absorption and scattering), thereby improving the controllability of the modification effect.

This device controlled the laser power used for inducing modification by adjusting the current through a computer. At the same time, the computer coordinated the movement of the X-Y-Z stage to adjust the pulse state of the emitted laser through the phase-sensitive optical (PSO) function. When the X-Y-Z stage completed the specified movement distance, PSO controlled the femtosecond laser to output pulses for the FLPIM process based on the pre-set current and pulse quantity by the computer.

Characterization of the fabricated micro lens morphology was performed using a laser scanning confocal microscope (LSCM, VK-X200, Keyence, Japan). The HF solution etching process lasted for 150 min, with samples retrieved for morphology observation and analysis every 60 min.

3. Results and Discussion

We designed experiments to investigate the effects of the laser pulse energy, pulse quantity, and HF acid etching duration on the geometric dimensions of the micro lens morphology, in order to find suitable process intervals. Then, we prepared MLAs based on process parameters and measured their size and micro imaging performance.

3.1. Influence of Laser Parameters on Induced Modified Holes

We investigated the impact of varying the number of laser pulses (20–100 pulses) and the energy during the manufacturing process of micro modified holes on fused silica surfaces, and presented our findings in Figure 2. The micro modified holes formed are elliptical in shape, with the length of the minor and major axes represented on the vertical axes of Figures 2b and 2c, respectively.

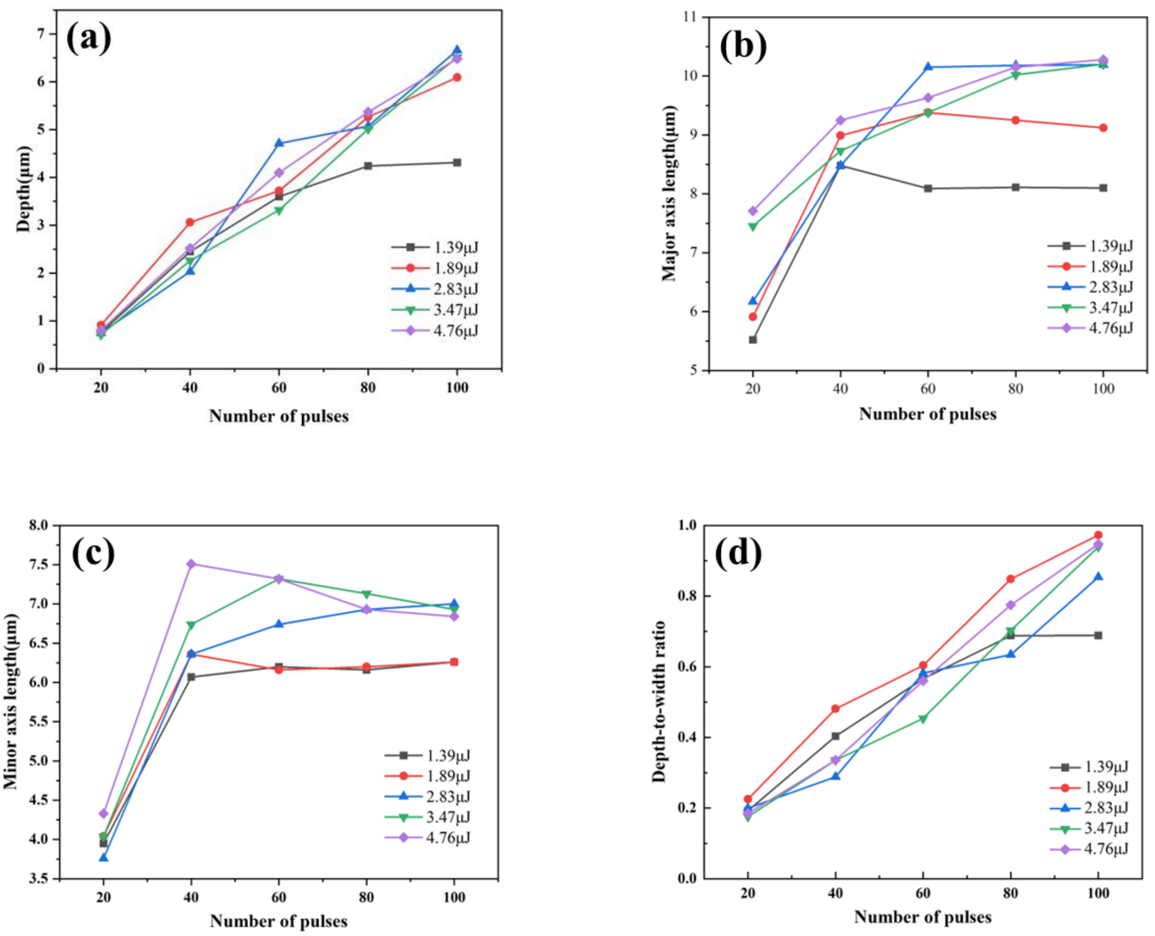

Figure 2. Influence of laser parameters on micro modified hole dimensions. (**a**) Variation in the depth of the modified holes; (**b**) variation in major axis length of the modified holes; (**c**) variation in minor axis length of the modified holes; (**d**) variation in depth-to-diameter ratio of the modified holes.

Figure 2a illustrates that under identical energy conditions, the etching depth of the micro lens increases notably with higher pulse counts. Furthermore, with elevated pulse energies, the rate of etching depth augmentation also escalates proportionally. At a single pulse energy of 1.39 μJ, minimal changes in the etching depth are observed. Whereas at 1.89 μJ, the depth increases sharply from 0.91 μm to 6.09 μm with an increasing pulse count. This means that in order to achieve precise control of the modification depth, energy exceeding 1.89 uJ cannot be used. Nevertheless, the maximum etching depth does not escalate indefinitely with higher pulse numbers. Even with a pulse energy increase to approximately 2.5 times (from 1.39 μJ up to 4.76 μJ) at pulse numbers of 100, the maximum etching depth only marginally increased from 6.0 μm to 6.8 μm.

Figure 2b,c depict that when the pulse count is below 40, both the major and minor axis lengths of the micro lens significantly increase with additional pulses. However, 40 pulses are the turning point. When beyond 60 pulses, these dimensions stabilize. This phenomenon can be attributed to the widening of the micro-hole surface area, where the laser edge energy falls below the material ablation threshold, thereby reducing the fused silica-removal capability. Consequently, further dimensional changes cease despite continued laser exposure on the fused silica pits. That is to say, there is a non-linear relationship between the depth of modified pores and the number of pulses. As the number of pulses increases, the lateral dimension of the modified holes will gradually reach its limit.

Figure 2d reveals that at a single pulse energy of 1.39 μJ, when the number of pulses is less than 80, the depth-to-diameter ratio of the micro modified holes increases linearly with the pulse count. Meanwhile, micro holes modified with 80 and 100 pulses exhibit nearly identical depth-to-diameter ratios, approximately 0.69. At higher single pulse energies of 1.89 μJ and above, the depth-to-diameter ratio also increases linearly with the pulse count, approaching 0.9 at 100 pulses. However, a larger depth-to-diameter ratio for the micro lens implies reduced curvature, leading to diminished magnification in microscopic imaging and increased distortion of the original image. Addressing these challenges may necessitate additional optical design strategies to mitigate substantial distortion effects [35].

In conclusion, taking into account these observation results, our study has discovered excellent laser parameters, namely the use of lower pulse energy (1.39 μJ–1.89 μJ) and a moderate number of pulses (60–80) to prepare MLAs.

3.2. Influence of Wet Etching Time on the Formation of Micro Lenses

According to Step 2, we explored the influence of the HF solution etching time on the dimensions and surface quality of the micro lens. Using a femtosecond laser with a single pulse energy of 1.39 μJ and 60 pulses, the material underwent modification, followed by observing the morphology changes of the micro lens after etching in the HF solution for different durations, as depicted in Figure 3. The etching times in Figure 3a–d are 0, 60, 120, and 150 min, respectively.

Initially, the morphology around the micro lens appears disorderly with a rough surface (Figure 3a). As the etching time progresses, the diameter of the micro lens gradually increases, approaching a perfect circular contour. Early in the etching process, rough striped structures are visible inside the micro lens (shown in Figure 3b,c). With prolonged etching durations, the etching process reaches saturation, and the internal striped structures gradually disappear, leading to a smoother surface morphology. This indicates that complete etching of the laser-modified region has occurred in the HF acid solution, when the etching time reaches 150 min.

Figure 3e illustrates the transition of the HF solution from an initially anisotropic to an isotropic behavior. Notably, significant differences in etching rates are observed between the regions modified via femtosecond laser treatment and those that remain unmodified. Regarding the contour width, the HF solution exhibits an efficient etching capability and rapid etching rate on the sidewalls formed through femtosecond laser modification. After 120 min, the modified areas begin to diminish, resulting in a gradual slowdown in the etching rate for the contour width. In terms of the etching depth, the modified region at the bottom of the micro lens is rapidly removed by the HF solution, achieving complete etching within the initial 60 min. As time went on, the etching depth hardly changed. Obviously, the etching rate in the vertical direction is much higher than that in the radial direction.

This difference is attributed to the fact that the femtosecond laser modification intensity is mainly concentrated in the vertical direction. the strongly induced modified region is primarily confined within the beam waist, resulting from the direct interaction between the femtosecond laser and the material. In contrast, the modification in the horizontal direction is mainly influenced by refracted light beams, which are scattered by the modified region in the vertical direction. Due to the attenuation of the energy of these refracted beams, the modification effect in the horizontal direction is not as strong as that in the vertical direction. Consequently, during etching with HF acid, a faster etching rate is observed in the vertical direction. As the etching progresses, the area exposed to the HF solution exhibits isotropic etching characteristics similar to the original material. At this point, wet etching has been completed. Only by achieving complete wet etching can micro lenses with extremely low surface roughness be obtained.

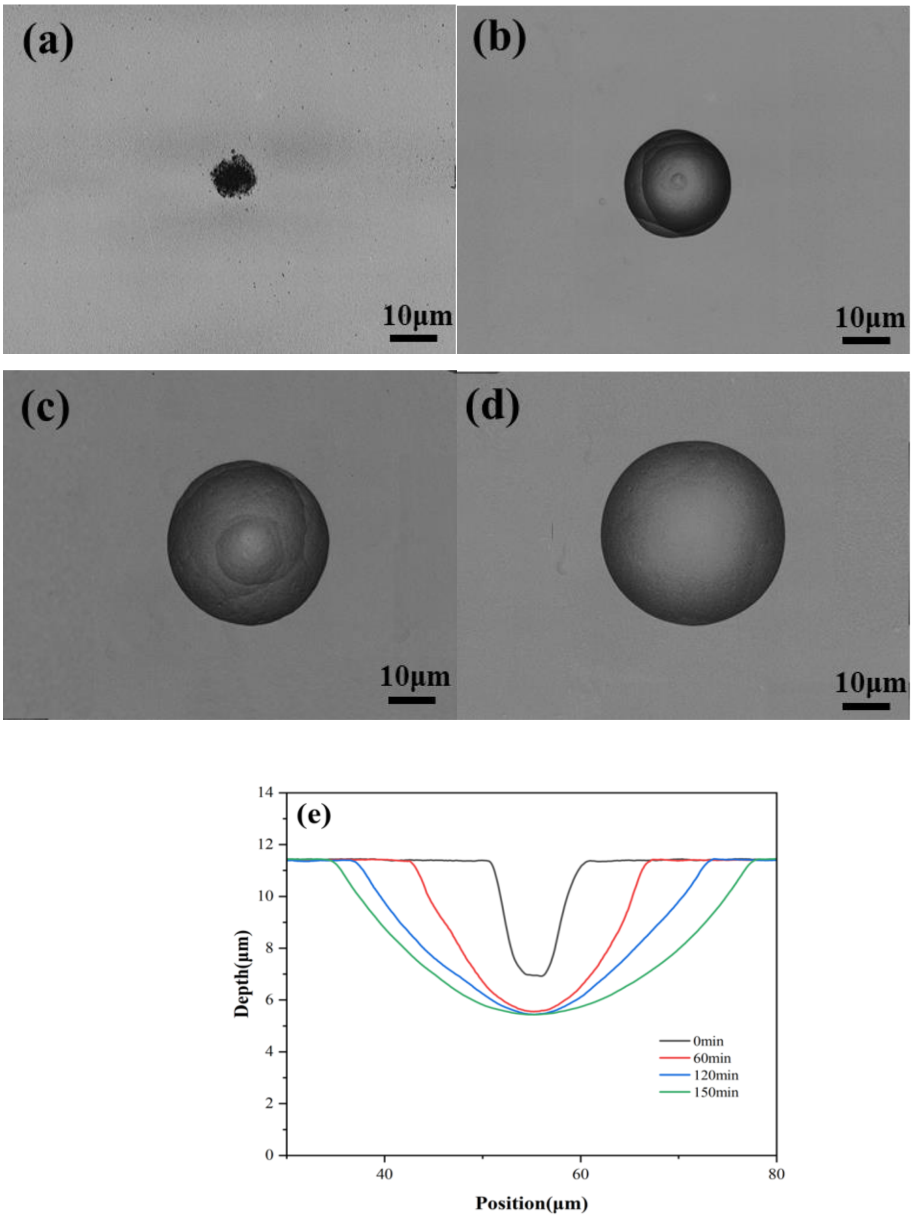

Figure 3. Morphological changes of micro lens under different HF solution etching times. (**a**) 0 min; (**b**) 60 min; (**c**) 120 min; (**d**) 150 min, scale bar in Figure 3a,b is 10 μm; (**e**) variation in micro lens contour profiles with the etching time.

3.3. Controlled Fabrication of the Micro Lens

Furthermore, we prepared individual micro lenses. Under constant laser energy conditions, the formation of micro lens contours can be precisely regulated by varying the number of laser pulses. As depicted in Figure 4a,b, the depths of the micro lenses increase linearly with pulse numbers, and the measurement results are 2.3 μm, 4.05 μm, 6.05 μm, 8.06 μm, and 9.84 μm, corresponding to pulse numbers of 20, 40, 60, 80, and 100, respectively. Similarly, the diameter of the micro lens also increases approximately linearly with an increase in the number of pulses. Under different pulse numbers (20–100), the diameters of the micro lens achieved are measured to be 23.91 μm, 32.76 μm, 39.05 μm, 44.57 μm, and 48.04 μm, respectively.

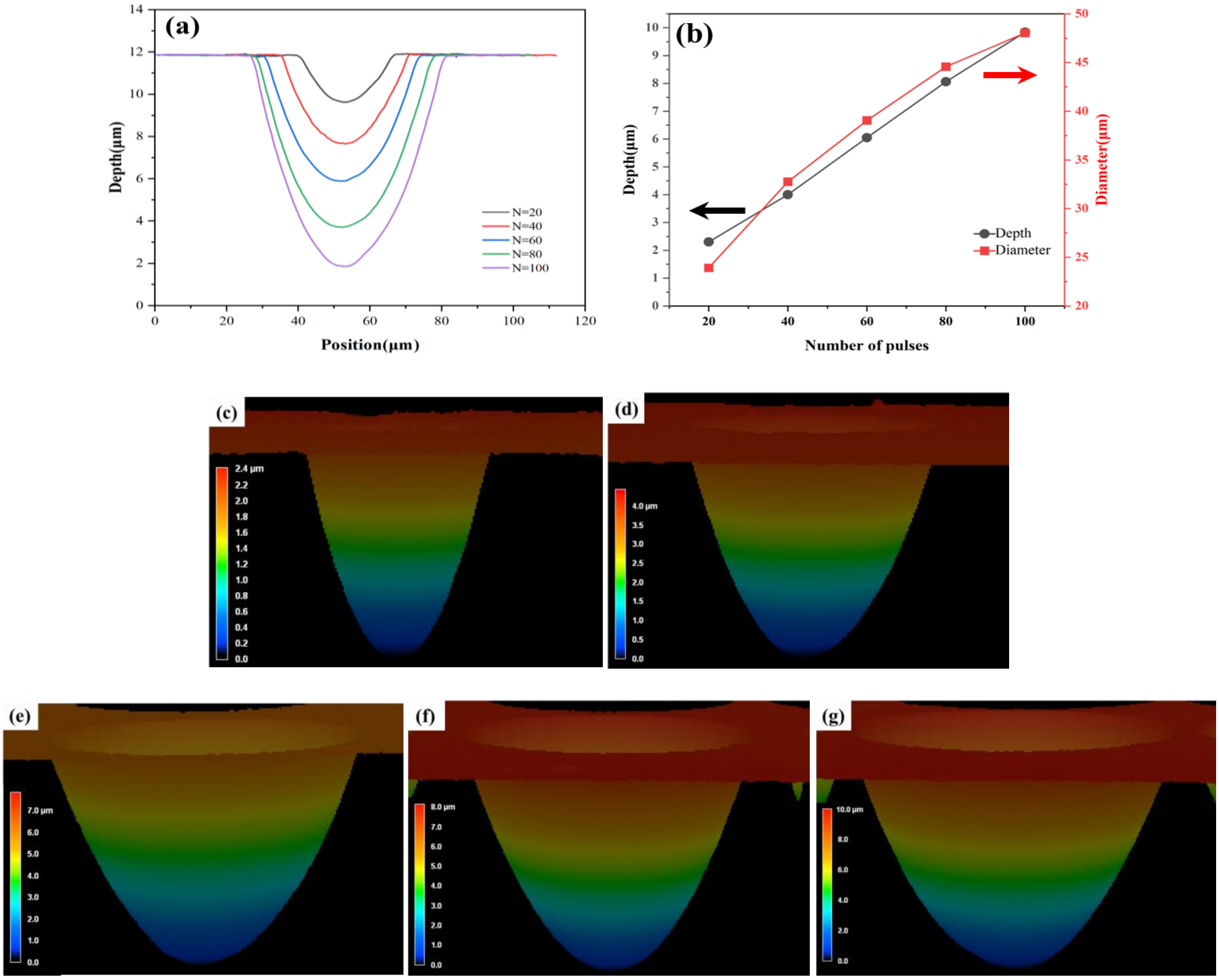

Figure 4. Controlled fabrication of micro lens profiles. (**a**) Profile curves of micro lens fabricated under different pulse numbers; (**b**) depth and diameter of the micro lens fabricated under different pulse numbers. The black arrow represents the depth curve of the left coordinate axis, and the red arrow represents the diameter curve of the right coordinate axis; (**c**–**g**) three-dimensional profiles of micro lens fabricated under different pulse numbers: (**c**) 20 pulses; (**d**) 40 pulses; (**e**) 60 pulses; (**f**) 80 pulses; (**g**) 100 pulses.

In addition, higher single pulse energies lead to an increased depth and width of the micro lens profiles. This is due to the enlarging of the laser processing area on the surface of fused silica, resulting in a larger etched area. Figure 4c–g present the three-dimensional morphology of an individual micro lens etched with pulse numbers ranging from 20 to 100. It is worth noting that regardless of the number of pulses, each micro lens exhibits smooth contours and excellent surface quality. This is the result of complete etching. That is to say, we have found suitable laser parameters and the wet etching time. By modulating the number of pulses, we can effectively prepare the expected size and shape of the micro lens without affecting its surface smoothness.

3.4. Fabrication of MLAs

Based on the aforementioned experimental findings, we successfully produced two types of 9 × 9 micro lens arrays, depicted in Figure 5a,b. Each MLA consists of 81 micro lenses, covering an area of approximately 0.16 mm^2. The center-to-center spacing of each micro lens is 50 μm. The micro lens exhibits perfectly circular and uniform surface profiles. The contour measurements of these arrays are presented in Figure 5c. Among them, the red curve in Figure 5c shows the measurement result of the micro lens profiles in the solid box area of Figure 5a.

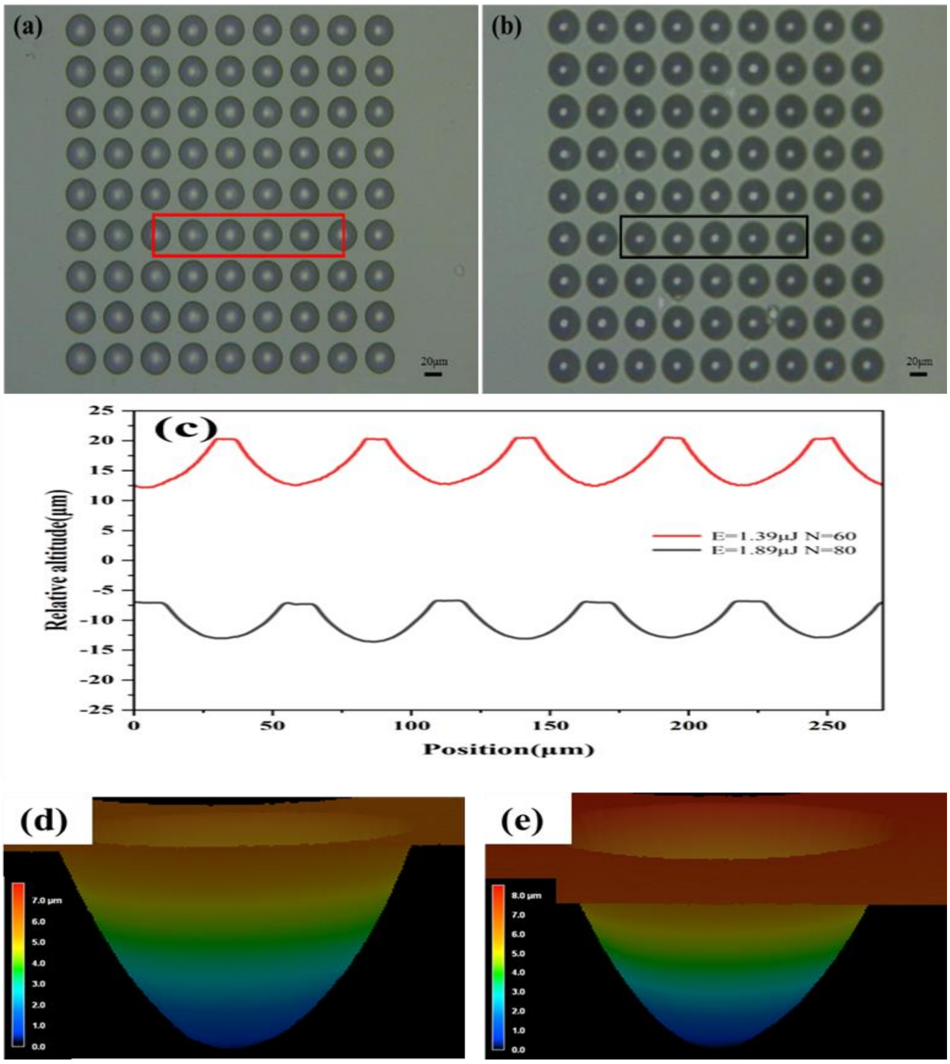

Figure 5. MLA schematics. (**a**) Micro lens array fabricated with a single pulse energy of 1.39 μJ and 60 pulses, scale bar: 20 μm; (**b**) micro lens array fabricated with a single pulse energy of 1.89 μJ and 80 pulses, scale bar: 20 μm; (**c**) profiles of the two micro lens arrays. The red curve represents the profile measurement result of the micro lenses within the red box in Figure 5a. The gray curve represents the profiles measurement result of the micro lenses within the gray box in Figure 5b; (**d**,**e**) three-dimensional views of individual micro lens structures from the two micro lens arrays.

The results show that using a single pulse energy of 1.39 μJ and 60 pulses, the fabricated micro lenses have a diameter of approximately 39.7 μm and a depth of about 19.5 μm. Using the roughness measurement module of an LSCM, ten micro lenses are selected to measure the roughness of the bottom of the micro lenses (each measurement area is 1 μm × 1 μm). The measurement result shows that the average roughness is about 30 nm. The gray curve in Figure 5c, corresponding to the measurement result within the solid box area of Figure 5b, reveals that using a single pulse energy of 1.89 μJ and 80 pulses, the fabricated micro lens has a diameter of about 44.2 μm and a depth of approximately 22.8 μm, with an average surface roughness of approximately 50 nm (the measurement method is the same as above). Obviously, as the power and number of pulses increase, the depth and diameter of the implemented micro lens array also increase accordingly, as we have learned from our previous process research. Figure 5d,e depict the three-dimensional morphology of a representative micro lens from each array type captured under laser scanning confocal microscopy. Both arrays demonstrate exceptional surface morphology, smoothness, and uniformity. In both arrays, each lens exhibits a consistent geometric shape without any obvious visual defects. These superior characteristics are attributed to the minimal scattering observed during femtosecond laser processing and the meticulous optimization of process parameters [36].

3.5. Imaging Performance Test of MLAs

As we know, the image plane of a concave lens is in the negative direction. The expressions for the focal length f and numerical aperture (NA) that determine the imaging performance of micro concave lenses are as follows [6]:

$$f = -\frac{h^2 + \left(\frac{D}{2}\right)^2}{2h(n-1)} \tag{1}$$

$$NA = \frac{D}{2|f|} \tag{2}$$

where h is the height of the micro lens, D is the diameter, n is the refractive index of the micro lens material, f is the focal length, and NA is the numerical aperture of the micro lens. The focal lengths of the micro lens arrays in Figure 5a,b are calculated to be −43.303 μm and −48.223 μm, respectively. It is worth noting that the numerical aperture (NA) of both MLAs is 0.458. That is to say, this study can also achieve a micro lens array with a constant aperture and variable focal length.

Finally, imaging performance tests were conducted with the optical setup depicted in Figure 6a. A halogen lamp served as the illumination source, directing light through a brown mask featuring a transparent letter 'N' (approximately 7 mm in size on the letter mask). The MLAs fabricated focused this light onto an objective lens positioned opposite, enabling a CCD to capture bright-field and dark-field images of the letter 'N' on the pseudo-focal plane of the MLAs without inserting the letter mask, and we observed the transparency of two manufactured MLAs, as shown in Figure 6b,c. Obviously, each micro lens structure in the array has good transparency and exhibits excellent roundness in their contours. When inserting the letter mask template, the imaging effects of the two MLAs are shown in Figure 6(d1–d3) and Figure 6(e1–e3), respectively. Both demonstrate clear imaging capabilities overall, with each micro lens exhibiting nearly consistent imaging performance within the same array, which indirectly indicates excellent uniformity of the array structure. Using a higher magnification 50× objective lens for local observations, it was found that the imaging performance of a single micro lens is also satisfactory, as depicted in Figure 6(d2,e2). By shifting the letter mask upward to adjust the relative distance between the mask and MLA, the imaging effect of the letter "N" can be further magnified, while maintaining clear imaging quality, as shown in Figure 6(d3,e3). Compared with Figure 6(d2), the imaging magnification of Figure 6(d3) has increased by about 3.0 times. In addition, the imaging magnification of Figure 6(e3) has increased by about 1.3 times compared to Figure 6(e2).

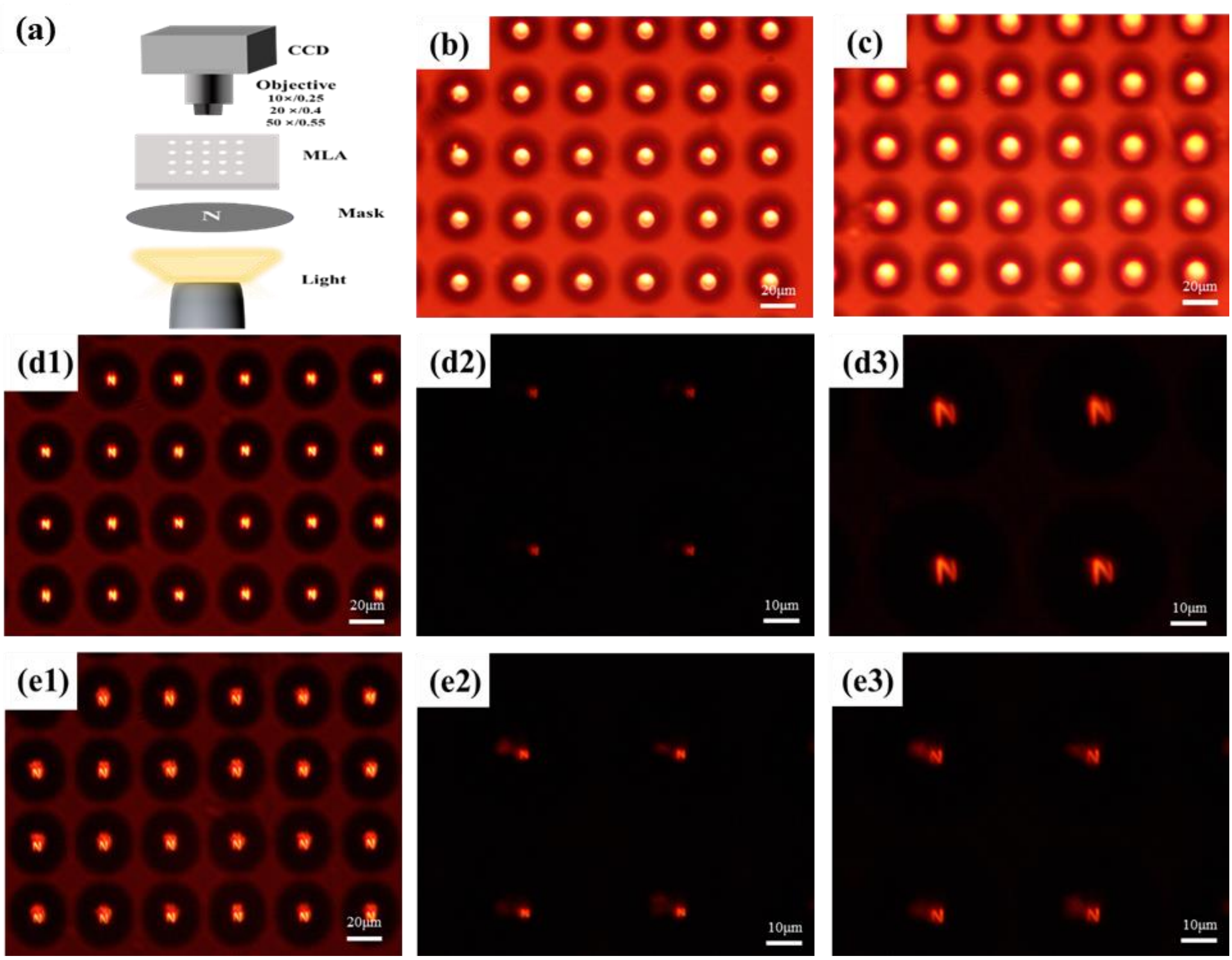

Figure 6. Imaging performance testing of the two MLAs shown in Figure 5a,b. (**a**) Optical path diagram of the imaging analysis system. The system is equipped with optional imaging objectives; (**b**,**c**) place the MLA shown in Figure 5a,b in the imaging analysis system, respectively. The CCD imaging results without the mask using an imaging objective of 20×. The scales are 20 µm; (**d1**–**d3**) CCD imaging results of the MLA shown in Figure 5a after inserting the mask N. The objective lenses used are 20×, 20×, and 50× in sequence. Among them, Figure 6(**d3**) is the imaging pattern obtained by moving the mask upwards based on Figure 6(**d2**). (**e1**–**e3**) CCD imaging results under the MLA shown in Figure 5b using the same testing method, corresponding to Figure 6(**d1**)–(**d3**). The scales in Figure 6(**d1**,**e1**) are 20 µm. The scales in Figure 6(**d2**,**d3**) and Figure 6(**e2**,**e3**) are 20 µm.

4. Conclusions

In summary, further improving the controllability of MLA preparation technology has become urgent in the new generation of MOSs. To achieve this, we introduced an innovative method called femtosecond laser penetration-induced modification-assisted wet etching (FLPIM-EL). Utilizing this technique, we successfully fabricated MLAs of tens of microns on the surface of fused silica. These micro lenses exhibited excellent morphology and smooth surfaces. In the first step, known as step 1-FLPIM, a penetrating induced modification method was adopted. This approach effectively mitigated the absorption and scattering effects caused by the modified layer from previous laser pulses, enhancing the overall controllability of the process. In step 2, an HF solution was utilized to wet etch the modified layer completely. By adjusting the single pulse energy and pulse number of the laser, the size of the laser-modified regions was precisely controlled, thereby regulating the dimensions and depths of the micro lens. This provides a viable approach to creating micro lens arrays with a constant NA with variations in the focal length, specifically, as follows:

In this paper, we have achieved two different types of 9 × 9 MLAs on fused silica with the FLIM-EL technique: one using 60 pulses with an energy of 1.39 μJ, and the other using 80 pulses with an energy of 1.83 μJ. The depths of the two MLAs were 19.5 μm and 22.8 μm, respectively, and the heights were 39.7 μm and 44.2 μm, respectively. The surface roughness was as low 30 nm. It is important to note that the two MLAs have the characteristic of a fixed NA (0.458) but different focal lengths (−43.303 μm and −48.223 μm). Meanwhile, the MLAs exhibits significant uniformity and excellent imaging performance, enabling the clear imaging of mask patterns at adjustable magnifications (1.3×–3.0×). This study will further advance the potential applications of tunable MOSs. For example, in AR/VR devices, it is used to enhance the depth of the field effect and achieve a more natural virtual scene interaction; in optical fiber communication, it is used to optimize the coupling efficiency of optical signals, thereby improving the reliability of signal transmission.

Author Contributions: J.W. and W.Z. conceived of the project. J.W. and W.Z. purchased equipment and built the experimental platform. K.C. performed the experiment and wrote the paper. G.W. and K.Y. assisted in data testing. J.W. helped in reviewing and editing the manuscript. All authors have read and agreed to the published version of the manuscript.

Funding: This work was supported by the project National Key Research and Development Program of China (2023YFB4606701), Chinese Academy of Sciences (XDC0150200, XDC0150201), National Natural Science Foundation of China (52405519) and Special Foundation of Director of Ningbo Institute of Materials Technology & Engineering (2021SZKY0309) for the financial support.

Institutional Review Board Statement: Not applicable.

Informed Consent Statement: Not applicable.

Data Availability Statement: The original contributions presented in the study are included in the article; further inquiries can be directed to the corresponding author/s.

Conflicts of Interest: The authors declare no conflicts of interest.

References

1. Tan, J.; Wang, G.; Li, Y.; Chen, Q. Femtosecond Laser Fabrication of Refractive/Diffractive Micro-Optical Components on Hard Brittle Materials. *Laser Photon. Rev.* **2023**, *17*, 2200692. [CrossRef]
2. Li, M.; Yang, Q.; Chen, F.; Yong, J.; Biao, H.; Fang, Y.; Hou, X. Integration of Great Water Repellence and Imaging Performance on a Superhydrophobic PDMS microlens Array by Femtosecond Laser Microfabrication. *Adv. Opt. Mater.* **2019**, *21*, 1800994. [CrossRef]
3. Xu, M.; Li, J.; Chang, X.; Chen, C.; Lu, H.; Wang, Z. Self-assembled microlens array with controllable curvatures for integral imaging 3D display. *Opt. Lasers Eng.* **2024**, *180*, 108322. [CrossRef]
4. Liu, F.; Bian, H.; Zhang, F.; Yang, Q.; Shan, C.; Li, M.; Ho, X.; Chen, F. IR Artificial Compound Eye. *Adv. Opt. Mater.* **2020**, *8*, 2070013. [CrossRef]
5. Zhou, W.; Li, R.; Li, M.; Tao, P.; Wang, X.; Dai, S.; Song, B.; Zhang, W.; Lin, C.; Shen, X.; et al. Fabrication of microlens array on chalcogenide glass by wet etching-assisted femtosecond laser direct writing. *Ceram. Int.* **2022**, *48*, 18983–18988. [CrossRef]
6. Liu, X.; Yang, S.; Yu, L.; Chen, Q.; Zhang, Y.; Sun, H. Rapid Engraving of Artificial Compound Eyes from Curved Sapphire Substrate. *Adv. Funct. Mater.* **2019**, *29*, 1900037. [CrossRef]
7. Jin, X.; Keke, W.; Jian, C.; Ping, L.; Jiahua, Z. The micro-optic photovoltaic behavior of solar cell along with microlens curved glass substrate. *Energy Conv. Manag.* **2015**, *96*, 315–321. [CrossRef]
8. Shen, X.; Wang, S.; Zhou, H.; Tuokedaerhan, K.; Chen, Y. Improving thin film solar cells performance via designing moth-eye-like nanostructure arrays. *Results Phys.* **2021**, *20*, 103713. [CrossRef]
9. Jisoo, H.; Youngmin, K.; Son-gi, P.; Jong-Ho, H.; Sung-Wook, M.; Sin-Doo, L.; Byoungho, L. 3D/2D convertible projection-type integral imaging using concave half mirror array. *Opt. Express* **2010**, *18*, 20628–20637. [CrossRef]
10. Jorissen, L.; Oi, Y.; Wakunami, K.; Ichihashi, Y.; Lafruit, G.; Yamamoto, K.; Bekaert, P.; Jackin, B. Holographic Micromirror Array with Diffuse Areas for Accurate Calibration of 3D Light-Field Display. *Appl. Sci.* **2020**, *10*, 7188. [CrossRef]
11. Kumaresan, Y.; Rammohan, A.; Dwivedi, P.K.; Sharma, A. Large area IR microlens arrays of chalcogenide glass photoresists by grayscale maskless lithography. *ACS Appl. Mater. Interfaces* **2013**, *5*, 7094–7100. [CrossRef]
12. Liiu, J.; Liu, J.; Deng, Q.; Feng, J.; Zhou, S.; Hu, S. Intensity modulation based optical proximity optimization for the maskless lithography. *Opt. Express* **2020**, *28*, 548–557. [CrossRef]

13. Zhu, X.; Fang, W.; Lei, J.; Li, Z.; Xie, F.; Cao, Y.; Zhang, Y.; Qin, F.; Li, X. Supercritical lens array in a centimeter scale patterned with maskless UV lithography. *Opt. Lett.* **2020**, *45*, 1798–1801. [CrossRef]
14. Robert, K.; Helmut, S. Thermal reflow of polymers for innovative and smart 3D structures: A review. *Mater. Sci. Semicond. Process* **2018**, *92*, 58–72. [CrossRef]
15. Bute, M.; Dhole, S.D.; Bhoraskar, V.N.; Abhyankar, A.; Terashima, C.; Gosavi, S.; Fujishima, A. Benzophenone doped polydimethylsiloxane: Resist platform for MeV electron beam lithography assisted microlens array fabrication. *Microelectron. Eng.* **2021**, *250*, 111632. [CrossRef]
16. Zhenbin, L.; Miao, X.; Hongbo, L.; Yunsheng, D. A polyvinyl alcohol microlens array with controlled curvature on discontinuous hydrophobic surface. *J. Mol. Liq.* **2020**, *319*, 114372. [CrossRef]
17. Sang, B.; Kisoo, K.; Sun, Y.; Kyung, J.; Ki, J. Multifocal microlens arrays using multilayer photolithography. *Opt. Express* **2020**, *28*, 9082–9088. [CrossRef]
18. Nam, H.J.; Jung, D.-Y.; Yi, G.-R.; Choi, H. Close-packed hemispherical microlens array from two-dimensional ordered polymeric microspheres. *Langmuir* **2006**, *22*, 7358–7363. [CrossRef] [PubMed]
19. Liu, X.; Chen, Q.; Guan, K.; Ma, Z.; Yu, Y.; Li, Q.; Tian, Z.; Sun, H. Dry-etching-assisted femtosecond laser machining. *Laser Photon. Rev.* **2017**, *11*, 1600115. [CrossRef]
20. Zhu, J.; Li, Q.; Chem, Q.; Liu, B.; Wei, Z. Precise and smooth structure on InP fabricated by femtosecond laser direct writing-assisted wet etching. *Opt. Laser Technol.* **2024**, *176*, 110944. [CrossRef]
21. Vorobyev, Y.A.; Guo, C. Direct femtosecond laser surface nano/microstructuring and its applications. *Laser Photon. Rev.* **2013**, *7*, 385–407. [CrossRef]
22. Li, J.; Zhong, S.; Huang, J.; Qiu, P.; Wang, P.; Li, H.; Qin, C.; Miao, D.; Xu, S. Laser-guided anisotropic etching for precision machining of micro-engineered glass components. *Int. J. Mach. Tools Manuf.* **2024**, *198*, 104152. [CrossRef]
23. Low, D.K.Y.; Xie, H.; Xiong, Z.; Lim, G.C. Femtosecond laser direct writing of embedded optical waveguides in aluminosilicate glass. *Appl. Phys. A-Mater. Sci. Process* **2005**, *81*, 1633–1638. [CrossRef]
24. Agnė, B.; Greta, M.; Tomas, J.; Jokūbas, S.; Tomas, B.; Rokas, V.; Titas, T.; Julien, B.; Simas, S.; Valda, S.; et al. Fe mtosecond Laser Assisted 3D Etching Using Inorganic-Organic Etchant. *Materials* **2022**, *15*, 2817. [CrossRef]
25. Wang, H.; Zhang, F.; Yang, Q.; Li, M.; Hoou, X.; Chen, F. Chalcogenide Glass IR Artificial Compound Eyes Based on Femtosecond Laser Microfabrication. *Adv. Mater. Technol.-USA* **2022**, *8*, 2200741. [CrossRef]
26. Daniel, N.; Detlef, K.; Kore, H. Femtosecond laser assisted selective etching of microchannels in lithium niobate. *Opt. Express* **2023**, *31*, 37618–37629. [CrossRef]
27. Sundaram, S.K.; Mazur, E. Inducing and probing non-thermal transitions in semiconductors using femtosecond laser pulses. *Nat. Mater.* **2002**, *1*, 217–224. [CrossRef]
28. Deng, Z.; Chen, F.; Yang, Q.; Bian, H.; Du, G.; Yong, J.; Shan, C.; Hou, X. Dragonfly-Eye-Inspired Artificial Compound Eyes with Sophisticated Imaging. *Adv. Funct. Mater.* **2016**, *26*, 1995–2001. [CrossRef]
29. Richter, S.; Miese, C.; Döring, S.; Zimmermann, F.; Withford, M.J.; Tünnermann, A.; Nolte, S. Laser induced nanogratings beyond fused silica-periodic nanostructures in borosilicate glasses and ULE. *Opt. Mater. Express* **2013**, *3*, 1161–1166. [CrossRef]
30. Yao, H.; Pugliese, D.; Lancy, M.; Dai, Y. Ultrafast Laser Direct Writing Nanogratings and their Engineering in Transparent Materials. *Laser Photonics Rev.* **2024**, 2300891. [CrossRef]
31. Bian, H.; Wei, Y.; Yang, Q.; Chen, F.; Zhang, F.; Guangqing, D.; Jiale, Y.; Xun, H. Direct fabrication of compound-eye microlens array on curved surfaces by a facile femtosecond laser enhanced wet etching process. *Appl. Phys. Lett.* **2016**, *109*, 221109. [CrossRef]
32. Hu, Y.; Rao, S.; Wu, S.; Wei, P.; Qiu, W.; Wu, D.; Xu, B.; Ni, J.; Yang, L.; Li, J.; et al. All-Glass 3D Optofluidic Microchip with Built-in Tunable microlens Fabricated by Femtosecond Laser-Assisted Etching. *Adv. Opt. Mater.* **2018**, *6*, 1701299. [CrossRef]
33. Li, R.; Li, C.; Yan, M.; Lin, C.; Dai, S.; Song, B.; Xu, T.; Zhang, P. Fabrication of chalcogenide microlens arrays by femtosecond laser writing and precision molding. *Ceram. Int.* **2023**, *49*, 15865–15873. [CrossRef]
34. Wang, B.; Zheng, J.; Qi, J.; Guo, M.; Gao, B.; Liu, X. Integration of Multifocal Microlens Array on Silicon Microcantilever via Femtosecond-Laser-Assisted Etching Technology. *Micromach-Basel* **2022**, *13*, 218. [CrossRef]
35. David, B.; Nathan, H. Multiscale lens design. *Opt. Express* **2009**, *17*, 10659–10674. [CrossRef]
36. Haotian, D.; Dongfeng, Q.; Xiaomeng, W.; Yuhan, L.; Shiyong, S.; Jianguo, Z.; Xiang, S.; Xueyun, L.; Jing, W.; Hongyu, Z. Femtosecond laser writing of infrared microlens arrays on chalcogenide glass. *Opt. Laser Technol.* **2023**, *159*, 108953. [CrossRef]

materials

Article

Investigations on the Surface Integrity and Wear Mechanisms of TiAlYN-Coated Tools in Inconel 718 Milling Operations

Francisco J. G. Silva [1,2,*], Naiara P. V. Sebbe [1,3], Rúben D. F. S. Costa [2,3], André F. V. Pedroso [1,3], Rita C. M. Sales-Contini [1,4], Marta L. S. Barbosa [3] and Rui P. Martinho [1]

[1] ISEP, Polytechnic Institute of Porto, Rua Dr. António Bernardino de Almeida, 4249-015 Porto, Portugal; napvs@isep.ipp.pt (N.P.V.S.); afvpe@isep.ipp.pt (A.F.V.P.); rita.sales@fatec.sp.gov.br (R.C.M.S.-C.); rpm@isep.ipp.pt (R.P.M.)
[2] Associate Laboratory for Energy, Transports and Aerospace (LAETA-INEGI), Rua Dr. Roberto Frias, 400, 4200-465 Porto, Portugal; rdcosta@inegi.up.pt
[3] Department of Mechanical Engineering, Faculty of Engineering, University of Porto, Rua Dr. Roberto Frias, 400, 4200-465 Porto, Portugal; martabarbosa8c@gmail.com
[4] Technological College of São José dos Campos, Centro Paula Souza, Avenida Cesare Mansueto Giulio Lattes, 1350 Distrito Eugênio de Melo, São José dos Campos 12247-014, Brazil
* Correspondence: fgs@isep.ipp.pt; Tel.: +351-228340500

Abstract: Inconel 718 is a Ni superalloy with superior mechanical properties, even at high temperatures. However, due to its high hardness and low thermal conductivity, it is considered a difficult-to-machine material. This material is widely used in applications that require good dimensional stability, making the milling process the most used in machining this alloy. The wear resulting from this process and the quality of the machined surface are still challenging factors when it comes to Inconel 718. TiAlN-based coating has been used on cutting tools with Yttrium as a doping element to improve the process performance. Based on this, this work evaluated the machined surface integrity and wear resistance of cutting tools coated using Physical Vapor Deposition (PVD) HiPIMS with TiAlYN in the end milling of Inconel 718, varying the process parameters such as cutting speed (v_c), feed per tooth (f_z), and cutting length (L_{cut}). It was verified that the L_{cut} is the parameter that exerts the most significant influence since, even at small distances, Inconel 718 already generates high tool wear (TW). Furthermore, the main wear mechanisms were abrasive and adhesive wear, with the development of a built-up edge (BUE) under a125 m/min feed rate (f) and a L_{cut} = 15 m. Chipping, cracking, and delamination of the coating were also observed, indicating a lack of adhesion between the coating and the substrate, suggesting the need for a good interlayer or the adjustment of the PVD parameters.

Keywords: milling; Inconel 718; TiAlYN coatings; HiPIMS technique; tool wear mechanisms; surface integrity

1. Introduction

The class of materials known as Inconel are Ni-Cr-based superalloys, recognised for having superior mechanical properties and good fatigue and creep behaviour up to 700 °C [1]. In their composition, generally, some elements, such as Al, Ti, Nb, Co, Cu, W, and Fe, are added, with the aim to improve their mechanical properties and corrosion resistance [2]. Within this class, Inconel 718 stands out. This material is a precipitation-hardened superalloy, with elements such as Ni and Cr contributing to its corrosion resistance [3,4]. Furthermore, Inconel 718 combines its resistance to corrosion [4] with excellent mechanical properties at high temperatures and good weldability [5], and is widely used in aircraft, gas turbines, turbocharger rotors, nuclear reactors, liquid fuel rockets, critical rotating parts, airfoils, etc. [6–9]. It can represent 30% of the total weight of an aircraft engine [10,11].

However, due to its properties, such as high hardness and low thermal conductivity, conventional machining and forming processes are challenging, making this alloy a difficult-to-machine material [12–14]. During machining, the work hardening of this alloy and its reactivity with the cutting tool material at high temperatures plastically deform the cutting tool, resulting in an inferior surface quality of the machined part [15]. This fact, added to the tendency of this alloy to adhere to the surface of cutting tools, makes machining even more difficult [16]. However, machining is still widely used in industries to produce high-precision and quality parts [17]. Of the machining processes, milling, a more flexible process with great dimensional accuracy, is the most used in the machining of Inconel 718.

Many authors have based their research on milling Inconel 718 [18–23], emphasising the fact that it is a challenging material when it comes to conventional machining processes. For example, Liao et al. [24] analysed the end milling of Inconel 718 under various cutting speeds (v_c) with carbide tools. It was found that, at low speeds, the increase in cutting temperature and strain hardening were the main problems generated in the slot milling of this alloy, causing chipping of the cutting tool and its subsequent failure. When milling at medium speeds, there was a reduction in the cutting force due to the softening caused by the precipitation γ' of Inconel 718. However, the chips were welded when the v_c was further increased, and their flow changed. With this, the authors observed an optimal v_c range for the end milling of Inconel 718.

On the other hand, Mayiar et al. [25] optimised end milling parameters, such as v_c, feed rate, and the depth of cut, when milling Inconel 718. The authors carried out nine tests on an L9 orthogonal arrangement of the Taguchi method. The analysis was based on surface roughness (SR) and the material removal rate (MRR), and an analysis of variance (ANOVA) was also applied to identify the most significant factor in the process. Based on the results, it was verified that the ideal cutting parameters would be 75 m/min, 0.06 mm/tooth and 0.4 mm for cutting depth, with v_c being the parameter with the most significant influence on the milling process. Therefore, to optimise the process, improve the tool life, reduce wear and ensure good surface integrity, machining parameters must be correctly selected, as well as the cutting conditions, environment, and the choice of the cutting tools' materials [15]. Thus, research involving machining is still a hot topic today, and efforts are being oriented toward improving the machining process, especially regarding materials that are difficult to machine [26].

Thus, analysing recent studies and the factors involved in the milling of Inconel 718, the set of ideal cutting parameters can be predicted. These studies are essential not only for Inconel 718 but also for all processing and milling operations involving difficult-to-machine materials. Furthermore, the cutting forces developed in the process are also important and must be considered [27], as they offer information about the performance and stability of milling and, consequently, are related to wear and surface integrity [28].

One of the main problems faced during the milling of Inconel 718 is the rapid wear of cutting tools, as critical shear and temperature forces are generated during the process, which leads to premature tool failure [29]. Furthermore, the cutting tool directly impacts the process, which means that much research is based on creating new geometries for these tools [30] and the development of coatings capable of improving the process performance. Furthermore, ultrasonic vibration can also be used to reduce the wear that tools are exposed to [31]. The hardness values of the coatings, low friction coefficients, and thermal specifications directly influence the process performance [32]. These coatings can be applied to various surfaces for different industries, as well as used in injection moulds [33,34]. In this scenario, when comparing the performance and efficiency of the process, recent works have made their analyses based on the comparison between coated and uncoated cutting tools in the machining of Inconel 718, as is the case of the work by Ucun et al. [35], in which the effect of a coating material on tool wear (TW) was analysed during the milling of Inconel 718, with uncoated and DLC-coated tools (WC-Co), while changing the feed rates and cutting depths. These authors found that the use of the coating improved the

SR and reduced the formation of burrs and the built-up edge (BUE), making the process performance better than when using uncoated tools.

The coatings are typically produced by two different processes, called Chemical Vapor Deposition (CVD) and Physical Vapor Deposition (PVD) [36]. These two processes include specific techniques. For example, PVD can be divided into two main processes: evaporation and sputtering [37], related to how particles can be extracted from the target. Sputtering is used more in applications that require a good surface quality [38] and has assumed extreme importance within the PVD deposition process group, with the development of new technologies and processes that aim to generate coatings with better mechanical properties, as is the case with the PVD HiPIMS (High Power Impulse Magnetron Sputtering) process. In the HiPIMS process, coatings with residual compressive stress are generated [39–41], which is extremely important in the milling process [42], as these stresses provide greater resistance to the tool edge, and, as a result, the quality of the machined surface is better.

However, much progress needs to be made in this area, as this can make the edges of cutting tools more susceptible to wear, which means that there are still many challenges regarding how to improve wear resistance with the use of different coatings when milling Inconel 718. The TiAlN-based coating is widely used and performs well in high-speed machining, with excellent oxidation resistance [43]. In addition, TiAlN-based coatings feature high hardness and good thermal stability [44]. However, wear resistance is still an area of much study and research. In this context, aiming to improve the tool's performance, doping elements have been added to TiAlN [45–48]. In addition to improving wear resistance, these elements can enhance corrosion resistance, hardness, adhesion, and toughness [17]. One element that can be used as a doping element is Yttrium [49]. The importance of adding Yttrium to the TiAlN-based coating is related to improved mechanical properties and oxidation resistance [50]. This phenomenon occurs due to the segregation of the element through grain refinement during film growth and its ability to form a protective film due to Yttrium's strong affinity for oxygen [51]. Aninat et al. [52] found that adding Y generated greater hardness and better mechanical properties; however, it reduced the compressive stress. In turn, Moser et al. [53] analysed the thermal stability of the $Ti_{1-x}Al_xN$ coating with the addition of Y through the DC magnetron sputtering process and found that at higher temperatures, after annealing, there was an increase in hardness. Furthermore, through the characterisation and morphology generated, it was seen that Y slows down the decomposition process of supersaturated phases. Even in studies regarding the characteristics and behaviour of the TiAlYN coating, there is still a significant gap in the literature regarding its wear behaviour and performance during the machining process, with most works having focused on its characterization.

Furthermore, there are still many challenges regarding the machining of Inconel 718, specifically the milling process, as many studies only address turning [54]. Even with coatings, the wear generated in the machining process is still a topic that should be further explored. Much information can be taken from models and simulations that can predict wear behaviour [55], as well as the quality of the machined surface, quickly and economically [56]. However, these models are complex and depend on prior knowledge, in addition to being little explored in milling, especially for materials that are difficult to machine, such as Inconel 718. The wear occurring during the milling process can provide data on the productivity of the process, the need to adjust the machining parameters, the materials involved, and their interaction and affinity to understand whether they are correct or whether an adjustment is necessary [26].

Therefore, this work evaluates the influence of machining parameters, such as v_c, feed per tooth (f_z), and cutting length (L_{cut}), on the surface integrity and wear behaviour of end mills coated with TiAlYN through the PVD HiPIMS process during the machining of Inconel 718. Therefore, this work aims to fill the gap regarding the use of Yttrium as a doping element and provide insight into the milling of Inconel 718.

2. Materials and Methods

This section will describe the materials used in the experimental work and the equipment used to perform the analyses.

2.1. Materials

2.1.1. Workpiece Material

The workpiece material was made of Inconel 718, an austenitic Ni-Cr-based superalloy. This material was supplied as a round bar with a 158 mm diameter (Ø), and prepared to a length of 30 mm for carrying out the tests. It underwent the following heat treatments:

- Solution annealing at 970 °C, followed by quenching in water;
- Precipitation hardening at 718 °C for 8 h, oven cooling at 621 °C for 8 h, and air cooling.

This workpiece was purchased from the company Paris Saint-Denis Aéro (Grândola, Portugal). The material's mechanical properties are presented in Table 1, and its respective chemical composition (%wt) is shown in Table 2.

Table 1. Mechanical properties of the Ni superalloy Inconel 718.

Material Property	Value
Yield strength [MPa]	1200
Tensile strength [MPa]	1427
Hardness [HBW]	441

Table 2. Chemical composition of Inconel 718 (wt%) [56].

Elements (%wt)							
Ni	Cr	Fe	Nb	Mo	Ti	Al	Co
53.89	18.05	17.78	5.35	2.90	0.96	0.51	0.20
Cu	Si	Mg	B	C	P	N	Mg
0.10	0.08	0.078	0.039	0.023	0.010	0.007	0.0017

2.1.2. Substrate and Tool Geometry

The employed tools are end mills. The substrate of the tools is a cemented carbide WC-Co, grade 6110, with Cobalt (~6 wt%) as a binder and an average grain size of 0.3 µm. These tools were provided by INOVATOOLS, S.A. (Leiria, Portugal). The tool geometry is characterised in Table 3.

Table 3. The geometry of the WC-Co end mills used in the experimental work.

Tool Geometry	Dimensions
Cutting Ø	6 mm
Total length	57 mm
Maximum cutting depth	13 mm
Number of flutes	4
Rake angle	12°
Clearance angle	10°
Chamfer	45°; 0.20 mm
Helix angle	35°

2.2. Methods

2.2.1. PVD Coating

Before coating deposition, the cutting tools were cleaned with acetone in an ultrasonic bath. This cleaning was performed in two phases: the first lasted around 15 min, and then the acetone was renewed before the second cleaning phase, which lasted 5 min.

A TiAlYN coating thickness of 2.4 µm was deposited via the PVD HiPIMS process using CemeCom CC800/HiPIMS equipment (CemeCon, AG, Wuersele, Germany) with four target holders. The adopted deposition parameters can be observed in Table 4. These parameters were selected from successful previous experiments on similar substrates using different targets. The rotation speed applied for the substrate holder was 1 rpm, ensuring that the deposited coatings presented high homogeneity throughout the deposition process.

Table 4. Parameters of the deposition of TiAlYN coating.

Deposition Parameters	TiAlYN Layer
Reactor gases	Ar^{+} + Kr + N_2
Deposition time [min]	233
Target amount/composition	4/TiAlY
Pressure [mPa]	600
Bias voltage [V]	−60
Temperature [°C]	520
Holder rotational speed [rpm]	1

2.2.2. Machining Parts

Machining tests were performed using CNC machining centre HAAS VF-2 (H.A.A.S. Automation, Oxnard, CA, USA), with three axes to machine, a maximum speed of 10,000 rpm, and a maximum power (P_{in}) of 20 kW. A spiral milling strategy was chosen as the part was supplied with a circular geometry. Thus, milling occurred from the centre towards the periphery of the workpiece and tests were conducted using cutting fluid with 5% oil in water, Alusol SL 61 XBB, which is a semi-synthetic metalworking fluid.

Regarding the milling parameters, because the strategy chosen was a spiral to avoid wear-related phenomena, the radial depth of the cut was kept constant. Another parameter was the axial depth of the cut (a_{p}, or ADOC). This parameter was suggested by the cutting tool supplier, therefore, initially, values of 0.2 mm and 0.1 mm were applied. However, these values caused the tool to fail and break shortly after the initial plunge. Due to this, the value of 0.08 mm was defined for this parameter, which was kept constant for all tests, as finishing milling operations was the goal to simulate. In addition, as the tool Ø = 6 mm, the value of the radial depth of cut (a_{e} or RDOC) was defined considering 75% of this value, i.e., 4.5 mm. This parameter also remained constant for all conditions tested. The parameters v_{c}, f_{z}, and L_{cut} were varied, determined based on the provided substrate of the tool. Regarding f_{z}, the centre value (100%) was 0.0700 mm/tooth and varied by 25% for less and 50% for more. This parameter was varied as it is known to have a high impact on wear and influence the quality of the machined surface. For L_{cut}, values of 5 m and 15 m were selected, aiming to analyse the progression of wear throughout the machining of the workpiece. For v_{c}, values of 75, 100, and 125 m/min were used, with the purpose of comparing and analysing the influence of cutting speed on the resulting wear and surface integrity. All parameters and test conditions are shown in Table 5, and Figure 1 illustrates the workpiece with its corresponding spiral marks. To fix this workpiece, a self-centring bushing with three jaws, Bison 3575 (BISON-BIAL, Bliesk Podiaski, Poland), was used, and the tools were fixed with an ISO40 DIN69871 cone, an ER32 H70 collet holder, an ISO 7388-2 tie rod, and an ER DIN 6499 collet from the same manufacturer.

Table 5. Parameters and conditions used in milling tests.

Reference	v_c [m/min]	f_z [mm/tooth]	L_{cut} [m]	a_p [mm]	a_e [mm]	T [min]
S75F75L5	75.0000	0.0525	5.0000	0.0800	4.5000	5.9854
S75F75L15	75.0000	0.0525	15.0000	0.0800	4.5000	17.9563
S75F100L5	75.0000	0.0700	5.0000	0.0800	4.5000	4.4880
S75F100L15	75.0000	0.0700	15.0000	0.0800	4.5000	13.4640
S75F150L5	75.0000	0.1050	5.0000	0.0800	4.5000	2.9919
S75F150L15	75.0000	0.1050	15.0000	0.0800	4.5000	8.9759
S100F75L5	100.0000	0.0525	5.0000	0.0800	4.5000	4.4880
S100F75L15	100.0000	0.0525	15.0000	0.0800	4.5000	13.4639
S100F100L5	100.0000	0.0700	5.0000	0.0800	4.5000	3.3659
S100F100L15	100.0000	0.0700	15.0000	0.0800	4.5000	10.0978
S100F150L5	100.0000	0.1050	5.0000	0.0800	4.5000	2.2440
S100F150L15	100.0000	0.1050	15.0000	0.0800	4.5000	6.7319
S125F75L5	125.0000	0.0525	5.0000	0.0800	4.5000	3.5904
S125F75L15	125.0000	0.0525	15.0000	0.0800	4.5000	10.7711
S125F100L5	125.0000	0.0700	5.0000	0.0800	4.5000	2.6928
S125F100L15	125.0000	0.0700	15.0000	0.0800	4.5000	8.0783
S125F150L5	125.0000	0.1050	5.0000	0.0800	4.5000	1.7952
S125F150L15	125.0000	0.1050	15.0000	0.0800	4.5000	5.3856

Figure 1. Workpiece material and its spiral marks.

2.2.3. Machined SR Analysis

Regarding the roughness of the machined surface, this was measured using a Mahr Perthometer M2 profilometer (Mahr, Gottingen, Germany) (Figure 2). The test was carried out following DIN EN ISO 21920-3:2021 [57]. Each test was performed with a cut-off value (λ_c) of 0.8 mm and a measurement length of 5.6 mm. Moreover, as errors may occur due to the acceleration and deceleration of the probe at the time of measurement, the first and last measurement segments of 0.8 mm were not considered. In addition, measurements were taken in the radial and tangential directions, and a minimum of five measurements were taken in different areas due to the possibility of variation in the values obtained in the centre and on the periphery of the workpiece. With these, the arithmetic average roughness value (R_a) was determined.

Figure 2. Mahr Perthometer M2 profilometer.

Thus, roughness analysis was performed to evaluate the process stability and performance of the cutting tool, which can be related to TW and the best milling conditions for which it is possible to obtain the best quality and surface integrity.

2.2.4. Characterisation of Wear Mechanisms

Before analysing the cutting tools' wear, they underwent ultrasonic cleaning with acetone as a cleaning agent. Afterwards, the wear suffered by the machining tools was evaluated through Scanning Electron Microscopy (SEM) analysis, according to ISO 8688-2:1986 [58]. This standard recommends analysing the presence of all wear phenomena and adopting the one with the most significant influence as a life criterion. Thus, the VB3 was selected, and the wear measurements were performed in "Position 1". For this, an FEI QUANTA 400 FEG scanning electron microscope was used (F.E.I., Hillsboro, OR, USA), equipped with an EDAX Genesys Energy Dispersive X-Ray Spectroscopy microanalysis system (EDAX Inc., Mahwah, NJ, USA). The analyses were carried out using BackScattered Electrons Diffraction (BSED), with magnification varying between 100× and 2000×, and using a beam potential of 15 kV, which was sporadically reduced to 10 kV.

Furthermore, Energy-Dispersive X-Ray Spectroscopy (EDS) (EDAX Inc., Mahwah, NJ, USA) analysis was used to check and confirm the occurrence of material adhered to the tool. The top view (TOP), rake face (RF), and clearance face (CF) of all tools were analysed. In addition, for better identification, a reference was created for the four cutting teeth of the tool, with numbers 1 to 4 used to identify them.

3. Results and Discussion

3.1. Roughness Analysis of the Machined Surface

The SR was measured after each tested condition to analyse the machined surface quality in the tangential and radial directions. No notable differences were observed between the values obtained in different directions. All test conditions were compared using the SR values obtained, which were organised and grouped according to Figure 3 and are shown in Table 6. The figure is divided by test conditions in the graph's X axis and three groups corresponding to each f_z, as a percentage of the initial value (0.07 mm/tooth). SR values are displayed according to the Y axis. It should be noted that, according to the identification of the tools, the number after the "S" indicates the v_c and the number after the "L" indicates the L_{cut} used in the machining test.

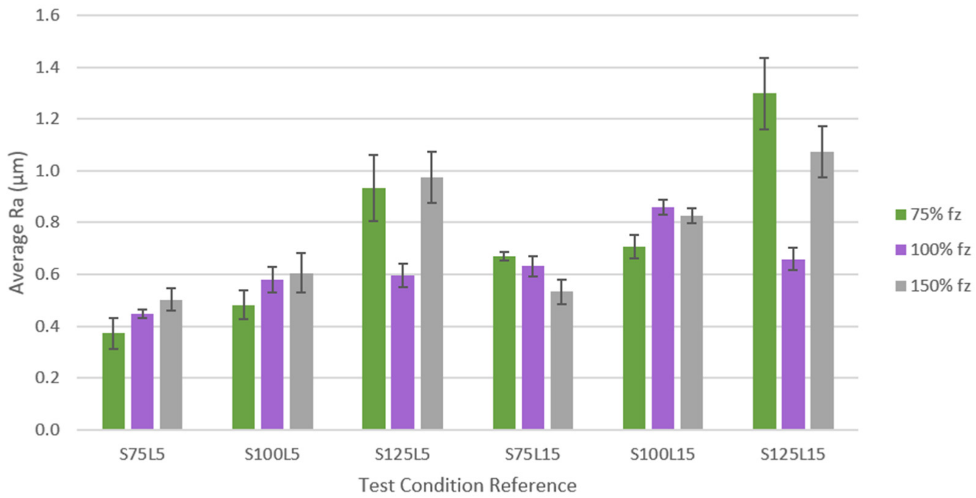

Figure 3. Comparison of SR values obtained for all conditions tested.

Table 6. R_a values for all conditions tested.

Reference	Average R_a Value (µm)
S75F75L5	0.372 ± 0.0060
S75F75L15	0.670 ± 0.0155
S75F100L5	0.448 ± 0.0176
S75F100L15	0.631 ± 0.0382
S75F150L5	0.502 ± 0.0434
S75F150L15	0.533 ± 0.0472
S100F75L5	0.483 ± 0.0542
S100F75L15	0.708 ± 0.0444
S100F100L5	0.578 ± 0.0493
S100F100L15	0.859 ± 0.0301
S100F150L5	0.605 ± 0.0755
S100F150L15	0.827 ± 0.0279
S125F75L5	0.935 ± 0.1270
S125F75L15	1.299 ± 0.2759
S125F100L5	0.595 ± 0.0454
S125F100L15	0.659 ± 0.0431
S125F150L5	0.975 ± 0.0988
S125F150L15	1.073 ± 0.0999

It can be seen that by increasing the L_{cut}, the SR values also increased, which was an already expected result, as Inconel 718 is a difficult-to-machine material that, even for small L_{cut} values, can generate high levels of TW, and, consequently, greater SR values and a poorer quality of the machined surface [59].

The influence of the f_z is not evident for the conditions tested at a v_c = 75 m/min since for a L_{cut} = 5 m, when the f_z increased, the roughness also increased. On the other hand, for a L_{cut} = 15 m, when the f_z was increased, the SR decreased. Usually, for lower values of f_z, the quality of the machined surface is better, i.e., the roughness of the machined surface has lower values [60], meaning that the quality of the machined surface could be impaired with the increase in f_z [56]. However, for conditions with a L_{cut} = 15 m, this scenario was not observed since there was an improvement in the surface quality obtained. This could have been generated by stabilising the wear behaviour on the tool's cutting edge, homogenising the wear effect on the edge.

Therefore, under the conditions tested at a v_c = 75 m/min, the maximum value of R_a was obtained for the condition that used 75% f_z and a L_{cut} = 15 m, i.e., for condition S75F75L15. The lowest R_a value was obtained for the condition with 75% f_z and a L_{cut} = 5 m, corresponding to the S75F75L5 condition. Thus, it can be seen that for 75% f_z, when increasing the L_{cut} from 5 m to 15 m, the difference in roughness was the most notable among the tested conditions.

In the same way as for the conditions tested at 75 m/min, under the conditions tested at 100 m/min, when the L_{cut} was increased, the roughness also increased, making this parameter's influence evident. Furthermore, for a L_{cut} = 5 m, the same was observed as in the previous case: when the f_z increased, the roughness of the machined surface also increased. However, for a L_{cut} = 15 m, when increasing the f_z from 75% to 100%, the roughness increased significantly, and when increasing the f_z to 150%, the roughness decreased slightly compared to 100% f_z. Therefore, by increasing the f_z, the roughness of the machined surface tends to be worse. Thus, it appears that this parameter greatly influences the roughness of the machined surface [61].

In the same way as in the conditions at 75 m/min and 100 m/min, in the case of using 125 m/min, when increasing the L_{cut} from 5 m to 15 m, the SR also increases. Regarding the f_z, there seems to be some instability in the process under conditions at 75% of this parameter, given the discrepancy in the values obtained. However, for 100% and 150% of this parameter, for both 5 m and 15 m, it is observed that when the parameter increases, the roughness also increases, and the quality of the machined surface decreases.

In general, it can be seen that average R_a values tend to increase for higher L_{cut} values, a trend that is registered for all conditions tested. In some conditions, this increase is more pronounced, as is the case in conditions S75F75, S100F100, and S125F75. On the other hand, this increase is slight in some conditions, for example, in conditions S75F150, S125F100, and S125F150.

Regarding the f_z, it is observed that this parameter also influences the roughness of the machined surface [62], but this influence is not so evident, as a common trend is not observed across all conditions. Therefore, when comparing this parameter, it is clear that for conditions S75L5 and S100L5, increasing this parameter worsens the quality of the machined surface. For the S75L15 condition, increasing this parameter results in a lower SR. On the other hand, for conditions S125L5 and S125L15, a decrease in roughness was observed when increasing from 75% of this parameter to 100%, followed by an increase in roughness when increasing to 150% of the f_z. For the S100L15 condition, the opposite occurred: the roughness increased, followed by a decrease, when varying the f_z. However, in general, increasing the f_z increases the roughness of the surface [63].

Furthermore, concerning the v_c, it is observed that the higher this parameter, the more the roughness of the machined surface rises and the lower the surface quality. This is not commonly observed, as the tendency is for SR to decrease as this parameter increases [64]. This phenomenon probably occurred because Inconel 718 is a material that is difficult to machine, the amount of wear suffered at these v_cs was high, and high abrasive wear was usually observed, which can lead to cutting tool chipping [65]. The only case in which it was observed that by increasing the v_c the R_a was lower was for 100% f_z, with a L_{cut} = 15 m, when increasing the v_c from 100 m/min to 125 m/min.

As for standard deviation (SD), it is known that this refers to the difference in measurements at the centre and periphery of the part. In the latter, the measurement tends to be higher, as it is the end of the spiral path, and, consequently, the wear is also higher. Conditions S125F75L5 and S125F75L15 showed a more significant SD. These two conditions, as previously mentioned, suffered from instability in the process. However, this higher SD result may be related to the sustained abrasive wear of the tool, which can lead to a difference in the SR recorded from the centre to the periphery of the part [66].

For a more concise and accurate validation, *t*-tests for two samples with different variances were conducted on Microsoft® Excel™ software to statistically assess the differences between the setups while varying a parameter, and to assess whether this parameter was the most influential when moving from one milling setup to another. A *p*-value of 0.05 was considered significant for the effects. The statistical tests started by comparing R_a results from different L_{cut} values and verifying the influence of this parameter while fixing s and f; for example, the *t*-test that compared the R_a from the S75F75L5 setup with the one from the S75F75L15 produced a P(T <= t) two-tailed value of $2 \times 10^{-4} < 0.05$, which means that there is a statistical difference between the two trials' mean values. Table 7 summarises the aftermath of the statistical tests. All data and statistical results can be found in Appendix A.

Table 7. Drawn conclusions from the performed *t*-tests.

Condition	Comments
L_{cut} influence	For low values of *s* and *f*, L_{cut} has the most influence. However, as the values of *s* and *f* increase, its influence on the surface quality becomes less prominent. In the case of S75F150L5 vs. S75F150L15, surface quality is not affected by the L_{cut}. For cases with conditions S100F150L15 and above, there is a noticeable blend of the influence of all three parameters together.
f influence	*f* is the most influential parameter on the surface quality and this influence is more pronounced when accompanied by an increasing in *s* within the setup. However, due to phenomena such as three-body abrasion, some outliers are to be seen, since the milling setup has proven to be catastrophic to TiAlYN-coated tools.
s influence	*s* has proven to be the most sensitive parameter, when in conjunction with *f* and L_{cut}. In some cases, it is visible that the increase in *s* leads to a different variance in the measured values, but sometimes it does not. Nonetheless, for the most extreme setups carried out, *s* is a very influential parameter regarding surface quality.

In general, it can be said that the quality of the machined surface was satisfactory, with good SR results. The exceptions were conditions S125F75L5 and S125F75L15, which experienced instability during the process, and, consequently, their results were discrepant. One of the main characteristics of surface integrity is the presence of compressive residual stresses [67], which are generated through the HiPIMS deposition technique [68] and which also prevent cohesive failures [69]. This fact is very beneficial for producing a machined surface with low roughness and a good surface quality to the machined part [56].

3.2. Wear Measurements and Characterisation

As explained in Section 2.2.4, the TW measurement was carried out following ISO 8688-2:1986 [58] for the top view of the tools (VB3). To compare all test conditions, the values obtained for VB3 were organised and grouped according to Figure 4; the sum is shown in Table 8. Figure 2 is divided by test conditions in the X axis of the graph, with three groups corresponding to each f_z, as a percentage of the initial value (0.07 mm/tooth) in the Y axis. It should be noted that, according to the identification of the tools, the number after the "S" indicates the v_c and the number after the "L" indicates the L_{cut} used in the machining test.

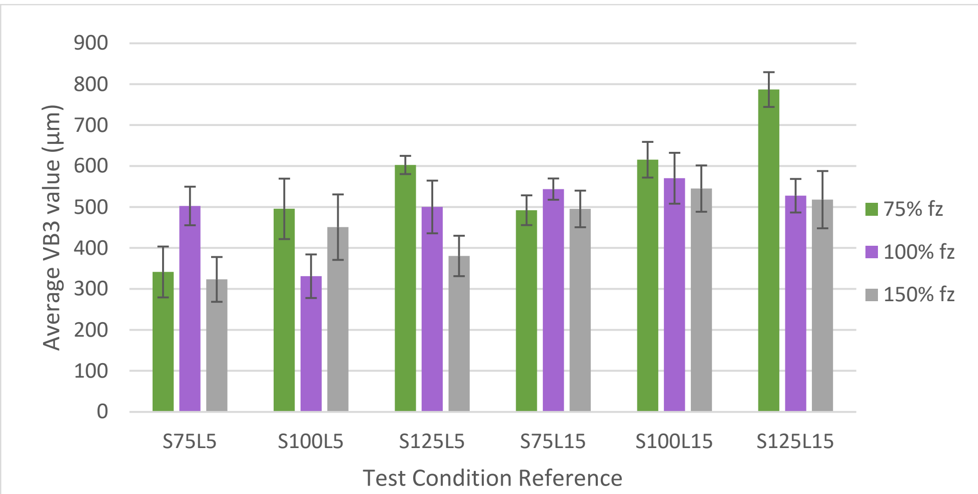

Figure 4. Comparison of VB3 values obtained for all conditions tested.

Table 8. Average values of VB3 for all conditions tested.

Reference	Average VB3 Value (μm)
S75F75L5	341.67 ± 124.349
S75F75L15	492.15 ± 72.7340
S75F100L5	502.68 ± 94.3731
S75F100L15	543.75 ± 25.8692
S75F150L5	323.43 ± 109.361
S75F150L15	495.38 ± 89.2471
S100F75L5	495.77 ± 147.663
S100F75L15	615.55 ± 43.5210
S100F100L5	331.09 ± 106.354
S100F100L15	570.41 ± 62.1473
S100F150L5	450.84 ± 79.8641
S100F150L15	545.21 ± 56.4712
S125F75L5	602.74 ± 22.1942
S125F75L15	786.95 ± 85.0253
S125F100L5	500.13 ± 128.609
S125F100L15	527.68 ± 41.0967
S125F150L5	380.68 ± 98.4872
S125F150L15	518.06 ± 70.0723

For conditions tested at a v_c = 75 m/min, the influence of the L_{cut} is evidently clear when the L_{cut} increases from 5 m to 15 m. However, at 100% f_z, this increase was slightly higher. Regarding the influence of the variation in the f_z on the flank wear (*VB* as ISO 8688-2:1986 [58] of the tools, for a L_{cut} = 5 m the lowest value obtained was for condition S75F150L5. Wear increased when increasing the f_z from 75% to 100% and decreased when increasing to 150%. In turn, the same trend was observed for the cases tested at a L_{cut} = 15 m; increased wear from 75% to 100% f_z, and a reduction as the increase continued to 150%. At 100% f_z, and a L_{cut} = 15 m, the maximum *VB* was observed. It was also noted that the condition of a L_{cut} = 5 m and 100% f_z presented greater wear than conditions with a L_{cut} = 15 m and 150% f_z.

For conditions tested at 100 m/min, the same situation as in the previous case is observed regarding the L_{cut}. When increasing from 5 m to 15 m, the resulting VB3 is higher. This is due to the properties of Inconel 718, such as the thermomechanical tool load, which generates high abrasive damage [65]. However, no clear influence of the f_z parameter is observed. For a L_{cut} = 5 m, when increasing from 75% to 100% f_z, the VB3 decreases, and when increasing it to 150%, the VB3 increases, but with a lower value than in the first condition (F75L5). On the other hand, for a L_{cut} = 15 m, when the f_z is increased, the VB3 decreases in all f_z conditions.

The fact that a common trend for f_z is not observed may be related to the chip formation mechanism, which varies under each condition and is related to the productivity of the milling process [70]. It seems that the formation of thinner chips is the most common cause of a poor process performance, as they are easier to break, and this causes higher abrasion and, consequently, much wear on the cutting tool. Thus, the chip section should be thicker to lead to greater integrity and extraction flow, but if the thickness is too high it can overload the cutting edge and, consequently, breakage can occur [56].

Under the conditions tested at 125 m/min, the influence of L_{cut} was also observed. In all conditions, VB3 increased when L_{cut} increased. This is due to the properties of Inconel 718, which causes abrasive damage and can consequently lead to tool chipping [65]. However, for 100% of the f_z, this increase was lessened. Furthermore, the conditions with 75% f_z presented the highest VB3, higher for 15 m than the L_{cut} = 5 m.

Regarding the influence of the f_z for a L_{cut} = 5 m, when the f_z was increased, the wear was reduced. The same occurred for a L_{cut} = 15 m. In other words, under these conditions, when the L_{cut} was increased, VB3 decreased.

In general, it can be observed that there is no clear trend for f_z, making its influence more challenging to analyse and detect. As already mentioned, the f_z is directly related to the productivity of the process and the chip formation mechanism. Furthermore, Inconel 718, as a difficult-to-machine material, can generate serrated or segmented chips that affect the machined surface's integrity [71] and result in different trends for f_z.

As for the v_c used in each condition, it can be observed that when this parameter is increased in conditions with 75% f_z, VB3 also increases. For conditions at 100% f_z, a clear trend cannot be identified. Regarding a L_{cut} = 5 m and 100% f_z conditions, wear decreases when increasing from 75 m/min to 100 m/min and increases when increasing to 125 m/min. However, in the last condition, the VB3 is similar to the first condition. In turn, for 150% f_z, wear increases when increasing the v_c from 75 m/min to 100 m/min and decreases when increasing to 125 m/min at both L_{cut} values.

Therefore, when the v_c is increased, the resulting wear also increases. This increase in *VB* is in line with the roughness obtained and the quality of the surface of the machined part. But, usually, an increased v_c results in a better surface quality and the smoother cutting behaviour of the cutting tools [72].

3.3. Analysis of Wear Mechanisms

3.3.1. v_c of 75 m/min

Regarding the type of *VB* identified for tools tested at 75 m/min, Figure 5 illustrates the top view of the cutting tools tested under conditions S75F150L5 and S75F150L15, making it possible to observe the influence of the L_{cut} on the resulting wear.

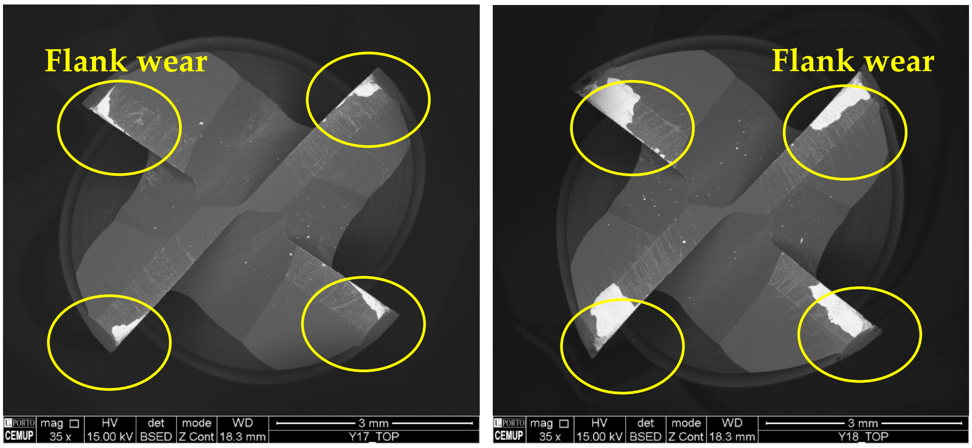

(**a**) (**b**)

Figure 5. Top view of the tools tested at a v_c of 75 m/min and 35× magnification: (**a**) S75F150L5 and (**b**) S75F150L15.

As for the wear mechanism, it can be said that for 75 m/min conditions, mainly abrasion wear and adhesive wear were observed, both on the substrate and on the coating. In addition, in some conditions, delamination and cracking of the coating occurred. Mechanical mechanisms such as abrasion and adhesion are common in terms of the wear suffered by cutting tools in the milling process [73]. Figure 6 illustrates the abrasive wear that occurred on the substrate of the cutting tool under the S75F75L5 and S75F75L15 conditions, where, for 15 m, the wear is more developed. Abrasive wear was detected for all the tests, and was more significant and more intense for the L_{cut} = 15 m.

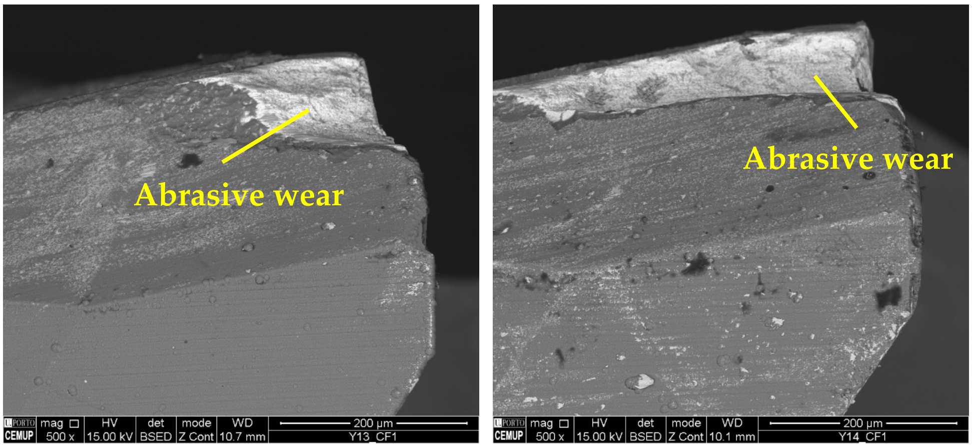

(**a**) (**b**)

Figure 6. Abrasive wear: (**a**) clearance face (CF1) of S75F75L5 at 500× magnification and (**b**) clearance face (CF1) of S75F75L15 at 500× magnification.

As for the presence of adhered material, it was found in all conditions and in great quantities. This is an expected result, since Inconel 718 usually tends to adhere to cutting tools [74]. Figure 7 illustrates the presence of adhered material on the top view of the S75F75L5 condition.

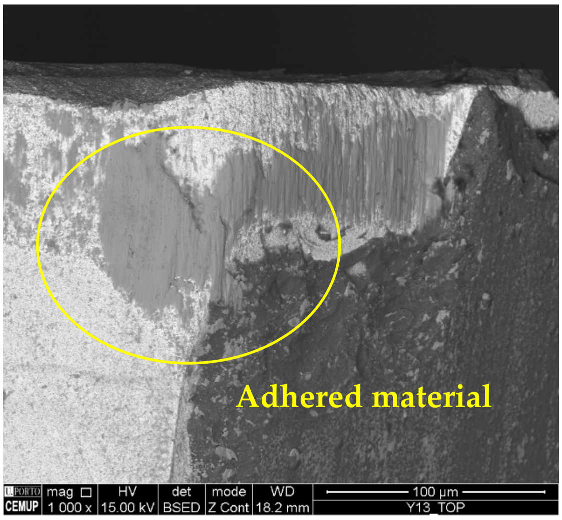

Figure 7. Adhered material: top view of S75F75L5 at 1000× magnification.

The wear mechanisms identified in the coating were abrasive, workpiece material adhesion, delamination, and cracks. Abrasive and adhesive wear were observed at a lower intensity on the tool substrate. Material adhesion causes more abrasion and can lead to coating delamination [59]. Figure 6 illustrates the wear mechanisms identified in the coating. In Figure 8a, abrasive wear and adhered material can be observed in the S75F100L15 condition, and in Figure 8b, delamination and cracking can be seen in a cutting tool tested in the S75F75L15 condition. Furthermore, it can be stated that the wear mechanisms identified in the cutting tool's coating were more intense under the conditions tested at the L_{cut} = 15 m.

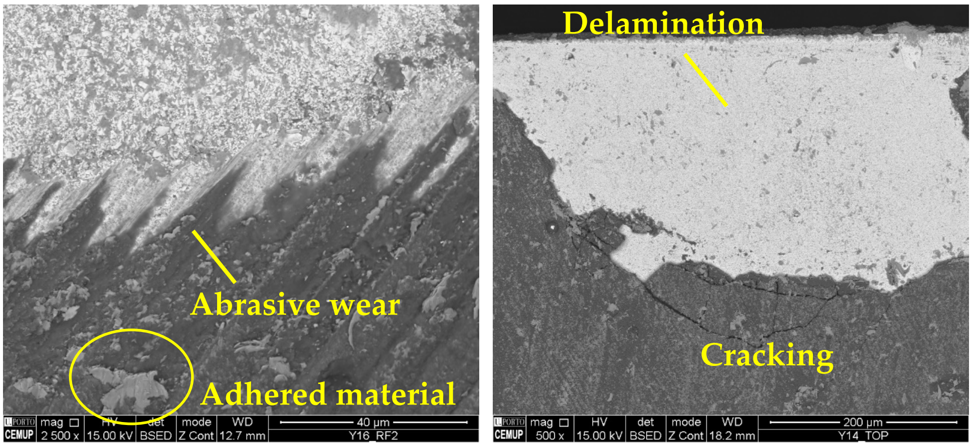

(**a**) (**b**)

Figure 8. Coating wear mechanisms: (**a**) abrasive wear and adhered material in the RF2 of the S75F100L15 condition at 2500× magnification and (**b**) delamination and cracking in the top view of the S75F75L15 condition at 500× magnification.

Thus, it appears that the increase in L_{cut} caused the development of increased wear mechanisms, such as abrasion and adhesion of the material to the tool surface. It can be said that the adhesion of the material is promoted as the test progresses, as the material accumulates in the grooves left on the tool's surface as a result of grinding [56]. Therefore, at a longer L_{cut}, the amount of accumulated material will be higher and, consequently, more abrasive wear will occur, which can lead to coating delamination. Under these conditions, delamination occurred in almost all situations, which also indicates a low adhesion of the coating to the tool substrate. In addition, the lowest wear among all the conditions was for S75F100L5 and S75F150L5, but, as it is the condition with the lowest v_c (75 m/min), the machining process was less productive and this could increase the industrial costs.

3.3.2. v_c of 100 m/min

Figure 9 illustrates the top view of the S100F100L5 and S100F100L15 conditions, where it is possible to observe the influence of the L_{cut} on the machining in these conditions.

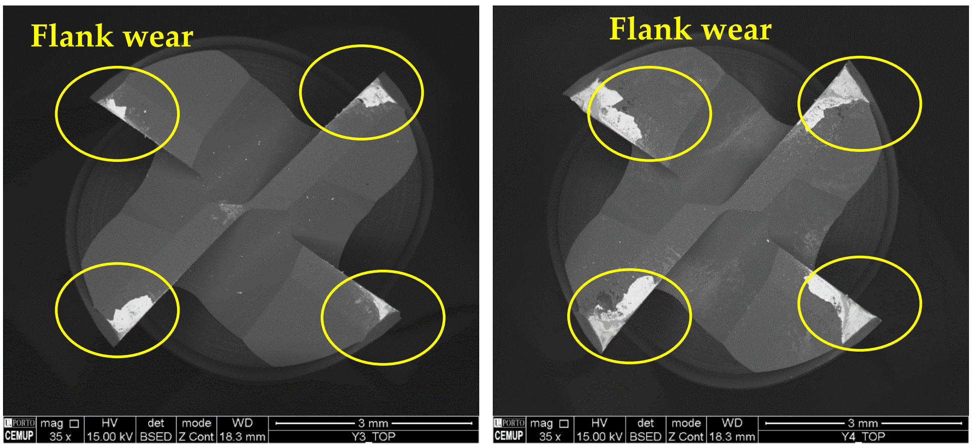

(**a**) (**b**)

Figure 9. Top view of the tools tested at a v_c of 100 m/min at 35× magnification: (**a**) S100F100L5 and (**b**) S100F100L15.

As mentioned, the impact of the L_{cut} seems to significantly increase the resulting wear, as can be seen from the measurements carried out and clearly seen in the images obtained.

As for the influence of f_z, due to the frictional wear to which the tool is subject at lower values of this parameter [75], the wear mark is broader for tools tested with a lower f_z, i.e., wear is more pronounced and deeper than in tools tested with higher values. This can modify the geometry of the tools and is also related to the chip generation process [17].

The predominant wear mechanisms on the tool substrate and coating were abrasion and material adhesion, the latter being more intense than in the cases tested at 75 m/min. It is seen that Inconel 718 commonly adheres to cutting tools [74]. The abrasive wear was more intense on the clearance face of the tools, as shown in Figure 10, and this type of wear is frequent when machining this alloy [76].

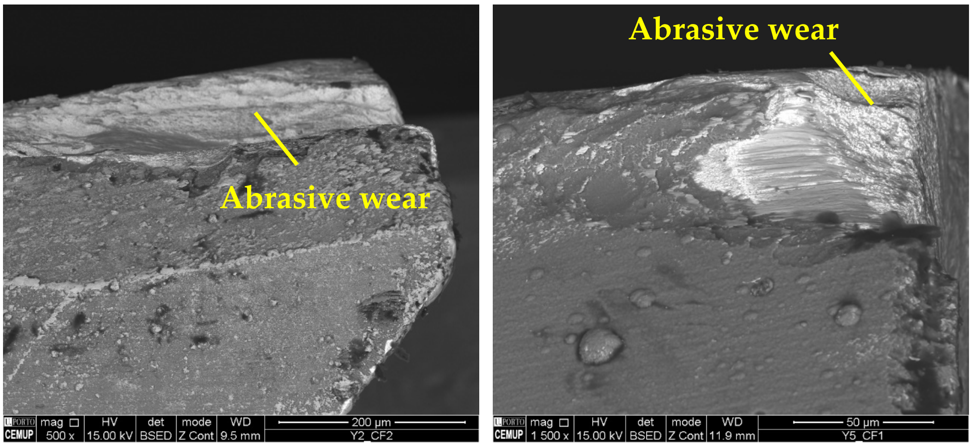

(**a**) (**b**)

Figure 10. Abrasive wear: (**a**) clearance face (CF2) of S100F75L15 at 500× magnification and (**b**) clearance face (CF1) of S100F150L5 at 1500× magnification.

Figure 11 illustrates the adhesion of the material to the tool substrate under the S100F150L15 condition, and three zones in which the analysis was carried out. This wear was registered on the tools' flank, edges, and rake face. In this case, EDS analysis was performed to confirm that it was Inconel 718, according to the chemical composition resulting from the analysis. Figure 12 illustrates the results of the EDS analysis for the three corresponding zones.

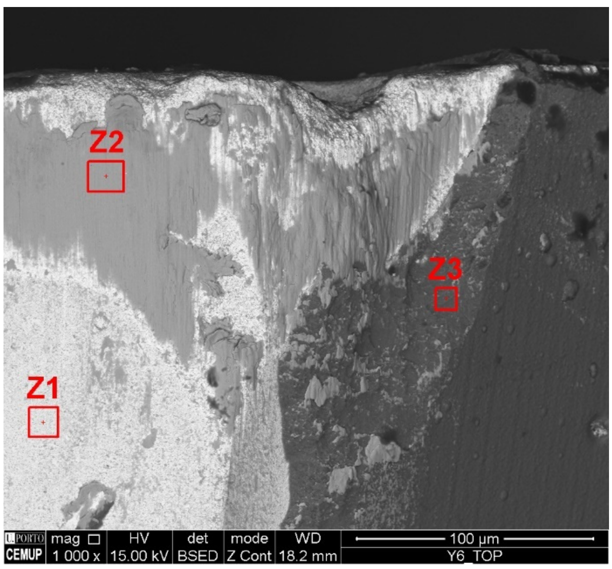

Figure 11. Condition S100F150L15 indicates material adhesion and has three zones for EDS analysis.

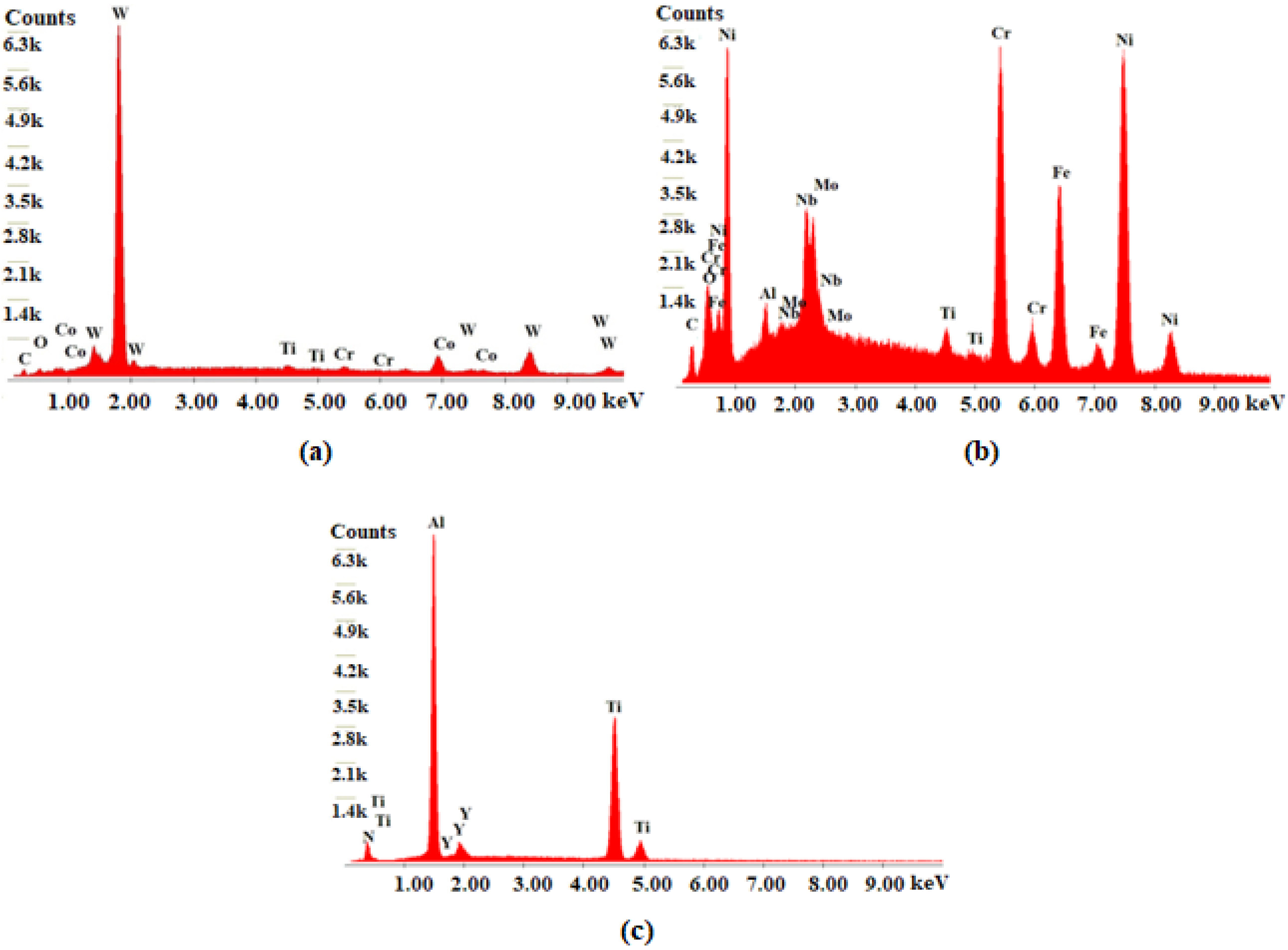

Figure 12. EDS spectra analysis of the three zones of S100F150L15: (**a**) Z1—tool substrate, (**b**) Z2—adhered machined material, and (**c**) Z3—coating.

According to the EDS analysis, zone 1, rich in tungsten, refers to the tool substrate; zone 2, in turn, is rich in Ni and with other elements present that are part of the composition of Inconel 718, indicating that it is machined material that is adhered to the substrate of the tool; and zone 3, indicating the constituent elements of the coating. Therefore, the coherence of the results obtained, based on the chemical composition of the areas indicated in the image, can be observed.

Regarding the wear mechanisms identified in the coating, delamination, chipping, and cracking can also be observed in addition to material adhesion and abrasion. Figure 13 illustrates cracking and delamination identified on the coating, and Figure 14 the chipping and delamination as well. This chipping may negatively affect process performance [77] due to the change in the cutting tool's geometry [78]. Another aspect is related to cracking propagation. Some authors, such as Zhang et al. [79] and Shuai et al. [80], suggest that the presence of an interlayer could provide high strength to the coating, and that, with this, the resistance to crack propagation increases. Furthermore, thinner layers significantly increase the resistance to crack propagation and protect the coating from delamination, improving its adhesion [81,82].

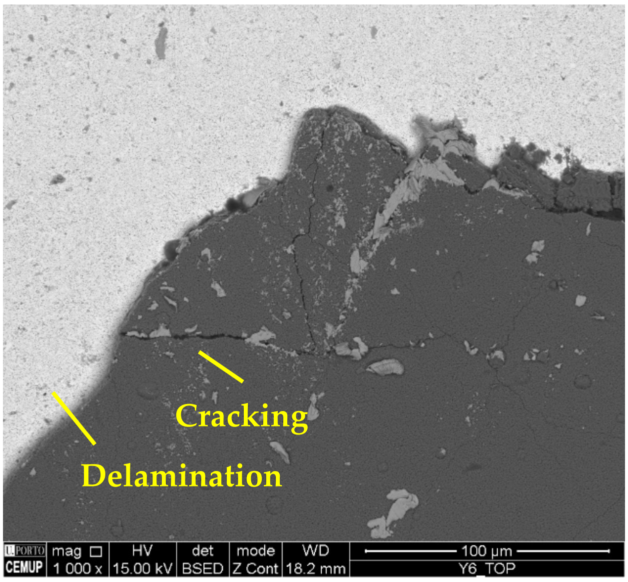

Figure 13. Delamination and cracking in the top view of S100F150L15 at 1000× magnification.

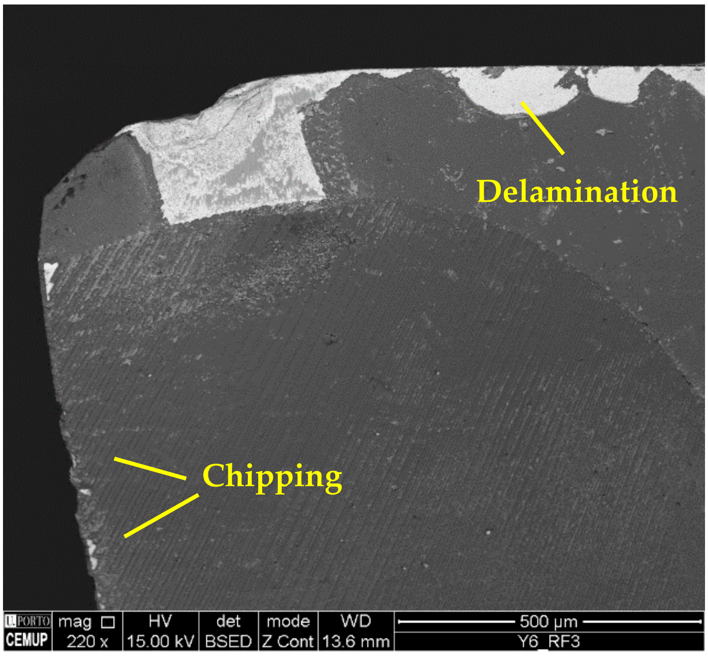

Figure 14. Delamination and chipping in RF3 of S100F150L15 at 220× magnification.

3.3.3. v_c of 125 m/min

Figure 15 illustrates the top view of two tools tested at 125 m/min under the S125F100L5 and S125F100L15 conditions. As seen in Section 3.3.2. the difference between these two conditions was not pronounced regarding VB3, even when the v_c increased. It can be observed that the maximum TW was similar, but in the 15 m condition it was more significant and expanded towards the centre of the cutting tool. However, in other conditions, as expected, the severity of the wear increased for higher values of L_{cut}, which further intensified the wear phenomena.

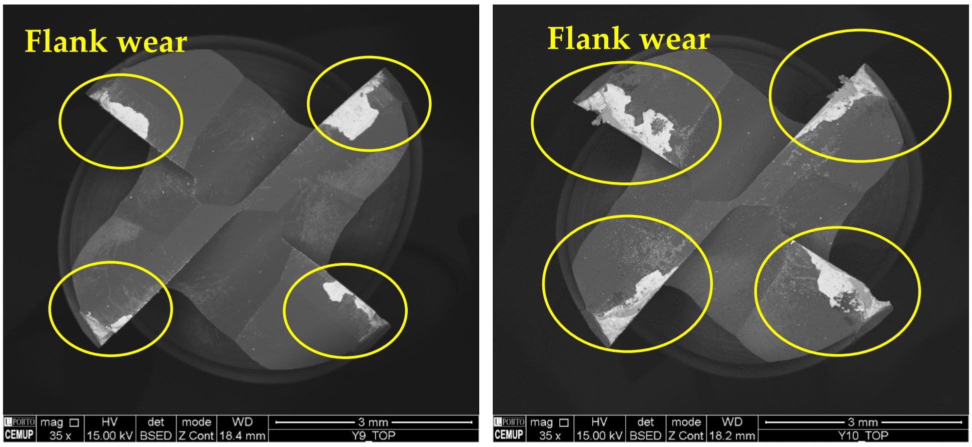

(**a**) (**b**)

Figure 15. Top view of the tools tested at a v_c of 125 m/min at 35× magnification: (**a**) S125F100L5 and (**b**) S125F100L15.

As in previous cases, the main wear mechanisms observed were abrasion and adhesion. However, under these conditions, the wear was higher and more expressive, with the beginning of the development of a BUE under the conditions tested at a L_{cut} = 15 m. The beginning of the development of a BUE indicates a large amount of adhered material, which tends to generate severe wear [83], as this mechanism increases abrasive wear and, consequently, leads to the occurrence of the delamination of the coating. Figure 16 illustrates the abrasive wear and material adhesion, both on the coating and the tool substrate, and Figure 17 illustrates the beginning of BUE development.

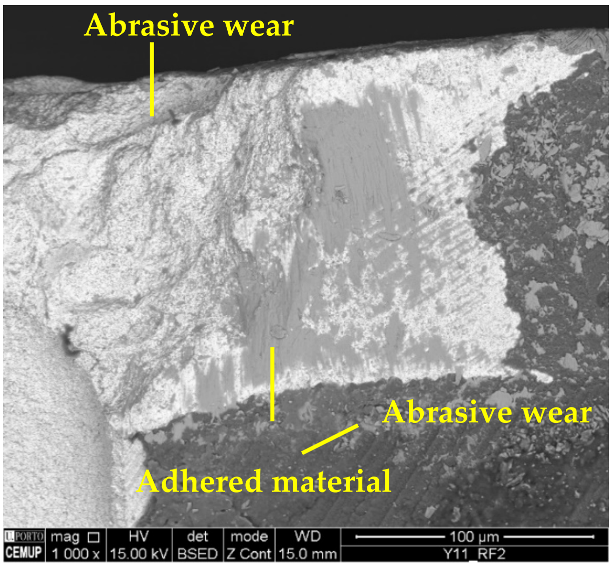

Figure 16. Wear mechanisms in condition S125F150L5: abrasive and adhesive wear on the tool substrate and coating.

It should be noted that the BUE is more common at a lower v_c, and changes the tool's geometry, which can accelerate TW [59]. The machining of Inconel 718 can be reasonably aggressive on cutting tools, promoting high levels of wear [76]. Furthermore, cracking, chipping, and delamination were observed in the coating. The formation of chips impairs the performance of the machining process, as this type of wear changes the geometry of the cutting tools, which causes the chip generation mechanisms to be modified, and consequently, the quality of the product obtained is lower [84]. Figure 18 illustrates the cracks in the coating seen under the S125F75L15 and S125F100L5 conditions, and Figure 19 illustrates chipping (S125F100L5) and delamination (S125F150L5).

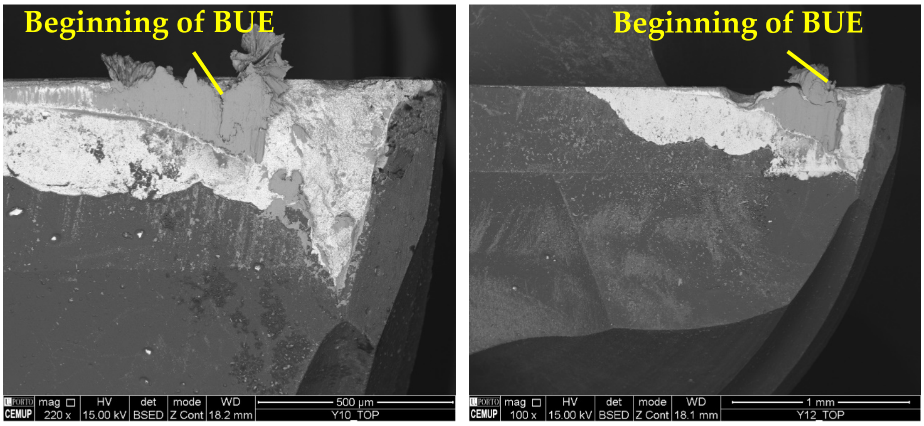

(**a**) (**b**)

Figure 17. Beginning of BUE development: (**a**) top view of S125F100L15 with 220× magnification and (**b**) top view of S125F150L15 with 100× magnification.

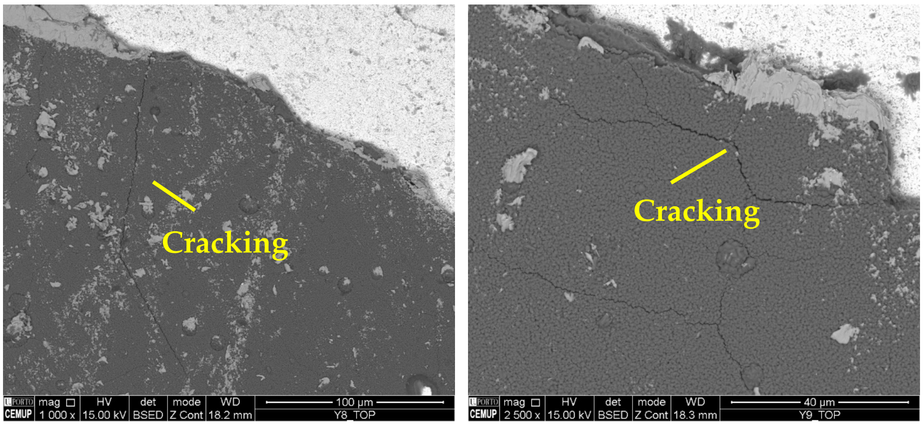

(**a**) (**b**)

Figure 18. Cracking in the coating: (**a**) top view of S125F75L15 at 1000× magnification and (**b**) top view of S125F100L5 at 2500× magnification.

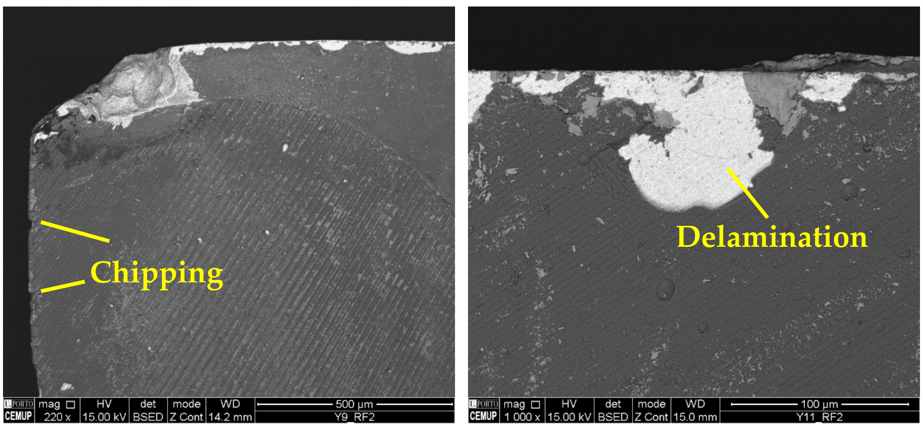

(**a**) (**b**)

Figure 19. Coating wear mechanisms: (**a**) chipping in RF2 of S125F100L5 condition at 220× magnification and (**b**) delamination in RF2 of S125F150L5 condition at 1000× magnification.

From the wear mechanisms identified, the difficulty of milling operations with Inconel 718 can be seen. But not only Inconel 718 brings this difficulty, which results in severe wear mechanisms; authors such as Martinho et al. [85] have analysed and detected similar mechanisms as a result of the machining of other materials that are also considered difficult to machine.

4. Conclusions

The present work describes a comparative evaluation of milling parameters regarding their influence on the quality of the machined surface and the resulting tool wear. Machining parameters such as v_c, f_z, and L_{cut} were altered for this evaluation. Regarding the results obtained, the following conclusions can be drawn:

- The machining parameters influence the process, with the L_{cut} having the highest influence;
- The lowest roughness values for the machined surface were obtained using the S75F75L5 condition;
- Due to sustained TW, the v_c had no apparent influence on roughness;
- Regarding the SD observed in SR measurements, it can be stated that the change in the measurements from the centre to the periphery of different conditions was induced by the increased TW observed during the path followed by the tool for the machining strategy adopted;
- The greatest *VB* was observed for the S125F75L15 condition, and the lowest for the S75F150L5 condition, which were clearly influenced by the L_{cut};
- For higher v_c and L_{cut} values, the wear developed was more intense;
- The predominant wear mechanisms were abrasive and adhesive wear on the coating and the tool substrate. Delamination, chipping, and cracking were also observed in the coated tools;
- At a L_{cut} of 15 m and v_c of 125 m/min, BUE development was generated;
- Even at a L_{cut} = 5 m, much wear was observed, which indicates the difficulty of machining Inconel 718, leading to the realisation that these cutting tools are unsuitable for these kinds of operations with higher L_{cut} values.

Therefore, the results show a need to improve the process further, especially regarding the high wear on the coating. The coatings' adhesion must also be improved, since coating delamination was observed under all conditions. Therefore, adding an interlayer before applying the coating now used is suggested, with the aim to improve its adhesion and reduce cracking propagation, consequently improving the process performance. Furthermore, the wear behaviour of this coating in cutting tools of different geometries can be compared with the results obtained in this work. Moreover, the results clearly indicate the need for a new study focused on the coating deposition parameters and the optimisation of machining parameters.

In addition, as a limitation of this study, the difficulty of machining Inconel 718 is highlighted, as well as the use of few machining conditions, making it necessary to expand them so that this analysis would be more complete. Based on this, for future work we recommend the use of more samples and machining conditions, as well as the use of a interlayer coating in order to avoid delamination, and the comparison of this coating's behaviour with other coatings and with uncoated tools. In addition, we recommend carrying out a statistical analysis of the results obtained.

Author Contributions: Conceptualisation: F.J.G.S., R.C.M.S.-C. and R.P.M.; methodology: N.P.V.S. and R.C.M.S.-C.; validation: F.J.G.S., R.C.M.S.-C. and R.P.M.; formal analysis: R.D.F.S.C., R.C.M.S.-C. and M.L.S.B.; investigation: N.P.V.S. and F.J.G.S.; data curation: N.P.V.S., R.D.F.S.C., M.L.S.B. and F.J.G.S.; writing—original draft preparation: N.P.V.S. and F.J.G.S.; writing—review and editing: A.F.V.P. and F.J.G.S.; visualisation: A.F.V.P., F.J.G.S., R.C.M.S.-C., M.L.S.B. and R.P.M.; supervision: F.J.G.S. and R.C.M.S.-C.; project administration: F.J.G.S.; funding acquisition: F.J.G.S. All authors have read and agreed to the published version of the manuscript.

Funding: The work is developed under the "DRIVOLUTION—Transition to the factory of the future", with the reference DRIVOLUTION C644913740-00000022 research project, supported by European Structural and Investments Funds with the "Portugal2020" program scope.

Data Availability Statement: No new data were created.

Acknowledgments: The authors thank ISEP, INEGI, and FEUP for their institutional support. The authors also acknowledge Rui Rocha from CEMUP Lab due to his contribution on the SEM analyses and interpretation, and to Ricardo Alexandre from INOVATOOLS company due to his availability to provide free of charge the tools used in this work, as well as Victor Moreira due to his collaboration in machining tests.

Conflicts of Interest: The authors declare no conflicts of interest.

Appendix A

Here lies the statistical analysis on the influence of each parameter on surface quality.

Table A1. *t*-test: two samples with different variances, comparison between their L_{cut} values, part 1.

	S75F75L5	**S75F75L15**	**S75F100L5**	**S75F100L15**	**S75F150L5**	**S75F150L15**	**S100F75L5**	**S100F75L15**	**S100F100L5**	**S100F100L15**	**S100F150L5**	**S100F150L15**
Mean	0.372	0.670	0.448	0.631	0.502	0.533	0.483	0.708	0.578	0.859	0.605	0.827
Variance	0.005	0.000	0.000	0.002	0.002	0.003	0.004	0.002	0.003	0.001	0.007	0.001
Observations	5	5	5	5	5	5	5	5	5	5	5	5
Hypothesised mean Difference	0		0		0		0		0		0	
df	5		6		8		8		7		5	
t Stat	−9.612		−8.683		−0.954		−6.430		−9.728		−5.501	
P(T <= t) one-tail	0.000		0.000		0.184		0.000		0.000		0.001	
t critical one-tail	2.015		1.943		1.860		1.860		1.895		2.015	
P(T <= t) two-tail	0.000		0.000		0.368		0.000		0.000		0.003	
t critical two-tail	2.571		2.447		2.306		2.306		2.365		2.571	

Table A2. *t*-Test: two samples with different variances, comparison between their L_{cut} values, part 2.

	S125F75L5	**S125F75L15**	**S125F100L5**	**S125F100L15**	**S125F150L5**	**S125F150L15**
Mean	0.935	1.299	0.595	0.659	0.975	1.073
Variance	0.020	0.095	0.003	0.002	0.012	0.012
Observations	5	5	5	5	5	5
Hypothesised mean Difference	0		0		0	
df	6		8		8	
t Stat	−2.398		−2.039		−1.392	
P(T <= t) one-tail	0.027		0.038		0.101	
t critical one-tail	1.943		1.860		1.860	
P(T <= t) two-tail	0.053		0.076		0.201	
t critical two-tail	2.447		2.306		2.306	

Table A3. *t*-Test: two samples with different variances, comparison between their *f* values, part 1.

	S75F75L5	S75F100L5	S75F75L15	S75F100L15	S100F75L5	S100F100L5	S100F75L15	S100F100L15	S125F75L5	S125F100L5	S125F75L15	S125F100L15
Mean	0.372	0.448	0.670	0.631	0.483	0.578	0.708	0.859	0.935	0.595	1.299	0.659
Variance	0.005	0.000	0.000	0.002	0.004	0.003	0.002	0.001	0.020	0.003	0.095	0.002
Observations	5	5	5	5	5	5	5	5	5	5	5	5
Hypothesised Mean Difference	0		0		0		0		0		0	
df	5		5		8		7		5		4	
t Stat	−2.435		1.891		−2.592		−5.614		5.036		4.584	
P(T <= t) one-tail	0.029		0.059		0.016		0.000		0.002		0.005	
t critical one-tail	2.015		2.015		1.860		1.895		2.015		2.132	
P(T <= t) two-tail	0.059		0.117		0.032		0.001		0.004		0.010	
t critical two-tail	2.571		2.571		2.306		2.365		2.571		2.776	

Table A4. *t*-Test: two samples with different variances, comparison between their *f* values, part 2.

	S75F100L5	S75F150L5	S75F100L15	S75F150L15	S100F100L5	S100F150L5	S100F100L15	S100F150L15	S125F100L5	S125F150L5	S125F100L15	S125F150L15
Mean	0.448	0.502	0.631	0.533	0.578	0.605	0.859	0.827	0.595	0.975	0.659	1.073
Variance	0.000	0.002	0.002	0.003	0.003	0.007	0.001	0.001	0.003	0.012	0.002	0.012
Observations	5	5	5	5	5	5	5	5	5	5	5	5
Hypothesised Mean Difference	0		0		0		0		0		0	
df	5		8		7		8		6		5	
t Stat	−2.295		3.238		−0.608		1.571		−6.987		−7.607	
P(T <= t) one-tail	0.035		0.006		0.281		0.077		0.000		0.000	
t critical one-tail	2.015		1.860		1.895		1.860		1.943		2.015	
P(T <= t) two-tail	0.070		0.012		0.563		0.155		0.000		0.001	
t critical two-tail	2.571		2.306		2.365		2.306		2.447		2.571	

Table A5. *t*-Test: two samples with different variances, comparison between their *f* values, part 3.

	S75F75L5	S75F150L5	S75F75L15	S75F150L15	S100F75L5	S100F150L5	S100F75L15	S100F150L15	S125F75L5	S125F150L5	S125F75L15	S125F150L15
Mean	0.372	0.502	0.670	0.533	0.483	0.605	0.708	0.827	0.935	0.975	1.299	1.073
Variance	0.005	0.002	0.000	0.003	0.004	0.007	0.002	0.001	0.020	0.012	0.095	0.012
Observations	5	5	5	5	5	5	5	5	5	5	5	5
Hypothesised Mean Difference	0		0		0		0		0		0	
df	7		5		7		7		8		5	
t Stat	−3.509		5.527		−2.633		−4.514		−0.500		1.542	
P(T <= t) one-tail	0.005		0.001		0.017		0.001		0.315		0.092	
t critical one-tail	1.895		2.015		1.895		1.895		1.860		2.015	
P(T <= t) two-tail	0.010		0.003		0.034		0.003		0.631		0.184	
t critical two-tail	2.365		2.571		2.365		2.365		2.306		2.571	

Table A6. *t*-Test: two samples with different variances, comparison between their *s* values, part 1.

	S75F75L5	S100F75L5	S75F75L15	S100F75L15	S75F100L5	S100F100L5	S75F100L15	S100F100L15	S75F150L5	S100F150L5	S75F150L15	S100F150L15
Mean	0.372	0.483	0.670	0.708	0.448	0.578	0.631	0.859	0.502	0.605	0.533	0.827
Variance	0.005	0.004	0.000	0.002	0.000	0.003	0.002	0.001	0.002	0.007	0.003	0.001
Observations	5	5	5	5	5	5	5	5	5	5	5	5
Hypothesised Mean Difference	0		0		0		0		0		0	
df	8		5		5		8		6		6	
t Stat	−2.739		−1.623		−4.948		−9.368		−2.369		−10.72	
P(T <= t) one-tail	0.013		0.083		0.002		0.000		0.028		0.000	
t critical one-tail	1.860		2.015		2.015		1.860		1.943		1.943	
P(T <= t) two-tail	0.025		0.165		0.004		0.000		0.056		0.000	
t critical two-tail	2.306		2.571		2.571		2.306		2.447		2.447	

Table A7. *t*-Test: two samples with different variances, comparison between their *s* values, part 2.

	S100F75L5	S125F75L5	S100F75L15	S125F75L15	S100F100L5	S125F100L5	S100F100L15	S125F100L15	S100F150L5	S125F150L5	S100F150L15	S125F150L15
Mean	0.483	0.935	0.708	1.299	0.578	0.595	0.859	0.659	0.605	0.975	0.827	1.073
Variance	0.004	0.020	0.002	0.095	0.003	0.003	0.001	0.002	0.007	0.012	0.001	0.012
Observations	5	5	5	5	5	5	5	5	5	5	5	5
Hypothesised Mean Difference	0		0		0		0		0		0	
df	5		4		8		7		7		5	
t Stat	−6.543		−4.227		−0.513		7.611		−5.945		−4.744	
P(T <= t) one-tail	0.001		0.007		0.311		0.000		0.000		0.003	
t critical one-tail	2.015		2.132		1.860		1.895		1.895		2.015	
P(T <= t) two-tail	0.001		0.013		0.622		0.000		0.001		0.005	
t critical two-tail	2.571		2.776		2.306		2.365		2.365		2.571	

Table A8. *t*-Test: two samples with different variances, comparison between their *s* values, part 3.

	S75F75L5	S125F75L5	S75F75L15	S125F75L15	S75F100L5	S125F100L5	S75F100L15	S125F100L15	S75F150L5	S125F150L5	S75F150L15	S125F150L15
Mean	0.372	0.935	0.670	1.299	0.448	0.595	0.631	0.659	0.502	0.975	0.533	1.073
Variance	0.005	0.020	0.000	0.095	0.000	0.003	0.002	0.002	0.002	0.012	0.003	0.012
Observations	5	5	5	5	5	5	5	5	5	5	5	5
Hypothesised Mean Difference	0		0		0		0		0		0	
df	6		4		5		8		5		6	
t Stat	−8.009		−4.551		−6.031		−0.965		−8.762		−9.774	
P(T <= t) one-tail	0.000		0.005		0.001		0.181		0.000		0.000	
t critical one-tail	1.943		2.132		2.015		1.860		2.015		1.943	
P(T <= t) two-tail	0.000		0.010		0.002		0.363		0.000		0.000	
t critical two-tail	2.447		2.776		2.571		2.306		2.571		2.447	

References

1. Qi, H.; Azer, M.; Ritter, A. Studies of Standard Heat Treatment Effects on Microstructure and Mechanical Properties of Laser Net Shape Manufactured INCONEL 718. *Metall. Mater. Trans. A* **2009**, *40*, 2410–2422. [CrossRef]
2. Thomas, A.; El-Wahabi, M.; Cabrera, J.M.; Prado, J.M. High Temperature Deformation of Inconel 718. *J. Mater. Process Technol.* **2006**, *177*, 469–472. [CrossRef]
3. Ding, R.G.; Huang, Z.W.; Li, H.Y.; Mitchell, I.; Baxter, G.; Bowen, P. Electron Microscopy Study of Direct Laser Deposited IN718. *Mater. Charact.* **2015**, *106*, 324–337. [CrossRef]
4. Smith, D.H.; Bicknell, J.; Jorgensen, L.; Patterson, B.M.; Cordes, N.L.; Tsukrov, I.; Knezevic, M. Microstructure and Mechanical Behavior of Direct Metal Laser Sintered Inconel Alloy 718. *Mater. Charact.* **2016**, *113*, 1–9. [CrossRef]
5. Zhao, X.; Chen, J.; Lin, X.; Huang, W. Study on Microstructure and Mechanical Properties of Laser Rapid Forming Inconel 718. *Mater. Sci. Eng. A* **2008**, *478*, 119–124. [CrossRef]
6. Hosseini, E.; Popovich, V.A. A Review of Mechanical Properties of Additively Manufactured Inconel 718. *Addit. Manuf.* **2019**, *30*, 100877. [CrossRef]
7. Liu, F.; Lin, X.; Song, M.; Zhao, W.; Chen, J.; Huang, W. Effect of Intermediate Heat Treatment Temperature on Microstructure and Notch Sensitivity of Laser Solid Formed Inconel 718 Superalloy. *J. Wuhan Univ. Technol.-Mater. Sci. Ed.* **2011**, *26*, 908–913. [CrossRef]
8. Blackwell, P.L. The Mechanical and Microstructural Characteristics of Laser-Deposited IN718. *J. Mater. Process Technol.* **2005**, *170*, 240–246. [CrossRef]
9. Lu, Y.; Wu, S.; Gan, Y.; Huang, T.; Yang, C.; Junjie, L.; Lin, J. Study on the Microstructure, Mechanical Property and Residual Stress of SLM Inconel-718 Alloy Manufactured by Differing Island Scanning Strategy. *Opt. Laser Technol.* **2015**, *75*, 197–206. [CrossRef]
10. Lal Virdi, R.; Singh Chatha, S.; Singh, H. Performance Evaluation of Inconel 718 under Vegetable Oils Based Nanofluids Using Minimum Quantity Lubrication Grinding. *Mater. Today Proc.* **2020**, *33*, 1538–1545. [CrossRef]
11. Ma, L.; Zhang, L.; Guo, F.; Du, W.; Luo, Y. High-Temperature Mechanical Behavior Assessment Based on a Developed Constitutive Model of Inconel 718 Fabricated by Selective Laser Melting. *Adv. Eng. Mater.* **2021**, *23*, 2100232. [CrossRef]
12. Roy, S.; Kumar, R.; Anurag; Panda, A.; Das, R.K. A Brief Review on Machining of Inconel 718. *Mater. Today Proc.* **2018**, *5 Pt 3*, 18664–18673. [CrossRef]
13. Outeiro, J.C.; Pina, J.C.; M'Saoubi, R.; Pusavec, F.; Jawahir, I.S. Analysis of Residual Stresses Induced by Dry Turning of Difficult-to-Machine Materials. *CIRP Ann.* **2008**, *57*, 77–80. [CrossRef]
14. Shokrani, A.; Dhokia, V.; Newman, S.T. Hybrid Cooling and Lubricating Technology for CNC Milling of Inconel 718 Nickel Alloy. *Procedia Manuf.* **2017**, *11*, 625–632. [CrossRef]
15. Ezugwu, E.O.; Wang, Z.M.; Okeke, C.I. Tool Life and Surface Integrity When Machining Inconel 718 with PVD- and CVD-Coated Tools. *Tribol. Trans.* **1999**, *42*, 353–360. [CrossRef]
16. Pedroso, A.F.V.; Sousa, V.F.C.; Sebbe, N.P.V.; Silva, F.J.G.; Campilho, R.D.S.G.; Sales-Contini, R.C.M.; Jesus, A.M.P. A Comprehensive Review on the Conventional and Non-Conventional Machining and Tool-Wear Mechanisms of INCONEL®. *Metals* **2023**, *13*, 585. [CrossRef]
17. Sousa, V.F.C.; Da Silva, F.J.G.; Pinto, G.F.; Baptista, A.; Alexandre, R. Characteristics and Wear Mechanisms of TiAlN-Based Coatings for Machining Applications: A Comprehensive Review. *Metals* **2021**, *11*, 260. [CrossRef]
18. Sharman, A.; Dewes, R.C.; Aspinwall, D.K. Tool Life When High Speed Ball Nose End Milling Inconel 718™. *J. Mater. Process Technol.* **2001**, *118*, 29–35. [CrossRef]
19. Le Coz, G.; Dudzinski, D. Temperature Variation in the Workpiece and in the Cutting Tool When Dry Milling Inconel 718. *Int. J. Adv. Manuf. Technol.* **2014**, *74*, 1133–1139. [CrossRef]
20. Çelik, A.; Sert Alağaç, M.; Turan, S.; Kara, A.; Kara, F. Wear Behavior of Solid SiAlON Milling Tools during High Speed Milling of Inconel 718. *Wear* **2017**, *378–379*, 58–67. [CrossRef]
21. Li, W.; Guo, Y.B.; Barkey, M.E.; Jordon, J.B. Effect Tool Wear During End Milling on the Surface Integrity and Fatigue Life of Inconel 718. *Procedia CIRP* **2014**, *14*, 546–551. [CrossRef]
22. Feng, Y.; Pan, Z.; Liang, S.Y. Temperature Prediction in Inconel 718 Milling with Microstructure Evolution. *Int. J. Adv. Manuf. Technol.* **2018**, *95*, 4607–4621. [CrossRef]
23. Yan, S.; Zhu, D.; Zhuang, K.; Zhang, X.; Ding, H. Modeling and Analysis of Coated Tool Temperature Variation in Dry Milling of Inconel 718 Turbine Blade Considering Flank Wear Effect. *J. Mater. Process Technol.* **2014**, *214*, 2985–3001. [CrossRef]
24. Liao, Y.S.; Lin, H.M.; Wang, J.H. Behaviors of End Milling Inconel 718 Superalloy by Cemented Carbide Tools. *J. Mater. Process Technol.* **2008**, *201*, 460–465. [CrossRef]
25. Maiyar, L.M.; Ramanujam, R.; Venkatesan, K.; Jerald, J. Optimization of Machining Parameters for End Milling of Inconel 718 Super Alloy Using Taguchi Based Grey Relational Analysis. *Procedia Eng.* **2013**, *64*, 1276–1282. [CrossRef]
26. Sebbe, N.P.V.; Fernandes, F.; Sousa, V.F.C.; Silva, F.J.G. Hybrid Manufacturing Processes Used in the Production of Complex Parts: A Comprehensive Review. *Metals* **2022**, *12*, 1874. [CrossRef]
27. Li, H.Z.; Zeng, H.; Chen, X.Q. An Experimental Study of Tool Wear and Cutting Force Variation in the End Milling of Inconel 718 with Coated Carbide Inserts. *J. Mater. Process Technol.* **2006**, *180*, 296–304. [CrossRef]
28. Kuo, C.-P.; Ling, C.-C.; Chen, S.-H.; Chang, C.-W. The Prediction of Cutting Force in Milling Inconel-718. *Int. J. Adv. Manuf. Technol.* **2006**, *27*, 655–660. [CrossRef]

29. Mahmood, J.; Mustafa, G.; Ali, M. Accurate Estimation of Tool Wear Levels during Milling, Drilling and Turning Operations by Designing Novel Hyperparameter Tuned Models Based on LightGBM and Stacking. *Measurement* **2022**, *190*, 110722. [CrossRef]
30. Aslantas, K.; Alatrushi, L.K.H. Experimental Study on the Effect of Cutting Tool Geometry in Micro-Milling of Inconel 718. *Arab. J. Sci. Eng.* **2021**, *46*, 2327–2342. [CrossRef]
31. Wang, J.; Yan, Y.; Li, C.; Geng, Y. Material Removal Mechanism and Subsurface Characteristics of Silicon 3D Nanomilling. *Int. J. Mech. Sci.* **2023**, *242*, 108020. [CrossRef]
32. Sahab, A.R.M.; Saad, N.H.; Kasolang, S.; Saedon, J. Impact of Plasma Spray Variables Parameters on Mechanical and Wear Behaviour of Plasma Sprayed Al_2O_3 3%wt TiO_2 Coating in Abrasion and Erosion Application. *Procedia Eng.* **2012**, *41*, 1689–1695. [CrossRef]
33. Nogueira, F.R.; Pedroso, A.F.V.; Sousa, V.F.C.; Sebbe, N.P.V.; Sales-Contini, R.C.M.; Barbosa, M.L.S. A Brief Review of Injection-Mould Materials Hybrid Manufacturing Processes. In *Flexible Automation and Intelligent Manufacturing: Establishing Bridges for More Sustainable Manufacturing Systems*; Silva, F.J.G., Pereira, A.B., Campilho, R.D.S.G., Eds.; Springer Nature: Cham, Switzerland, 2024; pp. 796–806.
34. Silva, F.; Martinho, R.; Andrade, M.; Baptista, A.; Alexandre, R. Improving the Wear Resistance of Moulds for the Injection of Glass Fibre–Reinforced Plastics Using PVD Coatings: A Comparative Study. *Coatings* **2017**, *7*, 28. [CrossRef]
35. Ucun, İ.; Aslantas, K.; Bedir, F. The Performance Of DLC-Coated and Uncoated Ultra-Fine Carbide Tools in Micromilling of Inconel 718. *Precis. Eng.* **2015**, *41*, 135–144. [CrossRef]
36. Sousa, V.F.C.; Silva, F.J.G.; Alexandre, R.; Fecheira, J.S.; Silva, F.P.N. Study of the Wear Behaviour of TiAlSiN and TiAlN PVD Coated Tools on Milling Operations of Pre-Hardened Tool Steel. *Wear* **2021**, *476*, 203695. [CrossRef]
37. Baptista, A.; Silva, F.; Porteiro, J.; Míguez, J.; Pinto, G. Sputtering Physical Vapour Deposition (PVD) Coatings: A Critical Review on Process Improvement and Market Trend Demands. *Coatings* **2018**, *8*, 402. [CrossRef]
38. Depla, D.; Mahieu, S.; Greene, J.E. Chapter 5-Sputter Deposition Processes. In *Handbook of Deposition Technologies for Films and Coatings*, 3rd ed.; Martin, P.M., Ed.; William Andrew Publishing: Boston, MA, USA, 2010; pp. 253–296. [CrossRef]
39. Machunze, R.; Ehiasarian, A.P.; Tichelaar, F.D.; Janssen, G.C.A.M. Stress and Texture in HIPIMS TiN Thin Films. *Thin Solid. Films* **2009**, *518*, 1561–1565. [CrossRef]
40. Ferreira, F.; Oliveira, J.C.; Cavaleiro, A. CrN Thin Films Deposited by HiPIMS in DOMS Mode. *Surf. Coat. Technol.* **2016**, *291*, 365–375. [CrossRef]
41. Alhafian, M.-R.; Chemin, J.-B.; Fleming, Y.; Bourgeois, L.; Penoy, M.; Useldinger, R.; Soldera, F.; Mücklich, F.; Choquet, P. Comparison on the Structural, Mechanical and Tribological Properties of TiAlN Coatings Deposited by HiPIMS and Cathodic Arc Evaporation. *Surf. Coat. Technol.* **2021**, *423*, 127529. [CrossRef]
42. Sousa, V.F.C.; Silva, F.J.G.; Lopes, H.; Casais, R.C.B.; Baptista, A.; Pinto, G.; Alexandre, R. Wear Behavior and Machining Performance of TiAlSiN-Coated Tools Obtained by Dc MS and HiPIMS: A Comparative Study. *Materials* **2021**, *14*, 5122. [CrossRef]
43. Mitsuo, A.; Uchida, S.; Nihira, N.; Iwaki, M. Improvement of High-Temperature Oxidation Resistance of Titanium Nitride and Titanium Carbide Films by Aluminum Ion Implantation. *Surf. Coat. Technol.* **1998**, *103–104*, 98–103. [CrossRef]
44. Liew, W.Y.H.; Lim, H.P.; Melvin, G.J.H.; Dayou, J.; Jiang, Z.-T. Thermal Stability, Mechanical Properties, and Tribological Performance of TiAlXN Coatings: Understanding the Effects of Alloying Additions. *J. Mater. Res. Technol.* **2022**, *17*, 961–1012. [CrossRef]
45. Tomaszewski, Ł.; Gulbiński, W.; Urbanowicz, A.; Suszko, T.; Lewandowski, A.; Gulbiński, W. TiAlN Based Wear Resistant Coatings Modified by Molybdenum Addition. *Vacuum* **2015**, *121*, 223–229. [CrossRef]
46. Yi, J.; Chen, S.; Chen, K.; Xu, Y.; Chen, Q.; Zhu, C.; Liu, L. Effects of Ni Content on Microstructure, Mechanical Properties and Inconel 718 Cutting Performance of AlTiN-Ni Nanocomposite Coatings. *Ceram. Int.* **2019**, *45*, 474–480. [CrossRef]
47. Liu, Z.R.; Chen, L.; Du, Y.; Zhang, S. Influence of Ru-Addition on Thermal Decomposition and Oxidation Resistance of TiAlN Coatings. *Surf. Coat. Technol.* **2020**, *401*, 126234. [CrossRef]
48. Yang, K.; Xian, G.; Zhao, H.; Fan, H.; Wang, J.; Wang, H.; Du, H. Effect of Mo Content on the Structure and Mechanical Properties of TiAlMoN Films Deposited on WC–Co Cemented Carbide Substrate by Magnetron Sputtering. *Int. J. Refract. Metals Hard Mater.* **2015**, *52*, 29–35. [CrossRef]
49. Münz, W.-D. Oxidation Resistance of Hard Wear Resistant $Ti_{0,5}Al_{0,5}N$ Coatings Grown by Magnetron Sputter Deposition. *Mater. Corros.* **1990**, *41*, 753–754. [CrossRef]
50. Mo, J.; Wu, Z.; Yao, Y.; Zhang, Q.; Wang, Q. Influence of Y-Addition and Multilayer Modulation on Microstructure, Oxidation Resistance and Corrosion Behavior of $Al_{0.67}Ti_{0.33}N$ Coatings. *Surf. Coat. Technol.* **2018**, *342*, 129–136. [CrossRef]
51. Choi, W.S.; Hwang, S.K.; Lee, C.M. Microstructure and Chemical State of Ti1−xYxN Film Deposited by Reactive Magnetron Sputtering. *J. Vac. Sci. Technol. A* **2000**, *18*, 2914–2921. [CrossRef]
52. Aninat, R.; Valle, N.; Chemin, J.-B.; Duday, D.; Michotte, C.; Penoy, M.; Bourgeois, L.; Choquet, P. Addition of Ta and Y in a Hard Ti-Al-N PVD Coating: Individual and Conjugated Effect on the Oxidation and Wear Properties. *Corros. Sci.* **2019**, *156*, 171–180. [CrossRef]
53. Moser, M.; Kiener, D.; Scheu, C.; Mayrhofer, P.H. Influence of Yttrium on the Thermal Stability of Ti-Al-N Thin Films. *Materials* **2010**, *3*, 1573–1592. [CrossRef]
54. Alauddin, M.; El Baradie, M.A.; Hashmi, M.S.J. End-Milling Machinability of Inconel 718. *Proc. Inst. Mech. Eng. B J. Eng. Manuf.* **1996**, *210*, 11–23. [CrossRef]

55. Niyas, S.; Winowlin Jappes, J.T.; Adamkhan, M.; Brintha, N.C. An Effective Approach to Predict the Minimum Tool Wear of Machining Process of Inconel 718. *Mater. Today Proc.* **2022**, *60*, 1819–1834. [CrossRef]
56. Sousa, V.F.C.; Fernandes, F.; Silva, F.J.G.; Costa, R.D.F.S.; Sebbe, N.; Sales-Contini, R.C.M. Wear Behavior Phenomena of TiN/TiAlN HiPIMS PVD-Coated Tools on Milling Inconel 718. *Metals* **2023**, *13*, 684. [CrossRef]
57. *ISO 21920-3:2021*; Geometrical Product Specifications (GPS)-Surface Texture: Profile—Part 3: Specification Operators. International Organization for Standardization: Geneva, Switzerland, 2021.
58. *ISO 8688-2:1986*; Tool Life Testing in Milling–Part 2: End Milling. International Organization for Standardization: Geneva, Switzerland, 1986.
59. Sebbe, N.P.V.; Fernandes, F.; Silva, F.J.G.; Sousa, V.F.C.; Sales-Contini, R.C.M.; Campilho, R.D.S.G.; Pedroso, A.F.V. Wear Behavior Analysis of TiN/TiAlN Coated Tools in Milling of Inconel 718. In *Flexible Automation and Intelligent Manufacturing: Establishing Bridges for More Sustainable Manufacturing Systems*; Springer Nature: Cham, Switzerland, 2024; pp. 784–795. [CrossRef]
60. Kumar, S.; Saravanan, I.; Patnaik, L. Optimization of Surface Roughness and Material Removal Rate in Milling of AISI 1005 Carbon Steel Using Taguchi Approach. *Mater. Today Proc.* **2020**, *22*, 654–658. [CrossRef]
61. Airao, J.; Chaudhary, B.; Bajpai, V.; Khanna, N. An Experimental Study of Surface Roughness Variation in End Milling of Super Duplex 2507 Stainless Steel. *Mater Today Proc* **2018**, *5 Pt 1*, 3682–3689. [CrossRef]
62. Buj-Corral, I.; Vivancos-Calvet, J.; Domínguez-Fernández, A. Surface Topography in Ball-End Milling Processes as a Function of Feed per Tooth and Radial Depth of Cut. *Int. J. Mach. Tools Manuf.* **2012**, *53*, 151–159. [CrossRef]
63. Čep, R.; Janásek, A.; Petru, J.; Sadilek, M.; Mohyla, P.; Valíček, J.; Harničárová, M.; Czán, A. Surface Roughness after Machining and Influence of Feed Rate on Process. In *Precision Machining VII*; Key Engineering Materials; Trans Tech Publications Ltd.: Wollerau, Switzerland, 2014; Volume 581, pp. 341–347. [CrossRef]
64. Ramesh, S.; Karunamoorthy, L.; Palanikumar, K. Surface Roughness Analysis in Machining of Titanium Alloy. *Mater. Manuf. Process.* **2008**, *23*, 174–181. [CrossRef]
65. Zimmermann, R.; Welling, D.; Venek, T.; Ganser, P.; Bergs, T. Tool Wear Progression of SiAlON Ceramic End Mills in Five-Axis High-Feed Rough Machining of an Inconel 718 BLISK. *Procedia CIRP* **2021**, *101*, 13–16. [CrossRef]
66. Liang, X.; Liu, Z. Tool Wear Behaviors and Corresponding Machined Surface Topography during High-Speed Machining of Ti-6Al-4V with Fine Grain Tools. *Tribol. Int.* **2018**, *121*, 321–332. [CrossRef]
67. Childerhouse, T.; M'Saoubi, R.; Franca, L.; Weston, N.; Crawforth, P.; Jackson, M. The Influence of Machining Induced Surface Integrity and Residual Stress on the Fatigue Performance of Ti-6Al-4V Following Polycrystalline Diamond and Coated Cemented Carbide Milling. *Int. J. Fatigue* **2022**, *163*, 107054. [CrossRef]
68. Tillmann, W.; Grisales, D.; Stangier, D.; Thomann, C.-A.; Debus, J.; Nienhaus, A.; Apel, D. Residual Stresses and Tribomechanical Behaviour of TiAlN and TiAlCN Monolayer and Multilayer Coatings by DCMS and HiPIMS. *Surf. Coat. Technol.* **2021**, *406*, 126664. [CrossRef]
69. Breidenstein, B.; Denkena, B. Significance of Residual Stress in PVD-Coated Carbide Cutting Tools. *CIRP Ann.* **2013**, *62*, 67–70. [CrossRef]
70. Rahman, M.A.; Bhuiyan, M.S.; Sharma, S.; Kamal, M.S.; Imtiaz, M.M.M.; Alfaify, A.; Nguyen, T.-T.; Khanna, N.; Sharma, S.; Gupta, M.K.; et al. Influence of Feed Rate Response (FRR) on Chip Formation in Micro and Macro Machining of Al Alloy. *Metals* **2021**, *11*, 159. [CrossRef]
71. Liu, C.; Wan, M.; Zhang, W.; Yang, Y. Chip Formation Mechanism of Inconel 718: A Review of Models and Approaches. *Chin. J. Mech. Eng.* **2021**, *34*, 34. [CrossRef]
72. Korkut, I.; Donertas, M.A. The Influence of Feed Rate and Cutting Speed on the Cutting Forces, Surface Roughness and Tool–Chip Contact Length during Face Milling. *Mater. Des.* **2007**, *28*, 308–312. [CrossRef]
73. Akhtar, W.; Sun, J.; Sun, P.; Chen, W.; Saleem, Z. Tool Wear Mechanisms in the Machining of Nickel Based Super-Alloys: A Review. *Front. Mech. Eng.* **2014**, *9*, 106–119. [CrossRef]
74. De Bartolomeis, A.; Newman, S.T.; Jawahir, I.S.; Biermann, D.; Shokrani, A. Future Research Directions in the Machining of Inconel 718. *J. Mater. Process Technol.* **2021**, *297*, 117260. [CrossRef]
75. Sousa, V.F.C.; Silva, F.J.G.; Pinto, A.G.; Campilho, R.D.S.G.; Barbosa, M.L.S.; Costa, R.D.F.S. Milling a Titanium Alloy Using Different Machining Parameters: A Comparative Study on Tool Wear, Tool Life and Performance. In *Flexible Automation and Intelligent Manufacturing: The Human-Data-Technology Nexus*; Kim, K.-Y., Monplaisir, L., Rickli, J., Eds.; Springer International Publishing: Cham, Switzerland, 2023; pp. 149–156.
76. Zhou, J.; Bushlya, V.; Avdovic, P.; Ståhl, J.E. Study of Surface Quality in High Speed Turning of Inconel 718 with Uncoated and Coated CBN Tools. *Int. J. Adv. Manuf. Technol.* **2012**, *58*, 141–151. [CrossRef]
77. Sousa, V.F.C.; Silva, F.J.G. Recent Advances in Turning Processes Using Coated Tools—A Comprehensive Review. *Metals* **2020**, *10*, 170. [CrossRef]
78. Sousa, V.F.C.; Silva, F.J.G. Recent Advances on Coated Milling Tool Technology—A Comprehensive Review. *Coatings* **2020**, *10*, 235. [CrossRef]
79. Zhang, L.; Zhong, Z.; Qiu, L.; Shi, H.; Layyous, A.; Liu, S. Coated Cemented Carbide Tool Life Extension Accompanied by Comb Cracks: The Milling Case of 316L Stainless Steel. *Wear* **2019**, *418–419*, 133–139. [CrossRef]
80. Shuai, J.; Zuo, X.; Wang, Z.; Guo, P.; Xu, B.; Zhou, J.; Wang, A.; Ke, P. Comparative Study on Crack Resistance of TiAlN Monolithic and Ti/TiAlN Multilayer Coatings. *Ceram. Int.* **2020**, *46*, 6672–6681. [CrossRef]

81. Vereschaka, A.; Grigoriev, S.; Sitnikov, N.; Oganyan, G.; Sotova, C. Influence of Thickness of Multilayer Composite Nano-Structured Coating Ti-TiN-(Ti,Al,Cr)N on Tool Life of Metal-Cutting Tool. *Procedia CIRP* **2018**, *77*, 545–548. [CrossRef]
82. Vereschaka, A.A.; Grigoriev, S.; Sitnikov, N.N.; Bublikov, J.I.; Batako, A.D.L. Effect Produced by Thickness of Nanolayers of Multilayer Composite Wear-Resistant Coating on Tool Life of Metal-Cutting Tool in Turning of Steel AISI 321. *Procedia CIRP* **2018**, *77*, 549–552. [CrossRef]
83. Narutaki, N.; Yamane, Y.; Hayashi, K.; Kitagawa, T.; Uehara, K. High-Speed Machining of Inconel 718 with Ceramic Tools. *CIRP Ann.* **1993**, *42*, 103–106. [CrossRef]
84. Ning, Y.; Rahman, M.; Wong, Y.S. Investigation of Chip Formation in High Speed End Milling. *J. Mater. Process Technol.* **2001**, *113*, 360–367. [CrossRef]
85. Martinho, R.P.; Silva, F.J.G.; Martins, C.; Lopes, H. Comparative Study of PVD and CVD Cutting Tools Performance in Milling of Duplex Stainless Steel. *Int. J. Adv. Manuf. Technol.* **2019**, *102*, 2423–2439. [CrossRef]

materials

Article

Simulation and Algorithmic Optimization of the Cutting Process for the Green Machining of PM Green Compacts

Yuchen Zhang, Dayong Yang *, Lingxin Zeng, Zhiyang Zhang and Shuping Li

School of Mechanical and Automotive Engineering, Guangxi University of Science and Technology, Liuzhou 545006, China
* Correspondence: dyyang@gxust.edu.cn; Tel.: +86-158-1711-2731

Abstract: Powder metallurgy (PM) technology is extensively employed in the manufacturing sector, yet its processing presents numerous challenges. To alleviate these difficulties, green machining of PM green compacts has emerged as an effective approach. The aim of this research is to explore the deformation features of green compacts and assess the impact of various machining parameters on the force of cutting. The cutting variables for compacts of PM green were modeled, and the cutting process was analyzed using Abaqus (2022) software. Subsequently, the orthogonal test ANOVA method was utilized to evaluate the significance of each parameter for the cutting force. Optimization of the machining parameters was then achieved through a genetic algorithm for neural network optimization. The investigation revealed that PM green compacts, which are brittle, undergo a plastic deformation stage during cutting and deviate from the traditional model for brittle materials. The findings indicate that cutting thickness exerts the most substantial influence on the cutting force, whereas the speed of cutting, the tool rake angle, and the radius of the rounded edge exert minimal influence. The optimal parameter combination for the cutting of PM green compacts was determined via a genetic algorithm for neural network optimization, yielding a cutting force of 174.998 N at a cutting thickness of 0.15 mm, a cutting speed of 20 m/min, a tool rake angle of 10°, and a radius of the rounded edge of 25 µm, with a discrepancy of 4.05% from the actual measurement.

Keywords: algorithm optimization; powder metallurgy; finite element; green compacts

1. Introduction

Conventional machining is almost always performed by removing excess material to ensure that the workpiece meets machining standards [1,2]; however, this type of machining wastes a large amount of material, with such waste being inconsistent with the main idea of green machinery manufacturing [3]. Powder metallurgy (PM) is used to manufacture metal parts by extruding metal powder to form green compacts and then sintering them, which is more material-efficient than traditional machining [4] and has been applied in many manufacturing fields [5–9]. However, it is almost impossible to process PM products in a single mold, and they require a small amount of processing [10].

The processing of PM products post-sintering presents substantial challenges, which inhibits the advancement of the powder metallurgy field [11,12]. Further innovation in the powder metallurgy (PM) industry has been hindered by several challenges. Ceramic machining shares similarities with PM machining; both processes involve the use of green compacts, which are subsequently sintered. However, after sintering, ceramic green compacts become difficult to process [13]. To address this issue in the ceramics industry, green compacts are processed before sintering [14]. This technique offers valuable insights for the powder metallurgy field [15] and suggests a potential strategy to alleviate the processing difficulties encountered in PM [16]. Green machining has become crucial in powder metallurgy material preparation, with the aim of achieving precise geometric features through the machining of green compacts before sintering and before addressing the challenges associated with machining these materials [17–19]. Paradis et al. [20] investigated the cold sintering process for surface-modified iron particles and revealed that this approach encourages the formation of a co-continuous phosphate phase among iron powder particles, which significantly improves the strength and density of the green compacts. These attained relative densities that reached 95%, and the transverse fracture strength was approximately 75 MPa, nearly sixfold greater than that of traditional powdered metal iron green compacts. This advancement underscores the growing academic interest in the green machining of PM green compacts, spotlighting it as a pivotal area of research.

While investigating the green compact machining mechanism, Robert-Perron et al. [21] observed that the tensile properties of parts machined in the green state were akin to those of parts machined post-sintering, as evidenced by experiments on cylindrical PM green compact sintering performance. This finding suggests that pre-sintering does not detrimentally impact the material properties. Moreover, Yang et al. [22] have elucidated unique material removal techniques such as particle shear deformation, stripping, and plowing/extrusion through geometric modeling of the green machining process of PM. The warm mold compaction method was shown to significantly decrease the porosity during the powder metallurgy process. Shi et al. [23] have explored the impact of warm mold compaction on the mechanical properties of iron-based powder metallurgy sintering and revealed that specimens prepared via warm mold compaction exhibited increased hardness, tensile strength, and yield strength.

Complementing the detailed studies on green machining mechanisms, extensive research has been conducted on machined surface quality, surface roughness minimization, and multi-objective optimization. For instance, according to research by Kulkarni Harshal et al. [24], the quality of machined surfaces improves with decreasing feed rate. Moreover, Goncalves et al. [25] observed from turning tests that increasing the radius of the rounded edge reduces surface roughness. Moreover, Kumar et al. [26] utilized the Gray–Taguchi approach for multiple objectives in the optimization of aerospace-grade alloys constructed of titanium, showing, through statistical assessment, that the speed of cutting substantially affects the quality of the machined surface.

Although extensive research has been conducted on various aspects of machining, the impact of cutting force has not been thoroughly explored. Although most researchers believe that the cutting force is small [16], due to the low strength of powder metallurgy green compacts, the workpieces are susceptible to damage by the cutting force during machining [27]. Hence, a systematic analysis of the way different machining parameters influence the cutting force is vital for a deeper understanding of the cutting characteristics of materials.

Despite the paucity of research on cutting forces within the realm of PM green machining utilizing optimization algorithms, employing these algorithms for cutting force optimization could provide a detailed understanding of how different machining parameters interact with the force of cutting. This knowledge is crucial for enhancing the quality and productivity of machined parts.

Therefore, this study sets out to achieve the following objectives:

1. Investigate deformation characteristics—to investigate the deformation characteristics of PM green compacts during the cutting process and evaluate the influence of various machining parameters on cutting forces.
2. Develop a simulation model—to develop a cutting process model for PM green compacts using Abaqus (2022) software for simulation.
3. Assess parameter significance—to use orthogonal test ANOVA methods to assess the significance of different machining parameters on cutting forces.
4. Optimize machining parameters—to optimize machining parameters through the application of a genetic algorithm for neural network optimization.
5. Validate the model—to validate the developed cutting model with experimental procedures.
6. Analyze cutting force variations—to analyze the variations in cutting forces under different machining parameters to determine the optimal cutting conditions.

By addressing these objectives, this research aims to contribute to a deeper understanding of PM green machining and to propose effective strategies for optimizing the cutting process.

2. Finite Element Modeling

2.1. Microstructure of Materials

When examining the various preparation processes for green PM compact materials, it was observed that the material porosity of powder metallurgy green compacts produced through different pressing techniques exhibited variability [28]. The microstructural morphology of the PM green compact materials is depicted in Figure 1a, revealing an approximate porosity of 12% within the material. For modeling purposes, Abaqus was employed, and, to alleviate the computational demands of computer simulation, a singular microstructure representative of the pore structure in PM green compacts was addressed. By arbitrarily placing five pore structures on the workpiece model substrate, the simulation was confined to the upper right quadrant of the model, as illustrated in Figure 1b.

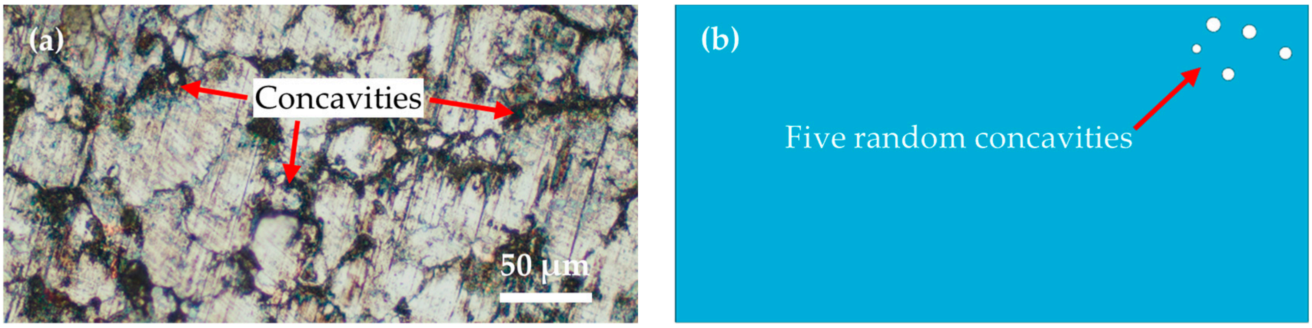

Figure 1. Microscopic morphology of the PM green compacts and modeling of the workpieces. (**a**) Microscopic topography of the PM green compacts. (**b**) Model of the workpiece.

2.2. Model Parameters

In the simulation, the workpiece was treated as a plastic body, and the tool was treated as an analytically rigid entity. The material parameters were established through a literature review and information assessment from tests on PM green compact materials. This research involved conducting tensile, strength, and compressive assessments on green compact test samples, and each test was performed six times to ascertain the reliability of the results and to calculate average values. The data compiled from these tests are organized in Table 1, which presents the pertinent performance parameters for PM–green compact materials. Table 2 shows the chemical composition of the green compact material.

Table 1. Mechanical characteristics of green compact materials constructed via powder metallurgy.

Performance	Density (g/cm^3)	Vickers Hardness (HV)	Tensile Strength (MPa)	Compressive Strength (MPa)	Elastic Modulus (GPa)	Poisson's Ratio
Parameter	7.1	87	3.9	98	210	0.018

Table 2. Chemical composition of the green compact material.

Chemical Composition	Fe	C	O	S	Mn	Mo	Ni	Cu
Proportion (%)	96.0586	0.002	0.07	0.0074	0.136	0.506	1.75	1.47

To facilitate a more intuitive understanding of the material removal process in simulated PM green compacts during cutting and to assist in the analysis of relevant experimental parameters, the initial parameters for the tool model were a rounded edge radius of 10 μm, an angle for the tool rake of 10°, and a clearance angle of 20°. The selection of a carbide-coated tool as the tool material was based on parameters provided by the tool manufacturer. The feed rate in this study is constant at 0.2 mm/r.

Figure 2a illustrates the machined surface of the specimen as captured by an electron microscope, revealing that the primary mode of material removal from the PM green compact specimen during cutting is predominantly plastic deformation. Similarly, Figure 2b displays images of the chips that underwent plastic deformation, which were also observed under an electron microscope. Consequently, this study adopts the Johnson–Cook model [29], a model extensively applied to the task of delineating the strength thresholds and failure mechanisms of metallic materials under conditions of significant strains and high strain rates, which are notably prevalent in simulations of metal cutting [30]. The parameters for the Johnson–Cook constitutive model applicable to PM green compact materials are detailed in Table 3 and are derived from experimental data that were subsequently fitted to the primary data and refined through modeling.

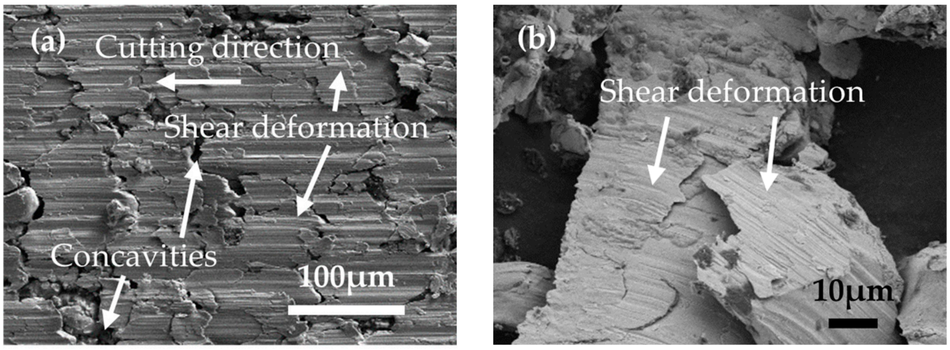

Figure 2. Machined surfaces and chips observed with an electron microscope. (**a**) Machined surfaces. (**b**) Chips.

Table 3. Variables for PM green compacts in the Johnson–Cook constitutive algorithm.

Parameter	*A* (MPa)	*B* (MPa)	*C*	*m*	*n*	*T*m (°C)	*T*r (°C)
Value	101	91	0.127	1.46	0.213	1861	25

2.3. Meshing and Assembly

In this study, the contact between the tool and the workpiece is set as surface-to-surface contact in the explicit analysis because the contact surface between the tool and the workpiece continuously changes during the cutting process. To simulate the cutting scenario, the bottom and left sides of the workpiece are fixed. The cutting edge of the tool is in contact with the entire workpiece material. In the contact properties, both the tangential behavior and normal behavior of the tool are established. For the tangential behavior, the friction formulation is set to penalty with a friction coefficient of 0.5. The normal behavior contact pressure–overclosure relationship is set to "hard" contact. In this model, a triangular mesh is utilized to address the dynamic deformation characterized by particle shear, detachment, and plowing/extrusion processes, deviating from the conventional rectangular mesh approach [26]. A total of 43,542 triangular meshes were created from the partitioned workpiece. In this paper, when dividing triangular meshes, free meshing is used. The maximum angle does not exceed 120°, the minimum angle is not less than 30°, and the ratio of the longest edge to the shortest edge is between 1 and 2. To optimize the computational effectiveness, the mesh density is increased in the upper right section while remaining sparser in other areas. This mesh distribution is depicted in Figure 3a. Figure 3b depicts the workpiece and tool following assembly and highlights the cutting simulation area positioned in the upper right corner.

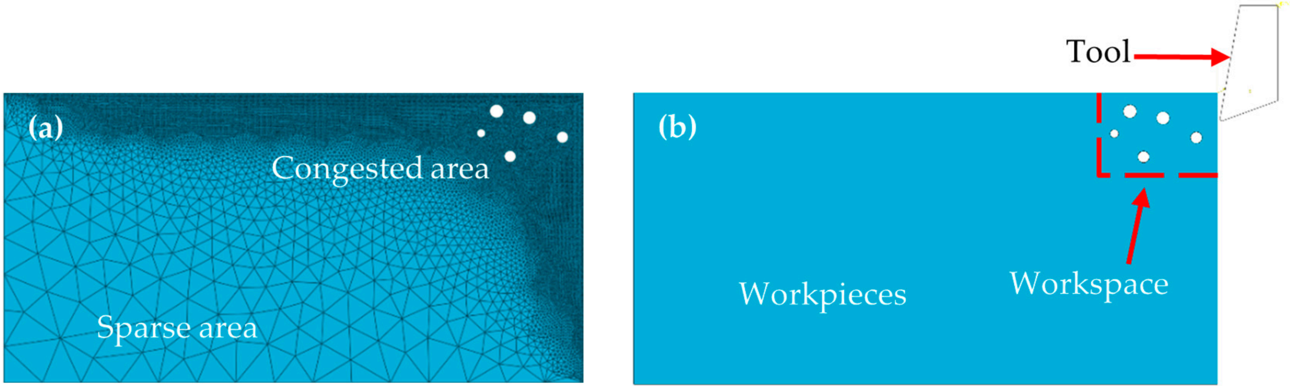

Figure 3. Diagrams of model meshing and assembly. (**a**) Mesh distribution. (**b**) Overall assembly.

2.4. Experimental Validation and Data Analysis

The simulation models were subjected to experimental verification to assess their accuracy. Figure 4a displays the PM green compact specimen used in this study. Multiple orthogonal cutting trials were conducted on these specimens, following which a white light interferometer, as shown in Figure 4b, was utilized to examine and measure the machined surface quality of the green compacts. The parameters employed during these cutting experiments were aligned as closely as possible with those of the simulation model, and these experiments are depicted in Figure 4c.

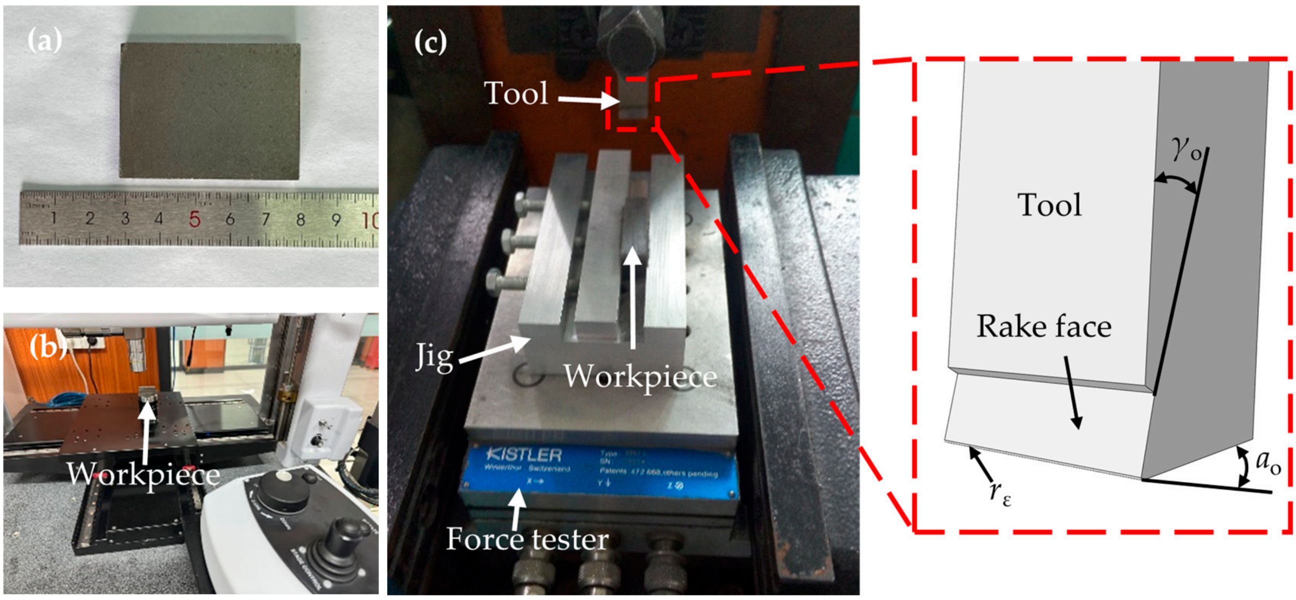

Figure 4. Experimental specimens and equipment. (**a**) PM green compacts specimen. (**b**) White light interferometer. (**c**) Cutting experiment on raw green compacts.

Figure 5 compares the simulated and experimental values of the cutting force exerted on the PM green compact specimens across different cutting thicknesses, with the cutting speed maintained at 5 m/min. Each value is the average of six experiments. For a cutting thickness of 0.12 mm, the discrepancy between the simulated value and the experimental value was 7.37%, while at other measured points, the variation did not exceed 5%, confirming the reliability of the model.

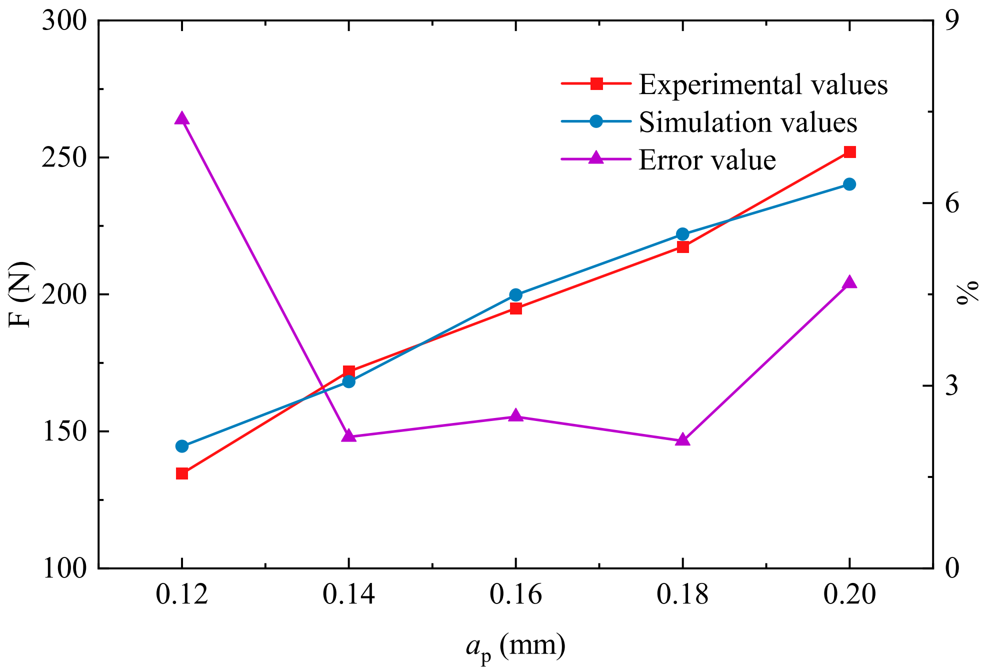

Figure 5. Cutting forces across various cutting thicknesses at a cutting speed of 5 m/min.

In this study, the evaluation criteria for surface quality are the size and depth of the concavities on the machined surface of the workpiece. During these tests, a constant speed of cutting of 65 m/min and a thickness of 0.15 mm were maintained. Figure 6a presents the simulation outcomes, while Figure 6b shows the corresponding experimental outcomes, with the left side of Figure 6e illustrating the height curve of the profile. The concavity depth in the simulation plot on the right side measures 56 µm with a width of 179 µm, whereas the experimental result on the left side shows a concavity depth of 59 µm and a width of 175 µm, yielding errors of 5.1% and 2.3%, respectively, as shown in Figure 6f. These results indicate that the simulation and experimental outcomes are closely matched, with the machined surface quality remaining satisfactory and the concavities exhibiting a small and shallow morphology. Figure 6c shows the simulation results for a cutting speed of 65 m/min and cutting thickness of 0.35 mm, and Figure 6d shows the experimental results, with the right side of Figure 6g showing the height curve of the profile. The concavity depth and width on the right side of the simulation plot are 60 µm and 205 µm, respectively. In contrast, the experimental results on the left side show a concavity depth of 63 µm and a width of 219 µm, with errors of 4.8% and 6.4%, respectively, as shown in Figure 6h. This comparison reveals that, while the simulation and experimental results generally align, the quality of the machined surface is inferior, characterized by a significant presence of burrs and large, deep concavities. In conclusion, the experimental evidence supports the validity of the model.

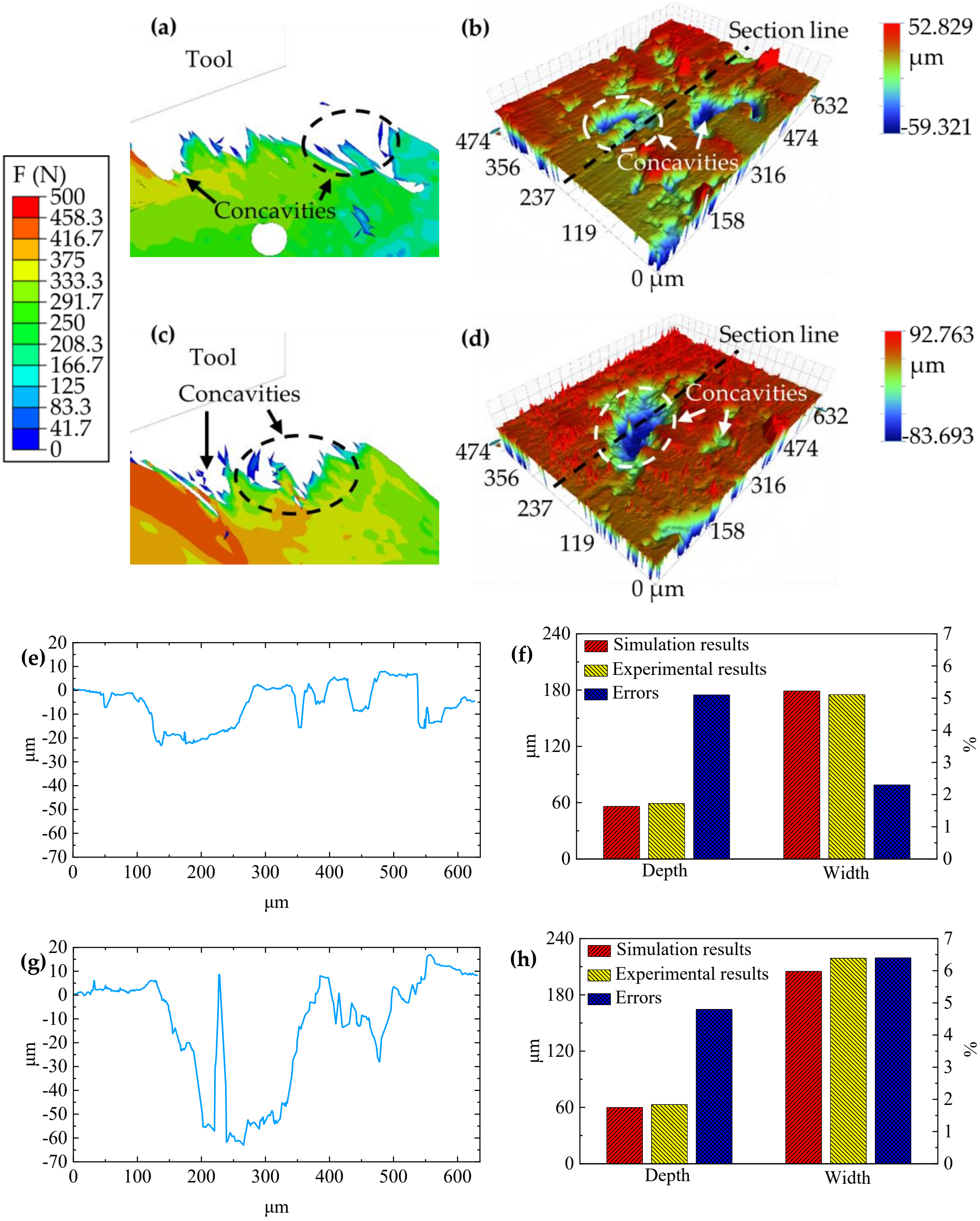

Figure 6. Analysis of machined surfaces through simulation and experimental approaches. (**a**) Simulated outcomes detailing the surface characteristics when employing a cutting speed of 65 m/min and a cutting thickness of 0.15 mm. (**b**) Corresponding experimental observations for a cutting regime characterized by a speed of 65 m/min and a thickness of 0.15 mm. (**c**) Simulation data for the surface generated at a cutting speed of 65 m/min, with the cutting thickness increased to 0.30 mm. (**d**) Experimental validation for the conditions set in panel c. (**e**) A detailed height profile of the machined surface for a cutting thickness of 0.15 mm. (**f**) A comparative analysis of the depth and width dimensions of the craters formed at a cutting thickness of 0.15 mm. (**g**) Height profile for the cutting thickness (0.35 mm). (**h**) Detailed comparison of crater dimensions—both depth and width—at a cutting thickness of 0.35 mm.

3. Results and Discussion

3.1. Analysis of the Cutting Process

The examination of the cutting process begins with its initial phase. Figure 7a,b illustrate the process for which the thickness of cutting was consistently 0.15 mm, whereas Figure 7c,d explore the process at a thickness of 0.35 mm.

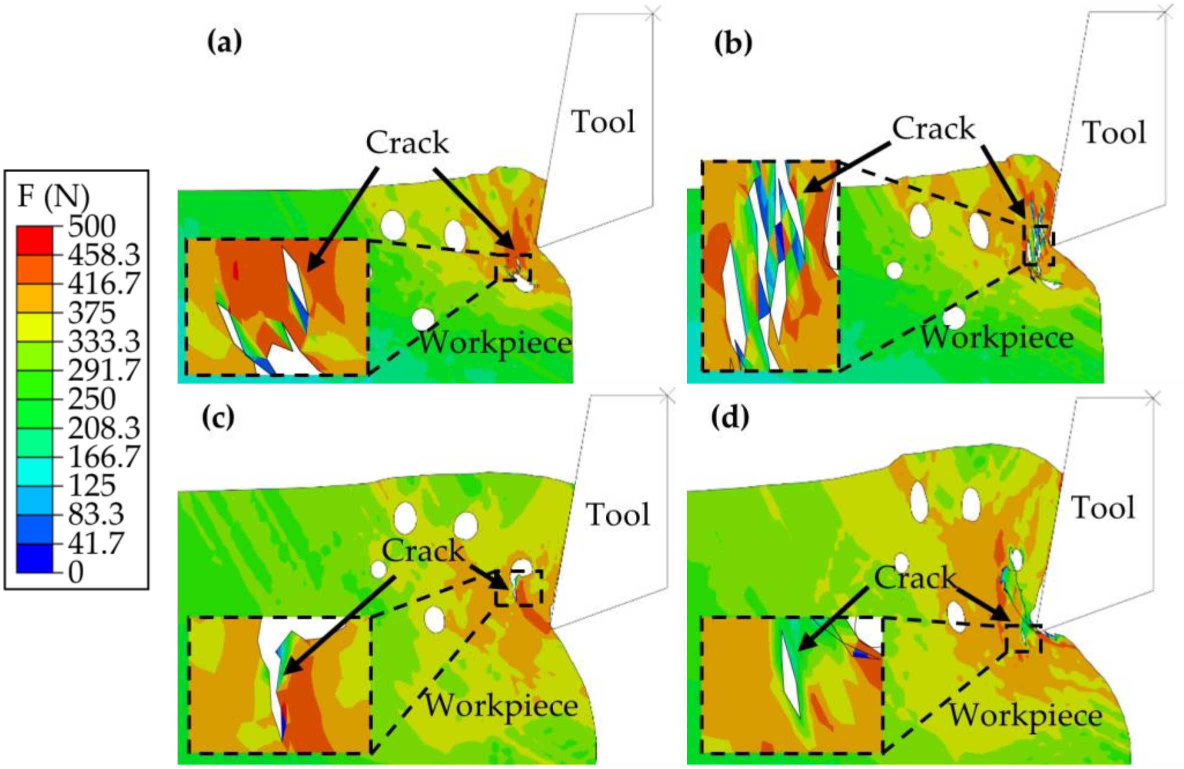

Figure 7. Initial phase of the cutting process. (**a**,**b**) Cutting at a thickness of 0.15 mm. (**c**,**d**) Cutting at a thickness of 0.35 mm.

Upon contact between the tool and the PM green compact specimen, the specimen at a cutting thickness of 0.15 mm exhibited cracking on the lower left side of the tool, as shown in Figure 7a, away from the specimen edge. Conversely, at a cutting thickness of 0.35 mm, cracking was observed on the upper left side of the tool, as illustrated in Figure 7c, which was also distant from the specimen edge. Notably, these cracks originated within the specimen, near the pores, diverging from typical crack initiation at the tool contact point. This unique pattern is attributed to the specimens being composed of unsintered metal powder compacts, which prevents them from behaving as monolithic entities. The stress concentration, which leads to crack formation at both cutting thicknesses, was located near the pores.

As the cutting advanced to the positions depicted in Figure 7b,d, the specimen with a cutting thickness of 0.15 mm exhibited further crack propagation and the emergence of numerous smaller cracks but without the formation of a machined surface. This phenomenon is attributed to the initial cracks being situated far from the specimen surface, which hinders their extension to the surface and causes them to propagate internally instead. In contrast, for the specimen with a thickness of 0.35 mm, cracks rapidly extended from the pore vicinity to the surface, culminating in the formation of a machined surface and additional cracks extending toward the lower left.

The analysis then progresses to the intermediate phase of the cutting process, with Figure 8a,b focusing on a cutting thickness of 0.15 mm and Figure 8c,d focusing on a thickness of 0.35 mm.

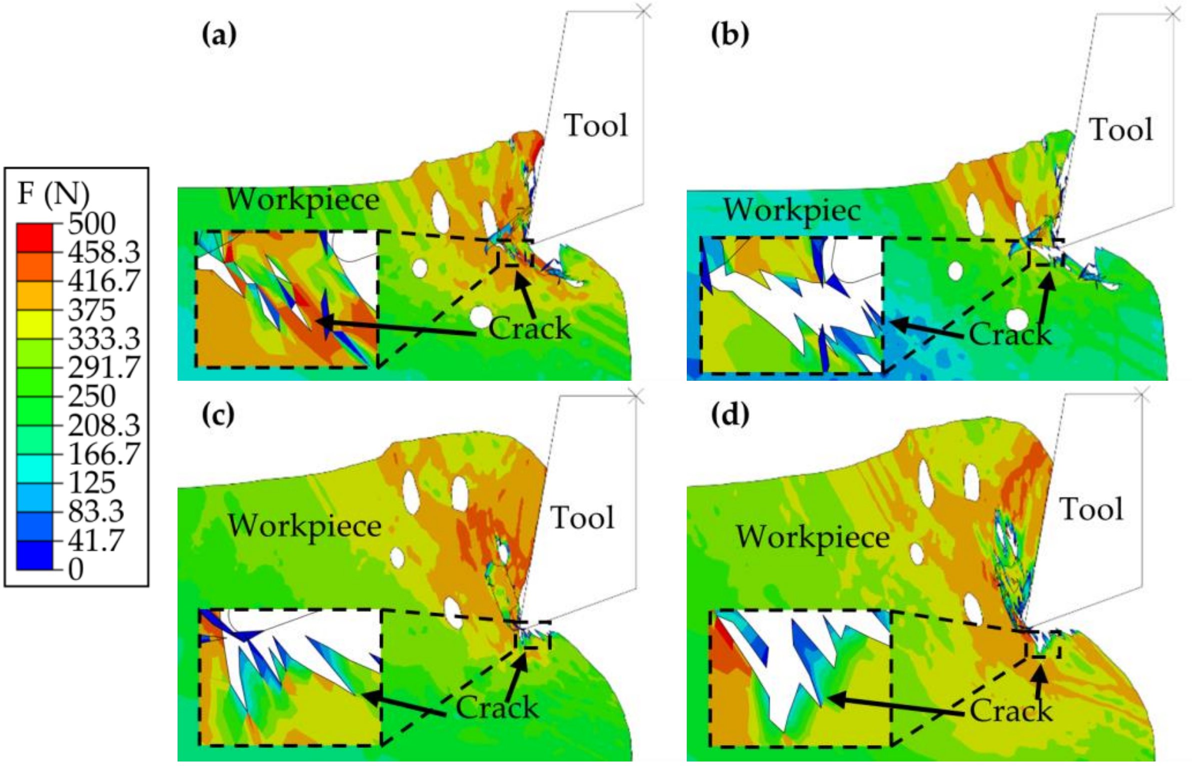

Figure 8. Mid-section analysis of the cutting process: (**a**,**b**) Cutting at a thickness of 0.15 mm; (**c**,**d**) Cutting at a thickness of 0.35 mm.

During the cutting phases depicted in Figure 8a,c, the machined surface on the specimen at a cutting thickness of 0.15 mm was formed, with a crack initiating within the specimen and propagating toward the left pore. Conversely, at a cutting thickness of 0.35 mm, the machined surface exhibited a crater originating from a preceding crack moving toward the lower left. As cutting proceeded to the stages shown in Figure 8b,d, the primary deformation zone in the 0.15 mm thick specimen continued to fracture, generating numerous small chips. This process resulted in a superior machined surface quality attributed to the absence of significant cracks on the machined surface. On the other hand, for the specimen with a cutting thickness of 0.35 mm, the previously formed cracks extended further downward, echoing the process outlined in Figure 7d. This process led to the formation of additional cracks extending toward the lower left, contributing to a rougher and inferior machined surface quality.

These findings underscore the profound impact of cutting thickness on the regularity of crack formation as well as the quality of the machined surfaces of the samples. It was determined that employing a smaller cutting thickness could diminish crack formation and enhance machined surface quality. In contrast, a greater cutting thickness is likely to facilitate crack propagation and increase surface roughness, thereby compromising the structural integrity and overall performance of the workpiece.

Subsequently, the analysis transitions to the latter stages of the cutting process. Figure 9a,b illustrate the cutting dynamics for a thickness of 0.15 mm, whereas Figure 9c,d depict the process for a thickness of 0.35 mm.

As the cutting process progresses beyond the stages illustrated in Figures 7 and 8, the previously observed patterns of crack formation cease to apply. Over time, the specimens cease to develop new cracks, as depicted in Figure 9a,c. Subsequently, the machined surfaces undergo stretching, which causes a decrease in surface quality, as shown in Figure 9b,d. After a certain duration, the specimens develop a new crack, reverting to the conditions observed in Figure 7a,c, thereby initiating the next cycle. This observation underscores the way in which, despite being classified as a brittle material, PM green compacts exhibit a deformation stage that does not fully conform to the brittle material cutting model. As demonstrated in Figure 9, the deformation stage in specimens with a 0.15 mm cutting thickness is less pronounced than that in specimens with a cutting thickness of 0.35 mm. The prolonged deformation stage in the latter results in significant concavity on the machined surface, culminating in the formation of a large, deep crater that adversely impacts surface quality. Figure 10 further elucidates this phenomenon. Figure 10a,b present the simulation and experimental findings for chip formation at a cutting thickness of 0.15 mm, respectively, while Figure 10c,d showcase the corresponding outcomes at a cutting thickness of 0.35 mm.

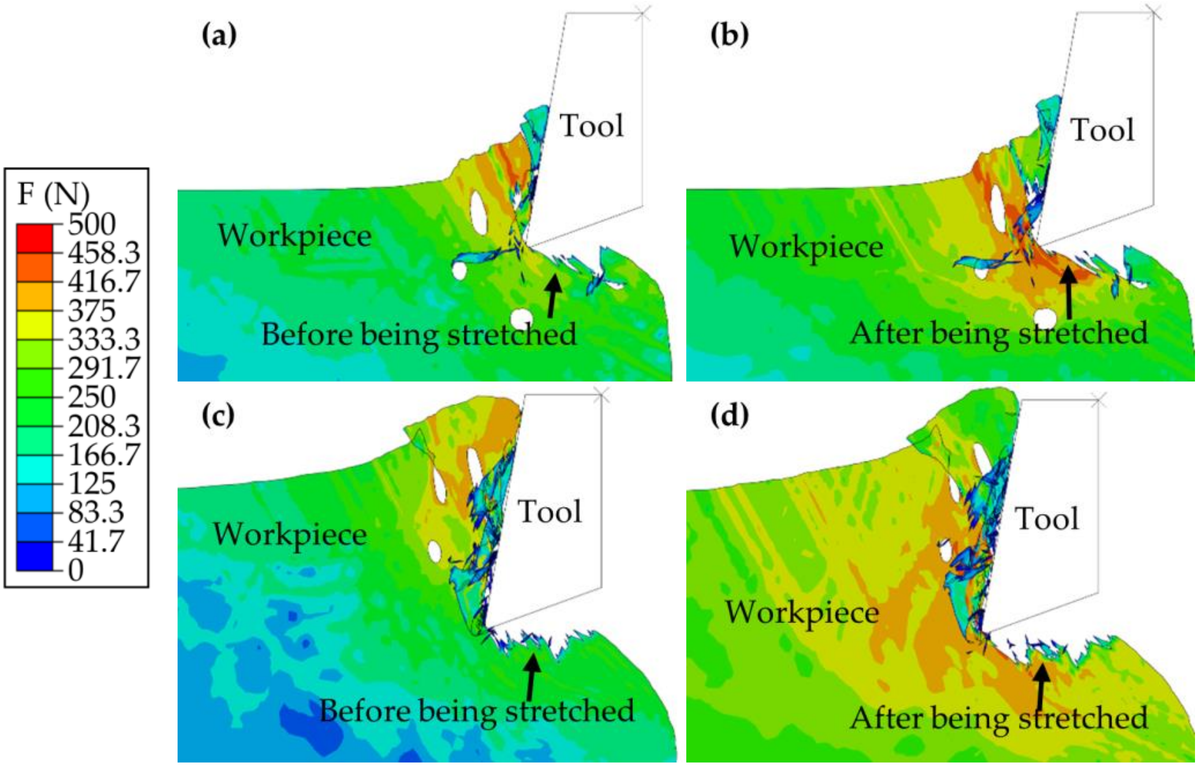

Figure 9. Latter stages of the cutting process (**a**,**b**) at a thickness of 0.15 mm and (**c**,**d**) at a thickness of 0.35 mm.

Figure 10a shows that the specimen subjected to a cutting thickness of 0.15 mm exhibits a distinct direction of stress propagation due to the action of the tool. The stress predominantly affects the upper part of the specimen, manifesting in a linear and parallel orientation. This force distribution facilitates the formation of chips, which are neither excessively large nor small, and significantly reduces the cutting force and the deformation phase of the specimen. Conversely, the stress pattern in the specimen with a cutting thickness of 0.35 mm is less defined, resulting in increased cutting force, an extended deformation phase, and a compromised machined surface quality, as illustrated in Figure 10c.

At a cutting thickness of 0.15 mm, the chips produced have a more consistent size and shape and are devoid of oversized or undersized anomalies. Similarly, this thickness maintains the regularity in chip size and shape, preventing any excessively large or small chips. At a thickness of 0.35 mm, however, the chips display considerable variation in size and shape, with a tendency toward larger dimensions accompanied by numerous smaller fragments. The congruence between the simulation results and the experimental results lends further credence to the accuracy of the model.

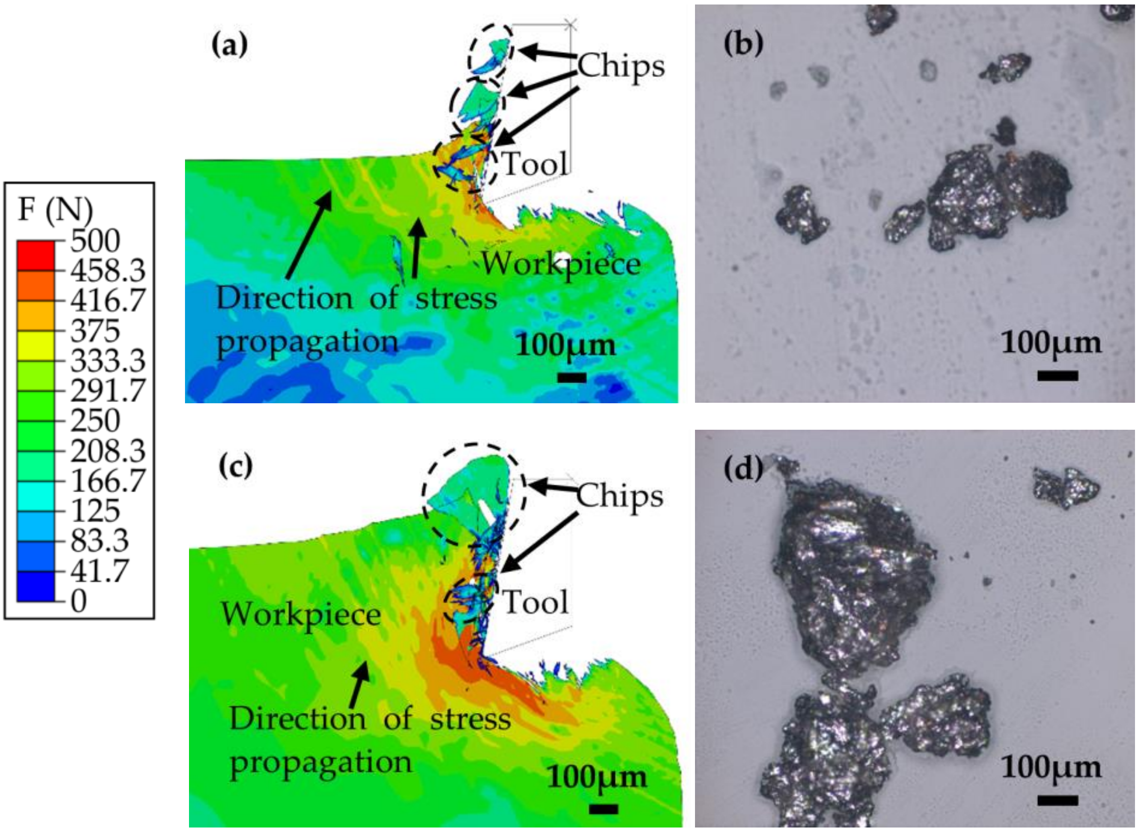

Figure 10. Analysis of specimen forces and chip formation during cutting. (**a**) Simulation of chip formation at a cutting thickness of 0.15 mm. (**b**) Experimental observation of chip formation at a cutting thickness of 0.15 mm. (**c**) Simulation of chip formation at a cutting thickness of 0.35 mm. (**d**) Experimental observation of chip formation at a cutting thickness of 0.35 mm.

3.2. Significance Analysis of the Cutting Force Factors

Orthogonal testing, which is a strategic experimental design method, is employed to systematically scrutinize the influence of various factors on a system or process. The aim of orthogonal testing is to identify the most favorable process conditions, parameter configurations, or design solutions by gaining a thorough understanding of these factors and their interplay while minimizing the number of experiments needed. To enrich the dataset, a 4-factor, 5-level orthogonal test was devised. Parameters such as the cutting thickness (a_p), cutting speed (v_c), tool rake angle (γ_o), and radius of the rounded edge (r_ε) were central to the study.

The cutting thickness (a_p) levels ranged from 0.15 mm to 0.35 mm and were chosen to capture a broad spectrum of practical applications. The cutting speed (v_c) levels varied from 5 m/min to 65 m/min, reflecting common machining conditions. Tool rake angle (γ_o) levels were selected based on typical tool geometries used in machining PM green compacts, and the radius of the rounded edge (r_ε) levels were chosen to study the effect of tool edge sharpness.

Analysis of variance is widely used as a statistical method to assess the mean differences across distinct groups. The four-factor ANOVA represents an extended application of ANOVA and is tailored for studies involving four independent variables. The integration of orthogonal tests with ANOVA facilitates a more detailed and systematic exploration of the impacts of multiple factors on a system, thus providing deeper insight into system optimization [31–34]. The subsequent section will outline the computation process of the four-factor ANOVA employed in this study, including the determination of main effects and interactions. This approach is aimed at providing a more transparent interpretation of the test outcomes. The detailed simulation data are listed in Table 4.

Table 4. Simulation data for the cutting force.

Test Number (i)	Four Factors				F_H (y_i)
	a_p (mm)	v_c (m/min)	γ_o (°)	r_ε (μm)	
1	0.15	5	0	10	183.564
2	0.15	20	10	25	184.028
3	0.15	35	20	15	186.512
4	0.15	50	5	30	189.603
5	0.15	65	15	20	186.964
6	0.2	5	20	25	212.920
7	0.2	20	5	15	230.748
8	0.2	35	15	30	212.350
9	0.2	50	0	20	237.716
10	0.2	65	10	10	245.292
11	0.25	5	15	15	263.694
12	0.25	20	0	30	275.158
13	0.25	35	10	20	273.018
14	0.25	50	20	10	280.353
15	0.25	65	5	25	284.094
16	0.3	5	10	30	308.031
17	0.3	20	20	20	296.932
18	0.3	35	5	10	330.820
19	0.3	50	15	25	312.766
20	0.3	65	0	15	340.883
21	0.35	5	5	20	443.402
22	0.35	20	15	10	432.286
23	0.35	35	0	25	433.532
24	0.35	50	10	15	420.143
25	0.35	65	20	30	371.171

The methodology for computing the data in Table 4 is delineated below [34,35]:
Calculate the total sum of squares (SS_T):

$$SS_T = \sum_{i=1}^{n}\sum_{j=1}^{k} y_{ij}^2 - CT \tag{1}$$

where y_{ij} denotes the cutting force for each set of simulations, and CT is the correction factor:

$$CT = \frac{\left(\sum_{i=1}^{n}\sum_{j=1}^{k} y_{ij}\right)^2}{nk} \tag{2}$$

Calculate the sum of squares for each factor (SS_F) and the error (SS_E):

$$SS_F = \frac{\sum(\text{factor sum})^2}{\text{number of levels}} - CT \tag{3}$$

$$SS_E = SS_T - \sum SS_F \tag{4}$$

Determine the degrees of freedom (DF), mean square (MS), and F value:

$$DF = \text{number of levels} - 1 \tag{5}$$

$$MS = \frac{SS}{DF} \tag{6}$$

$$F = \frac{MS_F}{MS_E} \tag{7}$$

In Table 5, the terms "**", "ns", and "/" indicate highly significant effects, nonsignificant effects, and not applicable, respectively. The critical values $F_{0.05}$ and $F_{0.01}$ are obtained from F distribution tables and represent the threshold values at the 5% and 1% significance levels, respectively. These values are used to determine whether the observed F values indicate a statistically significant effect of the factors on the response variable.

Table 5. ANOVA results for the cutting force.

Variation Source	Square of Deviance	Degree of Freedom	Sum of Mean Squares	F	Significance	$F_{0.05}$	$F_{0.01}$
a_p (mm)	162,374.456	4	40,593.614	177.781	**	3.84	7.01
v_c (m/min)	113.973	4	28.493	0.125	ns		
γ_o (°)	2244.428	4	561.107	2.457	ns		
r_ε (μm)	1479.226	4	369.807	1.620	ns		
Error	1826.676	8	228.335	/	/		
Summation	168,038.759	24	/	/	/		

Table 5 presents the ANOVA results for the cutting force. The analysis reveals that the cutting thickness (a_p) significantly impacts the cutting force, with an F value of 177.781, which is much higher than the critical values $F_{0.05}$ = 3.84 and $F_{0.01}$ = 7.01, indicating a highly significant effect. Conversely, the cutting speed (v_c), tool rake angle (γ_o), and radius of the rounded edge (r_ε) have F values of 0.125, 2.457, and 1.620, respectively, which are all lower than the critical value $F_{0.05}$. This suggests that these factors do not have a statistically significant impact on the cutting force.

3.3. Optimization of the Cutting Force Parameters

The orthogonal experimental ANOVA that was previously discussed enabled the identification of the influence of various parameters on system performance through a structured experimental design and data analysis approach. Nevertheless, for complex issues, conventional experimental designs and statistical methods might encounter difficulties due to vast parameter spaces, nonlinear relationships, or multimodality.

This study considers four principal parameters for cutting, namely, the cutting thickness (a_p), cutting speed (v_c), tool rake angle (γ_o) and radius of the rounded edge (r_ε), as well as their respective cutting force values. Figure 11 depicts the trend of the mean level k for each parameter.

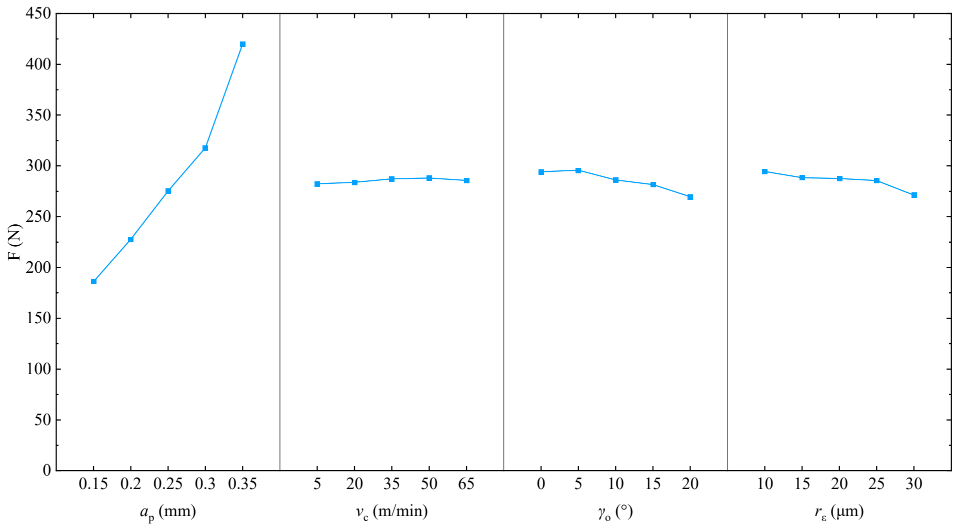

Figure 11. Trend of mean-level k for each factor.

While cutting thickness significantly influences cutting force, developing algorithms to determine cutting forces remains essential since cutting force is also affected by other parameters such as cutting speed, tool rake angle, and radius of the rounded edge. The interactions among these factors necessitate more sophisticated models for accurate prediction. Optimization algorithms can enhance prediction accuracy and balance multiple objectives, such as minimizing cutting force while maximizing surface quality and production efficiency. Therefore, developing these algorithms is crucial for improving the accuracy and efficiency of the cutting process and provides valuable references for related research.

To comprehensively assess the influence of these four factors on cutting force and to enhance optimization, this study adopts the GANN, an advanced optimization method [36–38].

Genetic algorithms (GAs) are optimization techniques that emulate natural selection and genetic processes, using simulations of genetic inheritance, mutation, and selection to iteratively refine model parameters, thereby attaining an optimal solution. In this context, GAs adjust the weights and biases within the neural network to better represent the intricate relationships between cutting forces and their parameters.

Neural networks, which are known for their robust nonlinear modeling capability, excel at fitting complex input–output relationships. However, their training requires extensive data and parameter adjustments, with a tendency to converge to local optima. To mitigate these issues, this research integrates the global search capability of genetic algorithms with the fitting ability of the neural network, establishing an effective optimization framework for cutting force optimization challenges. MATLAB (2021a) software will be employed to develop and execute the genetic algorithm program.

In this study, data on cutting parameters—cutting speed, tool rake angle, and radius of the rounded edge—and corresponding cutting force measurements were collected. Subsequently, a feedforward neural network with input, hidden, and output layers was designed.

In this research, the weights and biases of the neural network serve as the optimization variables for the genetic algorithm to minimize the prediction error of the neural network. These parameters are encoded as individuals within the genetic algorithm, which then undergoes evolutionary optimization until an optimal set of weights and biases is identified. To assess the performance of the neural network model, a fitness function is defined, which calculates the prediction error to serve as a criterion for evaluating the genetic algorithm.

The number of input layer nodes in the neural network depends on the number of cutting parameters, with one output layer node. There are two hidden layers with sizes of 10 and 8. The weight and bias parameters for the genetic algorithm have upper and lower bounds of 1 and -1, with a maximum generation number of 100 and a population size of 50. Through these processes, the integration of the genetic algorithm with the neural network for cutting force optimization is effectively realized.

Optimal results were achieved with a cutting thickness of 0.15 mm, a cutting speed of 20 m/min, a tool rake angle of 10°, and a radius of the rounded edge of 25 μm, leading to a cutting force of 174.998 N. When these parameters are simulated in the model, the resultant cutting force is 168.189 N, which indicates an error of 4.05%. This result underscores the accuracy and success of cutting force optimization.

4. Conclusions

In this article, Abaqus (2022) software facilitated the modeling of PM green compacts, followed by an analysis of the simulation results using orthogonal test ANOVA and an advanced analysis utilizing MATLAB (2021a) software in conjunction with the GANN. The principal findings are summarized as follows:

(1) A refined model of PM compacts was developed, yielding an average cutting force error of 3.8% within a cutting thickness range of 0.12–0.20 mm. Additionally, the average errors for the concavity depth and width on the machined surface were 5.0% and 4.4%, respectively.

(2) PM green compacts, characterized as brittle materials, exhibit plastic deformation during cutting, deviating from the traditional cutting model for brittle materials. This

observation offers fresh perspectives on cutting PM green compacts, thus improving the understanding of their machining dynamics.

(3) The cutting thickness has the most substantial impact on the cutting force, while the speed of cutting, the tool rake angle, and the radius of the rounded edge have minimal effects. This finding underscores the importance of cutting thickness control in PM green compact machining to prevent damage due to excessive cutting force.

(4) The optimization of the neural network using genetic algorithms determined the ideal parameter set for cutting PM green compacts, as follows: a cutting thickness of 0.15 mm, a cutting speed of 20 m/min, a tool rake angle of 10°, and a radius of the rounded edge of 25 μm. This parameter set led to a cutting force of 174.998 N with a 4.05% deviation from the actual measurement, which provides a valuable reference for machining PM green compacts.

Author Contributions: All authors contributed to the study conception and design. Material preparation, data collection and analysis were performed by Y.Z., D.Y. and L.Z. The first draft of the manuscript was written by Y.Z.; manuscript proofreading was undertaken by Z.Z. and S.L. All authors commented on previous versions of the manuscript. All authors have read and agreed to the published version of the manuscript.

Funding: This work was supported by the National Natural Science Foundation of China (no.52165055) and the Doctoral foundation of Guangxi University of Science and Technology (no. XKB 19Z25).

Institutional Review Board Statement: Not applicable.

Informed Consent Statement: Not applicable.

Data Availability Statement: All data to support the results of this study are included in this article.

Acknowledgments: We sincerely thank Guangxi University of Science and Technology for their generous sponsorship. We also express our appreciation to M.Z.'s team for their crucial support in providing the necessary experimental equipment, which greatly facilitated our research.

Conflicts of Interest: The authors declare no conflicts of interest.

References

1. Zeng, K.; Wu, X.; Jiang, F.; Shen, J.Y.; Zhu, L.F.; Li, L. A comprehensive review on the cutting and abrasive machining of cemented carbide materials. *J. Manuf. Process.* **2023**, *108*, 335–358. [CrossRef]
2. Du, J.G.; Tian, B.; Duan, L.Y.; Ming, W.Y.; Liu, K.; He, W.B. Traditional and non-traditional machining technology of metallic glass. *Int. J. Adv. Manuf. Technol.* **2022**, *120*, 2879–2902. [CrossRef]
3. Li, Y.; Zhang, X.H.; Hao, J.Y.; Huang, Q.B. The impact of green technology innovation on global value chain upgrading in China's equipment manufacturing industry. *Front. Environ. Sci.* **2022**, *10*, 1044583. [CrossRef]
4. Zhu, J.H.; Zhou, H.; Wang, C.; Zhou, L.; Yuan, S.Q.; Zhang, W.H. A review of topology optimization for additive manufacturing: Status and challenges. *Chin. J. Aeronaut.* **2021**, *34*, 91–110. [CrossRef]
5. Erdem, M.; Cinici, H.; Gokmen, U.; Karakoc, H.; Turker, M. Mechanical and ballistic properties of powder metal 7039 aluminium alloy joined by friction stir welding. *Trans. Nonferrous Met. Soc. China* **2016**, *26*, 74–84. [CrossRef]
6. Tijo, D.; Kumari, S.; Masanta, M. Hard and wear resistance TiC-composite coating on AISI 1020 steel using powder metallurgy tool by electro-discharge coating process. *J. Braz. Soc. Mech. Sci. Eng.* **2017**, *39*, 4719–4734. [CrossRef]
7. Zharov, M.V. Comparative Analysis of Features of Technologies for Obtaining Quality Spherical Powder of Nickel Aluminide NiAl. *Metallurgist* **2023**, *66*, 1401–1411. [CrossRef]
8. Boujelbene, M.; Ezeddini, S.; Ben Said, L.; Bayraktar, E.; Alhadri, M.; Aich, W.; Ghachem, K.; Kolsi, L. Analysis of surface integrity of intermetallic composite based on titanium-aluminum machined by laser cutting. *Opt. Laser Technol.* **2023**, *161*, 109187. [CrossRef]
9. Egorov, M.S.; Egorova, R.V. Characteristics of the Formation of Structure and Properties of Dispersed-Hardened Charges at the Hot Stamping of Complex Shape Products. *Metallurgist* **2023**, *66*, 1436–1441. [CrossRef]
10. Zhong, B.; Wang, Y.R.; Wei, D.S.; Zhang, K.S.; Wang, J.L. Multiaxial fatigue life prediction for powder metallurgy superalloy FGH96 based on stress gradient effect. *Int. J. Fatigue* **2018**, *109*, 26–36. [CrossRef]
11. Sun, F.J.; Qu, S.G.; Li, G.; Pan, Y.X.; Li, X.Q. Comparison of the machinability of titanium alloy forging and powder metallurgy materials. *Int. J. Adv. Des. Manuf. Technol.* **2016**, *85*, 1529–1538. [CrossRef]
12. da Silva, G.C.; Saraiva, Q.M.; Carneiro, J.R.G.; Santos, I.A.; José, A.S. New milling methodology for sealing planes in AlSi9Cu3(Fe) alloy machined with PCD tool. *Int. J. Adv. Manuf. Technol.* **2021**, *113*, 3211–3223. [CrossRef]

13. Dong, X.J.; Wu, J.Q.; Yu, H.L.; Zhou, Q.; Wang, W.Q.; Zhang, X.Q.; Zhang, L.; Li, L.; He, R.J. Additive manufacturing of silicon nitride ceramics: A review of advances and perspectives. *Int. J. Appl. Ceram. Technol.* **2022**, *19*, 2929–2949. [CrossRef]
14. Yin, Y.K.; Xu, J.Y.; Ji, M.; Li, L.F.; Chen, M. A critical review on sintering and mechanical processing of 3Y-TZP ceramics. *Ceram. Int.* **2023**, *49*, 1549–1571. [CrossRef]
15. Attia, U.M. Cold-isostatic pressing of metal powders: A review of the technology and recent developments. *Crit. Rev. Solid State Mater. Sci.* **2021**, *46*, 587–610. [CrossRef]
16. Kulkarni, H.; Dabhade, V. Green machining of powder-metallurgy-steels (PMS): An overview. *J. Manuf. Process.* **2019**, *44*, 1–18. [CrossRef]
17. Chen, C.; Huang, B.Y.; Liu, Z.M.; Li, Y.X.; Zou, D.; Liu, T.; Chang, Y.M.; Chen, L. Additive manufacturing of WC-Co cemented carbides: Process, microstructure, and mechanical properties. *Addit. Manuf.* **2023**, *63*, 103410. [CrossRef]
18. Parvizi, S.; Hashemi, S.M.; Asgarinia, F.; Nematollahi, M.; Elahinia, M. Effective parameters on the final properties of NiTi-based alloys manufactured by powder metallurgy methods: A review. *Prog. Mater. Sci.* **2021**, *117*, 100739. [CrossRef]
19. Bram, M.; Ebel, T.; Wolff, M.; Cysne Barbosa, A.P.; Tuncer, N. Applications of Powder Metallurgy in Biomaterials. In *Advances in Powder Metallurgy*; Woodhead Publishing: Cambridge, UK, 2013; pp. 520–554.
20. Paradis, L.; Waryoba, D.; Robertson, K.; Ndayishimiye, A.; Fan, Z.M.; Rajagopalan, R.; Randall, C.A. Densification and Strengthening of Ferrous-Based Powder Compacts Through Cold Sintering Aided Warm Compaction. *Adv. Eng. Mater.* **2022**, *24*, 2200714. [CrossRef]
21. Robert-Perron, E.; Blais, C.; Pelletier, S. Tensile properties of sinter hardened powder metallurgy components machined in their green state. *Powder Metall.* **2009**, *52*, 80–83. [CrossRef]
22. Yang, D.Y.; Lu, L.S.; Wan, Z.P. Material Removal Mechanism of Green Machining on Powder Metallurgy Parts during Orthogonal Cutting. *Adv. Mater. Sci. Eng.* **2020**, *2020*, 1962602. [CrossRef]
23. Shi, Q.L.; Chen, D.; Pan, Q.Q.; Peng, J.G. Study on the Influence of Warm Die Compaction Behavior on the Mechanical Properties of Iron-Based Powder Materials. *J. Mater. Eng. Perform.* **2023**, *33*, 5655–5666. [CrossRef]
24. Kulkarni, H.; Dabhade, V.V.; Blais, C. Analysis of machining green compacts of a sinter-hardenable powder metallurgy steel: A perspective of material removal mechanism. *CIRP J. Manuf. Sci. Technol.* **2023**, *41*, 430–445. [CrossRef]
25. Goncalves, M.; Sanchez, L.E.D.; Franca, T.V.; Fortulan, C.A.; da Silva, R.H.L.; Foschini, C.R. Analysis of the tool nose radius influence in the machining of a green ceramic material. *Int. J. Adv. Manuf. Technol.* **2019**, *105*, 3117–3125. [CrossRef]
26. Kumar, P.; Karsh, P.K.; Misra, J.P.; Kumar, J. Multi-objective optimization of machining parameters during green machining of aerospace grade titanium alloy using Grey-Taguchi approach. *Proc. Inst. Mech. Eng. Part E* **2021**. [CrossRef]
27. Yang, D.Y.; Zhang, Y.C.; Wang, R.; Wei, F.R.; Zeng, L.X.; Liu, M. Finite Element Modeling and Optimization Analysis of Cutting Force in Powder Metallurgy Green Compacts. *Processes* **2023**, *22*, 3186. [CrossRef]
28. Bidulska, J.; Bidulsky, R.; Grande, M.A.; Kvackaj, T. Different Formation Routes of Pore Structure in Aluminum Powder Metallurgy Alloy. *Materials* **2019**, *12*, 3724. [CrossRef]
29. Shokry, A. On the constitutive modeling of a powder metallurgy nanoquasicrystalline $Al_{93}Fe_3Cr2Ti_2$ alloy at elevated temperatures. *J. Braz. Soc. Mech. Sci.* **2019**, *41*, 118. [CrossRef]
30. Sun, Y.; Li, G.H.; He, Z.; Kong, X.C. The advance of research on constitutive model used in finite element simulation of metal cutting. *Proc. Inst. Mech. Eng. C J. Mech. Eng. Sci.* **2022**, *236*, 4921–4945. [CrossRef]
31. Hüseyin, G.; Yunus, E.G. Optimization and evaluation of dry and minimum quantity lubricating methods on machinability of AISI 4140 using Taguchi design and ANOVA. *Proc. Inst. Mech. Eng. Part C J. Mech. Eng. Sci.* **2020**, *235*, 1211–1227.
32. Naik, A.B.; Reddy, A.C. Optimization of Tensile Strength in TIG Welding Using Taguchi Method and Analysis of Variance (ANOVA). *Therm. Sci. Eng. Prog.* **2018**, *8*, 327–339. [CrossRef]
33. Savković, B.; Kovăc, P.; Stoić, A.; Dudić, B. Optimization of Machining Parameters Using the Taguchi and ANOVA Analysis in the Face Milling of Aluminum Alloys AL7075. *Teh. Vjesn.* **2020**, *27*, 1221–1228.
34. Deng, C.S.; Hsia, K.L. Analysis of the optimisation of parameters for the laser machining of timber. *Int. J. Adv. Manuf. Technol.* **2017**, *89*, 3721–3729. [CrossRef]
35. Kruzel, R.; Dembiczak, T.; Wachowicz, J. Optimization of Spark Plasma Sintering Technology by Taguchi Method in the Production of a Wide Range of Materials: Review. *Materials* **2023**, *16*, 5539. [CrossRef] [PubMed]
36. Elkatatny, S.; Alsharekh, M.F.; Alateyah, A.I.; El-Sanabary, S.; Nassef, A.; Alawad, M.O.; Kamel, M.; BaQais, A.; El-Garaihy, W.H.; Kouta, H. Optimizing the Powder Metallurgy Parameters to Enhance the Mechanical Properties of Al-4Cu/xAl_2O_3 Composites Using Machine Learning and Response Surface Approaches. *Appl. Sci.* **2023**, *13*, 7483. [CrossRef]
37. Wen, H.N.; Jin, J.S.; Tang, X.F.; Wang, X.Y.; Yang, H.Y.; Zhang, Y.D.; Zhang, M.; Deng, L.; Wei, Q.S.; Chen, J.Z.; et al. Machine learning-assisted constitutive modeling of a novel powder metallurgy superalloy. *Int. J. Mech. Sci.* **2023**, *260*, 108654. [CrossRef]
38. Dreano, A.; Favre, J.; Desrayaud, C.; Chanin-Lambert, P.; Wimmer, A.; Zaeh, M.F. Computational design of a crack-free aluminum alloy for additive manufacturing br. *Addit. Manuf.* **2022**, *55*, 102876.

materials

Article

Twin-Tool Orientation Synchronous Smoothing Algorithm of Pinch Milling in Nine-Axis Machine Tools

Dongdong Song [1,2,*], Shuai Zhu [1], Fei Xue [2,*], Yagang Feng [3] and Bingheng Lu [2]

1 College of Mechanical and Electronic Engineering, Northwest A&F University, No.3 Taicheng Road, Yangling District, Xianyang 712100, China; zs1124@nwafu.edu.cn
2 State Key Laboratory for Manufacturing Systems Engineering, Xi'an Jiaotong University, West Building 5, No. 99 Yan Cheung Road, Yanta District, Xi'an 710054, China; bhlu@mail.xjtu.edu.cn
3 Xi'an Aerospace Huawei Chemical & Biotechnology Co., Ltd., No. 289 Feitian Road, Aerospace Industry Park, Chang'an District, Xi'an 710054, China; fyg315@126.com
* Correspondence: sdd1213@nwafu.edu.cn (D.S.); xuefei82@xjtu.edu.cn (F.X.)

Abstract: Pinch milling is a new technique for slender and long blade machining, which can simultaneously improve the machining quality and efficiency. However, two-cutter orientation planning is a major challenge due to the irregular blade surfaces and the structural constraints of nine-axis machine tools. In this paper, a method of twin-tool smoothing orientation determination is proposed for a thin-walled blade with pinch milling. Considering the processing status of the two cutters and workpiece, the feasible domain of the twin-tool axis vector and its characterization method are defined. At the same time, an evaluation algorithm of global and local optimization is proposed, and a smoothing algorithm is explored within the feasible domain along the two tool paths. Finally, a set of smoothly aligned tool orientations are generated, and the overall smoothness is nearly globally optimized. A preliminary simulation verification of the proposed algorithm is conducted on a turbine blade model and the planning tool orientation is found to be stable, smooth, and well formed, which avoids collision interference and ultimately improves the machining accuracy of the blade with difficult-to-machine materials.

Keywords: pinch milling; twin-tool orientation; smoothing orientation planning method; feasible domain

1. Introduction

Pinch milling uses two cutters that can simultaneously mill the opposing surfaces of two blades from top to top, which can significantly improve machining efficiency and quality. Turbine blades are typically elongated components, distinguished by thin walls, asymmetry, and twisted free surfaces. A twin-tool orientation, formed by three rotary axes, plays a crucial role in machining complex parts like a turbine blade. Each tool orientation requires continuous and smooth transitions, but it is very difficult to simultaneously plan these tool orientations. Meanwhile, inappropriately defined tool orientations in such applications can cause fatal collisions and damage the in-processing part, and unsmooth segments of tool orientation may lead to unwanted vibrations due to sudden fluctuations in tool movements and, thus, limit the full production capabilities of multiaxis machine tools and inevitably impact machining precision.

In order to obtain smooth tool orientation, many studies have been conducted to achieve optimal tool orientation. For example, the tool-sweep surface-based method [1], curvature matching method [2–4], multipoint machining method [5–7], and simultaneous optimization with feed direction [8,9]; all share the goal of selecting a noninterference and collision-free tool orientation. Meanwhile, Mi et al. [10] presented a feasible C-space computation algorithm for triangular mesh models to plan smooth tool orientation along a tool path. Chen et al. [11] presented a reference plane to generate a set of smoothly aligned tool orientations along a tool path. Gong et al. [12] proposed a method to find the optimal tool orientation based on a ruled surface; the optimization objective function was set to minimize the vibration of rotary axes. Hong et al. [13] described a practical method for tool orientation generation for ball cutters commonly used in complex-surface-finish machining. Dong et al. [14] proposed a multiscale tool orientation generation method that considers both the machining strip width and roughness scales. Sun et al. [15] presented the prediction of an automatic tool axis orientation algorithm that avoids chatter while improving productivity.

In recent years, researchers' attention has also been directed to smoothing tool orientation, and researchers have proposed many typical methods, such as the shortest-path linking method [16], interpolation method [17,18], and optimization-based method [19–21]. Yuan et al. [22] proposed a method for generating smooth tool orientation by considering the relationship between tool orientation and strip width for five-axis machining with flat-end cutters. Dong et al. [23] proposed a multiscale tool orientation smoothness method that considers both machining strip width and roughness scales. On this basis, a novel method based on the best curvature matching was used to generate smoothing tool orientation [24]. Yana et al. [25] proposed a mathematical framework to generate smoothing tool axis variation even on partial surfaces lacking G2 and/or G1 continuities. Wang et al. [26] constructed a selection strategy for the smoothing tool axis from the discrete domain of feasible orientations. All the technology deeply improved the smoothness of tool orientation vector sequences.

The above theoretical studies are dedicated to planning smoothing tool axis vectors in single-tool machining. But pinch milling has two cutters, and any nonsmooth tool axis direction can seriously affect the cutting process. In early stages, the twin-tool milling path is planned [27], the opposite cutting contact points and paths are planned, the twin-tool orientation is characterized, and the initial dual-tool axis vectors are also planned. However, in actual machining, it was found that the angle between the cutters changed discontinuously and unevenly, which limited the cutting speed of the machine tool and caused obvious vibration during cutting processes. Meanwhile, the envelope surface is jointly constructed by the tool and workpiece at the cutting contact, which plays a crucial role in the cutting process. The state of the tool orientation has a significant impact on the formation of the envelope surface and the machining quality of the workpiece surface. It is a key item in the twin-tool cutting process. Therefore, smoothness orientation planning for pinch milling is an enormous challenge.

In this paper, the twin-tool orientation synchronous smoothing algorithm is proposed for thin-wall blades used in pinch milling. Considering the two cutters' structural layouts, the twin-tool orientations and coupling relationship are characterized; a method is also proposed for defining the feasible region of the cutters. In order to guarantee the smoothness of the tool orientations, the tool axis vector is parameterized and tool posture curve of global optimization is formulized, and the evaluation algorithm of local optimization is investigated. Finally, the twin-tool orientation selection and optimization scheme is explored within the feasible domain along the two tool paths. Furthermore, the smoothness tool orientation is planned for a typical turbine blade.

2. Twin-Tool Orientations Identification

2.1. The Method of Pinch Milling

Pinch milling is a method that involves simultaneously milling both sides of an irregular blade profile from top to top, using two tools concurrently. The milling process is shown in Figure 1; two tools are oppositely and simultaneously assigned to mill the dorsal (convex) and basin (concave) surfaces, and the directions along blade height are the feed directions for the two tools. Meanwhile, it considers the shape and size characteristics of the leading and trailing edges in order to avoid collisions between the two cutters, which are milled along the length direction with either one of the twin tools.

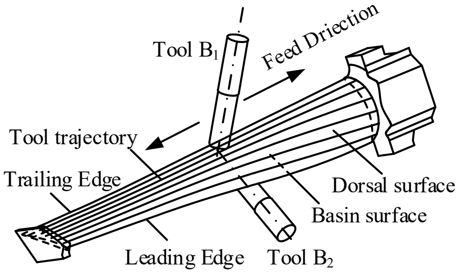

Figure 1. The method of pinch milling.

At the top-to-top contact point, the tool axes orientations of the two cutters should influence each other, and the rotation angle of the workpiece simultaneously affects the cutting angle of the tool.

2.2. Twin-Tool Orientations Description

In pinch milling, in addition to the translations along the length direction of the blade, two cutters can be rotated with the workpiece axis to adapt to complex curved surfaces. As shown in Figure 2, the local coordinate system O_L–X_L–Y_L–Z_L is defined at the cutter contact (CC) point C. The X_L-axis is defined along the instantaneous cutting direction, the Z_L-axis is defined along the direction of local surface normal, and the Y_L-axis is defined by the X_L- and Z_L-axes with the right-hand-rule. The tool orientation is determined with an inclination angle α_L around the Y_L-axis and a tilt angle λ_L around the Z_L-axis. The tool orientation for the other tool is also determined by the same rule.

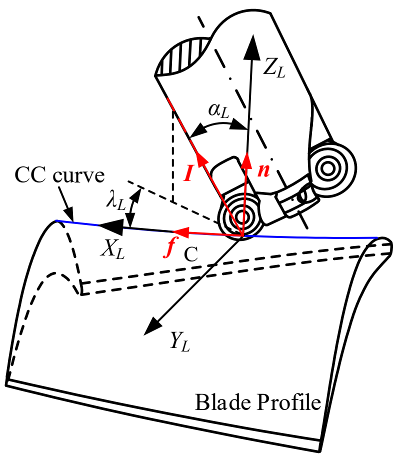

Figure 2. Definition of tool orientation angles.

In the local coordinate system O_L–X_L–Y_L–Z_L, the unit vectors $\boldsymbol{f}$, $\boldsymbol{n}$, and $\boldsymbol{I}$ are defined along the direction of the X_L-axis, Z_L-axis, and tool-axis, respectively. Then, the inclination angle α_L and the tilt angle λ_L can be derived as follows:

$$\begin{aligned} \alpha_L &= \cos^{-1}(\boldsymbol{n} \cdot \boldsymbol{I}) = \cos^{-1}(xx_n + yy_n + zz_n) \\ \lambda_L &= \cos^{-1}\left(\frac{\boldsymbol{I} \cdot \boldsymbol{f}}{\sin \alpha_L}\right) = \cos^{-1}\left(\frac{xx_f + yy_f + zz_f}{\sin \alpha_L}\right) \end{aligned} \quad (1)$$

where $\boldsymbol{f} = [x_f, y_f, z_f]$, $\boldsymbol{n} = [x_n, y_n, z_n]$, $\boldsymbol{I} = [x, y, z]$.

Considering structural constraints of pinch milling, the two tools can only horizontally swing and parallel each other. As Figure 3, in the workpiece coordinate system O_W–X_W–Y_W–Z_W, the points C_1 and C_2 are top-to-top cutting contacts, $\boldsymbol{a_1}$ and $\boldsymbol{a_2}$ are supposed to be the tool orientations at the opposite cutting points, respectively, $\boldsymbol{n_1}$ and $\boldsymbol{n_2}$ are supposed to be the normal vectors at the point on the dorsal and basin surfaces respectively, then $\boldsymbol{m_1}$ and $\boldsymbol{m_2}$ are the projection vectors of $\boldsymbol{n_1}$ and $\boldsymbol{n_2}$ onto the plane Y_W–O_W–Z_W.

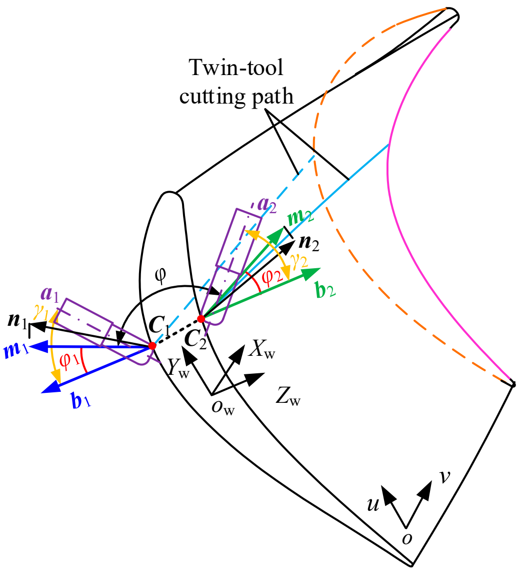

Figure 3. Twin-tool orientations constraint relationship of the CC point.

Assuming normal vector $\boldsymbol{n_1}$ is $[x_1, y_1, z_1]$ and normal vector $\boldsymbol{n_2}$ is $[x_2, y_2, z_2]$, then $[0, y_1, z_1]$ is expressed as the vectors $\boldsymbol{m_1}$, and $[0, y_2, z_2]$ is expressed as the vectors $\boldsymbol{m_2}$. The angle between the vectors $\boldsymbol{m_1}$ and $\boldsymbol{m_2}$ is denoted as φ, which can be expressed as

$$\varphi = \cos^{-1}\left(\frac{y_1 y_2 + z_1 z_2}{\sqrt{y_1{}^2 + z_1{}^2}\sqrt{y_2{}^2 + z_2{}^2}}\right) \tag{2}$$

The vectors $\boldsymbol{b_1}$ and $\boldsymbol{b_2}$ are the projection vectors of $\boldsymbol{a_1}$ and $\boldsymbol{a_2}$ onto the plane Y_W–O_W–Z_W, respectively. Suppose that the angle between $\boldsymbol{m_1}$ and $\boldsymbol{b_1}$ is φ_1, and the angle between $\boldsymbol{m_2}$ and $\boldsymbol{b_2}$ is $\boldsymbol{\varphi_2}$, then the relationship among φ_1, φ, and φ_2 can be expressed as follows:

$$\varphi_1 + \varphi + \varphi_2 = \pi \tag{3}$$

Suppose that the angle between $\boldsymbol{a_1}$ and $\boldsymbol{b_1}$ is γ_1, which is the rotation angle from $\boldsymbol{a_1}$ to $\boldsymbol{b_1}$; Similarly, the angle between $\boldsymbol{a_2}$ and $\boldsymbol{b_2}$ is γ_2, which is the rotation angle from $\boldsymbol{a_2}$ to $\boldsymbol{b_2}$. Then translating the vectors into the same plane X_W–O_W–Z_W, $\boldsymbol{a_1}$ and $\boldsymbol{a_2}$ can be calculated and expressed as

$$\begin{aligned} \boldsymbol{a}_1 &= (\sin\gamma_1(y_{\mathrm{n}1}\sin\varphi_1 + z_{\mathrm{n}1}\cos\varphi_1), y_{\mathrm{n}1}\cos\varphi_1 - z_{\mathrm{n}1}\sin\varphi_1\ , \\ &\quad \cos\gamma_1(y_{\mathrm{n}1}\sin\varphi_1 + z_{\mathrm{n}1}\cos\varphi_1)) \\ \boldsymbol{a}_2 &= (\sin\gamma_2(y_{\mathrm{n}2}\sin(\varphi+\varphi_1) + z_{\mathrm{n}2}\cos(\varphi+\varphi_1)), -y_{\mathrm{n}2}\cos(\varphi+\varphi_1) + z_{\mathrm{n}2}\sin(\varphi+\varphi_1), \\ &\quad -\cos\gamma_2(y_{\mathrm{n}2}\sin(\varphi+\varphi_1) + z_{\mathrm{n}2}\cos(\varphi+\varphi_1))) \end{aligned} \tag{4}$$

where $\boldsymbol{n}_1 = [x_{\mathrm{n}1}, y_{\mathrm{n}1}, z_{\mathrm{n}1}]$, and $\boldsymbol{n}_2 = [x_{\mathrm{n}2}, y_{\mathrm{n}2}, z_{\mathrm{n}2}]$.

2.3. Twin-Tool Orientations Coupling Relationship

Local coordinate systems $O_{\mathrm{L}1}X_{\mathrm{L}1}Y_{\mathrm{L}1}Z_{\mathrm{L}1}$ and $O_{\mathrm{L}2}X_{\mathrm{L}2}Y_{\mathrm{L}2}Z_{\mathrm{L}2}$ are established at the point C_1 and C_2 according to the right-hand rule; $\boldsymbol{f_1}$ is the unit vector of tool feed direction at the point C_1, and $\boldsymbol{f_2}$ is the unit vector of the tool feed direction at the point C_2. If the tool axis vector $\boldsymbol{a_1}$ and $\boldsymbol{a_2}$ are all unit vectors, the inclination angle $\alpha_{\mathrm{L}1}$ and tilt angle $\lambda_{\mathrm{L}1}$ of the cutter at the dorsal surface can be derived as follows:

$$\alpha_{\mathrm{L}1} = \cos^{-1}\left(\frac{\begin{array}{l}\sin\gamma_1(y_{\mathrm{n}1}\sin\varphi_1 + z_{\mathrm{n}1}\cos\varphi_1)x_{\mathrm{n}1} + (y_{\mathrm{n}1}\cos\varphi_1 - z_{\mathrm{n}1}\sin\varphi_1\ )y_{\mathrm{n}1} \\ +z_{\mathrm{n}1}\cos\gamma_1(y_{\mathrm{n}1}\sin\varphi_1 + z_{\mathrm{n}1}\cos\varphi_1)\end{array}}{\sqrt{(y_{\mathrm{n}1})^2 + (z_{\mathrm{n}1})^2}}\right) \tag{5}$$

$$\lambda_{L1} = \cos^{-1}\left(\frac{\begin{array}{l}\sin\gamma_1(y_{n1}\sin\varphi_1 + z_{n1}\cos\varphi_1)x_{f1} + (y_{n1}\cos\varphi_1 - z_{n1}\sin\varphi_1\ )y_{f1} \\ +\cos\gamma_1(y_{n1}\sin\varphi_1 + z_{n1}\cos\varphi_1)z_{f1}\end{array}}{\sin\alpha_{L1}\sqrt{(y_{n1})^2 + (z_{n1})^2}}\right) \quad (6)$$

where $\boldsymbol{f}_1 = [x_{f1}, y_{f1}, z_{f1}]$.

Similarly, the inclination angle α_{L2} and tilt angle λ_{L2} of the cutter at the basin surface can be derived as follows:

$$\alpha_{L2} = \cos^{-1}\left(\frac{\begin{array}{l}\sin\gamma_2(y_{n2}\sin(\varphi+\varphi_1) + z_{n2}\cos(\varphi+\varphi_1))x_{n2} + (-y_{n2}\cos(\varphi+\varphi_1) + z_{n2}\sin(\varphi+\varphi_1))y_{n2} \\ +(-\cos\gamma_2(y_{n2}\sin(\varphi+\varphi_1) + z_{n2}\cos(\varphi+\varphi_1)))z_{n2}\end{array}}{\sqrt{(y_{n2})^2 + (z_{n2})^2}}\right) \quad (7)$$

$$\lambda_{L2} = \cos^{-1}\left(\frac{\begin{array}{l}\sin\gamma_2(y_{n2}\sin(\varphi+\varphi_1) + z_{n2}\cos(\varphi+\varphi_1))x_{f2} + (-y_{n2}\cos(\varphi+\varphi_1) + z_{n2}\sin(\varphi+\varphi_1))y_{f2} \\ +(-\cos\gamma_2(y_{n2}\sin(\varphi+\varphi_1) + z_{n2}\cos(\varphi+\varphi_1)))z_{f2}\end{array}}{\sin\alpha_{L2}\sqrt{(y_{n2})^2 + (z_{n2})^2}}\right) \quad (8)$$

where $\boldsymbol{f}_2 = [x_{f2}, y_{f2}, z_{f2}]$.

It will be seen that the rotation angle φ_1 simultaneously determines the inclination angles α_{L1} and α_{L2}, as well as the tilt angles λ_{L1} and λ_{L2} of the tool axis vectors, resulting in mutual influence between the two tool axis vectors without a linear relationship. Meanwhile, the sizes of α_{L1} and λ_{L1} of the tool orientation $\boldsymbol{a_1}$ are directly affected by the parameter of the angle γ_1, and the sizes of α_{L2} and λ_{L2} of the tool orientation $\boldsymbol{a_2}$ are directly affected by the parameter of the angle γ_2. This phenomenon indicates that there is a mutually dependent coupling relationship between the two tool axis vectors, meaning that when the parameters of one tool axis vector change, it triggers corresponding changes in the parameters of the other tool axis vector. This interrelated state directly influences the machining conditions during the twin-tool cutting process. Therefore, adjustments to the parameters of either tool axis vector require careful consideration of their impact on the overall machining state.

3. Tool Orientation Smoothing Optimization Formulation

3.1. Identification of Twin-Tool Orientation Accessible Region

Due to the structural constraints of the pinch milling, the two tool movement spaces are all imposed limitations, and we thoroughly delved into the mutual influence relationship. Based on the parameters of φ_1, γ_1, and γ_2, we can solve the preliminary feasible space of all tool axis vectors, which all satisfy the structural constraints. This specific space is defined as the feasible domain of $Q(\alpha_{L1}, \lambda_{L1}, \alpha_{L2}, \lambda_{L2})$ and can be specifically described as

$$Q(\alpha_{L1}, \lambda_{L1}, \alpha_{L2}, \lambda_{L2}) = \{\boldsymbol{a}_1, \boldsymbol{a}_2 |\ \varphi_1, \gamma_1, \gamma_2\} \quad (9)$$

Under the premise of satisfying the structural constraints on pinch milling, due to multiple factors such as tool size, blade, and fixture shapes, the tool axis vector cannot cover all ranges within the feasible domain Q. In addition, more constraints are considered to avoid collisions and interferences. On the top-to-top cutting contact, the parameters are calculated based on tool data and local geometric data of the curved surface, such as the distance d_e between the tool and the machine tool or workpiece, the effective cutting radius R_e of the tool, the radius of curvature ρ_k at the contact point, and the distance d_s between the tool bottom and the workpiece. Using these data, we can determine a collision-free or interference-free tool axis vector space. In the twin-tool milling process, any of these tools must be ensured to avoid collisions and interferences. Therefore, the feasible domain is further restricted and marked as $R_1(\alpha_{L1}, \lambda_{L1}, \alpha_{L2}, \lambda_{L2})$ and can be specifically described as

$$R_1(\alpha_{L1}, \lambda_{L1}, \alpha_{L2}, \lambda_{L2}) = \{\boldsymbol{a}_1, \boldsymbol{a}_2 |\ d_e > 0, R_e < \rho_k, d_s > 0\} \quad (10)$$

Meanwhile, the geometry of the cutting surface is affected by the angle of the tool orientation, which manifests as excessive residual heights, as well as overcutting and undercutting phenomena, thereby affecting the machining quality of the workpiece surface. Thus, under the condition of the allowable scallop height $h_{\max}$ and chord error δ_{tmax} requirements, the reachable motion space of the tool axis vector can be determined, which is defined as the feasible region $R_2(\alpha_{L1}, \lambda_{L1}, \alpha_{L2}, \lambda_{L2})$ under geometric error constraints, and is expressed as

$$R_2(\alpha_{L1}, \lambda_{L1}, \alpha_{L2}, \lambda_{L2}) = \{\boldsymbol{a}_1, \boldsymbol{a}_2 |\ h_r < h_{\mathrm{rmax}}, \delta_{\mathrm{tr}} < \delta_{\mathrm{tmax}}\} \tag{11}$$

where h_r is the actual scallop height and δ_{tr} is the actual chord error corresponding to the two-tool axis vectors.

The true feasible region is actually the intersection of all feasible regions considered under the constraints, thus forming a closed area reachable by the twin-tool axis vectors, as shown in Figure 4. This area is defined as the feasible region $\Omega(\alpha_{L1}, \lambda_{L1}, \alpha_{L2}, \lambda_{L2})$ for the posture of dual tools, and is represented as

$$\Omega(\alpha_{L1}, \lambda_{L1}, \alpha_{L2}, \lambda_{L2}) = Q \cap R_1 \cap R_2 \tag{12}$$

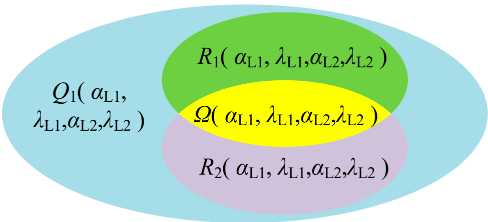

Figure 4. Twin-tool orientations feasible region.

Assuming that the feasible region of $\boldsymbol{a}_1$ is $\Omega_1(\alpha_{L1}, \lambda_{L1})$, and the feasible region of $\boldsymbol{a}_2$ is $\Omega_2(\alpha_{L2}, \lambda_{L2})$, the final feasible region is the union of the feasible regions of the two tool axis vectors. The equivalent expression Ω is represented as

$$\Omega(\alpha_{L1}, \lambda_{L1}, \alpha_{L2}, \lambda_{L2}) = \Omega_1(\alpha_{L1}, \lambda_{L1}) \cup \Omega_2(\alpha_{L2}, \lambda_{L2}) \tag{13}$$

In addition, to clearly describe the positions of the dual tool axis vectors in the workpiece coordinate system $O_W X_W Y_W Z_W$, a Gaussian sphere of unit tool axis vectors is constructed at the origin O_W. Meanwhile, the unit vector $\boldsymbol{a}_1$ and $\boldsymbol{a}_2$ are translated to the origin O_W, respectively, so that $\boldsymbol{a}_1$ and $\boldsymbol{a}_2$ are equivalent to a particle on the Gaussian sphere, and the corresponding feasible regions Ω_1 and Ω_2 represent the ranges of motion of the particles on the Gaussian sphere surface, as shown in Figure 5. However, the inclination angle α_L and tilt angle λ_L only describe the tool's posture in the local coordinate system at the contact point, and its tool axis vector is actually a directional vector in the workpiece coordinate system, which can be represented as (i, j, k). Therefore, the feasible region Ω of twin-tool orientation can be re-expressed as

$$\Omega(i_{W1}, j_{W1}, k_{W1}, i_{W2}, j_{W2}, k_{W2}) \leftrightarrow \Omega(\alpha_{L1}, \lambda_{L1}, \alpha_{L2}, \lambda_{L2}) \tag{14}$$

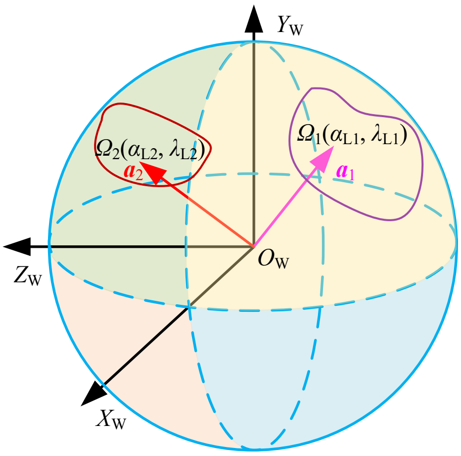

Figure 5. Feasible region in the workpiece coordinate system.

3.2. Global Smoothness of Twin-Tool Orientation

In multiaxis machining, it is expected that the tool axis vectors change continuously and uniformly along the contact points to achieve global smoothing of the tool axis vectors. However, the tool axis vectors formed during trajectory planning may have excessive or uneven angular changes, as shown in Figure 6, and the concept of "smoothness" is inherently complicated and often inconsistent. For unit tool axis vectors, rotation angle of tool orientation is equivalent to the trajectory of a particle moving on the spherical surface. The smoothing is transformed into a curve fitting problem at the particle, which means finding a smooth curve that ensures all tool axis vectors lie on this curve.

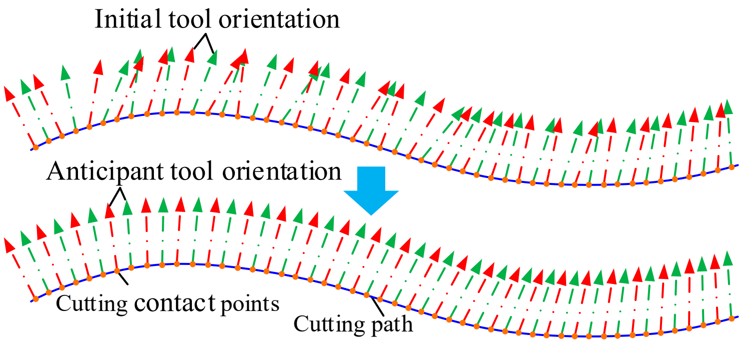

Figure 6. Global smoothness of tool orientation.

Assuming the tool axis vector at the cutting contact point is defined as $\boldsymbol{a}_{ck}$, and the values are $[a_{i,ck}, a_{j,ck}, a_{k,ck}]$, where the subscripts i, j, k represent the component values in each axis of the coordinate system, and the subscript ck indicates the position of the cutting contact point), and the corresponding control vertex is $\boldsymbol{a}_i$, then the parametric B-spline curve can be defined by the basis functions $N_{i,q}(s)$, control points $\boldsymbol{a}_i$, and degree n with the following form:

$$P_c(s) = \sum_{i=0}^{n} N_{i,q}(s)\boldsymbol{a}_i \tag{15}$$

The basis functions $N_{i,q}(s)$ are functions of the geometric parameter s and knot vector $S = [s_0, s_1, \ldots, s_{n+1}]$, and are defined as follows:

$$\begin{aligned} & N_{i,0}(s) = \begin{cases} 1, & s \in [s_i, s_{i+1}] \\ 0, & s \notin [s_i, s_{i+1}] \end{cases} \quad s \in [0,1] \\ & N_{i,q}(s) = \frac{s-s_i}{s_{i+p}-s_i}N_{i,q-1}(s) + \frac{s_{i+p+1}-s}{s_{i+p+1}-s_{i+1}}N_{i+1,q-1}(s), \ \ q \geq 1 \end{aligned} \tag{16}$$

Meanwhile, in order to achieve the analytical solution of control points, the number of basis functions and control points in Equation (14) is set equal to the number of tool axis vector a_k, which allows for the linear system to be solved for the control points. For this, the knot vector S is solved based upon the angles between the tool axis vector $\boldsymbol{a}_k$. Thus, the parameter values $\bar{s}_k$ are assigned to each tool axis vector $\boldsymbol{a}_k$, which can be expressed as

$$\begin{cases} d = \sum_{k=1}^{n} \sqrt{\cos^{-1}(\boldsymbol{a}_k \cdot \boldsymbol{a}_{k-1})} \\ \bar{s}_0 = 0,\ \bar{s}_n = 1 \\ \bar{s}_k = \bar{s}_{k-1} + \dfrac{\sqrt{\cos^{-1}(\boldsymbol{a}_k \cdot \boldsymbol{a}_{k-1})}}{d}, k = 1, \cdots, n-1 \end{cases} \tag{17}$$

Using the assigned parameter values $\bar{s}_k$, the knot vector is solved as follows:

$$\begin{cases} s_0 = \cdots = s_{\mathrm{p}} = 0,\ s_{n+1} = \cdots = s_{n+q+1} = 1 \\ s_{j+n} = \frac{1}{q} \sum_{k=j}^{j+n-1} \bar{s}_k, j = 1, \cdots, n-q \end{cases} \tag{18}$$

Based on the defined knot vector S and the assigned parameter values $\bar{s}_k$, the control point $\boldsymbol{a}_i$ can be solved through the line system of equations and represented as

$$\underbrace{\begin{bmatrix} N_{0,q}(\bar{s}_0) & \cdots & N_{n,q}(\bar{s}_0) \\ \vdots & \ddots & \vdots \\ N_{0,q}(\bar{s}_n) & \cdots & N_{n,q}(\bar{s}_n) \end{bmatrix}}_{\Phi} \underbrace{\begin{bmatrix} \boldsymbol{a}_0{}^T \\ \vdots \\ \boldsymbol{a}_n{}^T \end{bmatrix}}_{\Gamma} = \underbrace{\begin{bmatrix} \boldsymbol{a}_{\mathrm{c}0}{}^T \\ \vdots \\ \boldsymbol{a}_{\mathrm{c}n}{}^T \end{bmatrix}}_{\mathrm{Y}} \tag{19}$$
$$\Gamma = \Phi^{-1}\mathrm{Y}$$

Once the knot vector S and control points $\boldsymbol{a}_i$ have been determined, the B-spline curve $P_{\mathrm{c}}(\mathrm{s})$ of the tool axis can be obtained from Equation (14), which is called the tool posture curve $P_{\mathrm{c}}(\mathrm{s})$, and describes the trajectory of a particle on the spherical surface, representing the angle variation of the tool axis vector at the contact point. Therefore, new tool axis vectors are interpolated the contact point along the tool path; all tool axis vectors are located on the tool posture curve, and the global smoothing tool axis vector can be obtained.

3.3. Local Smoothness of Twin-Tool Orientation

All cutting contact points are all expected to have tool axis vectors that achieve global smoothness variation. However, the optimized cutting axis vector may not be in the feasible region, resulting in the uncertainty of the local cutting contact, so it is necessary to further solve the local optimization problem of the cutting axis vector. For the discrete data, the variation of the tool axis vector can be described as local angular velocity, which can be approximately represented by mean angular velocity in each interval between two neighboring tool orientations. Assuming that the tool center has a constant feed rate, the average angular velocity at unit speed of the tool axis vector between the ith interval can be expressed as

$$\omega_i = \frac{\theta_i}{\ell(c_i c_{i+1})} \tag{20}$$

where θ_i is the angle between tool axis vectors $\boldsymbol{a}_i$ and $\boldsymbol{a}_{i+1}$, and $\ell(c_i c_{i+1})$ stands for the arc length between the two cutting contact points.

In real situations, usually, two consecutive cutting contact points are close, and θ_i is small, so the approximate relationship between angles and arc length can be expressed as

$$\begin{aligned} \ell(c_i c_{i+1}) &\approx \|c_i c_{i+1}\| \\ \theta_i &\approx \sin\theta_i \approx \|\boldsymbol{a}_{i+1} - \boldsymbol{a}_i\| \end{aligned} \tag{21}$$

Therefore, the angular speed ω_i are re-expressed as

$$\omega_i = \frac{\|\boldsymbol{a}_{i+1} - \boldsymbol{a}_i\|}{\|c_i c_{i+1}\|} \tag{22}$$

The smoothness of angular velocity can be achieved by minimizing the harmonic mean of ω_i or the almost constant ω_i along the tool path to ensure the optimal tool axis vector. Then, the objective function for the optimization problem can be formulated as

$$\begin{aligned} &H = \min_{\{a_1,a_2,\cdots,a_n\}} \sum_{i=1}^{n-1} {\omega_i}^2 \\ &\text{s.t. } \alpha_i, \beta_i \in \Omega \end{aligned} \tag{23}$$

The optimal tool axis vector is sought to achieve uniform and smooth variation of the tool axis at adjacent consecutive contact points within the feasible region.

3.4. Twin-Tool Orientation Selection and Optimization Schemes

As long as the optimization algorithm is clearly defined, the tool posture determination process can be carried out. For the pinch milling, both the orientation of two tools are required to have continuous and smooth changes along the cutting path. Therefore, the selection and optimization process is established to solve the optimal tool axis vector; the flowchart of twin-tool smoothness orientation planning is shown in Figure 7.

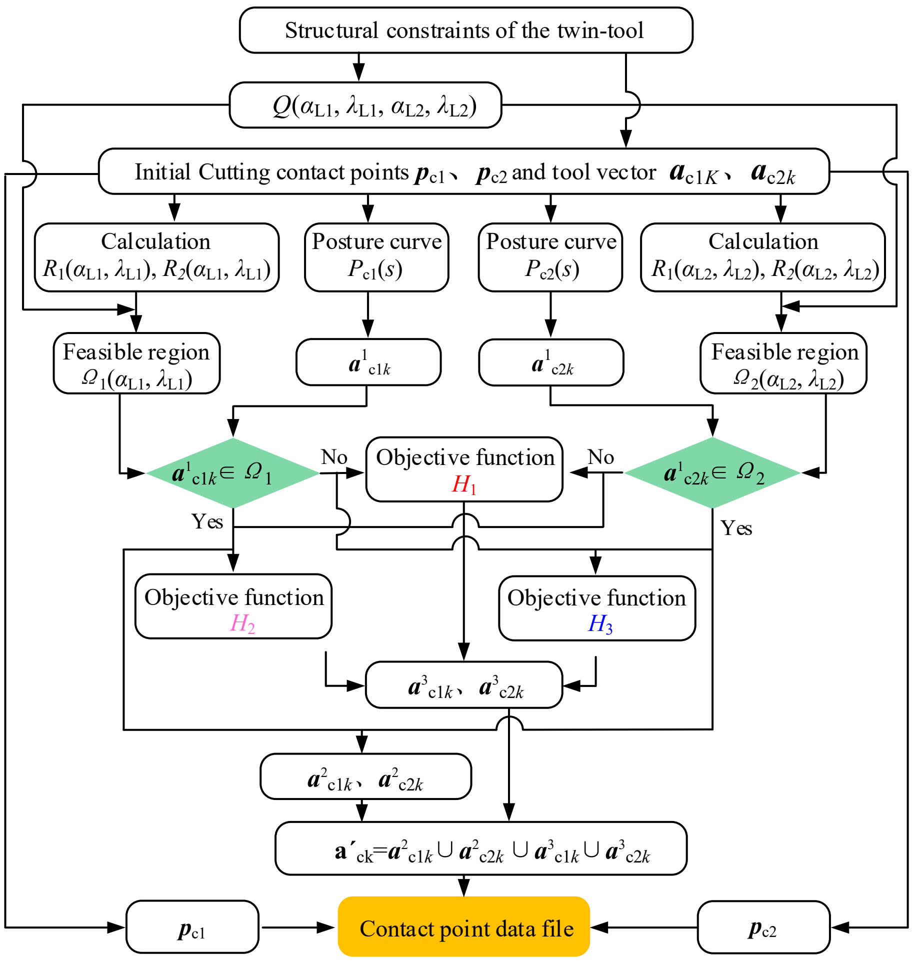

Figure 7. Flowchart of twin-tool orientation for pinch milling.

For the two cutters on the dorsal and basin surfaces of the blade, all reachable regions $Q(\alpha_{L1}, \lambda_{L1}, \alpha_{L2}, \lambda_{L2})$ of the twin-tool axis vector are determined based on the structural constraints. And the feasible domain $\Omega(\alpha_{L1}, \lambda_{L1}, \alpha_{L2}, \lambda_{L2})$ is calculated based on the cutting contact points $\boldsymbol{p}_{c1}$ and $\boldsymbol{p}_{c2}$ on the cutting path and the tool axis vectors $\boldsymbol{a}_{c1k}$ and $\boldsymbol{a}_{c2k}$. At the same time, the tool posture curves $P_{c1}(s)$ and $P_{c2}(s)$ are determined corresponding to the primitive tool axis, and the global optimal vectors $\boldsymbol{a}^1{}_{c1k}$ and $\boldsymbol{a}^1{}_{c2k}$ are solved. If $\boldsymbol{a}^1{}_{c1k}$ and $\boldsymbol{a}^1{}_{c2k}$ both belong to Ω, simultaneous optimization vectors on both sides can be achieved, which can be expressed as $\boldsymbol{a}^2{}_{c1k}$ and $\boldsymbol{a}^2{}_{c2k}$. However, it is difficult to achieve simultaneous optimization in the actual calculation process. For $\boldsymbol{a}^1{}_{c1k}$ and $\boldsymbol{a}^1{}_{c2k}$, which do not belong to Ω, it is necessary to ensure that the change in angular velocity for each of the cutters is minimized. The objective function H_1 is represented as

$$\begin{aligned} & H_1 = \min_{\{a_{c11}, a_{c21}, \cdots, a_{c1n}, a_{c2n}\}} \sum_{i=1}^{n-1} \left({\omega_{c1i}}^2 + {\omega_{c2i}}^2 \right) \\ & \text{s.t. } \boldsymbol{a}^1_{c1k} \notin \Omega,\ \boldsymbol{a}^1_{c2k} \notin \Omega \end{aligned} \tag{24}$$

If $\boldsymbol{a}^1{}_{c1k}$ belongs to Ω and $\boldsymbol{a}^1{}_{c2k}$ does not belong to Ω, then the objective function H_2 is represented as

$$\begin{aligned} & H_2 = \min_{\{a_{c11}, a_{c21}, \cdots, a_{c1n}, a_{c2n}\}} \sum_{i=1}^{n-1} {\omega_{c1i}}^2 \\ & \text{s.t. } \boldsymbol{a}^1_{c1k} \in \Omega,\ \boldsymbol{a}^1_{c2k} \notin \Omega \end{aligned} \tag{25}$$

If $\boldsymbol{a}^1{}_{c1k}$ does not belong to Ω and $\boldsymbol{a}^1{}_{c2k}$ belongs to Ω, then the objective function H_3 is represented as

$$\begin{aligned} & H_3 = \min_{\{a_{c11}, a_{c21}, \cdots, a_{c1n}, a_{c2n}\}} \sum_{i=1}^{n-1} {\omega_{c2i}}^2 \\ & \text{s.t. } \boldsymbol{a}^1_{c1k} \notin \Omega,\ \boldsymbol{a}^1_{c2k} \in \Omega \end{aligned} \tag{26}$$

In the actual optimization process, $\boldsymbol{a}^3{}_{c1k}$ and $\boldsymbol{a}^3{}_{c2k}$ are defined as the local optimal vectors. If $\boldsymbol{a}^1{}_{c1k}$ belongs to Ω, $\boldsymbol{a}^3{}_{c1k}$ is the same as $\boldsymbol{a}^1{}_{c1k}$. If $\boldsymbol{a}^1{}_{c2k}$ belongs to Ω, $\boldsymbol{a}^3{}_{c2k}$ is the same as $\boldsymbol{a}^1{}_{c2k}$, otherwise, they are not the same. Therefore, the final tool axis vector $\boldsymbol{a}'{}_{ck}$ can be expressed as

$$\boldsymbol{a}'{}_{ck} = \boldsymbol{a}^2_{c1k} \cup \boldsymbol{a}^3_{c1k} \cup \boldsymbol{a}^2_{c2k} \cup \boldsymbol{a}^3_{c2k} \tag{27}$$

Based on the above algorithm, all the smoothness orientations can be calculated for the top-to-top contact point, and are all optimal tool axis vectors.

4. Simulation and Experimental Verifications

4.1. Twin-Tool Orientation Smoothness Planning

The implementation of the presented twin-tool orientation optimization algorithm was successfully carried out using C++. A turbine blade is used to test the algorithm, as shown in Figure 8, and the length and rotational diameter of the blade are 633 and 165 mm, respectively. It can be seen from this CAD model that the blade body is thin-wall, asymmetric, and torque-shaped; planning the path and tool axis vector for two opposing milling cutters is a complex and challenging task, and, hence, a good test example for the proposed algorithm. The tool path is assumed to be generated from the upper stream procedures.

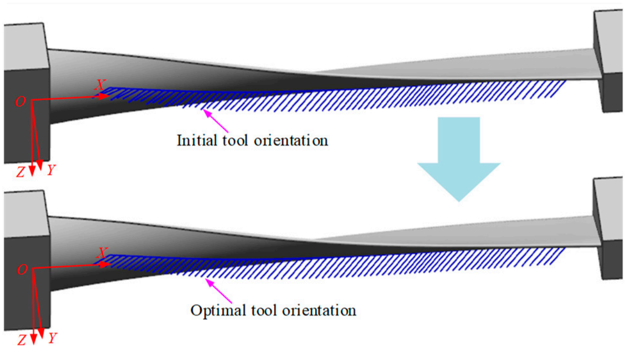

(**a**) the tool orientation on dorsal surface of blade

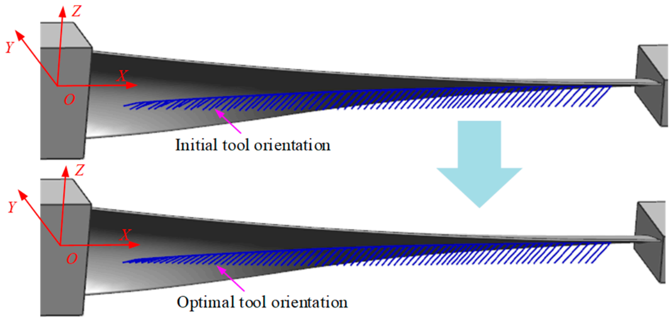

(**b**) the tool orientation on basin surface of blade

Figure 8. The final twin-tool orientation for pinch milling.

Two of the same torus-shaped milling cutters with the radius R of 16 mm and the corner radius r of 6 mm are employed to synchronously mill the oppose surface of the blade, respectively. For the opposing cutting contact points and initial twin-tool axis vectors generated during the path planning of blade profiles, there is no interference during the machining process of the blade surface, and it also satisfies the structural constraints of the two cutters layout. However, there is an obvious nonsmooth phenomenon among the tool axis vectors, and the tool axis vectors are not in a unified sequence.

Using this optimization method, the feasible domain of the two cutters axis vectors are calculated at each cutting contact point, and the tool posture curve is constructed; then, the optimal twin-tool axis vectors are planned through global and local algorithms. The results are shown in Figure 8. By comparing and analyzing the optimization results, it is found that the cutting contact point positions on the path remain unchanged, and the cutting parameters before and after optimization are macroscopically consistent. However, the optimized tool axis vector has visually visible smoothness and changes uniformly along the path, while avoiding interference during the machining process.

The average angular velocities between the initial and optimal tool axis vectors were calculated separately, and the results are shown in Figure 9. The variations in angular velocities are not entirely consistent on both surfaces of the blade, but the significant angle variations between the initial tool axis vectors have been corrected, i.e., the maximum value of the initial tool orientation on the basin surface is 0.5302, and the final is 0.4646. Moreover, the amplitude of variation in average angular velocity after optimization is relatively reduced, and the variations of adjacent tool axes are decreased. It can be seen that the algorithm given obtains continuously changing tool axis vectors with relatively uniform amplitudes of variation, and the planning twin-tool orientation is nearly smoothness.

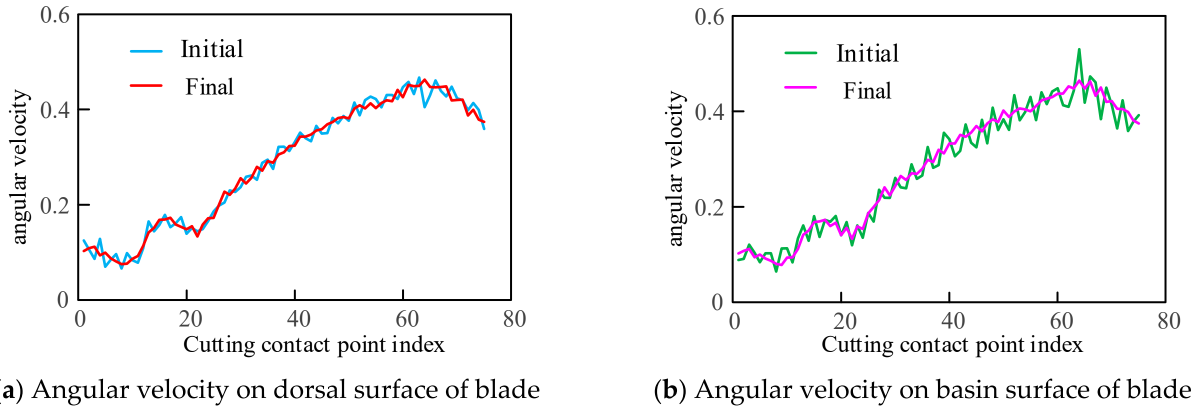

Figure 9. Comparison of angular velocity by initial and finial tool orientation.

4.2. Pinch Milling Experimental

The nine-axis machine tool for pinch milling was used to validate the proposed tool orientation optimization algorithm. The two cutters are arranged symmetrically with respect to the workpiece rotation, which are both the same torus-shaped milling cutters. Any cutter has an independent rotational speed, which is set to 2200. The material of the blade is 1Cr12Ni2W1Mo1V, which is a difficult-to-machine material. The material of the two cutters is hard alloy. Using the planned optimal tool axis vector, the pinch milling process is implemented for the blade, as shown in Figure 10. It is shown that the twin-tool orientation continuously and uniformly varies along the tool path, the milling process is smoothest, the cutting speed is increased by 46% for the initial process, the noise during the cutting process is noticeably reduced, and cutting stability is achieved along the entire path. The machined surface is smooth and flawless, with no visible interference marks, which is feels delicate and smooth to the touch with low roughness. Meanwhile, the product's size and shape closely match the specialized inspection mold, and the machining accuracy fully meets the preset requirements. Therefore, the algorithm is very beneficial for ensuring good machining quality of the blade surface. Additionally, it can better leverage the performance of the machine tool to enhance processing efficiency.

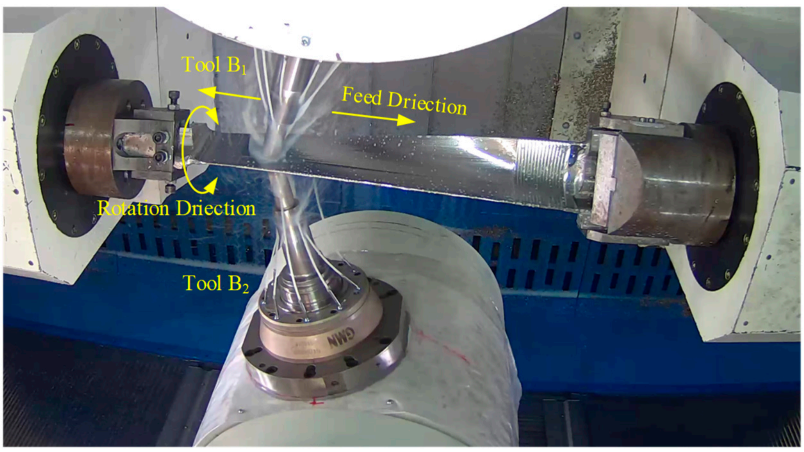

Figure 10. Pinch milling experiment of blade materials.

5. Conclusions

In this research, the twin-tool orientation smoothness planning method is proposed for thin-wall blade with pinch milling. Based on the two cutters structural layout, we clarify the coupling relationship of twin-tool posture, and a calculation method of the feasible region is defined considering multiple constraints. Then, the tool posture curve is constructed for tool orientation, and the global and local optimal planning algorithms are studied within the feasible domain. Furthermore, taking the tool axis vector on the tool posture curve as the optimal value and aiming for the minimum average angular velocity change, the twin-tool synchronization smoothing planning method is proposed for pinch milling.

The optimal twin-tool axis vector are successfully planned for a typical turbine blade using the proposed method, and are nearly smooth, and the collision-free requirement is guaranteed. By simulation and verification experiments, it is shown that the tool axis vectors of two cutters change uniformly along the path, and the pinch milling processing is very smooth. Therefore, efficient and high-precision processing of pinch milling can be achieved, ultimately improving the machining accuracy of the blade with difficult-to-machine materials.

Author Contributions: D.S.: Conceptualization, formal analysis, data curation, writing—original draft, writing—review and editing. S.Z.: Data curation, writing—review and editing. F.X.: Conceptualization, project administration, writing—review and editing. Y.F.: Investigation, data curation. B.L.: Project administration, writing—review and editing. All authors have read and agreed to the published version of the manuscript.

Funding: This research was funded by the Open Foundation of State Key Laboratory for Manufacturing Systems Engineering (grant no. sklms2022013), as well as the National Key R&D Program of China (grant no. 2022YFD2001300).

Institutional Review Board Statement: Not applicable.

Informed Consent Statement: Not applicable.

Data Availability Statement: The data will be provided as required.

Acknowledgments: The authors thank the Northwest A&F University and State Key Laboratory for Manufacturing Systems Engineering. We would also like to thank the National Key R&D Program of China.

Conflicts of Interest: Author Yagang Feng was employed by the company Xi'an Aerospace Huawei Chemical & Biotechnology Co., Ltd. The remaining authors declare that the research was conducted in the absence of any commercial or financial relationships that could be construed as a potential conflict of interest.

References

1. Jun, C.S.; Cha, K.; Lee, Y.S. Optimizing Tool Orientations for 5-Axis Machining by Configuration-Space Search Method. *Comput. Aided Des.* **2003**, *35*, 549–566. [CrossRef]
2. Li, H.; Feng, H.Y. Efficient Five-Axis Machining of Free-Form Surfaces with Constant Scallop Height Tool Paths. *Int. J. Prod. Res.* **2007**, *42*, 2403–2417. [CrossRef]
3. Wang, N.; Tang, K. Five-axis Tool Path Generation for a Flat-end Tool Based on iso-Conic Partitioning. *Comput. Aided Des.* **2008**, *40*, 1067–1079. [CrossRef]
4. Zhang, X.; Zhang, J.; Zheng, X.W.; Pang, B.; Zhao, W.H. Tool orientation optimization of 5-axis ball-end milling based on an accurate cutter/workpiece engagement model. *CIRP J. Manuf. Sci. Technol.* **2017**, *19*, 106–116. [CrossRef]
5. Warkentin, A.; Ismail, F.; Bedi, S. Multi-point Tool Positioning Strategy for 5-AxisMashining of Sculptured Surfaces. *Comput. Aided Geom. D* **2000**, *17*, 83–100. [CrossRef]
6. He, Y.; Chen, Z.T. Optimising tool positioning for achieving multi-point contact based on symmetrical error distribution curve in sculptured surface machining. *Int. J. Adv. Manuf. Technol.* **2014**, *73*, 707–714. [CrossRef]
7. Tsainis, A.M.; Papazafeiropoulos, G.; Stergiou, C. A novel convex hull method for optimum multi-point 5-axis tool positioning for machining of complex sculptured surfaces. *Int. J. Adv. Manuf. Technol.* **2019**, *103*, 4369–4383. [CrossRef]
8. Fard, B.; Javad, M.; Feng, H.Y. Effective Determination of Feed Direction and Tool Orientation in Five-Axis Flat-End Milling. *J. Manuf. Sci. Eng.* **2010**, *132*, 061011. [CrossRef]
9. Lu, Y.A.; Ding, Y.; Zhu, L.M. Simultaneous Optimization of the Feed Direction and Tool Orientation in Five-Axis Flat-end Milling. *Int. J. Prod. Res.* **2015**, *54*, 4537–4546. [CrossRef]
10. Mi, Z.P.; Yuan, C.M.; Ma, X.H.; Shen, L.Y. Tool orientation optimization for 5-axis machining with C-space method. *Int. J. Adv. Manuf. Technol.* **2017**, *88*, 1243–1255. [CrossRef]
11. Chen, L.; Xu, K.; Tang, K. Collision-free tool orientation optimization in five-axis machining of bladed disk. *J. Comput. Des. Eng.* **2015**, *2*, 197–205. [CrossRef]

12. Gong, Z.; Li, B.R.; Zhang, H.; Ye, P.Q. Tool orientation optimization method based on ruled surface using genetic algorithm. *Int. J. Adv. Manuf. Technol.* **2022**, *118*, 571–584. [CrossRef]
13. Hong, X.Y.; Hong, R.J.; Lin, X.C. Tool orientations' generation and nonlinear error control based on complex surface meshing. *Int. J. Adv. Manuf. Technol.* **2019**, *105*, 4279–4288. [CrossRef]
14. Dong, J.S.; He, J.M.; Liu, S.; Wan, N.; Chang, Z.Y. A multi-scale tool orientation generation method for freeform surface machining with bull-nose tool. *Micromachines* **2023**, *14*, 1199. [CrossRef] [PubMed]
15. Chao, S.; Altintas, Y. Chatter free tool orientations in 5-axis ball-end milling. *Int. J. Mach. Tools Manuf.* **2016**, *106*, 89–97.
16. Plakhotnik, D.; Lauwers, B. Graph-based optimization of five-axis machine tool movements by varying tool orientation. *Int. J. Adv. Manuf. Technol.* **2014**, *74*, 307–318. [CrossRef]
17. Tulsyan, S.; Altintas, Y. Local tool path smoothing for five-axis machine tools. *Int. J. Mach. Tools Manuf.* **2015**, *96*, 15–26. [CrossRef]
18. Ho, M.C.; Hwang, Y.R.; Hu, C.H. Five-axis tool orientation smoothing using quaternion interpolation algorithm. *Int. J. Mach. Tools Manuf.* **2003**, *43*, 1259–1267. [CrossRef]
19. Farouki, R.T.; Li, S.Q. Optimal Tool Orientation Control for 5-Axis CNC Milling with Ball-end Cutters. *Comput. Aided Geom. D* **2013**, *30*, 226–239. [CrossRef]
20. Zhou, K.; Tang, J. Tool position and orientation global optimization intrinsic geometry of strip-width-maximization manufacture technology for sculptured surface. *J. Mech. Eng.* **2020**, *56*, 192–201.
21. Xu, J.T.; Zhang, D.Y.; Sun, Y.W. Kinematics performance oriented smoothing method to plan tool orientations for 5-axis ball-end CNC machining. *Int. J. Mech. Sci.* **2019**, *157–158*, 293–303. [CrossRef]
22. Yuan, C.M.; Mi, Z.P.; Jia, X.H.; Lin, F.M.; Shen, L.Y. Tool orientation optimization and path planning for 5-axis machining. *J. Syst. Sci. Complex.* **2020**, *34*, 83–106. [CrossRef]
23. Kwon, S.H.; Han, C.Y. Least variation in tool orientation control for 5-axis CNC machining. *Comput. Aided Geom. Des.* **2022**, *96*, 102116. [CrossRef]
24. Dong, J.S.; Chang, Z.Y.; Chen, P.; He, J.M.; Wan, N. Tool orientation optimization method based on the best curvature matching. *Int. J. Adv. Manuf. Technol.* **2023**, *124*, 127–142. [CrossRef]
25. Yana, C.; Lee, C.H.; Li, X.Y.; Zhang, Y.M.; Min, K. A multi-objective tool-axis optimization algorithm based on covariant field functional. *J. Manuf. Syst.* **2018**, *48*, 30–37. [CrossRef]
26. Wang, Q.R.; Feng, Y.X.; Zhang, Z.X.; Tan, J.R. Tool orientation sequence smoothing method based on the discrete domain of feasible orientations. *Int. J. Adv. Manuf. Technol.* **2017**, *92*, 4501–4510. [CrossRef]
27. Song, D.D.; Xue, F.; Wu, D.D.; Zhang, J.; Zhang, X.; Zhao, W.H.; Lu, B.H. Iso-parametric path-planning method of twin-tool milling for turbine blades. *Int. J. Adv. Manuf. Technol.* **2018**, *98*, 3179–3189. [CrossRef]

materials

MDPI

Article

Experimental Modeling, Statistical Analysis, and Optimization of the Laser-Cutting Process of Hardox 400 Steel

Mehdi Safari *, Seyed Mohammad Abtahi and Jalal Joudaki

Department of Mechanical Engineering, Arak University of Technology, Arak 38181-46763, Iran
* Correspondence: m.safari@arakut.ac.ir; Tel./Fax: +98-86-33400672

Abstract: Fiber laser cutting machines are widely used in industry for cutting various sheet metals. Hardox steel is widely used in the construction of machinery and equipment that are subjected to wear and impact due to its anti-wear properties and good impact resistance. In this experimental study, the effect of input parameters including laser output power (LOP), laser-cutting speed (LCS), and focal point position (FPP) of fiber laser on the surface roughness and kerf width of Hardox 400 steel sheets are studied. In addition, the optimization of input parameters to achieve the desired surface roughness and kerf width are investigated and analyzed using the response surface methodology (RSM). The experiments are performed using a 4 kW fiber laser-cutting machine and the output results including surface roughness and kerf width are measured using roughness meters and optical microscope. The results of the analysis of variance (ANOVA) for surface roughness and kerf width show that the FPP and LCS are the most significant process parameters affecting the surface roughness and kerf width. With a positive focal point, the surface roughness decreases while the kerf width increases. With increasing the laser-cutting speed, both the surface roughness and kerf width decrease.

Keywords: laser-cutting process; Hardox 400 steel; surface roughness; kerf width; design of experiments

1. Introduction

The laser-cutting process (LCP) for sheet metals has increased significantly in recent years due to its high production speed and cutting surface accuracy, which leads to improved industrial production processes. The LCP is a non-contact method that utilizes the energy of a focused laser beam without the use of hard tooling, making it easy to cut complex geometries. With this method, the challenges of cutting hard materials using conventional methods are eliminated, the heat-affected zone (HAZ) is very small, the kerf width is very small, and there is very little residual stress and distortion [1,2]. Most researchers prefer to consider the main parameters affecting the LCP in their research, which include the intensity of the beam power, the diameter of the laser beam, the type and pressure of the assistant gas, the pulse frequency, the cutting speed, and the position of the focal point relative to the workpiece surface. This is because these parameters can be easily controlled and are the most effective parameters for measuring cut quality. The most common output parameters that indicate surface quality and have been studied by researchers are surface roughness and kerf width [2]. Hardox steel is a trademark that encompasses a wide range of high-strength, wear-resistant steels that retain their physical and mechanical properties over a wide temperature range and are widely used in industrial applications. These steels are used in environments involving severe wear and impact due to their exceptional toughness, hardness, and high wear resistance [3,4]. Hardox 400 steel has high wear resistance, fatigue resistance, and impact resistance. Due to these properties, it is widely used in earthmoving and mining equipment, agriculture, recycling, cement, and concrete production. For example, it is a reliable choice for the production of dump truck bodies, stone crusher equipment, bulldozer blades and concrete mixers, and agricultural and waste equipment due to the harsh working conditions [5]. Due to the physical and chemical properties of this steel, the use of traditional machining leads to rapid tool wear with an average surface roughness [6–8]. Since this steel exhibits high thermal conductivity, melt viscosity, and absorption then the LCP can be an efficient and suitable alternative process [9,10]. In recent years, researchers have investigated and studied the possibility of LCP of various materials. Very few researchers have investigated and studied laser-cutting conditions on Hardox steel. Gheorghe and Girdu [11] conducted an experimental study on CO_2 laser cutting of Hardox 400 steel and the effect of process parameters including laser output power (LOP), gas pressure (GP), and laser-cutting speed (LCS) on the kerf width based on a full factorial design to improve kerf characterizations. They found that LOP has the most significant effect on kerf width. In the interaction between LOP and GP at constant LCS, the minimum kerf was obtained when setting the LOP and GP to intermediate values. In another study by the same researchers [12], they optimized LCP parameters to increase process productivity and reduce energy costs on Hardox 400 steel. The findings of this study show that cutting efficiency is highly influenced by LCS and subsequently by LOP, emphasizing the importance of optimizing LCS and LOP combinations to achieve cost-effective and efficient production processes. Mileșan et al. [13] conducted an experimental study on the LCP of Hardox 400 steel sheets and showed that low surface roughness is obtained at high speeds and low powers, and increasing the LOP leads to an increase in laser focus energy density and surface roughness. Gondalia and Sharma [14] investigated the effect of various LCP parameters such as LCS, LOP, GP, and pulse frequency on Hardox 400 with a thickness of 8 mm using oxygen gas. This study was conducted to establish relationships between these parameters and improve cut quality, which includes surface roughness and kerf. Prajapati et al. [15] investigated the effect of CO_2 laser machine parameters such as LOP, GP, LCS, and thickness on the surface roughness of Mild Steel and Hardox 400. The experiments were designed based on the Taguchi L27 orthogonal array with three different levels of each input parameter. ANOVA was performed to interpret the results. The results showed that LCS and workpiece thickness plays a significant role in surface roughness. Design of experiments (DOE) using the response surface method (RSM) is a mathematical and statistical method used to model and analyze problems in which one response (output variable) is affected by several independent variables (input variables). The goal of RSM is to optimize the response by finding the best combination of input variables, which involves using designed experiments to collect data, fitting models to the data, and using optimization techniques to find the combination of variables that maximizes or minimizes the response. This method helps to understand the effect of LCP on cut quality and predict the results of different parameter settings by developing regression models and using statistical analysis such as ANOVA. It is also very efficient for optimizing LCP, as it can handle complex and nonlinear relationships and interactions between parameters that are common in LCP. It also allows for the optimization of multiple responses simultaneously, which is important for achieving a balance between different aspects of cut quality [16–18]. Nguyen et al. [18] in an experimental and comparative study to optimize LCP parameters on Stainless Steel 304 concluded that the RSM predicts optimal conditions more accurately than Taguchi. The RSM was strongly recommended for identifying optimal parameter settings and interactions, and the Taguchi method can be a suitable method for screening important variables for cases where experimentation is costly and time consuming. Sharma and Kumar [19] successfully applied the RSM using the Box–Behnken design (BBD) with analysis of LCP parameters on the responses of laser cutting of aluminum metal matrix composite and optimized it, validating the predicted model with experimental data and showing the importance and accuracy of the model. Wang et al. [20] discuss LCP for nickel-based superalloys in an experimental study and investigates the LCP parameters and their effects on surface roughness using the RSM. The results of the ANOVA showed that the data fit well with the predicted nonlinear regression model. The main parameters of LCS, LOP, and focal length had the most significant effect on the temperature around the cutting area, in that order. Vishnu Vardhan et al. [21] investigated the experimental process parameters of LCP including LOP, LCS, and GP to improve the surface quality of SS 314 stainless steel. The LCP parameters were optimized using the RSM to minimize surface roughness. Eltawahni et al. [22] investigated the LCP of AISI316L stainless steel by process parameters such as LOP, LCS, FPP, nitrogen pressure, and nozzle diameter and applied the RSM to develop the mathematical models and optimize the kerf width, surface roughness, and operational cost. Vora et al. [23] studied the advantages of fiber laser for the LCP of titanium alloy Ti6Al4V. The LOP, LCS, and GP were selected as the input parameters, and surface roughness, kerf, bead height, and material removal rate (MRR) were selected as the output variables. The effects of the input variables were analyzed through ANOVA, main effect plots, residual plots, and contour plots. Safari et al. [24] conducted an experimental study on the LCP of polymethyl methacrylate (PMMA) using the RSM to analyze the effects of process variables on surface roughness, kerf, and taper angle. The results showed that LBD has a significant effect on surface roughness, while LOP and LCS affect kerf and taper angle. Multi-objective optimization was also used to determine the optimal conditions and minimize surface roughness, kerf, and taper angle. Jadhav and Kumar [25] investigated the effect of process parameters including LOP, LCS, and GP on surface roughness using RSM in an experimental study on LCP of AISI 304 stainless steel with an optimization process to minimize surface roughness. Kotadiya et al. [26] investigated the LCP of stainless steel in an experimental study and analyzed process parameters including LOP, LCS, and GP using RSM to optimize responses including surface roughness and kerf, and it was found that LOP has the most significant effect on the responses.

To the authors' knowledge, few pieces of research have been reported on the LCP of Hardox 400 steel, especially with a fiber laser source. The Hardox 400 steel is widely used in various industries due to its special physical and chemical properties. It should be noted that laser cutting has been used in industries for more than 30 years but still, it has some unknown aspects that lead to unoptimized cutting. The irradiated heat produces microstructural changes and a little deviation in flatness (usually bowing and wrapping) but the manufacturers cut the sheets with these unwanted phenomena because of its speed and low cost (good productivity). By the way, laser cutting is used widely without thinking about these defects. This manuscript aims to find the cutting condition that minimized the surface roughness and minimized kerf width. This article is an attempt to focus on surface roughness and kerf width in laser cutting. Therefore, in this work the LCP of Hardox 400 steel will be studied and the effects of some important process parameters such as laser output power (LOP), laser-cutting speed (LCS), and focal point position (FPP) of the surface roughness and kerf width are investigated.

2. Materials and Methods

The experiments were carried out with an industrial fiber laser machine with a maximum power of 4 kW (Figure 1). The examined material is a Hardox 400 steel sheet (SSAB Steel industry company, Stockholm, Sweden) with a thickness of 8 mm. For implementing the tests, a 330 mm $\times$ 130 mm sample was prepared. The steel was provided by a certified steel supplier and the chemical composition of the Hardox 400 steel sheet is shown in Table 1.

In this study, the RSM (Box–Behnken type) was used to investigate the relationship between input variables and output responses. To investigate the changes in surface roughness and kerf width, the input variables of laser output power (LOP), laser-cutting speed (LCS), and focal point position (FPP) were selected as influential factors of the LCP based on a review of previous research [12,14,15,24]. Accordingly, the experimental design was performed using three parameters and three different levels, as shown in Table 2. The effect of process parameters and their interactions were analyzed using analysis of variance (ANOVA), the mathematical model was determined based on the results of the experimental design, and finally, process variables were optimized. Minitab software (Minitab 18.1) was used for experimental design and data analysis, and the list of experiments according to RSM is shown in Table 3. It should be noted that different DOE techniques exist, such as full-factorial and Taguchi. The full-factorial design is used when the effect of input parameters is an always ascending or always descending function and it is usually used as a 2-level full-factorial DOE design. So, the data will be analyzed by $2^3 = 8$ experiments. When the researcher guesses that the output variable firstly increases and then decreases (or vice versa) by the input parameter, it is necessary to use the RSM method. Also, the effect of the interaction of the input variables and the square of the input variables can be discussed in this method. Using a 3-level full-factorial DOE design can lead to including higher-order terms such as cubic terms and their third-order interactions and some fourth-order terms in the calculation, which is very complicated and is avoided by the researchers. So, the RSM is used for DOE in this study.

Figure 1. Fiber Laser Machine for LCP of Hardox 400 steel.

Table 1. Chemical composition of Hardox 400 steel [5].

Alloy Element	Fe	C	Si	Mn	P	S	Cr	Ni	Mo	B
Weight Percent (%)	Base	0.32	0.70	1.60	0.025	0.010	2.50	1.50	0.60	0.004

Table 2. The levels of process parameters in LCP of Hardox 400 steel.

Input Variable	Units	Levels		
		I	II	III
LOP	W	1900	2300	2700
LCS	mm/min	1000	1300	1600
FPP	mm	0	+1	+2

Table 3. List of experiments for LCP of Hardox 400 according to RSM.

Experiment Number	LOP (W)	LCS (mm/min)	FPP (mm)
1	2300	1000	2
2	1900	1000	1
3	2300	1300	1
4	2300	1300	1
5	2300	1000	0
6	1900	1300	2
7	2700	1600	1
8	2700	1300	2

Table 3. *Cont.*

Experiment Number	LOP (W)	LCS (mm/min)	FPP (mm)
9	2300	1300	1
10	2300	1600	0
11	1900	1300	0
12	2700	1300	0
13	1900	1600	1
14	2700	1000	1
15	2300	1600	2

In Figure 2, the straight cuts with a length of 80 mm were made on a Hardox 400 steel sheet according to the list of experiments designed based on RSM (Table 3).

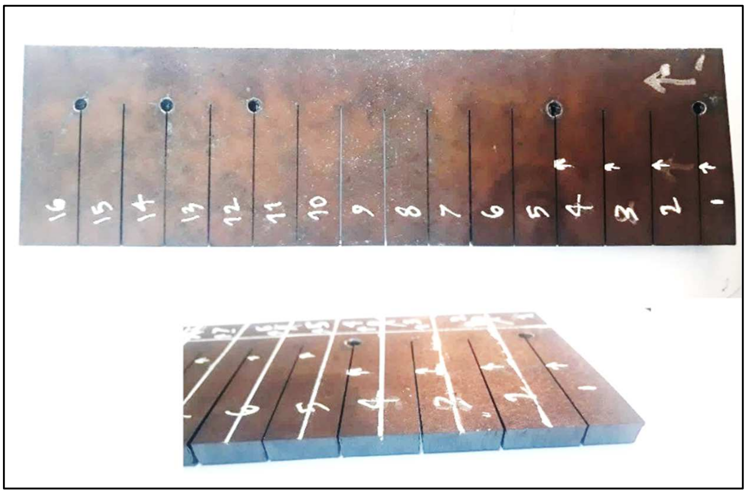

Figure 2. The laser cut specimens after LCP.

OLYMPUS DP73 optical microscope (OLYMPUS, Tokyo, Japan) with 100× magnification was used to measure the kerf width. In Figure 3, a sample of kerf width measurements using the optical microscope is shown. The kerf width was measured at five points and the average of the data was used for data analysis using Minitab software.

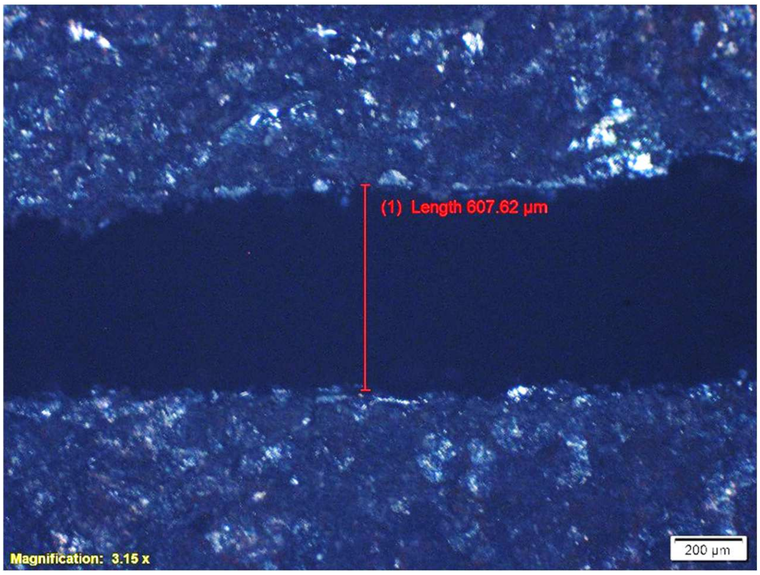

Figure 3. Measurement of kerf width using OM software (DP73 Firmware (Ver. 2.116)).

A surface roughness instrument (Surfscan200) (Surfscan, Rocklin, CA, USA) was used to measure the surface roughness (Figure 4). The nominal accuracy of this device is 0.001 μm, and the stylus probe scans the surface with 4 mm as evaluation length (0.8 mm sampling length or cut-off length × 5 sampling lengths) and 0.4 mm pre-travel and 0.4 mm post-travel lengths. The average surface roughness value (Ra) is calculated according to the ISO 21920-3:2021 standard [27]. To measure the surface roughness of the samples, the measurements were carried out in three zones of the surface for each sample. The instrument probe scans the surface roughness along the direction of the laser-scanning direction, and the average value was considered as the final surface roughness of the cutting groove.

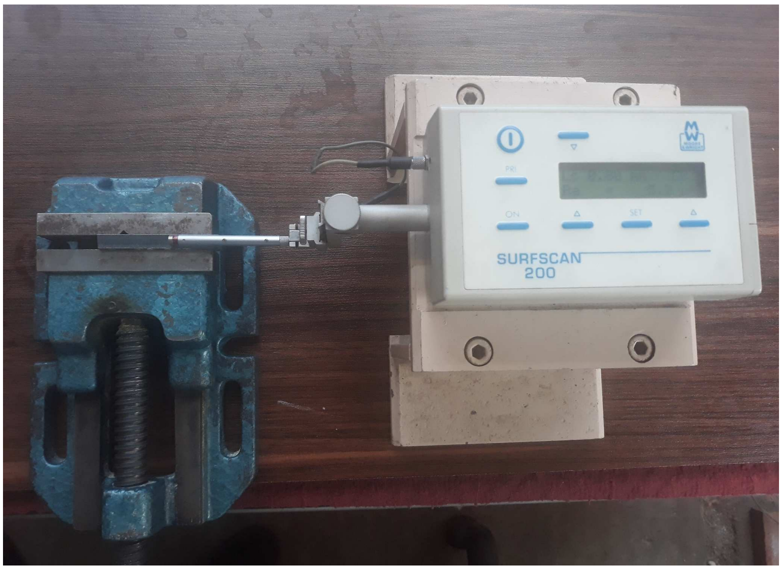

Figure 4. The surface roughness measurement apparatus.

3. Results and Discussion

To determine the effect of each parameter and the interactions of the parameters on the surface roughness and kerf width, ANOVA was used. It should be noted that in the ANOVA results, a *p*-value less than 0.05 shows that the investigated parameter is effective on the expected output. In addition, in the ANOVA results, the R-sq and R-sq (adj) values are also provided, which indicate that the data fit the regression model and are of very high accuracy.

3.1. Surface Roughness Analysis

The results of the ANOVA for surface roughness are shown in Table 4. FPP and LCS are the effective parameters in the process, while LOP has the least effect. The results of the ANOVA for surface roughness are also shown graphically in a Pareto chart in Figure 5. The red line in Figure 5 is called the reference line and the variable that crosses the line is a significant parameter. It is calculated from the T-distribution function.

Figure 6 presents the Normal Probability Plot for the surface roughness. Observing that the data points align approximately linearly along the regression line, we can conclude that the data follow a normal distribution and that the linear regression model fits the experimental data well. The distance of points from the red line (Residual) shows the quality of interpolation, and the coefficient of determination (R^2) is calculated according to the closeness of the points to the line. From Table 4 it can be reported that the R^2 is 96.56% for surface roughness.

Table 4. ANOVA results for surface roughness.

Source	DF	Adj SS	Adj MS	F-Value	*p*-Value
Model	7	54.0436	7.7205	28.06	0.000
Linear	3	44.6275	14.8758	54.07	0.000
LOP (W)	1	0.0450	0.0450	0.16	0.698
LCS (mm/min)	1	18.3012	18.3012	66.52	0.000
FPP (mm)	1	26.2812	26.2812	95.53	0.000
Square	2	4.6636	2.3318	8.48	0.013
LOP (W) × LOP (W)	1	3.3116	3.3116	12.04	0.010
LCS (mm/min) × LCS (mm/min)	1	1.6635	1.6635	6.05	0.044
2-Way Interaction	2	4.7525	2.3762	8.64	0.013
LOP (W) × FPP (mm)	1	1.6900	1.6900	6.14	0.042
LCS (mm/min) × FPP (mm)	1	3.0625	3.0625	11.13	0.012
Error	7	1.9258	0.2751		
Lack-of-Fit	5	1.7391	0.3478	3.73	0.225
Pure Error	2	0.1867	0.0933		
Total	14	55.9693			
S = 0.524509	R-sq = 96.56%	R-sq (adj) = 93.12%			

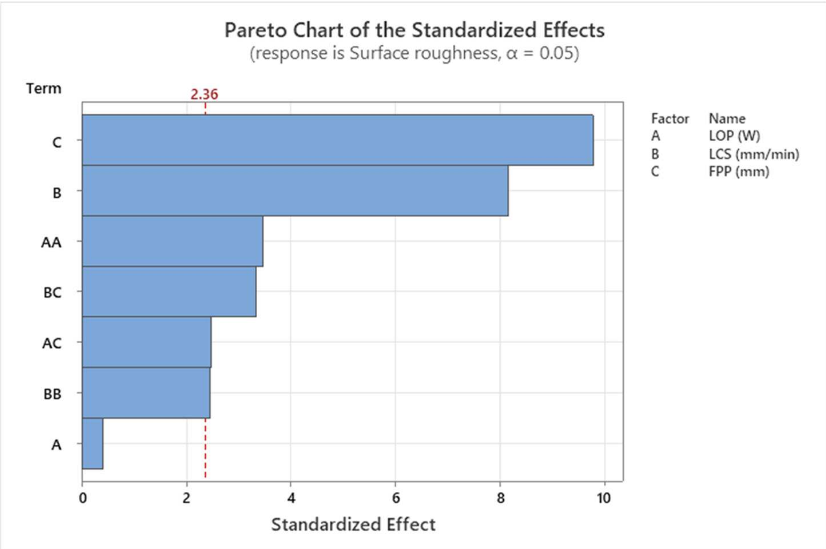

Figure 5. Pareto chart for surface roughness.

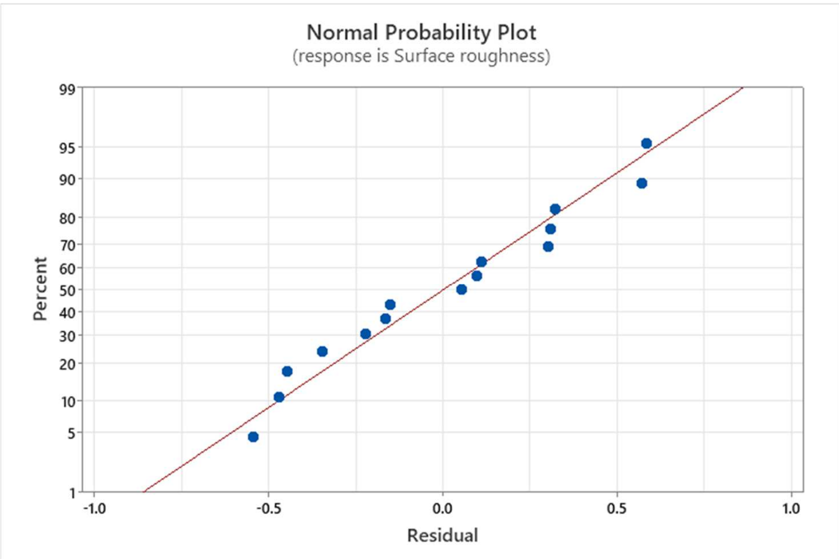

Figure 6. Normal Probability Plot for the surface roughness.

Based on the obtained results, the regression equation for the prediction of surface roughness for LCP of Hardox 400 steel sheet is given by Equation (1):

$$\text{Surface roughness} = 49.6 - 0.02571\ \text{LOP} - 0.02146\ \text{LCS} + 5.72\ \text{FPP} + 0.000006\ \text{LOP} \times \text{LOP} + 0.000007\ \text{LCS} \times \text{LCS} - 0.001625\ \text{LOP} \times \text{FPP} - 0.002917\ \text{LCS} \times \text{FPP} \quad (1)$$

The effect of the main parameters such as LOP, LCS, and FPP on the surface roughness is shown in Figure 7. In this research, the focus position has been set between 0 and 2 mm above the surface of the sheet. As is seen in Figure 7, with the increase in laser power, the surface roughness decreases due to the entry of more thermal energy into the cutting area and complete melting in this area. Consequently, with a further increase in laser power, due to the destruction of more areas of the sheet in the cutting area, the roughness of the cutting surface increases. In addition, with increasing the LCS, surface roughness decreased. This is because the thermal energy has less time to melt the cut surface and increase surface roughness. The laser energy density should also be applied to the workpiece surface in an appropriate range and for a specified time to prevent an increase in surface roughness.

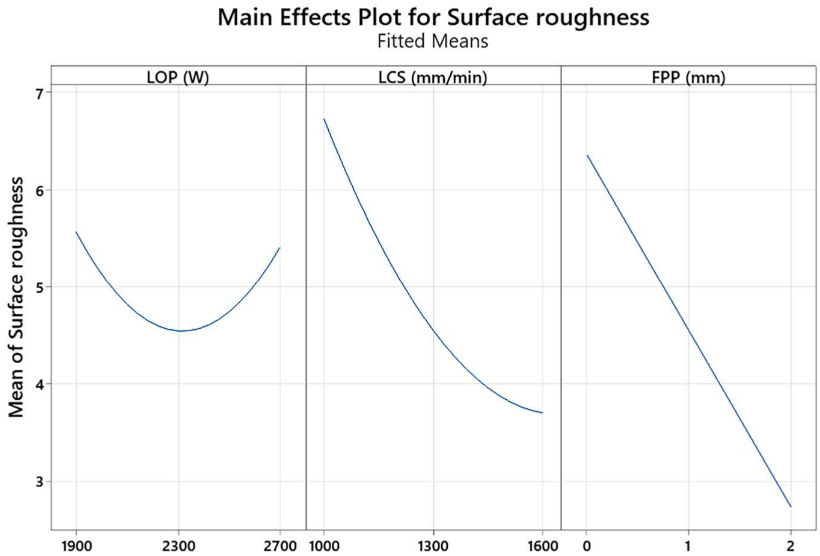

Figure 7. Main effect plot for surface roughness.

It is concluded from Figure 7 that the surface roughness is decreased with increasing the distance from the focal point of the laser beam from above the surface of the sheet. The reason is that increasing the positive focus allows the gas to react better with the melt in the front of the cut, generating additional heat in the cut gap, melting it, and moving it down the gap, resulting in a smoother surface. Figure 8 shows the contour plot of the interaction effects of FPP and LCS on the surface roughness of the cutting area of the sheet. It is found from Figure 8 that with increasing positive FPP and LCS, the surface roughness decreases. As the FPP increases, the focus of the laser's heat beam is positioned above the workpiece, allowing the oxygen gas to react thermally with the workpiece, adding a thermal energy source to the cutting process that melts the material. With increasing speed, the molten material is expelled from the cutting groove along with the oxygen GP, improving the surface quality of the cut.

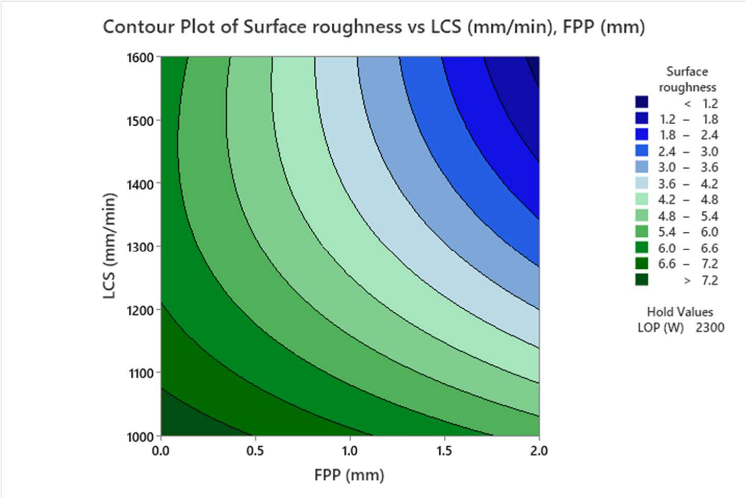

Figure 8. Contour Plot of the Interaction Effects of FPP and LCS on Surface Roughness.

3.2. Kerf Width Analysis

The results of the ANOVA for kerf width are shown in Table 5. FPP and LCS are the most significant process parameters affecting kerf width, while LOP has the least effect. The results of the ANOVA for kerf width are also shown graphically in Figure 9, the Pareto chart. The observed value for the coefficient of determination (R^2) indicates a high degree of fit between the model and the experimental data.

Table 5. ANOVA results for kerf width.

Source	DF	Adj SS	Adj MS	F-Value	*p*-Value
Model	4	78,604.7	19,651.2	89.31	0.000
Linear	3	74,496.3	24,832.1	112.85	0.000
LOP (W)	1	234.4	234.4	1.07	0.326
LCS (mm/min)	1	3065.4	3065.4	13.93	0.004
FPP (mm)	1	71,196.5	71,196.5	323.56	0.000
Square	1	4108.4	4108.4	18.67	0.002
FPP (mm) × FPP (mm)	1	4108.4	4108.4	18.67	0.002
Error	10	2200.4	220.0		
Lack-of-Fit	8	2135.6	266.9	8.24	0.113
Pure Error	2	64.8	32.4		
Total	14	80,805.1			
S = 14.8337		R-sq = 97.28%	R-sq (adj) = 96.19%		

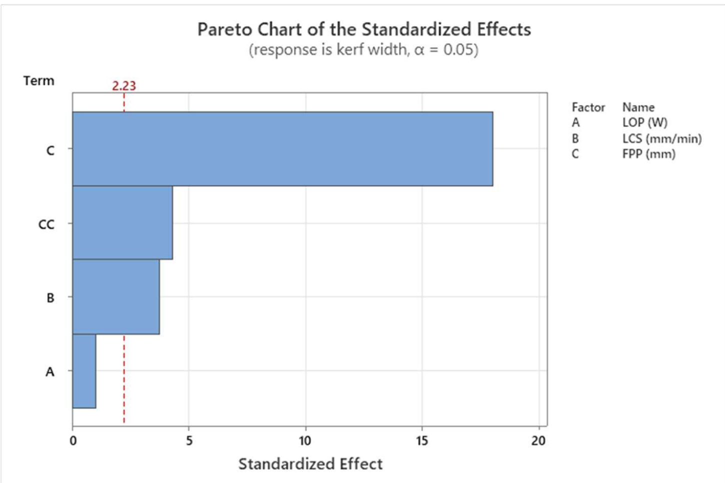

Figure 9. Pareto chart for kerf width.

Figure 10 presents the Normal Probability Plot for the kerf width. Observing that the data points align approximately linearly along the regression line, we can conclude that the data follows a normal distribution and that the linear regression model fits the experimental data well. The coefficient of determination (R^2) is 97.28% for kerf width which shows the good quality of the interpolated equation.

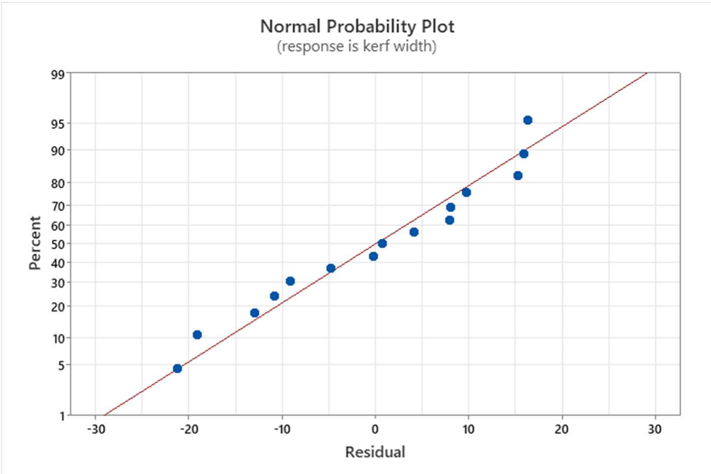

Figure 10. Normal Probability Plot for the kerf width.

According to Equation (2), the regression equation for the kerf width of the Hardox 400 sheet is as follows:

$$\text{Kerf width} = 604.6 + 0.0135\ \text{LOP} - 0.0652\ \text{LCS} + 28.0\ \text{FPP} + 33.17\ \text{FPP} \times \text{FPP} \quad (2)$$

Figure 11 shows the effect of the main parameters such as LOP, LCS, and FPP on the kerf width. It is seen that the kerf width is increased after increasing the LOP. The reason for this is that by increasing the LOP, the amount of thermal energy entered into the cut area increases, and then the volume of the molten area increases, which leads to an increase in the kerf width. Also, with increasing the positive FPP, the kerf increases. This is because the laser beam is focused above the workpiece, allowing the oxygen gas to react exothermically with the workpiece more easily, adding another heat energy source to the cutting process. With the increase in the amount of energy beam and the creation of a larger molten zone, the kerf increases. With increasing the LCS, the kerf decreases. This is because the high-energy laser beam passes through the cutting zone more quickly and the heat energy does not stay, so less material is melted in the cutting zone.

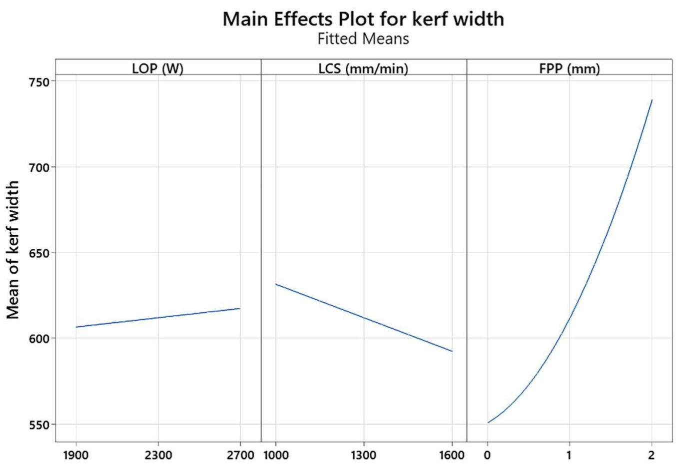

Figure 11. Effect of main parameters on kerf width.

Figure 12 presents the contour plot of the interaction effects of LCS and FPP on kerf width. The interaction plot indicates that kerf width decreases with increasing the LCS and also with decreasing the positive FPP towards the sheet surface. Increasing the LCS reduces the concentration of the heat energy impact point, and the FPP approaching the cutting surface prevents the oxygen gas from having optimal exothermic reaction conditions with the workpiece, reducing the heat energy and consequently resulting in less melting in the kerf.

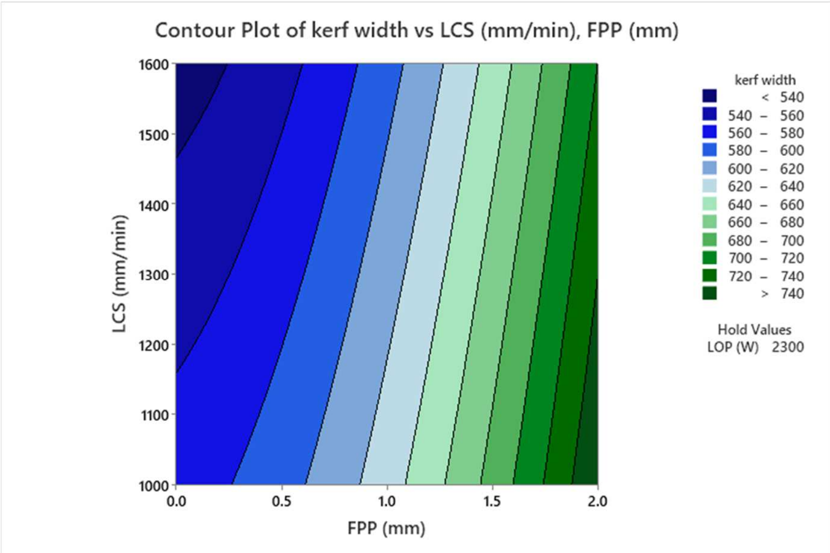

Figure 12. Contour plot of the interaction effects of FPP and LCS on kerf width.

3.3. Process Optimization

The effect of process parameters on the characteristics of the cutting area in the LCP is very complex. This complexity arises from the fact that changes in various parameters in LCP affect both surface roughness and kerf width. Figure 13 shows the optimization settings for the minimum surface roughness. The results show that if only surface roughness optimization is considered, the optimal average surface roughness is around 1 µm if the LOP is 2457 watts, the LCS is 1600 mm/min, and the FPP is +2 mm above the sheet surface.

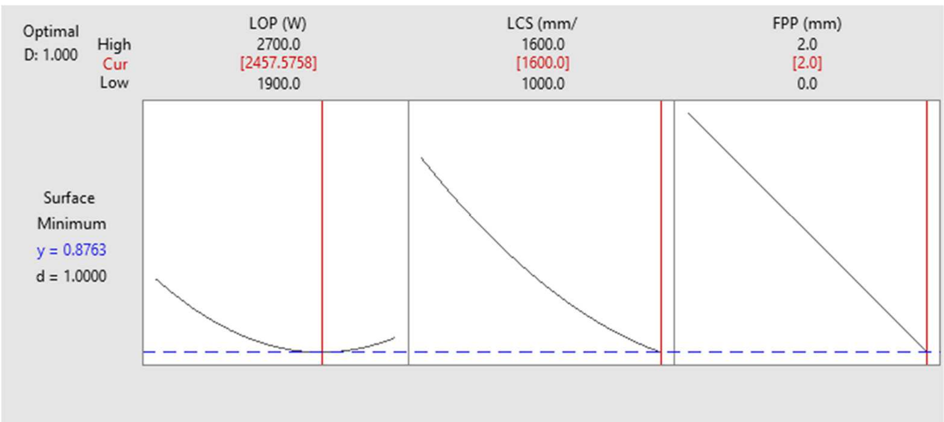

Figure 13. Surface Roughness Optimization of the cutting area.

Figure 14 shows the optimization settings for the minimum kerf. The results show that if only kerf optimization is considered, the optimal kerf is 0.525 mm if the LOP is 1900 W, the LCS is 1600 mm/min, and the FPP is zero.

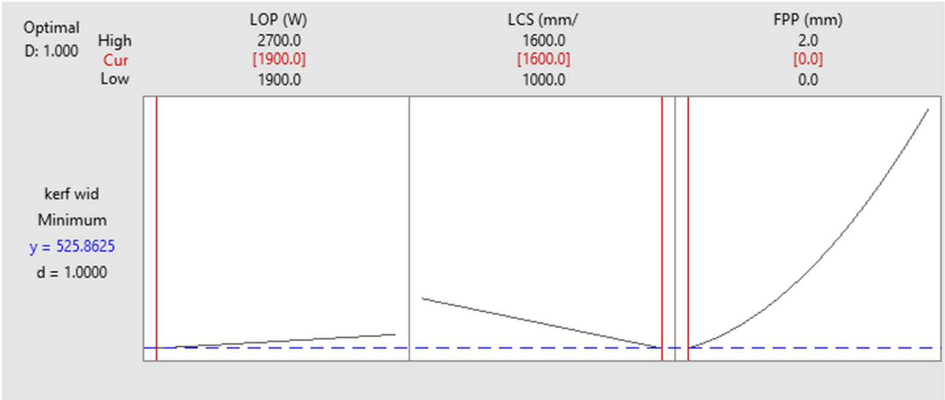

Figure 14. Kerf Optimization of the cutting area.

In the optimization of process parameters, one of the best choices for optimization is to minimize both surface roughness and kerf width together. The results of multi-objective optimization of the LCS of the Hardox 400 steel sheet in Figure 15 show that if the LOP is set to 2287 watts, the LCS is 1600 mm/min and the FPP is +1 mm above the sheet surface, the optimized surface roughness of the cut area will be 3.67 µm and the kerf width will be 0.593 mm.

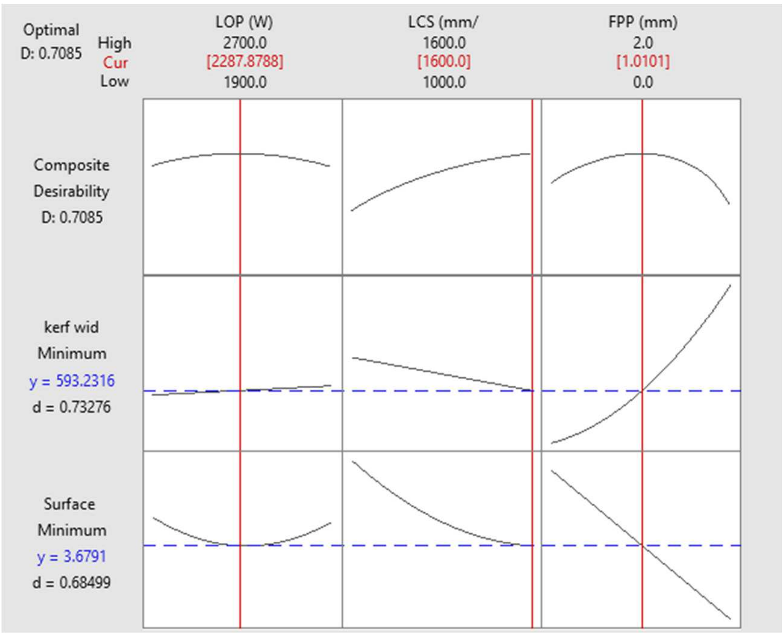

Figure 15. Optimization of both surface roughness and kerf width.

Multi-objective optimization in manufacturing processes needs to consider the desirability function. As can be seen in Figures 13 and 14, the optimum condition for individually minimizing the surface roughness and kerf width is different. This means that both of the output variables cannot be absolutely optimized and cannot be absolutely minimized concurrently. For a better understanding of the concept of multi-objective optimization, we need to define individual desirability function (d) and composite desirability function (D). Three types of optimization can be defined known as follows: smaller is the best (minimize), larger is the best (maximize), and nominal value is the best (target value). Individual desirability function (d) is defined as a scale in the range of [0, 1] according to the difference from maximum or minimum value. This method is proposed by Derringer and Suich and is applied in many pieces of optimization software such as Minitab. The individual desirability function (d) for the minimized condition is defined as Equation (3).

$$d(y) = \left(\frac{y-U}{L-U}\right)^r \tag{3}$$

where r is a user defined parameter ($r > 0$). A zero value of d shows completely undesirability for the response and total desirability obtained when d is 1. Figures 13 and 14 shows that the individual desirability is 1. But for combined optimization it is needed to define and use composite desirability function (D). The composite desirability function is calculated by the product (geometric mean) of the individual desirability function (d) of each output variable (Equation (4)).

$$D(y) = \left(\prod_{j=1}^{n}\left(d_j(y)\right)^{w_j}\right)^{\frac{1}{\sum_{j=1}^{n} w_j}} \tag{4}$$

where $d_j(y)$ is the individual desirability of j'th output variable and w_j is the weight function of it. As can be seen in Figure 15, the individual desirability of surface roughness and kerf width is 0.68499 and 0.73276 and the composite desirability is 0.7085. This value of d and D shows that simultaneous optimization is just fair and better surface roughness or better kerf width can be obtained according to the desire of the industry. The readers can study [28,29] for more details and discussion about the desirability function in multi-objective optimization.

At last, it is worth noting that, the current study aims to find a relation between the process parameters (LOP, LCS, and FPP) and surface roughness and kerf width. This aim can be achieved by using deep learning approaches such as Support Vector Regression (SVR) methods, and meta-heuristic optimization methods (ANN, GA, PSO, . . .). These approaches need a high volume of data and the accuracy extremely depends on the volume of data. For example, 70% of the data will be used for the training of the neural network, and the remaining 30% used for evaluation of the trained network, while it cannot yield any closed-form equation for easy use. The DOE methods use a moderate volume of data and are appropriate for process optimization. Implementation of the new methods for prediction of the output process with more complicated models can be an attractive object for researchers.

4. Conclusions

In this experimental study, the laser-cutting process (LCP) of Hardox 400 steel sheets was investigated using the RSM and the regression model proposed a very high accuracy equation for prediction of surface roughness and kerf width. Input parameters of the LCP were selected as laser output power (LOP), laser-cutting speed (LCS), and focal point position (FPP), while surface roughness and kerf width were considered as output variables. The following results can be obtained from the present study:

- The results of the ANOVA for surface roughness and kerf width showed that the FPP and LCS are the most significant process parameters affecting the surface roughness and kerf width. After increasing the FPP, the surface roughness decreased and the kerf width increased. After increasing the LCS, the surface roughness and kerf width decreased.
- Regression equations for surface roughness and kerf width were obtained, which can significantly contribute to improving the LCP, increasing cut quality, reducing waste, increasing efficiency, and reducing costs.
- The normal probability plots and the coefficient of determination (R2) value for surface roughness and kerf width show that the proposed model by RSM can fit well with the experimental data.

- The results show that if only surface roughness is optimized, the optimal average surface roughness is around 1 μm obtained by 2457 W LOP, 1600 mm/min LCS, and +2 mm FPP conditions.
- The results show that if only kerf width is optimized, the optimal kerf width is 0.525 mm and obtained by 1900 W LOP, 1600 mm/min LCS, and zero FPP conditions.
- The multi-objective optimization to minimize both surface roughness and kerf width simultaneously was carried out and the results show that the optimized condition (2287 W LOP, 1600 mm/min LCS, and +1 mm FPP) leads to 3.67 μm surface roughness and 0.593 mm kerf width.

Author Contributions: Conceptualization, M.S.; methodology, S.M.A. and J.J.; software, S.M.A.; validation, M.S.; formal analysis, M.S. and J.J.; investigation, S.M.A.; resources, S.M.A.; data curation, M.S.; writing—original draft preparation, M.S., S.M.A. and J.J.; writing—review and editing, M.S. and J.J.; visualization, M.S.; supervision, M.S.; project administration, M.S.; funding acquisition, M.S. All authors have read and agreed to the published version of the manuscript.

Funding: This research received no external funding.

Institutional Review Board Statement: Not applicable.

Informed Consent Statement: Not applicable.

Data Availability Statement: The original contributions presented in the study are included in the article, further inquiries can be directed to the corresponding author.

Conflicts of Interest: The authors declare no conflicts of interest.

References

1. Kannatey-Asibu, E. *Principles of Laser Materials Processing*, 1st ed.; Wiley: Hoboken, NJ, USA, 2009.
2. Alsaadawy, M.; Dewidar, M.; Said, A.; Maher, I.; Shehabeldeen, T.A. A comprehensive review of studying the influence of laser cutting parameters on surface and kerf quality of metals. *Int. J. Adv. Manuf. Technol.* **2024**, *130*, 1039–1074. [CrossRef]
3. Kuntoglu, M. Machining induced tribological investigations in sustainable milling of Hardox 500 steel: A new approach of measurement science. *Measurement* **2022**, *201*, 111715. [CrossRef]
4. Konat, Ł.; Zemlik, M.; Jasiński, R.; Grygier, D. Austenite Grain Growth Analysis in a Welded Joint of High-Strength Martensitic Abrasion-Resistant Steel Hardox 450. *Materials* **2021**, *14*, 2850. [CrossRef] [PubMed]
5. Hardox® 400—Get Wear-Resistant, Easy to Form Steel—SSAB. Available online: https://www.ssab.com/en/brands-and-products/hardox/product-program/400 (accessed on 14 May 2023).
6. Dzioba, I.; Pała, R. Strength and Fracture Toughness of Hardox-400 Steel. *Metals* **2019**, *9*, 508. [CrossRef]
7. Mamundi Azaath, L.; Natarajan, U. Investigation on the tool worn surface morphology and machining characteristics of the Hardox steel using minimum quantity lubrication. *Int. J. Mater. Res.* **2021**, *112*, 486–497. [CrossRef]
8. Krolczyk, G.M.; Krolczyk, J.B.; Maruda, R.W.; Legutko, S.; Tomaszewski, M. Metrological changes in surface morphology of high-strength steels in manufacturing processes. *Measurement* **2016**, *88*, 176–185. [CrossRef]
9. Ramos, J.; Moralejo, S.; Figueras, J.; Lamikiz, A. Composition and surface state influence in laser process for steel sheets. *DYNA* **2020**, *95*, 497–502. [CrossRef] [PubMed]
10. Szataniak, P.; Novy, F.; Ulewicz, R. HSLA steels-comparison of cutting techniques. In Proceedings of the 23rd International Conference on Metallurgy and Materials: METAL, Brno, Czech Republic, 21–23 May 2014.
11. Girdu, C.C.; Gheorghe, C.; Radulescu, C.; Cirtina, D. Influence of Process Parameters on Cutting Width in CO_2 Laser Processing of Hardox 400 Steel. *Appl. Sci.* **2021**, *11*, 5998. [CrossRef]
12. Girdu, C.C.; Gheorghe, C. Energy Efficiency in CO_2 Laser Processing of Hardox 400 Material. *Materials* **2022**, *15*, 4505. [CrossRef] [PubMed]
13. Mileșan, M.; Gîrdu, C.C.; Cîrtînă, L.; Rădulescu, C. Mathematical Modelling Study of Hardox400 Steel Parts' Roughness and Hardness, Cut with CO_2 Laser. *J. Mech. Eng.* **2020**, *66*, 127–141. [CrossRef]
14. Gondalia, V.R.; Sharma, A.K. Parametric Investigation and Optimization of CO_2 Laser Cutting process used for Cutting Hardox-400 materials. *Int. J. Sci. Eng. Appl.* **2013**, *2*, 123–129. [CrossRef]
15. Prajapati, B.D.; Patel, R.J.; Khatri, B.C. Parametric Investigation of CO_2 Laser Cutting of Mild Steel and Hardox-400 Material. *Int. J. Emerg. Technol. Adv. Eng.* **2013**, *3*, 204–208.
16. Rao, S.; Sethi, A.; Das, A.K.; Mandal, N.; Kiran, P.; Ghosh, R.; Dixit, A.R.; Mandal, A. Fiber laser cutting of CFRP composites and process optimization through response surface methodology. *Mater. Manuf. Process.* **2017**, *32*, 1612–1621. [CrossRef]
17. Khdair, A.I.; Melaibari, A.A. Experimental evaluation of cut quality and temperature field in fiber laser cutting of AZ31B magnesium alloy using response surface methodology. *Opt. Fiber Technol.* **2023**, *77*, 103290. [CrossRef]

18. Nguyen, V.; Altarazi, F.; Tran, T. Optimization of Process Parameters for Laser Cutting Process of Stainless Steel 304: A Comparative Analysis and Estimation with Taguchi Method and Response Surface Methodology. *Math. Probl. Eng.* **2022**, *2022*, 6677586. [CrossRef]
19. Sharma, V.; Kumar, V. Application of Box-Behnken design and response surface methodology for multi-optimization of laser cutting of AA5052/ZrO 2 metal−matrix composites. *Proc. Inst. Mech. Eng. Part J. Mater. Des. Appl.* **2018**, *232*, 652–668. [CrossRef]
20. Wang, J.; Sun, Z.; Gu, L.; Azimy, H. Investigating the effect of laser cutting parameters on the cut quality of Inconel 625 using Response Surface Method (RSM). *Infrared Phys. Technol.* **2021**, *118*, 103866. [CrossRef]
21. Vardhan, T.V.; Mahender, T.; Vempati, S.; Balram, Y. Optimization of laser machining parameters of SS 314 using response surface methodology. *Mater. Today Proc.* **2023**, *in press*. [CrossRef]
22. Eltawahni, H.A.; Hagino, M.; Benyounis, K.Y.; Inoue, T.; Olabi, A.G. Effect of CO_2 laser cutting process parameters on edge quality and operating cost of AISI316L. *Opt. Laser Technol.* **2012**, *44*, 1068–1082. [CrossRef]
23. Vora, J.; Chaudhari, R.; Patel, C.; Pimenov, D.Y.; Patel, V.K.; Giasin, K.; Sharma, S. Experimental Investigations and Pareto Optimization of Fiber Laser Cutting Process of Ti6Al4V. *Metals* **2021**, *11*, 1461. [CrossRef]
24. Safari, M.; Joudaki, J.; Rezaei, M. Investigation of Laser Cutting of Thin Polymethyl Methacrylate Sheets by Response Surface Methodology. *Int. J. Eng.* **2024**, *37*, 484–495. [CrossRef]
25. Jadhav, A.; Kumar, S. Laser cutting of AISI 304 material: An experimental investigation on surface roughness. *Adv. Mater. Process. Technol.* **2019**, *5*, 429–437. [CrossRef]
26. Kotadiya, D.J.; Kapopara, J.M.; Patel, A.R.; Dalwadi, C.G.; Pandya, D.H. Parametric analysis of process parameter for Laser cutting process on SS-304. *Mater. Today Proc.* **2018**, *5*, 5384–5390. [CrossRef]
27. *ISO 21920-3:2021*; Geometrical Product Specifications (GPS)—Surface Texture: Profile Method—Rules and Procedures for the Assessment of Surface Texture. International Organization for Standardization: Geneva, Switzerland, 2021.
28. Costa, N.R.; Lourenço, J.; Pereira, Z.L. Desirability Function Approach: A Review and Performance Evaluation in Adverse Conditions. *Chemometr. Intell. Lab. Syst.* **2011**, *107*, 234–244. [CrossRef]
29. Akteke-Öztürk, B.; Weber, G.W.; Köksal, G. Desirability Functions in Multiresponse Optimization. In *Optimization in the Natural Sciences. Communications in Computer and Information Science*; Plakhov, A., Tchemisova, T., Freitas, A., Eds.; Springer: Cham, Switzerland, 2015; Volume 499. [CrossRef]

materials

MDPI

Article

Material Removal Mechanism of SiC Ceramic by Porous Diamond Grinding Wheel Using Discrete Element Simulation

Zhaoqin Zhang, Jiaxuan Xu, Yejun Zhu *, Zhongxing Zhang and Weiqi Zeng

College of Engineering, Nanjing Agricultural University, Nanjing 210031, China;
9213011329@stu.njau.edu.cn (Z.Z.); xujiaxuan@stu.njau.edu.cn (J.X.); 15970311437@163.com (Z.Z.);
zengwq@stu.njau.edu.cn (W.Z.)
* Correspondence: yjzhu@njau.edu.cn; Tel.: +86-152-5095-2212

Abstract: SiC ceramics are typically hard and brittle materials. Serious surface/subsurface damage occurs during the grinding process due to the poor self-sharpening ability of monocrystalline diamond grits. Nevertheless, recent findings have demonstrated that porous diamond grits can achieve high-efficiency and low-damage machining. However, research on the removal mechanism of porous diamond grit while grinding SiC ceramic materials is still in the bottleneck stage. A discrete element simulation model of the porous diamond grit while grinding SiC ceramics was established to optimize the grinding parameters (e.g., grinding wheel speed, undeformed chip thickness) and pore parameters (e.g., cutting edge density) of the porous diamond grit. The influence of these above parameters on the removal and damage of SiC ceramics was explored from a microscopic perspective, comparing with monocrystalline diamond grit. The results show that porous diamond grits cause less damage to SiC ceramics and have better grinding performance than monocrystalline diamond grits. In addition, the optimal cutting edge density and undeformed chip thickness should be controlled at 1–3 and 1–2 um, respectively, and the grinding wheel speed should be greater than 80 m/s. The research results lay a scientific foundation for the efficient and low-damage grinding of hard and brittle materials represented by SiC ceramics, exhibiting theoretical significance and practical value.

Keywords: porous diamond; DEM; SiC; self-sharpening; grinding

1. Introduction

SiC ceramics are hard and brittle materials with high mechanical strength, excellent chemical stability, a small thermal expansion coefficient, and high resistance to wear and corrosion. They have been widely applied in aero-engine components and satellite optical mirrors [1,2]. In general, diamond grinding wheels, composed of monocrystalline diamond grit (M-diamond), serve as the main method for the manufacturing of SiC ceramics. Though this grit type has superior mechanical properties, macro-fractures still occur [3–5]. The grit type seriously affects the service life of the grinding wheel and produces a large amount of irreversible surface/subsurface damage on the SiC surface as the wheel wears [6]. Conventional M-diamond grits cannot satisfy the requirements of the high-efficiency and low-damage processing of SiC ceramics. Thus, porous diamond grits (P-diamond) have been developed [7,8]. Moreover, numerous microporous structures, which create micro-edges, are produced on its surface. On the one hand, when the workpiece material is ground by this grit type, the undeformed chip thickness decreases dramatically due to the increase in the micro-cutting edges, which allow for hard and brittle materials to be removed mainly in a plastic form, reducing the subsurface damage caused by stress concentration [9,10]. On the other hand, the grit produces microporous fragmentation during the grinding process, forming new micro-edges, which improve the grinding efficiency. Therefore, the P-diamond grit has a broad application prospect in the highly efficient and low-damage grinding of hard and brittle materials.

Several studies have been carried out to reveal the generation mechanism of the pore on the grit, considering the superior material properties of P-diamond grit. Ohashi et al. [11], Mehedi et al. [12], and Takasu et al. [13] focused on studying how to use thermo-chemical corrosion technology to prepare P-diamond grits. Finally, the diamond surface was corroded in a mixed high-temperature gas flow environment of hydrogen and nitrogen, and P-diamond abrasives were successfully prepared. Wang Junsha et al. [14–16] also used corrosion methods to compare the differences in corrosion degree and morphology of diamond {100} and {111} crystal planes caused by corrosion agents such as Fe, Co, and Ni. They further explored and optimized the chemical reaction mechanism of these corrosion agents on M-diamond, thereby optimizing the corrosion process. Lee et al. [17] and Jeong et al. [18] used femtosecond laser technology to drill holes on the surface of diamond abrasive particles to prepare P-diamond abrasive particles. They also verified that femtosecond laser drilling on diamond produces good roundness, no microcracks, and no thermal damage.

Studies on P-diamond grit preparation have been greatly advanced, and the pore structure has less influence on the grits' strength. Nevertheless, investigations on the material removal mechanism using P-diamond grits are still limited. Li et al. [19,20] used a mechanical model of stress distribution at the interface between the surface modified layer and the matrix of brittle materials, providing a theoretical basis for optimizing the toughness domain grinding process of brittle materials. Mao et al. [21] used a toughness domain critical grinding depth model for hard and brittle materials, indicating that at the toughness domain grinding scale, the surface roughness and damage depth of hard and brittle materials were significantly reduced. Zhou et al. [22] established a two-dimensional finite element model for the single-abrasive grain grinding of silicon carbide and analyzed the influence of the grinding edge radius and grinding wheel speed on the formation of silicon carbide chips. Numerous scholars at home and abroad have used single-abrasive particle scratch experiments to validate the above model and support its effectiveness. Guo et al. [23] and Rasim et al. [24] derived a quantitative chip-forming model and explored the effect of different rake angles of abrasive particles on material removal forms. The study showed that the size of the rake angle of abrasive particles significantly affects the ductile/brittle removal transformation of the material. Jin et al. [25] found through single-abrasive scratch experiments on fused quartz glass that only by reducing the scratch depth can crack formation be avoided. Based on this, a new method for predicting the surface quality of brittle material processing was proposed by combining the chip thickness model with finite element simulation. These research models were simulated using the finite element model. However, mesh distortion easily occurred during the finite element simulation process, leading to the computation's convergence, especially in the grinding process. In addition, the simulation method cannot sufficiently clarify the physical phenomena in microscale processing. Therefore, studies on the material removal mechanism of SiC ceramics with P-diamond grit still remain in the bottleneck stage.

In recent years, the molecular dynamics (MD) method, which is essentially similar to the discrete element method (DEM), has been utilized to study the precision machining of brittle materials. Liu et al. [26] investigated the material removal behavior of SiC by diamond grit at the nanoscale by using MD. They found that plastic deformation and through-crystal fracture occurred in monocrystalline SiC. Meanwhile, Zhao et al. [27,28] and Li et al. [29] investigated the brittle/ductile transition conditions of silicon by MD. This method differs significantly from the finite element simulation method. It involves constructing a discrete unit ensemble based on the nature of the substance itself and then analyzing the physical behavior from a micro or macro perspective. This approach provides explanations that cannot be achieved through finite element analysis. In addition, this method avoids mesh distortion and other issues that may arise during the calculation process.

Consequently, this paper proposes a discrete element simulation model for the P-diamond grit grinding of SiC hard and brittle materials. The model reveals the removal mechanism of the SiC material by P-diamond grit grinding at the microscopic scale and explores the influence laws of grinding parameters and pore parameters on material removal. At the same time, the model determines the difference in grinding performance between P-diamond abrasive and P-diamond grit, so as to provide a more scientific theoretical basis for optimizing the grinding parameters. The research results of this paper will lay a scientific foundation for the efficient and low-damage grinding of hard and brittle materials represented by SiC ceramics, which has important theoretical significance and practical value.

2. Grinding Model

2.1. Model of SiC Ceramics by DEM

SiC ceramics are typically brittle materials that are difficult to machine, and their mechanical properties are similar to those of diamond. In this paper, Altair EDEM 2021 (Altair, Baltimore, MD, USA) was used to construct a physical model for grinding SiC ceramics with P-diamond grit grains. The SiC model was designed as a rectangular block 80 μm × 40 μm × 30 μm, and more than 97,000 particle cells were generated. The boundary conditions of the remaining surfaces were fixed. The Hertz–Mindlin bonded contact model was used to associate each particle according to Equation (1) [30], as follows:

$$F_n^e = -K_{nHz} h^{\frac{3}{2}} \tag{1}$$

where F_n^e denotes the elastic contact force between two particles; h is the overlap value between adjacent particles, and h = −g. The contact stiffness parameter K_{nHz} is calculated as follows:

$$K_{nHz} = \frac{4}{3} E^* \sqrt{R^*} \tag{2}$$

where E* is the effective modulus of elasticity defined by the Young's moduli E_i and E_j and Poisson's ratios v_i and v_j of two contacting particles:

$$\frac{1}{E^*} = \frac{1 - v_i^2}{E_i} + \frac{1 - v_j^2}{E_j} \tag{3}$$

and R* is the effective radius of the particle:

$$R^* = \frac{1}{R_i} + \frac{1}{R_j} \tag{4}$$

The material properties, particle properties, and specific values involved in the model building process are listed in Table 1. The effect of the SiC discrete element model is displayed in Figure 1.

Table 1. Material property for SiC model [31–35].

Material Property	Value
Particle radius (μm)	0.5
Poisson rate (μ)	0.142
Density (kg/m^3)	3215
Shear modulus (GPa)	192
Coefficient of restitution	0.5
Coefficient of static friction	0.5
Coefficient of rolling friction	0.01
Normal stiffness per unit area (kN/m^3)	1.156×10^{10}
Shear stiffness per unit area (kN/m^3)	9×10^9
Critical normal stress (MPa)	640
Critical shear stress (MPa)	270
Bonded disk radius (μm)	0.5

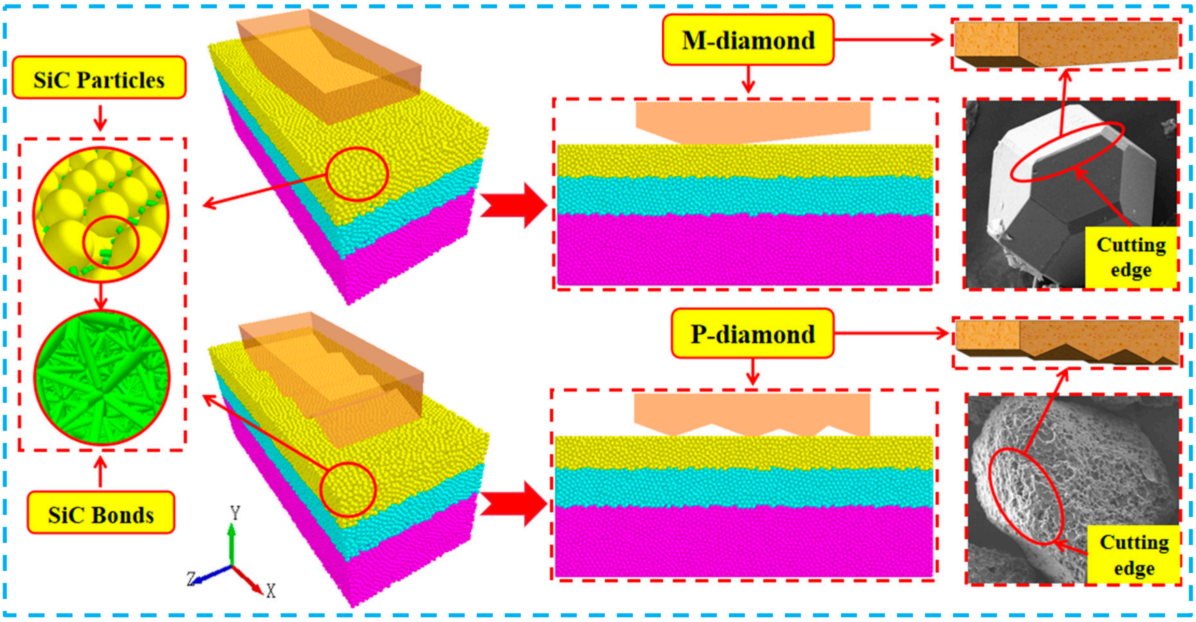

Figure 1. Model of SiC ceramics grinded by P-diamond grit.

2.2. Model of Diamond Grit by DEM

The P-diamond grit is obtained using the etching process. Figure 1 illustrates that the M-diamond grit has a relatively smooth appearance and a small number of grinding edges. However, the surface of the P-diamond grit is rougher, with many grinding edges on the surface. In addition, the grits are typically attached to the grinding wheel's substrate, moving circularly. The P-diamond grits are extended in the grit modeling given that the trajectory of each grit involved in grinding at the micrometer level is approximately a straight line. Thus, each grinding edge on its surface lies flat on a beveled surface. The height of the bevel is the tangential thickness of a single grit, and the depth of the cut of each grinding edge on the bevel should be incrementally increased. The rake angle of the grit is set at a constant value of 160°, to which the material properties of diamond are assigned. Subsequently, the M-diamond grits are modeled using the same approach. The material properties and specific values involved in the modeling process of P-diamond and M-diamond grits are listed in Table 2, and the schematic of the DEM model of porous diamond grinding SiC ceramics is shown in Figure 1.

Table 2. Material property for diamond grit modeling [36–38].

Material Property	Value
Poisson rate (μ)	0.14
Density (kg/m^3)	3500
Shear modulus (GPa)	700
Coefficient of restitution	0.5
Coefficient of static friction	0.5
Coefficient of rolling friction	0.01

2.3. Simulation Program

The grinding performance of P-diamond grit is affected by three key factors: cutting edge density, grinding wheel speed, and undeformed chip thickness. The term "cutting edge density" is used to describe the number of cutting edges per unit of cutting thickness on the surface of the abrasive grain. The grinding wheel speed is defined as the linear speed of the grinding wheel. Undeformed chip thickness refers to the thickness of a single cut of each abrasive grain when cutting between the grinding wheel and the workpiece. These parameters are of great significance in the grinding process, as they have a notable impact on the quality of the workpiece surface, its roughness, and the extent of damage to the workpiece. For each grinding factor, three groups of experiments were conducted using the controlled experiment method and the control variable method. The effects of cutting edge density, grinding wheel speed, and undeformed chip thickness on the material removal of SiC ceramics by P-diamond grit were investigated, considering the amount of damage to the SiC bonds, the change in the energy of the SiC particles, and the magnitude of the total grinding force as the characterizing quantities. During the simulation process, the diamond grit model grinds the surface of the SiC model based on the predetermined scheme, retaining factors that affect the grinding of SiC ceramics, such as the grinding angle. Table 3 shows the specific simulation scheme.

Table 3. Simulation scheme for grinding SiC ceramics with P-diamond grit.

Parameter	Diamond Types	Cutting Edge Density (μm^{-1})	Grinding Wheel Speed (m/s)	Undeformed Chip Thickness (μm)
Cutting edge density	M-diamond	-	120	2
	P-diamond	1, 2, 3, 4, 5	120	2
Grinding wheel speed	M-diamond	-	35, 50, 80, 120, 160	2
	P-diamond	2	35, 50, 80, 120, 160	2
Undeformed chip thickness	M-diamond	-	120	1, 2, 3, 4
	P-diamond	2	120	1, 2, 3, 4

3. Results and Discussion

3.1. Effect of Micro-Cutting Edge Density on Material Removal Process of SiC Ceramics

Generally, the grinding process is mainly composed of four stages: scratch, plowing, chip formation, and grit detachment. Figure 2 displays the changes in the number of accumulated damages in each surface, subsurface, and inner layer of bonds when SiC ceramics are ground by diamond grits with different cutting edge densities during the scratch and plowing stages. The SiC surface with a depth of 5 μm is defined as the surface layer, a depth of 5–10 μm represents the subsurface layer, and a depth of 10–15 μm depicts the inner layer. This definition is extended to the following figure representations. When the M-diamond grit is utilized, more than 5.98×10^3 bonds on the surface are damaged. The values of damaged bonds on the subsurface and inner layer are 2.55×10^3 and 1.44×10^3, respectively. By contrast, when the P-diamond grit is applied, the number of damaged bonds in all layers of SiC is lower than that of M-diamond grits. When the micro-cutting edge density is 1/μm, the number of damage bonds on the SiC surface layer, subsurface layer, and inner layer is 1.46×10^3, 0.95×10^3, and 0.85×10^3, respectively. As the micro-cutting edge density increases gradually to 5/um, the number of damaged bonds on each layer slightly increases. However, the number remains significantly lower than that of the M-diamond grit. Figure 3 shows the distribution of damage to the SiC model at the scratch and plowing stages for P-diamond with different cutting edge densities and M-diamond grits. Evidently, the damage areas are mainly concentrated on the surface layer with a tendency to extend downward and to the sides when ground by M-diamond grit. In addition, the damage is concentrated on the surface layer when ground by P-diamond grit, and the depth of damage is minimal (Figure 3b,c). Thus, the damage to the SiC bond is more pronounced when subjected to M-diamond grit. However, the effect of micro-cutting edge density on the damage to the SiC bond is small.

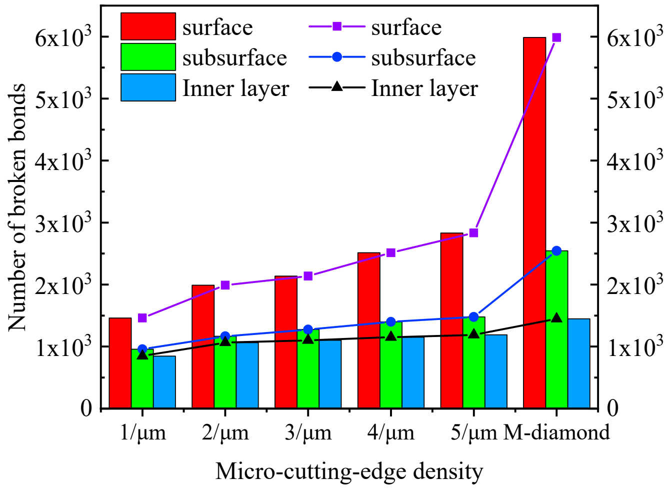

Figure 2. Number of broken bonds in each SiC layer at stages of scratch and plowing.

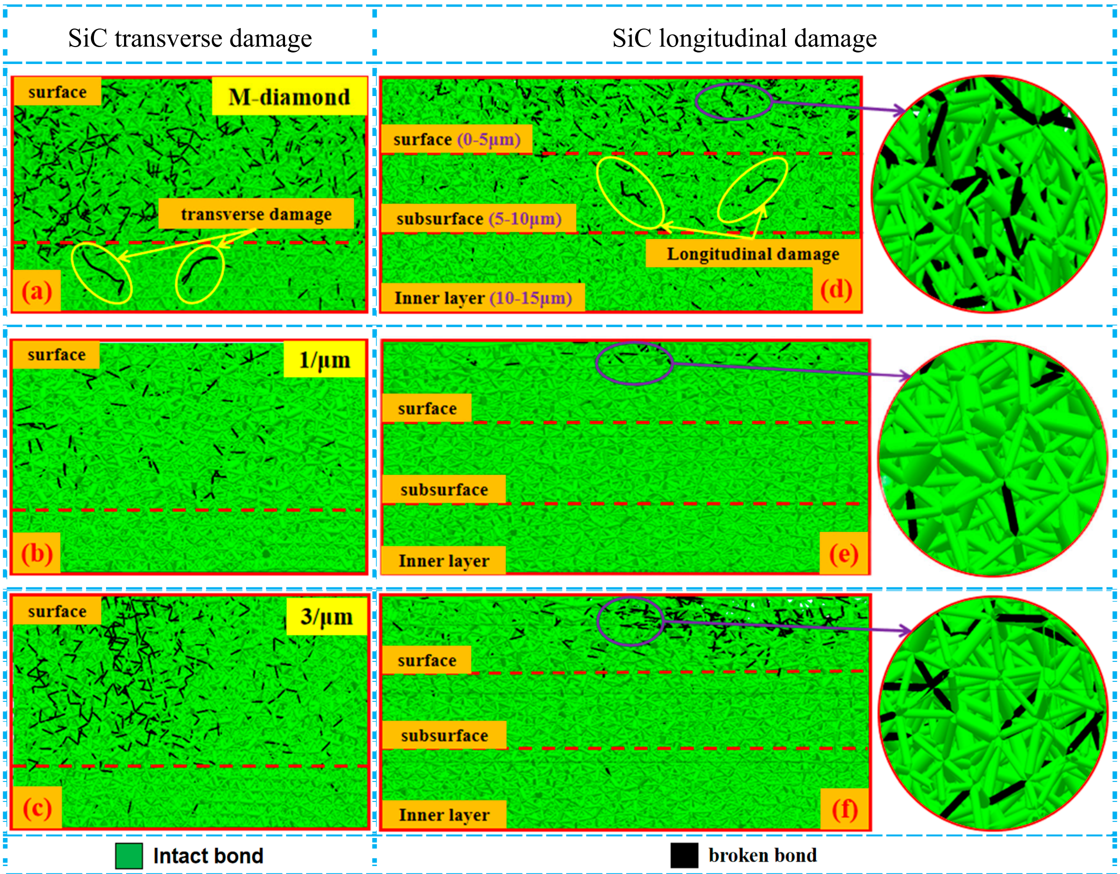

Figure 3. Distribution of broken bond conditions in each SiC layer at scratch plowing stages: (**a**–**c**) represent the transverse bond damage in the surface layer of SiC after diamond grit grinding with different cutting—edge densities. (**d**–**f**) indicate the longitudinal damage of bonding bonds in each layer of SiC.

During the chip formation stage, as the grit gradually cuts into the SiC surface and the chips are formed, the damage degree of SiC ceramics ground by M-diamond or P-diamond grits further increases. Figure 4 shows that the number of damaged bonds on the surface increases to 5.33×10^4 (88.78%) when M-diamond grit is applied. The number of damaged bonds on the subsurface and inner layers also increases to 2.91×10^4 and 1.82×10^4, respectively, compared with that at the scratch plowing stage. Figure 5 shows the SiC removal mechanism for diamond grit grinding, and Figure 6a shows the distribution of damage to SiC bonds during the grinding of the M-diamond grit under this stage. The depth of the damaged area on SiC gradually extends from the surface layer to the subsurface and inner layers. Moreover, a breakage bond extension phenomenon can be observed on both sides of the surface layer. The bond damage trend is consistent with the phenomenon in Figure 5. The damage area of SiC ground by P-diamond grit also increases gradually and becomes more apparent as the micro-cutting edge density increases. The surface, subsurface, and inner layer of SiC can sustain bond damage ranging from 3.42×10^4 to 5.11×10^4, 1.55×10^4 to 2.51×10^4, and 0.78×10^4 to 1.63×10^4, respectively (Figure 4). Compared with M-diamond, the maximum reduction in the number of damages to SiC bonds was 35.76%, 46.86%, and 57.31%, whereas the minimum reduction was 4.09%, 13.87%, and 10.17%. Figure 6b,c show that although the amount of bond damage in each layer of SiC increases slightly as the micro-cutting edge density increases, this damage remains primarily concentrated on the surface layer, with relatively short extension lengths of damaged bonds. Moreover, the overall damage extent is still less than that in the case of M-diamond grit grinding. At this stage, the SiC bond is significantly damaged when ground by M-diamond grit, and the damage depth continues to increase. The increase in micro-cutting edge density increases the damage on the SiC bond, but it is still mainly concentrated in the surface layer, resulting in a more stable grinding process.

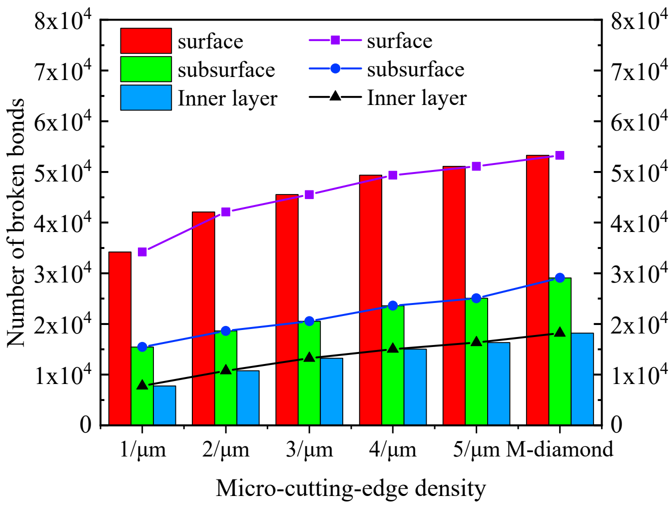

Figure 4. Number of cumulative broken bonds in each layer of SiC at stage of chip formation.

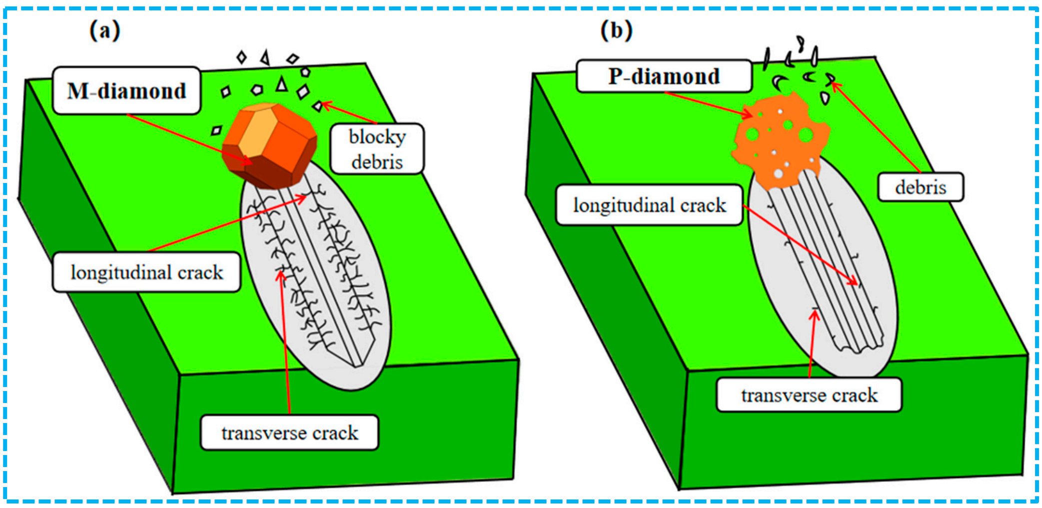

Figure 5. SiC removal mechanism for diamond grit grinding: (**a**) M-diamond, (**b**) P-diamond.

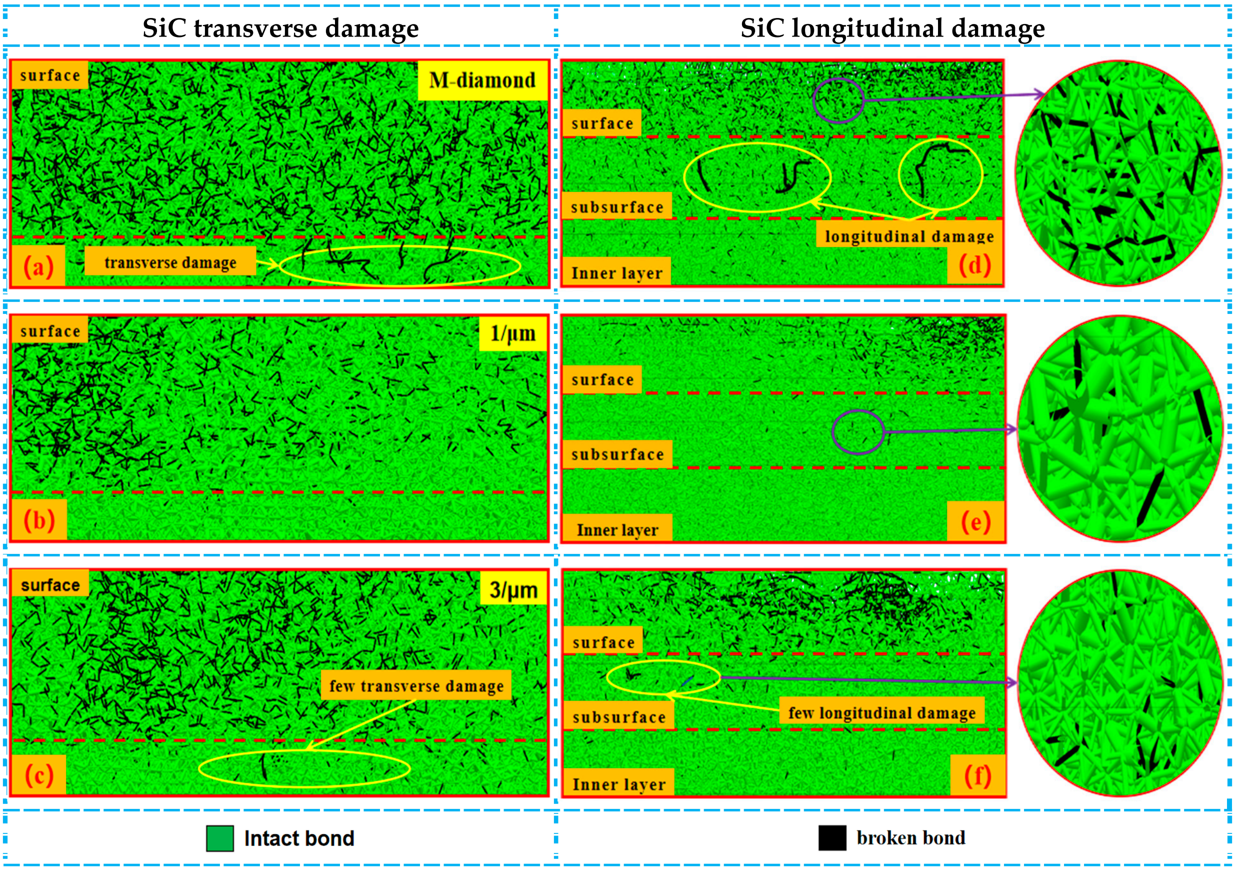

Figure 6. Distribution of cumulative damage conditions of bonding bonds in each layer of SiC at chip formation stage: (**a**–**c**) represent the transverse bond damage in the surface layer of SiC after diamond grit grinding with different cutting—edge densities. (**d**–**f**) indicate the longitudinal damage of bonding bonds in each layer of SiC.

During the detachment stage, the grit gradually cuts out of the SiC surface. The degree of damage by M-diamond and P-diamond grits to SiC bonds gradually tends to flatten. For M-diamond grit, the number of damage bonds on the SiC surface, subsurface, and inner layer is 6.39×10^4, 3.66×10^4, and 2.40×10^4, respectively (Figure 7). However, when grinding using P-diamond grit, the damaged bond number ranges from as small as 4.97×10^4, 2.17×10^4, and 1.08×10^4 to as large as 6.11×10^4, 3.18×10^4, and 1.98×10^4, respectively. Compared with M-diamond grit, P-diamond grit damages bonds in the minimum percentage of 77.78%, 59.29%, and 45% and in the maximum percentage of 95.62%, 86.88%, and 82.5% at the same time and parameters. Figure 8a shows a large amount of visible damage to the SiC subsurface layer bonded to the inner layer during M-diamond grinding. Moreover, Figure 8b,c show that the damage to the SiC bond during P-diamond grinding is mainly concentrated on the surface layer, with a small amount of damage occurring in the subsurface layer. Meanwhile, the damage in the subsurface layer increases as the micro-cutting edge density increases. However, the damage is not evident on the inner layer. When the density of the micro-cutting edge reaches 5/μm, the material removal performance of P-diamond is similar to that of M-diamond. The damage to the SiC bond caused by M-diamond grit is significant and extends throughout the entire process. The damaged depth and concentration are noticeable. On the contrary, the damage degree of SiC ground by P-diamond grit is minimal, and the damaged depth and area are mainly concentrated on the surface layer of SiC. Few instances are observed on the subsurface and inner layers. However, with the increase in micro-cutting edge density, the number of SiC damaged bonds increases simultaneously.

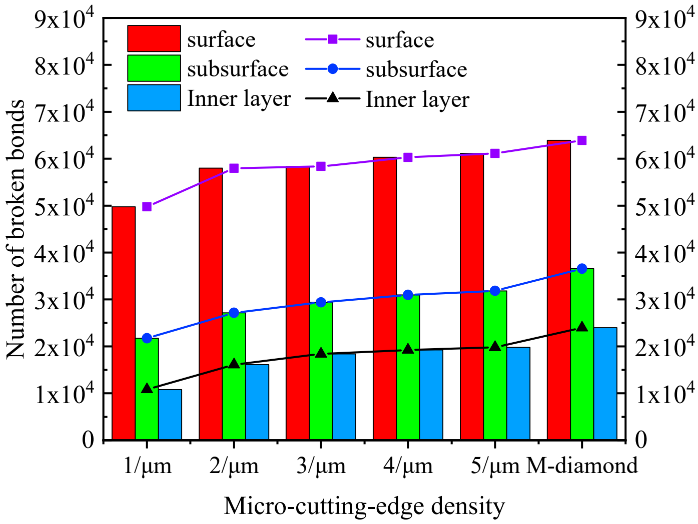

Figure 7. Number of cumulative broken bonds in each layer of SiC in grit detachment stage.

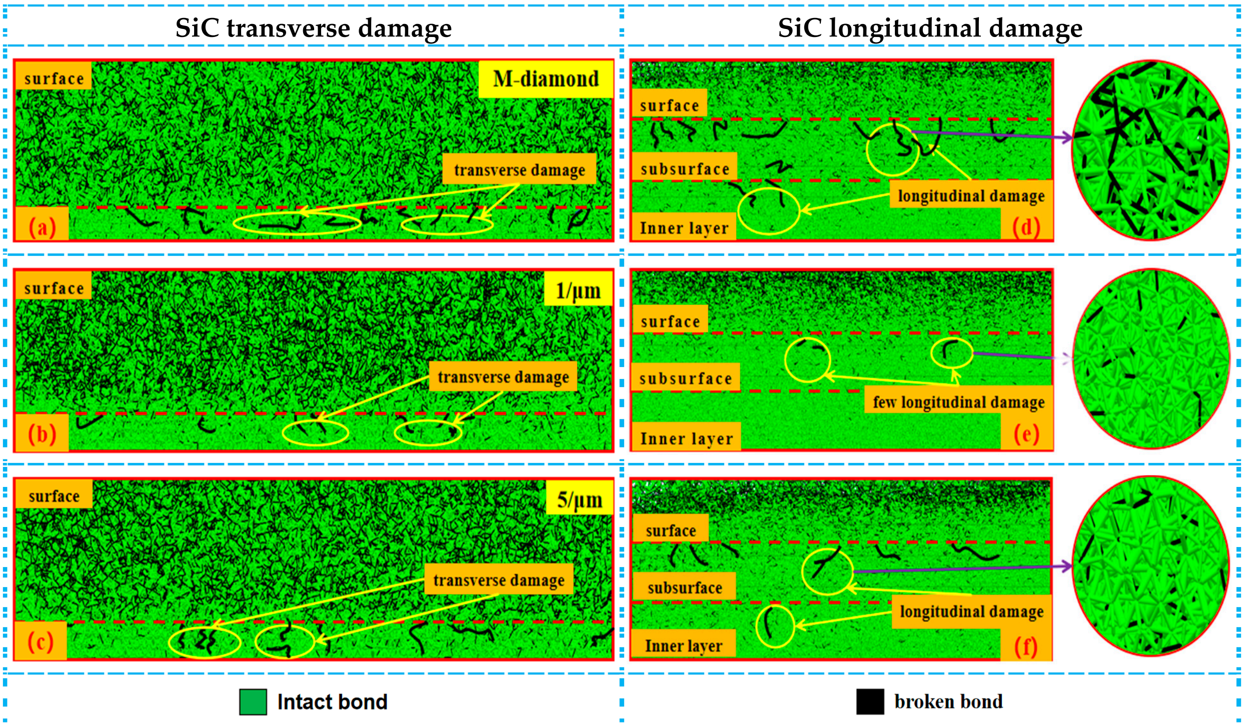

Figure 8. Distribution of cumulative damage conditions of bonds in each layer of SiC at grit detachment stage: (**a**–**c**) represent the transverse bond damage in the surface layer of SiC after diamond grit grinding with different cutting—edge densities. (**d**–**f**) indicate the longitudinal damage of bonding bonds in each layer of SiC.

The removal capacity of diamond grit for SiC ceramics can be characterized by the amount of damaged bonds. The grinding process of P-diamond grit is "gentler," whereas that of M-diamond grit is more "vigorous" because the surface of the P-diamond grit has numerous micro-cutting edges with a different undeformed chip thickness. During the scratch plowing stage, the SiC surface is initially contacted by the cutting edge of the P-diamond grit with small undeformed chip thickness. The bond of the SiC surface layer gradually breaks under the grinding force, without causing subsurface or inner layer damage. During the chip forming stage, micro-cutting edges on the grit surface participate in grinding as the grit deepens. SiC bonds continue to break, causing damage primarily on the surface layer. This damage gradually extends to subsurface and inner layers as the density of micro-cutting edges increases, but the amount of damaged bonds remains small. During grit detachment, smaller undeformed chip thickness micro-cutting edges detach from the SiC surface, while larger ones maintain contact. Additionally, significant grinding residual stress persists on the SiC surface layer, resulting in gradual surface-focused SiC fracture. Additionally, at increased cutting edge densities, the damage to SiC layer bonding gradually approximates that caused by M-diamond grit grinding. P-diamond grit improves the grinding of SiC, reducing subsurface and inner layer damage compared to M-diamond grit. This is due to reduced damage from bonds on SiC layers. However, its effectiveness decreases with increasing micro-cutting edge density. Therefore, P-diamond grit's micro-cutting edge density should be controlled at 1–3/μm.

The breakage of SiC bonds is caused by the kinetic energy of SiC particles when subjected to the grinding force of diamond grit. This energy causes SiC particles to break free from each other, resulting in bond breakage. The kinetic energy of SiC particles and the severity of the bond breakage increase with proximity to the surface of the diamond grit. Chip formation produces the most concentrated SiC damage. A significant difference in the kinetic energy of SiC particles during the grinding process is observed between M-diamond and P-diamond grit with different micro-cutting edge densities. Figure 9a illustrates that during the grinding of SiC with M-diamond grit, a considerable number of active particles are present in the SiC surface layer. These particles are distributed throughout the grinding area, with their kinetic energy decreasing from the grinding zone to the two sides. This results in a noticeable delayed extension phenomenon. However, when grinding SiC with P-diamond grit, the number of active particles on the surface layer is limited, and the distribution of these particles is relatively concentrated, with less extension to the sides. However, as the density of the grinding edge increases, the number of active particles in the surface layer of SiC gradually increases, and the degree of elongation and dispersion slowly increases. This phenomenon is also supported by the data presented in Figure 9b. The extent of SiC damaged bonds incurred during the grinding process is directly proportional to the kinetic energy of the SiC particles in each layer. This energy is, in turn, related to the magnitude of the grinding force applied to the SiC particles. The undeformed chip thickness of M-diamond grit is larger than that of P-diamond grit. Furthermore, the grinding force generated on the SiC particles affects a wide range. The P-diamond grit is characterized by the presence of numerous surface pores, which results in a relatively small undeformed chip thickness. Consequently, the grinding force generated on SiC particles is diminished, and the impact range is concentrated. Consequently, the kinetic energy of the SiC particles ground by P-diamond grit can be significantly reduced, as well as the range of energy transfer. However, the effect intensifies as the density of the micro-cutting edge increases, thereby reducing the stability of the P-diamond grit. When SiC particles are subjected to grit with higher kinetic energy and a wider energy transfer range, there is a greater likelihood of the SiC bond experiencing centralized breakage and extension. Furthermore, the grinding performance of the grit becomes increasingly unstable, resulting in more severe damage to the material. In conclusion, the overall grinding performance of P-diamond grit is more stable, significantly reducing the propensity of SiC subsurface and inner layer bond damage during the grinding process. Nevertheless, the effect diminishes with increasing the density of the cutting edge. Nevertheless, it still possesses certain advantages over M-diamond grit.

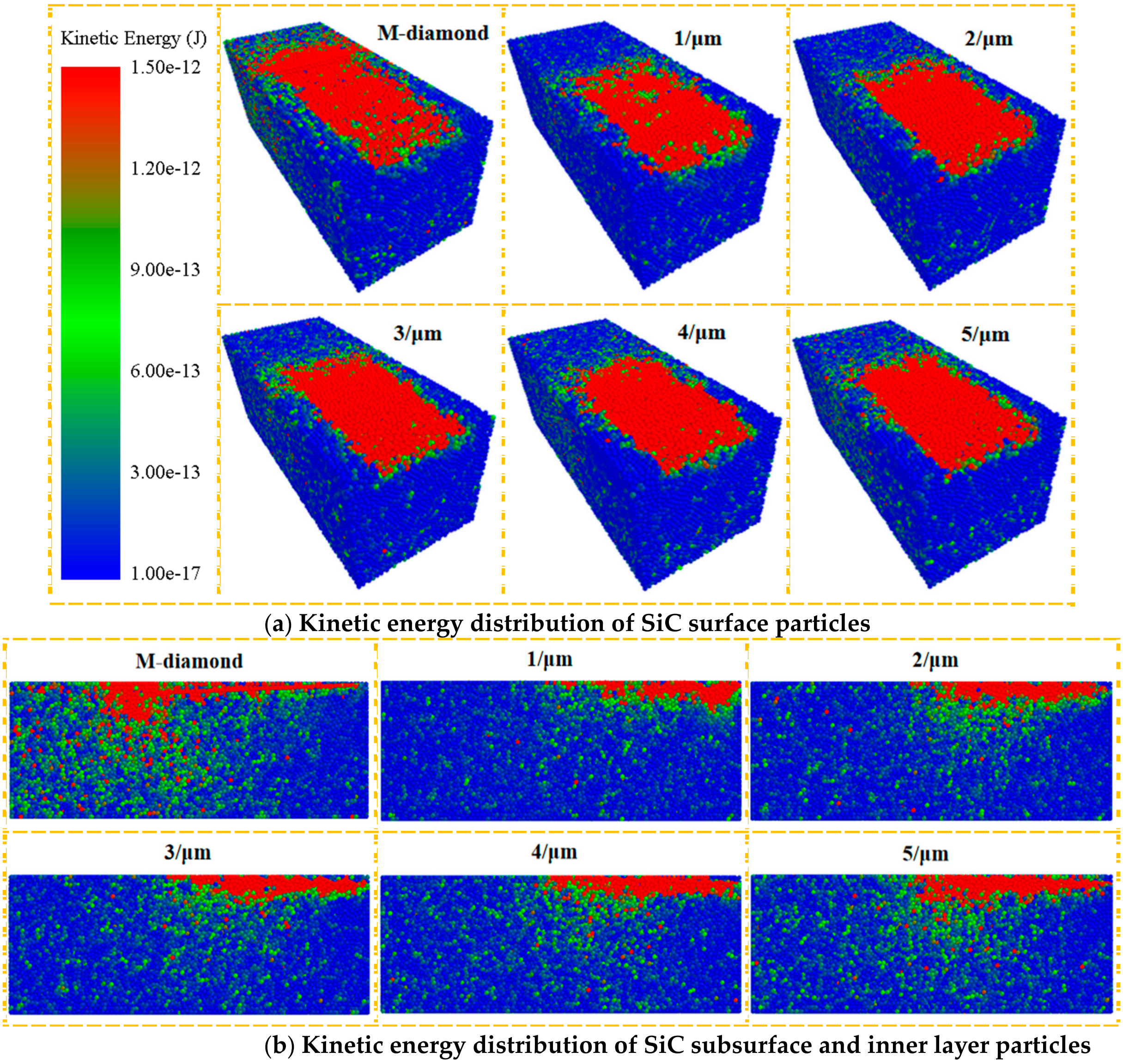

Figure 9. Distribution of kinetic energy of particles in each layer when diamond grits with different cutting edge densities grind SiC at chip formation stage.

3.2. The Effect of Grinding Wheel Speed on the Material Removal Process of SiC Ceramics

The grinding wheel speed is one of the most important grinding parameters that affect the material removal process. Figure 10 shows the statistics of changes in the number of accumulated damages in each surface, subsurface, and inner bond layer when ground by M-diamond and P-diamond grits with a cutting edge density of 2/μm at the scratch plowing stage. The amount of damaged bonds in each layer ground by M-diamond grit decreases as the grinding wheel speed increases. When the grinding wheel speed is 35 m/s, the number of damaged bonds is 9.99×10^3 on the surface, 5.49×10^3 on the subsurface, and 3.53×10^3 on the inner layer. When the grinding wheel speed is increased to 160 m/s, the number of damaged bonds in each layer decreases to 5.38×10^3, 2.39×10^3, and 1.26×10^3. However, when the P-diamond grit is utilized, the amount of damaged bonds on each layer is considerably less than that of M-diamond grit. When the grinding wheel speed is 35 m/s, the amount of damaged bonds on each layer is 5.06×10^3, 2.91×10^3, and 2.57×10^3. When the grinding wheel speed reaches 160 m/s, the number of damaged bonds decreases to 1.0×10^3, 0.71×10^3, and 0.67×10^3. Figure 11 shows a cloud diagram of the distribution of damage conditions in each layer when M-diamond grit and P-diamond grit grinds SiC at different grinding wheel speeds at this stage. The damage trends of the bonds in various layers when grinding SiC with P-diamond grit at different grinding wheel speeds are similar to those of M-diamond grit. However, the damage depth is shallower than that of M-diamond. At this stage, the damage to the SiC bond is more significant when using M-diamond grinding at different speeds. The damage caused by P-grinding is slightly weaker, but the trend of bond damage with respect to grinding wheel speed remains the same for both methods.

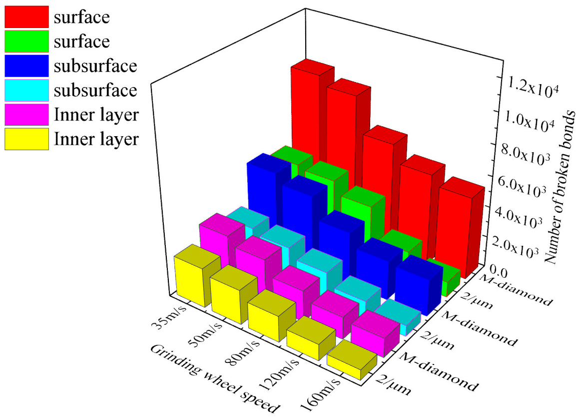

Figure 10. Number of broken bonds in each layer of SiC at scratch plowing stage.

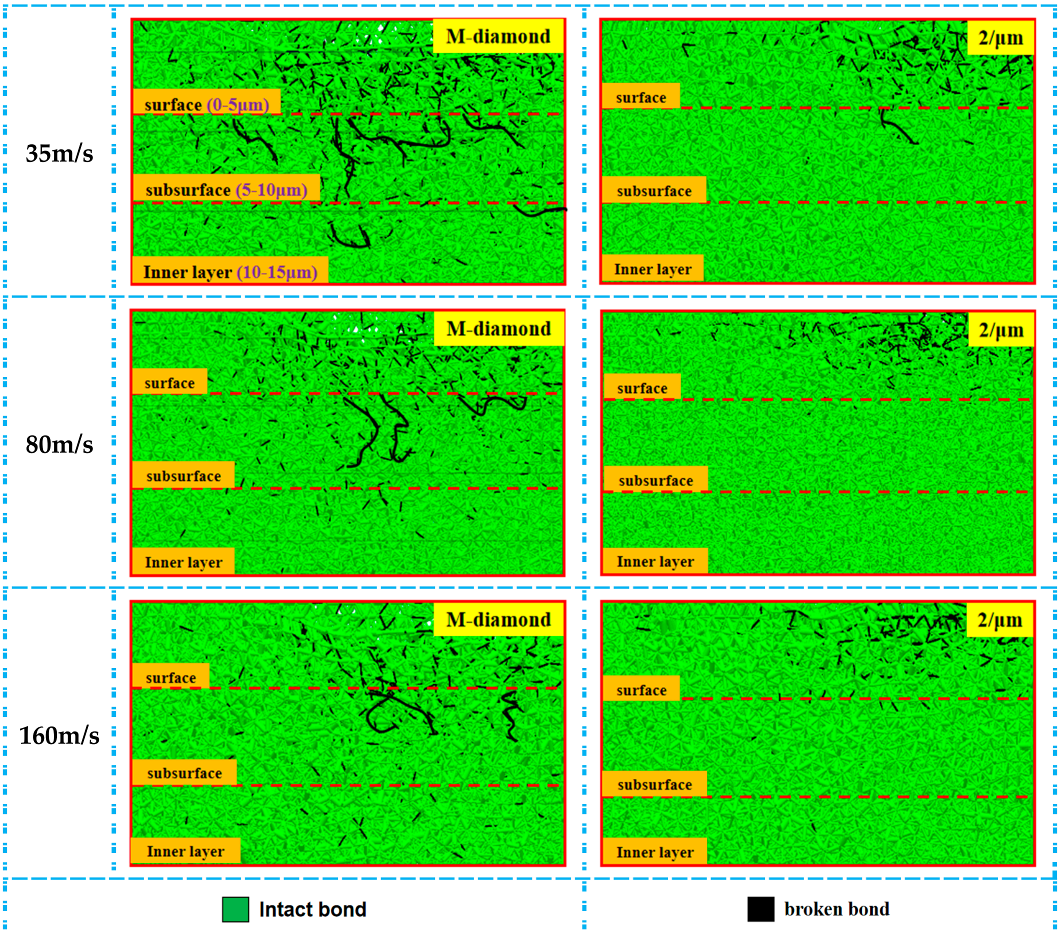

Figure 11. Distribution of cumulative damage conditions of bonds in each SiC layer at scratch plowing stage.

During the chip formation stage, the influence of grinding wheel speed on the damage area of SiC bonds is further intensified, and the overall damage trend of the bonds is still consistent with that in the scratch plow stage. In addition, the damage to the SiC bond ground by M-diamond grit is more severe than that of P-diamond grit. Figure 12 shows the statistics of changes in the number of accumulated damages in each surface, subsurface, and inner bond layer when SiC is ground by M-diamond grit and P-diamond grit at different grinding wheel speeds. When the grinding wheel speed is 35 m/s, the accumulation of surface, subsurface, and inner bond damage in the case of M-diamond grit grinding reaches 6.46×10^4, 3.91×10^4, and 2.53×10^4, respectively. In the case of P-diamond grit grinding, the accumulation of bond damage for each layer is 5.92×10^4, 2.83×10^4, and 1.71×10^4. These values are 8.46%, 27.54%, and 32.61% lower than those of M-diamond. Figure 13 shows a cloud diagram of the distribution of damage conditions in each layer when M-diamond grit and P-diamond grit grind SiC at different grinding wheel speeds at this stage. The degree of damage to SiC by the two types of diamond grit is almost equal at a grinding wheel speed of 35 m/s. The amount of SiC bond damage is minimized when the grinding wheel speed is 160 m/s. The accumulation of bond damage in each SiC layer of ground by M-diamond grit decreases to 4.70×10^4, 2.52×10^4, and 1.55×10^4. The depth of damage extends from the subsurface layer to the inner layer. In the case of P-diamond grit grinding, the accumulation of bond damage in each layer decreases to 3.96×10^4, 1.73×10^4, and 0.97×10^4, which is 15.75%, 31.49%, and 37.46% lower than that of M-diamond, respectively, and the depth of the damage is mainly concentrated on the surface layer. Figure 12 also shows that the material damage of SiC is severer when the grinding wheel speed is in the range of 35 m/s to 80 m/s. For the case of M-diamond grit, the extent of bond damage in each layer of SiC decreases by 3.98%, 8.72%, and 9.47%. By contrast, for the P-diamond grinding case, where the counterpart decreases by 14.34%, 16.83%, and 20.09%, the decreasing trend of damage is moderate. By increasing the grinding wheel speed from 80 m/s to 160 m/s, the amount of bond damage of each SiC layer ground by M-diamond grit can be reduced by 24.36%, 29.28%, and 32.45%, respectively. However, in the case of P-diamond grinding, the decrease is 21.96%, 26.6%, and 28.98%, a significant decrease in the bond damage trend. Therefore, to ensure the grinding performance of diamond grit, the critical grinding wheel speed is set to approximately 80 m/s. The tendency for bond damage decreases with increasing grinding wheel speed but is still more significantly affected by M-diamond grinding. For SiC grinding, a grinding wheel speed of more than 80 m/s is slightly more favorable.

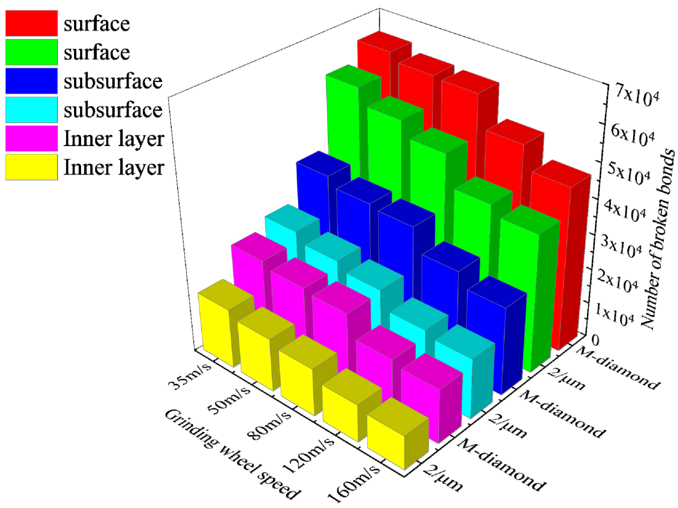

Figure 12. Number of broken bonds in each layer of SiC at stage of chip formation.

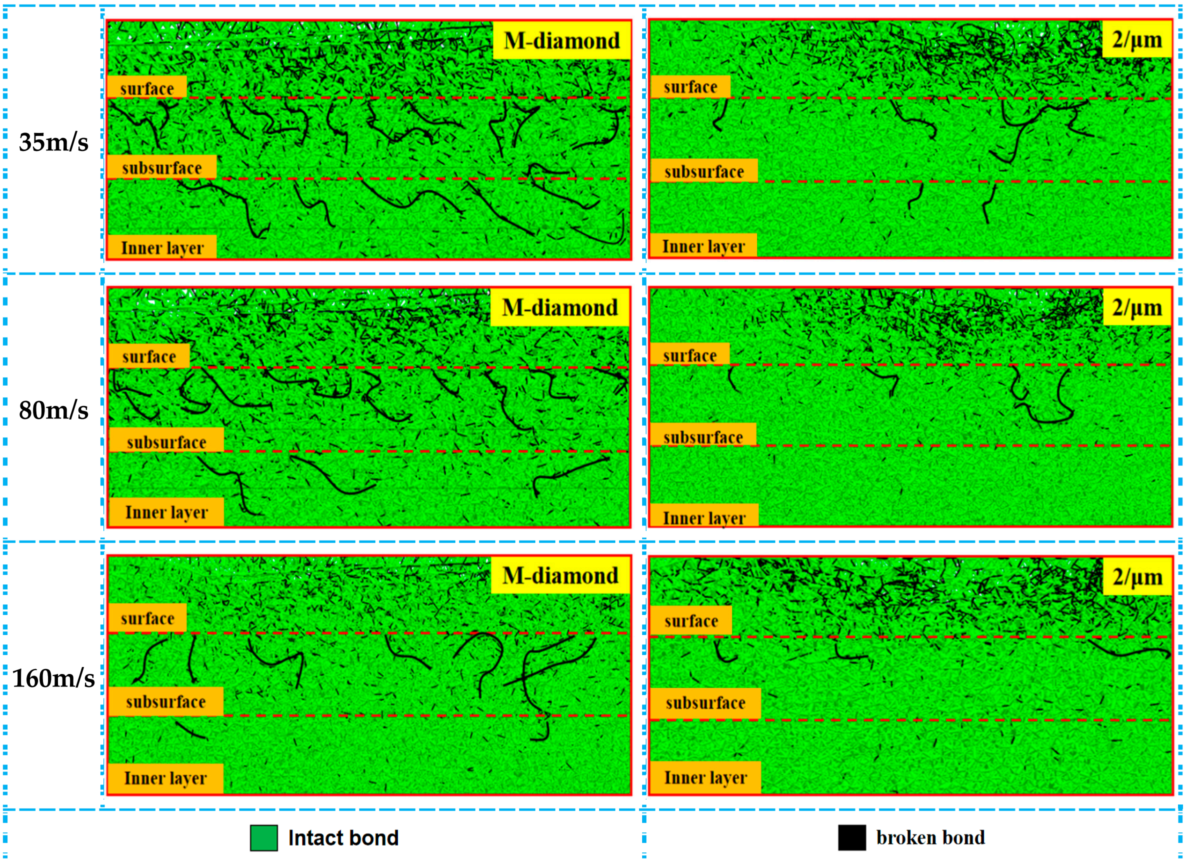

Figure 13. Cumulative damage distribution of bond bonds in SiC layers at different grinding wheel speeds during the chip formation stage.

During the grit detachment stage, the damage to the SiC bonds caused by both diamond grits gradually levels off. However, the amount of damage to the bonds increases slightly due to the grinding edges of the P-diamond surfaces still acting on the SiC surfaces. Nevertheless, the damage is much less than that caused by M-diamonds after grinding. Figure 14 shows the statistical changes in the number of accumulated damages in each surface, subsurface, and inner bond layer when the M-diamond grit and P-diamond grit grind SiC at different grinding wheel speeds at the grit detachment stage. When the grinding wheel speed is 35 m/s, the cumulative damages to the bonds of each layer of SiC at the end of M-diamond grinding are quantified as 6.92×10^4, 4.26×10^4, and 2.81×10^4. By contrast, the cumulative bond damages in each SiC layer at the end of P-diamond grinding are 6.71×10^4, 3.71×10^4, and 2.25×10^4. Figure 15 shows a cloud diagram of the distribution of damage conditions in each layer when M-diamond grit and P-diamond grit grind SiC at different grinding wheel speeds at this stage. Although the amount of bond damage is less in the latter case, the overall damage to the SiC bond is severe for both diamond grits at low speeds. When the grinding wheel speed increases to 80 m/s, the cumulative bond damages of each SiC layer after M-diamond grinding are 6.61×10^4, 3.88×10^4, and 2.53×10^4. Moreover, the cumulative bond damages in each SiC layer at the end of P-diamond grinding are 6.29×10^4, 3.43×10^4, and 2.04×10^4, which decreases by 4.81%, 11.65%, and 19.47% compared with the former values. The degree of SiC bond damage becomes significantly less for P-diamond than for M-diamond at this speed. When the grinding wheel speed is increased to 160 m/s, the cumulative bond damages in each SiC layer after M-diamond grinding are 6.19×10^4, 3.51×10^4, and 2.31×10^4. Moreover, the cumulative damage of the bond of each SiC layer at the end of P-diamond grinding is 5.13×10^4, 2.35×10^4, and 1.31×10^4. Compared with the M-diamond grit, it decreases by 17.08%, 33.22%, and 42.80%, exhibiting remarkable reduction and low damage. At this grinding wheel speed, P-diamond demonstrates superior grinding performance to M-diamond. Furthermore, the damage depth is concentrated on the surface layer of SiC.

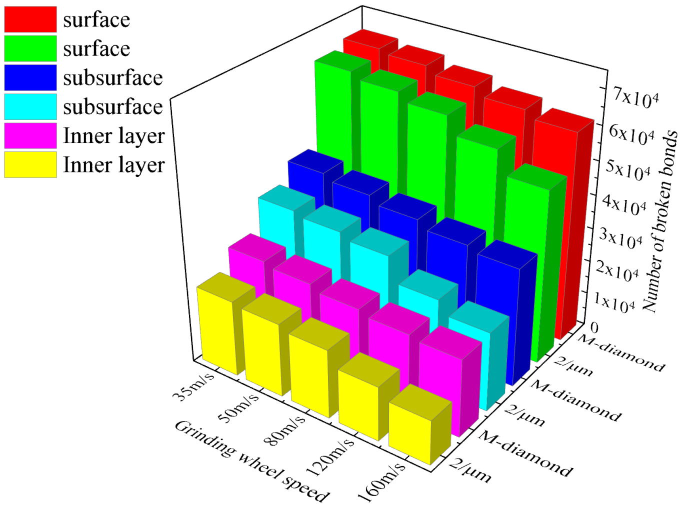

Figure 14. Number of broken bonds in each layer of SiC at stage of grit detachment.

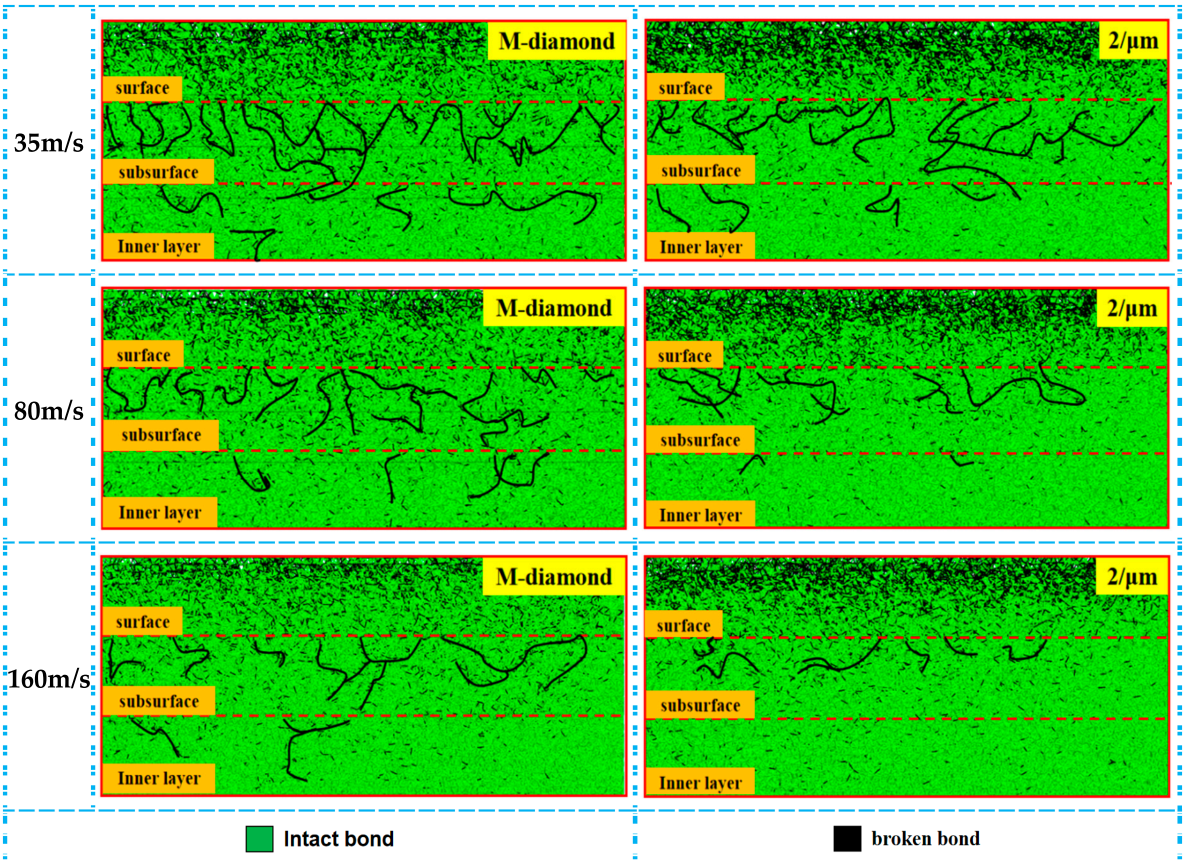

Figure 15. Distribution of cumulative damage conditions of bonds in each SiC layer at grit detachment stage.

During grinding, diamond grit extrusion and shearing can lead to SiC particle collisions. Particle collisions and energy increase as the grinding wheel speed rises. This raises the SiC/diamond contact area temperature, softening it and reducing the tangential grinding force. This minimizes SiC bond damage. The normal grinding force remains constant. Overall, the SiC layer bond strength damage is reduced. Figure 16 demonstrates that as the grinding wheel speed increases, the concentration of active particles on the SiC surface increases, whereas the dispersion of active particles in the subsurface and inner layers gradually increases, enhancing the energy transfer effect. However, in M-diamond grit grinding, the number of active particles and the degree of dispersion of SiC layers are greater than those achieved with P-diamond grit grinding. Meanwhile, Figure 17 shows that the average internal energy contained in the SiC surface particles gradually increases as the grinding wheel speed increases. SiC particles after M-diamond grit grinding have a higher internal energy than P-diamond grit grinding. Tangential and normal grinding forces during the process are influenced by the M-diamond grit surface and cutting depth of larger edges, causing diverse effects. Despite higher kinetic and internal energies, no significant surface temperature concentration is observed, leading to poor softening in the contact area. However, the presence of a large range of active particles leads to deeper bond damage. Although the SiC particles are considerably influenced by the grinding edges on the surface of the P-diamond grit, the tangential and normal grinding forces are generally smaller, thereby reducing the impact range. This finding results from numerous grinding edges with varying cutting depths on the P-diamond surface. Consequently, the elevated kinetic and internal energy in SiC particles raises the temperature of the contact area, inducing a softening effect that minimizes damage to the SiC layer bonds. In brief, the speed of the grinding wheel has a notable influence on the efficiency of P-diamond grit grinding. Boosting the speed of the wheel enhances the stability of the grinding process. Therefore, the risk of causing harm to the SiC subsurface and inner layers is minimized during grinding.

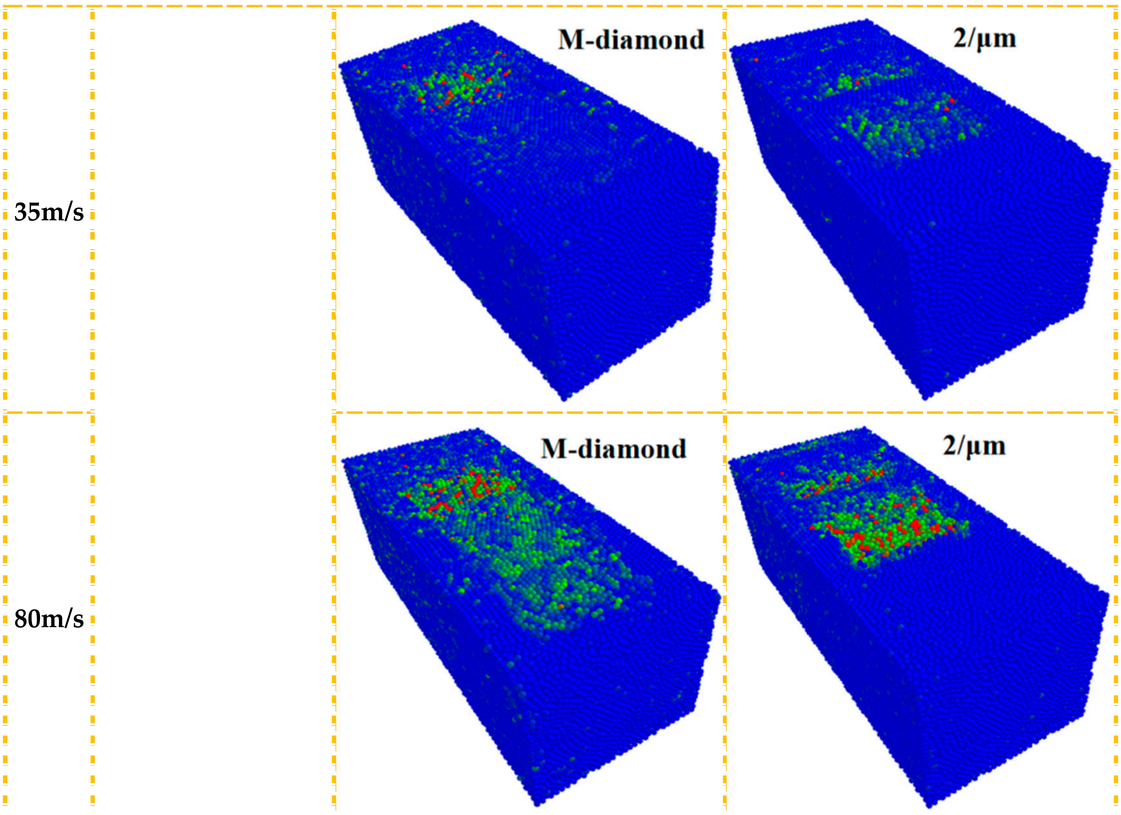

Figure 16. *Cont.*

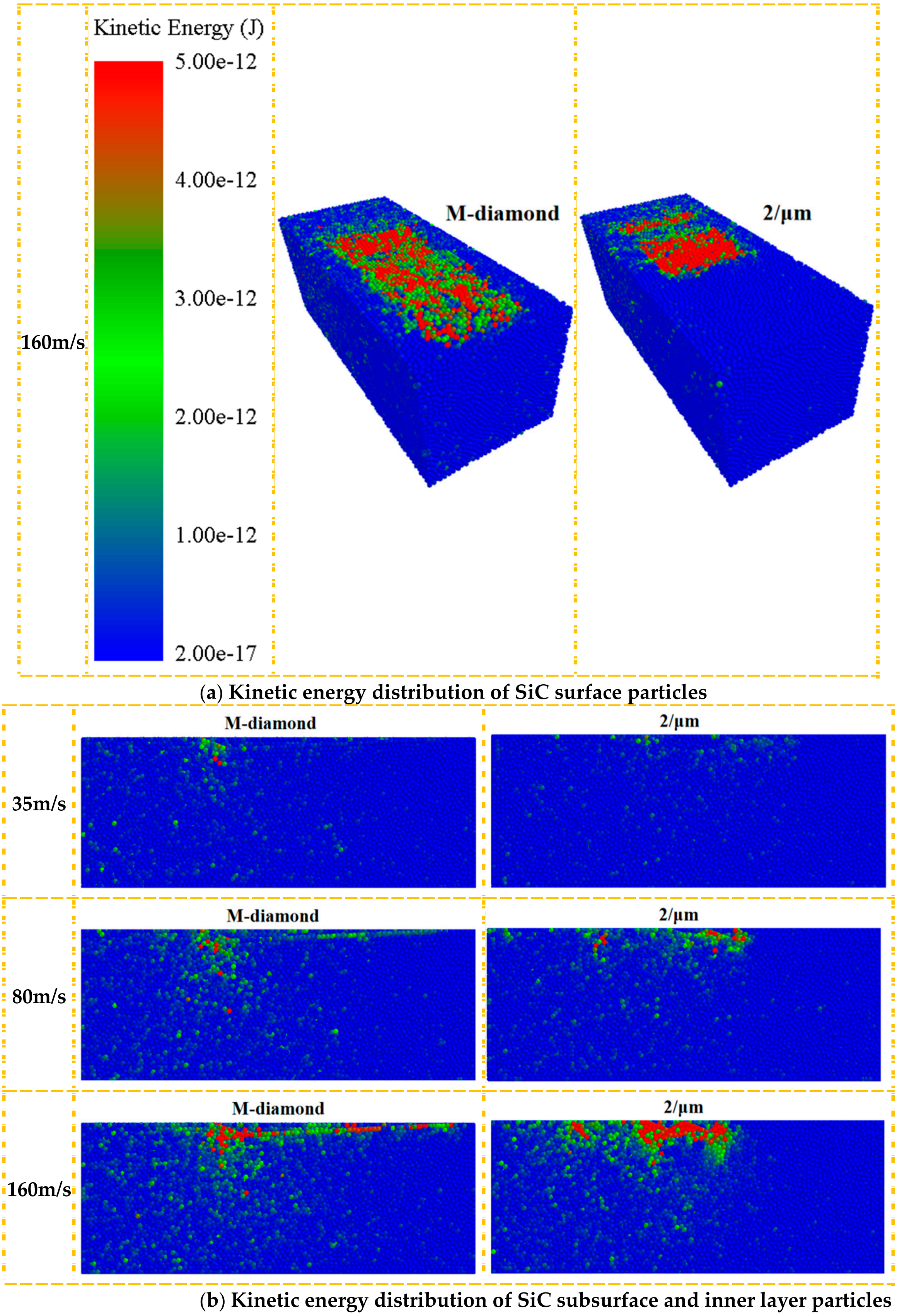

Figure 16. Distribution of kinetic energy of particles in each layer when diamond grit with different grinding wheel speeds grinds SiC at chip formation stage.

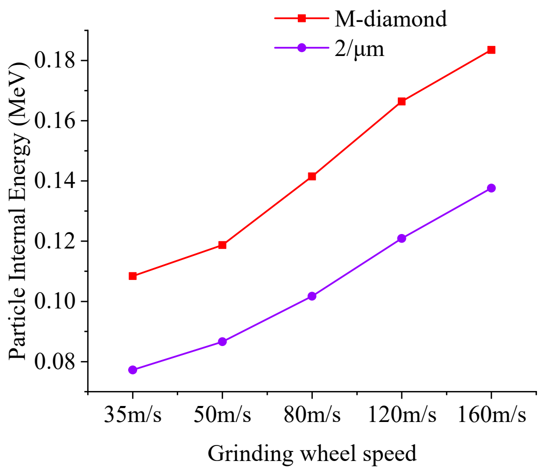

Figure 17. Variation in the average internal energy in the SiC surface particles at different grinding speeds during the chip formation stage.

3.3. Effect of Undeformed Chip Thickness on SiC Ceramic Removal

The effect of undeformed chip thickness on the diamond grinding of SiC is significant, and the extent of diamond grit damage to SiC bonds varies with different grit thicknesses. Figure 18 shows the changes in the cumulative number of flaws in each surface, subsurface, and inner bond layer as M-diamond grit with different undeformed chip thicknesses and P-diamond grit with the micro-cutting edge density of 2/μm grind SiC using scratch plowing. During the scratch plowing stage, the bond damages in each layer of M-diamond grit used to grind SiC are 0.48×10^4, 0.16×10^4, and 0.10×10^4 when the thickness of the undeformed chip is 1 μm. Meanwhile, the bond damages in each layer of P-diamond grit grinding are 0.12×10^4, 0.075×10^4, and 0.067×10^4. When the undeformed chip thickness increases to 4 μm, the bond damages in each layer reach 1.64×10^4, 0.99×10^4, and 0.61×10^4 for M-diamond grit grinding. Moreover, the bond damages in each layer reach 0.88×10^4, 0.39×10^4, and 0.26×10^4 in P-diamond grit grinding. Figure 19 shows a cloud plot of the distribution of the damage condition of each layer when grinding SiC with M-diamond grit and P-diamond grit using different undeformed chip thicknesses. The quantity of SiC bond damages increases as the thickness of the undeformed chip increases. In addition, the number of bond damages increases significantly with the use of M-diamond grit grinding. Furthermore, the depth of bond damage in each SiC layer exhibits a linear increase. At this stage, M-diamond grinding causes more significant damage to the SiC bond at different undeformed chip thickness, whereas P-diamond grinding causes slightly weaker damage. However, the damage trends for both methods increase linearly with the increase in undeformed chip thickness.

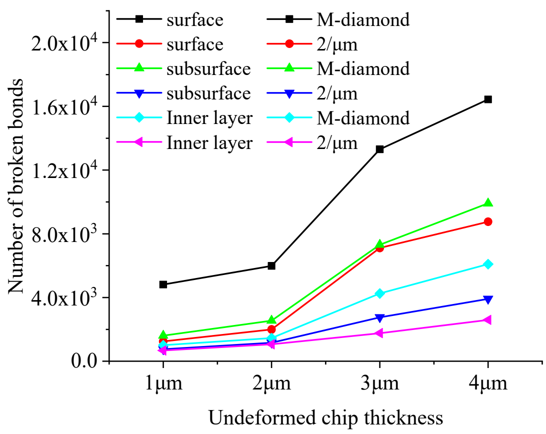

Figure 18. Number of broken bonds in each SiC layer at scratch plowing stage.

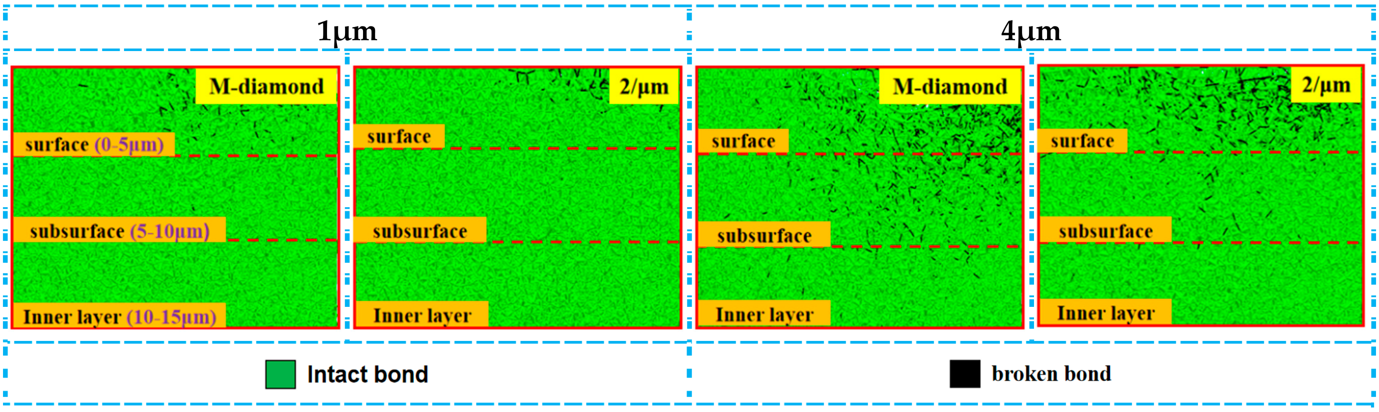

Figure 19. Distribution of cumulative damage conditions of bonds in each layer of SiC at scratch plowing stage.

During the chip formation stage, the damage to the SiC bond increases substantially with the increase in the undeformed chip thickness. Figure 20 shows the changes in the cumulative number of flaws in each surface, subsurface, and inner bond layer upon SiC grinding by the M-diamond grit with different undeformed chip thickness and P-diamond grit with chip formation. When the undeformed chip thickness increases from 1 μm to 4 μm, the number of cumulative damages of superficial bonds increases from 2.97×10^4 to 8.55×10^4, that of subsurface bonds increases from 1.12×10^4 to 5.92×10^4, and that of inner bonds increases from 0.57×10^4 to 4.14×10^4 in the M-diamond grit grinding of SiC. By contrast, the amount of accumulated bond damage in each layer increases from 2.42×10^4, 0.68×10^4, and 0.38×10^4 to 6.28×10^4, 3.45×10^4, and 2.30×10^4, respectively, when the P-diamond grit was used to grind SiC. The average increase in SiC bond fracture in the case of M-diamond grinding is 77.43%, whereas that in the case of P-diamond grinding is 74.97%, indicating that the SiC bond damage by P-diamond grit is slightly affected by the undeformed chip thickness. Figure 21 shows a cloud plot of the distribution of the damage condition of each layer when grinding SiC with M-diamond grit and P-diamond grit using different undeformed chip thicknesses at this stage. As the undeformed chip thickness increases, the depth of bond damage in each SiC layer increases linearly. The depth of damage is shallow when the undeformed chip thickness is small. In the case of M-diamond grit grinding, the bond damage depth extends to the SiC subsurface layer, whereas the damage depth is concentrated on the surface layer in P-diamond grinding. When a single grit has a larger cutting thickness, the depth of SiC bond damage in both types of diamond grit grinding is extended to the subsurface layer or even the inner layer. However, in P-diamond grit grinding, the depth of damage is slightly smaller. The SiC bond damage at this stage is significantly affected by the undeformed chip thickness, but P-diamond grits can significantly reduce the large bond break caused by the increased undeformed chip thickness. The optimum undeformed chip thickness should be between 1 and 2 μm to achieve less damage.

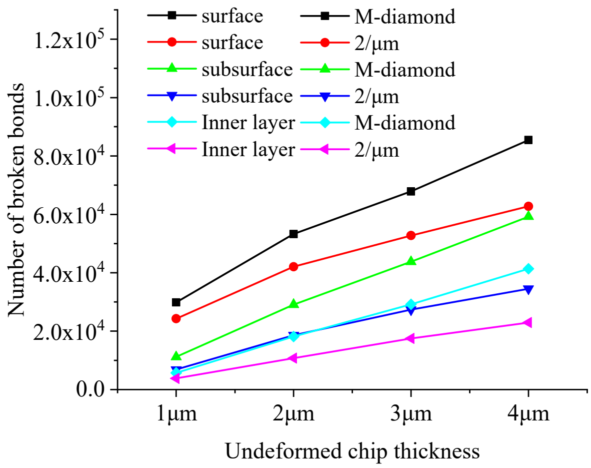

Figure 20. Number of broken bonds in each SiC layer at chip formation stage.

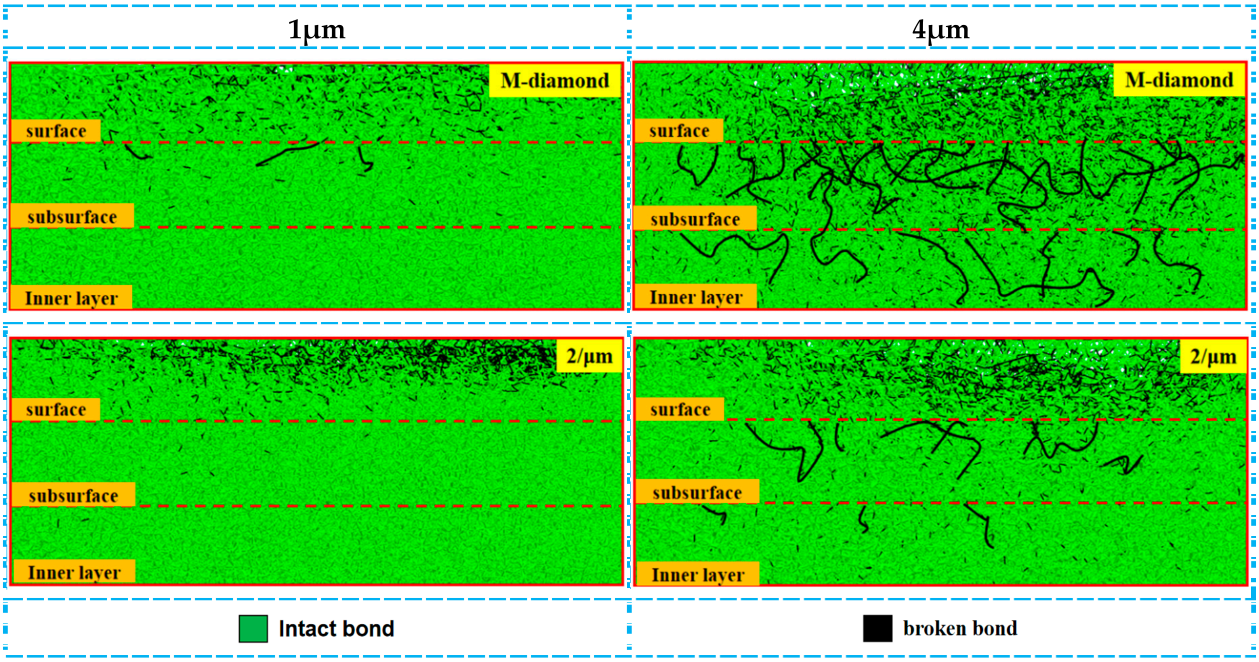

Figure 21. Distribution of cumulative damage conditions of bonds in each SiC layer at chip formation stage.

During the grit detachment phase, the degree of SiC bond disruption by both diamond grits gradually levels off, but the undeformed chip thickness continues to increase. Figure 22 shows the changes in the cumulative number of flaws in each surface, subsurface, and inner bond layer under M-diamond grit with different undeformed chip thickness and P-diamond grit grinding SiC with grit detachment. When the undeformed chip thickness is 1 μm, the cumulative damage quantities of bond in each SiC layer at the end of M-diamond grit grinding are finally 3.21×10^4, 1.24×10^4, and 0.66×10^4 and 3.03×10^4, 0.87×10^4, and 0.52×10^4 for P-diamond grit grinding, indicating a decrease by 5.21%, 29.63%, and 20.75% year-on-year. When the undeformed chip thickness increases to 4 μm, the cumulative damage quantities of the bond in each SiC layer at the end of M-diamond grit grinding are 9.19×10^4, 6.55×10^4, and 4.65×10^4 and 7.66×10^4, 4.87×10^4, and 3.99×10^4 for P-diamond grit grinding, exhibiting a decrease by 16.63%, 25.67%, and 14.11% year-on-year. Figure 23 shows a cloud plot of the distribution of the damage condition of each layer when grinding SiC with M-diamond and P-diamond grits under different undeformed chip thicknesses at this stage. When the undeformed chip thickness is 1 µm, the depth of the SiC bond damage extends to the subsurface layer after M-diamond grinding. By contrast, the depth of bond damage after P-diamond grinding is still concentrated on the surface layer. When the undeformed chip thickness is 4 µm, both diamond types experience more severe SiC bond damage during grinding. M-diamond grinding results in a greater depth of bond damage, reaching the inner layer and causing a large number of broken bonds. P-diamond, on the contrary, experiences shallower bond damage. In summary, using a smaller undeformed chip thickness can reduce the SiC bond damage and its depth. However, larger undeformed chip thickness can exacerbate bond damage, which can be severe regardless of the diamond grit type.

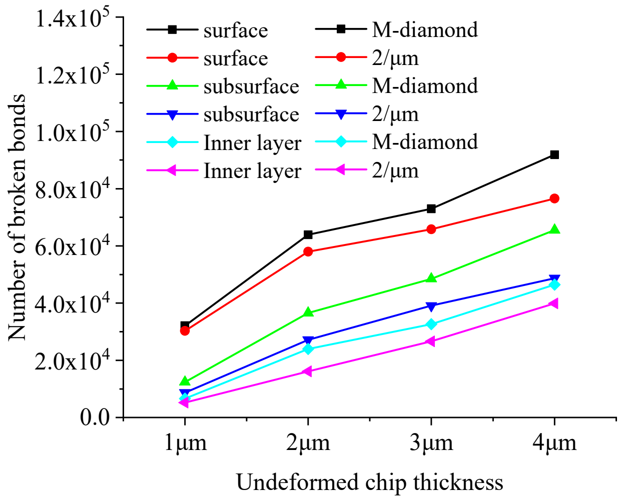

Figure 22. Number of broken bonds in each SiC layer at stage of grit detachment.

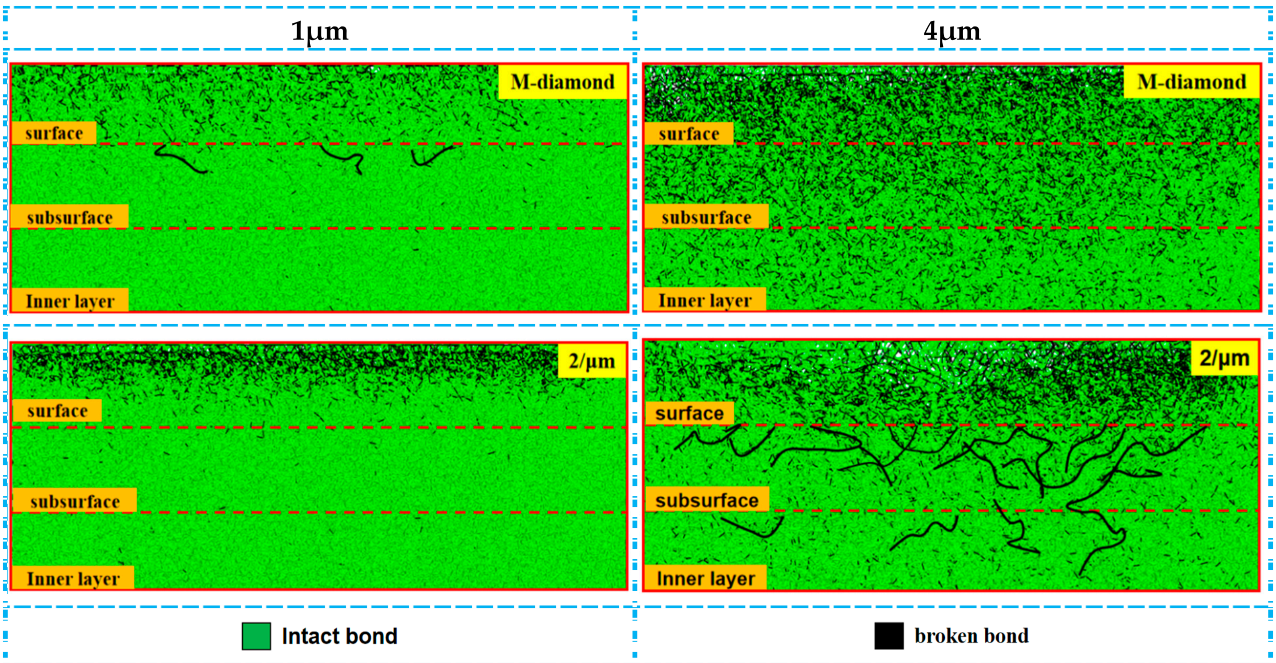

Figure 23. Distribution of cumulative damage conditions of bonds at grit detachment stage.

The effective area of the grinding edge on the diamond grit's surface interacting with the SiC particles also increases as the undeformed chip thickness increases. This phenomenon leads to intensified collisions between the particles and elevated kinetic energy, resulting in a rapid increase in the amount of damage to the bonds. Figure 24 shows the variation in the total grinding force exerted on SiC when grinding with M-diamond grit and P-diamond grit with different undeformed chip thicknesses at the chip formation stage. The data show that the total grinding force increases linearly with the undeformed chip thickness. However, when grinding SiC, the grinding force generated by the P-diamond grit is significantly lower than that generated by the M-diamond grit. The grinding force magnitude varies and affects the SiC particles differently. Figure 25 shows a cloud diagram of the magnitude distribution of the kinetic energy of the particles in the different SiC layers when grinding with the two grit types in the corresponding case. The impact of M-diamond grit on SiC particles increases step by step with the undeformed chip thickness. This condition intensifies the energy transfer effect and linearly elevates the number and distribution of active particles in each layer, substantially increasing the amount of bond damage. The P-diamond grit, on the contrary, generates less grinding force than the M-diamond grit despite the increased effect under different undeformed chip thickness conditions. Thus, the number of active particles is reduced, the distribution is more concentrated, and the amount of bond damage is less. In summary, the effect of undeformed chip thickness on the grinding performance of the two diamond grits is significant. P-diamond, compared with M-diamond, greatly reduces the grinding force and damage to SiC when the undeformed chip thickness is small, resulting in more stable grinding. However, when the condition of undeformed chip thickness is large, the tendency of SiC to incur large area damage increases.

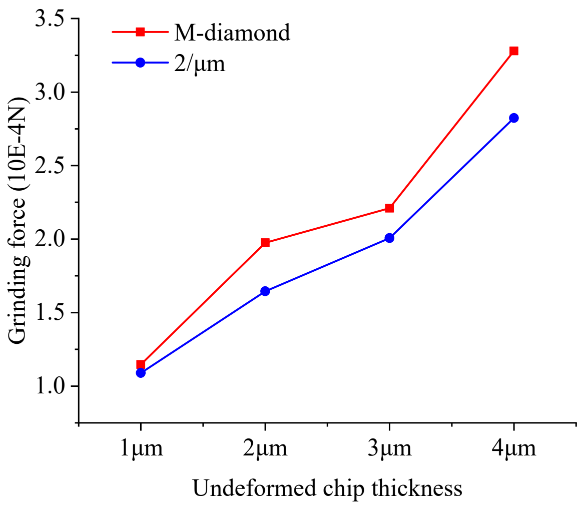

Figure 24. Variation in total grinding forces on SiC during diamond grit grinding with different undeformed chip thicknesses at the chip formation stage.

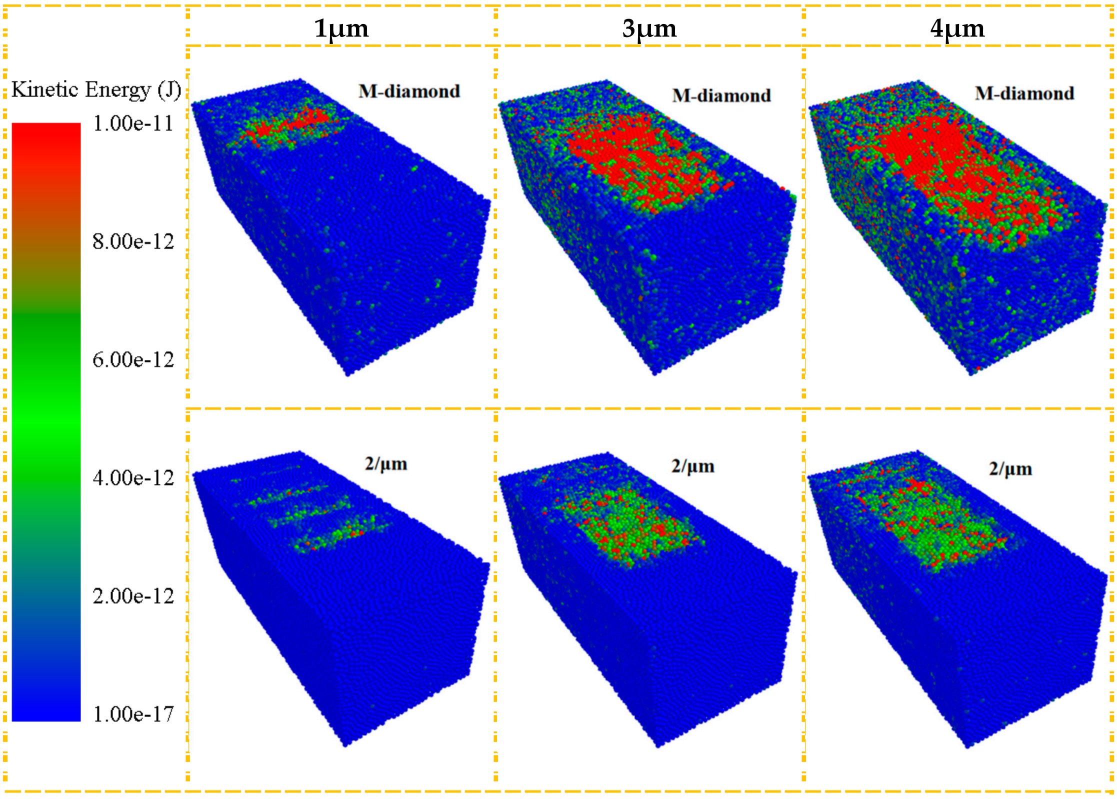

(**a**) Kinetic energy distribution of SiC surface particles

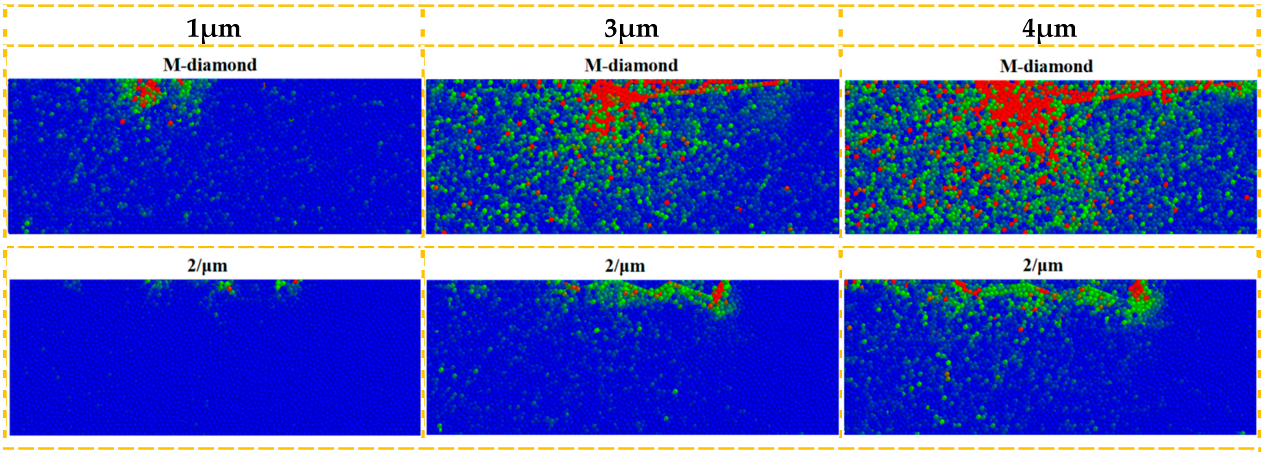

(**b**) Kinetic energy distribution of SiC subsurface and inner layer particles

Figure 25. Distribution of kinetic energy of particles in each layer when diamond grit with different undeformed chip thicknesses grinds SiC at chip formation stage.

4. Conclusions

In this paper, a discrete element simulation model of SiC ceramic material grinding by P-diamond grit grains is established by the DEM. The controlled experimental simulation method is used to compare with M-diamond grit grains to reveal the mechanism of removing SiC ceramic materials by P-diamond grit grains from a microscopic point of view, and then the grinding parameters are optimized. In the future, this model can be employed to simulate and analyze the remaining grinding parameters (grinding angle, feed rate, etc.), as well as to further investigate the wear mechanism of porous diamond grits. The conclusions of this paper can provide new research ideas and a theoretical basis for the efficient and low-damage research of hard and brittle materials. The specific conclusions are as follows:

1. Compared to the more "aggressive" removal process of M-diamond grits, P-diamond grits are more "gentle" in removing SiC materials. Moreover, the damage to SiC ceramics caused by P-diamond grits is low, mainly concentrated in the surface layer of SiC. However, this damage degree increases with the increase in cutting edge density, so the optimal cutting edge density should be controlled within 1–3 μm.
2. Grinding SiC materials with P-diamond grits can cause workpiece damage due to the skin effect. The damage degree decreases with an increase in grinding wheel speed. When the grinding wheel speed exceeds 80 m/s, the removal of SiC during grinding becomes more efficient.
3. The results show that the undeformed chip thickness is very significant to the damage of SiC layers. In order to minimize the tendency and extent of such damage, the optimum undeformed chip thickness should be controlled between 1 and 2 μm.
4. Under reasonable grinding and pore parameters, P-diamond causes less damage to SiC materials than M-diamond. This finding indicates that P-diamond has better grinding performance than M-diamond.

Author Contributions: Conceptualization, Y.Z. and Z.Z. (Zhaoqin Zhang); methodology, Y.Z.; software, Z.Z. (Zhaoqin Zhang) and Z.Z. (Zhongxing Zhang); validation, Z.Z. (Zhaoqin Zhang) and W.Z.; writing—original draft preparation, Z.Z. (Zhaoqin Zhang); writing—review and editing, Y.Z.; investigation, Z.Z. (Zhaoqin Zhang) and J.X.; funding acquisition, Y.Z. All authors have read and agreed to the published version of the manuscript.

Funding: This research was funded by the Natural Science Foundation of Jiangsu Province (No. BK20210407), the National Natural Science Foundation of China (NSFC) (No. 52305474).

Institutional Review Board Statement: Not applicable.

Informed Consent Statement: Not applicable.

Data Availability Statement: The raw data supporting the conclusions of this article will be made available by the authors on request.

Conflicts of Interest: All authors declare no conflicts of interest.

References

1. Boyle, R.J.; Gnanaselvam, P.; Parikh, A.H.; Ameri, A.A.; Bons, J.P.; Nagpal, V.K. Design of stress constrained SiC/SiC ceramic matrix composite turbine blades. *J. Eng. Gas Turbines Power* **2021**, *143*, 051013. [CrossRef]
2. Zhong, J.; Xu, Q. High-temperature mechanical behaviors of SiO_2-based ceramic core for directional solidification of turbine blades. *Materials* **2020**, *13*, 4579. [CrossRef] [PubMed]
3. Wang, Y.; Fan, L.; Chen, H. Effect of strength and toughness of ceramic particles on impact abrasive wear resistance of iron matrix composites. *Mater. Today Commun.* **2023**, *35*, 105689. [CrossRef]
4. Luo, Q.; Chen, J.; Lu, J.; Ke, C.; Hu, G.; Huang, H. Fabrication and Application of Grinding Wheels with Soft and Hard Composite Structures for Silicon Carbide Substrate Precision Processing. *Materials* **2024**, *17*, 2079. [CrossRef] [PubMed]
5. Liu, S.; Liu, M.; Liu, T.; Xiao, H.; Xiao, B. Wear characteristics of brazing diamond abrasive wheel on high efficiency grinding ferrous metals. *Wear* **2023**, *514*, 204580. [CrossRef]
6. Dai, J.; Cao, S.; Wang, Z.; Liu, X.; Zhang, Y.; Chen, H. Experimental investigation on the feasibility of high-efficiency and precision grinding of silicon carbide ceramics with monolayer brazed diamond wheel. *Mater. Today Commun.* **2023**, *37*, 107037. [CrossRef]
7. Li, J.; Liu, X.; Wan, L.; Fang, W.-J.; Yan, Y.-G.; Li, Y.-Y.; Gao, P.-Z. Using the thermochemical corrosion method to prepare porous diamonds. *Ceram. Int.* **2021**, *47*, 35002–35012. [CrossRef]
8. Peng, Y.; Ren, J.; Jia, C.; Zhong, G.; Ma, Q.; Zhang, W. Structural design and mechanical properties of porous structured diamond abrasive tool by selective laser melting. *Ceram. Int.* **2023**, *49*, 6508–6521. [CrossRef]
9. Kacalak, W.; Lipiński, D.; Szafraniec, F. Selected Aspects of Precision Grinding Processes Optimization. *Materials* **2024**, *17*, 607. [CrossRef]
10. Jamshidi, H.; Budak, E. An analytical grinding force model based on individual grit interaction. *J. Mater. Process. Technol.* **2020**, *283*, 116700. [CrossRef]
11. Ohashi, T.; Sugimoto, W.; Takasu, Y. Catalytic etching of synthetic diamond crystallites by iron. *Appl. Surf. Sci.* **2012**, *258*, 8128–8133. [CrossRef]

12. Mehedi, H.A.; Hébert, C.; Ruffinatto, S.; Eon, D.; Omnes, F.; Gheeraert, E. Formation of oriented nanostructures in diamond using metallic nanoparticles. *Nanotechnology* **2012**, *23*, 455302. [CrossRef] [PubMed]
13. Takasu, Y.; Konishi, S.; Sugimoto, W.; Murakami, Y. Catalytic formation of nanochannels in the surface layers of diamonds by metal nanoparticles. *Electrochem. Solid-State Lett.* **2006**, *9*, C114. [CrossRef]
14. Wang, J.; Wan, L.; Chen, J.; Yan, J. Micropatterning of diamond crystallites via cobalt-catalyzed thermochemical etching. *J. Mater. Sci.* **2017**, *52*, 709–720. [CrossRef]
15. Wang, J.; Wan, L.; Chen, J.; Yan, J. Surface patterning of synthetic diamond crystallites using nickel powder. *Diam. Relat. Mater.* **2016**, *66*, 206–212. [CrossRef]
16. Wang, J.; Wan, L.; Chen, J.; Yan, J. Anisotropy of synthetic diamond in catalytic etching using iron powder. *Appl. Surf. Sci.* **2015**, *346*, 388–393. [CrossRef]
17. Lee, G.C.B.; Su, S.; Li, J.; Sugden, K.; Roohpour, N.; Yan, H.; Ye, H. Analysis of femtosecond laser surface patterning on bulk single-crystalline diamond. *J. Exp. Nanosci.* **2012**, *7*, 662–672. [CrossRef]
18. Jeong, B.; Lee, B.; Kim, J.H.; Choi, J.-A.; Yang, J.; Sall, E.; Heo, D.; Jang, J.; Kim, G.-H.; Yashin, V. Drilling of sub-100μm hourglass-shaped holes in diamond with femtosecond laser pulses. *Quantum Electron.* **2020**, *50*, 201. [CrossRef]
19. Li, W.; Long, G.; Shi, F.; Zhou, S.; Yin, J.; Yang, J. Influence of the fiber orientation on 3D C/C–SiC composite material and its formation mechanism of the machining surface. *Int. J. Adv. Manuf. Technol.* **2022**, *118*, 2725–2742. [CrossRef]
20. Li, W.; Jiao, Y.; Jiang, H.Y.; Ren, Y.-H.; Ibrahim, A.M.M. Investigation of mechanical force acting on the surface modified-substrate layer area during the chemical-mechanical micro-grinding of monocrystalline silicon. *Int. J. Mech. Sci.* **2022**, *228*, 107482. [CrossRef]
21. Mao, C.; Liang, C.; Zhang, Y.; Zhang, M.; Hu, Y.; Bi, Z. Grinding characteristics of CBN-WC-10Co composites. *Ceram. Int.* **2017**, *43*, 16539–16547. [CrossRef]
22. Zhou, W.; Su, H.; Dai, J.; Yu, T.; Zheng, Y. Numerical investigation on the influence of cutting-edge radius and grinding wheel speed on chip formation in SiC grinding. *Ceram. Int.* **2018**, *44*, 21451–21460. [CrossRef]
23. Guo, C.; Shi, Z.; Mullany, B.; Linke, B.; Yamaguchi, H.; Chaudhari, R.; Hucker, S.; Shih, A. Recent advancements in machining with abrasives. *J. Manuf. Sci. Eng.* **2020**, *142*, 110810. [CrossRef]
24. Rasim, M.; Mattfeld, P.; Klocke, F. Analysis of the grain shape influence on the chip formation in grinding. *J. Mater. Process. Technol.* **2015**, *226*, 60–68. [CrossRef]
25. Jin, W.W.B. Micro-milling of fused silica based on instantaneous chip thickness. *J. Mater. Process. Technol.* **2020**, *285*, 116786. [CrossRef]
26. Liu, Y.; Li, B.; Kong, L. Molecular dynamics simulation of silicon carbide nanoscale material removal behavior. *Ceram. Int.* **2018**, *44*, 11910–11913. [CrossRef]
27. Zhao, P.; Zhao, B.; Pan, J.; Wu, J. Nano-grinding process of single-crystal silicon using molecular dynamics simulation: Nano-grinding parameters effect. *Mater. Sci. Semicond. Process.* **2022**, *143*, 106531. [CrossRef]
28. Zhao, P.; Zhao, B.; Pan, J.; Wu, J. Superimpose mechanism of surface generation process in grinding of monocrystalline silicon using molecular dynamics simulation. *Mater. Sci. Semicond. Process.* **2022**, *147*, 106684. [CrossRef]
29. Li, M.; Guo, X.; Kang, R.; Guo, D.; Zhou, P. Study on the transformation and control mechanism of amorphous damage during the grinding process of monocrystalline silicon considering grain shapes by MD method. *Tribol. Int.* **2023**, *187*, 108720. [CrossRef]
30. Daniel, G.; Jiri, Z. *Discrete Element Method in the Design of Transport Systems*; Springer: Cham, Switzerland, 2019. [CrossRef]
31. Okuzono, Y.; Hirata, Y.; Matsunaga, N.; Sameshima, S. Young's Modulus and Poisson's Ratio of Liquid Phase-Sintered Silicon Carbide. *Key Eng. Mater.* **2011**, *1318*, 98–101. [CrossRef]
32. Kiyashko, M.V.; Grinchuk, P.S.; Kuznetsova, T.A.; Kren, A.P.; Abuhimd, H.M. Determination of elastic modulus of SiC-based composite ceramics. *Tech. Phys. Lett.* **2021**, *47*, 150–153. [CrossRef]
33. Heidenreich, B.; Kraft, H.; Bamsey, N.; Such-Taboada, M. Shear properties of C/C-SiC sandwich structures. *Int. J. Appl. Ceram. Technol.* **2022**, *19*, 54–61. [CrossRef]
34. Chai, P.; Li, S.; Li, Y.; Yin, X. Study on damage of 4H-SiC single crystal through indentation and scratch testing in micro–nano scales. *Appl. Sci.* **2020**, *10*, 5944. [CrossRef]
35. Zhou, P.; Sun, T.; Shi, X.; Li, J.; Zhu, Y.; Wang, Z. Atomic-scale study of vacancy defects in SiC affecting on removal mechanisms during nano-abrasion process. *Tribol. Int.* **2020**, *145*, 106136. [CrossRef]
36. Barhoumi, M.; Rocca, D.; Said, M.; Lebègue, S. Elastic and mechanical properties of cubic diamond and silicon using density functional theory and the random phase approximation. *Solid State Commun.* **2021**, *324*, 114136. [CrossRef]
37. Kawasaki, K.; Tanaka, D.; Yamada, H.; Ohmagari, S.; Mokuno, Y.; Chayahara, A.; Tamagawa, T.; Hironaka, Y.; Yamanoi, K.; Tsukamoto, M.; et al. Direct-drive implosion experiment of diamond capsules fabricated with hot filament chemical vapor deposition technique. *Phys. Plasmas* **2021**, *28*, 104501. [CrossRef]
38. Shen, X.; Wu, K.; Sun, H.; Sang, L.; Huang, Z.; Imura, M.; Koide, Y.; Koizumi, S.; Liao, M. Temperature dependence of Young's modulus of single-crystal diamond determined by dynamic resonance. *Diam. Relat. Mater.* **2021**, *116*, 108403. [CrossRef]

materials

MDPI

Article

Micro-Milling of Additively Manufactured Al-Si-Mg Aluminum Alloys

Qiongyi He [1], Xiaochong Kang [2] and Xian Wu [3,*]

1 School of Mechanical Engineering, Tianjin University of Technology and Education, Tianjin 300350, China; hqyyhy@vip.163.com
2 Jimei Industrial College, Xiamen 361022, China; kxc215@163.com
3 College of Mechanical Engineering and Automation, Huaqiao University, Xiamen 361021, China
* Correspondence: xianwu@hqu.edu.cn

Abstract: Additively manufactured aluminum alloy parts attract extensive applications in various felids. To study the machinability of additively manufactured aluminum alloys, micro-milling experiments were conducted on the additively manufactured AlSi7Mg and AlSi10Mg. By comparing the machinability of Al-Si-Mg aluminum alloys with different Si content, the results show that due to the higher hardness of the AlSi10Mg, the cutting forces are higher than the AlSi7Mg by about 11.8% on average. Due to the increased Si content in additively manufactured Al-Si-Mg aluminum alloys, the surface roughness of AlSi10Mg is 26.9% higher than AlSi7Mg on average. The burr morphology of additively manufactured aluminum alloys in micro-milling can be divided into fence shape and branch shape, which are, respectively, formed by the plastic lateral flow and unseparated chips. The up-milling edge exhibits a greater burr width than the down-milling edge. Due to the better plasticity of AlSi7Mg, the burr width of the down-milling edge is 28.1% larger, and the burr width of the up-milling edge is 10.1% larger than the AlSi10Mg. This research can provide a guideline for the post-machining of additively manufactured aluminum alloys.

Keywords: additively manufactured aluminum alloys; processability; burr formation

1. Introduction

With the rapid development of lightweight design in various fields, such as aerospace, transportation, and automotive industries, more and more integrated structural components are being adopted. Lightweight manufacturing is gradually becoming a trend and greatly promotes the application of lightweight alloys in these fields. Aluminum alloy materials have excellent properties, such as low weight, good specific strength and stiffness, and higher plasticity, making them the preferred alloy for achieving a structural lightweight design [1–3]. The widespread application of aluminum alloy has promoted the rapid development of aluminum alloy materials and its machining technology. Traditional aluminum alloy components are mainly prepared by melting, casting, and forging, requiring a lot of time and energy. At present, with the continuous improvement of high-end equipment technology, higher requirements are put forward for the manufacturing technology of aluminum alloy components with complex and precise structures. This not only requires the manufacturing process to be efficient and precise but also to have high flexibility and adaptability requirements for its production and manufacturing process.

Additive manufacturing technology, also known as 3D printing technology, can directly manufacture parts layer-by-layer based on a digital model of the parts. Additive manufacturing technology can rapidly manufacture complex components as a whole. It has been widely applied in many fields, such as aerospace, biomedical, and rail transit [4–6]. With the rapid development of metal additive manufacturing technology, many researchers have reported on the additive manufacturing of aluminum alloys. Li et al. achieved the additive manufacturing of high-strength aluminum alloys through the laser powder bed fusion (LPBF) process [7]. Liu et al. prepared high-strength aluminum alloys with strengths exceeding 600 MPa using a pulse laser arc hybrid process [8]. At present, aluminum alloy additive manufacturing technology has been applied in industrial production to achieve the complex structural customization of products and shorten market response time [9–11].

Although metal additive manufacturing technology presents advantages in terms of flexibility and efficiency, due to limitations in machining principles, the aluminum alloy parts prepared by additive manufacturing often cannot meet machining requirements regarding simultaneous machining accuracy and surface quality. Additionally, it usually requires subsequent post-processing, such as mechanical machining and polishing [12–14]. Compared to metal materials prepared by casting and forging, metal materials prepared through additive manufacturing have significant differences in microstructure and mechanical properties, such as hardness and yield strength [15–17], which cause corresponding changes in their machinability in the mechanical machining process. Wu et al. found significant differences in the cutting machinability of additively manufactured titanium alloy compared to the forged titanium alloy. They pointed out that the machining parameters must be adjusted for the additively manufactured blank [18]. Randolph et al. performed single-point turning on additively manufactured A205 aluminum alloys; the results indicated that additively manufactured A205 material presented good ultra-precision turning performance [14]. Segebad et al. investigated the influence of build-up direction on chip formation in the orthogonal cutting of additively manufactured AlSi10Mg [19]. Tan et al. studied the ultrasonic elliptical vibration-assisted cutting of selective laser melting (SLM) additively manufactured AlSi10Mg alloy and found it can suppress surface defects and improve surface quality [20]. Although many researchers have conducted extensive studies on the cutting machinability of various additively manufactured metal materials [21–23], there are few reports on the effect of the Si phase in additively manufactured aluminum alloy on micro-milling machinability in the existing literature.

This paper focuses on the subsequent post-milling of the additively manufactured Al-Si-Mg aluminum alloys. Micro-milling experiments were conducted on AlSi7Mg and AlSi10Mg using a micro end mill. The milling force, surface roughness, and burr formation have been analyzed. The cutting performance of additively manufactured aluminum alloys with different Si contents was studied. The results can provide theoretical guidance for industrial applications in the production of aluminum alloy parts by additive manufacturing.

2. Experimental Procedures

In this work, micro-milling research was performed on a five-axis machine center (JDGR 200T, Beijing Jingdiao Group, Beijing, China), which is specially designed for the machining of micro components, as shown in Figure 1. This machine can provide a maximum spindle rotating speed of 24,000 rpm and a repeated position accuracy of 2 μm. The tool used in the experiment was a micro end mill with two flutes made of fine-grained cemented carbide (MSE 230, NS Tool Co., Ltd., Tokyo, Japan), which is specially designed for micro machining. Tool diameter was measured to 1 mm, the edge length was 2.5 mm, handle diameter was 4 mm, and helix angle was 30°; tool structure parameters are shown in Figure 2.

When reducing weight is the main goal, additively manufactured aluminum alloys are a common choice for aerospace and high-performance racing applications. The Al-Si-Mg alloys present excellent laser machining performance and attract much attention in the additive manufacturing field of selective laser melting (SLM) processes. Hence, the Al-Si-Mg alloys have been selected to study the micro-milling machinability. The used workpiece materials in this work were AlSi7Mg and AlSi10Mg aluminum alloys prepared by the SLM process, produced by Falcon Tech Co., Ltd., Wuxi, China. In SLM, the laser power was 340 kW, the scanning speed was 1400 m/s, the scanning interval was 90 μm, and layer thickness was 30 μm. The printing orientation deflects a 67° angle from the length direction of the workpiece. The workpiece was cut into the suitable size of 35 × 9 × 3 mm by wire electric discharge machining (WEDM) and pre-machined by conventional milling. The chemical compositions and mechanical properties along the horizontal direction are listed in Tables 1 and 2, based on the previous literature [24,25]. Table 2 shows that the additively manufactured aluminum alloys present different mechanical properties due to different Si contents. In comparison, the yield strength of AlSi10Mg aluminum alloy is slightly lower in yield strength but slightly higher in material hardness.

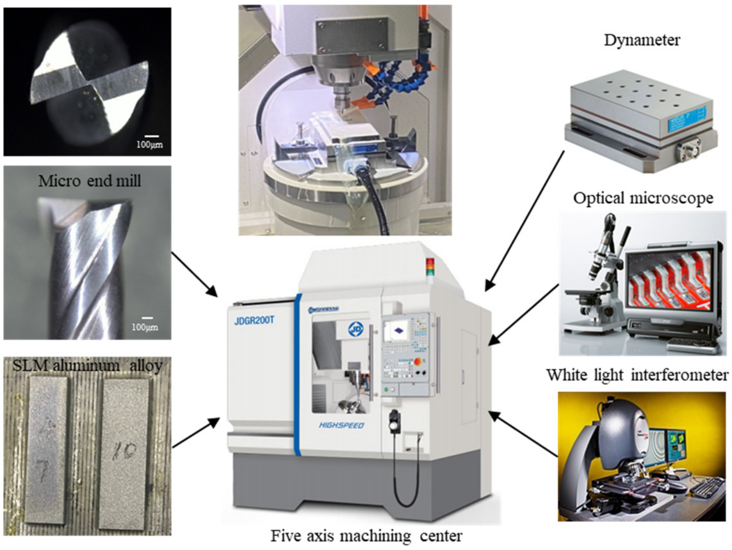

Figure 1. Micro-milling experiments.

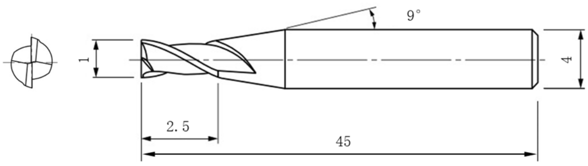

Figure 2. Tool structure parameters of micro end mill (mm).

Table 1. The chemical compositions of the additively manufactured aluminum alloys.

Material	Si wt%	Mg wt%	Fe wt%	Zn wt%	Ti wt%	Ni wt%	Al wt%
AlSi7Mg	7	0.36	0.1	0.016	0.006	0.004	Bal
AlSi10Mg	10	0.36	0.1	0.016	0.006	0.004	Bal

Table 2. The mechanical properties of the additively manufactured aluminum alloys.

Material	Yield Strength (MPa)	Elongation (%)	Hardness (HV)
AlSi7Mg	299	14.3	110.5
AlSi10Mg	280	8.1	120.7

In this work, straight groove micro-milling experiments were carried out on the top surface of the SLM samples with a water-based cutting fluid. The micro-milling machinability of two different alloy materials made by the SLM process was compared through single-factor experiments. Based on the previous preliminary experiments, the processing parameters used are listed in Table 3. Based on the fixed machining parameters n = 14,331 rpm, f_z = 2 µm/Z, and a_p = 20 µm, the spindle speed varied in the range of (9554~23,885) rpm, the corresponding cutting velocity was (30~75) m/min, the feed rate was selected to vary in the scope of (1~4) µm/Z, and the variation range of the milling depth was (20~50) μm. During micro-milling experiments, the cutting force in the micro-milling process was measured using a dynameter (9257B, Kistler, Winterthur, Switzerland) with a sampling frequency of 20 kHz. The cutting force data were then analyzed by Dyno Ware software to obtain the cutting force results. After micro-milling, the burr width was tested using the optical microscope (VHX-1000, Keyence, Osaka, Japan), and the surface roughness Ra was inspected following the feed direction at the middle position of the machined groove using a white light interferometer (NewView 7300, Zygo, Middlefield, CT, USA).

Table 3. Processing parameters.

Parameter Name and Unit	Value
Spindle speed n/rpm	9554, 14,331, 19,108, 23,885
Feed rate f_z μm/Z	1, 2, 3, 4
Milling depth a_p μm	20, 30, 40, 50

3. Results and Discussions

3.1. The Cutting Force Comparison

In micro-milling experiments, the milling force signal in the machining process was recorded using a dynameter, and the difference value between the peaks and valleys in the milling force signal was used as the milling force results. The changes in the milling force of two additively manufactured aluminum alloys under different machining parameters are shown in Figure 3. The recorded milling force includes three cutting force components perpendicular to each other: Fx is the main cutting force, Fy is the feed force, and Fz is the axial force. Through comparison, we found that the main cutting force component was the largest, followed by the feed force component, and the axial force component was far less than the other two force components.

As the spindle speed increased from 9554 to 23,885 rpm, the milling forces of two additively manufactured aluminum alloys showed a slightly increase trend. Among them, three cutting force components of AlSi7Mg increased from 0.52 N, 0.36 N, and 0.13 N to 0.84 N, 0.49 N, and 0.23 N, respectively, while three cutting force components of AlSi10Mg increased from 0.56 N, 0.38 N, and 0.23 N to 0.92 N, 0.63 N, and 0.35 N, respectively. The increase in the main component of the milling force was more significant than the axial component. Due to the good plasticity of aluminum alloys, it is easy for them to adhere to tool surfaces and form a built-up edge. Within the cutting speed range in this experiment, as the cutting speed increases, more built-up edges adhere to the tool surface, leading to a gradual increase in the milling force. It is necessary to exceed this cutting velocity scope to obtain a smaller cutting force. As the feed rate and milling depth increase, three cutting force components of two additively manufactured aluminum alloys also gradually increase. This is because the increase in these two milling parameters directly results in an increase in the cutting area during the machining process, an increase in the required cutting power, and the corresponding cutting forces also increase.

Comparing three cutting force components of two additively manufactured aluminum alloys with different Si contents, it was found that the cutting force components of AlSi10Mg during micro-milling were relatively higher than the AlSi7Mg alloy. By counting three cutting force components of two additive manufactured aluminum alloys under different machining parameters and calculating the average value, we found that the main cutting force component Fx, feed force component Fy, and axial force component Fz of AlSi10Mg were, respectively, 21.9%, 10.4%, and 30.7% higher than that of AlSi7Mg. It can be inferred from the mechanical properties of two additively manufactured aluminum alloys that the hardness of AlSi10Mg material is slightly higher than that of AlSi7Mg, which is the main reason for the increased milling force.

The resultant forces were also calculated (except the cutting force components). The resultant force comparison of two additively manufactured aluminum alloys under different machining parameters is shown in Figure 4. From the results, it was found that the resultant forces of AlSi10Mg were also larger than that of AlSi7Mg. The average resultant forces were about 11.8% larger with the increased Si content in AlSi10Mg aluminum alloys.

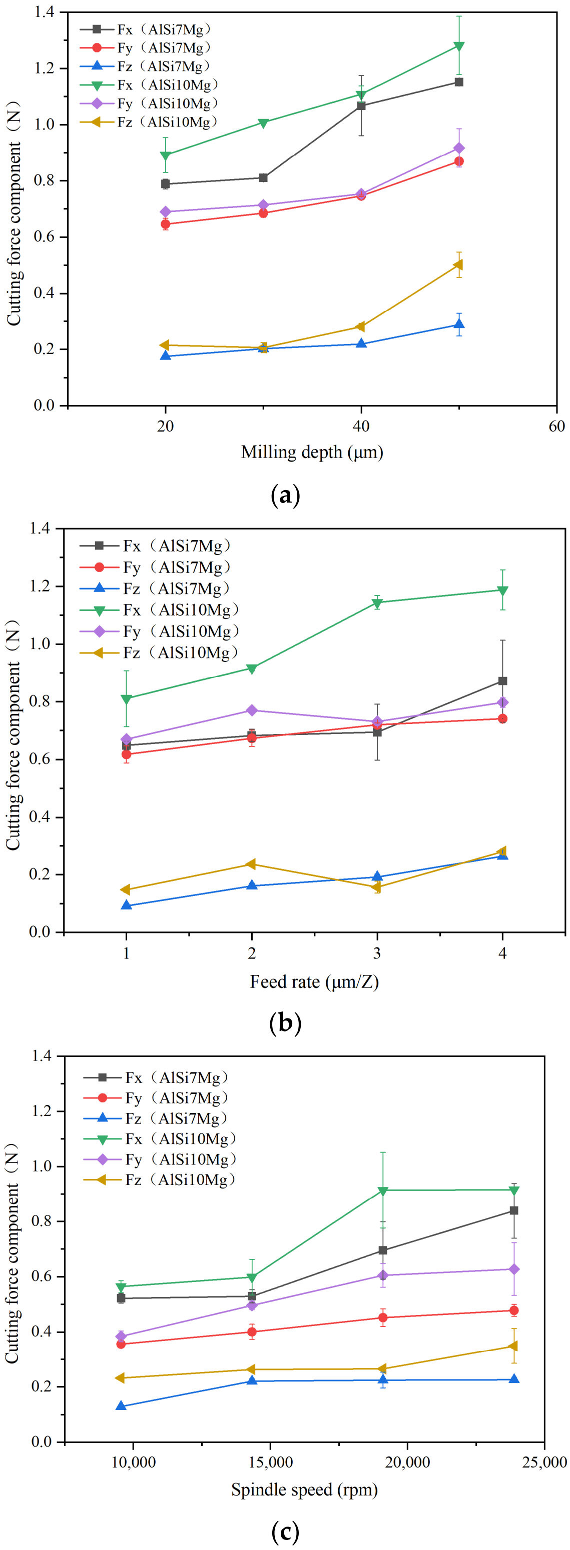

Figure 3. The milling force components comparison between additively manufactured AlSi7Mg and AlSi10Mg alloys. (**a**) The milling force components under different spindle speeds. (**b**) Milling force components under different feed rates. (**c**) Milling force components under different milling depths.

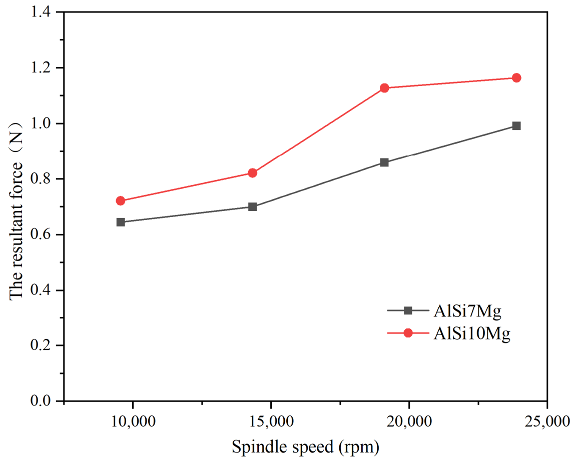

(**a**)

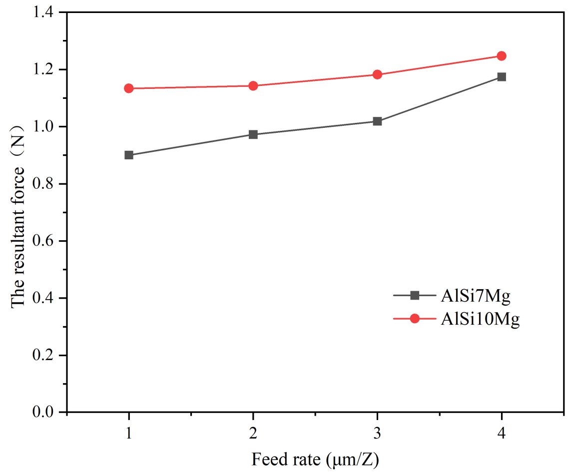

(**b**)

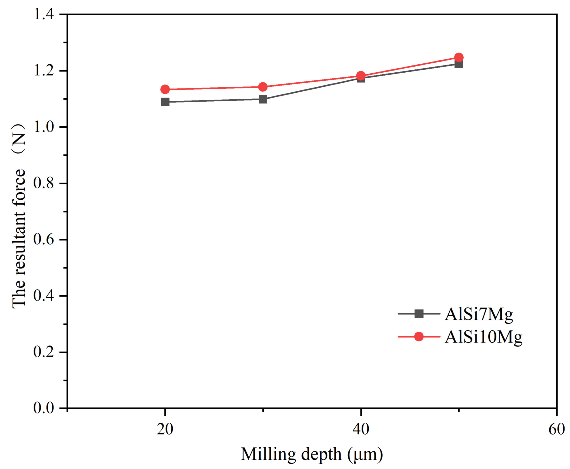

(**c**)

Figure 4. The resultant force comparison between additively manufactured AlSi7Mg and AlSi10Mg alloys. (**a**) The resultant force under different spindle speeds. (**b**) The resultant force under different feed rates. (**c**) The resultant force under different milling depths.

3.2. The Surface Roughness Comparison

In industrial production, the surface roughness is commonly used to reflect the surface quality of the mechanically processed workpieces. The main measurement methods of surface roughness include the contact and non-contact methods. Due to the fact that microgroove machined parts by micro-milling are narrow, with only a width of 1 mm, the probe in the contact measurement method cannot enter the micro-grooves to measure the surface roughness. Therefore, in this experiment, the non-contact method was employed to inspect the surface roughness Ra of the milled surface by a white light interferometer, as shown in Figure 5. Surface roughness, Ra, was measured following the feed direction at the middle position of the machined surface and was repeated three times at different positions; their average value is in the experimental results.

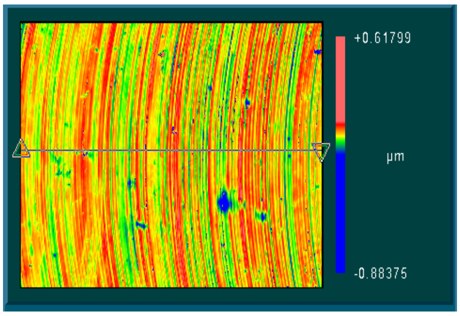

(**a**)

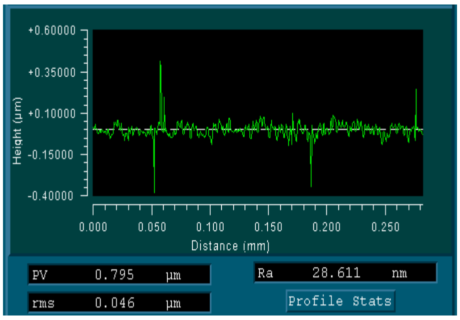

(**b**)

Figure 5. Surface roughness measurement (material: additively manufactured AlSi10Mg, parameters: n = 14,331 rpm, f_z = 2 μm/Z and a_p = 30 μm). (**a**) Surface morphology and roughness measurement direction. (**b**) Surface profile and roughness Ra.

The surface roughness of two additively manufactured aluminum alloys with different machining parameters is shown in Figure 6. From the results, with the change in machining parameters, the variation in the surface roughness trend of two additively manufactured aluminum alloys was nearly consistent. As the spindle speed increased, the inspected surface roughness showed a gradually decreasing trend. Higher cutting speeds can achieve a good machining surface quality. When the feed rate rises from 1 to 2 μm/Z, the surface roughness slightly decreases first; when the feed rate rises from 2 to 4 μm/Z, there is a significant upward trend in surface roughness. It can be seen that the surface roughness is also influenced by the minimum cutting thickness and size effect, and when the cutting thickness is too small, it forms a larger machining surface roughness. As the milling depth rises, the surface roughness slightly increases, and the effect of milling depth on the machining surface roughness seems relatively smaller than the other two machining parameters.

Comparing two additively manufactured aluminum alloy materials, it was found that the inspected surface roughness of the AlSi7Mg was relatively smaller than that of the AlSi10Mg. By calculating the averaged surface roughness of two additively manufactured aluminum alloys under different machining parameters, it was found that the surface roughness of the AlSi10Mg was 26.9% higher than that of the AlSi7Mg. This result indicates that an increase in Si content in the additively manufactured aluminum alloy will, to some extent, deteriorate the machined surface quality. From Figure 5, it was observed that there were some micro pits on the surface morphology and profile of the micro-milled surface.

During SLM, the Si phase in the aluminum alloy is easy to oxidize; then, the hard SiO_2 particle formed can fall off in the cutting process and is unfavorable to obtain a good surface quality. Hence, the increase in the Si phase in the additively manufactured aluminum alloy results in higher surface roughness in micro-milling.

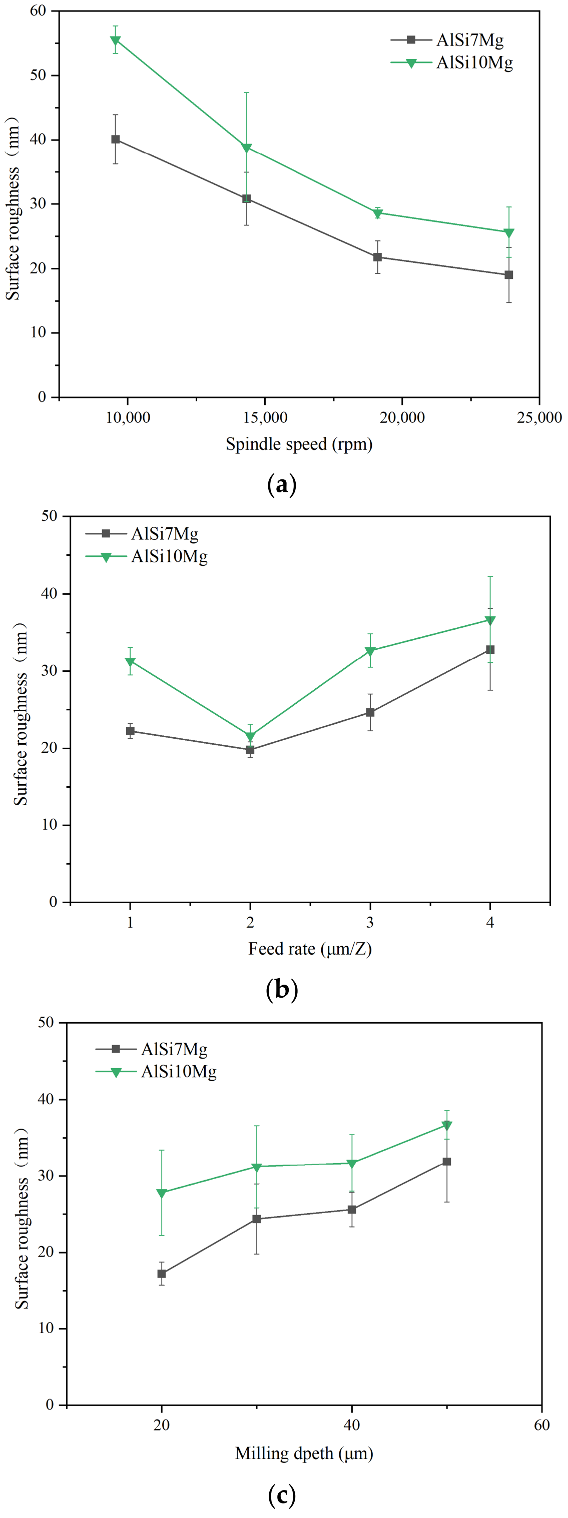

Figure 6. The surface roughness comparison between additively manufactured AlSi7Mg and AlSi10Mg alloys. (**a**) Surface roughness under different spindle speeds. (**b**) Surface roughness under different feed rates. (**c**) Surface roughness under different milling depths.

3.3. The Burr Formation Comparison

The burr located on the top edge is a common trouble that affects the machining quality and the subsequent assembly. The top burr morphologies observed during the micro-milling of the additively manufactured aluminum alloys are shown in Figure 7. From the results, it was found that the top burrs exist on the top edges of both the top and bottom milling edges. The top burr can be classified into fence shape or branch shape based on their typical morphological characteristics. The fence shape burrs are continuous, with relatively uniform width and height, similar to continuous fences erected at the machined edge. The branch shape burrs are intermittent, and their orientation is relatively consistent with the obliques to the feed direction. They are connected to the top edge of the micro-grooves just like branches, and this burr width varies greatly along the feed direction. The micro-milling process is an intermittent cutting process, and the formation of the branch shape burrs is not very stable in this intermittent cutting process.

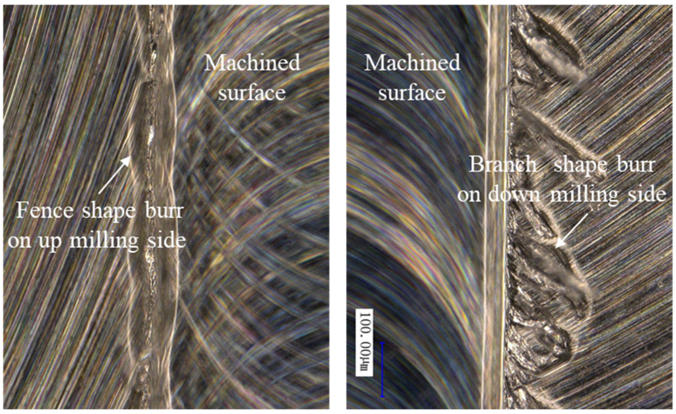

Figure 7. Burr morphology characteristics.

During the cutting process, the burrs in micro-milling are formed by two main reasons. When the cutting thickness is very small, even lower than the minimum cutting thickness, the machined material under the cutting edge does not flow along the tool rake surface but has plastically lateral flow due to the dramatic squeezing and plowing. This material plastic lateral flow behavior usually forms burrs standing upright to the machined edge, which is the fence-shaped burr, as shown in Figure 8. Additionally, some chips in the cutting process do not completely separate from the workpiece due to insufficient motivation or edge obstruction. These unseparated chips during the cutting process also form large burrs on the machined edge.

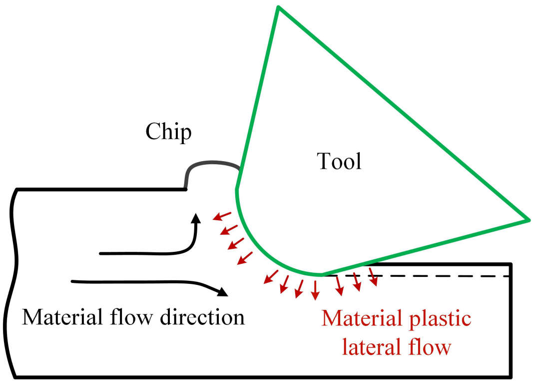

Figure 8. Material plastic lateral flow under the cutting edge.

The height and width of burrs are commonly used indicators to measure burr size. Among these two indicators, the burr width is relatively easier to measure. Therefore, in this experiment, the burr width is employed to assess burr size under different parameters. As exhibited in Figure 9, the burr width of the up-milling and down-milling edges is measured at different positions of the micro-milled groove; their averaged value is taken as the experimental results.

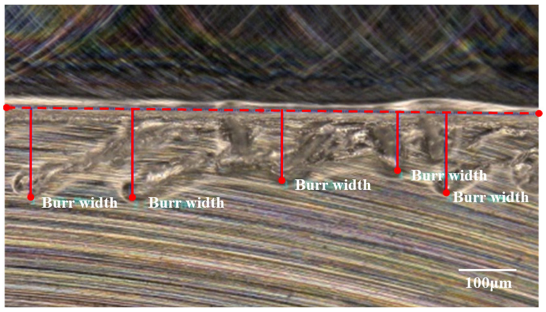

Figure 9. Burr width measurement.

The inspected burr width results with different machining parameters are shown in Figure 10. Comparing the burr size located on the up-milling and down-milling edges, the burr size on the down-milling edge are, to varying degrees, greater than those on the up-milling edge for both additively manufactured AlSi7Mg and AlSi10Mg. During the micro-milling process, with the tool rotating, the cutting edge cuts in at the up-milling edge, and its instantaneous cutting thickness gradually raises from zero to the maximum value, then cuts out at the down-milling edge, and the instantaneous cutting thickness gradually downwards to zero again, as exhibited in Figure 11. At the up-milling edge, due to the small instantaneous cutting thickness, the plastic lateral flow materials will generate fence burrs. The cutting edge pushes the unseparated chips along the cutting velocity direction from the machined edge to the unmachined area. These unseparated chips do not leave the machined edge, resulting in a smaller burr width. However, during the cutting process at the down-milling edge, the cutting edge will push some unseparated chips along the cutting velocity direction from the unmachined area to the machined edge. This behavior generates the branch-shaped burrs on the down-milling edge in each cutting pass. With the continuous feed of the tool, the branch-shaped burr continuously generates, obtaining a larger burr width.

From the results in Figure 10, the burr width of both the additively manufactured AlSi7Mg and AlSi10Mg alloys shows a consistent trend with the variation in machining parameters. As the spindle speed increases, the burr width of both materials in up-milling and down-milling edges gradually decreases. Since the feed rate increases from 1 to 3 μm/Z, the burr width gradually decreases first; when the feed rate becomes greater than 3 μm/Z, the burr width tends to stabilize and shows a slight upward trend. It can be observed that when the feed rate is too low, the cutting process is affected by the minimum cutting thickness and size effect, resulting in a larger burr width during the machining process. As the milling depth increases, the burr width of two materials in the up and down-milling edges generally shows an upward trend. With the milling depth increasing from 20 to 40 μm, the burr width is relatively stable. But since the milling depth rises from 40 to 50 μm, the burr width begins to show a relatively significant increase. When the milling depth is large, it is equivalent to a larger cutting width in the orthogonal cutting process. In this case, the larger and longer chips will be formed during the cutting process, and some of the remaining chips will be pushed and adhered to the workpiece edge, forming relatively large burr sizes.

Comparing the additively manufactured AlSi7Mg and AlSi10Mg aluminum alloys, it is found that the burr width of AlSi7Mg aluminum alloy material is relatively larger than that of AlSi10Mg. By calculating the average burr width of two materials under different processing parameters, it is indicated that the burr width on the up-milling edge of the AlSi7Mg material is 28.1% larger, and the burr width on the down-milling edge is 10.1%

higher than that of the AlSi10Mg. By comparing the mechanical properties of the additively manufactured AlSi7Mg and AlSi10Mg aluminum alloys, it was found that the elongation of the AlSi7Mg material is relatively higher than that of the AlSi10Mg; this indicates that its plasticity is relatively good and the burr size generated during micro-milling is larger.

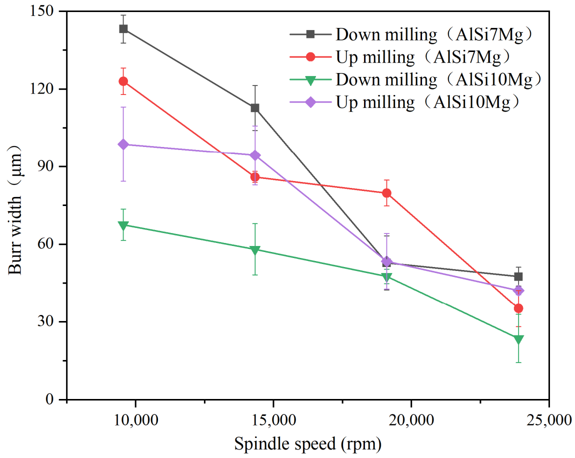

(**a**)

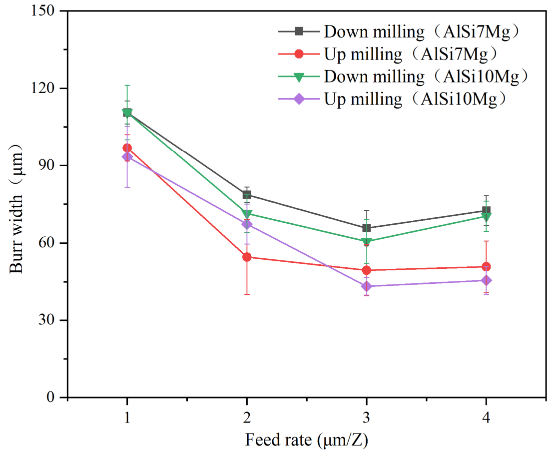

(**b**)

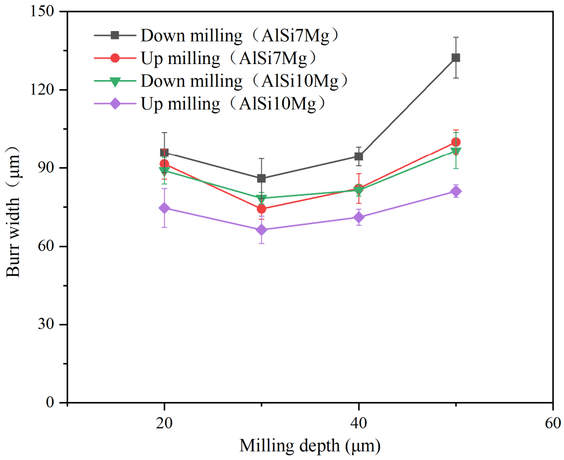

(**c**)

Figure 10. Burr width comparison between additively manufactured AlSi7Mg and AlSi10Mg alloys. (**a**) Burr width under different spindle speeds. (**b**) Burr width under different feed rates. (**c**) Burr width under different milling depths.

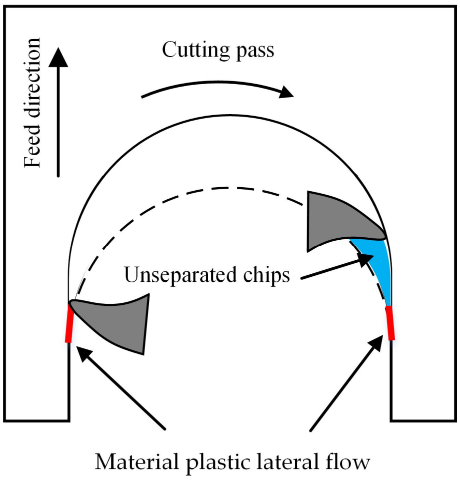

Figure 11. Burr formation in micro-milling.

4. Conclusions

In this paper, micro-milling experiments were performed on the additively manufactured AlSi7Mg and AlSi10Mg alloys with different Si contents. The effect of Si contents in the additively manufactured aluminum alloys on its micro-milling machinability was studied in terms of cutting force, surface roughness, and burr width. Based on the results, the conclusions can be drawn as follows:

1. The cutting force of the AlSi7Mg and AlSi10Mg alloys increases with the increase in cutting parameters. Because of the higher material hardness of AlSi10Mg, the cutting force component Fx is 21.9% higher, the feed force Fy is 10.4% higher, and the axial force Fz is 30.7% higher than AlSi7Mg, on average.
2. Surface roughness in the micro-milling of AlSi7Mg and AlSi10Mg alloys decreases with rising spindle speed and increases with rising feed rate and milling depth. The increased Si content of the additively manufactured aluminum alloys increases surface roughness. The surface roughness of AlSi10Mg is, on average, 26.9% higher than that of AlSi7Mg.
3. Burr morphology in the micro-milling of additively manufactured aluminum alloys can be divided into fence and branch shapes, and the burr width on the down-milling edge is greater than up milling edge. In terms of machining parameters, the burr width gradually decreases with increased spindle speed. Because of the minimum cutting thickness and size effect, the burr width first decreases and then slightly increases with the feed rate. As the milling depth increases, the burr width shows a gradual increasing trend. Due to the relatively better plasticity of the AlSi7Mg, the generated burr width during the machining process is 28.1% larger on the up-milling edge and 10.1% larger on the down-milling edge than that of the AlSi10Mg.

Author Contributions: Q.H. and X.W. guided the research idea and offered workpiece material, X.K. performed micro-milling experiments; Q.H. and X.W. were responsible for data analysis and writing the manuscript. All authors have read and agreed to the published version of the manuscript.

Funding: This work was supported by the Fujian Science and Technology Plan Project (2023H0011).

Institutional Review Board Statement: Not applicable.

Informed Consent Statement: Not applicable.

Data Availability Statement: The data that support this study are available within this article.

Conflicts of Interest: The authors declare no conflicts of interest.

References

1. Li, S.S.; Yue, X.; Li, Q.Y.; Peng, H.L.; Dong, B.X.; Liu, T.S.; Yang, H.Y.; Fan, J.; Shu, S.L.; Qiu, F.; et al. Development and applications of aluminum alloys for aerospace industry. *J. Mater. Res. Technol.* **2023**, *27*, 944–983. [CrossRef]
2. Shangguang, Y.; Wang, W.J.; He, A.R.; Ma, W.J.; Tian, H.L. Lightweight design for the aluminum alloy-carbon fiber hybrid structure of the EMU car body. *J. Mech. Sci. Technol.* **2023**, *37*, 6441–6452. [CrossRef]
3. Rometsch, P.A.; Zhu, Y.M.; Wu, X.H.; Huang, A.H. Review of high-strength aluminium alloys for additive manufacturing by laser powder bed fusion. *Mater. Des.* **2022**, *219*, 110779. [CrossRef]
4. Zhang, J.L.; Ye, J.L.; Song, B.; Li, R.D.; Shi, Y.S. Comparative study on microstructure and electrochemical corrosion resistance of Al7075 alloy prepared by laser additive manufacturing and forging technology. *J. Cent. South Univ.* **2021**, *28*, 1058–1067. [CrossRef]
5. Nzengue, A.G.B.; Mpofu, K.; Mathe, N.; Daniyan, I.; Muvunzi, R. An experimental investigation of selective laser process parameters on aluminium alloy (AlSi12). *Procedia CIRP* **2023**, *118*, 638–642. [CrossRef]
6. Kotadia, H.R.; Gibbons, G.; Das, A.; Howes, P.D. A review of Laser Powder Bed Fusion Additive Manufacturing of aluminium alloys: Microstructure and properties. *Addit. Manuf.* **2021**, *46*, 102155. [CrossRef]
7. Li, Q.; Li, G.; Lin, X.; Zhu, D.; Jiang, J.; Shi, S.; Liu, F.; Huang, W.; Vanmeensel, K. Development of a high strength Zr/Sc/Hf-modified Al-Mn-Mg alloy using Laser Powder Bed Fusion: Design of a heterogeneous microstructure incorporating synergistic multiple strengthening mechanisms. *Addit. Manuf.* **2022**, *57*, 102967. [CrossRef]
8. Liu, D.; Wu, D.; Ge, C.; Lu, H.; Chen, Z.; Liu, M.; Wang, Y.; Niu, F.; Ma, G.; Luo, K.; et al. Superior strength of laser-arc hybrid additive manufactured Al-Zn-Mg-Cu alloy enabled by a tunable microstructure. *Addit. Manuf.* **2023**, *68*, 103526. [CrossRef]
9. Fan, H.J.; Wang, Y.; Zhang, H.Q.; Guo, W.; Li, J.S.; Xu, S.B.; Li, H.X.; Liu, P. A review of laser additive manufacturing (LAM) aluminum alloys: Methods, microstructures and mechanical properties. *Opt. Laser Technol.* **2024**, *175*, 110722. [CrossRef]
10. Zhu, Z.G.; Hu, Z.H.; Seet, H.L.; Liu, T.T.; Liao, W.H.; Ramamurty, U.; Nai, S.M.L. Recent progress on the additive manufacturing of aluminum alloys and aluminum matrix composites: Microstructure, properties, and applications. *Int. J. Mach. Tools Manuf.* **2023**, *190*, 104047. [CrossRef]
11. Mao, Y.; Chen, H.; Xiong, J. Research progress in laser additive manufacturing of aluminum alloys: Microstructure, defect, and properties. *J. Mater. Res. Technol.* **2024**, *30*, 695–716. [CrossRef]
12. Malakizadi, A.; Mallipeddi, D.; Dadbakhsh, S.; M'Saoubi, R.; Krajnik, P. Post-processing of additively manufactured metallic alloys—A review. *Int. J. Mach. Tools Manuf.* **2022**, *179*, 103908. [CrossRef]
13. Lizzul, L.; Sorgato, M.; Bertolini, R.; Ghiotti, A.; Bruschi, S. Influence of additive manufacturing-induced anisotropy on tool wear in end milling of Ti6Al4V. *Tribol. Int.* **2020**, *146*, 106200. [CrossRef]
14. Randolph, O.; Kazi, A.; Lin, T.; Zvanut, R.; Tai, B. Single point machining of A205 aluminum: A comparison of cast and additively manufactured materials. *J. Manuf. Process.* **2024**, *110*, 252–262. [CrossRef]
15. Biffi, C.A.; Bassani p Fiocchi, J.; Giuranno, D.; Novakovic, R.; Tuissi, A.; Ricci, E. Investigation of high temperature behavior of AlSi10Mg produced by selective laser melting. *Mater. Chem. Phys.* **2021**, *259*, 123975. [CrossRef]
16. Zhou, S.Y.; Wu, H.; Li, X.D.; Yin, J.; Wang, X.M.; Wang, H.Y.; Li, B.B.; Guo, X.P.; Yang, G. Effects of annealing on periodic microstructure and mechanical properties of inter-layer hammering hybrid wire arc additively manufactured aluminum alloy. *CIRP J. Manuf. Sci. Technol.* **2024**, *49*, 28–39. [CrossRef]
17. Schimbäck, D.; Kaserer, L.; Mair, P.; Mohebbi, M.S.; Staron, P.; Maier-Kiener, V.; Letofsky-Papst, I.; Kremmer, T. Advancements in metal additive manufacturing: In-situ heat treatment of aluminium alloys during the laser powder bed fusion process. *Mater. Sci. Eng. A* **2024**, *14*, 146102. [CrossRef]
18. Wu, X.; Chen, Z.; Ke, W.; Jiang, F.; Zhao, M.; Li, L.; Shen, J.; Zhu, L. Investigation on surface quality in micro milling of additive manufactured Ti6Al4V titanium alloy. *J. Manuf. Process.* **2023**, *101*, 446–457. [CrossRef]
19. Segebade, E.; Gerstenmeyer, M.; Dietrich, S.; Zanger, F.; Schulze, V. Influence of anisotropy of additively manufactured AlSi10Mg parts on chip formation during orthogonal cutting. *Procedia CIRP* **2019**, *82*, 113–118. [CrossRef]
20. Tan, R.K.; Zhao, X.S.; Liu, Q.; Guo, X.M.; Lin, F.T.; Yang, L.Q.; Sun, T. Investigation of Surface Integrity of Selective Laser Melting Additively Manufactured AlSi10Mg Alloy under Ultrasonic Elliptical Vibration-Assisted Ultra-Precision Cutting. *Materials* **2022**, *15*, 8910. [CrossRef]
21. Li, G.; Chandra, S.; Rashid, R.A.; Palanisamy, S.; Ding, S. Machinability of additively manufactured titanium alloys: A comprehensive review. *J. Manuf. Process.* **2022**, *75*, 72–99. [CrossRef]
22. Chen, Z.W.; Wu, X.; He, L.J.; Jiang, F.; Shen, J.Y.; Zhu, L.F. Comparative study on micro-milling machinability of titanium alloys prepared by different processes: Forging process, additive manufacturing process and heat-treatment process. *Precis. Eng.* **2024**, *88*, 164–176. [CrossRef]
23. Silva, T.E.F.; Amaral, A.; Couto, A.; Coelho, J.; Reis, A.; Rosa, P.A.R. Comparison of the machinability of the 316L and 18Ni300 additively manufactured steels based on turning tests. *Proc. Inst. Mech. Eng. Part L-J. Mater. -Des. Appl.* **2021**, *235*, 2207–2226. [CrossRef]

24. Li, X.; Zhu, Q.; Kong, S.; Kang, Y.; Wang, X.; Ni, J. Study on the structure and properties of the AlSi10Mg samples produced by 3D printing. *Mater. Sci. Technol.* **2019**, *27*, 16–21. (In Chinese)
25. Zou, T.; Chen, M.; Zhu, H.; Mei, S. Effect of Heat Treatments on Microstructure and Mechanical Properties of AlSi7Mg Fabricated by Selective Laser Melting. *J. Mater. Eng. Perform.* **2022**, *31*, 1791–1802. [CrossRef]

materials

Article

Study on Characteristics of Ultrasound-Assisted Fracture Splitting for AISI 1045 Quenched and Tempered Steel

Yinfang Jiang [1,2,*], Yangyang Wang [1], Xiancheng Liu [1], Deli Sha [1] and Mengcheng Zhu [1]

1 School of Mechanical Engineering, Jiangsu University, Zhenjiang 212000, China; 2212103064@stmail.ujs.edu.cn (Y.W.)
2 College of Mechanical Engineering, Nantong Institute of Technology, Nantong 226000, China
* Correspondence: 13914567669@163.com or yfjiang@ujs.edu.cn

Abstract: Ultrasonic vibration-assisted con-rod fracture splitting (UV-CFS) was used to carry out the fracture experiment of 1045 quenched and tempered steel. The effect of ultrasonic vibration on the fracture properties was studied, the fracture microstructure and the evolution of dislocations near the fracture were analyzed and the microscopic mechanism was analyzed. The results show that in the case of conventional fracture splitting without amplitude, the dimple and the fracture belong to ductile fracture. With the increase in ultrasonic amplitude, the plasticity and pore deformation of the con-rod samples decrease at first and then increase; when the amplitude reaches a certain point, the load required for cracking is reduced to a minimum and the ultrasonic hardening effect is dominant, resulting in a decrease in the plasticity of the sample, a cleavage fracture, a brittle fracture, the minimum pore deformation and high cracking quality. The research results also show that with the increase in ultrasonic amplitude, the fracture dislocation density decreases at first, then increases, and dislocation entanglement and grain breakage appear, then decrease, and multiple dislocation slip trajectories appear. The changes in the dislocation density and microstructure are consistent with the above results.

Keywords: con-rod fracture splitting; ultrasonic vibration; ultrasonic amplitude; cracking force; microstructure

1. Introduction

As the key parts of the engine, the con-rod bears a high thrust load, which has high requirements for its fatigue performance [1], which has high requirements for its fatigue performance. In order to improve the strength and anti-fatigue performance of the con-rod, there are higher requirements for its materials and processing methods [2]. The traditional con-rod machining requires the grinding, broaching and milling of the connecting surface of the con-rod cover and the con-rod body and then carries on the matching work between the con-rod cover and the con-rod body, which is tedious and costly.

Compared with the traditional method, con-rod fracture splitting (CFS) [3] has significant advantages; it fundamentally changes the con-rod production process, which can reduce the con-rod manufacturing process, reduce the investment in equipment and tools and save energy [4]. As a result, the production cost is greatly reduced, the product quality and bearing capacity are improved and a route of high quality, high precision and low cost is provided for the production of the con-rod [5].

At present, with con-rod fracture splitting, it is easy to produce quality defects on the fracture surface and serious deformation of the crank bore in the fracture process [6], so it puts forward higher requirements for the materials used for fracture splitting, requiring the materials to have the characteristic of brittle fracture at room temperature, which seriously limits the selection of cracking materials [7]. At present, the main cracking materials are powder metallurgy, high carbon steel, nodular cast iron and malleable cast iron [8], but the cost of powder metallurgy and high carbon steel is high, and the mechanical properties of cast iron make it difficult to meet the requirements of the con-rod, which hinders the development of fracture splitting.

Quenched and tempered 1045 steel has characteristics of low cost, high strength and good toughness, which meets the working environment of alternating the composite of the con-rod, and is very suitable for the manufacturing material of the con-rod [9]. However, the cracking force of quenched and tempered 1045 steel is too large, which makes it easy to produce large fracture deformation and poor cracking quality, so it is necessary to improve the cracking process of the con-rod [10].

Ultrasound has special potential to improve product quality, reduce production cost and improve production efficiency. At present, ultrasound is widely used in many important fields, such as machining, material forming and preparation, chemistry, medicine and health, textiles, energy saving and environmental protection, bioengineering and so on. The authors of [11,12] used Longitudinal–Torsional Ultrasonic-Assisted Milling (LTUAM) to process Ti-Al6-4V and successfully fabricated micro-dimpled surface textures on Ti-Al6-4V; compared with Conventional Milling (CM), a noticeable decrease in the cutting force was observed in LTUAM. Ni et al. [13] investigated the effect of ultrasonic vibration-assisted milling (UVAM) and minimum quantity lubrication (MQL) on the machining performance of TC4 alloy; the results show that cutting force features could be significantly affected under the UVAM and UVAM&MQL condition compared with that in general milling, and the uniform micro-textured surfaces with improved profile fluctuations could be obtained when applying the UVAM&MQL strategy.

Some scholars have found that the application of ultrasonic vibration in tensile tests of materials such as zinc, magnesium and nickel promotes grain refinement, improves material plasticity and reduces both yield stress and flow stress [14,15]. Storck et al. [16] found that ultrasonic vibration has both acoustic softening and hardening effects on materials. Wen et al. [17] discovered that when the applied ultrasonic amplitude is small, the softening effect predominates, leading to increased material plasticity, while at larger amplitudes, the hardening effect becomes dominant. Because the excessive amplitude leads to the early fracture of the material, and the plasticity of the material decreases to a certain extent, at this time, the hardening effect is dominant. And with the increase in amplitude, the deformation resistance of materials decreases at first and then increases [18]. When the amplitude reaches a certain value, the softening effect of the material is the most obvious, and the fracture is cup-cone-shaped with obvious necking, which is a typical ductile fracture. But with the continuous increase in the amplitude, the deformation resistance of the material increases and the elongation decreases. When the amplitude increases to a certain value, the section of the material changes to brittle transgranular fracture [19].

Although many people have conducted a series of studies on ultrasound-assisted technology, no one has applied ultrasound to CFS. Therefore, based on the new technology of ultrasonic vibration-assisted con-rod fracture splitting (UV-CFS), the effect of ultrasonic amplitude on the behavior of con-rod fracture splitting is studied systematically for the first time in this paper. Through the characterization of crack propagation and the cracking force, fracture morphology and dislocation structure of the con-rod, it is found that the reasonable combination of the acoustic "softening" and acoustic "hardening" effects of ultrasonic vibration can effectively reduce the cracking force and improve the brittleness of the material. In this study, ultrasonic vibration is introduced into con-rod fracture splitting for the first time, which reduces the harshness of the con-rod cracking material and provides a promising auxiliary process for con-rod fracture splitting.

2. Materials and Methods

2.1. Materials and Devices

The specimen material selected for this paper is tempered 1045 steel, whose chemical composition is shown in Table 1, and the mechanical parameter table is shown in Table 2.

Table 1. Chemical composition of 1045 steel (wt%).

C	Si	Mn	P	S	Cr	Ni	Cu
0.42~0.50	0.17~0.37	0.50~0.80	≤0.045	≤0.06~0.07	≤0.25	≤0.30	≤0.25

Table 2. Mechanical parameters of 1045 steel.

Material	E/MPa	Poisson's Ratio (v)	Yield Strength σ_s/MPa	Tensile Strength σ_b/MPa	Rupture Stress σ_f/MPa	Rupture Strain ε_f/MPa
1045 steel	210	0.3	710	993	1727	0.21545

The ultrasonic-assisted fracture splitting stretcher, as shown in Figure 1, consists of a stretcher, an ultrasonic-assisted fracture splitting machine and an ultrasonic power supply. The cracking device is mainly composed of an upper T-block, upper T-block fixed plate, upper pull rod, wedge tool head, right expansion sleeve, left expansion sleeve, sample placement plate, horn, horn fixed circular plate, horn fixed square plate, lower pull rod, transducer, lower T-block fixed plate, lower T-block and ultrasonic power supply.

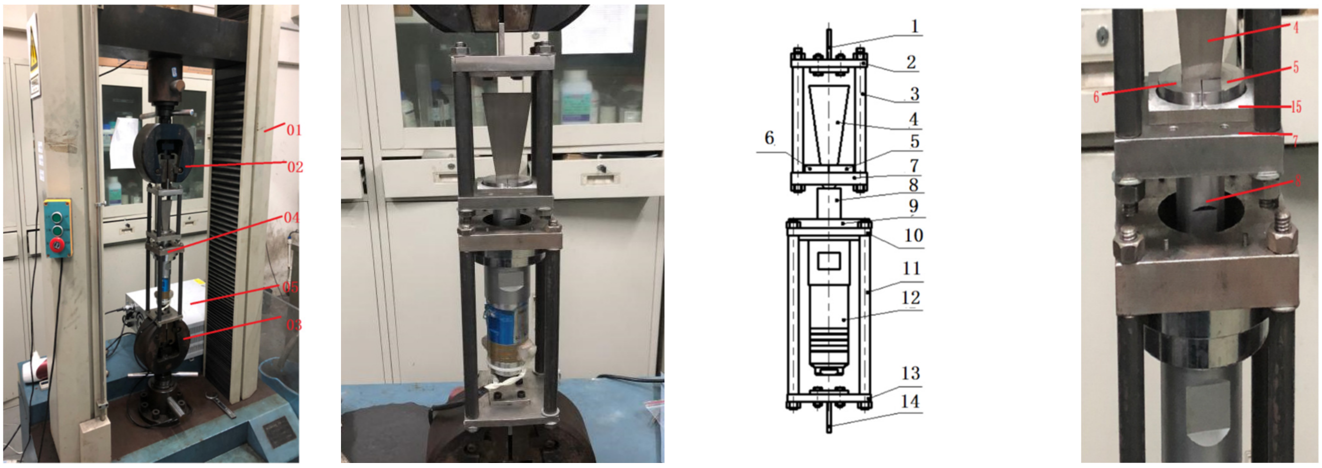

(**a**) (**b**) (**c**) (**d**)

Figure 1. (**a**) Ultrasonic-assisted fracture splitting stretcher, (**b**) cracking device, (**c**) schematic diagram of cracking unit, (**d**) installation of cracking sample. 01. Stretcher, 02. upper chuck, 03. lower chuck, 04. cracking unit, 05. ultrasonic power supply; 1. upper T-shaped block (clamping), 2. upper T-block fixing plate, 3. pull up rod, 4. wedge tool head, 5. right bulging sleeve, 6. left bulging sleeve, 7. sample placement plate, 8. horn, 9. horn fixed circular plate, 10. horn fixed square plate, 11. pull rod, 12. transducer, 13. lower T-block fixing plate, 14. lower T-shaped block (clamping), 15. sample.

The size of the wedge-shaped tool head was designed according to the half-wavelength theory; the length of the wedge-shaped tool head is about half the wavelength of ultrasonic wave propagation in 1045 steel. The wedge angle of the wedge-shaped tool head is designed to be 16°, the width of the smaller end face is 15 mm, the length between the upper and lower end faces is 135 mm and the thickness is 10 mm. The modal analysis of the tool head was carried out by using the Abaqus finite element analysis software to verify the size of the designed tool head to ensure that when the wedge tool head was connected with the horn, the stress amplitude at the small end of the wedge-shaped tool head was the maximum. The wedge-shaped tool head and the small end of the horn are closely connected and are fixed by M8 × 20 fine thread bolts.

The 1045 steel [20] used in the sample is quenched in brine at 840 °C and tempered for two hours at 520 °C. The hardness after heat treatment is around HRC 26. The cracking sample is shown in Figure 2. The crack groove is machined by a laser, the groove depth is

0.6 mm and the groove width is 0.2 mm. Ultrasonic vibration-assisted fracture splitting is shown in Figure 3. The stretcher adopts a microcomputer to control Electro-mechanical Universal Testing Machines (WDW-2000). The ZJS-2000 ultrasonic generator and piezoelectric ceramic transducer are adopted, and the vibration frequency is 20 KHz. Ultrasonic vibration is transmitted to the expansion sleeve through the wedge tool head and then to the sample.

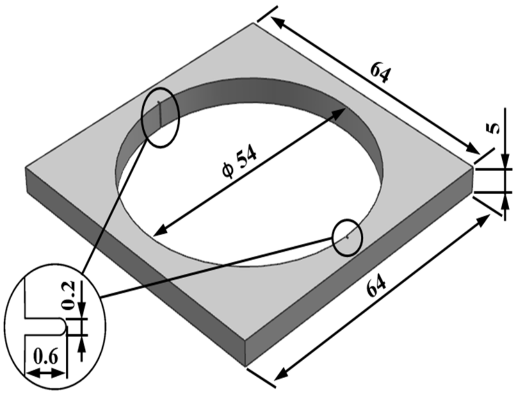

Figure 2. Cracking sample (unit: mm).

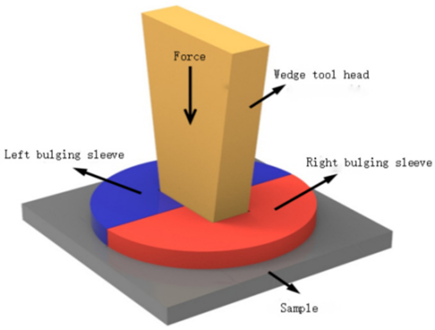

Figure 3. Schematic diagram of ultrasonic vibration-assisted cracking.

2.2. Cracking Force

The schematic diagram of the force analysis of the cracking unit is shown in Figure 4, the wedge-shaped tool head is treated as an isolator and the equilibrium equations for forces in the x and y directions are presented:

$$\sum F_y = 0,\ Q = 2(N_2 sin\frac{\alpha}{2} + F_2 cos\frac{\alpha}{2}) \tag{1}$$

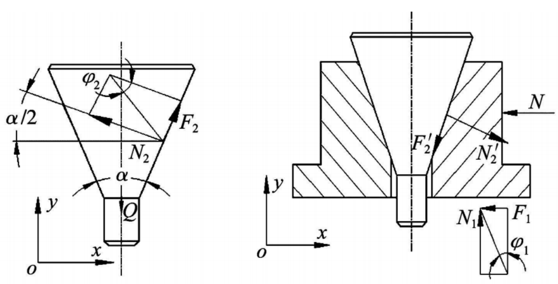

Figure 4. Schematic diagrams of force analysis of cracking unit.

The friction angle of the contact surface between the bulging sleeve and the supporting platform is φ_1, then there are the following:

$$\frac{F_1}{N_1} = tan\varphi_1 = \mu_1 \tag{2}$$

Let the friction angle of the contact surface between the wedge tool head and the bulging sleeve be φ_2, then there are the following:

$$\frac{F_2}{N_2} = tan\varphi_2 = \mu_2 \tag{3}$$

Treat the bulging sleeve as an isolated body, and then analyze the forces separately, and list the equilibrium equations for the forces in the x, y directions:

$$\sum F_x = 0,\ N = N_2{}'cos\frac{\alpha}{2} + F_2{}'sin\frac{\alpha}{2} - F_1 \tag{4}$$

$$\sum F_y = 0,\ N_1 = N_2{}'sin\frac{\alpha}{2} + F_2{}'cos\frac{\alpha}{2} \tag{5}$$

The ratio i_p of the cracking force N to the drawing force Q of the stretcher is obtained by combining and solving Formulas (1)–(5):

$$i_p = \frac{cos\frac{\alpha}{2} + tan\varphi_2 sin\frac{\alpha}{2} - tan\varphi_1 sin\frac{\alpha}{2} - tan\varphi_1 tan\varphi_2 cos\frac{\alpha}{2}}{2sin\frac{\alpha}{2} + 2tan\varphi_1 cos\frac{\alpha}{2}} \tag{6}$$

In the above formula, Q is the pulling force of the stretcher on the wedge-shaped rod, N is the cracking force, N_1 and N_2 are the pressure on the expanding sleeve and the wedge-shaped rod, respectively, F_1 and F_2 are the friction force, α is the angle of the wedge-shaped rod and μ_1 and μ_2 are the corresponding friction coefficients, respectively.

2.3. Characterization Methods

The fracture morphology of the sample was observed by a JSM-7800F field emission scanning electron microscope of Nippon Electronics Corporation (Beijing, China). The deformation degree of the sample was measured by a 19JPC universal toolmaker's microscope. Each sample was measured 3 times, and the average value was taken. The XRD was detected by a Japanese ultra X TTR III X-ray diffractometer, the accelerating voltage was 48 kV, the current was 100 mA, the scanning step was 0.02° and the range of the 2θ angle was 32–88°. TEM transmission was performed using a Nippon Electronics Corporation (Beijing, China) high-resolution transmission electron microscope with an accelerating voltage of 200 KV, a point resolution of 0.24 nm, tilt angle of samples: $\geq \pm 35°$.

In this experiment, the amplitude is controlled by adjusting the gear position of the ultrasonic generator, adjusting the ultrasonic amplitude to 0 μm, 6 μm, 15 μm, 25 μm and 30 μm, respectively, with 3 samples in each group. Initiate the tensile machine and apply tension until the specimen fractures completely at a fracture speed of 20 mm/min. Record the obtained tension and displacement data, and calculate the fracture force value using Equation (2). After fracture completion, document the deformation in the parallel fracture force direction of the specimen at different amplitudes (change in L before and after fracture) and the deformation in the perpendicular fracture force direction (change in H before and after fracture), as shown in Figure 5.

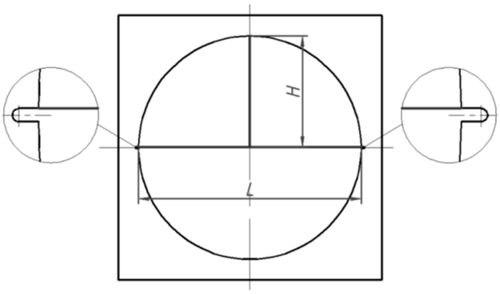

Figure 5. Definition of deformation.

3. Results

3.1. Effect of Ultrasonic Amplitude on Cracking Force

The variation curve of the cracking force of the sample and the displacement of the stretcher with different amplitude is shown in Figure 6. At the beginning of tension, the cracking force of the sample with ultrasonic amplitude decreased greatly compared with the sample without amplitude under the same displacement, and the decrease was more obvious with the increase in amplitude; when the sample was at low amplitude (6 μm, 15 μm), the cracking force at fracture decreased compared with that without amplitude, and when the sample was at high amplitude (25 μm, 30 μm), the cracking force at fracture was greater than that without amplitude. The deformation of the sample with ultrasonic vibration-assisted cracking is smaller than that without vibration. When the amplitude is 15 μm, the deformation of the sample at fracture is the smallest, and the load required for cracking is reduced by 53.2%, and the displacement of the stretcher is reduced by 43.1%. With the increase in amplitude, the cracking force and the displacement of the stretcher show a trend of decreasing at first and then increasing. In short, ultrasonic vibration can effectively delay the increase in the cracking force (Figure 7) and reduce the displacement of the stretcher; low-amplitude ultrasound can also reduce the cracking force; there may be an amplitude parameter most suitable for cracking near the amplitude of 15 μm.

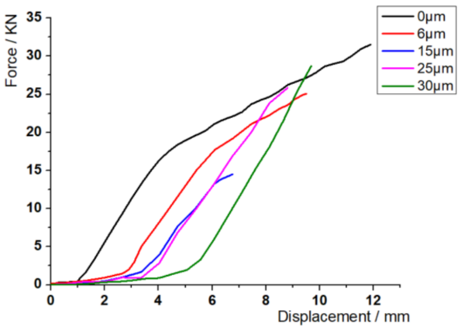

Figure 6. Force–displacement curves.

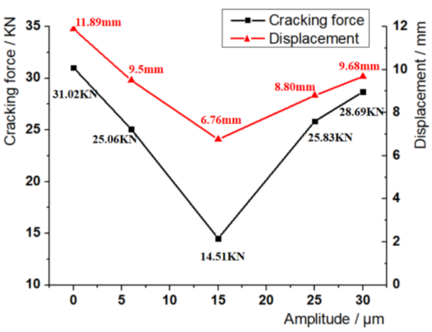

Figure 7. Amplitude–cracking force and amplitude–displacement curve.

3.2. Effect of Ultrasonic Amplitude on Hole Deformation

3.2.1. Macro-Deformation at the Cracking Section

Figure 8 shows the side macrograph of the cracking fracture at different amplitudes of 0 μm, 6 μm, 15 μm, 25 μm and 30 μm. The deformation of the fracture surface of the ordinary non-amplitude cracking sample is large, and there is necking. When the amplitude increases to 6 μm, the fracture necking phenomenon is more obvious, and there is an obvious 45° shear lip on the right side of the fracture surface. It shows that ultrasonic "softening" plays a dominant role when the amplitude is 6 μm. When the amplitude increases to 15 μm, the fracture surface is flat and the necking phenomenon disappears, indicating that "acoustic hardening" is dominant. When the amplitude continues to increase to 25 μm, the necking phenomenon begins to appear again from the side of the fracture, and the fracture surface is still flat. When the amplitude increases to 30 μm, the necking phenomenon is more obvious from the side of the fracture. It can be seen that the increase in ultrasonic amplitude will lead to the necking phenomenon of the fracture surface first enhanced, then weakened and then strengthened. When the amplitude is near 6 μm, "acoustic softening" is dominant, and the material hardens gradually with the increase in the amplitude. There is a threshold or turning point near the amplitude of 15 μm, and the material softens gradually when the amplitude is higher than this threshold.

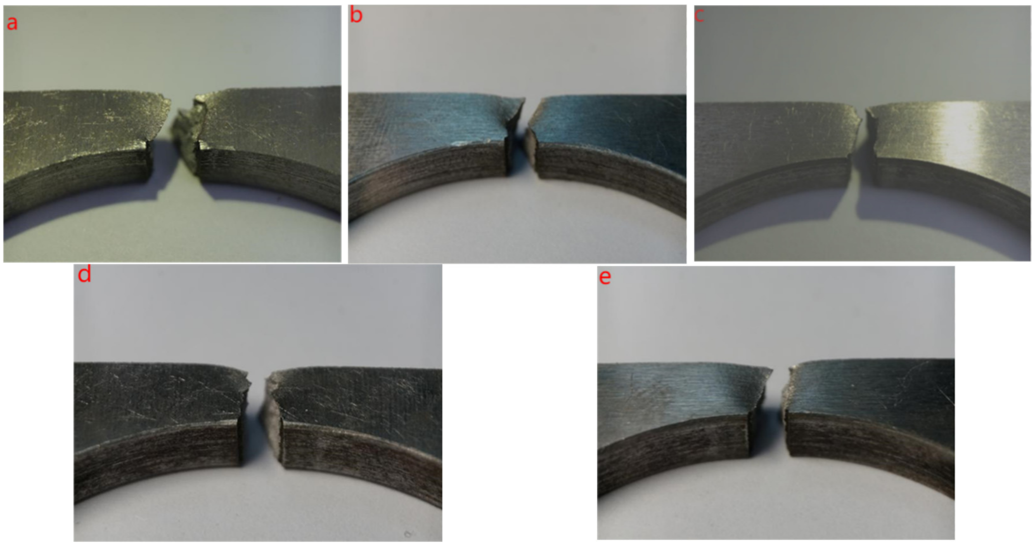

Figure 8. Macrograph of side and fracture after splitting of (**a**) 0 μm, (**b**) 6 μm, (**c**) 15 μm, (**d**) 25 μm, (**e**) 30 μm.

3.2.2. Hole Deformation after Cracking

Measured by the universal toolmaker's microscope, the results of hole deformation after cracking are shown in Table 3, and the trend curve of hole deformation under different amplitudes is shown in Figure 9. It can be seen from Figure 9 that the change in amplitude has little effect on (L/2) and has a great influence on H. The high-frequency vibration assistant can not necessarily reduce the deformation of the crank bore, and when the amplitude is 6 μm, the deformation of the sample increases sharply, which is significantly higher than that of the conventional non-vibration cracking, which may be because that the low-amplitude high-frequency vibration improves the plasticity of the sample, so that the "softening effect" plays a leading role. When the amplitude is 15 μm, the deformation in the H and L direction decreases, and the cracking quality is improved. The smallest deformation is produced on samples, and there may be a range of amplitude so that the "hardening effect" is dominant, which is more suitable for the cracking of the con-rod. When the amplitude is higher than 15 μm, the deformation of the crank bore increases continuously with the increase in the amplitude, even larger than that of the conventional cracking, which may be due to the transformation of more ultrasonic energy from high-frequency mechanical vibration to thermal energy transfers to the con-rod sample, which in turn improves the plasticity of the material.

Table 3. Measurement of hole size deformation.

NO.	Amp/µm	Before L/2/mm	After L/2/mm	Δ(L/2)/mm	Before H/mm	After H/mm	ΔH/mm	Deform/mm
1		26.940	26.739	0.201	26.718	27.423	0.705	0.906
2	0	26.933	26.718	0.215	26.708	27.428	0.720	0.935
3		26.899	26.665	0.234	26.634	27.362	0.728	0.962
4		26.960	26.635	0.325	26.817	28.305	1.488	1.813
5	6	26.863	26.523	0.340	26.713	28.128	1.415	1.755
6		26.930	26.583	0.347	26.655	28.145	1.490	1.837
7		26.945	26.727	0.218	26.869	27.255	0.386	0.604
8	15	26.864	26.632	0.232	26.734	27.130	0.396	0.628
9		26.835	26.597	0.238	26.708	27.101	0.393	0.631
10		26.945	26.690	0.255	26.723	27.354	0.631	0.886
11	25	26.860	26.597	0.263	26.321	27.060	0.739	1.002
12		26.935	26.668	0.267	26.708	27.404	0.696	0.963
13		27.028	26.711	0.317	26.302	27.282	0.980	1.297
14	30	26.946	26.648	0.298	26.450	27.423	0.973	1.271
15		26.867	26.563	0.304	26.653	27.708	1.055	1.359

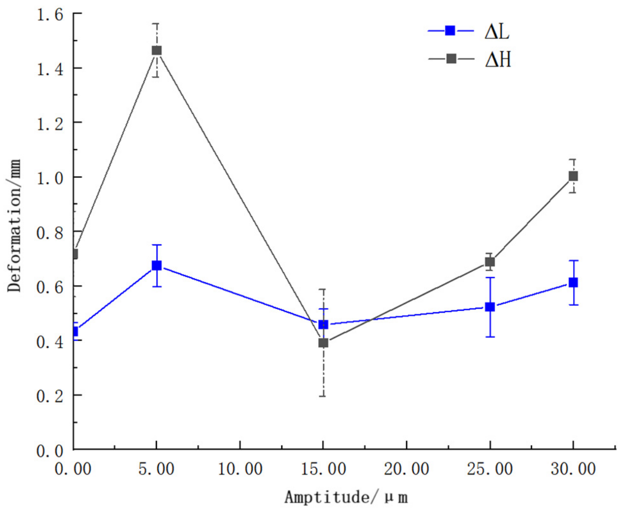

Figure 9. Trend curve of hole deformation of samples under different amplitude.

3.3. Effect of Ultrasonic Amplitude on Microstructure

Divide the macro-fracture into three regions: the initiation region, extension region and termination region. Figure 10 shows the fracture morphology of the sample under conventional cracking without amplitude. From the micrograph of each area of the fracture (Figure 10b–d), there are a large number of dimples in each area, so it can be inferred that the fracture form under no amplitude is mainly ductile fracture.

Figure 11 shows the fracture morphology of the sample when the amplitude is 6 µm. From the crack initiation area in Figure 11b, there are river patterns and cleavage steps near the fracture splitting notch, which belong to cleavage fracture. This is mainly because the ultrasonic vibration and stretcher formed stress superposition near the fracture splitting notch in the initiation area, which accelerated crack propagation in the initiation area and formed cleavage brittle fracture. There are a large number of dimples in the expansion area of Figure 11c and the termination area of Figure 11d, which belong to ductile fracture, from which it is inferred that cleavage fracture and ductile fracture coexist under the amplitude of 6 µm.

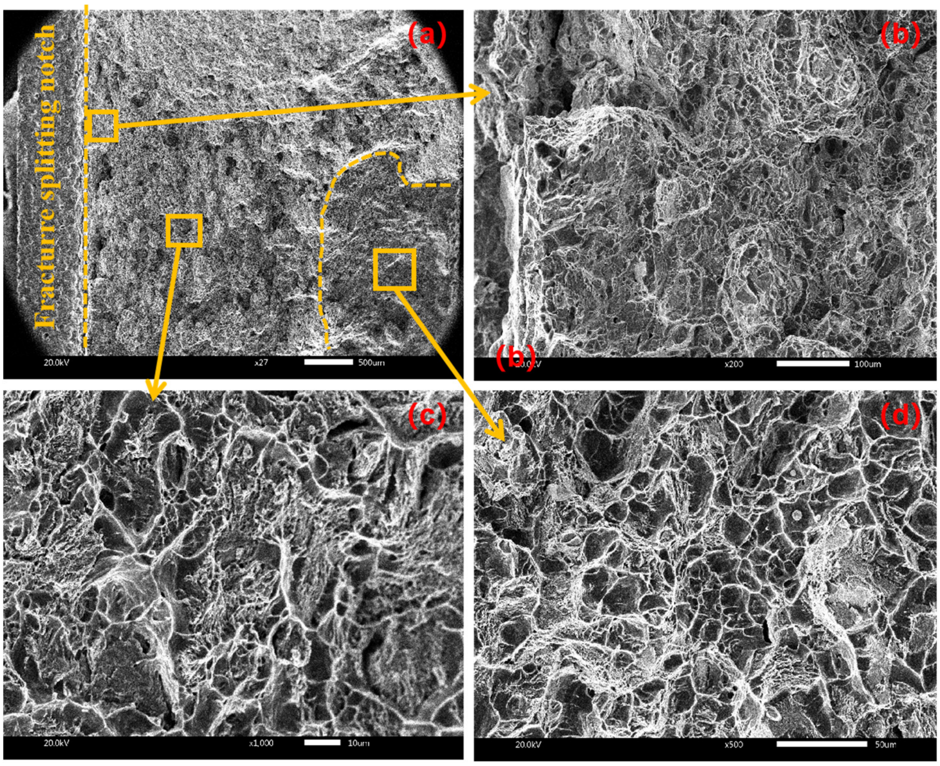

Figure 10. Fracture morphology at amplitude of 0 μm with (**a**) macroscopic fracture, (**b**) crack initiation area, (**c**) extension area, (**d**) termination area.

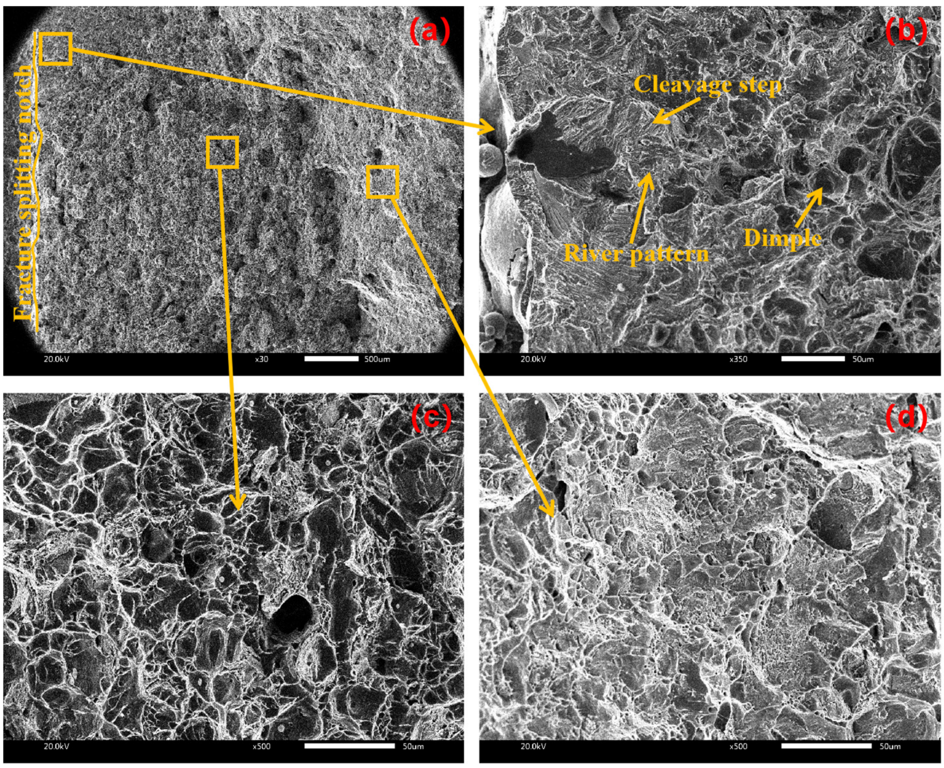

Figure 11. Fracture morphology at amplitude of 6 μm with (**a**) macroscopic fracture, (**b**) crack initiation area, (**c**) extension area, (**d**) termination area.

Figure 12 shows the fracture morphology of the sample with an amplitude of 15 μm. From the initiation area of Figure 12b, there are a large number of river patterns, which belong to cleavage fracture. From the expansion area of Figure 12c, there are many micropores and tearing edges, and the tearing edges are discontinuous, which belong to quasi-cleavage fracture. From the termination area in Figure 12d, there are lamellar delamination and a large number of short and curved tearing edges, which belong to quasi-cleavage fracture; there are also slip marks, and the slip line reflects the path of crack propagation to some extent. It is inferred that when the amplitude increases to 15 µm, the brittleness of the specimen increases, the direction of crack propagation increases and the transition from ductile fracture to cleavage fracture occurs.

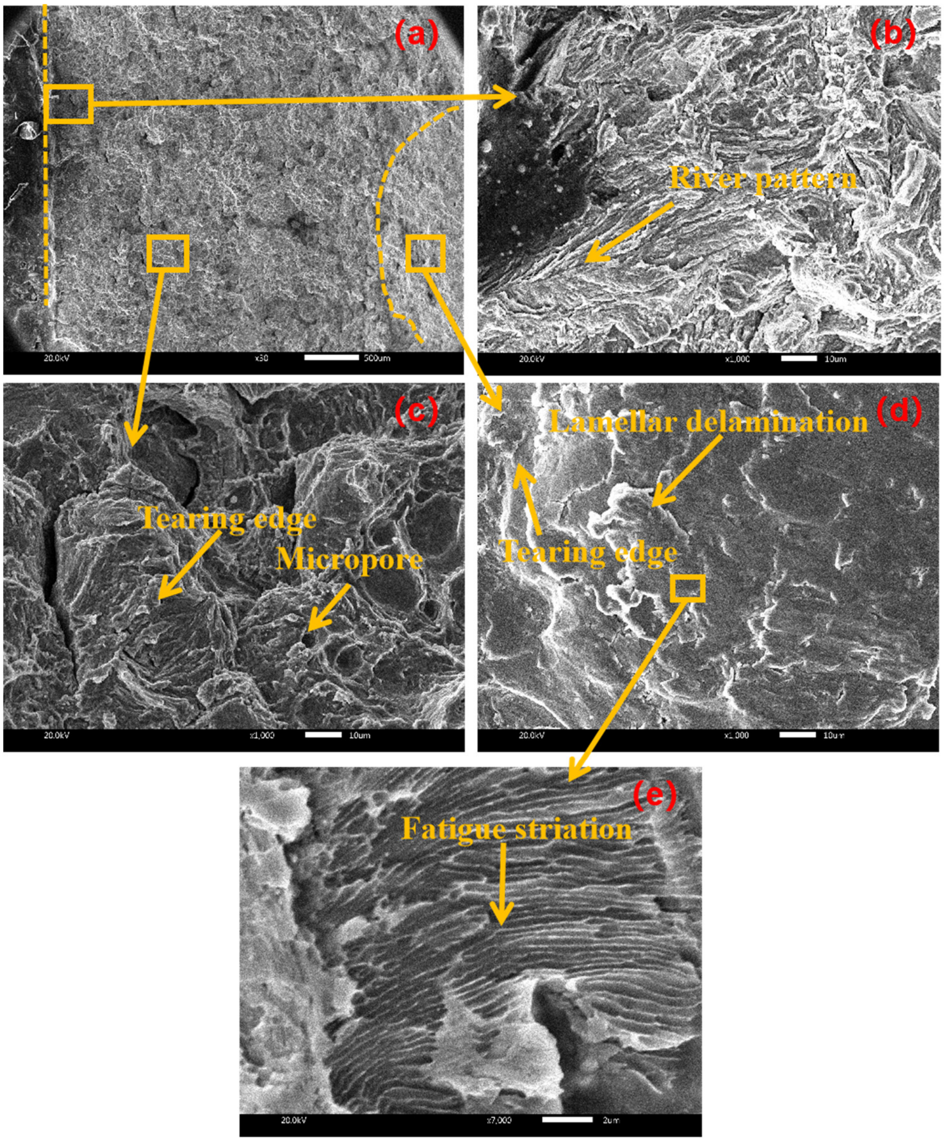

Figure 12. Fracture morphology at amplitude of 15 µm with (**a**) macroscopic fracture, (**b**) crack initiation area, (**c**) extension area, (**d**) termination area (**e**) local magnification.

Figure 13 shows the fracture morphology of the sample with amplitude 25 µm, which is similar to that of the sample with amplitude 6 µm. In Figure 13b, there are a large number of river flowers on the left side of the initiation area and dimples on the right side, indicating that the left side of the initiation area belongs to cleavage fracture and the right side belongs to ductile fracture; there are a large number of dimples in the expansion area of Figure 13c and the termination area of Figure 13d, which belong to ductile fracture. It is inferred that when the amplitude increases to 25 µm, the brittleness of the sample decreases and the plasticity increases.

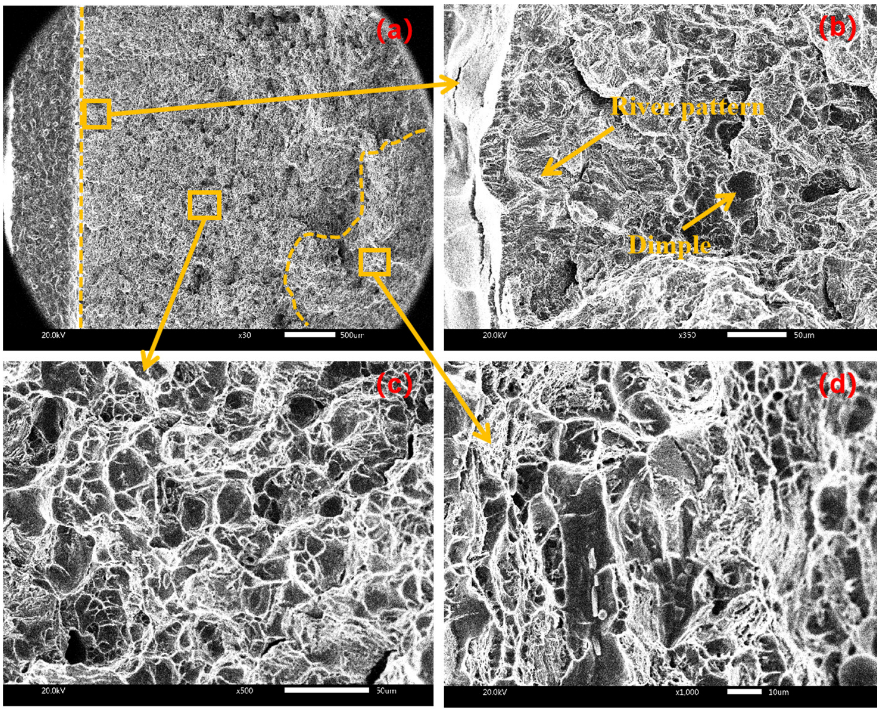

Figure 13. Fracture morphology at amplitude of 25 µm with (**a**) macroscopic fracture, (**b**) crack initiation area, (**c**) extension area, (**d**) termination area.

Figure 14 shows the fracture morphology of the sample when the amplitude is 30 µm. The left side of the initiation area is cleavage fracture, the right side is ductile fracture and there are a large number of dimples existing in the extension area and termination area, which are ductile fracture. It shows that when the amplitude is further increased, the plasticity of the sample is further strengthened.

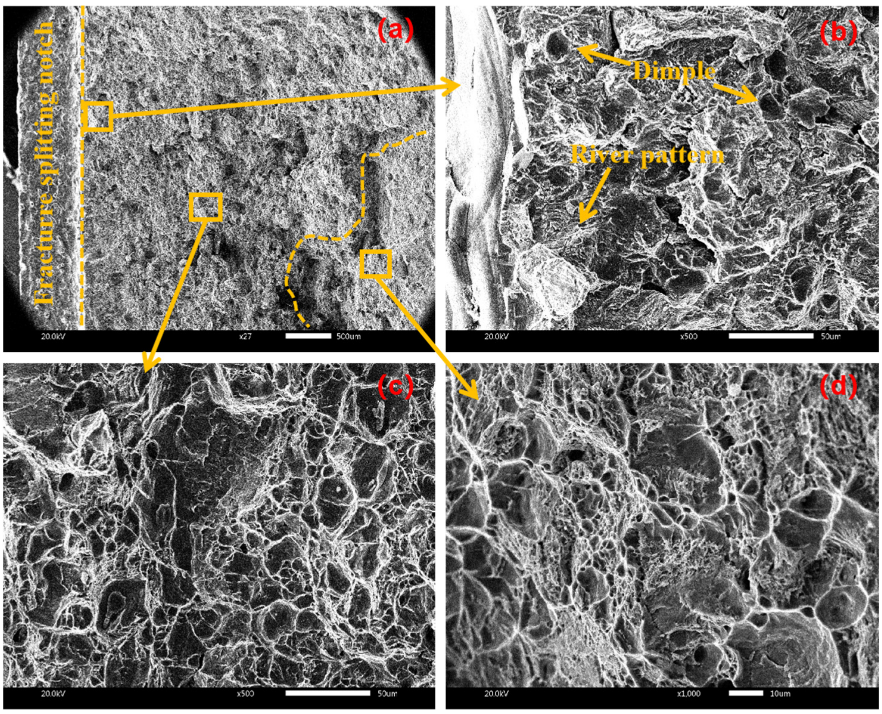

Figure 14. Fracture morphology at amplitude of 30 µm with (**a**) macroscopic fracture, (**b**) crack initiation area, (**c**) extension area, (**d**) termination area.

To sum up, in the case of conventional cracking without amplitude, the dimple characteristic and the fracture form belong to ductile fracture. When the ultrasonic amplitude increases from 6 μm to 30 μm, the plasticity and hole deformation of the con-rod sample decrease at first and then increase. When the amplitude is 15 μm, the fracture form of the con-rod sample is cleavage fracture; at this time, the brittleness is the highest, the hole deformation is the smallest and the cracking quality is the highest.

3.4. The Effect of Ultrasonic Amplitude on the Change in Dislocation

From the above research, the ultrasonic amplitude has a great influence on the cracking force, deformation, fracture morphology and ductile–brittle fracture mode of con-rod fracture splitting, so allowing us to better study the microscopic reasons for the above changes during con-rod fracture splitting. The influence of ultrasonic amplitude on the macro-force and deformation of con-rod fracture splitting is studied from the view of the microscopic dislocation motion by the combination of XRD detection analysis and TEM transmission analysis, and the fracture ductile–brittle transfer mechanism is also explained from the microscopic point of view.

3.4.1. XRD Analysis

The XRD test of the sample is mainly carried out by the X-ray diffraction experiment on the fracture surface of the cracking sample under different ultrasonic amplitude by an ultra X TTR III X-ray diffractometer. The accelerating voltage is 48 kV, the current is 100 mA, the scanning step is 0.02° and the range of angle 2θ is 32–88°. In Figure 15, we can find that as the ultrasonic amplitude increases from 0 μm to 15 μm and then to 30 μm, the diffraction peaks corresponding to the three crystal planes (110), (200) and (211) show the same law of first enhancement, then weakening and then enhancement, and the FWHM of the diffraction peak decreases at first, then increases and then decreases. This law shows that with the increase in ultrasonic amplitude, the grain size of the cracking material in the cracking area will change to a certain extent, and the grain size will become larger at first, then smaller and then larger. When the amplitude is 0–6 μm, the addition of ultrasound will improve the particle activity of the fracture material, enhance the recovery ability, release the internal stress of the material and increase the grain size to a certain extent. When the amplitude is in the range of 6–15 μm, ultrasound will cause dislocation entanglement and make the grains elongate and break, so that ultrasound can refine the grains to a certain extent, and when the amplitude is higher than 15 μm, the temperature effect caused by ultrasonic amplitude will cause the increase in temperature, resulting in the mutual annexation and growth of grains, then leading to grain enlargement. At the same time, it can also be seen from Figure 15 that the diffraction peaks of (110), (200) and (211) crystal planes keep increasing and decreasing with the increase in ultrasonic amplitude. And there will not be the phenomenon that the peak value of the crystal plane changes greatly while others' change inversely, indicating that ultrasonic fracture splitting does not affect the grain orientation or the preferred orientation along a certain plane of the cracking material.

MID Jade 6 diffraction peak processing software was used to calculate the FWHM of the diffraction peak under different amplitude. According to the relationship obtained by Dunn et al. [21–23], the dislocation density was obtained. The calculated dislocation densities of different crystal planes are shown in Figure 16.

In Figure 16, with the increase in ultrasonic amplitude, the dislocation changes in each crystal plane are complex, and the dislocation density of each crystal plane reaches the order of 1010 cm^{-2}. At different amplitude, the dislocation density of the (211) crystal plane is always higher than that of the other two crystal planes, which is mainly due to the maximum tensile stress on the (211) crystal plane and the faster deformation of the material during cold plastic deformation; the dislocation density also increases sharply at the same time; it also increases the resistance of dislocation movement. With the increase in ultrasonic amplitude, the dislocation density of each crystal plane decreases at first, then increases and then decreases. We can add the dislocation densities of (110), (200) and (211) together and find out the change rule of it. The total dislocation density curve under different amplitude is shown in Figure 17.

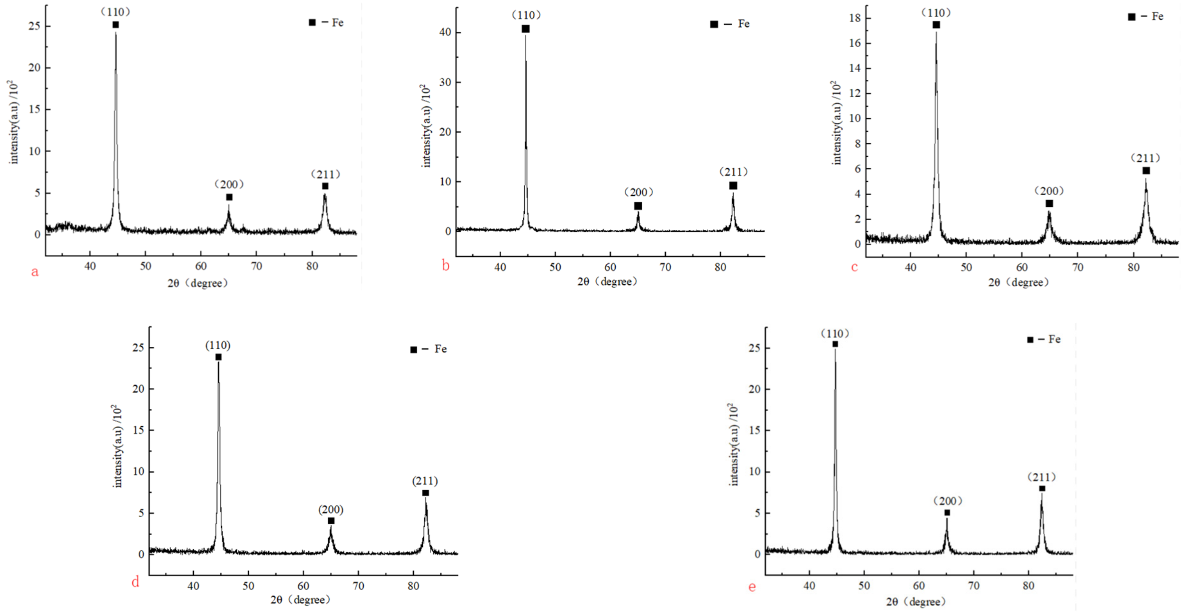

Figure 15. XRD pattern of sample fracture at different amplitude with (**a**) 0 µm, (**b**) 6 µm, (**c**) 15 µm, (**d**) 25 µm, (**e**) 30 µm.

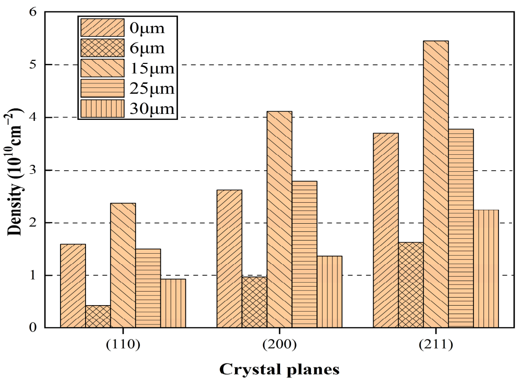

Figure 16. Dislocation density of different crystal planes at different amplitude.

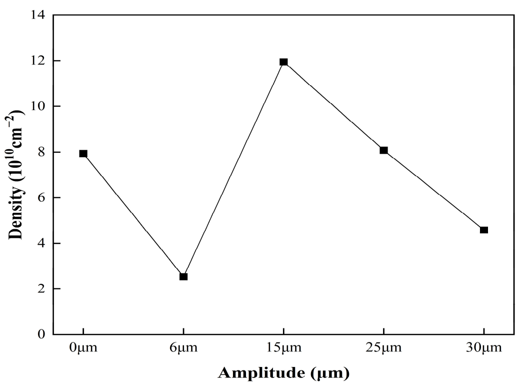

Figure 17. Curves of total dislocation density at different amplitude.

In Figure 17, the total dislocation density decreases at first and then increases and then decreases with the increase in amplitude. At low amplitude (0–6 µm), ultrasound can improve the particle activity of the con-rod during deformation, release the internal stress, annihilate the dislocation and decrease the dislocation density, and the larger the amplitude is, the more obvious this phenomenon is. When the amplitude is about 15 μm, the energy provided by ultrasound can not only completely release the internal stress of the material but also produce a new dislocation multiplication phenomenon. Due to the higher amplitude, the continuous increase in the amplitude will increase the strain rate of the material at the same time. As a result, the increment rate of dislocations increases, which means that the critical shear stress of the slip system is increased, slip is less likely to occur and the temperature is still in a low state; the material is not easy to recrystallize. These lead to the increase in dislocation density. When the amplitude reaches a larger value (25–30 μm), the increase in amplitude will highlight the temperature effect, resulting in an increase in the temperature of the material during cracking, then resulting in the enhancement of the dynamic characteristics of the atom and the critical shear stress required for the start-up of the slip system decreasing, which reduces the slip resistance between the dislocation motion and the crystal plane [24]. At the same time, the increase in temperature will also make the material more prone to recrystallization. All these will lead to the decrease in dislocation density.

3.4.2. TEM Analysis

Because the crack propagation area of the fracture surface always accounts for a large proportion of the fracture area under different amplitude, in order to compare the effect of amplitude on the dislocation of the fracture surface, we observe the change in the dislocation mechanism in the propagation area under different amplitude. The slice specimens in the vertical direction of the fracture crack propagation area were observed by a transmission electron microscope. First of all, the right part of the fracture surface of the cracked sample was cut from the middle of the fracture surface by WEDM to cut a sheet with a thickness of 200 μm and a length of 4 mm perpendicular to the depth of the fracture splitting notch, then the thickness was about 50 μm with metallographic sandpaper, and then the circle of ∅3 mm was punched out along the middle of the sheet on the punching machine, and then the central area of ∅3 mm was thinned to the desired thickness by an ion thinning instrument. Finally, different samples were observed by a transmission electron microscope (TEM). Their micrograph is shown in Figure 18, and the observed area is the region with a depth of 2 mm in the center of the fracture, and the mechanism of amplitude on the microstructure of cracking samples is analyzed.

In Figure 18, when the amplitude is 0 μm and only the tension machine is used for cracking, it belongs to static tension. The matrix material continues to deform in a certain direction after being subjected to the breaking force exerted by the expanding sleeve, so does the dislocation movement, as shown in Figure 18a; multiple dislocation lines and the dislocation slip direction TrP have been marked with a thick arrow. When two of the dislocation lines d1 and d2 meet and act on each other, the dislocation will be pinned. At the same time, the dislocation at the pinning point (usually impurity elements) will be blocked and difficult to move. However, the dislocation lines on both sides of the pinning point continue to move, which causes the dislocation to become arched. When the dislocation motion continues, two dislocation lines are connected. This mechanism forms a new dislocation d3 and produces an immovable dislocation segment [25]. This phenomenon results in the conventional con-rod fracture splitting requiring a larger maximum cracking force; at the same time, the con-rod itself also deforms greatly, which affects the quality of cracking processing. When the amplitude is 6 μm, the addition of ultrasound can effectively weaken the above directivity, improve the activity of particles and release the internal stress of the material, resulting in a certain reduction in dislocation density and the number of dislocation lines, as shown in Figure 18b. When the amplitude is further increased to 15 μm, the dislocation density increases, the dislocation entanglement is obvious and grain fragmentation and a grain size decrease appear at the same time, as shown in Figure 18c, which shows that the cracking fracture belongs to brittle cleavage fracture to a certain extent. When the amplitude is higher than a certain threshold, the thermal effect caused by ultrasound begins to dominate. When the amplitude is 25 μm, the thermal effect caused by ultrasound will trigger the partial recrystallization of the material, coarsening the internal polymerized grain, and constantly thermally activate the dislocation migration at the interface, resulting in dislocation slip; the energy of the system and dislocation density and interface energy continue to decrease. At the same time, this thermal effect is also conducive to the initiation of multi-slip systems, so that dislocations in different grains can cross the grain boundary through dislocation movement, so multiple slip characteristics can be found in the same grain, that is, the dislocations of each slip system move along their respective directions, as shown in Figure 18d. This will lead to the con-rod softening to some extent during cracking, and the fracture tends to ductile fracture. When the amplitude increases to 30 μm, the dislocation density further decreases, and the grain boundaries of recrystallized grains continue to become flat, coarse and obvious, as shown in Figure 18e, which ensures that the material tends to a lower energy state during cracking, thus more severe deformation can occur, and the con-rod tends to ductile fracture during cracking.

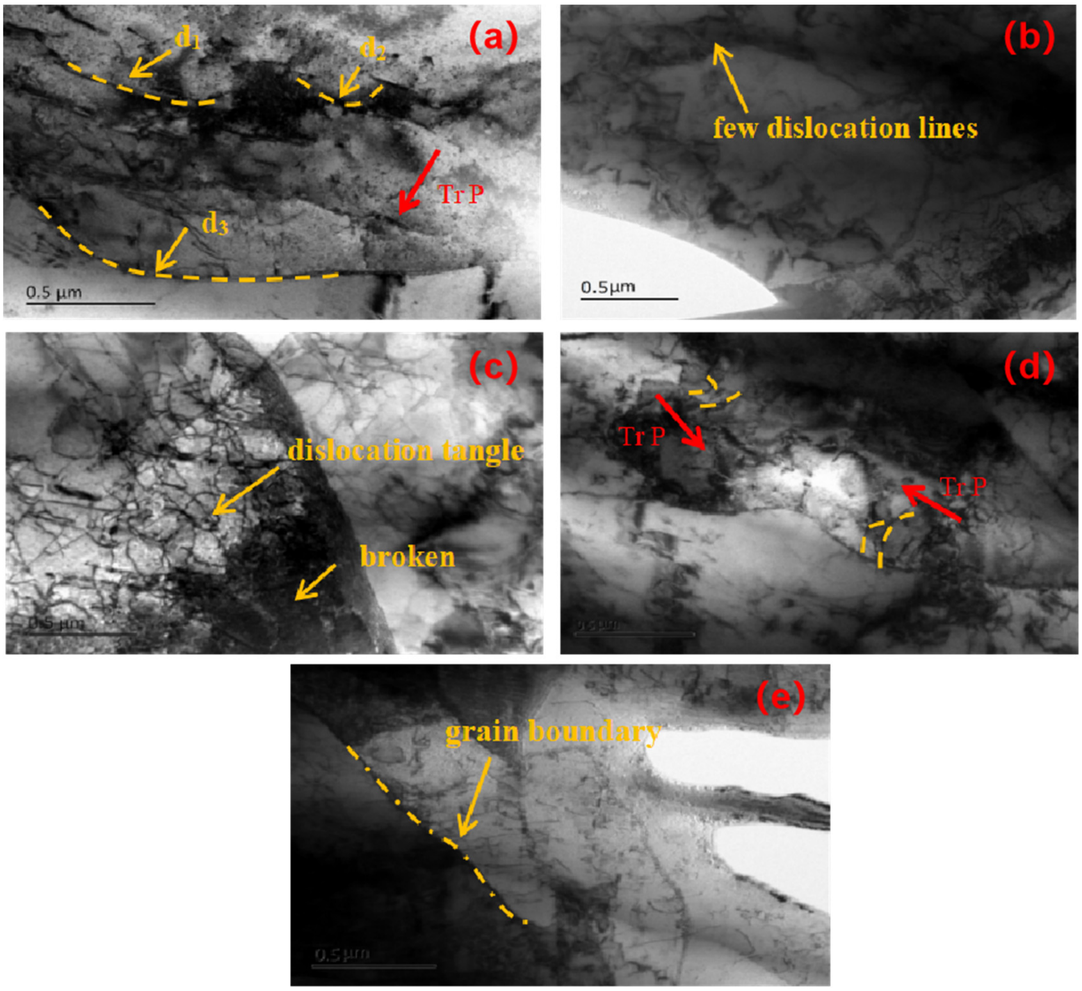

Figure 18. Micrograph of sample observed by TEM with (**a**) 0 μm, (**b**) 6 μm, (**c**) 15 μm, (**d**) 25 μm (**e**) 30 μm.

In summary, it can be seen from the micrographs of the transmission electron microscope under different amplitude in Figure 18 that the dislocation density at the fracture of the cracking sample decreases when the amplitude ranges from 0 μm to 6 μm, increases when the amplitude ranges from 6 μm to 15 μm and decreases when the amplitude ranges from 15 μm to 30 μm.

4. Discussion—An Analysis of the Mechanism of Ultrasound-Assisted Cracking

The results show that when the amplitude increases from 0 μm to 6 μm, low-amplitude vibration will increase the temperature of the crack tip, increase the mobility between atoms, reduce the resistance of the dislocation motion, increase the atomic transition frequency and the vacancy concentration, increase the self-diffusion of atoms in the matrix and the slip ability of dislocations, continuously release the internal stress of the material and the flow stress of the metal decreases obviously, weakening the stress concentration effect. And dislocations are easier to redistribute to form a more stable lattice in energy, which speeds up the mutual destruction of dislocations and decreases the density of dislocations. At the same time, due to the decrease in dislocation density and dislocation motion resistance, the dislocation emission at the crack tip becomes easier during cracking, which leads to the passivation of the crack tip, the improvement in the plasticity of the material and the fracture surface tends to ductile fracture. Finally, the deformation of the sample is intensified after cracking.

When the amplitude increases from 6 μm to 15 μm, due to the high amplitude, ultrasound can not only completely release the internal stress of the material but also cause new internal stress and dislocation density to increase again. At the same time, the mutual accumulation and entanglement of dislocations are caused by the characteristics of high ultrasonic frequency and a different direction of motion. And near the fracture splitting notch, due to the sudden change in the cross-section size of the sample and the large dislocation density, leading to lattice distortion and the force effect of stress field and the atom deviating from its equilibrium position, while the dislocation plug group means that many dislocations are concentrated together, the superposition of the force increases the total force, which will produce a great force near the dislocation plug group, so the stress superposition is concentrated in the dislocation plug group, causing the concentrated distribution of stress in the cracking trough. With the increase in amplitude, the dislocation density increases sharply, and the stress concentration becomes more obvious, making the hardening effect of the material more obvious, which makes the dislocation emission at the crack tip of the material become more difficult, and the plasticity of the material decreases. Thus, the fracture surface tends to brittle fracture and finally reduces the deformation degree of the sample after cracking. The peak value of the hardening stress peak increases with the increase in ultrasonic vibration energy, and the higher the vibration energy is, the more significant the hardening effect is [26]. This is consistent with the research findings of Xie et al. [27], which suggest that the hardening effect predominates when a large amplitude of ultrasonic vibration is applied during tensile testing. When the amplitude reaches 90% A (A is the maximum amplitude of the ultrasonic vibration device), the cross-section of the material is brittle transgranular fracture. When the ultrasonic vibration energy is high, the hardening effect is dominant, and the high vibration energy changes the deformation mechanism of the material, which leads to brittleness [28].

When the amplitude increases from 15 μm to 30 μm, because the ultrasonic amplitude is too large, the limiting effect of sleeve expansion on ultrasonic vibration is prominent, so that more ultrasonic energy is converted into thermal energy, and the thermal effect caused by ultrasound is dominant. During cracking, the temperature of the fracture surface is high, and the higher the amplitude is, the higher the temperature is, which leads to the intensification of dislocation annihilation and the decrease in dislocation density with the increase of in amplitude. At the same time, the thermal effect makes it easier to trigger the partial recrystallization of the material, the coarsening of material polymerization, the activation of the dislocation migration at the interface, the slip phenomenon and the continuous decrease in the dislocation density; these increase the plasticity of the material, lead to the fracture surface tending to ductile fracture and finally aggravate the deformation of the sample after cracking.

Under the premise of non-resonance, the realization of the cracking of the con-rod sample mainly depends on the tension of the stretcher, and the ultrasonic vibration only plays an auxiliary role. The ultrasonic vibration with appropriate amplitude should be selected to better realize the cracking of the con-rod.

The amplitude of high-frequency vibration has a great influence on the force, deformation and fracture of the con-rod in the cracking process. The influence of high-frequency vibration on the material deformation process includes the force effect, thermal effect and so on. On the one hand, due to the superposition of the force, the stress concentration is higher, and the crack appears at the bottom of the cracking tank earlier; on the other hand, after the material absorbs the vibration energy, the temperature and the activity of particles in the material increase, which provides energy for the movement of dislocations, so that the plasticity of the material is also partially improved. There is a possible critical amplitude near 15 μm, which can make the ultrasonic energy act on the con-rod in the form of mechanical vibration efficiently.

By observing the fracture surfaces of the samples with different amplitude, it is found that ultrasonic vibration can improve the brittleness of the root area of the fracture splitting notch, so that the crack appears and propagates at the root of the cracking tank earlier. The high-frequency vibration with an amplitude of 6 μm has little effect on cracking and shows ductile fracture in both the crack propagation area and the rapid fracture area. When the amplitude is 15 μm, the ultrasonic vibration promotes both the crack propagation area and the rapid fracture area, which improves the brittleness of the fracture surface and is more beneficial to the cracking of the con-rod. When the amplitude is 25 μm and 30 μm, the extrusion pressure between the expanding sleeve and the crank bore of the sample limits and weakens the effect of high-amplitude vibration, so that more ultrasonic energy is transferred from high-frequency mechanical vibration to thermal energy to the con-rod sample and then improves the plasticity of the material and makes the fracture surface ductile, which is not conducive to the cracking of the con-rod.

5. Conclusions

In order to expand the range of cracking con-rod materials and reduce the requirements of process parameters, ultrasonic-assisted con-rod fracture splitting was studied by using a con-rod material of quenched and tempered 1045 steel. The effects of amplitude on cracking force and deformation, ductile–brittle transition and dislocation change were tested and analyzed; the general law of the effect of different amplitude on cracking was found out, so as to better control the cracking quality. The main conclusions of this paper are as follows:

(1) When the amplitude increases from 0 μm to 15 μm and then to 30 μm, the cracking force and the displacement of the stretcher decrease at first and then increase. At 15 μm, the cracking force of the sample is the smallest and the deformation of the sample is the smallest.

(2) There is a threshold near the amplitude of 15 μm. When the amplitude is lower than this threshold, ultrasonic vibration plays a major role in cracking, and the low-amplitude “softening” and high-amplitude “hardening” effects of ultrasound are consistent with the experimental results.

(3) When the amplitude increases from 0 μm to 6 μm, the dislocation density decreases, the dislocation lines at the center depth of the fracture 2 mm become reduced and the direction of the dislocation movement becomes less obvious. When the amplitude increases from 6 μm to 15 μm, the dislocation density increases, resulting in dislocation entanglement and grain fragmentation. When the amplitude increases from 15 μm to 30 μm, the dislocation density decreases, and multiple dislocation slip trajectories appear.

(4) The increase in amplitude will lead to the decrease in dislocation density at first, then an increase and then a decrease; the plasticity of the fracture surface will increase, then decrease and then increase. The effect of amplitude on dislocation leads to the change in fracture morphology.

(5) There is a threshold near the amplitude of 15 μm. When the amplitude is this threshold, the minimum cracking force and sample deformation can be guaranteed, the fracture

surface is smooth without a necking phenomenon and the fracture surface is brittle and flat.

Author Contributions: Y.J.: conceptualization, methodology, writing—review and editing, project administration, supervision and project administration. Y.W.: investigation, data curation, writing–original draft and validation. X.L.: writing—review and editing, software, formal analysis and validation. D.S.: investigation, writing—review and editing, resources and visualization. M.Z.: investigation, project administration and visualization. All authors have read and agreed to the published version of the manuscript.

Funding: This work was supported by the National Natural Science Foundation of China (No. 51075193).

Institutional Review Board Statement: Not applicable.

Informed Consent Statement: Not applicable.

Data Availability Statement: The data will be provided as required.

Conflicts of Interest: The authors declare that they have no known competing financial interests or personal relationships that could have appeared to influence the work reported in this paper.

References

1. Bhamdare, A.; Atulkar, A.; Porwal, R. Design, static structural analysis and topology optimization of a four wheeler connecting rod. *Mater. Today Proc.* **2022**, *66*, 829–833. [CrossRef]
2. Kuldeep, B.; Ravikumar, K.P.; Guruprasad, B.S.; Tasneem, H.A.; Ashrith, H.S.; Shree, N.; Ali, M.M.; Bashir, M.N.; Ahamad, T. A novel composite connecting rod: Study on mechanical and dynamic behaviour through experimental and finite element approach. *Compos. Part C Open Access* **2023**, *12*, 100413. [CrossRef]
3. Shi, Z.; Kou, S. Inverse reconstruction of fracture splitting connecting rod and its strength and fatigue life. *J. Fail. Anal. Prev.* **2018**, *18*, 619–627. [CrossRef]
4. Zhang, F.; Zhang, Y. Setting of Natural Fracture Splitting Surface on Connecting Rod and Its Formation Mechanism. *Metals* **2020**, *10*, 590. [CrossRef]
5. Gu, Z.; Yang, S.; Ku, S.; Zhao, Y.; Dai, X. Fracture splitting technology of automobile engine connecting rod. *Int. J. Adv. Manuf. Technol.* **2005**, *25*, 883–887. [CrossRef]
6. Shi, Z.; Kou, S. Analysis of quality defects in the fracture surface of fracture splitting connecting rod based on three-dimensional crack growth. *Results Phys.* **2018**, *10*, 1022–1029. [CrossRef]
7. Liu, J.; Kou, S.; He, D. Comparative analysis of the fracture splitting deformation of the big end for C70S6, 36MnVS4 and 46MnVS5 connecting rods. *IOP Conf. Ser. Mater. Sci. Eng.* **2020**, *772*, 012113. Available online: https://iopscience.iop.org/article/10.1088/1757-899X/772/1/012113/pdf (accessed on 29 April 2024). [CrossRef]
8. Zhang, C.L.; Fang, W.; Cai, B.R.; Sun, X.H.; Liu, Y.Z. Austenite grain growth and its effect on splitting fracture property of a V–N microalloyed medium carbon steel connecting rod. *J. Iron Steel Res. Int.* **2019**, *26*, 875–881. [CrossRef]
9. Liu, B.X.; Fan, K.Y.; Yin, F.X.; Feng, J.H.; Ji, P.G. Effect of caliber rolling reduction ratios on the microstructure and mechanical properties of 45 medium carbon steel. *Mater. Sci. Eng. A* **2020**, *774*, 138954. [CrossRef]
10. Ji, Y.; Sun, X.; Zhao, F.; Zhang, C.; Jiang, B.; Liu, Y. Austenite grain growth behavior and its effects on fracture splitting performance of 36MnVS4 connecting rod for automobile engine. *Kov. Mater. Met. Mater.* **2018**, *56*, 113–120. [CrossRef]
11. Ouyang, J.; Qiu, Z.; Wang, L. Investigation of 2D ultrasonic-assisted micro-injection molding. *J. Mater. Process. Technol.* **2024**, *328*, 118397. [CrossRef]
12. Qin, S.; Zhu, L.; Wiercigroch, M.; Ren, T.; Hao, Y.; Ning, J.; Zhao, J. Material removal and surface generation in longitudinal-torsional ultrasonic assisted milling. *Int. J. Mech. Sci.* **2022**, *227*, 107375. [CrossRef]
13. Ni, C.; Zhu, L. Investigation on machining characteristics of TC4 alloy by simultaneous application of ultrasonic vibration assisted milling (UVAM) and economical-environmental MQL technology. *J. Mater. Process. Technol.* **2020**, *278*, 116518. [CrossRef]
14. Shao, G.; Li, H.; Zhang, X.; Zhan, M.; Xiang, Z. Characteristics and mechanism in ultrasonic vibration-assisted deformation of Ni-based superalloy thin-walled sheet by quasi-in-situ EBSD. *J. Alloys Compd.* **2022**, *908*, 164591. [CrossRef]
15. Huang, Y.; Zhang, Y.; Liao, J. Effects of process parameters on the mechanical properties and microstructure in ultrasonic vibration-assisted warm tensile deformation of AZ31 magnesium alloy. *Int. J. Lightweight Mater. Manuf.* **2024**, *7*, 378–383. [CrossRef]
16. Storck, H.; Littmann, W.; Wallaschek, J.; Mracek, M. The effect of friction reduction in presence of ultrasonic vibrations and its relevance to travelling wave ultrasonic motors. *Ultrasonics* **2022**, *40*, 379–383. [CrossRef]
17. Wen, T.; Wei, L.; Chen, X.; Pei, C.-L. Effects of ultrasonic vibration on plastic deformation of AZ31 during the tensile process. *Int. J. Miner. Metall. Mater.* **2011**, *18*, 70–76. [CrossRef]

18. Yao, Z.; Kim, G.Y.; Wang, Z.; Faidley, L.; Zou, Q.; Mei, D.; Chen, Z. Acoustic softening and residual hardening in aluminum: Modeling and experiments. *Int. J. Plast.* **2012**, *39*, 75–87. [CrossRef]
19. Zhong, C. Study on Plastic Forming of Aluminum Alloy with High Frequency Vibration. Master's Thesis, Shandong University, Jinan, China, 2015. (In Chinese)
20. Chen, L.; Wang, H.; Liu, D.; Ye, X.; Li, X.; Tang, G. Effects of electropulsing cutting on the quenched and tempered 45 steel rods. *J. Wuhan Univ. Technol.-Mater. Sci. Ed.* **2018**, *33*, 204–211. [CrossRef]
21. Jia, R.; Zhang, Y.; Zhang, Y.; Guo, H. The dislocation density in 4H-Si C epitaxial single crystals is calculated by XRD method. *Spectrosc. Spectr. Anal.* **2010**, *30*, 1995–1997. (In Chinese)
22. Zhang, J.; Wang, J.; Wang, Y.; Yang, H. The effect of the ratio of In source flow to group III flow on the properties of In Ga N/Ga N multiple quantum wells. *Acta Phys. Sin.* **2004**, *53*, 2467–2471. (In Chinese) [CrossRef]
23. Wang, X.; Cui, F.; Yan, G.; Li, Y. Study on the change of dislocation density in 40Cr cold rolling forming. *China Mech. Eng.* **2013**, *24*, 2248. Available online: http://www.cmemo.org.cn/CN/Y2013/V24/I16/2248 (accessed on 29 April 2024). (In Chinese)
24. Su, J.; Sun, H.; Ren, F.; Chen, X. Dislocation evolution analysis of XRD's TA10 titanium alloy after hot compression deformation. *J. Harbin Eng. Univ.* **2019**, *40*, 406–411. (In Chinese) [CrossRef]
25. Huang, P. In-Situ Transmission Electron Microscopic Study on the Size Effect and Temperature Effect of Titanium Alloy Deformation Mechanism. Master's Thesis, Zhejiang University, Hangzhou, China, 2019. (In Chinese)
26. Petch, N.J. The ductile-brittle transition in the fracture of α-iron: I. *Philos. Mag.* **1958**, *3*, 1089–1097. [CrossRef]
27. Xie, Z.-D.; Guan, Y.-J.; Yu, X.-H.; Zhu, L.-H.; Lin, J. Effects of ultrasonic vibration on performance and microstructure of AZ31 magnesium alloy under tensile deformation. *J. Cent. South Univ.* **2018**, *25*, 1545–1559. [CrossRef]
28. Zhou, X. Discussion on the Essence of Temperature and Load Rate Affecting Brittleness of Structural Steel and Brittle Fracture Control. Master's Thesis, Harbin Engineering University, Harbin, China, 2005. (In Chinese)

materials

Article

A Study of 2D Roughness Periodical Profiles on a Flat Surface Generated by Milling with a Ball Nose End Mill

Mihaita Horodinca *, Florin Chifan, Emilian Paduraru, Catalin Gabriel Dumitras, Adriana Munteanu and Dragos-Florin Chitariu

Digital Manufacturing Systems Department, Gheorghe Asachi Technical University of Iasi, 700050 Iasi, Romania; florin.chifan@academic.tuiasi.ro (F.C.); emilian.paduraru@academic.tuiasi.ro (E.P.); catalin-gabriel.dumitras@academic.tuiasi.ro (C.G.D.); adriana.munteanu@academic.tuiasi.ro (A.M.); dragos-florin.chitariu@academic.tuiasi.ro (D.-F.C.)
* Correspondence: mihaita.horodinca@academic.tuiasi.ro

Abstract: This paper presents a study of 2D roughness profiles on a flat surface generated on a steel workpiece by ball nose end milling with linear equidistant tool paths (pick-intervals). The exploration of the milled surface with a surface roughness tester (on the pick and feed directions) produces 2D roughness profiles that usually have periodic evolutions. These evolutions can be considered as time-dependent signals, which can be described as a sum of sinusoidal components (the wavelength of each component is considered as a period). In order to obtain a good approximate description of these sinusoidal components, two suitable signal processing techniques are used in this work: the first technique provides a direct mathematical (analytical) description and is based on computer-aided curve (signal) fitting (more accurate); the second technique (synthetic, less accurate, providing an indirect and incomplete description) is based on the spectrum generated by fast Fourier transform. This study can be seen as a way to better understand the interaction between the tool and the workpiece or to achieve a mathematical characterisation of the machined surface microgeometry in terms of roughness (e.g., its description as a collection of closely spaced 2D roughness profiles) and to characterise the workpiece material in terms of machinability by cutting.

Keywords: 2D roughness profiles; milling; ball nose end mill; measurement; characterisation; curve (signal) fitting; fast Fourier transform

1. Introduction

The surface roughness of steel work pieces machined by milling with ball nose cutters appears to be closely related to the interaction between the tool and the workpiece, and the machinability of the workpiece material by cutting. It depends mainly on the shape, geometry, and position of the tool (tilt angle, axial depth of cut, effective cutting diameter), the machining parameters (cutting speed, feed, and direction), the milling strategy (tool path pattern, step over distance), and the cutting forces (involved in the elastic deformations of the tool). Some non-systematic phenomena are also occasionally involved in the definition of this roughness: relative vibrations between tool and workpiece, self-excited vibrations, local variations in the hardness of the workpiece material, tool wear, cutting edge adhesion or fractures, etc. Therefore, under the most suitable milling conditions, the roughness is mainly characterised by a micro-geometry with a regular (periodic) shape, with equidistant pick (path) and feed interval scallops [1] on the pick and feed directions.

A better understanding of the interaction between tool and workpiece during any cutting (machining) process requires a thorough investigation of the surface roughness. The first approach to this investigation is the experimental sampling of the surface roughness description using appropriate equipment. The most common method to achieve this sampling is the use of contact profilometers [2–10] as a reliable but time-consuming method. Some other methods use the non-contact surface exploration by lasers [11], laser interferometry [12,13], laser confocal microscopes [14], optical systems [15–18], machine vision systems [19], or are inspired by research into the optical properties of surfaces (ability to split white light, diffractive properties) using scanning electron microscopy and atomic force microscopy [20].

As the description of a 3D surface roughness by sampling is generally obtained by joining many 2D roughness profiles (e.g., as a grid on pick and feed directions), the study of these surfaces mainly means a study of each of these 2D roughness profiles (2DRPs), often as a periodic evolution [2,4,5,8,11,15,16,18,20,21]. Some investigation techniques on this topic are available in the literature, most of which reveal the presence of numerous permanent sinusoidal components within these 2DRPs (as wavinesses [21], with dominants and some harmonics). Some previous studies indicate the availability of techniques to describe the components using synthetic rather than analytical methods, treating the 2DRPs mainly as digital time-dependent signals. The simplest synthetic description of the components can be obtained by digital filtering [22], in particular by selective band-pass filtering [8]. A relatively better approach to this synthetic description is possible using the power spectral density (by Fast Fourier Transform, FFT) of 2DRPs as time-dependent signals [2,7,8,19,21]. On an FFT spectrum (with amplitude on the y-axis and conventional frequency as the inverse of the wavelength on the x-axis), each significant sinusoidal component within a 2DRP is described as a peak. However, the availability of the FFT is generally seriously limited by the insufficiently low resolution of the conventional frequency (R_{cf}) on the spectrum. The use of a high sampling rate (or sampling frequency f_s) for 2DRP description (in order to have a high Nyquist limit $f_{Nq} = f_s/2$) should be mandatorily accompanied by a high number (N) of samples (or a large size length of 2DRP) in order to have a conveniently small resolution of conventional frequency $R_{cf} = f_s/N$. If this resolution is not small enough, some peaks in the spectrum will be missing or will have incorrectly described amplitudes (smaller than normal). This is a major inconvenience of the FFT that has not yet been resolved in these previous approaches. However, there is an additional drawback to the FFT analysis: the synthetic description of the sinusoidal components is incomplete (their phases at the origin of time are missing).

In some cases, the 2DRPs, considered as time-dependent signals, contain short sinusoidal components that do not persist permanently. For these situations (not considered in our work), where generally short oscillations (waves) occur transiently, the FFT analysis is not at all appropriate, but there are available other specific investigation techniques (inspired by the study of vibrations), e.g., based on Wavelet Transform (as Continuous Wavelet Transform [7], Frequency Normalised Wavelet Transform [23,24], and Wavelet Packet Transform [25]).

The main purpose of this work is focused on the study of periodic 2DRPs (considered as time-dependent signals) in order to determine the best analytical approximation of them (as a pattern), as close as possible to experimental evolutions, as a sum of significant sinusoidal components. Each sinusoidal component (analytically defined by the amplitude, a conventional angular frequency, and a phase at the conventional time origin) is a description of waviness on the machined surface of the workpiece. The inverse of the conventional frequency (as the conventional period) is the wavelength of the waviness.

Specifically, these 2DRPs are experimentally sampled in feed and pick directions (using a contact profilometer) on a theoretically flat surface milled with a ball nose end mill (on a steel workpiece in our approach). In order to analyse the 2DRP, a curve fitting procedure in Matlab R2019b (based on the Curve Fitting Toolbox) is favoured in this approach. In contrast to the FFT procedure (also discussed here), the curve fitting procedure can now be applied to relatively small (in length) 2DRPs, providing a high degree of accuracy in the analytical description of sinusoidal components. Similar to the FFT procedure, the curve fitting procedure has the same Nyquist limit ($f_{Nq} = f_s/2$); in other words, it is not possible to find out the analytical descriptions of sinusoidal components having conventional frequency above the Nyquist limit f_{Nq}. The curve fitting procedure allows for an interesting approach: a 2DRP in the analytical description can be artificially resized by mathematical extrapolation (increasing the number of samples N, while keeping the same sampling rate f_s). The accuracy of the FFT spectrum of this resized 2DRP is significantly improved due to a lower conventional frequency resolution, so that the FFT spectrum is now better suited to synthetically describe the content (in sinusoidal components) of a 2DRP.

There is an interesting option in the 2DRP analysis: one period of the synthetically described roughness pattern is obtained by a special kind of moving averaging. This averaging drastically reduces both the sinusoidal components harmonically uncorrelated and the noise. The analytical description of this pattern is also achieved by curve fitting.

The following sections of this paper are organised as follows: Section 2 presents the materials and methods, Section 3 presents the results and discussions, and Section 4 presents the conclusions.

2. Materials and Methods

A flat surface was milled on a workpiece made of 90MnCrV8 steel (hardness 60 HRC) using a 12 mm diameter, 3 flute, TiAlN coated carbide ball nose end mill (as GARANT Diabolo solid carbide ball nose slot drill HPC 12 mm, from the Hoffmann Group, Bucharest, Romania), tilted at 25 degrees to the pick direction and perpendicular to the feed direction, with the following cutting regime parameters: 5200 rpm, 1560 mm/min feed rate, constant axial cutting depth of 0.1 mm and 0.4 mm step over (with theoretically equal pick-interval scallops height [26]). Figure 1 shows a conceptual description of the down milling process (with the workpiece in cyan, the tool in red, the feed direction in green, and the direction of rotation in blue). The magenta-coloured straight line (d1) represents the pick direction, and the black straight line (d2) represents the feed direction, with both conventionally used for experimental sampling of 2DRP. Figure 2 shows a view of the tool and workpiece (with the cutting process stopped) on an OKUMA GENOS M460R-VE CNC vertical machining centre (Charlotte, NC, USA).

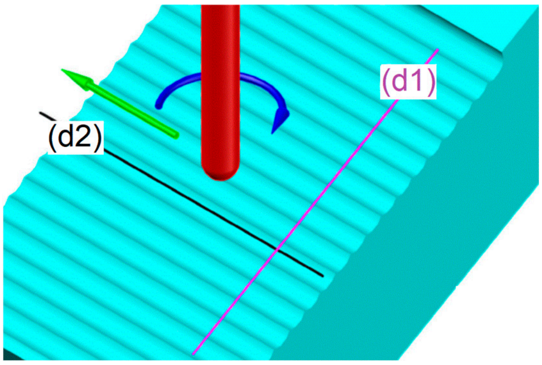

Figure 1. A conceptual description of the cutting process.

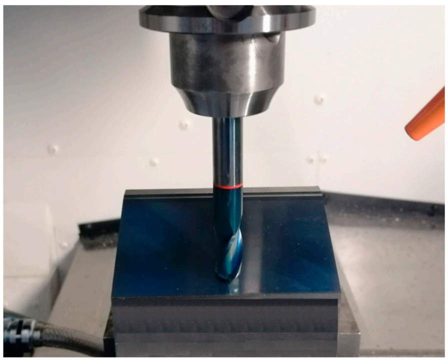

Figure 2. A view of the milling setup.

Figure 3 shows a view of the roughness sampling setup (using a SURFTEST SV-2100W4 contact profilometer, from Mitutoyo (Bucharest, Romania), with 0.0001 µm resolution, 2 µm stylus tip radius), with the flat milled surface placed in a horizontal position (here for sampling in pick direction).

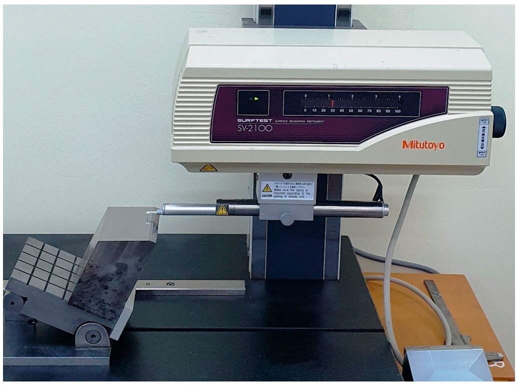

Figure 3. A view on the roughness sampling setup.

The numerical description of a 2DRP is delivered as a two-column .txt file describing N = 8000 equidistant samples (Δx = 0.5 µm sampling interval between samples on the x-axis, for a total distance of 4 mm). This file can be easily loaded into Matlab R2019b and analysed as a time-dependent signal (by FFT and curve (signal) fitting). Figure 4 shows a 4 mm long 2DRP, sampled in the pick direction (plotted in Matlab).

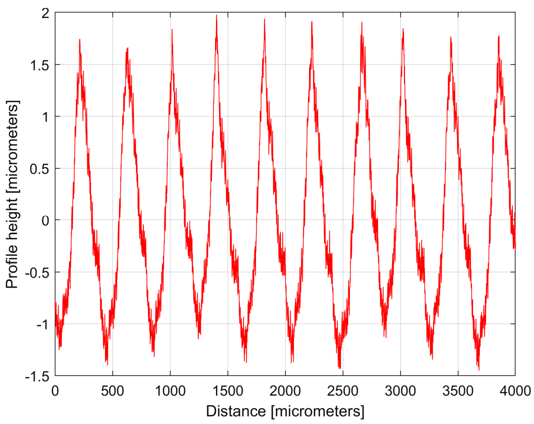

Figure 4. Graphical description of a 2DRP sampled on work piece, in the pick direction.

Here the profilometer resolution (0.0001 µm) was experimentally confirmed (as the minimum describable variation of the y-coordinate). As expected, there is a dominant periodic component within the 2DRP of Figure 4. A rough estimation indicates that this dominant has 10 periods, with each period being equal to the milling step over (400 µm), and an average pick-interval scallop height of 2.5 µm.

Figure 5 shows a partial view of the FFT spectrum of this 2DRP with real amplitudes (in Matlab). The 2DRP from Figure 4 was processed with FFT as a time-dependent signal (the x-coordinates of the samples are seen as signal samples time; the y-coordinates are seen as signal level). The sampling interval Δx on the x-axis (Δx = 0.5 µm) is seen as the conventional sampling period Δt on the t-axis. An x-coordinate on the x-axis of Figure 5 is equivalent to a conventional frequency or the inverse of a conventional period, or the inverse of a wavelength λ. A peak on the FFT spectrum (e.g., the highest peak 1, represented by an x-coordinate of 0.0025 µm^{-1} and a y-coordinate of 1.138 µm) indicates that there is a dominant sinusoidal component in the 2DRP with wavelength $\lambda = 1/x$ (e.g., $\lambda_1 = 1/0.0025$ = 400 µm for peak 1). This is exactly the step over value (pick feed) previously highlighted. In Figure 5, some other relevant peaks (2, 3, 4, and 5) represent sinusoidal components, harmonically correlated with the dominant, having the wavelengths $\lambda_1/2$ = 200 µm, $\lambda_1/3$ = 133.(3) µm, $\lambda_1/4$ = 100 µm, and $\lambda_1/5$ = 80 µm. The conventional sampling period Δt = 0.5 µm corresponds to the sampling frequency (rate) $fs = 1/\Delta t = 2$ µm^{-1} which is a conventional Nyquist limit (frequency) of $f_{Nq} = f_s/2 = 1$ µm^{-1}. In other words, the smaller synthetically describable wavelength of a sinusoidal component within the 2DRP by FFT spectrum is defined as $\lambda_{min} = (f_{Nq})^{-1} = (f_s/2)^{-1} = 1$ µm.

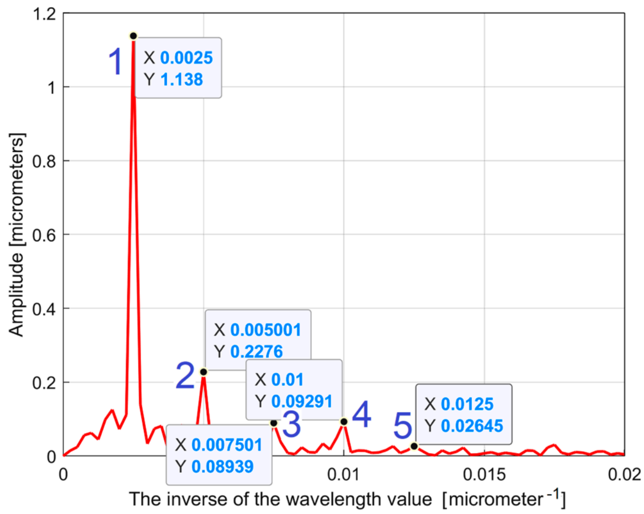

Figure 5. A partial view on the FFT spectrum of 2DRP from Figure 4.

However, as Figure 5 clearly shows, the conventional frequency resolution $R_{cf} = f_s/N$ = 2/8000 = 0.00025 µm^{-1} is not small enough in order to describe an accurate spectrum. In the spectrum from Figure 5 there are only $0.02/R_{cf}$ = 0.02/0.00025 = 80 samples. There are certainly other harmonics (with higher conventional frequencies) that are not visible in the spectrum. A longer 2DRP (obtained by increasing the number of samples at the same sampling frequency) significantly reduces the conventional frequency resolution. It should also be noted that the FFT spectrum does not provide the phase at the origin of the conventional time (x = 0) for sinusoidal components. A better approach proposed in this paper considers that within the $y(x)$ 2DRP there is a consistent deterministic part $y_d(x)$ and a less significant non-deterministic part $y_{nd}(x)$, mainly as noise, with $y(x) = y_d(x) + y_{nd}(x)$. In general, for periodic 2DRPs, this deterministic part $y_d(x)$ can be described as the sum of n sinusoidal components:

$$y_d(x) = \sum_{j=1}^{n} y_{dj}(x) = \sum_{j=1}^{n} A_j \cdot \sin(\omega_j \cdot x + \varphi_j) \tag{1}$$

In Equation (1), A_j are amplitudes, ω_j are conventional angular frequencies (related by wavelengths λ_j, with $\omega_j = 2\pi/\lambda_j$), and φ_j are conventional phase shifts at the origin (x = 0). Here, x (the current position of the profilometer stylus on the x-axis) plays the role of time.

The curve (signal) fitting procedure (using the Curve Fitting Tool from Matlab) allows for the values of A_j, ω_j, and φ_j to be determined with a good approximation. A sine model (as f(x) = a1*sin(b1*x + c1)) was used for a first fit, with x—coordinates as X data and y—coordinates as Y data. In this model, a1, b1, and c1 play the role of A_1, ω_1, and φ_1 values in defining the first sinusoidal component $y_{d1}(x)$. The first curve fit gives A_1 = 1.151 µm, ω_1 = 0.01558 rad/µm, and φ_1 = 4.1871 rad, whereby typically this curve fitting procedure finds the description of the highest amplitude component. It systematically searches for those suitable A_1, ω_1, and φ_1 values that satisfy the condition: $\sum\lfloor y(x) - y_{d1}(x) \rfloor = \min$. This first sinusoidal component $y_{d1}(x)$ is shown (as dominant) in blue in Figure 6, superimposed on $y(x)$, shown in red (an evolution already described in Figure 4). The component $y_{d1}(x)$ can be described mathematically as:

$$y_{d1}(x) = A_1 \cdot \sin(\omega_1 \cdot x + \varphi_1) = 1.151 \cdot \sin(0.01557 \cdot x + 4.1871\ ) \tag{2}$$

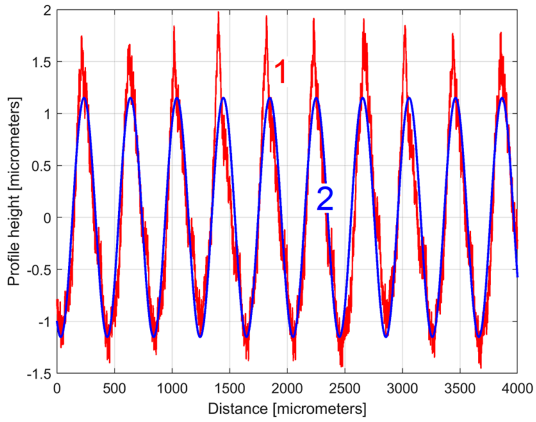

Figure 6. 1—The 2DRP from Figure 4; 2—The first (dominant) sinusoidal component ($y_{d1}(x)$) found by curve (signal) fitting (Equation (2)).

The description of $y_{d1}(x)$ from Equation (2) allows for the mathematical removal from $y(x)$, with the result shown in Figure 7 as the first residual ($r_1(x)$) of 2DRP, as $r_1(x) = y(x) - y_{d1}(x)$, after the first curve fitting (drawn at the same scale as Figure 6). The decrease in the y-coordinates of the residual profile is additional evidence of the quality of the mathematical description of $y_{d1}(x)$ found by curve fitting.

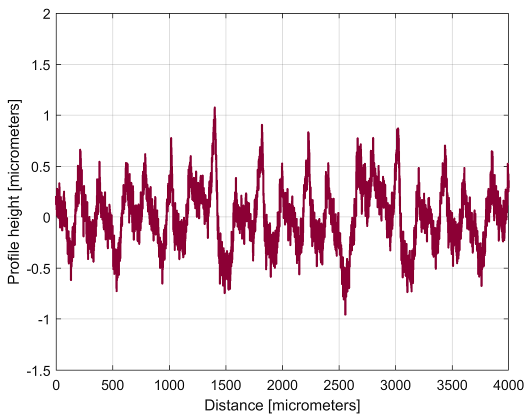

Figure 7. The first residual 2DRP after first analysis by curve fitting (as $r_1(x) = y(x) - y_{d1}(x)$).

It is clear that the dominant component $y_{d1}(x)$ does indeed fit $y(x)$. Its amplitude A_1 is close to that shown in the FFT spectrum (peak 1), and its wavelength $\lambda_1 = 2\pi/\omega_1 = 2\pi/0.01558 = 403.285$ µm is close to the step over value or pick feed (400 µm) during the milling process. The conventional frequency of $y_{d1}(x)$ is $1/\lambda_1 = 0.002479$ µm^{-1}, which is more precisely described by comparison with Figure 5, as related to the first peak (there $1/\lambda_1 = 0.0025$ µm). Related by the difference between the measured wavelength $\lambda_1 = 403.285$ µm (determined by curve fitting) and the pick feed (400 µm, as theoretical wavelength λ_1 generated by the CNC machining centre), a logical conclusion must be drawn: we suspect an inaccurate control of the x movement of the contact profilometer during the 2DRP measurement (involved in the measured λ_1) rather than inaccurate control of the pick feed during the milling process. In Figure 6, there are not exactly ten periods of the dominant $y_{d1}(x)$, as the ratio between the 2DRP length (4000 μm) and the theoretical wavelength (400 μm) suggests.

It is clear that this procedure can be repeated many times in an identical way (automatically, by programming in Matlab), and the mathematical description of the sinusoidal component $y_{dj}(x)$ can be found by curve fitting of the $(j-1)$th residual of 2DRP, as $r_{j-1}(x)$, described by Equation (3):

$$r_{j-1}(x) = y(x) - \sum_{k=1}^{j-1} y_{dk}(x) \tag{3}$$

Of course, in the curve-fitting procedure (as in the case of the FFT spectrum), exceeding of the Nyquist limit is forbidden ($\omega j < 2\pi f_{Nq}$ or $\lambda_j > (f_{Nq})^{-1}$).

Hypothetically, considering that $y_{nd}(x) = 0$, a perfect mathematical description of $y_d(x)$ (after n similar curve-fitting steps), should produce an $r_n(x) = 0$ for the nth residual of 2DRP (graphically represented as a straight line placed exactly on the x-axis).

The viability of this method of determining the mathematical description of a roughness profile (using a similar curve-fitting method developed in Matlab) has previously been demonstrated [27] in the analysis of other types of complex signals (vibration, active electrical power, instantaneous angular speed, etc.) containing many sinusoidal components.

3. Results and Discussion

3.1. Analysis of 2D Roughness Profiles in the Pick Direction by Curve Fitting

The analysis of the previously sampled 2DRP (Figure 4) was similarly performed using repetitively this curve fitting procedure a further 121 times. The mathematical description of these 122 sinusoidal components within $y(x)$ was found (these components having amplitudes greater than the resolution of the contact profilometer). Figure 8 shows the 2DRP (already shown in red in Figures 4 and 6) superimposed on an approximation of $y_d(x)$ by mathematical addition of these 122 sinusoidal components (shown in blue). In the same figure, the 122nd residual of 2DRP ($r_{122}(x)$), shown in purple, is superimposed. Figure 9 shows a zoomed section of area A from Figure 8.

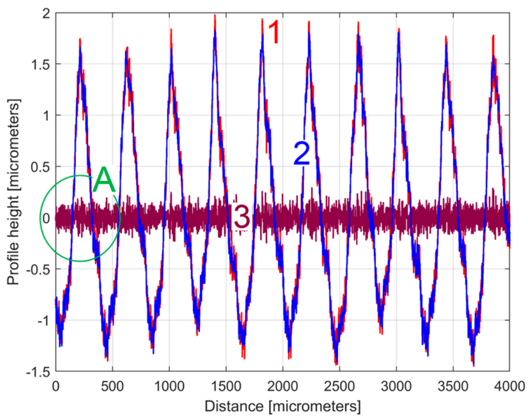

Figure 8. 1—The 2DRP; 2—An approximation of $y_d(x)$ through $y_{dh}(x)$ with 122 components; 3—The 122nd residual $r_{122}(x)$.

It is obvious that there is a good fit between the approximation of $y_d(x)$ and $y(x)$. Compared to Figure 7, there is a significantly smaller residual of 2DRP, which mainly describes the non-deterministic part $y_{nd}(x)$ of $y(x)$ and the measurement noise. In a simple approach, this noise—which does not significantly affect the fitting results—can be greatly reduced by numerical low-pass filtering.

As is well known [28], any evolution of a signal in time (or similar, e.g., this 2DRP in pick direction) can be well approximated as a sum of sinusoidal components. In our approach, it is more interesting to find the approximate analytical description of 2DRP (strictly related to the milling process) as a sum of harmonically correlated sinusoidal components (as $y_{dh}(x)$) with a fundamental at 0.01557 rad/μm as conventional angular frequency ω_1 (Equation (2)) related by pick feed or step over and some harmonics (at 2·0.01557 rad/μm, 3·0.01557 rad/μm, etc.). In other words, the deterministic part of $y(x)$ should be seen as $y_d(x) = y_{dh}(x) + y_{dnh}(x)$, where $y_{dnh}(x)$ is a sum of sinusoidal non-harmonically correlated components. Of course, this new type of approximation is available here because $y_{dh}(x)$ is dominant ($y_d(x) \approx y_{dh}(x)$).

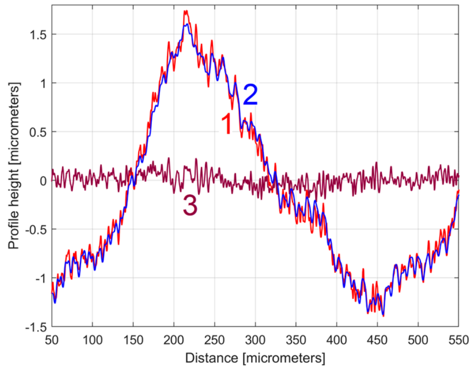

Figure 9. A zoom-in detail in area A from Figure 8.

Among the 122 identified sinusoidal components, 30 components (Hi) were found to be well harmonically correlated (and involved in the definition of $y_{dh}(x)$ from Equation (4)) with a good approximation, with the values of A_{Hi} (amplitudes), ω_{Hi} (conventional angular frequencies), and φ_{Hi} (phases in origin) given in Table 1.

$$y_{dh}(x) \approx \sum_{i=1}^{30} A_{Hi} \cdot \sin(\omega_{Hi} \cdot x + \varphi_{Hi}) \tag{4}$$

Table 1. The values of A_{Hi}, ω_{Hi}, and φ_{Hi} involved in the mathematical description of 30 well harmonically correlated sinusoidal components within $y_{dh}(x)$ of the 2DRP, in the pick direction.

Harmonic # (Hi)	Amplitude A_{Hi} [μm]	Conventional Angular Frequency ω_{Hi} [rad/μm]	Wavelength $\lambda_{Hi} = 2\pi/\omega_i$ [μm]	Phase φ_{Hi} at Origin (x = 0) [rad]
H1	A_{H1} = 1.148	ω_{H1} = 0.01557	λ_{H1} = 403.544	φ_{H1} = 4.2031
H2	0.2459	0.03118 (as 2.0025·ω_{H1})	201.53 (as λ_{H1}/2.0024)	1.412
H3	0.09367	0.04669 (as 2.9987·ω_{H1})	134.57 (as λ_{H1}/2.9988)	4.3261
H4	0.1116	0.06239 (as 4.0070·ω_{H1})	100.70 (as λ_{H1}/4.0074)	2.456
H5	0.02461	0.07848 (as 5.0404·ω_{H1})	80.061 (as λ_{H1}/5.0405)	3.085
H7	0.03816	0.1092 (as 7.0138·ω_{H1})	57.538 (as λ_{H1}/7.0135)	4.785
H8	0.009202	0.1245 (as 7.9961·ω_{H1})	50.467 (as λ_{H1}/7.9962)	5.8120
H9	0.0236	0.1404 (as 9.0173·ω_{H1})	44.752 (as λ_{H1}/9.0173)	3.4731
H10	0.02267	0.1558 (as 10.0064·ω_{H1})	40.328 (as λ_{H1}/10.0065)	4.6591
H11	0.0129	0.1714 (as 11.0083·ω_{H1})	36.658 (as λ_{H1}/11.0083)	1.21
H12	0.01171	0.1873 (as 12.0295·ω_{H1})	33.546 (as λ_{H1}/12.0296)	5.3275

Table 1. *Cont.*

Harmonic # (Hi)	Amplitude A_{Hi} [μm]	Conventional Angular Frequency ω_{Hi} [rad/μm]	Wavelength $\lambda_{Hi} = 2\pi/\omega_i$ [μm]	Phase φ_{Hi} at Origin ($x = 0$) [rad]
H13	0.01317	0.2027 (as 13.0186·ω_{H1})	30.997 (as $\lambda_{H1}/13.0188$)	1.796
H14	0.01174	0.2181 (as 14.0077·ω_{H1})	28.808 (as $\lambda_{H1}/14.0081$)	5.8364
H15	0.01097	0.2337 (as 15.0096·ω_{H1})	26.885 as $\lambda_{H1}/15.0100$)	5.3481
H16	0.01386	0.2493 (as 16.0016·ω_{H1})	25.203 (as $\lambda_{H1}/16.0117$)	3.097
H18	0.01152	0.2805 (as 18.0154·ω_{H1})	22.399 (as $\lambda_1/18.0162$)	5.5279
H19	0.0192	0.2961 (as 19.0173·ω_{H1})	21.219 (as $\lambda_{H1}/19.0180$)	0.628
H22	0.01029	0.3425 (as 21.9974·ω_{H1})	18.345 (as $\lambda_{H1}/21.9975$)	3.9651
H23	0.008842	0.3586 (as 23.0315·ω_{H1})	17.521 (as $\lambda_{H1}/23.0320$)	2.8171
H24	0.02065	0.3741 (as 24.0270·ω_{H1})	16.795 (as $\lambda_{H1}/24.0276$)	4.3321
H25	0.009471	0.3896 (as 25.0225·ω_{H1})	16.127 (as $\lambda_{H1}/25.0229$)	1.299
H26	0.01693	0.4053 (as 26.0308·ω_{H1})	15.502 (as $\lambda_{H1}/26.0317$)	1.822
H27	0.01081	0.4208 (as 27.0263·ω_{H1})	14.931 (as $\lambda_{H1}/27.0273$)	4.2351
H28	0.009238	0.4365 (as 28.0347·ω_{H1})	14.394 (as $\lambda_{H1}/28.0356$)	1.563
H29	0.007853	0.4524 (as 29.0559·ω_{H1})	13.888 (as $\lambda_{H1}/29.0570$)	0.7781
H31	0.01326	0.4833 (as 31.0405·ω_{H1})	13.000 (as $\lambda_{H1}/31.0418$)	0.5155
H32	0.01014	0.4985 (as 32.0167·ω_{H1}	12.604 (as $\lambda_{H1}/32.0171$)	3.9471
H38	0.008485	0.5924 (as 38.0475·ω_{H1})	10.606 (as $\lambda_{H1}/38.0487$)	5.7423
H41	0.02497	0.6392 (as 41.0533·ω_{H1})	9.829 (as $\lambda_{H1}/41.0565$)	1.478
H42	0.01782	0.6548 (as 42.0552·ω_{H1})	9.595 (as $\lambda_{H1}/42.0577$)	0.9996

Some harmonics in Table 1 are missing (e.g., H6, H17, H20, H21, etc.).

Figure 10 shows an equivalent of Figure 8 but with an approximation of $y_d(x)$ by $y_{dh}(x)$, according to Equation (4) and Table 1. Figure 11 shows a zoomed detail in area A of Figure 10 (similar to Figure 9).

A comparison of Figures 10 and 11 with Figures 8 and 9 shows that the fit is acceptable but less good than before, an aspect that is well highlighted by the evolution of the residual ($r_{30}(x)$). In particular, in some areas (e.g., B, C, and D in Figure 10) the fit between $y(x)$ and $y_{dh}(x)$ is locally less good. There are several reasons for this mismatch. Firstly, we should consider the angular position of the milling tool (due to its rotation). This position was not necessarily the same each time when its axis intersects the line (e.g., (d1) on Figure 1) where the 2DRP was sampled (the pick-interval scallops geometry on this line from the working piece is slightly different). Secondly, there is a variable flexional deformation of the milling tool in the direction of this line (pick feed direction).

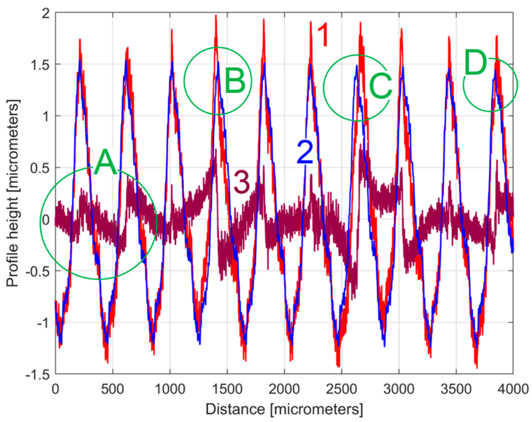

Figure 10. 1—The 2DRP; 2—An approximation of $y_d(x)$ with the profile $y_{dh}(x)$ with 30 components described in Table 1; 3—The 30th residual $r_{30}(x)$.

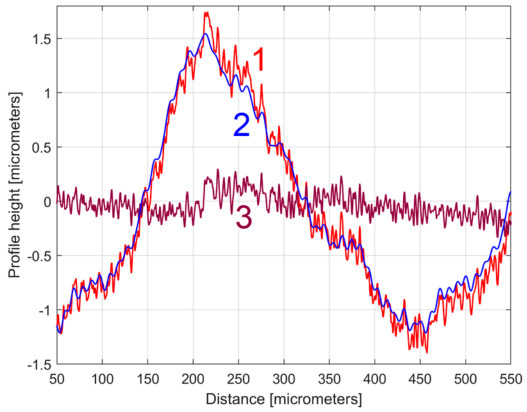

Figure 11. A zoom-in detail in area A from Figure 10.

However, in this approach, the evolution of $y_{dh}(x)$ (shown separately in Figure 12) provides one of the best characterisations of the 2DRP, which is systematically related to the interaction between the milling tool and the workpiece (and obviously by the properties of its material).

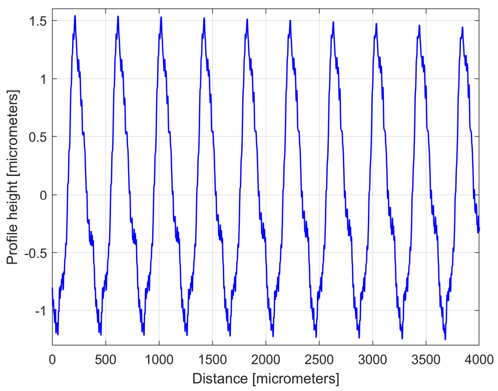

Figure 12. The evolution of the $y_{dh}(x)$ profile.

Due to a small imprecision in the curve (signal) fitting process, there is not a perfect harmonic correlation between the 30 components within $y_{dh}(x)$, as clearly indicated in Table 1 (with $\omega_{Hi} \approx Hi{\cdot}\omega_{H1}$ or $\lambda_{Hi} \approx \lambda_{H1}/Hi$), and the evolution of $y_{dh}(x)$ from Figure 12 is not strictly periodic, as expected.

This inconvenience can be easily avoided by roughly considering ω_{Hi} = $H_i \cdot \omega_{H1}$ in Equation (4). A more rigorous approach is to replace above the conventional angular frequency ω_{H1} with a more precisely equivalent value ω_{He1}, calculated as follows:

$$\omega_{He1} = (\sum_{i=1}^{30} \frac{A_{Hi}}{A_{H1}})^{-1} \cdot \sum_{i=1}^{30} \frac{A_{Hi}}{A_{H1}} \frac{\omega_{Hi}}{H_i} = 0.0155785 \text{ rad/}\mu\text{m} \tag{5}$$

In Equation (5), ω_{He1} is the weighting (by amplitude A_{Hi}) of the conventional angular frequency $\omega_{Hi}$of each harmonic, relative to the amplitude A_{H1} of the first harmonic H1 (as dominant). However, here particularly, there is no significant difference between ω_{H1} and ω_{He1}.

With this value ω_{He1}, the description of $y_{dh}(x)$ from Equation (4) can be rewritten as $y_{dhe}(x)$ according to Equation (6) and plotted according to Figure 13.

$$y_{dhe}(x) = \sum_{i=1}^{30} A_{Hi} \cdot \sin(H_i \cdot \omega_{He1} \cdot x + \varphi_{Hi}) \tag{6}$$

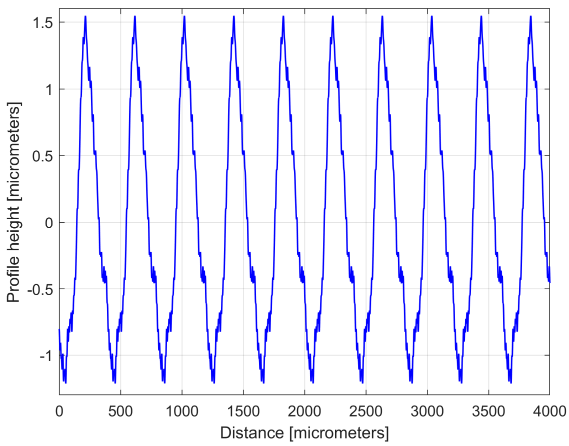

Figure 13. The evolution of the $y_{dhe}(x)$ profile.

This $y_{dhe}(x)$ profile can be accepted as a systematic characterisation (pattern) of the 2DRP in the pick direction. An even more interesting characterisation is obtained if this $y_{dhe}(x)$ profile is described by artificially shifting the origin on x-axis (x = 0) in the abscissa $(2\pi - \varphi_{H1})/\omega_{He1}$ of the first zero crossing (from negative to positive values) of the dominant sinusoidal component (H1 in Table 1). Now the profile $y_{dhe}(x)$ becomes $y_{dhe0}(x)$, described mathematically by Equation (7) and shown graphically in blue in Figure 14. Here, the magenta curve describes the dominant component (H1), also shifted to new origin (as $H1_0$), with ω_{H1} replaced by ω_{He1}.

$$y_{dhe0}(x) = \sum_{i=1}^{30} A_{Hi} \cdot \sin\left[H_i \cdot \omega_{He1} \cdot (x + \frac{2\pi - \varphi_{H1}}{\omega_{He1}}) + \varphi_{Hi}\right] \tag{7}$$

With Equation (7) rewritten as Equation (8), this motion to a new origin is equivalent to a positive phase shift (with $H_i \cdot (2\pi - \varphi_{H1})$) at the origin for each sinusoidal component.

$$y_{dhe0}(x) = \sum_{i=1}^{30} A_{Hi} \cdot \sin\left[H_i \cdot \omega_{He1} \cdot x + \varphi_{Hi} + H_i \cdot (2\pi - \varphi_{H1})\right] \tag{8}$$

Figure 15 shows a zoomed detail of Figure 14, with a first period of the $y_{dhe0}(x)$ profile and of the $H1_0$ sinusoidal component.

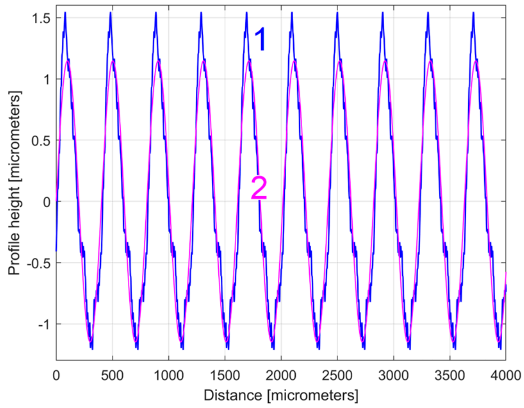

Figure 14. 1—The evolution of $y_{dhe0}(x)$ profile; 2—The evolution of the dominant component $H1_0$.

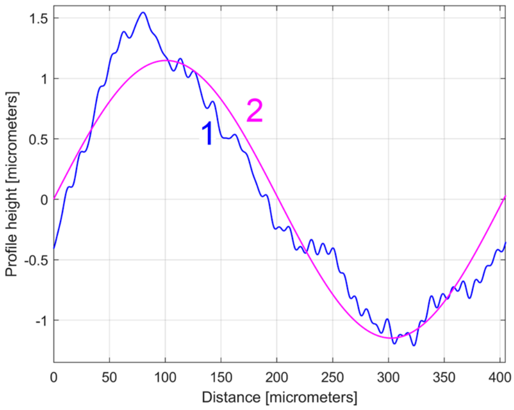

Figure 15. A detail of Figure 14 with the first period of the $y_{dhe0}(x)$ profile and $H1_0$.

This $y_{dhe0}(x)$ type of 2DRP is useful when comparing two (or more) 2DRPs sampled under similar conditions. In this approach, a second 2DRP was sampled on the same flat milled surface on a straight line parallel to (d1) on the pick direction, with a randomly chosen distance between (several millimetres).

As an equivalent to Figure 10, Figure 16 shows this new 2DRP (as $y(x)$, in red) with the same number of samples (8000) and sampling interval (Δx = 0.5 µm), overlaid with the $y_{dh}(x)$ profile (in blue) and the residual (in purple). This time only 12 harmonically related sinusoidal components inside $y_{dh}(x)$ were found (Table 2) among the 122 sinusoidal components in $y_d(x)$. The areas A–D mark some mismatches between the $y(x)$ and $y_{dh}(x)$ profiles.

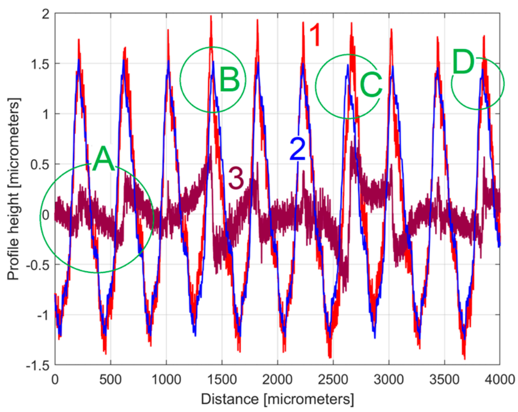

Figure 16. 1—A new 2DRP; 2—An approximation of $y_d(x)$ with $y_{dh}(x)$ profile having 12 components; 3—The 12th residual $r_{12}(x)$.

Table 2. The values A_{Hi}, ω_{Hi}, and φ_{Hi} involved in the mathematical description of 12 harmonically correlated sinusoidal components within $y_{dh}(x)$ of the 2nd 2DRP, sampled in the pick direction.

Harmonic # (Hi)	Amplitude A_{Hi} [µm]	Conventional Angular Frequency ω_{Hi} [rad/µm]	Wavelength $\lambda_{Hi} = 2\pi/\omega_i$ [µm]	Phase φ_{Hi} at Origin (x = 0) [rad]
H1	A_{H1} = 1.124	ω_{H1} = 0.01552	λ_{H1} = 404.8444	φ_{H1} = 0.4821
H2	0.2406	0.03099 (as 1.9968·ω_{H1})	202.7488 (as λ_{H1}/1.9968)	0.407
H3	0.08159	0.04671 (as 3.0097·ω_{H1})	134.5148 (as λ_{H1}/3.0097)	5.2621
H4	0.1232	0.06224 (as 4.0103·ω_{H1})	100.9509 (as λ_{H1}/4.0103)	6.1897
H5	0.0234	0.07745 (as 4.9903·ω_{H1})	81.1257 (as λ_{H1}/4.9903)	4.9971
H6	0.008268	0.09263 (as 5.9604·ω_{H1})	67.8310 (as λ_{H1}/5.9684)	0.205
H7	0.03793	0.1088 (as 7.0103·ω_{H1})	57.7499 (as λ_{H1}/7.0103)	3.7771
H9	0.01861	0.1404 (as 9.0464·ω_{H1})	44.7520 (as λ_{H1}/9.0464)	0.1429
H10	0.02616	0.1558 (as 10.0387·ω_{H1})	40.3285 (as λ_{H1}/10.0387)	3.6981
H11	0.01256	0.1712 (as 11.0309·ω_{H1})	36.7008 (as λ_{H1}/11.0309)	2.608
H13	0.01106	0.2026 (as 13.0541·ω_{H1})	31.0128 (as λ_{H1}/13.0541)	2.05
H22	0.0107	0.3425 (as 22.0683·ω_{H1})	18.3451 (as λ_{H1}/22.0683)	1.326

As an equivalent to Figure 14, Figure 17 shows the evolution of the $y_{dhe0}(x)$ profile (in green) superimposed on the evolution of the dominant component $H1_0$ (in brown).

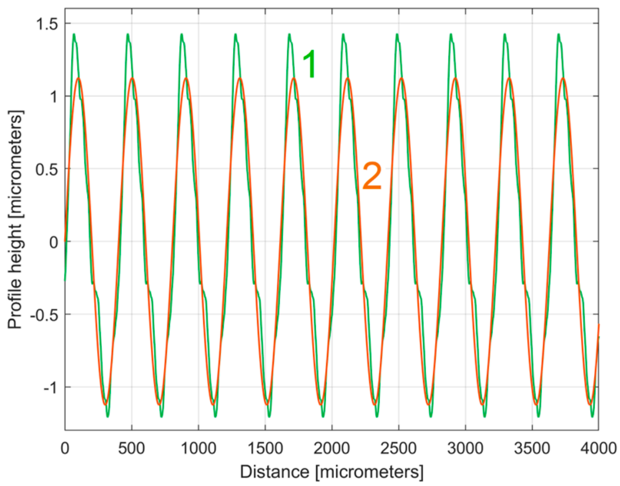

Figure 17. 1—The evolution of the $y_{dhe0}(x)$ profile; 2—The evolution of the dominant component $H1_0$. An equivalent of Figure 14.

It is interesting here to note the similarities (by comparison) between the $y_{dhe0}(x)$ profiles (from Figures 14 and 17) by their overlap in Figure 18. This is possible because both profiles start from a zero crossing (from negative to positive y-ordinates) of their dominant component $H1_0$. A zoomed detail of the first period of Figure 18 is shown in Figure 19.

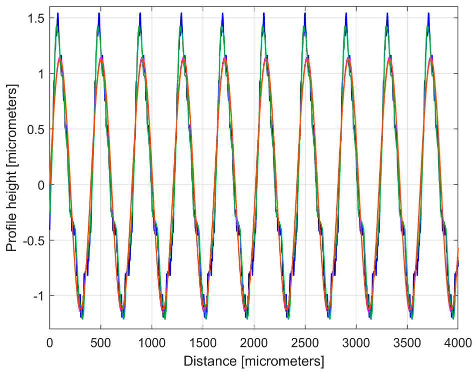

Figure 18. An overlap of both $y_{dhe0}(x)$ profiles (for 1st and 2nd 2DRP) and their dominants $H1_0$.

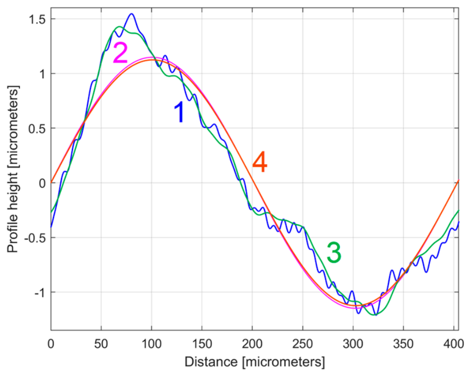

Figure 19. A zoomed detail of Figure 18: 1, 3—the $y_{dhe0}(x)$ profiles; 2, 4—the dominants $H1_0$.

As can be seen in Figure 18 and especially in Figure 19, there are strong similarities between the $y_{dhe0}(x)$ profiles 1 and 3 (and also between the dominant components $H1_0$ 2 and 4). This proves that the proposal of this $y_{dhe0}(x)$ pattern is a useful approach in a comparative analysis of 2DRPs sampled under similar conditions (especially direction) on a flat milled surface with a ball nose end mill.

3.1.1. Synthesis of a 2D Roughness Profile Pattern on a Period by Profile Averaging

There is another simple way of obtaining a synthetic (non-analytical) description of a pattern useful for characterizing the periodic 2DRPs graphically represented by m conventional periods: the y-coordinate of a point on this pattern (as $y_{ap}(x)$) is an average of the y-coordinates of m samples of 2DRP (calculated using a moving average, with m samples selectively selected for averaging). The distance (measured on the x-axis) between each two consecutive samples considered within the average is exactly the conventional period of the dominant H1, as the equivalent wavelength λ_{He1} calculated with $\lambda_{He1} = 2\pi/\omega_{He1}$. A y-coordinate value of this—pattern $y_{ap}(x)$ is determined by calculation as Equation (9):

$$y_{ap}(x) = \frac{1}{m}\sum_{i=0}^{m-1} y(x + i{\cdot}\lambda_{He1}) \qquad \text{with } x = 0 \div \lambda_{He1} \tag{9}$$

The length of this $y_{ap}(x)$ pattern is exactly the conventional period (the wavelength λ_{He1}). A better approach is to describe this $y_{ap}(x)$ pattern starting from the zero crossing of the dominant H1 (as $y_{ap0}(x)$, Equation (10)), where this starting point still has the x-coordinate $(2\pi - \varphi_{H1})/\omega_{He1}$.

$$y_{ap0}(x) = \frac{1}{m}\sum_{i=0}^{m-1} y\left(x + \frac{2\pi - \varphi_{H1}}{\omega_{He1}} + i{\cdot}\lambda_{He1}\right) \qquad \text{with } x = 0 \div \lambda_{He1} \tag{10}$$

Here, x is the x-coordinate of a generic point on the pattern $y_{ap0}(x)$. In Equation (10), in almost all previous equations (except Equation (5)) and in the sampled 2DRP, the x-coordinate is described numerically as $x = l{\cdot}\Delta x$ for the lth sample, $l = 1 \div N$. Here above, $x + (2\pi - \varphi_{H1})/\omega_{He1} + i{\cdot}\lambda_{He1}$ and $x + i{\cdot}\lambda_{He1}$ in Equation (9) are also x-coordinates (numerically described) of samples placed on 2DRP.

Figure 20 shows this $y_{ap0}(x)$ pattern, established by averaging, for the first sampled 2DRP (with $m = 9$). This averaging (acting as a form of digital filtering) greatly attenuates the non-sinusoidal components (noise) as well as the harmonic uncorrelated components with the dominant H1, but it retains the harmonically correlated (averaged) components if they occur systematically. In other words, it is expected that this $y_{ap0}(x)$ pattern is similar with the first period of the $y_{dhe0}(x)$ profile (already shown in Figure 15). This is fully confirmed in Figure 21, where the $y_{ap0}(x)$ pattern, the $y_{dhe0}(x)$ profile, and the dominant $H1_0$ (the first periods) are overlapped.

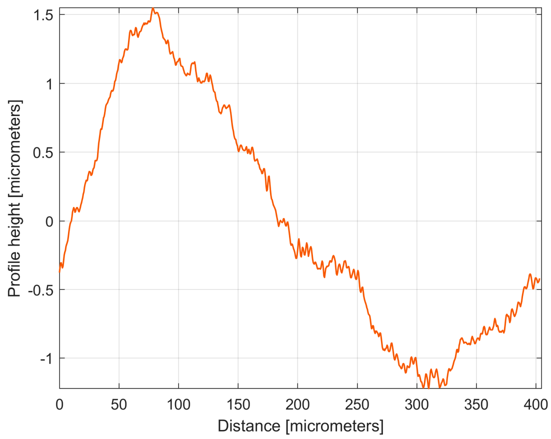

Figure 20. The $y_{ap0}(x)$ pattern of the first 2DRP.

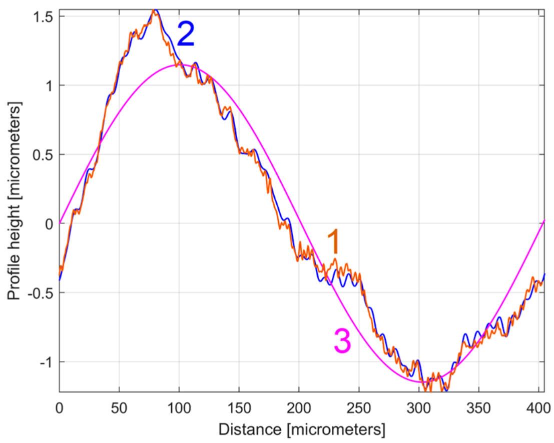

Figure 21. 1—The $y_{ap0}(x)$ pattern of the first 2DRP; 2—The first period of the $y_{dhe0}(x)$ profile; 3—The dominant $H1_0$.

Similar considerations can be made for the $y_{ap0}(x)$ pattern of the 2nd 2DRP sampled in the pick direction, as shown in Figure 22.

There is an interesting utility of these $y_{ap0}(x)$ patterns, similar to the utility of the first periods of the $y_{dhe0}(x)$ profiles, already shown in Figure 19. It allows us to synthetically characterize the roughness profiles, possibly for comparison. As an example, Figure 23 shows the overlap of the $y_{ap0}(x)$ patterns for both sampled 2DRPs in the pick direction.

As expected, there is a very good similarity between the $y_{ap0}(x)$ patterns, which is even better than between the $y_{dhe0}(x)$ profiles (from Figure 19).

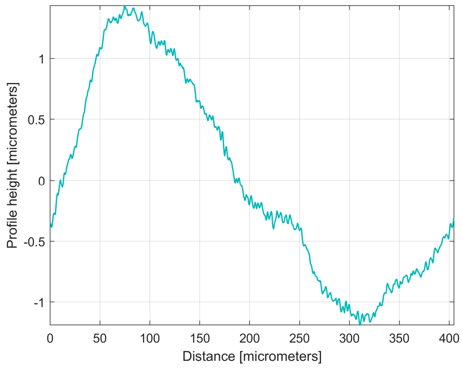

Figure 22. The $y_{ap0}(x)$ pattern of the 2nd 2DRP.

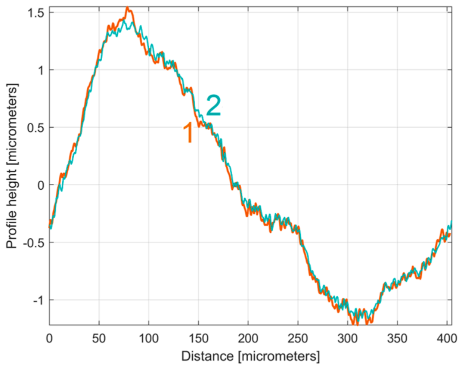

Figure 23. A graphical overlapping of the $y_{ap0}(x)$ patterns: 1—for 1st 2DRP; 2—for 2nd 2DRP.

There is an interesting and simpler way to obtain a more trustworthy mathematical description of the $y_{dhe0}(x)$ profiles (as $y_{dhe0t}(x)$) through analysis by curve (signal) fitting of the mathematically extended $y_{ap0}(x)$ patterns over a large number of periods (e.g., 10), while keeping the same sampling interval Δx = 0.5 µm. Figure 24 shows the $y_{ap0}(x)$ pattern for the 1st 2DRP, the first period of the $y_{dhe0t}(x)$ profile, and the residual $y_{ap0}(x) - y_{dhe0t}(x)$. The $y_{dhe0t}(x)$ profile is described as the sum of 30 harmonically correlated sinusoidal components found in the extended $y_{ap0}(x)$ pattern. Now, by comparison with the results from Figure 21, the similarity between the $y_{ap0}(x)$ pattern and the $y_{dhe0t}(x)$ profile is consistently improved.

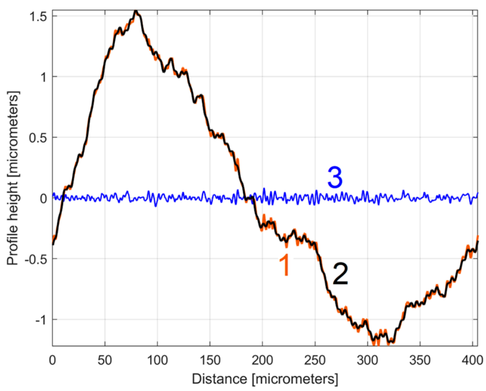

Figure 24. 1—The $y_{ap0}(x)$ pattern for 1st 2DRP; 2—The first period from the $y_{dhe0t}(x)$ profile; 3—The residual $y_{ap0}(x) - y_{dhe0t}(x)$.

The first periods from these $y_{dhe0t}(x)$ profiles (for each 2DRP, each one as a sum of 30 harmonically correlated sinusoidal components) obtained using this new approach are shown in Figure 25.

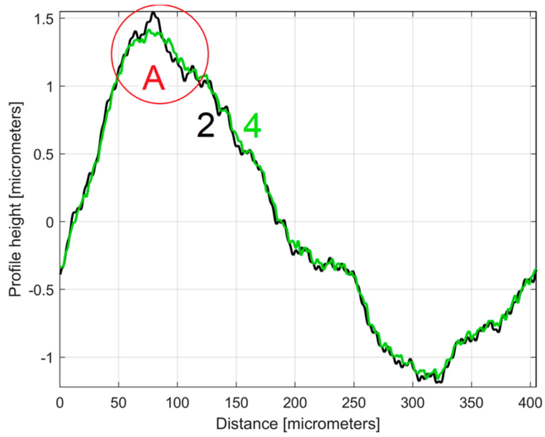

Figure 25. The first period of the $y_{dhe0t}(x)$ profiles: 2—for 1st 2DRP; 4—for 2nd 2DRP.

Compared to Figure 19 (where the profiles $y_{dhe0}(x)$ are overlapped), in Figure 25 the $y_{dhe0t}(x)$ profiles are much more similar, with the exception of area A. As expected, there are very strong similarities between the $y_{dhe0t}(x)$ profiles of Figure 25 and the $y_{ap0}(x)$ patterns of Figure 23.

3.1.2. An Approach on FFT Spectrum in 2D Roughness Profile Description

There is another interesting resource that can be exploited related to the mathematical description of the $y_{dh}(x)$ profile, and in particular the $y_{dhe}(x)$ profile. As already mentioned in Section 1, the length of any of two analytical profiles can be artificially increased by mathematical extrapolation (by increasing the number of samples from N to $p{\cdot}N$), while keeping the same sampling rate f_s (or the same sampling interval Δx = 0.5 µm). In this way, the conventional frequency resolution (as R_{cfe}) of the FFT spectrum for each of the two extrapolated profiles ($R_{cfe} = f_s/pN$) is significantly reduced (by p times compared to the spectra of the original profiles having $R_{cf} = f_s/N$ conventional frequency resolution), while the Nyquist limit remains unchanged. The quality description of the sinusoidal profile components by means of the FFT spectrum increases significantly.

As a first example, related by the first 2DRP, Figure 26 shows partially (in the range $0 \div 0.02$ µm^{-1} of conventional frequency) the FFT spectrum for the $y(x)$ profile (in red, a spectrum already presented before in Figure 5)—and for the extrapolated $y_{dhe}(x)$ profile (in blue, with $p = 10$). Figure 27 presents both spectra over an extended conventional frequency range ($0 \div 0.08$ µm^{-1}), with the first 27 harmonic correlated sinusoidal components (with $\omega_{Hi} = H_i \cdot \omega_{He1}$).

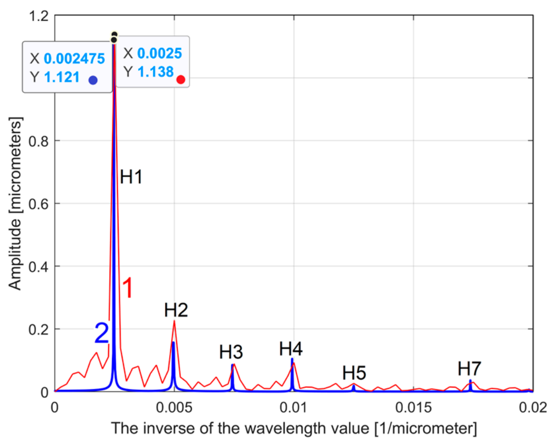

Figure 26. A partial view of the FFT spectrum: 1—of the $y(x)$ profile; 2—of the extrapolated $y_{dhe}(x)$ profile, with $p = 10$. The peaks H1–H7 depict harmonic correlated components.

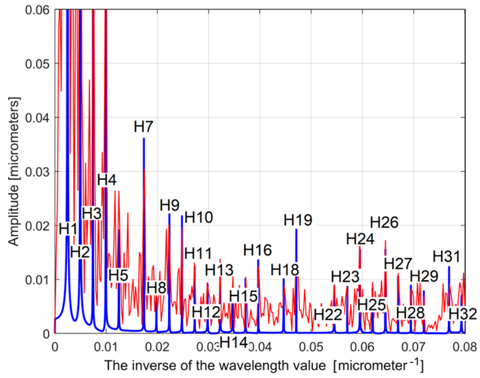

Figure 27. An extended view of the FFT spectra of the $y(x)$ profile (in red) and the extrapolated $y_{dhe}(x)$ profile, with p = 10 (in blue). The peaks H1–H32 depict harmonic correlated components.

Because in this approach the conventional angular frequencies ω_{H1} and ω_{He1} have very similar values (Table 1 and Equation (5)), the FFT spectrum of the extrapolated $y_{dh}(x)$ and $y_{dhe}(x)$ profiles are very similar. Changing the origin of the $y_{dhe}(x)$ profile (to produce the $y_{dhe0}(x)$ profile) does not produce any change on the FFT spectrum (which is insensitive to the phase shifting). The FFT spectra of the extrapolated $y_{dhe}(x)$ and $y_{dhe0}(x)$ profiles are identical.

It is obvious that the FFT spectrum of the extrapolated $y_{dhe}(x)$ profile can also be used as a pattern to compare two (or more) 2DRPs, sampled on the same surface, under identical conditions. The similarities between the partial FFT spectra of the extrapolated $y_{dhe}(x)$ profiles (with p = 10) found in both 2DRPs analysed before, are clearly highlighted in Figure 28, with a zoom on the y-axis shown in Figure 29. In both figures, in order to facilitate the comparison, the FFT spectrum of extrapolated $y_{dhe}(x)$ of the 2nd analysed 2DRP has been artificially shifted by 0. 02 μm upwards and 0.0005 μm^{-1} to the right.

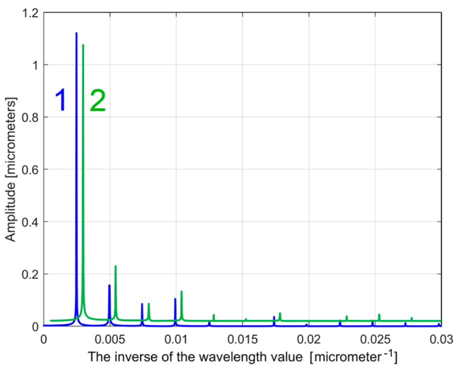

Figure 28. A partial view of the FFT spectra of extrapolated $y_{dhe}(x)$ profiles with p = 10; 1—for 1st 2DRP; 2—for 2nd 2DRP (shifted).

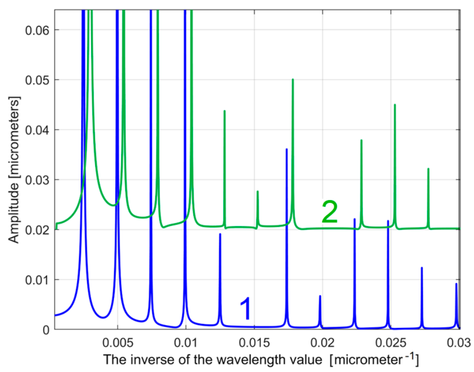

Figure 29. A zoomed image on y-axis of the FFT spectra from Figure 28.

A simpler and more reliable approach is to examine the resources provided by the compared FFT spectra of mathematically extended $y_{ap0}(x)$ patterns (related by both 2DRPs) over a large number of periods.

3.2. Analysis of 2D Roughness Profiles in the Feed Direction

A similar study can be made on the 2DRPs sampled on the same machined surface, in the feed direction, parallel to (d2), under identical conditions, number of samples, and sampling rate (sampling interval). Each of these 2DRPs is expected to describe a periodic succession of feed-interval scallops, as traces left by the tips of the milling tool edges during its rotation and feed motion. For a milling tool having three teeth, a 5600 rpm rotation speed, and a feed rate of 1560 mm/min, the conventional period of these feed-interval scallops should be equal to the feed per tooth f_t = 0.1 mm.

Figure 30 shows a first 2DRP sampled in the feed direction (coloured in red), the deterministic harmonically correlated part $y_{dh}(x)$ (as a sum of 11 components, coloured in blue), and the residual $r_{11}(x)$ coloured in purple. Figure 31 shows the overlap of the first two periods of the dominant $H1_0$ (curve 1), the first two periods of the profile $y_{dhe0}(x)$ (curve 2), and the pattern $y_{ap0}(x)$—with m = 11—extrapolated on two periods (curve 3). As expected, there is a relatively good fit between them.

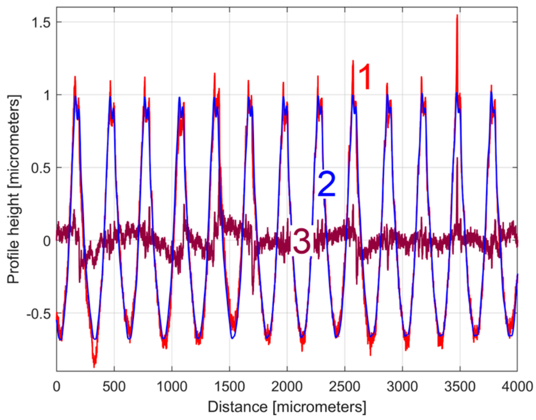

Figure 30. 1—A first 2DRP; 2—The profile $y_{dh}(x)$ with 11 components; 3—The 11th residual $r_{11}(x)$.

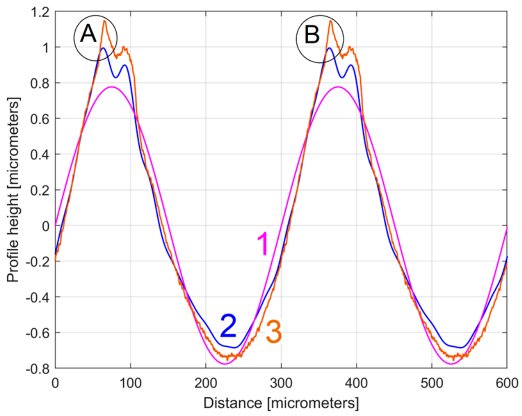

Figure 31. Some results of the analysis of the first 2DRP. Two conventional periods of: 1—the dominant component $H1_0$; 2—the profile $y_{dhe0}(x)$; 3—the pattern $y_{ap0}(x)$.

Unexpectedly, the conventional angular frequency ω_{He1} = 0.020921 rad/µm defines the wavelength $\lambda_{He1} = 2\pi/\omega_{He1}$ = 300.32 µm, as a conventional period, three times greater than the feed per tooth (100 µm), but practically equal to the feed per rotation f_r of the milling tool. This means that the 2DRP in the feed direction reveals an abnormal behaviour of the milling tool, since because it turns off of its axis (with run out [3]), a single tooth is involved in the definition of the final machined surface (roughness). Obviously, the theoretical 2DRP in the feed direction consists mainly of a group of 2D curve (trochoidal) arcs, as parts of the trajectories of points on the teeth cutting edges. Figure 32 shows a conceptual simulation (without milling tool run-out) of these identical trochoidal trajectories (Tr1, Tr2, and Tr3) at a high feed rate (for clarity of approach). Figure 33 describes these trajectories with a particular run-out of milling tool: the centre of tool rotation is in opposite direction to the point involved in generating the trajectory Tr2. In both figures, for down milling, the theoretical 2DRP is described by arcs between the lowest intersection points of the trajectories.

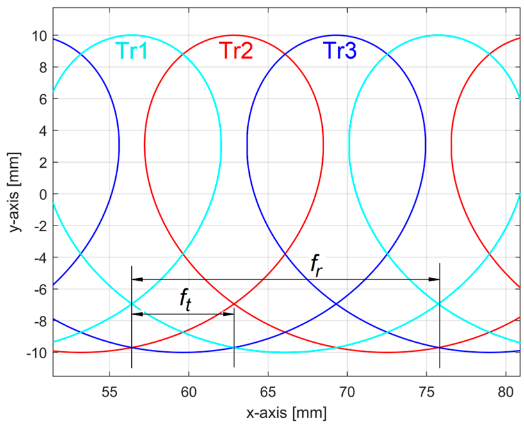

Figure 32. A simulation of 2D trajectories of points placed on teeth cutting edges (no run-out).

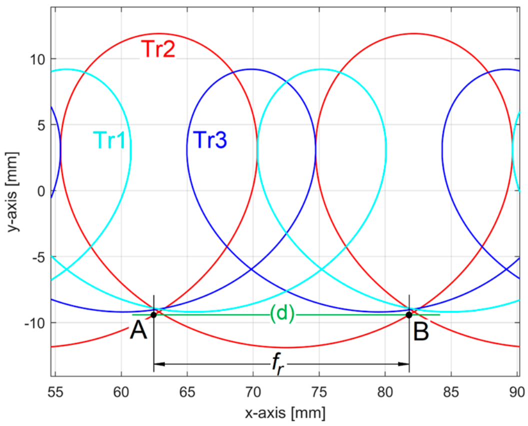

Figure 33. A simulation of 2D trajectories of points placed on teeth cutting edges (with run-out).

If the run-out is large enough, then the theoretical 2DRP is described by arcs placed on a single trochoidal trajectory as in Tr2 in Figure 33. Here, (d) is the workpiece surface reference line before milling. A conventional period of the dominant component in 2DRP is equal with the feed per rotation (f_r) and not with the feed per tooth ($f_t = f_r/3$). The points A, B in Figure 33 are located in the areas A, B in Figure 31. We should mention that, as opposed to Figure 33, Figure 31 does not have the same scale on the x and y-axis.

A similar and comparative study can be made in relation to a second 2DRP sampled on a straight line (feed direction) as a parallel direction to (d2) in Figure 1. As opposed to the analysis of the 2DRP in the pick direction, now this second 2DRP was sampled along a straight line carefully placed as accurately as possible over a whole number of pick intervals. A correct comparison requires that the first and second theoretical 2DRP should be the result of the trajectories of the same points on the teeth cutting edges.

The equivalent of Figure 30 is shown in Figure 34 and the equivalent of Figure 31 is depicted in Figure 35. As expected, similar to Figure 31, there is a relatively good fit between the dominant component $H1_0$, the $y_{dhe0}(x)$ profile, and the pattern $y_{ap0}(x)$.

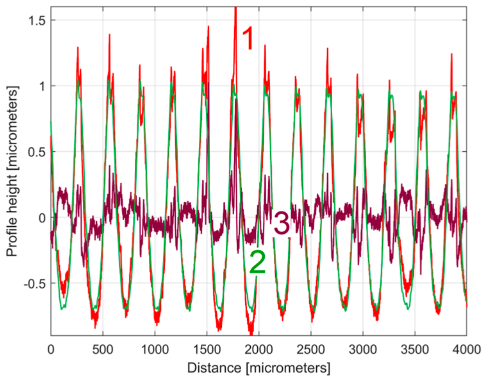

Figure 34. 1—A second 2DRP; 2—The profile $y_{dh}(x)$ having 11 components; 3—The 11th residual $r_{11}(x)$.

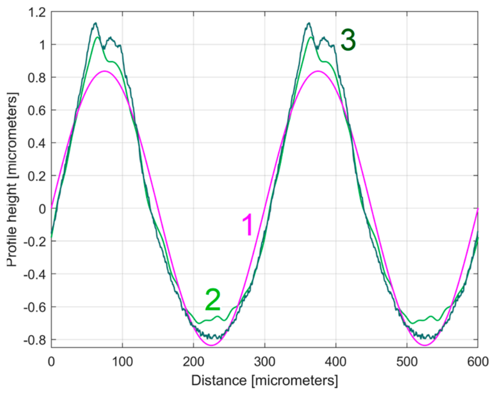

Figure 35. Some results of the analysis of the second 2DRP. Two conventional periods of: 1—the dominant component $H1_0$; 2—the profile $y_{dhe0}(x)$; 3—the pattern $y_{ap0}(x)$.

As previously stated, related by the first 2DRP in the feed direction, the same abnormal behaviour of the milling tool persists, because for the run-out it is the case that a single tooth is involved in defining the final machined surface, and the conventional angular frequency ω_{He1} = 0.020946 rad/µm defines the wavelength $\lambda_{He1} = 2\pi/\omega_{He1}$ = 299.97 µm, as a conventional period or feed per rotation f_r (very close to that determined for the first profile), which is three times greater than the feed per tooth (100 µm).

A comparison of Figures 31 and 35 shows that, similar to the study in the pick direction, there are also strong similarities between these two different 2DRPs sampled in the feed direction. Figure 36 shows two periods of the overlapped profiles $y_{dhe0}(x)$, Figure 37 shows the overlap of the extended patterns $y_{ap0}(x)$ with two periods, and Figure 38 shows the first two overlapped periods of the $y_{dhe0t}(x)$ profiles.

However, it should be noted that the coincidence of these two $y_{dhe0}(x)$ profiles (Figure 36) is less good than in the case of the $y_{dhe0}(x)$ profiles for 2DRPs sampled in the pick direction (Figure 19). A similar conclusion can be drawn for the fit of the $y_{ap0}(x)$ patterns (by comparing Figures 23 and 37) or for the $y_{dhe0t}(x)$ profiles (Figures 25 and 38). The main reason for these mismatches is the lack of certainty that the two analysed 2DRPs were generated by the same points of the tool edges (an error that must be eliminated for an accurate analysis).

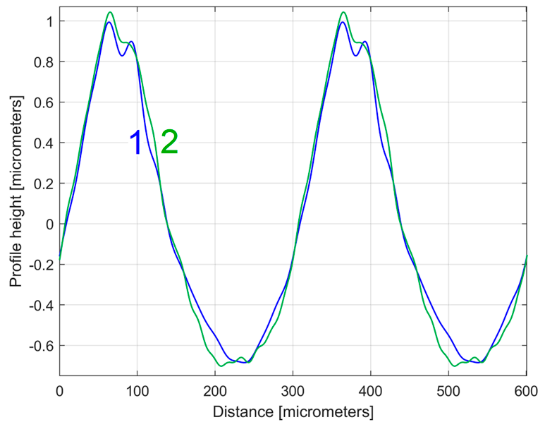

Figure 36. An overlap of the $y_{dhe0}(x)$ profiles (two periods) for the 1st and 2nd 2DRP (1 and 2).

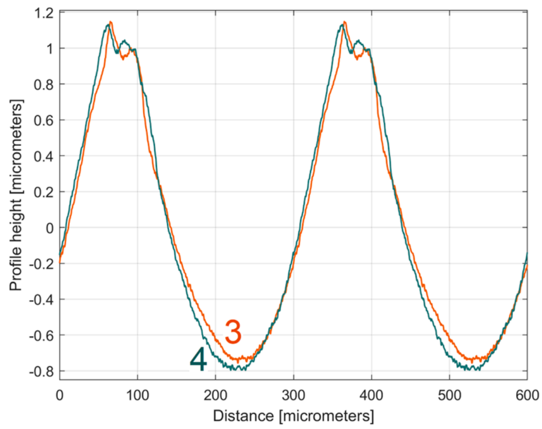

Figure 37. An overlap of the $y_{ap0}(x)$ patterns (two periods) for the 1st and 2nd 2DRP (3 and 4).

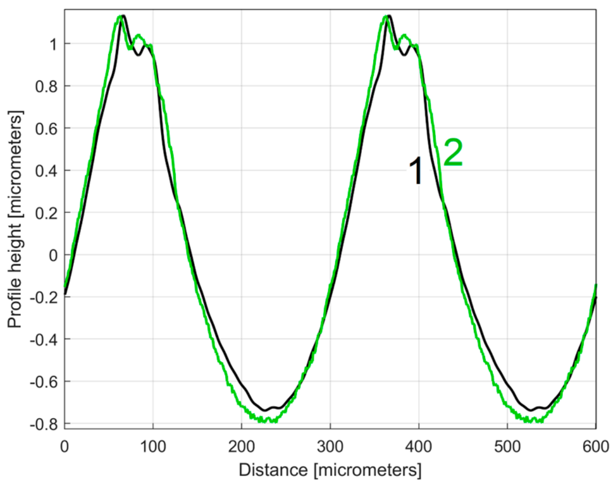

Figure 38. The first two periods of the $y_{dhe0t}(x)$ profiles: 1—for the 1st 2DRP; 2—for the 2nd 2DRP.

As already stated before, the description of the $y_{dhe0t}(x)$ profiles is more reliable (in relation to the $y_{ap0}(x)$ patterns) than the description of the $y_{dhe0}(x)$ profiles.

It is also possible to make a comparison between the FFT spectra of the extrapolated $y_{dhe}(x)$ profiles of both 2DRPs, with $p = 10$, as Figure 39 indicates, with zooming in on the y-axis, as shown in Figure 40. For easier comparison, the FFT spectrum of the extrapolated $y_{dh}(x)$ of the 2nd analysed 2DRP has been artificially shifted by 0.01 μm upwards and 0.0005 μm^{-1} to the right.

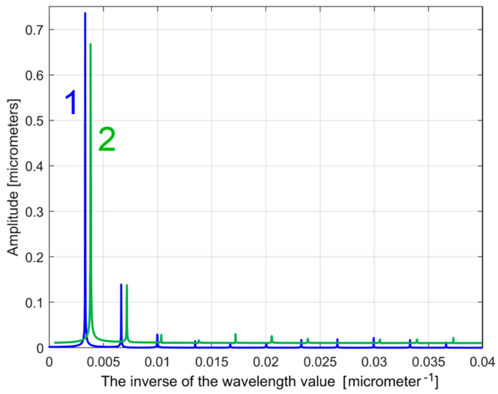

Figure 39. A partial view of the FFT spectra of the extrapolated $y_{dhe}(x)$ profiles with p = 10: 1—for the first 2DRP; 2—for the second 2DRP (shifted).

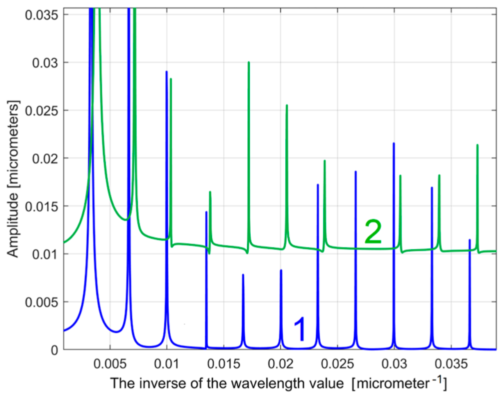

Figure 40. A zoomed image on the y-axis of the FFT spectra from Figure 39.

The similarities between spectra of the extrapolated $y_{dhe}(x)$ profiles are certainly related by conventional peak frequencies but less certainly related by the peak amplitudes.

4. Conclusions

The proposed method for analysing and finding (by curve/signal fitting) the mathematical description of the periodic part of an experimental 2D roughness profile, 2DRP (as a sum of sinusoidal components harmonically correlated), provides reliable results, experimentally confirmed, useful for the characterisation of the milled surface (as a sum of wavinesses in two perpendicular directions), the interaction between the tool and workpiece during the milling process (in particular of flat surfaces machined with a ball nose end mill, constant step over), and the machinability of workpiece materials by a cutting process.

This paper proposes an analytical definition of a periodic profile as the best systematic characterisation (pattern) of an experimental 2DRP sampled with a contact profilometer (in pick and feed directions). A very similar periodic profile (but without an analytical description) is generated by a special type of sample averaging within the experimental 2DRP. These periodic profiles are useful for comparison purposes between different experimental 2DRPs, or to validate a predictive model for 2DRP [12,29,30], or to obtain the mathematical description of the microgeometry of a milled surface.

As suggested during the review of this paper, a possible approach would be to use a curve fitting formula using the milling process parameters (and also tool condition and characteristics) as variables. This will be a challenge for a future approach. In the current approach (valid for any type of evolution of a physical quantity with a dominant periodic component), the fitting formula (a sinusoidal function), repetitively applied to obtain the best characterisation of the 2DRP profile as the sum of significantly harmonically correlated sinusoidal components (used as a pattern), indirectly provides some information related to the milling process, such as the peak to peak amplitude of the resultant is the pick-interval or feed-interval scallop height, and the conventional angular frequency of the fundamental describes the pick feed (pick direction 2DRP) or feed per tooth (feed direction 2DRP) as a relationship between tool rotation speed and feed rate. The analysis of the shapes of the experimental 2DRP patterns and the highlighting of differences with the theoretical patterns allows for the qualitative description of some anomalies of the machining process, such as the tool run-out (already shown in this paper), tool wear or cutting edges fracture, elastic bending deformation of the tool, etc.

This paper proves that the mathematical extrapolation of the analytically defined periodic profile of 2DRP improves the availability of a known but underutilized method of roughness analysis based on the spectrum of the periodic profile (seen as a time-dependent signal) generated by Fast Fourier Transform (FFT), with a low (conventional) frequency resolution.

Of course, generalisation of these results to the analysis of other types of milled surfaces, machined on other milling machines, with other types of tools on other workpiece materials (and possibly using other roughness sampling methods), is entirely feasible in a future approach.

As a future approach, we also intend to extend this study to the investigation of the 3D mathematical description of the roughness microgeometry of the complex milled surfaces, experimentally sampled with a suitable optical system.

Author Contributions: Conceptualization, M.H. and F.C.; methodology, M.H., E.P., C.G.D. and A.M.; software M.H. and C.G.D.; validation F.C., E.P. and A.M.; investigation E.P., M.H. and D.-F.C.; resources C.G.D. and D.-F.C.; data curation, M.H., E.P., C.G.D., A.M. and D.-F.C.; writing—original draft preparation, M.H., F.C., C.G.D. and A.M.; writing—review and editing, E.P. and D.-F.C.; supervision and project administration, M.H. and C.G.D.; funding acquisition, C.G.D. All authors have read and agreed to the published version of the manuscript.

Funding: This work was supported by Gheorghe Asachi Technical University of Iasi, Romania.

Institutional Review Board Statement: Not applicable.

Informed Consent Statement: Not applicable.

Data Availability Statement: The data presented in this paper are available upon request addressed to the corresponding author. The data are not publicly available due to privacy.

Acknowledgments: Many thanks to Mitutoyo Romania for the donation of the roughness measuring equipment. We would like to thank our colleagues Neculai-Eugen Seghedin and Eugen Carata who previously equipped the department with several modern CNC machines and equipment. Some of these were used in this study. We also thank our colleague Florentin Cioata for his support and advice.

Conflicts of Interest: The authors declare no conflicts of interest.

References

1. Chen, J.S.; Huang, Y.K.; Chen, M.S. A study of the surface scallop generating mechanism in the ball-end milling process. *Int. J. Mach. Tools Manuf.* **2005**, *45*, 1077–1084. [CrossRef]
2. Costes, J.P. A predictive surface profile model for turning based on spectral analysis. *J. Mater. Process. Technol.* **2013**, *213*, 94–100. [CrossRef]
3. Ren, Z.; Fang, Z.; Kobayashi, G.; Kizaki, T.; Sugita, N.; Nishikawa, T.; Kugo, J.; Nabata, E. Influence of tool eccentricity on surface roughness in gear skiving. *Precis. Eng.* **2020**, *63*, 170–176. [CrossRef]
4. Álvarez-Flórez, J.; Buj-Corral, I.; Vivancos-Calvet, J. Analysis of roughness, force and vibration signals in ball-end milling processes. *J. Trends Dev. Mach. Assoc. Technol.* **2015**, *19*, 1–4.
5. Zahaf, M.Z.; Benghersallah, M. Surface roughness and vibration analysis in end milling of annealed and hardened bearing steel. *Measur. Sens.* **2021**, *13*, 100035. [CrossRef]
6. Bai, J.; Zhao, H.; Zhao, L.; Cao, M.; Duan, D. Modelling of surface roughness and studying of optimal machining position in side milling. *Int. J. Adv. Manuf. Technol.* **2021**, *116*, 3651–3662. [CrossRef]
7. Grzesik, W.; Brol, S. Wavelet and fractal approach to surface roughness characterization after finish turning of different workpiece materials. *J. Mater. Process. Technol.* **2009**, *209*, 2522–2531. [CrossRef]
8. Drbúl, M.; Martikáň, P.; Bronček, J.; Litvaj, I.; Svobodová, J. Analysis of roughness profile on curved surfaces. *MATEC Web Conf.* **2018**, *244*, 01024. [CrossRef]

9. Dumitras, C.G.; Chitariu, D.F.; Chifan, F.; Lates, C.G.; Horodinca, M. Surface Quality Optimization in Micromachining with Cutting Tool Having Regular Constructive Geometry. *Micromachines* **2022**, *13*, 422. [CrossRef]
10. Seyedi, S.S.; Shabgard, M.R.; Mousavi, S.B.; Heris, S.Z. The impact of SiC, Al_2O_3, and B_2O_3 abrasive particles and temperature on wear characteristics of 18Ni (300) maraging steel in abrasive flow machining (AFM). *Int. J. Hydrogen Energy* **2021**, *46*, 33991–34001. [CrossRef]
11. Krolczyk, G.; Legutko, S. Experimental analysis by measurement of surface roughness variations in turning process of duplex stainless steel. *Metrol. Meas. Syst.* **2014**, *XXI*, 759–770. [CrossRef]
12. Shang, S.; Wang, C.; Liang, X.; Cheung, C.F.; Zheng, P. Surface roughness prediction in ultra-precision milling: An extreme learning machine method with data fusion. *Micromachines* **2023**, *14*, 2016. [CrossRef]
13. Wang, N.; Jiang, F.; Zhu, J.; Xu, Y.; Shi, C.; Yan, H.; Gu, C. Experimental study on the grinding of an Fe-Cr-Co permanent magnet alloy under a small cutting depth. *Micromachines* **2022**, *13*, 1403. [CrossRef] [PubMed]
14. Li, J.; Xu, W.; Shen, T.; Jin, W.; Wu, C. Evaluating surface roughness of curved surface with circular profile based on arithmetic circular arc fitting. *AIP Adv.* **2023**, *13*, 125312. [CrossRef]
15. Kundrák, J.; Felhő, C.; Nagy, A. Analysis and prediction of roughness of face milled surfaces using CAD model. *Manuf. Technol.* **2022**, *22*, 555–572. [CrossRef]
16. Lazkano, X.; Aristimunno, P.X.; Aizpuru, O.; Arrazola, P.J. Roughness maps to determine the optimum process window parameters in face milling. *Int. J. Mech. Sci.* **2022**, *221*, 107191. [CrossRef]
17. Varga, J.; Ižol, P.; Vrabel', M.; Kaščák, L.; Drbúl, M.; Brindza, J. Surface Quality Evaluation in the Milling Process Using a Ball Nose End Mill. *Appl. Sci.* **2023**, *13*, 10328. [CrossRef]
18. Żurawski, K.; Żurek, P.; Kawalec, A.; Bazan, A.; Olko, A. Modeling of Surface Topography after Milling with a Lens-Shaped End-Mill, Considering Runout. *Materials* **2022**, *15*, 1188. [CrossRef]
19. Palani, S.; Natarajan, U. Prediction of surface roughness in CNC end milling by machine vision system using artificial neural network based on 2D Fourier transform. *Int. J. Adv. Manuf. Technol.* **2011**, *54*, 1033–1042. [CrossRef]
20. Lou, Z.; Yan, Y.; Wang, J.; Zhang, A.; Cui, H.; Li, C.; Geng, Y. Exploring the structural color of micro-nano composite gratings with FDTD simulation and experimental validation. *Opt. Express* **2024**, *32*, 2432–2451. [CrossRef]
21. Zeng, Q.; Qin, Y.; Chang, W.; Luo, X. Correlating and evaluating the functionality-related properties with surface texture parameters and specific characteristics of machined components. *Int. J. Mech. Sci.* **2018**, *149*, 62–72. [CrossRef]
22. Filtration Techniques for Surface Texture. Available online: https://guide.digitalsurf.com/en/guide-filtration-techniques.html (accessed on 15 February 2024).
23. Josso, B.; Burton, D.R.; Lalor, M.J. Frequency normalised wavelet transform for surface roughness analysis and characterisation. *Wear* **2002**, *252*, 491–500. [CrossRef]
24. Josso, B.; Burton, D.R.; Lalor, M.J. Wavelet strategy for surface roughness analysis and characterization. *Comput. Methods Appl. Mech. Eng.* **2001**, *191*, 829–842. [CrossRef]
25. Wang, X.; Shi, T.; Liao, G.; Zhang, Y.; Hong, Y.; Chen, K. Using wavelet packet transform for surface roughness evaluation and texture extraction. *Sensors* **2017**, *17*, 933. [CrossRef]
26. Hao, H.; He, D.; Li, Z.; Hu, P.; Chen, Y.; Tang, K. Efficient cutting path planning for a non-spherical tool based on an iso-scallop height distance field. *Chin. J. Aeronaut.* **2023**, *in press*, *uncorrected proof*. [CrossRef]
27. Horodinca, M.; Bumbu, N.-E.; Chitariu, D.-F.; Munteanu, A.; Dumitras, C.-G.; Negoescu, F.; Mihai, C.-G. On the behaviour of an AC induction motor as sensor for condition monitoring of driven rotary machines. *Sensors* **2023**, *23*, 488. [CrossRef]
28. Lecture: Sums of Sinusoids (of Different Frequency). Available online: http://www.spec.gmu.edu/~pparis/classes/notes_201/notes_2019_09_12.pdf (accessed on 15 February 2024).
29. Chen, C.-H.; Jeng, S.-Y.; Lin, C.-J. Prediction and analysis of the surface roughness in CNC end milling using neural networks. *Appl. Sci.* **2022**, *12*, 393. [CrossRef]
30. Peng, Z.; Jiao, L.; Yan, P.; Yuan, M.; Gao, S.; Yi, J.; Wang, X. Simulation and experimental study on 3D surface topography in micro-ball-end milling. *Int. J. Adv. Manuf. Technol.* **2018**, *96*, 1943–1958. [CrossRef]

materials

MDPI

Article

Experimental Investigation of Water Jet-Guided Laser Micro-Hole Drilling of C_f/SiC Composites

Binying Bao [1,2], Guangyi Zhang [2,*], Zhongan Chen [1,2], Yang Chao [2], Chunhai Guo [2] and Wenwu Zhang [2,*]

1 College of Mechanical Engineering, Zhejiang University of Technology, Hangzhou 310023, China; baobinying@nimte.ac.cn (B.B.); chenzhongan@nimte.ac.cn (Z.C.)
2 Ningbo Institute of Materials Technology and Engineering, Chinese Academy of Sciences, Ningbo 315201, China; chaoyang@nimte.ac.cn (Y.C.); guochunhai@nimte.ac.cn (C.G.)
* Correspondence: zhangguangyi@nimte.ac.cn (G.Z.); zhangwenwu@nimte.ac.cn (W.Z.)

Abstract: In this paper, water jet-guided laser (WJGL) drilling of C_f/SiC composites was employed and the effects of the processing parameters on the depth and quality of the micro-holes were systematically investigated. Firstly, the depth measurement showed that the increase in processing time and power density led to a significant improvement in micro-hole drilling depth. However, the enhancement of the water jet speed resulted in a pronounced decrease in the depth due to the phenomenon of water splashing. In contrast, the scanning speed, path overlap ratio, pulse frequency, and helium pressure exhibited less effect on the micro-hole depth. Secondly, the microstructural analysis revealed that the increase in power density resulted in the deformation and fracture of the carbon fibers, while the augmentation in water jet speed reduced the thermal defects. Finally, based on the optimization of the processing parameters, a micro-hole of exceptional quality was achieved, with a depth-to-diameter ratio of 8.03 and a sidewall taper of 0.72°. This study can provide valuable guidance for WJGL micro-hole drilling of C_f/SiC composites.

Keywords: water jet-guided laser; C_f/SiC composites; micro-hole drilling; influencing factor; microstructure analysis

1. Introduction

In the aerospace field, lightweight design is crucial for reducing the overall mass of the vehicle and plays a pivotal role in improving structural strength and safety. By adopting lightweight design, not only can the launch cost be lowered, but also the thrust-to-weight ratio of the engine is improved [1–3]. C_f/SiC ceramic composites possess substantially lower density than superalloys and are characterized by high-temperature resistance, high specific strength, and oxidation resistance. Additionally, by introducing continuous fibers, C_f/SiC composites address the brittleness of ceramic materials and may replace metals as a new generation of high-temperature structural materials [4–6]. Thus far, C_f/SiC composites have been applied to components such as combustion chambers, heat shields, wing leading edges, rocket nozzles, etc., in the context of ultra-high-speed vehicles [7–10].

Achieving precision machining of C_f/SiC composites is necessary to meet the requirements of assembly and application. However, the high hardness, anisotropy, and inhomogeneity of the fibers and distribution of pores of C_f/SiC composites present great challenges for their processing [11]. Traditional machining for C_f/SiC composites includes cutting, milling, drilling, etc., which has the advantages of a simple process, wide application, and high machining efficiency [12]. However, cutting forces in the direction of the perpendicular fiber layup can lead to delamination defects due to the low interlaminar bond strength of the material [13]. During drilling, the fibers are pulled out of the substrate by the axial force and generate burrs. The carbon fibers are removed mainly by fracture, resulting in a rough machined surface [14]. Moreover, the tool is subject to heavy wear. To minimize the defects present in conventional machining, various non-traditional machining methods have been developed. Rotary ultrasonic machining provides lower cutting forces and reduces tearing defects on the hole surface [15,16]. Abrasive water jet machining offers negligible thermal effects but is prone to cracking and delamination [17]. Laser processing is characterized by no mechanical stress and high energy density. However, one of the main disadvantages of laser ablation is the heat-affected zone [18]. To minimize the thermal damage, short-pulse lasers and ultrashort-pulse lasers were employed for C_f/SiC composite processing. However, the cutting surfaces of millisecond and nanosecond lasers are characterized by the presence of large amounts of debris and recast layers [19,20]. Picosecond and femtosecond lasers may reduce oxide generation but prolong processing time [21,22].

Water jet-guided laser (WJGL) processing technology combines a laser and water jet with minimal thermal effect, strong machining capability, and high adaptability [23–25]. In recent years, WJGL has been applied to composite materials processing by many researchers. Marimuthu et al. [26] drilled silicon carbide-reinforced aluminum matrix composites with WJGL and obtained holes without molten layers. Wu et al. [27] investigated the effects of laser power, feed speed, and water jet speed on the depth and width of carbon fiber-reinforced plastic (CFRP) cuts and analyzed the relationship between the direction of carbon fiber arrangement and cutting damage. Moreover, the parallel path layered scanning method was utilized to achieve the 10 mm thickness CFRP cutting. Cheng et al. [28] introduced a novel coaxial helical gas-assisted technique to improve WJGL processing capability. Eventually, a SiC_f/SiC composite microgroove with a maximum depth-to-width ratio of 13.6 and without recast layers, fiber pullout, and delamination was achieved. Hu et al. [29] studied the effect of laser power, scanning speed, and fill spacing on WJGL grooving of SiC_f/SiC composites. The experimental results showed that the processing parameters significantly affected the ablation depth, volume, and surface morphology. Therefore, different processing efficiency and quality requirements should be considered when selecting processing parameters.

Given the results of the literature review, the problem of high-quality deep-hole drilling of C_f/SiC composites requires an urgent solution, while the research on WJGL processing for C_f/SiC composites still lacks a detailed report. Therefore, this paper systematically investigates the effects of parameters such as the laser, water jet, and scanning path on the depth and morphology of WJGL micro-hole drilling of C_f/SiC composites. Based on optimizing the processing parameters, a high-quality micro-hole with a depth-to-diameter ratio of 8.03 and a depth of 4.1 mm was achieved. These micro-holes processed by WJGL can be applied in aerospace engines and brake disks. This paper presents a detailed analysis of the process of WJGL drilling of C_f/SiC composites and the mechanism of each factor, which can provide valuable guidance for high-quality deep-hole drilling.

2. Materials and Methods

2.1. Materials

The material used in the experiments was C_f/SiC ceramic composites with a 3-dimensional (3D) needle-punched structure (Zhejiang Hangyin New Material Technology Co., Hangzhou, China) measuring 58.2 mm × 10.0 mm × 4.1 mm, as shown in Figure 1c. The C_f/SiC composites consist of SiC matrix, carbon fibers, and pyrolytic carbon interface layer. Figure 1d shows its cross-sectional morphology, and the layered stacked carbon fibers can be divided into transversal and longitudinal carbon fibers, as shown in Figure 1e. The diameter of the carbon fiber is about 6–8 μm, and the volume fraction is about 40%. The characteristic parameters of C_f/SiC composites at room temperature are shown in Table 1.

Table 1. Characteristic parameters of the C_f/SiC composites at room temperature.

Properties	Parameters	Units
Diameter of carbon fiber	6–8	μm
Thickness of PyC	∼0.3	μm
Density	1.7	g/cm^3
Fiber volume fraction	∼40	%
Porosity	∼18	%
Tensile strength	>120	MPa
Bending strength	>250	MPa
Interlayer thermal conductivity	∼5	W/(m·K)
Size	58.2 × 10.0 × 4.1	mm

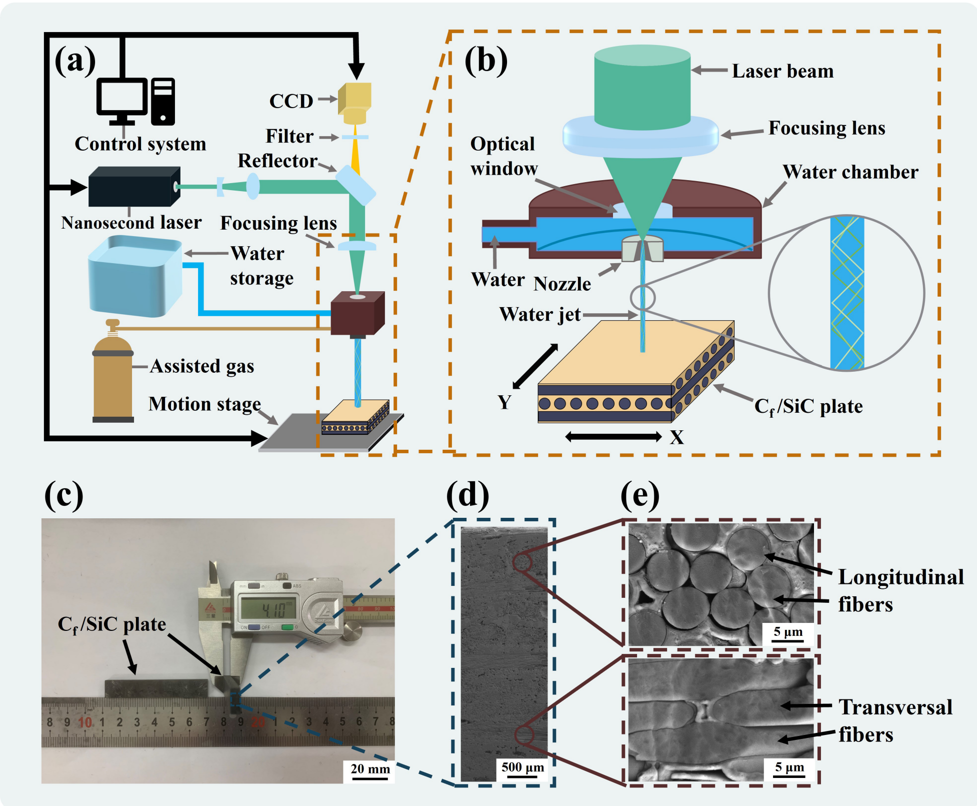

Figure 1. Water jet-guided laser (WJGL) processing system and experimental materials. (**a**) Schematic diagram of the WJGL processing system. (**b**) Schematic diagram of the principle of WJGL processing. (**c**) Macroscopic morphology of the C_f/SiC composites. (**d**) Cross-section morphology of the C_f/SiC composites. (**e**) Microstructure of the transversal and longitudinal carbon fibers.

2.2. WJGL System and Processing Principle

The experimental platform was a self-developed WJGL processing system. As shown in Figure 1a, the processing system mainly consists of the following components: control system, nanosecond laser, optical path system (including reflection lens, beam-expanding lens, focusing lens, and dichroic lens), charge coupled device (CCD), high-pressure water supply system, auxiliary gases, and motion stage. The laser source was a solid-state nanosecond laser with a wavelength of 532 nm. The auxiliary gas was helium, which coaxially surrounded the water jet to reduce the friction between the surface of the water jet and the air.

Figure 1b shows the principle of WJGL processing. First, the water supply system provides high-pressure deionized water into the water chamber, which is injected at the nozzle and forms a steady micro-water-jet. Then, the laser is coaxially aligned with the water jet and is focused through a focusing lens into the nozzle to couple with the water jet. The coupling error is reduced by CCD observation. Finally, the laser continuously undergoes total reflection in the water jet and is transmitted to the material to achieve processing.

2.3. Experimental Design

The effects of scanning speed, path overlap ratio, pulse frequency, helium pressure, processing time, power density, and water jet speed on the micro-hole depth and morphology of WJGL drilling of C_f/SiC composites were experimentally investigated. The experimental parameters are shown in Table 2. The laser power density I is calculated by the following equation:

$$I = \frac{P_{avg}}{f\tau A} \tag{1}$$

where P_{avg} is the average laser power, f is the pulse frequency, A is the irradiated area of the WJGL, and τ is the pulse width.

In pulsed lasers, power density represents the amount of energy irradiated per unit time by a single laser pulse per unit area of the target material. Power density typically determines whether the material reaches a threshold for destruction, ablation, and other effects.

During the experiments, the changes in the WJGL irradiated area and pulse width were negligible. Thus, the power density was proportional to the average laser power and inversely proportional to the pulse frequency. In the single-factor experiments, the other parameters were held constant, where the power density was 0.10 GW/cm^2, the pulse frequency was 10 kHz, the water jet speed was 100 m/s, the scanning speed was 0.3 mm/s, the path overlap ratio was 50%, the helium pressure was 5 kPa, and the processing time was 45 s. The holes obtained in the experiments were blind. Each set of experiments was conducted three times.

Table 2. Experimental parameters.

Parameter	Value	Units
Laser wavelength	532	nm
Pulse width	70–100	ns
Maximum average power	15	W
Repetition frequency	2.5, 5, 7.5, 10, 12.5, 15	kHz
Power density	0.01, 0.05, 0.10, 0.15, 0.20, 0.25	GW/cm^2
Water jet speed	40, 60, 80, 100, 120, 140	m/s
Scanning speed	0.1, 0.3, 0.5, 0.7, 0.9, 1.1	mm/s
Path overlap ratio	40, 50, 60, 70, 80, 90	%
Helium pressure	0, 5, 10, 20, 30, 40	kPa
Drilling time	15, 30, 45, 60, 75, 90	s
Nozzle diameter	100	μm

2.4. Drilling Strategy and Characterization

The laser scanning path during drilling was a top-down multilayer concentric circle filling path, as shown in Figure 2. Due to the characteristics of total reflection transmission of the laser in the water jet, the laser focus position does not need to be adjusted during the scanning process [30,31]. The diameter of the processed holes was fixed at 500 μm. The concentric circles were fixed at four. The laser scanned concentric circles from outside to inside and then returned to complete a cycle. When scanning adjacent concentric circles, the overlap area between the water jets is the overlap path, and the ratio of its width to the diameter of the water jet is the path overlap ratio. The path overlap ratio can be adjusted by adjusting the distance L between adjacent concentric circles.

After WJGL drilling, the surface morphology and 3D contours of the micro-holes were observed and the micro-hole depths were measured using a laser confocal microscope

(Keyence VX-200, Keyence Co., Osaka, Japan) at 500× magnification. The cross-sectional microstructure of the micro-holes was observed and elemental distribution was analyzed with a scanning electron microscope (Regulus-8230, Hitachi, Ltd., Tokyo, Japan). The splashing morphologies were captured with a high-speed camera (Qian Yan Lang X213M, Hefei Zhongke Junda Vision Technology Co., Hefei, China) at the rate of 1000 frames per second with 1280 × 1024 pixels.

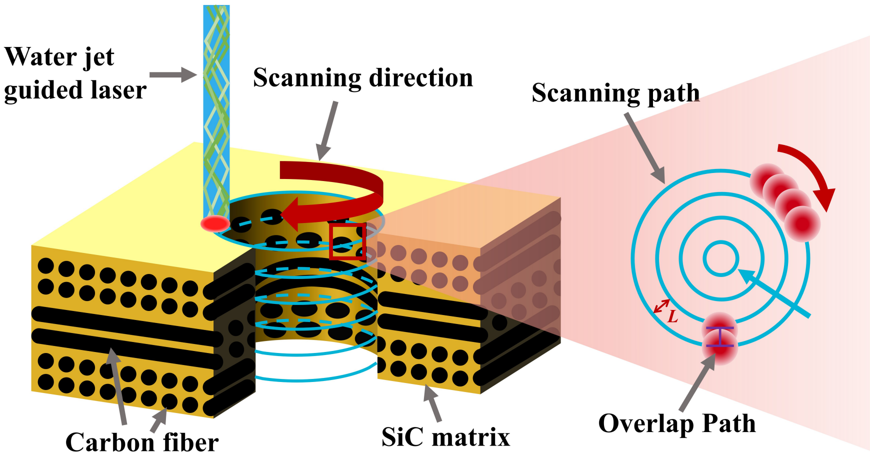

Figure 2. Scanning path of WJGL.

3. Results and Discussion

Different drilling depths were obtained by varying the level of each factor in the experiment. The significance of the factors on drilling depth was evaluated by the analysis of variance and range of it. From the experimental study, the variance of the seven factors, processing time, power density, water jet speed, scanning speed, path overlap ratio, pulse frequency, and helium pressure on drilling depth were 32,955.6 μm, 23,980.4 μm, 18,294.5 μm, 1274.8 μm, 811.8 μm, 2360.0 μm, and 5849.8 μm, respectively, as shown in Table 3. Their ranges are 536.3 μm, 491.8 μm, 378.4 μm, 97.1 μm, 85.6 μm, 136.9 μm, and 222.8 μm, respectively. These factors can be arranged in descending order of the variance and range, yielding the first three factors with greater effect and the last four factors with less effect. Therefore, the processing time, power density, and water jet speed were identified as significant factors, while the scanning speed, path overlap ratio, pulse frequency, and helium pressure were considered non-significant factors.

Table 3. The variance of each factor on the processing depth.

Factor	Depth 1	Depth 2	Depth 3	Depth 4	Depth 5	Depth 6	Range	Variance
Processing time	145.6	290.3	402.3	505.4	596.5	681.9	536.3	32,955.6
Power density	133.3	308.0	402.3	455.2	503.4	625.1	491.8	23,980.4
Water jet speed	692.6	599.6	430.2	402.3	355.6	314.2	378.4	18,294.5
Scanning speed	388.3	402.3	358.0	327.9	320.2	305.2	97.1	1274.8
Path overlap ratio	345.8	402.3	368.6	343.4	325.1	316.7	85.6	811.8
Pulse frequency	292.4	329.9	368.3	402.3	414.9	429.3	136.9	2360.0
Helium pressure	344.5	402.3	407.0	317.4	278.3	184.2	222.8	5849.8

3.1. Non-Significant Factors on Drilling Depths

3.1.1. Effect of Scanning Speed

As shown in Figure 3a, the micro-hole depth exhibits a primary increase followed by a decrease as the scanning speed increases from 0.1 mm/s to 1.1 mm/s. When the scanning speed was 0.1 mm/s, it took a long time for a single scanning cycle, resulting in low processing efficiency. The maximum processing depth of 402.3 μm was achieved when the scanning speed was 0.3 mm/s. As the scanning speed increased, the number of pulses per unit area and the overlap of adjacent pulses decreased, which reduced the laser energy absorbed by the material [32,33]. As a result, the volume of material reaching the ablation threshold decreased and the depth of micro-holes declined. However, since the processing time was fixed at 45 s, the increase in scanning speed raised the number of scanning cycles. Therefore, there was no significant decrease in the depth of the micro-holes.

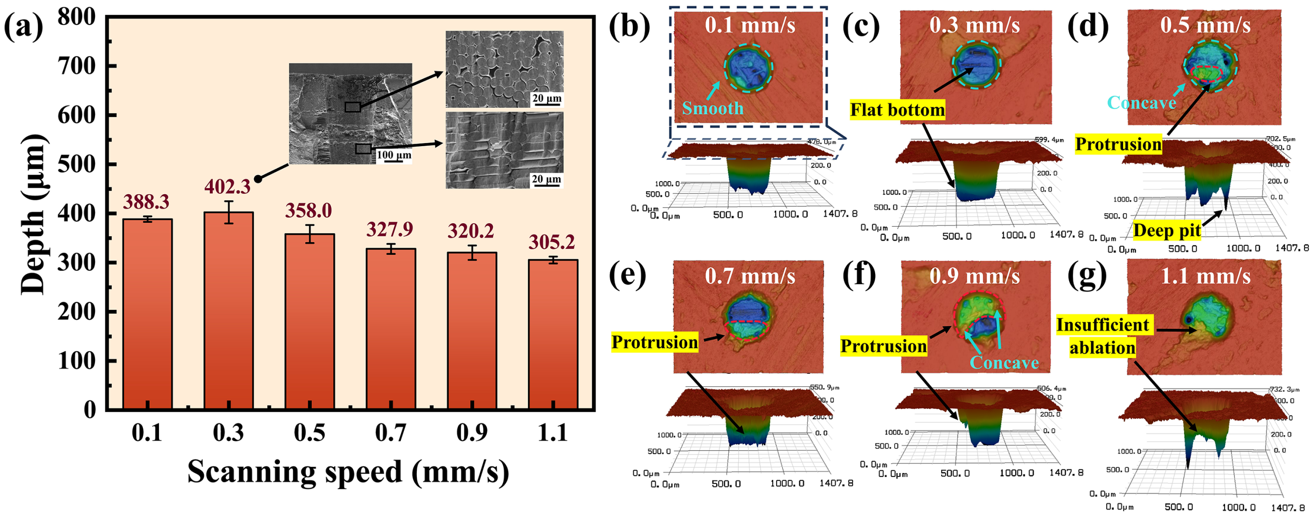

Figure 3. Depth and morphology of micro-holes at different scanning speeds. (**a**) Depth of micro-holes at different scanning speeds. (**b**–**g**) The entrance morphologies and 3D contours of the holes at scanning speeds of 0.1 mm/s, 0.3 mm/s, 0.5 mm/s, 0.7 mm/s, 0.9 mm/s, and 1.1 mm/s, respectively.

Figure 3b–g show the entrance morphology and 3D contours of the holes at scanning speeds of 0.1 mm/s, 0.3 mm/s, 0.5 mm/s, 0.7 mm/s, 0.9 mm/s, and 1.1 mm/s, respectively. From Figure 3d, it is evident that there are a few deep pits with small areas that may exist at the bottom of the hole, which may be attributed to the uneven distribution of pores and carbon fibers within the C_f/SiC composites [34]. Although the maximum depth is shown in the 3D contour, the deep pits were excluded in the analysis of micro-hole depths. From Figure 3b,c, it can be seen that the entrance contours of the ablated holes were smooth and the bottoms were flat when the scanning speed was 0.1 mm/s and 0.3 mm/s. However, as the scanning speed increased, the entrance contour appeared to be concave and a protrusion appeared at the bottom of the hole, and the area and height of the protrusion gradually increased, as shown in Figure 3d–f. At the scanning speed of 1.1 mm/s, there was insufficient ablation in the hole, as shown in Figure 3g. Due to the increased scanning speed, part of the material did not absorb enough laser energy to reach its ablation threshold and therefore remained in the hole.

The cross-sectional micro-morphology in Figure 3a demonstrates the exceptional cleanness of the sidewall processed by the WJGL at the scanning speed of 0.3 mm/s. The cut of transversal and longitudinal carbon fibers was smooth and no thermal damage or debris was observed in the processed area, which was similar to the cold ablation of femtosecond laser [35]. This result indicates that high-quality processing of C_f/SiC composites can be achieved by WJGL.

3.1.2. Effect of Path Overlap Ratio

Figure 4a shows the effect of the path overlap ratio on the micro-hole depth, which exhibits an initial increase followed by a decrease with the path overlap ratio. When the path overlap ratio was reduced from 50% to 40%, the micro-hole depth decreased from 402.3 μm to 345.8 μm. The reduced overlap between scanning paths led to an extended distance between adjacent concentric circles. As a result, less laser energy was absorbed per unit area of the material within a single cycle, leading to a reduction in the depth of processing. As the path overlap ratio increased from 50% to 90%, the micro-hole depth gradually decreased to 316.7 μm. The reduction in the distance between adjacent concentric circles provided a longer ablation of the material farther from the center of the circle. Consequently, the ablation depth near the edge of the hole was greater than that in the center of it.

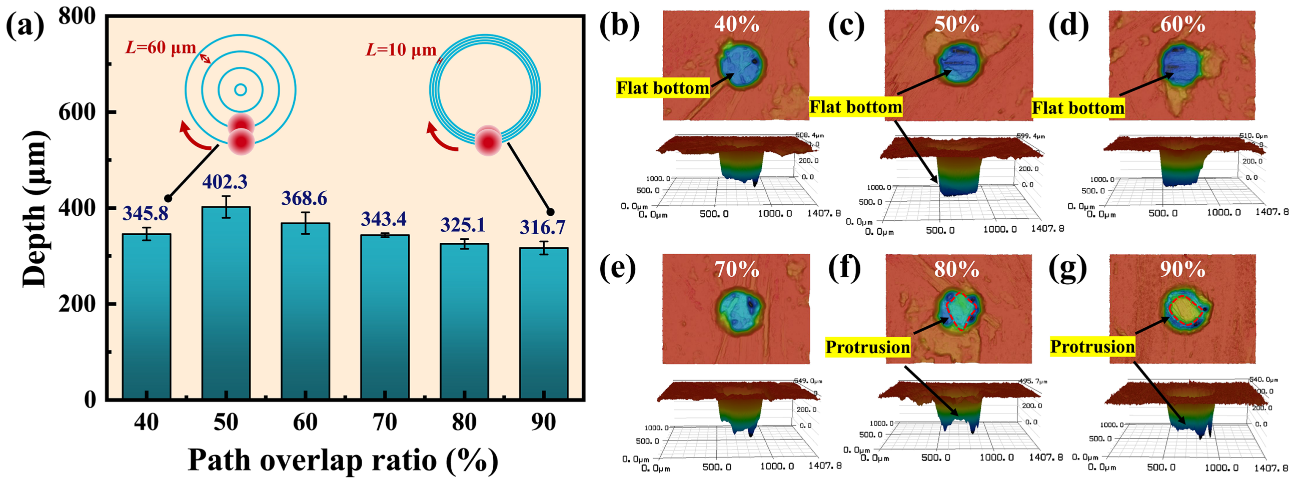

Figure 4. Depth and morphology of micro-holes at different path overlap ratios. (**a**) Depth of micro-holes at different path overlap ratios. (**b**–**g**) The entrance morphologies and 3D contours of the holes at path overlap ratios of 40%, 50%, 60%, 70%, 80%, and 90%, respectively.

Figure 4b–g show the entrance morphologies and 3D contours of the holes at path overlap ratios of 40%, 50%, 60%, 70%, 80%, and 90%, respectively. When the path overlap ratio was lower than 70%, the ablation in the hole was uniform and the bottom of the hole was flat, as depicted in Figure 4b–d, because the hole surface was completely covered by the concentric circle path. And since the diameter of the inner concentric circles was smaller, the number of scanning cycles increased. When the path overlap ratio reached 80% and above, protrusions started to appear in the center of the holes, as shown in Figure 4f,g. At this point, the surface of the holes could not be completely covered by the concentric circles of the path, and the material in the center of the hole was partially removed by heat conduction.

3.1.3. Effect of Pulse Frequency

As shown in Figure 5a, the depth of the micro-hole increased with pulse frequency. When the pulse frequency was increased from 2.5 kHz to 15 kHz, there was a corresponding increase in hole depth from 292.4 μm to 429.3 μm, reflecting a growth of 31.8%. Since the power density was kept constant, the increased pulse frequency raised the number of pulses per second radiated on the material without reducing the single-pulse energy. Therefore, the laser energy absorbed by the material per second was increased, resulting in an augmented ablation depth. However, the micro-hole depth was not proportionally increased with pulse frequency. At high pulse frequencies, a significant proportion of laser pulses were absorbed and reflected by the insufficiently ablated debris and bubbles produced by material sublimation [36]. In addition, the laser pulses were absorbed by the plasma generated in the processed area [37].

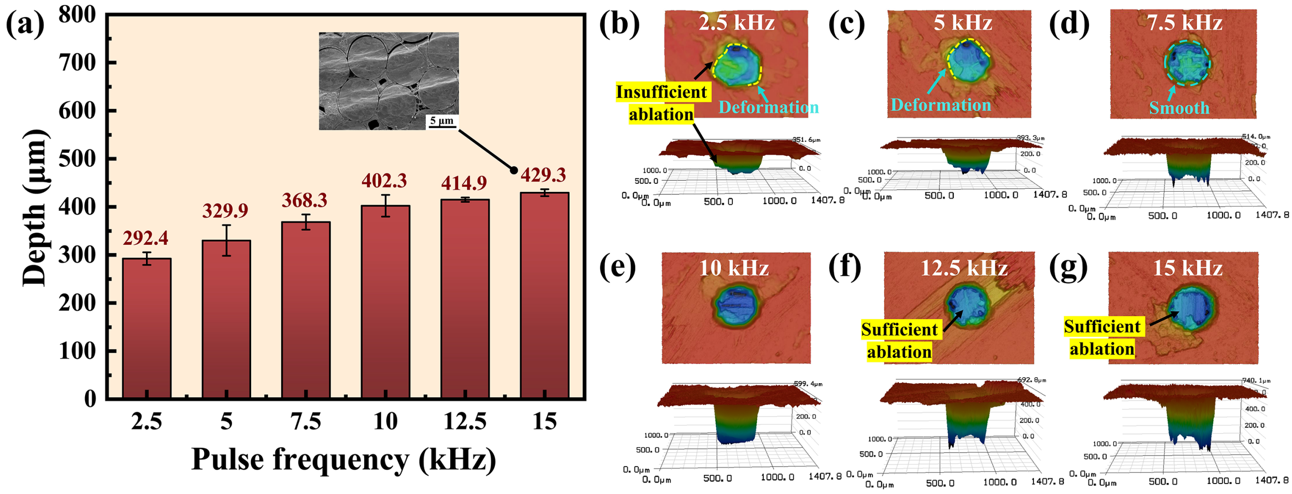

Figure 5. Depth and morphology of micro-holes at different pulse frequencies. (**a**) Depth of micro-holes at different pulse frequencies. (**b**–**g**) The entrance morphologies and 3D contours of the holes at pulse frequencies of 2.5 kHz, 5 kHz, 7.5 kHz, 10 kHz, 12.5 kHz, and 15 kHz, respectively.

At the pulse frequency of 2.5 kHz, insufficient ablation occurred and the entrance contour exhibited deformation, as shown in Figure 5b. Even when increased to 5 kHz, the entrance remained in deformation, as shown in Figure 5c. The low pulse frequency resulted in a limited amount of material being removed and therefore the entrance was deviated from the circle. However, the entrance and interior of the hole exhibited a smooth and sufficient ablation, as depicted in Figure 5d–g, when the pulse frequency exceeded 5 kHz.

From the microstructure of the carbon fibers cut at the frequency of 15 kHz in Figure 5a, it is evident that there was no molten layer or debris on the fiber surface, indicating a high cutting quality. It is worth noting that the study of Xing et al. [38] showed that a large amount of melt and recast layers were observed in the processed area when the pulse frequency was increased from 5 kHz to 15 kHz while cutting ceramic composites with a nanosecond laser. The heat accumulation on the machined surface increased due to the growing number of pulses deposited per unit area and the shortening of the gap between adjacent pulses, leading to more thermal defects. However, during WJGL processing, the water jet prevented thermal damage by cooling the material between pulses and scouring the molten materials generated by laser ablation [39]. This result demonstrates the superiority of WJGL processing of ceramic composites.

3.1.4. Effect of Helium Pressure

In the experiment, helium was used as an auxiliary gas to coaxially surround the water jet, thereby mitigating the interaction between the water jet and ambient air and enhancing the length of laminar flow [40]. The impact of helium pressure on micro-hole depth is illustrated in Figure 6a, with the absence of helium assistance represented by the pressure of 0 kPa. The micro-hole depth was 344.5 μm without helium assistance, while the maximum depth of 407.0 μm was achieved with the helium pressure of 10 kPa, representing an improvement of 18.1%. Since the distance between the nozzle and the workpiece was 25 mm, the water jet maintained a steady laminar flow over this length, resulting in the marginal increase in the processing depth. However, as the helium pressure increased from 10 kPa to 40 kPa, the micro-hole depth decreased from 407.0 μm to 184.2 μm.

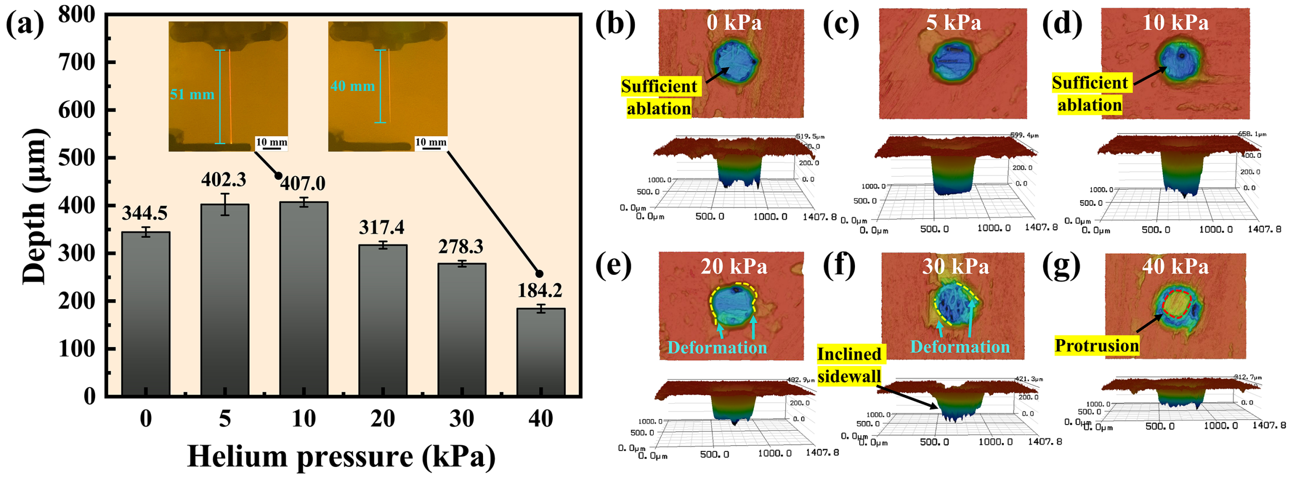

Figure 6. Depth and morphology of micro-holes at different helium pressures. (**a**) Depth of micro-holes at different helium pressures. (**b**–**g**) The entrance morphologies and 3D contours of the holes at helium pressures of 0 kPa, 5 kPa, 10 kPa, 20 kPa, 30 kPa, and 40 kPa, respectively.

To investigate the effect of helium pressure on WJGL processing, the laser transmission length in the water jet at the helium pressures of 10 kPa and 40 kPa was captured with a camera, as shown in Figure 6a. It is obvious that the laser transmission length in the water jet was able to reach 51 mm at a helium pressure of 10 kPa, while the transmission length was only 40 mm at the helium pressure of 40 kPa. The Reynolds number is an important indicator for assessing the stability of the water jet and the auxiliary gas. According to Lasheras et al. [41], when a gas is injected coaxially with the water jet, the Reynolds numbers of the water jet and the auxiliary gas are calculated as follows:

$$Re_w = \frac{\rho_w v_w d_w}{\mu_w} \tag{2}$$

$$Re_g = \frac{\rho_g v_g d_g}{\mu_g} \tag{3}$$

where Re_w and Re_g are the Reynolds numbers of the water jet and the gas, respectively. ρ_w and ρ_g, v_w and v_g, d_w and d_g, and μ_w and μ_g are the densities, velocities, equivalent diameters, and dynamic viscosities of the water jet and the gas, respectively.

The velocity of the helium increased with the growth of helium pressure, and the flow transitioned to turbulence when Re_g exceeded a critical value. During this period, the helium exhibited erratic movements and interacted with the water jet, resulting in a disturbance on its surface. The disturbance propagated downwards along the surface of the water jet, ultimately resulting in the fragmentation of the water jet. The laser transmission over the surface of the disturbed water jet was affected, resulting in a decrease in the processing depth.

As depicted in Figure 6b–d, the interior of the micro-holes was sufficiently ablated by WJGL when the helium pressure was 0 to 10 kPa, obtaining smooth entrances. However, when the helium pressure was above 10 kPa, the entrance contours underwent deformation, and protrusions and inclined sidewalls occurred due to insufficient ablation, as shown in Figure 6e–g.

High processing efficiency can be achieved without helium assistance during drilling at small depths. Due to the high price of helium, it is possible to process without gas assistance to save costs. Therefore, it is crucial to ascertain the optimal gas pressure for micro-hole processing.

3.2. Significant Factors for Drilling Depth

3.2.1. Effect of Processing Time

Figure 7a shows the relationship between micro-hole depth and processing time. When the processing time increased from 15 to 90 s, the hole depth was significantly increased from 145.6 µm to 681.9 µm. The increase in processing time resulted in a corresponding rise in the number of scanning cycles, leading to enhanced material ablation and consequently an increased depth of ablation. However, the pursuit of minimizing processing time while achieving micro-hole drilling should be emphasized. The efficiency of processing was defined as the drilling depth per second in each increasing 15 s. It can be seen from Figure 7a that the efficiency has been decreasing from 9.7 µm/s at 15 s to 5.7 µm/s at 90 s, indicating a reduction of 41.2%.

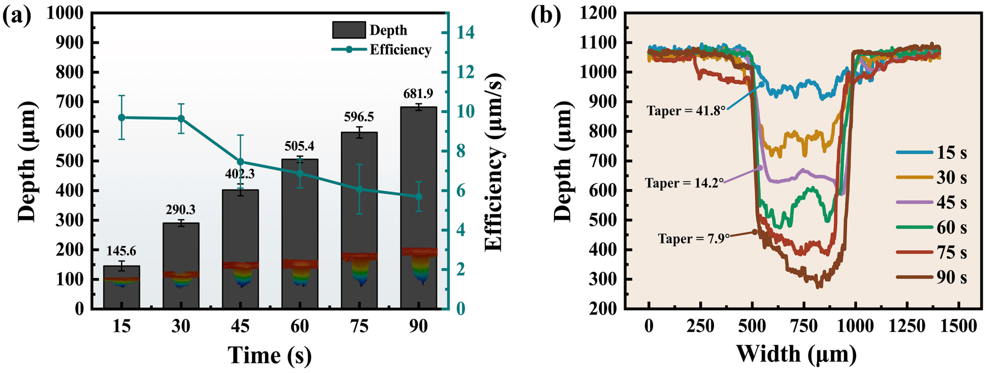

Figure 7. Depth and contour of micro-holes under different processing times. (**a**) Micro-hole depths at different processing times. (**b**) Cross-sectional contours of the micro-holes at different processing times.

The decrease in processing efficiency was attributed to a multitude of factors. The water jet would rebound upwards after reaching the bottom of the hole. The rebound process was characterized by the high flow velocity and the low air pressure surrounding the water jet, which resulted in the convergence of rebound water towards the water jet and subsequently led to fragmentation at the bottom of the water jet [42]. As the processing time grew, the depth of the micro-hole increased and the flow of water through the blind holes became more complicated. The rebound water, upon impacting the sidewall of the hole, may subsequently interact with the water jet, thereby exacerbating its instability. In addition, bubbles may be generated during water jet fragmentation as well as material evaporation under intense laser radiation, inducing cavitation effects. The laser was scattered by the bubbles in the water, which reduced the laser power [36]. As the depth of the hole increased, inadequate drainage at the bottom hindered prompt water discharge, resulting in challenges for the bubbles released from the hole [42].

In addition, it can be seen from the cross-sectional contours of the micro-holes in Figure 7b that the sidewall taper gradually decreased from 41.8° to 7.9° as the processing time increased. A significant amount of time during drilling was spent on reducing the sidewall taper. The sidewall taper resulted from the higher static pressure and laser power density in the central region of the water jet compared to its periphery [43]. WJGL continuously ablated the inclined sidewalls to achieve greater depth. Unlike the circular spot irradiated on a horizontal surface, the irradiation was elliptical on the inclined sidewall. The irradiated area of WJGL gradually increased as the sidewall taper decreased. According to Equation (1), the laser power density was reduced. As a result, more time was consumed for sidewall ablation when dealing with deeper micro-holes, which was one of the factors that contributed to the reduced processing efficiency.

3.2.2. Effect of Power Density

The enhancement of laser power density is pivotal for augmenting the capability of deep-hole processing. The material can only be removed when the power density reaches the ablation threshold. As shown in Figure 8a, the micro-hole depth exhibited a significant increase as the power density was elevated. When the laser power density was increased from 0.01 GW/cm² to 0.25 GW/cm², the depth increased from 133.3 µm to 625.1 µm, which was improved by 368.9%. The enhancement in power density arose from an augmentation in pulse energy, thereby increasing the energy absorption of the material. However, the rate of increase in hole depth exhibited a lower magnitude compared to the rate of increase in power density because the plasma shielding effect was found to be significantly enhanced at high pulse energies, leading to a more pronounced attenuation of the laser energy [44].

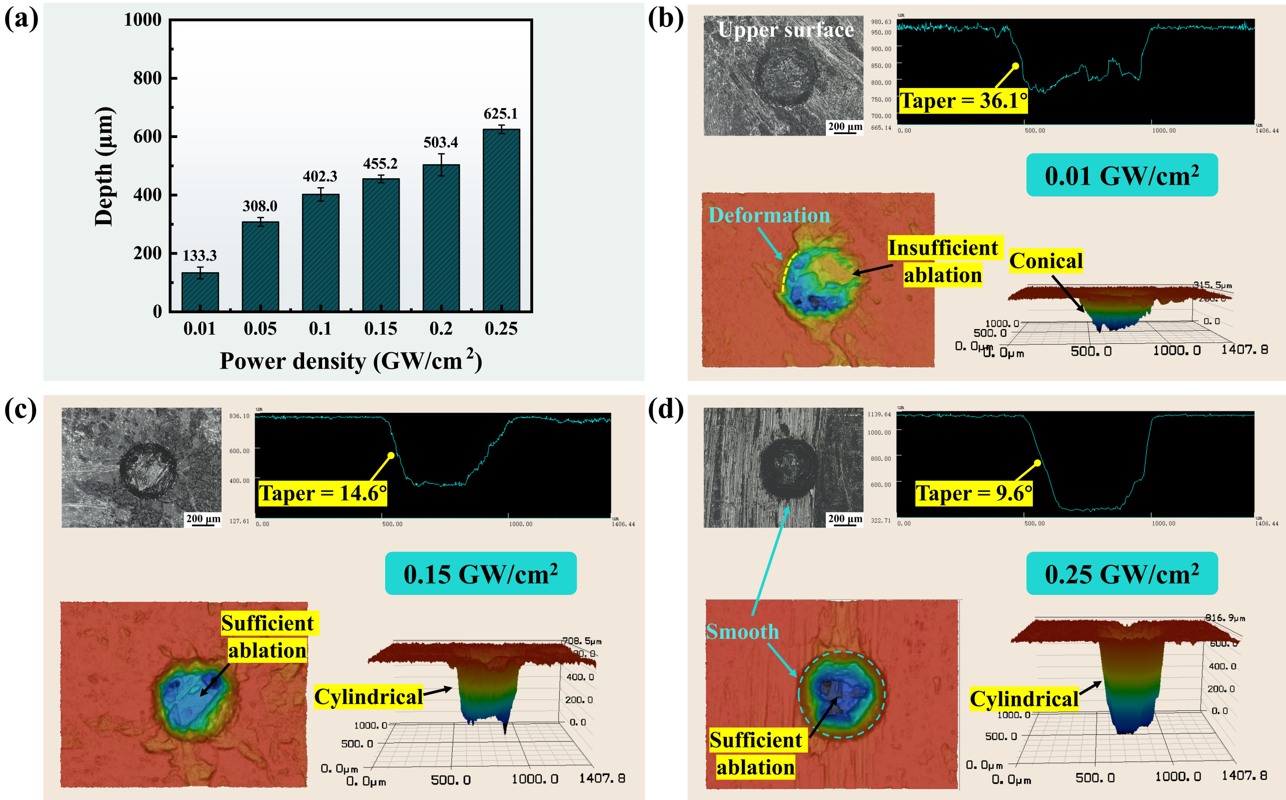

Figure 8. Micro-hole depth and morphology at different power densities. (**a**) Micro-hole depths at different power densities. (**b**–**d**) Hole entrance morphology, cross-sectional contours, and 3D contours at the power densities of 0.01 GW/cm², 0.15 GW/cm², and 0.25 GW/cm², respectively.

Figure 8b–d illustrate the upper surface morphologies and 3D contours of the micro-holes at power densities of 0.01 GW/cm², 0.15 GW/cm², and 0.25 GW/cm², respectively. It is evident from Figure 8b that insufficient ablation occurred when the power density was low, resulting in tapered sidewalls and a conical-shaped ablated hole. As shown in Figure 8c,d, as the power density increased, the material within the holes underwent sufficient ablation, and cylindrical holes were formed. Moreover, the sidewall taper was reduced from 36.1° to 9.6°, a reduction of 73.4%. From the upper surface morphologies of the holes, it can be seen that there was no fiber pull-out or breakage at the entrance of the holes.

As demonstrated in Figure 9, the microstructure of cross-sectional carbon fibers at different power densities was investigated. Due to the limited power of the laser source employed in the experiment, the pulse frequency was reduced to achieve power densities of 0.50 GW/cm² and 1.00 GW/cm² while maintaining the fixed laser power of 15 W. As shown in Figure 9a,b, a neat and clean cut of the longitudinal carbon fibers was obtained at the power density of 0.25 GW/cm². However, when the power density was increased to 0.50 GW/cm², a large amount of debris appeared on the fiber surface, as illustrated in Figure 9c,d. Furthermore, the results depicted in Figure 9e,f demonstrate that the carbon fiber experienced shrinkage and core protrusion upon increasing the power density to 1.00 GW/cm². Moreover, crevices were observed between the fibers. The heat was not able to be fully dissipated by the water jet at high power densities, thereby resulting in thermal damage. Fiber shrinkage and crevices were attributed to the higher sublimation temperature of the carbon fibers than the silicon carbide and pyrolytic carbon interface layers [45]. The energy at the edges of the water jet sublimated the silicon carbide matrix and the pyrolytic carbon interface layer but not the carbon fibers. In addition, the decomposition temperature of the core is higher than that of the outermost layer in the carbon fiber. As a result, the carbon fiber shrank, and the core protruded [46].

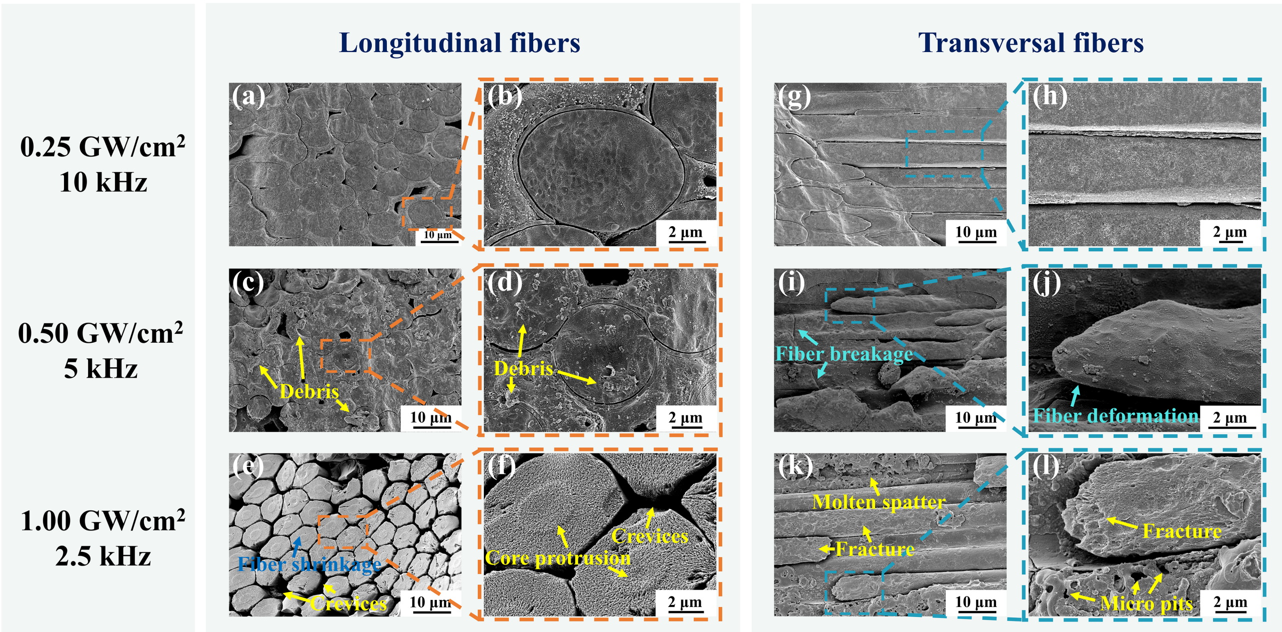

Figure 9. Microstructure of cross-sectional carbon fibers at different power densities. (**a**,**b**) Microstructure of longitudinal carbon fibers at the power density of 0.25 GW/cm². (**c**,**d**) Microstructure of longitudinal carbon fibers at the power density of 0.50 GW/cm². (**e**,**f**) Microstructure of longitudinal carbon fibers at the power density of 1.00 GW/cm². (**g**,**h**) Microstructure of transversal carbon fibers at the power density of 0.25 GW/cm². (**i**,**j**) Microstructure of transversal carbon fibers at the power density of 0.50 GW/cm². (**k**,**l**) Microstructure of transversal carbon fibers at the power density of 1.00 GW/cm².

As illustrated in Figure 9g,h, the transversal carbon fibers cut at the power density of 0.25 GW/cm² also exhibited excellent smoothness and cleanness. In contrast, fiber deformation and breakage were observed at the power density of 0.50 GW/cm², as shown in Figure 9i,j. When the laser energy increased, since the axial thermal conductivity of carbon fiber was higher than the radial direction [47], the heat was prone to propagate along the axial direction of the fiber and generated thermal stresses, leading to fiber deformation and breakage. As indicated in Figure 9k,l, molten spatter, fiber fracture, and micro pits were observed on the cut at the power density of 1.00 GW/cm². During processing at high power densities, the sharp absorption and explosion of laser energy by the plasma and the shock pressure generated by the rupture of microbubbles may lead to micro pits and fiber fracture [48]. Moreover, the heightened power density led to a propensity for laser energy deposition on the nozzle edge, thereby increasing the possibility of nozzle damage and subsequent additional costs.

In conclusion, the increase in power density led to a greater micro-hole depth but concurrently resulted in more thermal defects. Therefore, the selection of an appropriate power density is crucial in attaining efficient and minimally damaging processing.

3.2.3. Effect of Water Jet Speed

The effect of water jet speed on the depth of micro-holes is shown in Figure 10a. It is evident that the micro-hole depth decreased significantly as the water jet speed increased. When the water jet speed was increased from 40 m/s to 140 m/s, the micro-hole depth decreased from 692.6 µm to 314.2 µm, a reduction of 54.6%. In addition, the hole entrance and 3D contour were also deformed. As shown in Figure 10b, when the water jet speed was 40 m/s, the entrance was smooth and the material ablation was sufficient. As the water jet speed increased to 80 m/s, a protrusion appeared in the hole, as shown in Figure 10c. At the water jet speed of 140 m/s, the entrance of the hole exhibited deformation. Meanwhile, insufficient ablation and deep pits occurred within the hole, as shown in Figure 10d. Moreover, the sidewall taper increased from 5.4° to 14.9°.

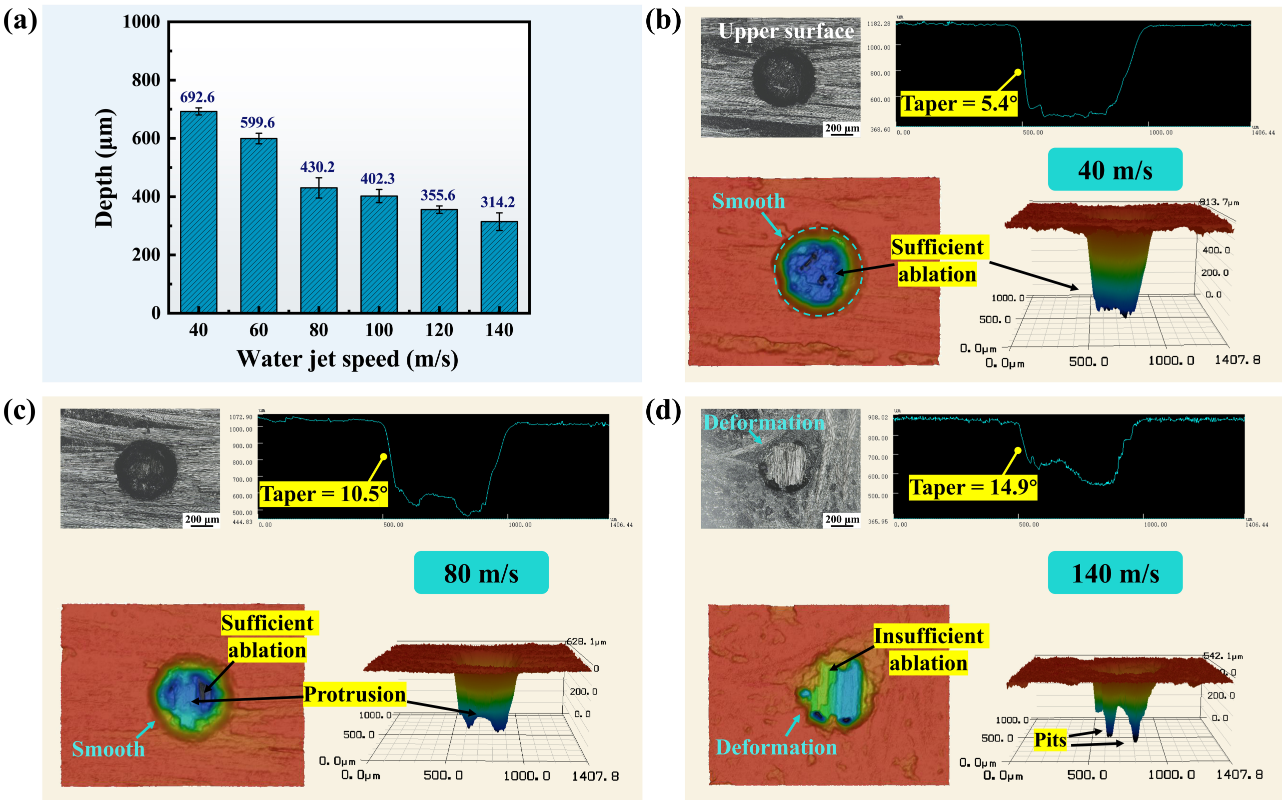

Figure 10. Depth and morphology of micro-holes at different water jet speeds. (**a**) Micro-hole depths at different water jet speeds. (**b**–**d**) Hole entrance morphology, cross-sectional contours, and 3D contours at the water jet speeds of 40 m/s, 80 m/s, and 140 m/s, respectively.

The reduction in micro-hole depth may be attributed to the phenomenon of water splashing occurring during the processing. During micro-hole drilling, splashing was formed by the water jet impinging on the bottom of the hole and subsequently ejecting along the sidewalls into the air. As illustrated in Figure 11a–c, as the water jet speed increased from 40 m/s to 140 m/s, the water jet impinged on the bottom of the micro-hole at a greater speed and sprayed more splashing droplets upwards, creating a larger mist in the air. The impingement of numerous splashing droplets on the water jet may result in deformation or even breakage of the water jet, which significantly affected the laser transmission [49]. In addition, the water jet was susceptible to being impacted and broken up by the water bouncing off the bottom of the hole with increased speed. To validate the role of splashing in the reduction in micro-hole depth, experiments were conducted by drilling on the edge of the workpiece. The center of the path was fixed on the edge of the workpiece. Figure 11d–f show that splashing was ejected downward while drilling on the edge at the water jet speeds of 40 m/s, 80 m/s, and 140 m/s, respectively. Therefore, there was no splashing and mist in the air. As illustrated in Figure 11g, the depths of drilling on the edge were 2390 μm, 2370 μm, and 2020 μm at the water jet speeds of 40 m/s, 80 m/s, and 140 m/s, respectively. The micro-hole depth decreased by only 15.4% when the water jet speed was increased from 40 m/s to 140 m/s. Therefore, the splashing resulting from the increasing water jet speed was identified as a significant factor influencing the drilling depth.

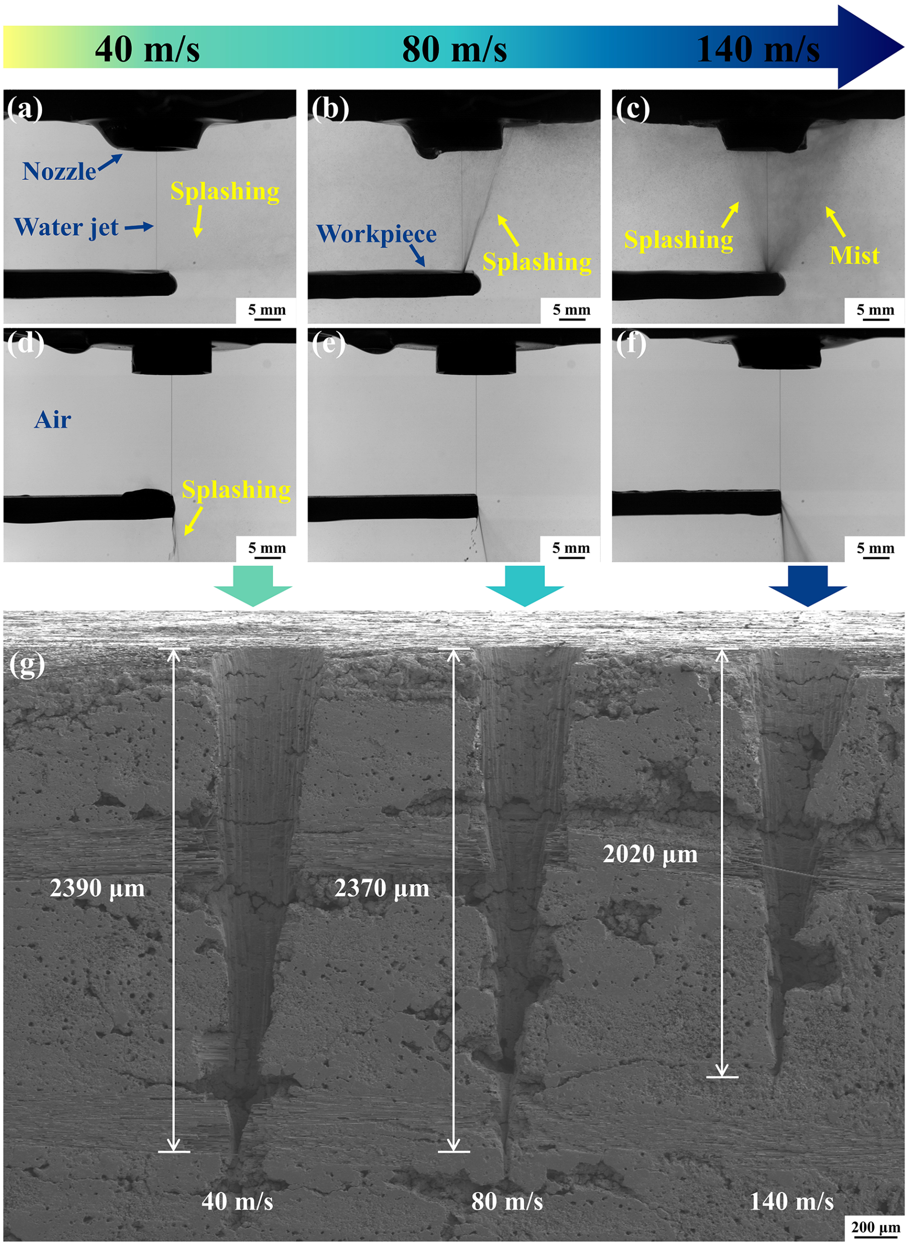

Figure 11. Splashing morphologies for drilling inside and on the edge of the workpiece. (**a**–**c**) Splashing morphologies at the water jet speeds of 40 m/s, 80 m/s, and 140 m/s for drilling inside the workpiece, respectively. (**d**–**f**) Splashing morphologies at the water jet speeds of 40 m/s, 80 m/s, and 140 m/s for drilling on the edge of the workpiece, respectively. (**g**) Micro-hole depths at the water jet speeds of 40 m/s, 80 m/s, and 140 m/s for drilling on the edge of the workpiece.

It is worth noting that the decrease in water jet speed could affect the drilling quality. As depicted in Figure 12a, debris with a diameter of about 20 μm was observed in the processed cross-section at the water jet speed of 40 m/s. As can be seen from the enlarged microstructural view in Figure 12b,c, a large amount of debris with small diameters was present on the surface of the fibers, accompanied by defects of fiber fracture and debonding. However, when the water jet speed was increased to 80 m/s, the surface of the cut appeared exceptionally clean, and only debris with a diameter of less than 1 μm was observed, as shown in Figure 12d–f. The element distribution was analyzed for cutting surfaces with water jet speeds of 40 m/s and 80 m/s, as shown in Figure 12g–i and j–l, respectively. The comparison of Figure 12i,l reveals that the concentration of oxygen and silicon elements was higher at the water jet speed of 40 m/s compared to the water jet speed of 80 m/s. The phenomenon of oxygen element aggregation can be observed in Figure 12h, the position of which corresponds to the position of the debris in Figure 12g. Therefore, the debris may be the oxide of silicon. The scouring and convective cooling effects of the water jet were enhanced when the water jet speed was increased to 80 m/s, preventing heat accumulation and debris adherence on the cut [50].

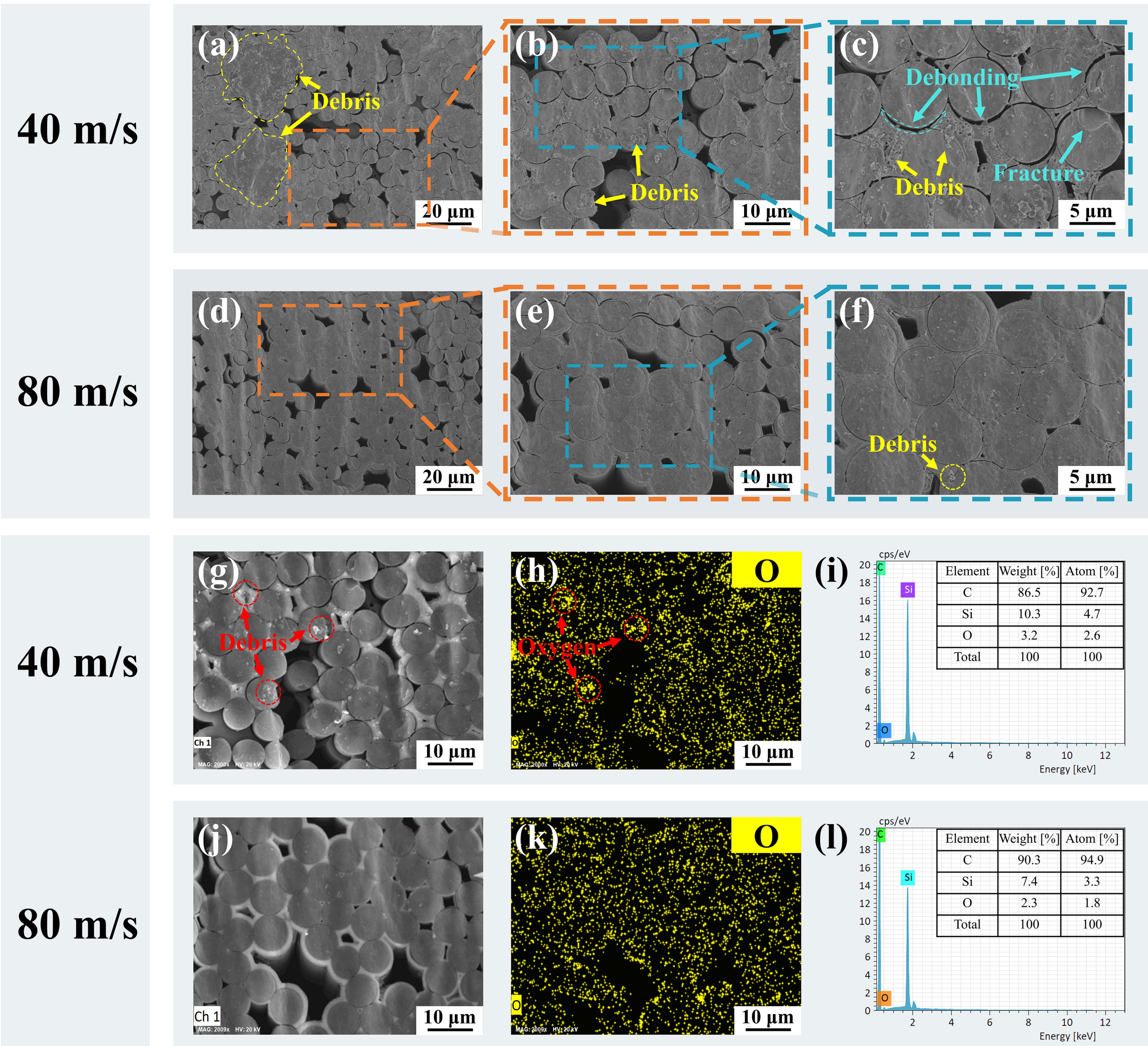

Figure 12. Cross-sectional microstructure analysis for different water jet speeds. (**a**–**c**) Cross-sectional microstructure at the water jet speed of 40 m/s. (**d**–**f**) Cross-sectional microstructure at the water jet speed of 80 m/s. (**g**–**i**) EDS spectra analysis of the cross-section at the water jet speed of 40 m/s. (**j**–**l**) EDS spectra analysis of the cross-section at the water jet speed of 80 m/s.

In conclusion, the decrease in the water jet speed and the increase in the power density contributed to greater processing efficiency but may lead to the additional thermal damage on the cut. According to the experimental results presented in Sections 3.2.2 and 3.2.3, the higher processing efficiency and lower thermal damage could be achieved simultaneously when the power density was 0.25 GW/cm² and the water jet speed was 80 m/s. Therefore, these two processing parameters were selected for deep-hole drilling in the experiment.

3.3. Micro Deep-Hole Drilling

The micro deep-hole drilling was conducted by optimizing the influential factors. The power density utilized was 0.25 GW/cm², accompanied by the pulse frequency of 10 kHz, the water jet speed of 80 m/s, the scanning speed of 0.3 mm/s, the path overlap ratio of 50%, and the helium pressure set at 10 kPa. The micro-hole with an average diameter of 510 μm, a depth of 4.1 mm, and a depth-to-diameter ratio of 8.03 was obtained, as illustrated in Figure 13a.

As shown in Figure 13b, the cross-section of the micro-hole exhibited no discernible heat-affected zone and featured a sidewall taper of only 0.72°. The diameter of the hole at the entrance was larger than at the internal and exit, which could be attributed to the longer processing time at the entrance, resulting in an extended impact of the water jet and heat transfer. In Figure 13d, it can be seen that the recast layers and debris existed on the fiber surface at the entrance, but the fibers were not deformed. The possible reasons for this phenomenon may be that the melt inside the hole was entrained by the water jet and deposited near the entrance during processing and that the longer processing time resulted in a minor amount of heat accumulation. In addition, the middle and exit region of the cross-section demonstrated exceptional processing quality, characterized by a smooth and clean cut without thermal defects, as shown in Figure 13f,h. In conclusion, high-quality micro-hole drilling of C_f/SiC composites could be achieved by WJGL with the selection of appropriate parameters.

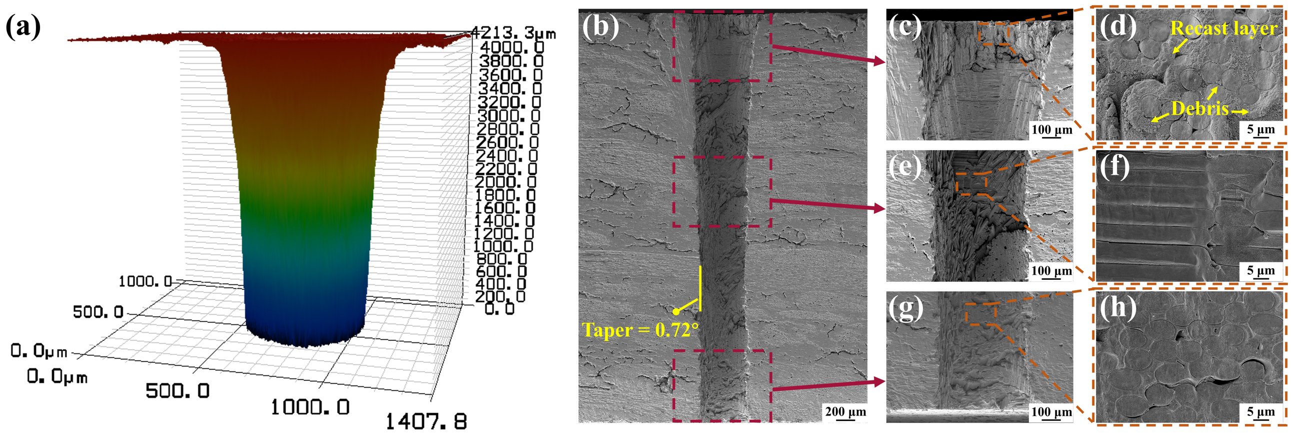

Figure 13. Morphology of the micro-hole with a depth of 4.1 mm drilled by WJGL. (**a**) The 3D contour of the micro-hole. (**b**) Cross-sectional morphology of the micro-hole. (**c**) Cross-sectional morphology of the entrance. (**d**) Microstructure of the entrance. (**e**) Cross-sectional morphology of the middle region. (**f**) Microstructure of the middle region. (**g**) Cross-sectional morphology of the exit. (**h**) Microstructure of the exit.

4. Conclusions

In this study, the effects of seven factors, namely processing time, power density, water jet speed, scanning speed, path overlap ratio, pulse frequency, and helium pressure, on the micro-hole depth and morphology of C_f/SiC composites drilled by WJGL were investigated. These factors can be classified into significant and non-significant categories. The significant factors include processing time, power density, and water jet speed. Their effects on the micro-hole processing can be summarized as follows:

- The processing efficiency declined with the increasing processing time. When the processing time was increased from 15 to 90 s, the processing efficiency decreased from 9.7 μm/s to 5.7 μm/s, a decrease of 41.2%;
- The increase in power density is essential for deep-hole drilling. As the power density increased from 0.01 GW/cm² to 0.25 GW/cm², the micro-hole depth increased from 133.3 μm to 625.1 μm. However, when the power density exceeded 0.25 GW/cm², thermal defects appeared on the cut because the residual heat could not be fully absorbed by the water jet;
- The increase in water jet speed facilitated the improvement of processing quality while resulting in a decrease in drilling depth. As the water jet speed increased from 40 m/s to 140 m/s, the splashing became progressively severe and interfered with the water jet, resulting in a decrease of 54.6% in the micro-hole depth. However, the elevated water jet speeds contribute to the cooling of the processing area and reduction in oxide accumulation.

The non-significant factors include scanning speed, path overlap ratio, pulse frequency, and helium pressure. The effects of these factors on micro-hole processing can be summarized as follows:

- The depth of the micro-holes exhibited a slight increase followed by a subsequent decrease as the scanning speed, path overlap ratio, and helium pressure were increased. The optimal scanning speed of 0.3 mm/s, a path overlap ratio of 50%, and a helium pressure of 10 kPa were determined to achieve the maximum drilling depth. In terms of drilling quality, as the scanning speed, path overlap ratio, and helium pressure continued to increase, the entrance of the hole exhibited deformation while insufficient ablation and protrusion formed within it;
- By increasing the pulse frequency, the drilling depth was increased, achieving a smoother entrance and sufficient ablation. However, when the pulse frequency was increased from 2.5 kHz to 15 kHz, the hole depth was only improved by 31.8%.

Based on the optimization of the processing parameters, the micro deep hole with an average diameter of 510 μm, a depth of 4.1 mm, a depth-to-diameter ratio of 8.03, and a sidewall taper of merely 0.72° was achieved. The microstructural observations of the cross-section revealed that the quality exhibited higher levels in the middle region and at the exit compared to those observed at the entrance. No thermal defects were observed in the middle region of the cross-section or at the exit, and the cut was smooth and clean. Therefore, the WJGL processing technology enables the realization of high quality micro deep-hole processing for C_f/SiC composites.

Due to the limitations of the laser and water pump pressure, higher laser power densities and water jet speeds could not be obtained in this study. Therefore, subsequent research can be carried out with higher levels of the parameters and the investigation of their potential interactions.

Author Contributions: Conceptualization, B.B., G.Z. and W.Z.; methodology, B.B. and G.Z.; software, G.Z., Z.C. and Y.C.; validation, Z.C. and Y.C.; formal analysis, B.B. and G.Z.; investigation, C.G.; resources, W.Z.; data curation, Z.C.; writing—original draft preparation, B.B. and Z.C.; writing—review and editing, B.B., G.Z., Y.C., C.G. and W.Z.; visualization, Y.C.; supervision, G.Z.; project administration, G.Z. and C.G.; funding acquisition, W.Z. All authors have read and agreed to the published version of the manuscript.

Funding: This research was funded by the National Natural Science Foundation of China (51805525), the Natural Science Foundation of Zhejiang Province (LY21E050018), the Innovation Guidance Foundation of the Innovation Academy for Light-duty Gas Turbine of the Chinese Academy of Sciences (CXYJJ20-QN-10), the Natural Science Foundation of Ningbo (2019A610111), the Open Subject of State Key Laboratory of Intelligent Manufacturing Equipment and Technology (IMETKF2024014), and the Ningbo Yongjiang Talent Introduction Programme (2022A-210-G).

Data Availability Statement: The data are contained within the article.

Conflicts of Interest: The authors declare no conflicts of interest.

Abbreviations

The following abbreviations are used in this manuscript:

WJGL	Water jet-guided laser
CFRP	Carbon fiber-reinforced plastics
3D	3-dimensional
CCD	Charge-coupled device

References

1. Sziroczak, D.; Smith, H. A review of design issues specific to hypersonic flight vehicles. *Prog. Aerosp. Sci.* **2016**, *84*, 1–28. [CrossRef]
2. Braga, D.F.; Tavares, S.; Da Silva, L.F.; Moreira, P.; De Castro, P.M. Advanced design for lightweight structures: Review and prospects. *Prog. Aerosp. Sci.* **2014**, *69*, 29–39. [CrossRef]
3. Siengchin, S. A review on lightweight materials for defence applications: A present and future developments. *Def. Technol.* **2023**, *24*, 1–17. [CrossRef]
4. Skinner, T.; Rai, A.; Chattopadhyay, A. Multiscale ceramic matrix composite thermomechanical damage model with fracture mechanics and internal state variables. *Compos. Struct.* **2020**, *236*, 111847. [CrossRef]
5. Shi, Y.; Kessel, F.; Friess, M.; Jain, N.; Tushtev, K. Characterization and modeling of tensile properties of continuous fiber reinforced C/C-SiC composite at high temperatures. *J. Eur. Ceram. Soc.* **2021**, *41*, 3061–3071. [CrossRef]
6. Almeida, R.S.; Besser, B.; Tushtev, K.; Li, Y.; Rezwan, K. Fatigue behavior and damage analysis of PIP C/SiC composite. *J. Eur. Ceram. Soc.* **2022**, *42*, 5391–5398. [CrossRef]
7. Naslain, R.R. SiC-matrix composites: Nonbrittle ceramics for thermo-structural application. *Int. J. Appl. Ceram. Technol.* **2005**, *2*, 75–84. [CrossRef]
8. Schmidt, S.; Beyer, S.; Immich, H.; Knabe, H.; Meistring, R.; Gessler, A. Ceramic matrix composites: A challenge in space-propulsion technology applications. *Int. J. Appl. Ceram. Technol.* **2005**, *2*, 85–96. [CrossRef]
9. Binner, J.; Porter, M.; Baker, B.; Zou, J.; Venkatachalam, V.; Diaz, V.R.; D'Angio, A.; Ramanujam, P.; Zhang, T.; Murthy, T. Selection, processing, properties and applications of ultra-high temperature ceramic matrix composites, UHTCMCs—A review. *Int. Mater. Rev.* **2020**, *65*, 389–444. [CrossRef]
10. Le, V.T.; San Ha, N.; Goo, N.S. Advanced sandwich structures for thermal protection systems in hypersonic vehicles: A review. *Compos. Part B Eng.* **2021**, *226*, 109301. [CrossRef]
11. Maddala, V.K.S.; Anitha, D.; Mishra, S.; Gupta, K.K.; Shahi, S.; Goud, N.U.R.; Dutt, A.; Talib, H.A. Machining of ceramic matrix composites: Challenges in surface integrity. *Mater. Today Proc.* **2023**. [CrossRef]
12. Rösiger, A.; Goller, R.; Langhof, N.; Krenkel, W. Influence of in-plane and out-of-plane machining on the surface topography, the removal mechanism and the flexural strength of 2D C/C-SiC composites. *J. Eur. Ceram. Soc.* **2021**, *41*, 3108–3119. [CrossRef]
13. Choudhary, A.; Chakladar, N.D.; Paul, S. Identification and estimation of defects in high-speed ground C/SiC ceramic matrix composites. *Compos. Struct.* **2021**, *261*, 113274. [CrossRef]
14. Diaz, O.G.; Luna, G.G.; Liao, Z.; Axinte, D. The new challenges of machining Ceramic Matrix Composites (CMCs): Review of surface integrity. *Int. J. Mach. Tools Manuf.* **2019**, *139*, 24–36. [CrossRef]
15. Singh, R.P.; Singhal, S. Rotary ultrasonic machining: A review. *Mater. Manuf. Process.* **2016**, *31*, 1795–1824. [CrossRef]
16. Júnior, M.G.; França, T.V.; Fortulan, C.A.; da Silva, R.H.L.; Foschini, C.R. Green ceramic machining benefits through ultrasonic-assisted turning: An experimental investigation. *Int. J. Adv. Manuf. Technol.* **2022**, *118*, 91–3104. [CrossRef]
17. Zhang, Y.; Liu, D.; Zhang, W.; Zhu, H.; Huang, C. Hole characteristics and surface damage formation mechanisms of Cf/SiC composites machined by abrasive waterjet. *Ceram. Int.* **2022**, *48*, 5488–5498. [CrossRef]
18. Nandam, S.R.; Rao, A.V.; Marla, D.; Gokhale, A.A.; Joshi, S.S. Analysis of laser-induced surface damage of single-crystal Ni-based superalloy towards improving machinability. *J. Manuf. Process.* **2024**, *118*, 357–375. [CrossRef]
19. Tong, Y.; Bai, S.; Zhang, H.; Ye, Y. Laser ablation behavior and mechanism of C/SiC composite. *Ceram. Int.* **2013**, *39*, 6813–6820. [CrossRef]
20. Zhang, T.; Liu, F.; Liu, Y.; Wu, C.; Liang, S.Y. Ultraviolet nanosecond laser-ablated groove analysis of 2.5 D Cf/SiC composites. *Crystals* **2023**, *13*, 223. [CrossRef]
21. Liu, Y.; Wang, C.; Li, W.; Zhang, L.; Yang, X.; Cheng, G.; Zhang, Q. Effect of energy density and feeding speed on micro-hole drilling in C/SiC composites by picosecond laser. *J. Mater. Process. Technol.* **2014**, *214*, 3131–3140. [CrossRef]
22. De Zanet, A.; Casalegno, V.; Salvo, M. Laser surface texturing of ceramics and ceramic composite materials—A review. *Ceram. Int.* **2021**, *47*, 7307–7320. [CrossRef]
23. Subasi, L.; Gokler, M.I.; Yaman, U. A process modeling approach for micro drilling of aerospace alloys with a waterjet guided laser system. *Opt. Laser Technol.* **2022**, *148*, 107682. [CrossRef]

24. Chao, Y.; Liu, Y.; Xu, Z.; Xie, W.; Zhang, L.; Ouyang, W.; Wu, H.; Pan, Z.; Jiao, J.; Li, S.; et al. Improving superficial microstructure and properties of the laser-processed ultrathin kerf in Ti-6Al-4V alloy by water-jet guiding. *J. Mater. Sci. Technol.* **2023**, *156*, 32–53. [CrossRef]
25. Gao, M.; Yuan, S.; Wei, J.; Niu, J.; Zhang, Z.; Li, X.; Zhang, J.; Zhou, N.; Luo, M. Optimization of processing parameters for waterjet-guided laser machining of SiC/SiC composites. *J. Intell. Manuf.* **2023**, 1–21. [CrossRef]
26. Marimuthu, S.; Dunleavey, J.; Liu, Y.; Smith, B.; Kiely, A.; Antar, M. Water-jet guided laser drilling of SiC reinforced aluminium metal matrix composites. *J. Compos. Mater.* **2019**, *53*, 3787–3796. [CrossRef]
27. Wu, Y.; Zhang, G.; Wang, J.; Chao, Y.; Zhang, W. The cutting process and damage mechanism of large thickness CFRP based on water jet guided laser processing. *Opt. Laser Technol.* **2021**, *141*, 107140. [CrossRef]
28. Cheng, B.; Ding, Y.; Li, Y.; Li, J.; Xu, J.; Li, Q.; Yang, L. Coaxial helical gas assisted laser water jet machining of SiC/SiC ceramic matrix composites. *J. Mater. Process. Technol.* **2021**, *293*, 117067. [CrossRef]
29. Hu, T.; Yuan, S.; Wei, J.; Zhou, N.; Zhang, Z.; Zhang, J.; Li, X. Water jet guided laser grooving of SiCf/SiC ceramic matrix composites. *Opt. Laser Technol.* **2024**, *168*, 109991. [CrossRef]
30. Zhang, G.; Zhang, Z.; Wang, Y.; Guo, C.; Zhang, W. Gas shrinking laminar flow for robust high-power waterjet laser processing technology. *Opt. Express* **2019**, *27*, 38635–38644. [CrossRef]
31. Liu, Y.; Wei, M.; Zhang, T.; Qiao, H.; Li, H. Overview on the development and critical issues of water jet guided laser machining technology. *Opt. Laser Technol.* **2021**, *137*, 106820. [CrossRef]
32. Liu, Y.; Zhang, R.; Li, W.; Wang, J.; Yang, X.; Cheng, L.; Zhang, L. Effect of machining parameter on femtosecond laser drilling processing on SiC/SiC composites. *Int. J. Adv. Manuf. Technol.* **2018**, *96*, 1795–1811. [CrossRef]
33. Qiao, H.; Zhihe, C.; Jianfeng, C.; Zhao, J. Experimental study on water jet guided laser micro-machining of mono-crystalline silicon. *Opt. Laser Technol.* **2021**, *140*, 107057. [CrossRef]
34. Jiao, H.; Chen, B.; Li, S. Removal mechanism of 2.5-dimensional carbon fiber reinforced ceramic matrix composites processed by nanosecond laser. *Int. J. Adv. Manuf. Technol.* **2021**, *112*, 3017–3028. [CrossRef]
35. Mirza, I.; Bulgakova, N.M.; Tomáštík, J.; Michálek, V.; Haderka, O.; Fekete, L.; Mocek, T. Ultrashort pulse laser ablation of dielectrics: Thresholds, mechanisms, role of breakdown. *Sci. Rep.* **2016**, *6*, 39133. [CrossRef] [PubMed]
36. Charee, W.; Tangwarodomnukun, V. Dynamic features of bubble induced by a nanosecond pulse laser in still and flowing water. *Opt. Laser Technol.* **2018**, *100*, 230–243. [CrossRef]
37. Wang, J.; Wu, Y.; Zhang, G.; Chao, Y.; Zhang, W. Experimental Research of CFRP Cutting by Using Water Jet Guided Laser Processing# br. *China Mech. Eng.* **2021**, *32*, 1608.
38. Xing, Y.; Liu, L.; Wu, Z.; Wang, X.; Huang, P.; Tang, L. Fabrication and characterization of micro-channels on Al_2O_3/TiC ceramic produced by nanosecond laser. *Ceram. Int.* **2018**, *44*, 23035–23044. [CrossRef]
39. Gobet, M.; Obi, S.; Pavius, M.; Takano, M.; Vago, N.; Lee, K.; Kozuki, Y.; Pauchard, A. Implementation of Short-Pulse Lasers for Wafer Scribing and Grooving Applications. *J. Laser Micro/Nanoeng.* **2010**, *5*, 16–20. [CrossRef]
40. Cadavid, R.; Wüstenberg, D.; Louis, H.; Pude, F.; Senne, T. Effect of helium atmospheres on abrasive suspension water jets. *Int. J. Adv. Manuf. Technol.* **2005**, *26*, 1246–1254. [CrossRef]
41. Lasheras, J.C.; Hopfinger, E. Liquid jet instability and atomization in a coaxial gas stream. *Annu. Rev. Fluid Mech.* **2000**, *32*, 275–308. [CrossRef]
42. Liang, J.; Qiao, H.; Zhao, J.; Cao, Z.; Zhang, Y.; Wang, S. Study on fluid flow characteristics and laser transmission mode of water jet–guided laser processing in blind hole. *Int. J. Adv. Manuf. Technol.* **2023**, *129*, 1717–1730. [CrossRef]
43. Liu, Q.; Zhao, Y.; Meng, J.; Zheng, Z.; Cao, C.; Zhao, G.; Zhao, C.; Liu, G.; Dai, D.; Song, Z. Experimental research and optimization of Ti-6Al-4V alloy microgroove machining based on waterjet-guided high-power laser. *Materials* **2022**, *15*, 7430. [CrossRef] [PubMed]
44. Zhu, H.; Wang, J.; Yao, P.; Huang, C. Heat transfer and material ablation in hybrid laser-waterjet microgrooving of single crystalline germanium. *Int. J. Mach. Tools Manuf.* **2017**, *116*, 25–39. [CrossRef]
45. Wei, L.; Yang, X.; Song, W.; Yan, M.; Zhao, C. Ablation behavior of three-dimensional braided C/SiC composites by oxyacetylene torch under different environments. *Ceram. Int.* **2013**, *39*, 463–468. [CrossRef]
46. Liu, C.; Zhang, X.; Wang, G.; Wang, Z.; Gao, L. New ablation evolution behaviors in micro-hole drilling of 2.5 D Cf/SiC composites with millisecond laser. *Ceram. Int.* **2021**, *47*, 29670–29680. [CrossRef]
47. Tian, T.; Cole, K.D. Anisotropic thermal conductivity measurement of carbon-fiber/epoxy composite materials. *Int. J. Heat Mass Transf.* **2012**, *55*, 6530–6537. [CrossRef]
48. Cao, Z.; Qiao, H.; Zhang, Y.; Chen, Y.; Zhao, J. Study on reducing burrs of super alloy through structures in water jet guided laser ablation. *J. Manuf. Process.* **2022**, *77*, 809–818. [CrossRef]
49. Arleo, F. Numerical Simulation of a Pure Water Jet inside an Orifice: Jet Stability and Effects of Droplets Collisions. Master's Thesis, Politecnico di Milano, Milan, Italy, 2009.
50. Wang, Y.; Zhang, Z.; Zhang, G.; Wang, B.; Zhang, W. Study on immersion waterjet assisted laser micromachining process. *J. Mater. Process. Technol.* **2018**, *262*, 290–298. [CrossRef]

materials

MDPI

Article

Surface Roughness Prediction of Titanium Alloy during Abrasive Belt Grinding Based on an Improved Radial Basis Function (RBF) Neural Network

Kun Shan [1,*], Yashuang Zhang [1], Yingduo Lan [1], Kaimeng Jiang [2], Guijian Xiao [2] and Benkai Li [3]

1 AECC Shenyang Liming Aero-Engine Co., Ltd., No. 6 Dongta Street, Dadong District, Shenyang 110862, China; zys800801@163.com (Y.Z.); lydlyd621@126.com (Y.L.)

2 College of Mechanical and Vehicle Engineering, Chongqing University, No. 174 Shazheng Street, Shapingba District, Chongqing 400444, China; jiangkmeng@outlook.com (K.J.); xiaoguijian@cqu.edu.cn (G.X.)

3 School of Mechanical and Automotive Engineering, Qingdao University of Technology, No. 777 Jialingjiang Road, Huangdao District, Qingdao 266520, China; lbk17082@163.com

* Correspondence: shankun8888@163.com

Abstract: Titanium alloys have become an indispensable material for all walks of life because of their excellent strength and corrosion resistance. However, grinding titanium alloy is exceedingly challenging due to its pronounced material characteristics. Therefore, it is crucial to create a theoretical roughness prediction model, serving to modify the machining parameters in real time. To forecast the surface roughness of titanium alloy grinding, an improved radial basis function neural network model based on particle swarm optimization combined with the grey wolf optimization method (GWO-PSO-RBF) was developed in this study. The results demonstrate that the improved neural network developed in this research outperforms the classical models in terms of all prediction parameters, with a model-fitting R^2 value of 0.919.

Keywords: titanium alloy; abrasive belt grinding; roughness prediction; neural network

1. Introduction

Titanium alloy is a very effective metal that has been utilized extensively in a variety of industries, including aerospace, vehicle production, medical equipment, and others [1–3]. However, due to their unique strength, hardness, and chemical stability, titanium alloys have consistently been difficult to machine. Among the various processing techniques, titanium alloy belt grinding has drawn a lot of attention as a popular and efficient processing technique [4]. Abrasive belt grinding realizes the flexible processing of titanium alloy workpieces, which achieves better surface quality and accuracy to meet the requirements of high-precision machining [5].

However, with the rapid expansion of manufacturing, processing, and other related industries, the quality standards for products are getting more and more strict, and the processing industry is increasingly shifting in favor of high efficiency, fine quality, and low cost [6–8]. To increase their competitiveness in the global market, manufacturers compete to produce "zero-defect" products, which necessitate parts with exceptional surface quality [9]. The modern processing industry will confront significant hurdles as a result of the difficulty in controlling surface roughness under various processing circumstances and the lack of clarity regarding the processing variables that influence surface roughness.

In recent years, with the advancement of intelligence, numerous sophisticated algorithms have been employed to forecast the surface roughness of workpieces and enhance their predictive power. The causes of high and low surface roughness, as well as roughness prediction and modeling, have currently been developed as a near-complete theoretical system [10–12]. Tian et al. [13] developed a prediction model for the association between different process factors and workpiece surface roughness using a BP neural network based on the experimental results. Li et al. [14] constructed a state parameter prediction model based on the BP neural network by performing grinding tests on samples of nickel-based superalloys, and the prediction accuracy of the model is 93.58%. Qi et al. [15] took the maximum cutting depth of the belt, the speed of the belt, and the feed rate of the workpiece as input parameters to establish the prediction model of polishing surface roughness of the belt based on the BP neural network. The results show that the predicted value is in good accordance with the experimental value. Different from the BP neural network, the RBF neural network [16–18] utilizes the Gaussian activation function, which can address some of the issues with the BP neural network, such as the lengthy training period, ease of local optimum, and so on. It can generalize well, make predictions quickly, and adapt better to various types of data.

However, researchers become dissatisfied with the direct use of classic algorithms when the study goes deeper and they discover flaws in the traditional algorithms. As a result, they start to think of ways to improve traditional algorithms. The most popular strategy is to combine optimization algorithms with conventional prediction models, and the most utilized particle swarm optimization (PSO) technique is the optimization algorithm. Zhang et al. [19] suggested a data-driven roughness prediction approach for the GH4169 superalloy and discovered that the PSO-BP-based roughness prediction algorithm had a positive impact on the prediction of the superalloy. Yang et al. [20] built the PSO-BP surface roughness prediction model by using the particle swarm optimization algorithm to optimize the initial weights and thresholds of the BP neural network. Wang et al. [21] designed a temperature prediction model using an RBF neural network and, then, used particle swarm optimization and Levenberg-Marquardt computation to create the PSO-LM-RBF prediction method with a reduced deviation of prediction results and a more stable model.

Therefore, to accurately predict the belt grinding surface roughness of titanium alloy, the PSO algorithm was utilized in this study to optimize the RBF network parameters, obtaining the optimal solution and improving the operation efficiency. In addition to this, the iterative formula was updated with the application of the GWO algorithm, which is employed to prevent the algorithm from losing its capacity to converge later on and enter the local optimum problem. Then, empirical programs and formulas are used to establish the structural framework of the neural network and to clarify the key parameter values that must be employed in the algorithm. Finally, the accuracy of the algorithm is verified by simulation.

The remainder of the paper is structured as follows: the second part describes the prediction method adopted in this study. The determination of experimental parameters and the experimental results are discussed and analyzed in the third part. Finally, we summarize the paper.

2. Methods

2.1. Data Acquisition

The experimental equipment was based on a precision CNC belt grinder (2MGY5580, SAMHIDA, Chongqing, China), as shown in Figure 1. The TC4 titanium alloy, with dimensions of 400 mm × 200 mm × 5 mm, and the #80 alumina belt were adopted for the experimental study. A single grinding length of 35 mm was used for the processing, which was conducted under constant pressure.

Researchers in this field have found that workpiece surface roughness in belt grinding is significantly influenced by variables including abrasive belt particle size, belt linear speed, feed speed, and grinding depth [22–24]. In particular, the belt particle size is significantly influenced by the test material and essentially stays the same throughout the test. Therefore, as stated in Table 1, three test factors are identified, including belt linear speed (v_s), feed speed (v_p), and grinding depth (a_p), and four horizontal orthogonal tests are conducted.

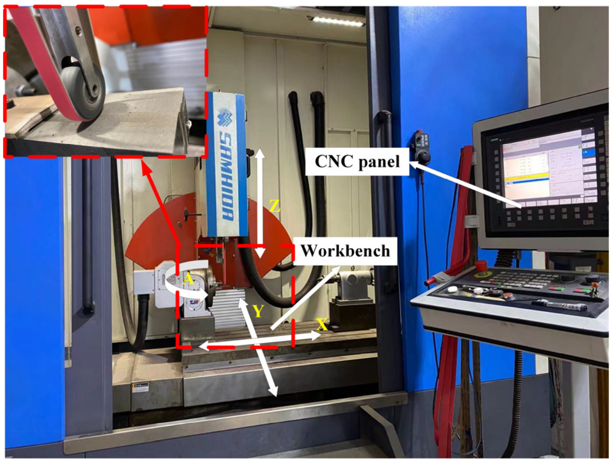

Figure 1. CNC belt grinding machine.

Table 1. Abrasive belt grinding factor level.

Level	v_s (m/s)	v_p (mm/Min)	a_p (mm)
1	7.8	200	3
2	11.5	300	6
3	15.6	400	9
4	19.5	500	12

The test scheme, as presented in Table 1, is designed, and a total of 64 grinding experiments are conducted in the pre-experiment. The selection of experimental parameters is mainly based on the performance of the machine tool and the maximum/minimum parameters based on engineering experience. In addition to this, the testing scheme takes into account the characteristics of the orthogonal test table and neural network (the more training samples, the higher the prediction accuracy). Therefore, we divided the parameters of vs. between 7.8–19.5 m/s, v_p between 200–500 mm/min, and a_p between 3–12 mm into four segments at equal intervals for orthogonal experiments. After grinding, a portable roughness measurement device was used to determine the surface roughness of the test titanium alloy. During the process, roughness detection is conducted for five different points, and the final surface roughness value is calculated by taking the arithmetic average of the five measurements. As a result, the dataset of grinding parameters and corresponding roughness was built. Table 2 displays some data from the dataset.

2.2. Data Pre-Processing

Normalization [25] of these collected data is required to eliminate units, balance orders of magnitude, and avoid sample features with low values from being unduly controlled. Test data in different units can affect the results. The normalization formula is as follows:

$$y = \frac{x_i - x_{\min}}{x_{\max} - x_{\min}} \tag{1}$$

where x_i is the sample data collected, and $x_{\max}$ and $x_{\min}$ are the maximum and minimum values of the sample data collected.

2.3. Prediction Model Based on GWO-PSO-RBF

2.3.1. RBF Neural Network

The RBF neural network uses a Gaussian excitation function, which can address some of the issues with classic BP neural networks, including their lengthy network training procedures and propensity to easily enter local optimums [17]. It has excellent generalization capabilities, and, for a given amount of input data, only a few neuron parameters and hidden layer weights are used in the operation, which significantly increases the prediction speed of RBF neural networks and renders them more flexible to diverse types of data.

Table 2. Experimental results under different processing parameter conditions (partial result).

v_s (m/s)	v_p (mm/Min)	a_p (mm)	Ra (μm)
7.8	200	3	0.916
7.8	200	6	0.977
7.8	200	9	1.543
7.8	200	12	1.379
11.5	300	3	1.14
11.5	300	6	1.259
11.5	300	9	1.112
11.5	300	12	0.945
15.6	400	3	0.989
15.6	400	6	0.99
15.6	400	9	0.948
15.6	400	12	0.833
19.5	500	3	0.724
19.5	500	6	0.827
19.5	500	9	0.936
19.5	500	12	0.956

There are three structural layers in the network used in this study. The first layer is used to input the machining parameters. In the second layer, the Gaussian function was used as the activation function to process the input parameters non-linearly. The third layer is the output layer to output the final roughness prediction results. This is shown in Figure 2.

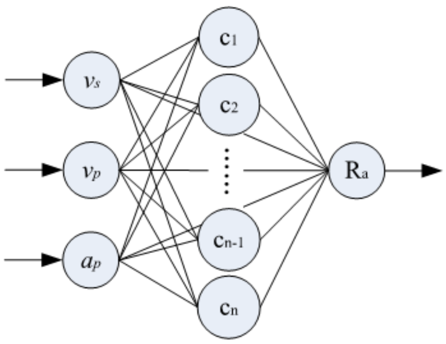

Figure 2. The structure of the RBF neural network [17].

The input vector is $x(t) = (x_1, x_2, \ldots, x_N)^T$ and there are three different types of processing parameters in this work, which is equal to the number of input vectors. The terms x_1, x_2, and x_3 represent v_s, v_p, and a_p, respectively. After the sample data pass through the intermediate layer, the output is a nonlinear activation function $h_j(t)$:

$$h_j(t) = \exp(-\frac{||x(t) - c_j(t)||^2}{2\sigma_j^2}), j = 1, 2 \cdots m \tag{2}$$

where c_j is the center of the jth node, σ_j is the width of the jth node, $||x(t) - c_j(t)||$ is the Euclidean distance between the sample and the node center, and m is the number of nodes in the middle layer. By weighting the output data of the intermediate layer, the roughness prediction result can be obtained, as shown in Equation (3):

$$y_i(t) = \sum_{j=i}^{m} \omega_{ji} h_j(t), i = 1, 2 \cdots, n \tag{3}$$

where w is the weight and n is the number of network outputs.

The parameters of the RBF neural network, such as c_j, σ_j, and w, need to be determined by iteration. To better optimize the above parameters, this study suggested a GWO-PSO hybrid optimization method to better optimize the parameters.

2.3.2. Particle Swarm Optimization Algorithm

Three parameters in the RBF neural network need to be set artificially: weight, node center, and radial basis width. The traditional RBF neural network often uses gradient descent iterative optimization, but this method not only has a poor training effect, taking a long time, but, also, it easily falls into local optimum so that the global effect cannot reach the best position. The parameter selection of the RBF neural network is, essentially, an optimization process, so the PSO optimization algorithm is used to optimize the parameters that need to be set manually in the RBF neural network and select the optimal values.

The particle swarm optimization algorithm [26] is an optimization method, which optimizes parameters by limiting the process of birds foraging in nature, and, finally, realizes the "survival of the fittest". The particle will continuously evolve during each update process, and the parameters it carries will adjust in line with this evolution. The particle will evolve into a new particle if the prediction error corresponding to the parameters of the evolved particle is lower than that of the non-evolved particle. On the other hand, the undeveloped particles are kept.

In this study, the position of the particle corresponds to the value of the parameters that the neural network needs to train. Particle fitness corresponds to the error size of the roughness prediction model. In the iterative process, each particle modifies its speed and direction to move closer to the parameter value that reduces the prediction error through guidance. The first is called individual extremum guidance and it refers to the parameter value that each particle in an iterative process determines to reduce its own mistake. The global extremum guidance is the parameter value that was attained by every particle during the iteration procedure with the minimum overall error.

These two extreme values are used by the particle swarm to determine how to update each particle's parameter, and the update formula is as follows:

$$v_{ij}^{k+1} = \omega v_{ij}^{k} + c_1 r_1 (pbest_{ij}^{k} - x_{ij}^{k}) + c_2 r_2 (gbest_{ij}^{k} - x_{ij}^{k}) \tag{4}$$

$$x_{ij}^{k+1} = x_{ij}^{k} + 0.5 \times v_{ij}^{k} \tag{5}$$

where $x_i^k = (x_{i1}^k, x_{i2}^k, \cdots, x_{ij}^k), i = 1, 2, \cdots, m$ is the parameter that the particle i contains, $v_i^k = (v_{i1}^k, v_{i2}^k, \cdots, v_{ij}^k)$ is the velocity of the particle i, w is the weight of the middle layer, k is the current iteration number, c_1 and c_2 are learning factors to balance the relative importance of two extreme values, and r_1 and r_2 are randomly assigned values between 0 and 1.

$$\omega = \omega_{\max} - (\omega_{\max} - \omega_{\min}) \times \frac{k}{k_{\max}} \tag{6}$$

where k represents the number of iterations so far and $k_{\max}$ represents the maximum number of iterations. The terms $w_{\max}$ and $w_{\min}$ represent the maximum and minimum weights, respectively, which are generally set to 0.9 and 0.4, respectively.

2.3.3. Grey Wolf Encirclement Optimization Strategy

The particle swarm is easy to aggregate in the final iteration, which reduces its searchability and causes the roughness prediction result to fall into the local optimum. Additionally, depending solely on the global optimum to direct parameter iteration will cause the subsequent iterations to move more slowly and reduce the capacity for convergence. The grey wolf method [27] will be incorporated into this study to enhance the parameter iteration formula and address the issues.

The grey wolf algorithm will decide which three people in the group have the smallest prediction error during the iterative update. The problem of diminishing convergence performance in the later stages of the algorithm is improved since other particles will surround the three elite individuals rather than the single optimal individual. The bounding search strategy, which is the most significant search strategy in the grey wolf algorithm, has the following mathematical representation:

$$X(k+1) = X_p(k) - A \times D \quad (7)$$

$$D = \left| C \times X_p(k) - X(k) \right| \quad (8)$$

where t is the number of iterations, $X_p(t)$ is the position vector of the prey, and $X(t)$ is the position vector of the grey wolf. The schematic diagram of its surroundings is shown in Figure 3.

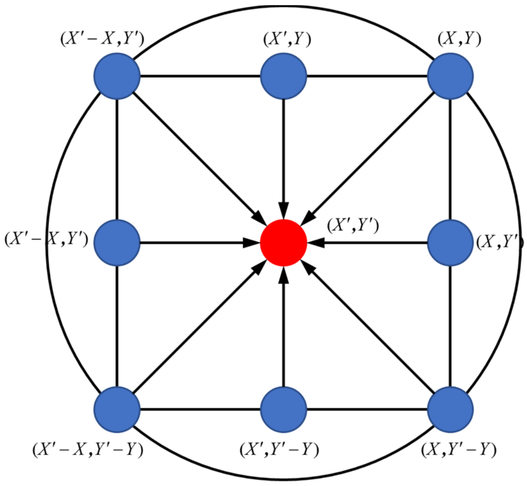

Figure 3. The encirclement strategy of the grey wolf algorithm [27].

As shown in Figure 3, assuming that the grey wolf is located in (X, Y) and the prey is located in (X', Y'), the grey wolf will move to $(X' - X, Y')$ by Equations (7) and (8) when $\vec{A} = (1,0)$ and $\vec{C} = (1,1)$. Different values of the coefficients $\vec{A}$ and $\vec{C}$ will produce different bounding effects, as shown in Figure 3, where $\vec{A}$ and $\vec{C}$ are coefficient vectors, which can be expressed by Equations (9) and (10), as follows:

$$\vec{C} = 2r_1 \quad (9)$$

$$\vec{A} = 2ar_2 - a \quad (10)$$

where r_1 and r_2 are random numbers of [0, 1], a is the control parameter linearly decreasing with the number of iterations in [0, 2], and the decreasing formula is as follows:

$$a = 2\left(1 - \frac{k}{k_{\max}}\right) \quad (11)$$

The introduction above states that the grey wolf algorithm employs the elite group advice, choosing the best three elite individuals as follows: the best solution α, the second best solution β, and the third best solution δ to guide the particle parameters. The three elite individuals will guide the particles in the form of bounding according to Equations (9) and (10). The guiding strategy formula is as follows:

$$D_\alpha = \left| C_1 \times X_\alpha(k) - X(k) \right| \quad (12)$$

$$D_\beta = \left|C_1 \times X_\beta(k) - X(k)\right| \tag{13}$$

$$D_\delta = |C_1 \times X_\delta(k) - X(k)| \tag{14}$$

where Equations (12)–(14) represent the distances between each particle and three elite individuals α, β, and δ, respectively; Equations (15)–(17) are the moving directions of particles to three elite individuals; and Equation (18) is used as the moving direction of particle swarm after combining the guidance of three elite individuals:

$$X_1(k) = X_\alpha(k) - A_1 \times D_\alpha \tag{15}$$

$$X_2(k) = X_\beta(k) - A_2 \times D_\beta \tag{16}$$

$$X_3(k) = X_\delta(k) - A_3 \times D_\delta \tag{17}$$

$$X(k+1) = \frac{X_1(k) + X_2(k) + X_3(k)}{3} \tag{18}$$

The performance of the particle swarm optimization algorithm can be enhanced by using the grey wolf algorithm bounding strategy in the update formula. Its updated formula will become Equation (20):

$$v_{ij}^k = \omega(X_{ij}^k - x_{ij}^k) + c_1 r_1 (pbest_{ij}^k - x_{ij}^k) + c_2 r_2 (gbest_{ij}^k - x_{ij}^k) \tag{19}$$

According to Formula (19), the update strategy of GWO is incorporated into the position update formula of PSO based on maintaining individual experience and the group optimal guiding strategy of PSO, which can somewhat alleviate the issues with the update formula of PSO, the prediction process is shown in Figure 4.

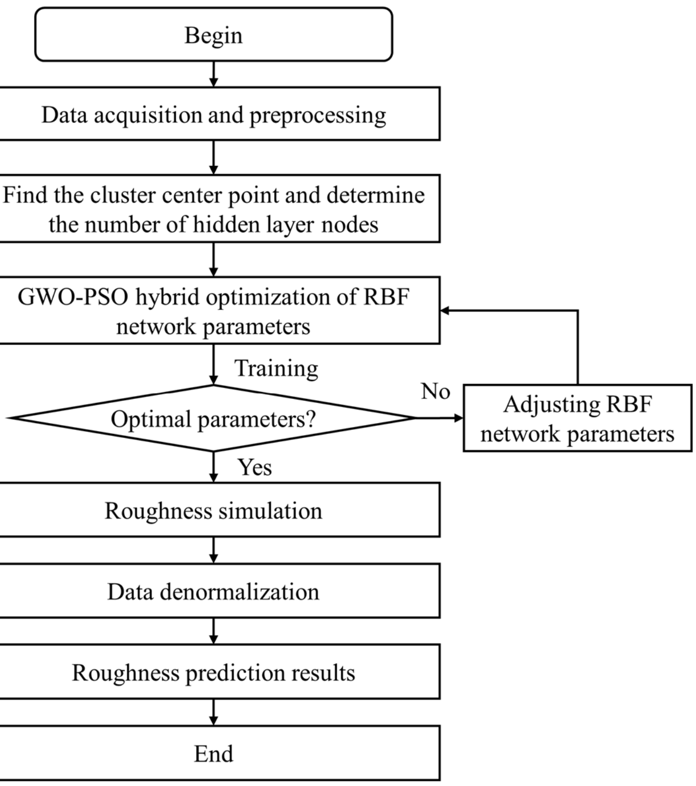

Figure 4. Roughness prediction by GWO-PSO-RBF neural network.

3. Experimental Results and Discussion

3.1. Experiment Details

3.1.1. Parameter Setting of RBF Neural Network

The nonlinear mapping issue in feedforward networks can be resolved by an intermediary layer, according to research and analysis [28–30]. As a result, there was just one intermediary layer in the RBF neural network used in this study. The number of nodes in the middle layer will influence the prediction effect of the network for different process parameters and prediction aims. This effect is, typically, calculated by the empirical formula below:

$$h = \sqrt{n + m} + \alpha \tag{20}$$

where n, h, and m are the number of nodes in the first, second, and third layer, respectively, and α is a random number of [1,10].

According to Equation (20), the range of the number of nodes in the middle layer can be roughly determined as [3,12]. Therefore, the influence of the number of nodes in the interval 3–16 on training error (MSE) was explored. Figure 5 shows the correspondence between the training error size and the number of hidden layer nodes. It can be seen that the training error tends to decrease with the increase in the number of nodes in this range, and the minimum error is obtained when the number of nodes is set to 12. When the number of nodes is greater than 12, the error increases slowly. Therefore, the number of nodes is determined to be 12.

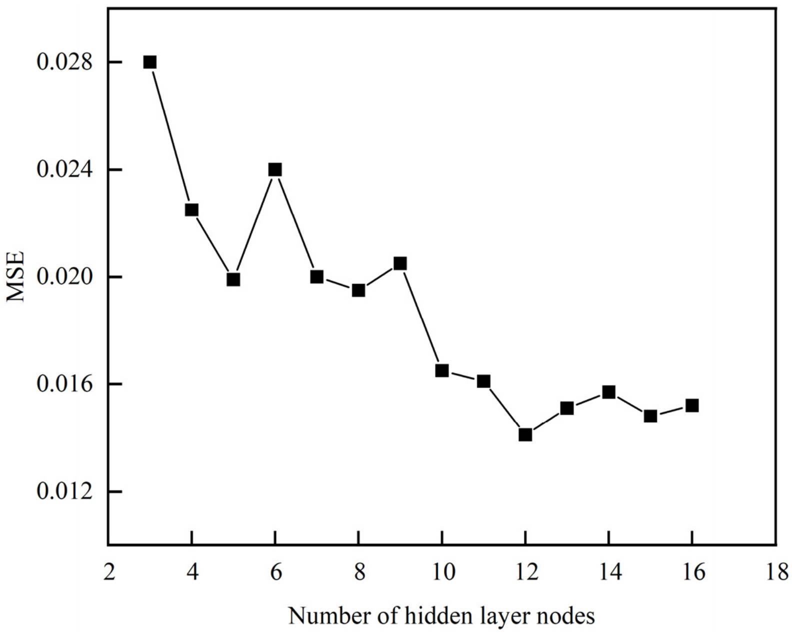

Figure 5. The change of the number of hidden layer nodes.

Three parameters, including initial weight, neuron center, and width, determine whether the network can converge to the minimum error and the training speed of the network during the training process. These three parameters will be constantly corrected in the subsequent iterative optimization process and approximate to the values that minimize the global error. The weights, neuron centers, and radial basis widths are initialized to random values between (0, 1).

Based on the above analysis, the RBF neural network structure in this paper is determined to be 3-12-1. In addition, the Gaussian function is used as the excitation function [31]. The initial weight, node center, and radial basis width are initially set as random numbers between (0, 1).

3.1.2. Parameter Setting of PSO Algorithm

Each particle in the PSO algorithm holds the values for its parameters. The position data used in this method are the RBF neural network parameters that need to be tuned. The number of particles $C = 100$ was selected. The dimension of the particle is the dimension of the solution space, which refers to the necessary information contained in the position of the particle, namely, the weight, the neuron center, and the radial basis width, and takes $D = 60$. The maximum number of iterations is $T_{\max} = 200$; maximum speed $V_{\max} = 1$; learning factor $c_1 = c_2 = 1.5$; and the inertia weight is updated iteratively according to Equation (6). The termination condition was that the global optimal fitness met the global accuracy requirements, and the MSE index was used as the particle fitness function, that is, the iteration was stopped when there were particles in the particle iteration process that made the global accuracy meet the requirements. In the particle position iteration formula, and are uniformly distributed random numbers between [0, 1].

3.2. Comparison of Model Fitting Results

Three prediction models of BP, RBF, and PSO-RBF neural networks are developed for comparison study to demonstrate the superiority of the upgraded GWO-PSO-RBF neural network prediction model established in this study. Figure 6 shows the prediction of the full data set using these four models on the roughness test data, respectively. The unoptimized RBF neural network performs better than the BP neural network fitting results when comparing the benefits and drawbacks of the four different types of neural network prediction effects. The optimized PSO-RBF neural network and GWO-PSO-RBF neural network are better than the ordinary RBF neural network, and the predicted value fits the true value more closely.

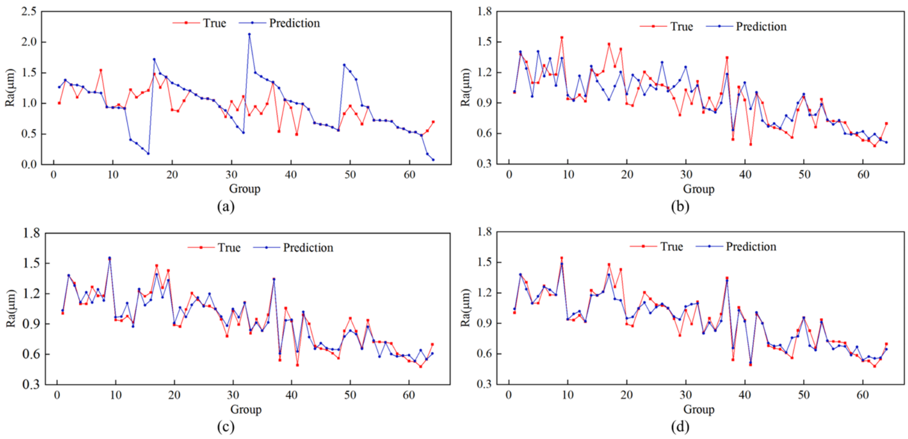

Figure 6. Comparison of prediction results of different models: (**a**) BP neural network; (**b**) RBF neural network; (**c**) PSO-RBF neural network; and (**d**) GWO-PSO-RBF neural network.

The scatter plots and regression lines for the four approaches are shown in Figure 7, where the ordinate represents the predicted values and the abscissa represents the true values. It can be seen that the GWO-PSO-RBF neural network scatter plot is near the fitting line and evenly scattered on both sides. The GWO-PSO-RBF neural network has the best prediction impact thanks to its determination coefficient of 0.919, which is higher than that of the other three models.

With the grinding parameters and the control variable technique, we exhibit the actual as well as the expected roughness in Figure 8. It can be found that when the belt linear speed is low under the condition of high feed speed and grinding depth reduction, large scratches appear on the grinding surface due to uneven grinding, machine vibration, and other factors (Figure 9b). When the belt linear speed and feed speed are high, the lower grinding depth occurs, and the uneven surface pits are produced by grinding due to the existence of factors such as grinding shedding and adhesion (Figure 9a). Due to the existence of these uncertainties, the predicted value learned by the model has a large error from the true value. It is worth noting that the proposed model has a better prediction effect on the whole.

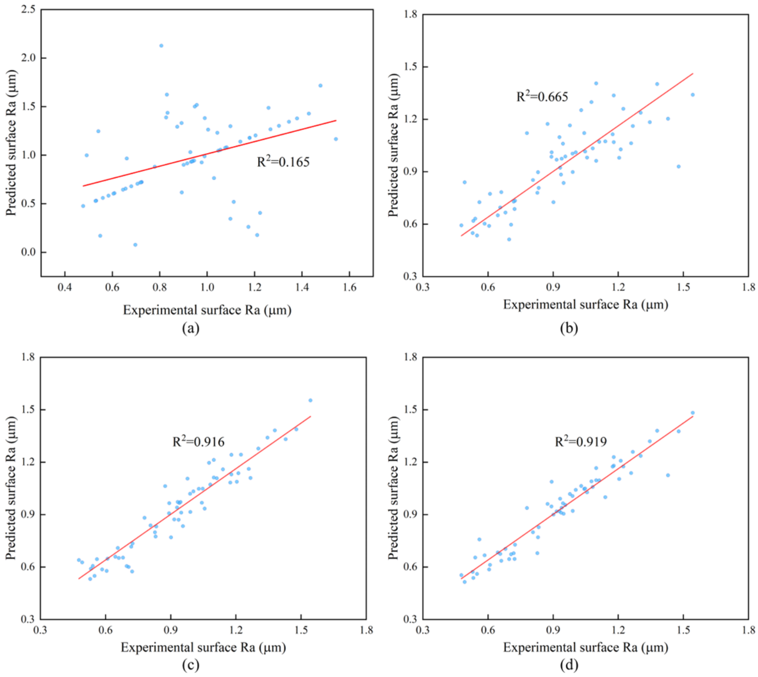

Figure 7. Scatter and regression lines between predicted and real values of the four models: (**a**) BP neural network; (**b**) RBF neural network; (**c**) PSO-RBF neural network; and (**d**) GWO-PSO-RBF neural network.

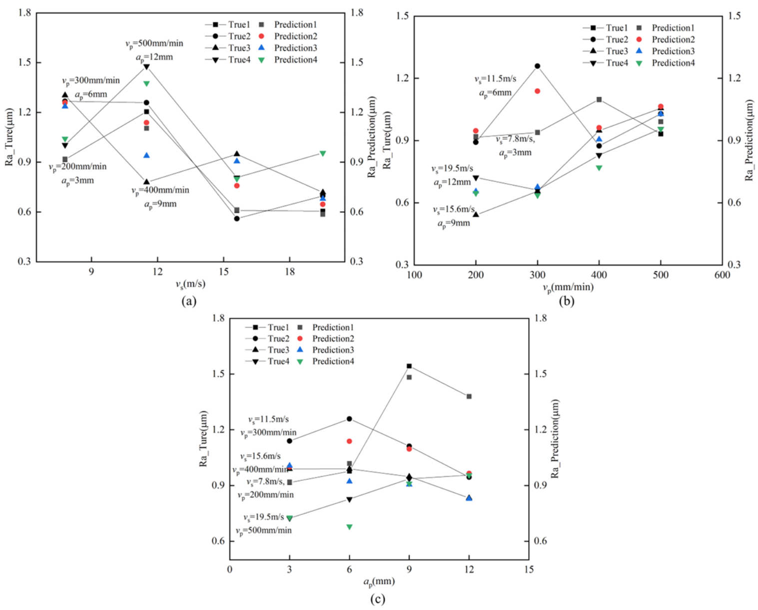

Figure 8. The effect of process parameter variation on roughness prediction: (a) v_s; (**b**) v_p; (**c**) a_p.

3.3. Comparison of Model Evaluation Results

In order to better illustrate the effect of the model, the mean square error (MSE), the root mean square error (RMSE), and the mean absolute percentage error (MAPE) of the prediction results are collected. Each model is simulated four times with the same random data, and the average of the results of the four times is taken as the reference value. The results for each model are summarized in Tables 3–5 along with the average values for each index.

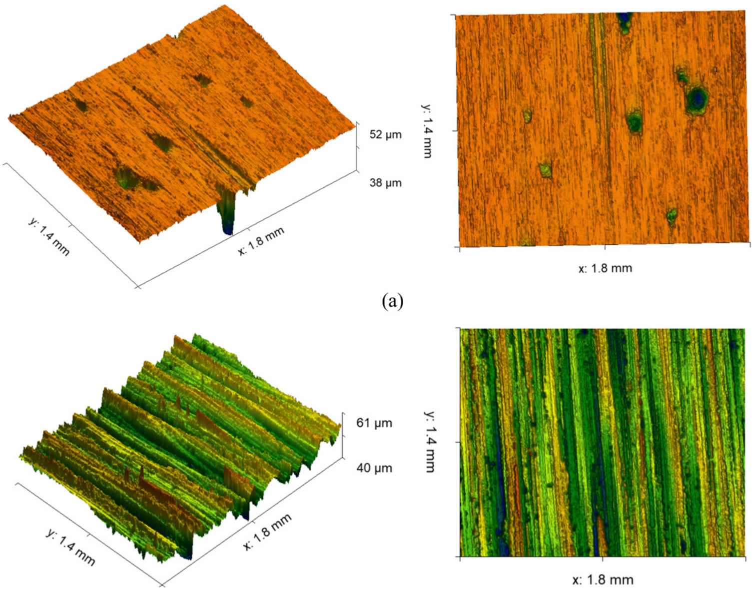

(a)

(b)

Figure 9. Surface topography of abrasive belt grinding: (**a**) the belt linear speed and feed speed are high during the lower grinding depth; (**b**) the belt linear speed is low under the condition of high feed speed and grinding depth.

Table 3. Comparison of results for MSE of each model under the test set.

Number	GWO-PSO-RBF	PSO-RBF	RBF	BP
1	0.004	0.007	0.047	0.242
2	0.011	0.008	0.084	0.283
3	0.005	0.024	0.061	0.291
4	0.008	0.013	0.052	0.192
Average value	0.007	0.013	0.061	0.252

Table 4. Comparison of results for RMSE of each model under the test set.

Number	GWO-PSO-RBF	PSO-RBF	RBF	BP
1	0.064	0.081	0.216	0.492
2	0.105	0.089	0.290	0.532
3	0.071	0.155	0.247	0.539
4	0.089	0.114	0.228	0.438
Average value	0.082	0.109	0.245	0.500

Table 5. Comparison of results for MAPE of each model under the test set.

Number	GWO-PSO-RBF	PSO-RBF	RBF	BP
1	0.046	0.070	0.208	0.498
2	0.067	0.072	0.214	0.512
3	0.102	0.107	0.321	0.472
4	0.071	0.068	0.198	0.384
Average value	0.071	0.079	0.235	0.466

According to the comparison of RMSE in Table 4, it can be seen that the evaluation result of the BP neural network model is 0.500, and that of the RBF neural network is

0.245. The result of PSO-RBF is 0.109. The result of GWO-PSO-RBF is 0.082. MSE is the mean square error, and its value is the square of RMSE. The average values of the above four models are 0.252, 0.061, 0.013, and 0.007, respectively. In general, the above three evaluation indexes of the GWO-PSO-RBF hybrid model are the smallest among the four algorithms, which can prove that it improves the accuracy and performance of the grinding roughness prediction to a certain extent, and can effectively predict the grinding roughness. In addition, the RBF neural network based on GWO-PSO optimization is superior to the PSO-RBF neural network in terms of optimization speed and optimization accuracy. Similarly, from Table 5, this index is 46.6% and 23.5%, respectively, after the roughness prediction by a single BP and RBF neural network. The prediction results of the hybrid model optimized by PSO and GWO-PSO decreased to 7.1% and 7.9%, respectively, indicating that the accuracy of the hybrid model combined with the optimization algorithm is higher than that of the single neural network prediction model.

By observing Figure 10, we can see that the single BP model has the worst three accuracy parameters and the lowest prediction accuracy. The prediction accuracy of the RBF neural network model is better than that of the BP neural network model, but the accuracy is still low. In general, whether it is PSO-RBF or GWO-PSO-RBF neural network, the prediction error index of the hybrid model is better than that of the single neural network model, indicating that the accuracy of the hybrid model combined with the optimization algorithm is higher than that of the single neural network prediction model. In addition, the proposed GWO-PSO-RBF neural network is slightly better than the PSO-RBF neural network, maintaining a smaller prediction error.

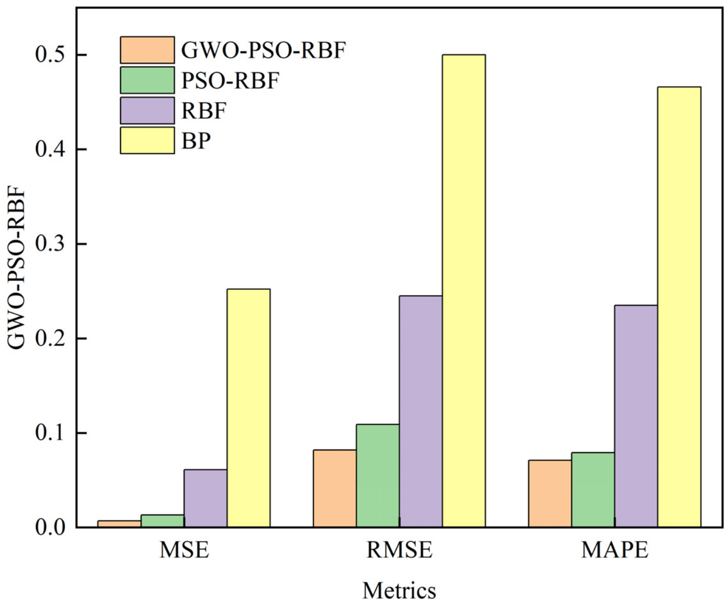

Figure 10. The average value of the three evaluation indicators.

4. Conclusions

In this chapter, a GWO-PSO hybrid optimized RBF neural network is established to establish the mapping relationship between grinding process parameters and the roughness of the titanium alloy abrasive belt to predict surface roughness. The PSO algorithm is used to optimize the parameters of the RBF network to obtain the optimal solution and improve the operation efficiency, and, then, the PSO algorithm is improved by the GWO algorithm to update the iterative formula, which effectively avoids the problem of falling into local optimum due to the decline of convergence ability in the later stage of the algorithm. Then, the structural framework of 3-12-1 is determined by an empirical formula and program debugging, and the main parameter values that need to be used in the algorithm are clarified. Finally, the simulation verifies the accuracy of the algorithm. The simulation results show that the GWO-PSO-RBF improved RBF neural network constructed in this paper can significantly improve the prediction accuracy of the algorithm, and has certain application values.

Author Contributions: Conceptualization, K.S. and B.L.; methodology, K.S., Y.L. and K.J.; validation, K.S.; investigation, K.S.; writing—original draft preparation, K.S. and Y.Z.; writing—review and editing, G.X.; supervision, K.S. All authors have read and agreed to the published version of the manuscript.

Funding: This research received no external funding.

Institutional Review Board Statement: Not applicable.

Informed Consent Statement: Not applicable.

Data Availability Statement: Data are contained within the article.

Conflicts of Interest: Author Kun Shan, Yashuang Zhang, and Yingduo Lan involved as a consultant and expert witness in Company AECC Shenyang Liming Aero-Engine Co.

References

1. Xiao, G.; Liu, X.; Song, K.; Zhang, T.; Huang, Y. Research on robotic belt grinding method of blisk for obtaining high surface integrity features with variable inclination angle force control. *Robot. Comput. Integr. Manuf.* **2024**, *86*, 102680. [CrossRef]
2. Chen, Y.; Yang, W.; Zhu, S.; Shi, Y. Microstructural, mechanical and in vitro biological properties of Ti6Al4V-5Cu alloy fabricated by selective laser melting. *Mater. Charact.* **2023**, *200*, 112858. [CrossRef]
3. Dai, B. Analysis and experimental research on titanium alloy cutting based on two-dimensional ultrasonic vibration assistance. *Diam. Abras. Eng.* **2020**, *40*, 92–96. [CrossRef]
4. Zhu, D.; Luo, S.; Yang, L.; Chen, W.; Yan, S.; Ding, H. On energetic assessment of cutting mechanisms in robot-assisted belt grinding of titanium alloys. *Tribol. Int.* **2015**, *90*, 55–59. [CrossRef]
5. Zheng, G.; Chen, K.; Zhang, X.; Zhang, X. Theoretical modeling and experimental research on the depth of radial material removal for flexible grinding. *Int. J. Adv. Manuf. Technol.* **2021**, *116*, 3355–3365. [CrossRef]
6. Kovilpillai, J.J.A.; Jayanthy, S. An optimized deep learning approach to detect and classify defective tiles in production line for efficient industrial quality control. *Neural Comput. Appl.* **2023**, *35*, 11089–11108. [CrossRef]
7. Xiao, G.; Zhu, B.; Zhang, Y.; Gao, H. FCSNet: A quantitative explanation method for surface scratch defects during belt grinding based on deep learning. *Comput. Ind.* **2023**, *144*, 103793. [CrossRef]
8. Zhang, J.; Song, W.; Bai, Y.; Han, B.; Li, L.; Zhu, H. Surface roughness prediction based on stepwise regression analysis. *Diam. Abras. Eng.* **2021**, *41*, 63–67. [CrossRef]
9. Fragapane, G.; Eleftheriadis, R.; Powell, D.; Antony, J. A global survey on the current state of practice in Zero Defect Manufacturing and its impact on production performance. *Comput. Ind.* **2023**, *148*, 103879. [CrossRef]
10. Cao, C.; Zhao, Y.; Song, Z.; Dai, D.; Liu, Q.; Zhang, X.; Meng, J.; Gao, Y.; Zhang, H.; Liu, G. Prediction and Optimization of Surface Roughness for Laser-Assisted Machining SiC Ceramics Based on Improved Support Vector Regression. *Micromachines* **2022**, *13*, 1448. [CrossRef]
11. Wang, R.; Cheng, M.N.; Loh, Y.M.; Wang, C.; Cheung, C.F. Ensemble learning with a genetic algorithm for surface roughness prediction in multi-jet polishing. *Expert Syst. Appl.* **2022**, *207*, 118024. [CrossRef]
12. Xu, X.; Ye, S.; Yang, Z.; Yan, S.; Zhu, D.; Ding, H. Analysis and prediction of surface roughness for robotic belt grinding of complex blade considering coexistence of elastic deformation and varying curvature. *Sci. China Technol. Sci.* **2021**, *64*, 957–970. [CrossRef]
13. Tian, F.; Lu, C. Research on Surface Roughness of Robotic Abrasive Belt Grinding Based on BP Neural Network. *Tool Engineer.* **2018**, *52*, 100–103. [CrossRef]
14. Li, Z.; Zou, L.; Yin, J.; Huang, Y. Investigation of parametric control method and model in abrasive belt grinding of nickel-based superalloy blade. *Int. J. Adv. Manuf. Technol.* **2020**, *108*, 3301–3311. [CrossRef]
15. Qi, J.; Zhang, D.; Li, S.; Chen, B. Modeling and prediction of surface roughness in belt polishing based on artificial neural network. *Proc. Inst. Mech. Eng. Part B J. Eng. Manuf.* **2018**, *232*, 2154–2163. [CrossRef]
16. Cheng, M.; Jiao, L.; Yan, P.; Li, S.; Dai, Z.; Qiu, T.; Wang, X. Prediction and evaluation of surface roughness with hybrid kernel extreme learning machine and monitored tool wear. *J. Manuf. Process.* **2022**, *84*, 1541–1556. [CrossRef]
17. Wang, J.; Chen, T.; Kong, D. Knowledge-based neural network for surface roughness prediction of ball-end milling. *Mech. Syst. Signal Process.* **2023**, *194*, 110282. [CrossRef]
18. Dong, H.; Gao, X.; Wei, M. Quality Prediction of Fused Deposition Molding Parts Based on Improved Deep Belief Network. *Comput. Intel. Neurosc.* **2021**, *2021*, 8100371. [CrossRef]
19. Zhang, Y.; Xiao, G.; Gao, H.; Zhu, B.; Huang, Y.; Li, W. Roughness Prediction and Performance Analysis of Data-Driven Superalloy Belt Grinding. *Front. Mater.* **2022**, *9*, 765401. [CrossRef]

20. Yang, Z.; Yu, P.; Gu, J. Research on prediction model of grinding surface roughness based on PSO-BP neural network. *Tool Technol.* **2017**, *51*, 36–40. [CrossRef]
21. Wang, T. Temperature prediction of granary based on improved RBF neural network. *Cereal Feed Ind.* **2021**, *5*, 12–15.
22. Gong, M.; Zou, L.; Li, H.; Luo, G.; Huang, Y. Investigation on secondary self-sharpness performance of hollow-sphere abrasive grains in belt grinding of titanium alloy. *J. Manuf. Process.* **2020**, *59*, 68–75. [CrossRef]
23. Xu, X.; Chu, Y.; Zhu, D.; Yan, S.; Ding, H. Experimental investigation and modeling of material removal characteristics in robotic belt grinding considering the effects of cut-in and cut-off. *Int. J. Adv. Manuf. Technol.* **2020**, *106*, 1161–1177. [CrossRef]
24. Jiang, G.; Zhao, Z.; Xiao, G.; Li, S.; Chen, B.; Zhuo, X.; Zhang, J. Study of Surface Integrity of Titanium Alloy (TC4) by Belt Grinding to Achieve the Same Surface Roughness Range. *Micromachines* **2022**, *13*, 1950. [CrossRef]
25. Guleria, V.; Kumar, V.; Singh, P.K. Prediction of surface roughness in turning using vibration features selected by largest Lyapunov exponent based ICEEMDAN decomposition. *Measurement* **2022**, *202*, 111812. [CrossRef]
26. Huang, Y.; Bai, Y. Intelligent Sports Prediction Analysis System Based on Edge Computing of Particle Swarm Optimization Algorithm. *IEEE Consum. Electron. Mag.* **2022**, *12*, 73–82. [CrossRef]
27. Wang, X.; Su, C.; Wang, N.; Shi, H. Gray wolf optimizer with bubble-net predation for modeling fluidized catalytic cracking unit main fractionator. *Sci. Rep.* **2022**, *12*, 7548. [CrossRef] [PubMed]
28. Shi, E.; Shang, Y.; Li, Y.; Zhang, M. A cumulative-risk assessment method based on an artificial neural network model for the water environment. *Environ. Sci. Pollut. Res.* **2021**, *28*, 46176–46185. [CrossRef]
29. Kabuba, J.; Maliehe, A.V. Application of neural network techniques to predict the heavy metals in acid mine drainage from South African mines. *Water Sci.Technol.* **2021**, *84*, 3489–3507. [CrossRef]
30. Xie, M.; Li, Z.; Zhao, J.; Pei, X. A Prognostics Method Based on Back Propagation Neural Network for Corroded Pipelines. *Micromachines* **2021**, *12*, 1568. [CrossRef]
31. Shymkovych, V.; Telenyk, S.; Kravets, P. Hardware implementation of radial-basis neural networks with Gaussian activation functions on FPGA. *Neural Comput. Appl.* **2021**, *33*, 9467–9479. [CrossRef]

materials

Review

Gear Hobs—Cutting Tools and Manufacturing Technologies for Spur Gears: The State of the Art

Norbert Hodgyai [1], Márton Máté [2], Gheorghe Oancea [1,*] and Mircea-Viorel Dragoi [1,*]

1 Department of Manufacturing Engineering, Transilvania University of Brasov, 500036 Brasov, Romania; norbert.hodgyai@unitbv.ro
2 Faculty of Technical and Human Sciences Târgu Mureș, Sapientia Hungarian University of Transylvania, 540485 Targu Mures, Romania; mmate@ms.sapientia.ro
* Correspondence: gh.oancea@unitbv.ro (G.O.); dragoi.m@unitbv.ro (M.-V.D.)

Abstract: The present work aims to provide the readers with a bird's-eye view of the general domain of cylindrical gear manufacturing technologies, including the cutting tools used, and related topics. The main scientific sources are explored to collect data about the subject. A systematization of the scientific works is completed, to emphasize the main issues the researchers have focused on in the past years in the domain. Several specific aspects are investigated: chip-forming process, cutting tool lifetime, the materials used to produce gear hobs, temperature and lubrication, the cutting tool geometry, cutting parameters, design methods, and optimization. Some gaps in the research have been identified, which are mainly related to the gear hob's design. These gaps, the organization of knowledge, the current requirements of the industry, and the actual socio-economic priorities form the basis for identifying new scientific research directions for the future in the area of spur gears manufacturing technologies and cutting tools. The main output of this work is a frame to guide the development of scientific research in the domain of spur gear production.

Keywords: cutting processes; chip formation; tool performance; gear hob; spur gear; gearing processes; gearing technologies; gear hob design; review; gap in literature; future research directions

1. Introduction

The first person who proposed a worm-derived generating tool for spur and worm gear-cutting was the German Christian Schiele. But 1856 was too early to introduce the method in serial manufacturing. After 33 years, the American George B. Grant patented the first known variant of a gear hobbing machine [1]. Finally, in Europe, the first entrepreneur who realized production of gear hobbing machines was the German Robert Herrmann Pfauter from Chemnitz. In this way, gear-cutting started, and the geometric precision of the manufactured gears presented a kind of amelioration. The cutting tool material was still carbon steel because the high-speed steel (HSS) was discovered at the beginning of the XX.-th century. The first official registration of the HSS marked as T1 was completed in 1910 by the company 'Crucible steel'. Once the HSS was discovered, the cutting tool durability presented a significant increase. However, the problem of the profile conservation was still unsolved. In 1907, the American Hans Baerbalck from Hamilton, Ohio patented an extension for the lathes [2] which allowed the profiling of the relief faces by an Archimedean spiral. Later, with the relieving lathe, the geometry of the gear hob was secured.

Parallel with the evolution of gear hobbing, other gear-generating methods were developed. In 1897, the American engineer and entrepreneur Edwin R. Fellows built the first gear shaper production machine, the famous '6-type', and later, patented a gear shaper cutter grinding machine [3]. It was the first method and machine able to generate internal spur gears, and this method persists almost 99% in machinery nowadays. It is true that a gear hobbing machine for internal gears was created in the early 1970s, but it is applicable only at large circumferences. Finally, in 1913, the Swiss engineer Max Maag patented his gear planing machine and the planing comb. The gear planing machine is the most complex kinematics-presenting machine tool ever created and the most precise; the planing comb is easy to manufacture due to its plain surfaces. But the productivity of this machine is weak, and thus, it remained in the actual machinery in the field of giant gears, where other methods and machines would not be more efficient. Another domain of gear manufacturing was brought to life by the automobile industry, and this is the domain of bevel and hypoid gears with curved teeth. The very special basic types (Gleason, Eloid, and Paloid) were patented, mathematical deductions were not published, and the majority of the deigning formulae were based on practical recommendations. Patent law acted as a shield to protect the mathematical models.

For the spur gears, the development was determined by the evolution of cutting tool materials, and later, the implementation of the numerical control in the structure of the machine tools. Firstly, the stabilization of the manufacturing technology of tungsten carbide inserts and the diversification of these (early 1980s) resulted in the appearance of the cutting insert-endowed gear hobs. The cutting performance increased fascinatingly, but the increased cutting speed and axial feed required more robust machines in order to avoid vibrations. Late, at the end of the 1990s, the physical vapour deposition (PVD) thin layer technologies induced the appearance of a new type of insert with superior mechanical and thermic properties. At the same time, thin layer-endowed carbide gear hobs arrived in the technological infrastructure, which led to a serious increase in the cutting speed and also opened the way to process hardened materials. With this, a grinding quality was nearly achieved. Finally, CNC gear hobbing machines can realize different types of numerically controlled crownings (possible only by grinding). These tooth surface modifications result in a more silent functioning. As can be seen, gear hobbing has come a long way, and has become one of the most popular and efficient gear-cutting methods.

According to the information published on a website [4], "The Global Gear Manufacturing Market is expected to reach USD 39.4 billion by 2025". The same source mentions as the main methods to produce gears being hobbing, shaping, and grinding, in this order, when it comes to their weight in the global production of gears. The relevance of the general domain of gears (production, manufacturing, control, cutting tools) is revealed also by other specialists [5], who devoted a literature review to the subject. Scholars mention in their publications that a considerable proportion of the gear hobbing is in the domain of gear-cutting, with a huge impact. So, gear hobbing machines represent approximately 50% of gear-cutting machines [4]. Other sources mention that the automotive industry uses the gear hobbing method, in a proportion of 70%, to obtain cylindrical gears [5,6]. The reason for such popularity of gear hobbing consists of its huge productivity in comparison with other cylindrical gear-cutting methods. Basically, there exist four fundamental cylindrical gear-cutting principles: copying using profiled disk mills, shaping using Fellow's cutters, planing by Maag's or Sunderland's planing combs, and finally, the subject of the present paper, hobbing using a gear hob derived from a basic worm.

A simple search on one of the most important scientific databases [7] while focusing on the keyword "gear" in "the title of articles" provides a list of more than 25,000 references. These statements are enough to emphasize the importance of the subject of the current review, dedicated to the most used cutting tool to manufacture gears—the gear hob—and to the gear hobbing technologies. The present work reveals some of the most important aspects approached by scientific researchers related to gear hobs usage, design, and manufacturing. Identifying some gaps in the achievements obtained so far in scientific research is the basis for formulating some possible future research directions meant to push the domain forward.

The next section of this article focuses on a literature review meant to reveal the main aspects approached by scientists in their published works. The beginning of the published research on gear hobs and gear hobbing is first presented, and then some main aspects of the problems in the gear hobbing processes are categorized, with six subsections, and in the gear hobs, with six subsections. This section highlights the main progress of each topic approached by scientific researchers and published in mainstream journals. Section 3 provides a discussion of the findings presented in the previous section, and is structured in three subsections that aim to systematize the literature, identify some gaps and bottlenecks in the current research, and propose some future research directions. The last section of this article, Conclusion, summarizes the main results of the work.

2. A Literature Review

The gear hobs and gear hobbing technologies belong to a very well-established domain. The gear hobbing process was patented in 1835, and the first specialized gear hobbing machine appeared in 1897 [4]. The first article on gear hobbing was published in 1963 [8]. Such a well-established domain, with a long history, is worthy of interest for scientific research. This literature review targets three main aspects related to the gear hobbing process and gear hobs: the cutting process itself, the design of gear hobs, and their manufacturing peculiarities, each of them with several specific issues.

2.1. The Gear Hobbing Processes

The gear hobbing process is one of the most complex cutting processes. This is because of the special needs in terms of the kinematics of the machine tools, the complexity of the cutting tool used, the chip-forming conditions, the specific geometry of the gear hob in terms of the cutting angles of the cutter, and so on.

A careful investigation of scientific production may reveal very interesting aspects the scientific researchers have faced.

2.1.1. The Mechanism of the Gear Hobbing Process

The mechanism of the gear hobbing process is considered one of the most complex generating processes. Litvin offers in his book known worldwide 'Gear Geometry and Applied Theory' [9] a clear definition and classification of the generating processes. The cylindrical gear surfaces generating process is described here as an example of two-parameter meshing. In this process, the rotation of the gear hob (the first parameter) combined with an imaginary axial shifting determined by the helix parameter forces the cutting edges to reconstruct the basic worm surface which contacts by lines the surfaces of a mobile generating rack. The second parameter is a translation along the axis of the workpiece, the named axial feed, in order to draw the tooth surfaces of the generating rack on their height, which means technologically the machining of the cut gear on whole width. If the cut gear is helical, the helix effect must be compensated for through an additional rotation of the rotary table. The corresponding settings are given in all machine tool handbooks.

The detailed geometric positions are described in a particular way in [10]. The kinematics of the meshing process is shown in Figure 1. This approach reveals the role of the gear hob in the process of involute surface generating with a mobile rack (we consider to mention here that there exists also the generation method with the standing rack, used in the construction principle of Maag's and Sunderland's planing machines). The figure describes the case of meshing a helical teethed cylindrical gear. Theoretically, the helical involute tooth surfaces contact along a straight line the generating surfaces of the rack Σ_1. The pitch plane of the rack rolls without slipping on the pitch cylinder C_1 of the machined gear. Let us consider now another rack, Σ_2, whose teeth are perfectly aligned with the ttooth gaps of rack Σ_1, like pattern and counterpattern.

The basic worm of the gear hob, reconstructed by the cutting edges in the helical motion, is considered an involute worm, which is in fact a helical teethed cylindrical gear, having a huge teeth declination angle, e.g., equal to the complementary angle of the pitch helix inclination angle. As a consequence, it contacts the rack surface by another straight line. Considering both racks, the helicoid involute surface of the basic worm and the helicoid surface of the machined, it can be concluded that the rack tooth surfaces contact by a plane, and the worm surface and machined tooth surface contact the corresponding rack surfaces along straight lines; thus, the worm surface and the machined gear tooth surface contact all the time at the intersection point of the lines mentioned before. In order to mesh the extent of the gear tooth surface, rack Σ_2 is forced to execute a rectilinear motion along the rack tooth direction; the motion denoted is with S_2. At the same time, rack Σ_1 executes a linear motion of direction S_1 perpendicular to the axis of the machined gear. Thus, reciprocated meshing of the surfaces is ensured. However, the construction of the gear hobbing machine does not admit the direction modification of motion S_2. This is set parallel to the axis of the machined gear—in most cases vertically. As a consequence, if machining helical teeth, the vertical feed motion must be summed to the tangential motion of rack Σ_1. This is completed by a differential mechanism in the case of classical machine tools, and by a program when using CNC gear hobbing machines. The main motions and cutting parameters in a gear hobbing operation are as follows:

- Main cutting motion as the rotation about the gear hob's own axis, characterized by the cutting velocity v_c, the rotation n_2, and the angular speed ω_2;
- Circular feed motion as the rotation of the blank about its own axis, characterized by the rotation n_1, and the angular velocity ω_1.
- Axial feed motion s_{ax} is the linear motion of the gear hob slider along the workpiece's axis.

As presented before, the circular feed is dependent on the rotation of the gear hob, the number of teeth of the cut gear, the axial feed, and the teeth inclination angle.

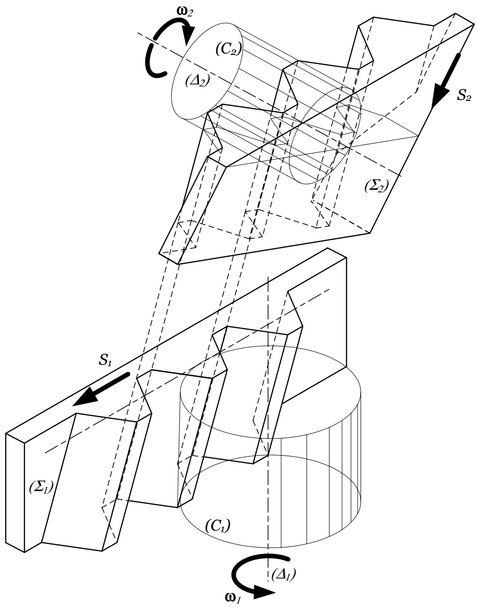

Figure 1. The generation principle of cylindrical gears with gear hobs [10].

2.1.2. Chip-Forming

The chip-forming at gear hobbing is a complex process, mainly because of the long cutting edge and its differently oriented zones. Due to its significant influence on the cutting forces, and the temperature in the cutting zone, the process of chip-forming raised the interest of specialists both in terms of theory and experiment. Ueda, Y., et al. [11] studied experimentally the chip-forming under the conditions of ultra-high-speed hobbing implemented on a gear grinding machine. To achieve such a high cutting speed, as fast as 2450 m/min, a large diameter gear hob was used with a grinding machine tool.

The workpiece material quality was SCM415 (equivalents: GB 15CrMo, JIS SCM415, DIN 15CrMo5) with 610 N/mm^2 tensile strength and 180 HBW hardness. The gear hobs were built with the WC-Co tungsten carbide. Due to the cutting tool material, experiments were completed in dry cutting conditions. To explore the hardness of the machined surface, tests were conducted using a micro-Vickers hardness tester at a load of 980 mN. After hobbing, the chips and gear surfaces were analyzed using a scanning electron microscope (SEM) and energy-dispersive X-ray spectrometer (EDX). Cross-sectional samples of chips were made using focused ion beam equipment and were inspected with a transmission electron microscope. The residual stress on the gear surface was measured using portable X-ray diffraction equipment. The main findings revealed that the quality and the hardness of the machined surface were high, and the wear of the hob was insignificant. The teeth quality of the surface machined on the gear was illustrated by images taken from the microscope. A comparison of the images taken from samples machined by a cutting speed of 200 m/min, and a feed rate of 0.3 mm/rev and 2450 m/min, 0.3 mm/rev, respectively, emphasizes the difference between the surface layers affected in the two cases. Despite the temperature rising with the cutting speed, the increase in temperature in the workpiece and the hob was small, because most of the heat was removed through the chips. A schematic model of the way the heat migrates and is distributed to the gear hob, workpiece, and chip is also presented for low and high cutting speeds, as shown in Figure 2 [11].

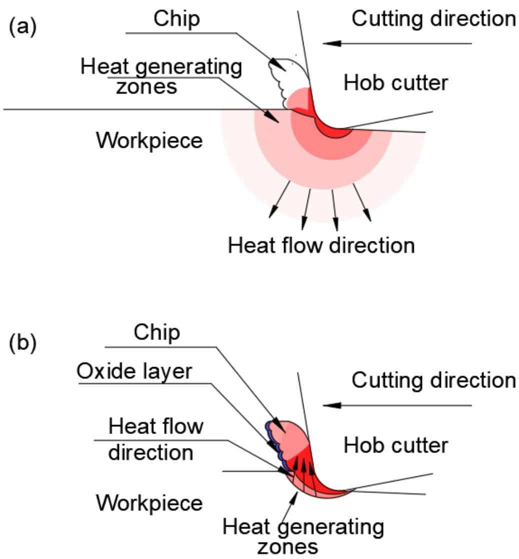

Figure 2. Schematic models for heat flow directions at different cutting speeds: (**a**) low cutting speed, (**b**) high cutting speed [11].

Because of the high temperature of the chips, they are highly oxidized. According to another conclusion, the color of the chip can be considered as a significantly accurate indicator of the temperature during their formation, and thus it can be used as a criterion for the optimization of cutting parameters. The color of the chips can also provide pieces of information to be used for enhancing the geometry of the cutting tool, i.e., the cutting angles. In order to obtain a consistent database for cutting geometry improvement, the chip-forming process was studied with highly sophisticated finite element method(FEM) models [12]. The results were confirmed by the experiments. Furthermore, the action of the chips on the gear flanks was modeled. A virtual machining environment was designed, aiming to study the chip-forming process without the need for experiments [13]. The research aimed to provide a tool to reduce cutting costs by determining the conditions to form un-deformed chips and to predict the cutting forces. The proposed method proved to be much faster and more accurate than the traditional numerical methods. A means to calculate the chip thickness is an analytically determined relationship [14]. Based on some variables (basically, the cutting parameters) and using non-linear regression of the experimental data, a mathematical relationship was developed to determine the maximum chip thickness. It was proved by case studies that the relationship was precise enough.

Despite the numerous research studies developed, the chip-forming process is still to be studied, to better understand its mechanics, and how it can be positively influenced by the gear hob's geometry. A general approach to chip-forming is presented in [14], regardless of the cutting process, but including gear hobbing. The final goal of the deep research is supposed to be the cutting force decrease.

Regarding the complexity of the chip-forming process during gear hobbing, one can admit that a chip results in a process of oblique cutting with a variable edge inclination angle (this is called the 'back rake angle', but in our opinion, the edge position by this angle determines much more the flow direction of the chip than it contributes to the chip-forming conditions; the phenomenon is controlled by the cutting speed and the orthogonal rake angle value). The nose radius in terms of turning can be adopted as the rounding radius by the gear hob tooth, meaning the circular arc edge part that links the side edge with the addendum edge. It is set in usual practice at the standard value, $\rho_0 = 0.38m_n$. It also must be mentioned here that the quality of the cut gear dedendum transition profile has an outstanding importance regarding the fatigue resistance and the load capacity of the cut gear. There exists research dealing with the influence of the rounding radius on the properties mentioned before [15]. It must be taken into consideration that the nose radius must be carefully correlated with the cutting parameters, especially the feed, because there exists a minimal limit chip thickness determined by these two parameters under which chip removal is not possible, and the cut surface result will be brittle and scaled. This problem was in extenso studied in [16] for a turning process, but we consider that the results can be admitted in the hobbing process too.

2.1.3. Cutting Forces

Chip-forming is just one of the aspects approached to design the gear hobbing process, another very important one being the cutting forces. An empirical formula to calculate the cutting force is developed, presented, and commented on [17]. It is based on experimental data, and some correction coefficients are used to consider the specific cutting conditions. This is a reason why the precision of the results is rather poor. The cutting factors considered are the maximum thickness of the chip, the modulus, the workpiece teeth number, the bevel angle of teeth, the axial feed, the cutting depth, and the number of teeth of the gear hob. Because of the complexity of the formula, it was further processed by advanced software means, to enhance it [18]. However, the newly obtained formula is applicable only for modules smaller than 30 mm. To find out more about the cutting forces, and to validate the theories related to cutting forces, different systems thought to measure the cutting force at gear hobbing were designed. One is based on the Kistler platform [18]. This allows obtaining by calculi, and based on the measured values, data about each component of the cutting force, as shown in Figure 3. The distribution of the magnitude of each force component is graphically represented depending on the nine successive orientations of the gear hob along its complete rotation. The graph gives a very good image of the way the gear hob is cyclically stressed.

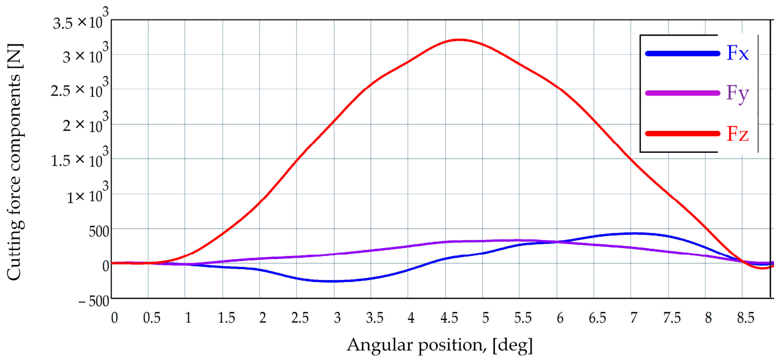

Figure 3. Cutting forces calculation for the hob's reference tooth during hobbing [18].

Another set of experiments was designed to perform measurements while hobbing gears made of brass [19]. Experiments were performed to study the similarities and/or differences between dry and wet machining. The monitored parameters were the profile precision, the tooth lead, and the cutting force by the other hand. In order to monitor the stability of the operation, a process capability indicator was introduced, as the quotient between the upper limit and the mean value difference and 3σ. Each experiment consisted of machining a sample of 45 gears. The conclusion was that in terms of gear precision, cutting forces, and process capability, the two are almost the same. It is to be noted that this conclusion cannot apply to other materials, especially if they are of harder machinability.

The cutting forces are used as one of the optimization criteria of the machining parameters [20]. Finding the best values of cutting parameters is often completed experimentally. This is a time-consuming task and generates supplementary costs. To avoid this, a special experimental system was designed, and it was used for the face hobbing of bevel gears.

One can appreciate that keeping under control the cutting forces at gear hobbing is an important objective since cutting forces have an important impact on the wear of cutting tools and they are always a source of vibration. As well, the energy consumption is directly influenced by the cutting forces. A deeper understanding of the way some factors such as cutting parameters, cutting conditions (dry, or wet), and the gear hob's geometry influence the cutting forces is desirable.

2.1.4. Temperature during the Gear Hobbing Process

It is obvious that the heat produced in the cutting area arises from two sources. The first one is the chip-forming process itself, which is discussed in a previous section. Here the heat is generated by the material deformation and flow. The second heat source is the friction between the different couples of actors involved in the gear hobbing process: the hob's rake face and the chip, respectively, and the relief face and the machined surface [21]. When it comes to friction, one of the main heat-generating phenomena, it can be reduced using cutting fluids. Their roles are both to cool the cutting area (help evacuate the heat) and to lubricate it, that is, to contribute to the decrease in friction forces. Despite the beneficial effects of the cutting fluids, they must be used under strict control, because of their bad impact on the environment and health. For these reasons, much research has been carried out on lubrication and cutting fluids. The main result was the appearance of bio-lubricants, able to successfully replace the mineral ones [22]. To diminish the bad effect of the cutting fluids, new techniques were developed. The cutting tools equipped with cutting inserts made of special materials (mono or multilayer-coated cemented carbides) can work without cooling. The so-called dry cooling techniques [23] eliminate the usage of cutting fluids or replace them with liquified gases delivered under high pressure (cryogenic cooling) [24]. Another approach aimed at giving up the cutting fluids in studies that targeted the durability of the cutting tools [25]. The study focused on the behavior of gear hobs made of special materials (designed to have high cutting capacity): powder metallurgical high-speed steel PM-HSS S390 and sintered tungsten carbide–cobalt WC-Co K30, under dry machining conditions, when cutting different types of materials. For an easy machinable one, 20 MnCr5, the findings were surprisingly good: the cutting speed could increase up to 350 m/min, and the durability was acceptable, even under dry machining conditions. On the contrary, if the workpiece was of a hard-to-be machined and highly abrasive one—EN-GJS-700-2—the results were disappointing. Even at a cutting speed as low as 50 m/min, the catastrophic wear occurred earlier than expected.

It was proved that the use of lubricants or cutting fluids increases the precision of gear hobbing [26]. A special technique that developed rapidly in recent years is lubrication by Minimum Quantity of Liquid (MQL). This combines the advantages of using lubrication and reducing the bad impact on the environment [25–30].

A comparison between dry machining, MQL lubrication, and wet machining (here referred to as flood lubrication) was completed [27]. It was emphasized that the lubricating conditions display particular aspects of gear hobbing, partially different from other cutting processes. Despite that gear hobbing usually needs more abundant lubrication than other processes, the conclusion was that the MQL technique provides the best results: much better than dry machining, and compared to wet machining, the advantages are bigger than the drawbacks.

Another experimental study [28] revealed that the MQL lubrication conditions are very suitable for gear hobbing. A flow rate as low as 100 mL/min offered good cutting conditions: the cutting depth did not have a significant influence on the quality of the machined spur gear. The effect of two non-mineral lubricants was compared in a specially designed study [29]. Eco-friendly lubricants based on synthetic ester and fatty alcohol were used in gear hobbing assisted by MQL. The general conclusion was that the fatty alcohol-based one offered better results, mostly in terms of heat transfer and friction decrease.

However, there is evidence that, in some cases, namely the finishing processes, lubrication cannot at all be eliminated [31,32].

In conclusion, one can say that there is still room for research on the temperature at gear hobbing: the way it influences the precision of the machined part and the wear of the gear hob, resulting in the development of efficient and eco-friendly ways to remove the heat from the cutting zone. As well, further clarification on how the cutting fluid can contribute to chip-forming, chip-breaking, and chip removal is needed. In these terms, inner cooling that feeds the gear hob with cutting fluid from its inside is a possible direction of research.

2.1.5. Wear and Durability of Gear Hobs

The wear and durability of the gear hob are closely connected, the first determining the second. This is why both here, and in the literature, they are treated together. While durability has direct implications for the effectiveness of the gear hobbing process, the wear of the hob directly and strongly influences the dimensional and geometrical precision and quality surface of the machined parts.

In the literature, much research that approaches lubrication [25–30] touches on aspects regarding the wear of the gear hob. This is normal, because the lubrication aims, among other things, to keep the cutting edge wear under control.

The gear hob wear is approached from different perspectives in the literature. Research on wear and durability is generally expensive, but when it comes to gear hobs, it becomes even more expensive because of the long time and many resources necessary to spend to obtain a result in experimental research. For this reason, scientific researchers focused on alternative ways to study the subject. An effective method to do that is simulation. Despite the very complex mathematical models needed to describe the phenomena involved, much research has been carried on based on this method.

Based on simulation methods, an interesting theoretical investigation tool was developed [33]. The evolution of the gear hob geometry affected by the wear is analyzed by this theoretical-experimental method. According to the simulation, several specific factors of the gear hobbing process can be predicted with acceptable accuracy, the most important of which are the temperature and cutting forces. In terms of gear hob wear rate, the predicted values are validated by experimental data. A study on the complex process of gear hobbing under conditions of high-speed and dry machining conditions [34] revealed interesting aspects about different forms of wear and how they evolve. The experimental research confirmed the simulated results, so they can be used confidently in the prediction of wear under different cutting parameters. The different ways each gear hob tooth acts to generate the tooth gaps on the machined gear determine different wear modes.

A special and very laborious study [35] was devoted to modeling the different wear types of the successive teeth of the gear hob involved in the cutting process. It showed the high complexity of chip-forming in a gear hobbing process. The form of wear, in terms of cutting theory, was considered the relief face wear, in the transition region between the addendum and the lateral edge, because this is the most stressed part of the tooth. It is defined as flank wear. Experimental research was performed to compare the evolution of the flank wear at a simple HSS-hob and a SUPERTIN-coated one. Results showed that the considered admissible value of the flank wear of 0.3 mm was achieved after a ten-times-larger number of cuts in comparison with the uncoated hob. The evolution of the wear was modeled using a computer program that considers the number of cuts, the equivalent chip thickness, the cutting length, and the cutting speed. Using this prediction model, the goal of the optimization was declared to be the uniform wear of all hob teeth. To achieve this, the vertical (axial) feed was completed with the tangential feed, resulting in a diagonal machining procedure. All experiments were performed with a flying cutter instead of a hob, but the results are accepted.

In gear applications, the designers often use specific tooth profile corrections of the tooth profile, aiming for different purposes. Accordingly, this involves modifications of the gear hob profile. A study [36] explains the way the cutting edge modified shape of the gear hob influences its wear, the shape of the chips, and the distribution of temperature in the gear hob's teeth. Simulations were used to provide models that can help understand the phenomena and save time devoted to experimental research. The similarity between the simulated results and those obtained experimentally is proved by pictures taken from the simulation and from chips physically obtained through the cutting process.

As mentioned before, research that deals mainly with high-speed gear hobbing [8] makes a very interesting conclusion about the wear of the cutting tool: the wear is not significantly affected by the increase in cutting speed, even if it reaches values in the domain of the ultra-high-speed (up to 2450 m/min).

Research [37] aimed to find out the extent to which the wear of the gear hob is influenced by the lubricant used in machining. The influence of the presence of alumina nanoparticles in the mineral lubricant was the particularity of the study. Two identical gears made of DIN1.7131 material were machined with identical gear hobs, using lubricants with and without alumina nanoparticles. Experimental research proved that the alumina nanoparticles have a beneficial contribution to reducing the craters and the wear of the flanks. The quality of the machined surfaces expressed by the roughness was better, as well.

The influence of the cutting speed on the gear hob wear under different lubrication conditions revealed that the general tendency is that the wear progresses faster when the cutting speed increases. The two lubrication methods were wet lubrication (wet machining—VM) and Minimum Quantity Lubrication (MQL). The cutting speed was varied in four steps within the range of 34.4 to 69.9 m/min. The type of wear analyzed is illustrated in Figure 4 [38].

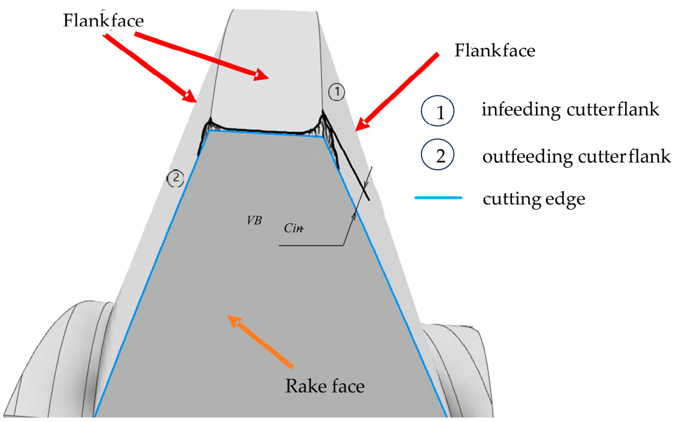

Figure 4. Locations and types of analyzed wears [38].

The number of teeth affected by the wear was also analyzed, and it was found that the teeth were differently worn depending on their position on the gear hob. The numbering of the teeth is shown in Figure 5. The study revealed that the bigger number of affected teeth reported was always in the case of MQL lubrication. The wear evolution was quite similar for the two lubrication methods, but there was identified a threshold value of the cutting speed of about 50 m/min. where the MQL method does not provide satisfactory results anymore.

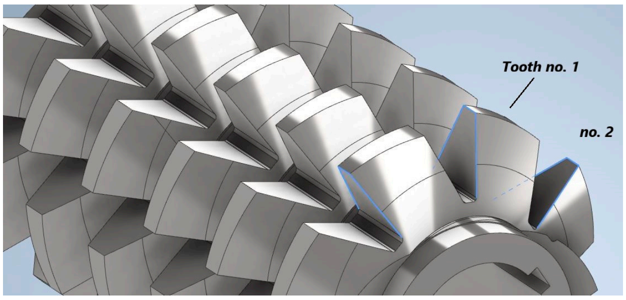

Figure 5. The numbering of the gear hob teeth [38].

Another issue that has a major impact on the wear of a gear hob is the cutting geometry [39]. To study the impact of the cutting angles, a gear hob equipped with cutting inserts was used. Such a constructive solution allows the easy building of gear hobs with different clearance and rake angles. In such a way, each side cutting edge obtains the desired clearance angle. The general conclusion is that the gear hobs equipped with indexable inserts present a much better wear resistance than the conventional ones. Despite the advantages provided by the increased durability of the gear hob, the authors do not mention that such cutting tools can be used only for roughing machining, because of their weakness in terms of profile precision, with bad implications for the geometrical precision of the machined gear, which needs to be finished by other processes.

The local wear of the finishing gear hob raised the attention of researchers [40]. Finishing by hobbing is usually applied as the final processing of the gears roughed by dry machining. The locally different wears of the finishing gear hob cause either low precision of the parts machined or premature tool replacement. Avoiding unbalanced wear can be achieved by an optimal design of the cutting process. To ease that, the local wear process was modeled. It was proved by experiments to be valid, so it became a useful design tool.

Because the tool wear investigation is a very expensive one, mainly in the case of gear hobs, a rapid method to characterize the wear was developed [37]. It was called “flute hobbing” and was first applied and verified for gear hobs made of PM-HSS. The wear of the gear hob was studied for a dry high-speed gear hobbing process.

The wear mechanism, in the case of gear hobbing, depends on the chip-forming model induced by the value of the cutting speed, and the cooling conditions, but firstly it is determined by the resulting tool-in-use geometry. Due to the helix effect, exactly as in the case of turning threads with large pitch values, the side rake and relief angles are strongly different on the attacking and the following flank. Gear hobbing, even in cases of very high cutting speeds, deals with small chip thickness; thus, crater wear on the rake face will never appear. Exactly as in the case of most gear-cutting tools, wear is prominent on the relief faces, due to the small side relief angle values. This is, in the case of gear hobs and generally in the case of gear-cutting tools, unavoidable, because of a compromise to keep the theoretical profile error in the limits of tolerance. However, deformation of the cutting edge occurs, and monitoring is always necessary to follow the evolution of the wear [39,40]. Looking more attentively at Figure 3 and considering that the gear hob’s helix is right-handed, exactly as shown in Figure 4, it is obvious that the left-side edge is the infeeding (attacking), while the right-side edge is the outfeeding (following) edge. Even in the case of Fellow’s cutters, there are significant differences considering the theoretical undetached chip section. Without any doubt, the infeeding edge supports more charge than the outfeeding one; thus, local temperatures are higher on this edge. Due to the large chip section, the cutting forces are also larger, but the tool-in-use relief angle is smaller. Thus, the elasto-plastic deformation of the resulting surface in the radial direction is more significant, and this leads to the accentuated wear phenomena on the relief face. In conclusion, the durability of the infeeding edge is always smaller than that of the outfeeding edge. The wear phenomena are influenced by the position of the analyzed tooth, regarding the rack-gear theoretical line of action. Despite the theoretical approaches, almost all based on [9], that consider a helical tool surface in the meshing process, teeth execute simple rotations about the gear hob's axis and, thus, have no chance to change their positions regarding the line of action. Special methods and means have been developed and presented to examine the shape of the cutting edge affected by wear [41–43]. As a conclusion, teeth situated at the lower and upper limits of the line of action are partially involved in the meshing process, while teeth situated in the middle, in the vicinity of the pitch point, are fully involved in the cutting process.

2.1.6. Other General Aspects of Gear Hobbing Processes

Beyond the particular aspects of the gear hobbing processes, presented above, general issues regarding the gear hobbing itself are widely present in industrial scientific research. Despite the focus of the current work being on the spur gear, it must be mentioned that much research is devoted to other kinds of gears, only a few of which are mentioned here: bevel [44–47], spiral [48–51], hypoid [52–56], and spherical [57].

It is more effective to use CNC machine tools' capabilities to generate sophisticated tool paths necessary to process special gears than using dedicated gear-cutting machines and cutting tools, which need special adjustments. The face hobbing is already a consecrated process for bevel spiral gears. Unfortunately, it cannot be applied for straight-teethed bevel gears, because the teeth profile results were deformed. However, using a six-axis CNC machine tool and a dedicated mathematical model, it is possible, to combine the two motions, one the cutting tool and one of the workpiece, to obtain rectilinear flanks of the teeth placed on a cone-shaped part [44]. Because the five and six-axis CNC machine tools are very expensive, the researchers looked for technical solutions to machine bevel gears with simpler equipment. Combining a three-axis CNC machine tool and a rotary table, it was possible to manufacture a spiral bevel gear [51]. Very sophisticated gears have been machined using a CNC hypoid generator and a dedicated mathematical model. To achieve this, online real-time programming was involved [53]. Using CNC machine tools, even big internal gears can be machined. A special new kind of cutting tool must be used. The problem is to manufacture a cutting tool that is basically a spherical-shaped one, on which the cutting edges must be placed. This is possible using a four-axis machine tool. Furthermore, such a machine tool was transformed, so that by reconfiguring it, along with spherical hobs, elliptical ones and arc surface hobs can be manufactured [57].

As one can see, the CNC machine tools are more versatile and capable of processing different types of gear hobs and complex gears. In terms of manufacturing the gear hobs, CNC machine tools might be useful to machine the relief face of the side cutting edges. Hence, a certain clearance angle can be obtained, which is not allowable by the classical turning process.

In conclusion, in this direction, there is much room for developing research toward new technical solutions for improving the geometry of the gear-cutting hobs.

Coming back to spur gears, some interesting aspects of the gear hobbing process are worthy of being presented. Simulation is an important means to gather pieces of information about phenomena, processes, and other things, using cheap but advanced computerized methods, instead of spending time, money, and resources for this purpose. Thus, a simulation was developed to study the process of gear hobbing spur and helical gears [58]. Based on the computer aided design (CAD) model of the gear, and involving the kinematic of the cutting process, a simulated model was obtained. The result offers 3D geometrical data useful for predicting cutting forces, cutting tool stress, and even previewing the tool wear evolution. Concluding, one may say that the simulation software system can be used for further research.

The simulation was used also to analyze the effect of the relative position (misalignment) of the gear hob and workpiece [59]. The purpose of the study was to identify some means to reduce the noise of the gears used in the automotive domain. A solution was replacing gear shaving with heat treatment followed by gear hobbing, which brings the advantage of the increase in the flank hardness. However, it was found that special attention must be paid to the positioning of the hob worm against the workpiece. Any misalignment has a big negative impact on the geometrical precision of the gear, measured by runout and pitch error. Also, the positioning errors affect the teeth profile. Simulating the gear hobbing process for different inputs regarding the tool positioning, quantitative appreciations could be made on the geometrical errors of the machined gear.

Cutting parameters have an important influence on the general way the cutting process operates. This statement applies even more in the case of gear hobbing, because of the difficult cutting conditions. This is why it is crucial to choose the best values of the cutting parameters. A correct selection of the parameters can be completed based on an optimization process. Much research was dedicated to optimizing the cutting parameters at gear hobbing [60–64]. Among many articles that deal with the subject, an outstanding one provides a method to optimize cutting parameters based on multi-objective optimization [64]. The particularity of the study is that it addressed the small sample problem. The objectives assumed for optimization (evaluation criteria) were the quality of the parts machined, processing time, the total cost of processing, and the carbon footprint (the total carbon emission) considered in all the aspects concerning the processing. The support vector machine (SVM) method was used to generate the first population of parameters, and to obtain the optimal parameters, the ant lion optimizer (ALO) algorithm was applied. In fact, two optimization methods were used and compared. A combination of algorithms and methods—(SVM), and ALO was used in a case study to provide better results in case of the small sample problem than IBPNN/DE, improved the back propagation neural network/differential evolution.

Despite that the spur gears are well established and consecrated, in some situations, they cannot provide sufficient functionality, especially in cases of high-speed gears. Replacing the involute gears (straight teeth) with involute-helix gears brings some considerable advantages: it reduces the noise in operating the gear capable of higher speed and increases the load capacity. This is because the new type of gear put together the advantages of involute and circular gears [65]. Of course, since the manufacturing process is not thought of for CNC machine tools, new dedicated gear hobs had to be designed. A specific mathematical model to describe the concave and convex sides of the teeth made this possible.

Accuracy is a key point in general in engineering and particularly in manufacturing and acquires special importance in the domain of gears. That is why it is widely approached by researchers, whether it is about gears themselves [22,59,66–68], gear hobs, or gearing machines [69].

The gearing process can generate errors (profile shape, dimensions, others) in the machined gears [69,70], stress [71], or other defects. The errors might be introduced by the cutting edge of the gear hob, misalignments [59], and the stress can be induced by the heat treatment or by the cutting regime. A very interesting study has investigated the influence of cutting parameters [71]—an investigation on how the hob speed, the axial feed, and the radial cutting depth induce stress at the base of the gear teeth (this is the place where usually cracks appear, or even the fracture occurs). According to the study, this is the sequence of the factors considering their importance in inducing stress in the gear. To measure the stress at the tooth root, the isotropic fixed ψ method was used.

The proportion of the factors' influence is shown in Figure 6 [71].

The influence of the rotation accuracy of a gear hobbing machine on the precision of the gears machined is investigated and discussed in [72]. The output of the investigation is very important because it can be used as a tool to select the correct values of the cutting parameters, aiming to obtain reliable gears. The results are all the more useful thanks to the 3D diagrams that illustrate the combined influence of pairs of input factors. Based on these 3D diagrams, optimization according to different goals can be performed.

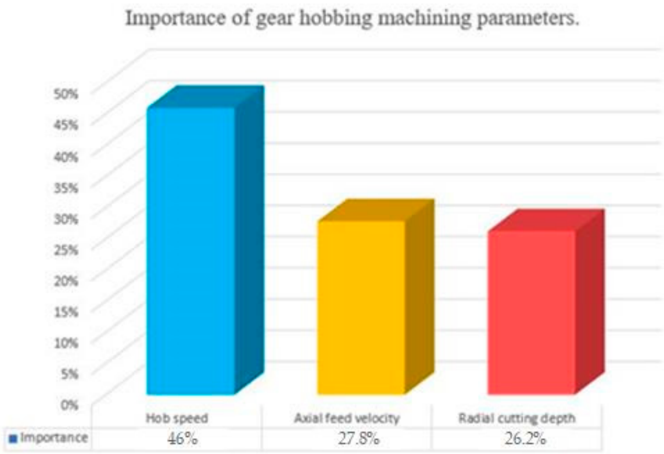

Figure 6. The importance of gear hobbing machining parameters [71].

An important advantage of the CNC gear-cutting machine tools is their capability to change the cutting parameters even during the cutting process if needed. Such a need appears whether severe variations of an output measure occur. To balance such output variations, an input parameter is accordingly adjusted. This is the basic principle of adaptive control [73]. This method was successfully applied to a CNC gearing machine tool [74]. The study was suggested by the relatively low effectiveness of the gearing processes, and the need to improve it. It is known that some input factors may vary during the cutting process (the cutting depth, the workpiece hardness/machinability, and others). To prevent an overload of the machine tools, the cutting parameters are chosen in such a way as to face properly the toughest cutting conditions. This means that for a certain period, the machine tool is underloaded. To bring the output to a normal value, a controllable input is increased. The relationship between the cutting torque (output measure) and the feed rate (controllable input) is exploited. First, a mathematical relationship between the two is established. This is used by a fuzzy controller able to determine (and deliver) the feedback to the machine tool. The feedback consists of an appropriate increase or decrease in the feed rate, according to the amount the torque deviates below or above a preset reference value. Applying this method, a decrease of 30–40% in the machining time is ascertained as being reported to the classic machining, and this can be considered a success.

2.1.7. Gear Hobbing Machine Tools

Machine tools are a very important element of the gear hobbing process. They influence decisively the precision, effectiveness, and the cost of the gear hobbing process. Furthermore, their capabilities determine the possibility of generating gears of various shapes. Obviously, the kinematics of the gear-cutting machine tools play a crucial role in the precision of the machined gears. This is a reason the researchers focused their attention on this domain. Studies have been carried out either to evaluate the precision of kinematics [75], and modeling [76], or to trace the transmission errors, aiming to improve them [77]. The novelty of this system consists of removing the uncertainty of the measuring system caused by the place of the encoders, on one hand, and the noise induced by the gears in the kinematic chain on the other hand. Individual circle grating encoders are connected at the ends of the two synchronized kinematic chains: at the spindle of the hob and of the workpiece. The design principle of the measuring system is presented in Figure 7 [77].

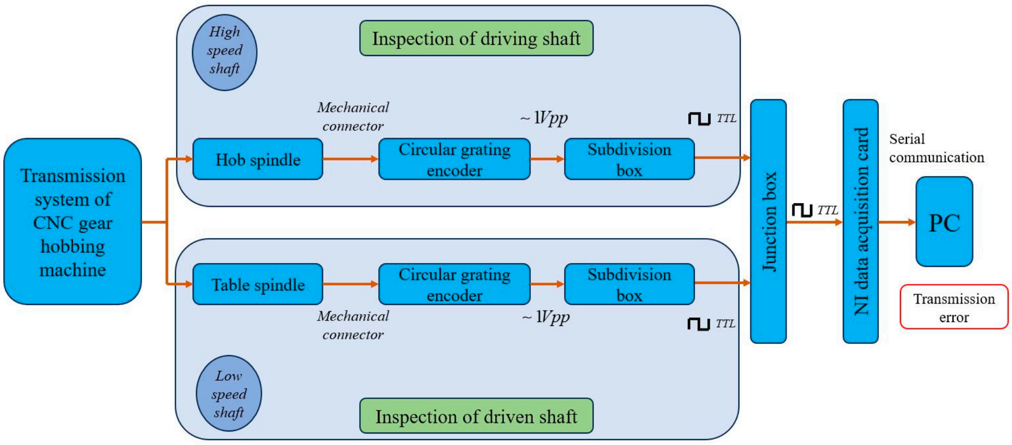

Figure 7. The design principle of transmission error in situ measuring system for gear hobbing machine [77] WPP (Volt Peak to Peak Voltage), TTL (Transistor-Ttransistor Logic, serial communication).

The proposed system, dedicated to locating the sources of transmission errors in the kinematic chains, was validated by experimental research. Using it, during the assembling process of a gear hobbing machine tool, adjustments can be applied to remove the transmission error sources. Furthermore, based on the statistical results of the evaluations, measures for improving the precision of the kinematic chains can be drawn.

The CNC machine tools are very agile in generating sophisticated tool paths, so they become important to the specialized machine tools for gear hobbing [68].

To conclude the review of the gear hobbing processes, one may say that any of the topics presented in this subsection leave room (more or less) for new research meant to improve the gear hobbing processes. Based on this assertion, and the gaps identified in the scientific research, some new future research directions will be stated by the end of this article.

2.2. Gear Hobs

The gear hobs are the main cutting tools used for manufacturing spur gears. Their most important feature is they ensure the effectiveness of the cutting process. The gear hobs are highly specialized to produce gears, to the same extent as the gear hobbing machine tools. Despite that the gear hobs are very well developed, much research is devoted to their improvement. For a very good understanding of the state of the art in the domain, a systematization of the problems related to gear hobs is necessary. A survey of the literature revealed the most important aspects of the research dedicated to gear hobs, as follows:

- The constructive solution (single block vs. cutting inserts);
- Design;
- Cutting materials;
- The rake face and regrinding;
- Undercuts.

2.2.1. The Constructive Solution

The basic constructive solutions for the gear hobs are single block and composite ones. The single block, or monolithic gear hobs, are made of a single material, and their teeth are cut in a cylindrical raw material. Their main characteristic is the good geometrical precision provided by the generating principle. This is why they are suitable for roughing, but are at the same time the most recommended solution for finishing the spur gears. Since the most used hobs are the single block ones [71–78], they are widely studied by researchers, so they are very present in the literature. The single block gear hobs can be better aligned to the geometrical precision requirements, but display some important disadvantages: relatively low effectiveness, and very importantly, they decrease in geometrical precision with every regrinding. The single block gear hobs are more complex in design and maintenance than the composite ones. Some of their particular aspects will be presented later in this article.

The composite gear hobs (known also as gear hobs with movable cutting inserts) form a narrower domain and they raise specific problems. The composite gear hobs are made of two parts: the main body, and the teeth. The teeth are made of a special material that offers better cutting properties, and they are mechanically assembled on the main body. This constructive solution was adopted because of the advantages they bring, but it is also affected by some drawbacks, as will be shown in the next paragraphs. The cutting inserts, by the material they are made of, are meant to provide better durability to the gear hobs and better stability to their dimensional precision because instead of being reground, they are replaced when worn. They are mechanically assembled on the body, so can easily be replaced when they become worn. The composite gear hobs mainly feature very good effectiveness of machining, and good durability, but have relatively low precision; thus, geometrical errors are transferred to the machined gears.

A general model of a composite gear hob was built [79]. The particular features of the gear hob so defined are as follows:

- A positive rake angle, which provides good cutting conditions through the way the cutting edge approaches the workpiece;
- A planar rake face, tilted against the gear hob's axis.

Different solutions were proposed to assemble the teeth on the main body: a line of teeth displaced rectilinearly, individual teeth, and even individual inserts for the left and right cutting edges. A computer program was used to determine the correct geometry and position of the cutting inserts. The authors also provided some recommendations/measures to be taken, aiming to increase the precision of the composite gear hobs: the cutting inserts are to be strictly placed in the correct position, modifying the shape of the cutting edge (replacing the straight one with appropriately curved ones), and keeping under control the angles of the teeth.

The composite gear hobs are produced in two constructive solutions: having the inserts placed parallel to the axis of the hob, or aligned to the helical rake face [77]. The second ensures equal rake angles for both the left and right flanks of the teeth, which is an advantage in terms of cutting conditions and inserts' durability. Whichever solution is chosen, the composite gear hobs suffer from low geometrical precision because of the difficulty of placing accurately the inserts in the desired position and orientation. Furthermore, usually, the cutting inserts have straight cutting edges, and this increases the geometrical imprecision because of the deviation of the straight line from the theoretical curved arc. However, there are available measures to improve the geometrical accuracy [79] by replacing the straight cutting edges with curvilinear ones and adjusting the cutting angles. Adjusting appropriately the orientation of the hob during the machining process, a uniform wear of all the inserts is achieved.

Further studies [80] offer solutions to improve the accuracy of composite gear hobs by modifying the shape of the inserts' cutting edges, aiming to make the shape approximation more precise and bring it closer to the theoretical shape. An advanced mathematical apparatus is involved, including analytical geometry and mathematical analysis. These special-shaped cutting edges increase the cost to manufacture the cutting inserts and the gear hob itself, but the cutting tool becomes as accurate, so it can be used even for finishing processes.

In conclusion, one may remark that the two types of gear hobs differ not only in the constructive solution but also in terms of their general design, manufacturing, and utilization. Briefly, the single block gear hobs feature good geometrical accuracy, and lower effectiveness (reported to the composite ones), which make them suitable mainly for finishing. Because of their low precision, but high effectiveness, composite gears are usually recommended for the roughing process.

2.2.2. Designing the Gear Hobs

Designing is the starting point in developing a gear hob. It is performed according to the requirements posed by the type of gear to be machined, its main geometrical features, the capabilities of the machine tool they will be used on, and the machine tool used to produce the gear hob, and the list can continue. All these conditions make the designing process of the gear hobs a very complex one. According to its complexity and importance, it has aroused the researchers' interest to a large extent (note that this section of the article targets exclusively the single block gear hobs).

Any gear-cutting tool must reproduce, through its relative motion referred to the machined gear, the generative part of the technological gear pair. As shown in Section 2.1.1, the generating part of the technological gear drive is a worm, which must be, according to Litvin's theory [9], an involute worm. The gear hob's edges must fit the involute worm's theoretical surface. Teeth must be provided with an adequate cutting geometry. In order to preserve the shape of the cutting edges, a relieving operation is applied. Litvin has also demonstrated that due to the helix effect, involute profile error is unavoidable, and can be kept under control only if the pitch helix angle fulfills $\lambda_0 \leq 2°30'$. In this case, the difference between an involute worm and a convolute worm is insignificant. The design of a gear hob consists in determining the main geometric elements of the basic worm, followed by the definition of the cutting geometry on the top edge, and finally, the computing of the second order relieve turning cutter and the relieve grinding wheel. The constructive elements of the gear hob are shown in Figure 8 [10].

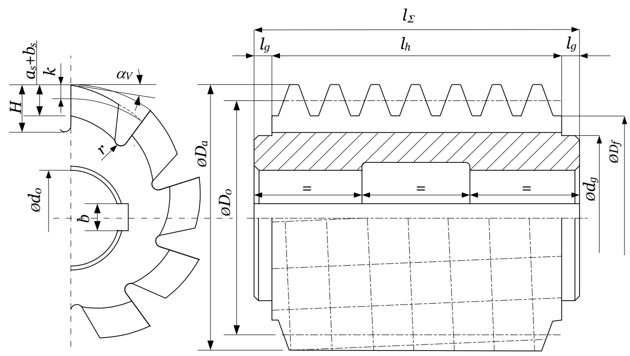

Figure 8. The principal constructive and geometric elements of a gear hob [10].

The design starts from the following initial data [10]: normal module m_n, number of threads (e.g., teeth) z_1, normal rack profile angle α_n and pitch helix angle λ_0. First, the front section data are computed as follows [10]:

$$\alpha_t = \arctan\frac{\tan\alpha_n}{\sin\lambda_0},\ m_t = \frac{m_n}{\cos\alpha_t} \tag{1}$$

With these, the basic and pitch cylinders diameters result as follows [10]:

$$D_0 = m_t\, z_1,\ \ D_b = D_0\cos\alpha_t \tag{2}$$

Starting from the normal pitch value $p_n = \pi\, m_n\, z_1$, the axial pitch value results as follows [10]:

$$p_{ax} = \frac{p_n}{\cos\lambda_0} \tag{3}$$

Now the nearest pitch value must be adopted, which can be set on the existing relieving machine; let us denote this with p_{ax}^{th}. The pitch diameter D_0 must be corrected in such way that the normal pitch must remain unaltered. This results also in the modification of the pitch helix angle. If considering an involute worm, the profile angle of the threading cutters α_s must be computed. These are equal to the basic helix angle [7]:

$$\alpha_s \equiv \lambda_b = \arctan\left(\frac{D_0}{D_b}\tan\lambda_0\right) \tag{4}$$

If deriving the gear hob from a ZN1-type worm, the equivalent normal profile angles α_{ne} are computed through the linearization of the curve obtained by intersecting the thread surfaces with a plane that is perpendicular to the pitch thread [9]. Finally, addendum and dedendum diameters D_a and D_f result by adding or deducting to the pitch diameter the tool tooth addendum or dedendum heights, in most cases.

The rake face of the gear hob is considered a helical ruled surface, and its leading helix is perpendicular to the pitch helix of the thread. As a conclusion, cutting edges result as the intersection of two helical surfaces. Here, additional corrections are needed.

The relief faces of the tooth are obtained by a helical relieving operation, first turning, and after the heat treatment, finishing by grinding. As a consequence of the relieving, the side relief faces result in conical helical surfaces. After resharpening, the characteristic diameters, including the pitch diameter, will decrease. In this case, the pitch helix angle increases, while the rake face helix angle decreases; thus, they will not anymore be perpendicular to each other. This phenomenon results in the deformation of the cutting edge form, which leads to the deformation of the generating worm while gear-cutting. As a consequence, theoretical profile errors, in the classical concept of the gear hob, are inevitable.

The most challenging issue in designing the gear hobs is the shape of the cutting edge. This is because even if the theoretical shape of the cutting edge can be determined by analytical methods based on the enveloping theory [81], it cannot be physically obtained due to technological restrictions (undercuts, effectiveness restrictions, machine tool kinematics, and others) [82–87]. That is why, when talking about the optimal profile shape, the scientists refer to the closest to the theoretic profile, which can be obtained in real manufacturing conditions.

A minimum modification of the tip fillet of the gear hob can avoid the undercuts of the teeth at the machined gear, without significantly affecting its geometrical precision [88]. A parametric model of a gear hob with a modified profile for big modules was created [89]. This allows easily adapting the design to specific technical requirements of the gear to be machined. The second-order cutting tools (relieving cutters for the clearance angle of the gear hob) were also designed. A gear hob was physically realized to prove the validity of the solution. As a side aspect of gear hob designing, the undercuts that occur during the gear hobbing and their effects on the gears machined are also approached in the research [90,91]. This is mentioned here only as a concern of the researchers, not as a directly linked aspect to gear hob design.

2.2.3. Cutting Materials

The gear hobs, mainly the small and medium-sized ones, used to be made of High-Speed-Steel (HSS). With the increasing demand for more and more effective cutting processes, new materials are needed to face successfully the harder and harder cutting conditions: high-speed cutting, the MQL lubricating method, or even dry machining. Also, the need for increased durability is a factor that prompted researchers to seek new performant cutting materials, which did not take long to appear. A study on dry gear hobbing [92] revealed that the powder-metallurgical High-Speed-Steel (PM-HSS) copes successfully with the tough conditions of such machining. A method to determine the correct values of cutting parameters for PM-HSS under dry machining is provided here.

The carbide hobs are very well suited for dry machining due to their high thermal stability, but this material quality seems to be still quite expensive. PM-HSS behaves even much better if coated with thin layers based on (Ti,Al)N, which adds good properties to resist the abrasion and hence to delay the wear [93].

A special technology allows coating the cutting inserts with thin layers of different materials. The technology is called physical vapor deposition (PVD) [94]. What is very important here is that the inserts can be repeatedly ground and again coated, thus significantly extending their operation time. An often-used coating material consists of an oxide based on Mn, Cr, and Fe in roughly even proportions, and important content of Si. A special preparation of the surface to be coated is required, so that the reshaped inserts show good results. Detailed investigation with advanced means of the coated surfaces of the cutting inserts revealed some shortcomings related mainly to the exfoliation phenomenon of the coating layer. A special preparation of the surface to be coated is required, so the coating provides good results. However, the repeated coating of the same cutting insert remains an important advantage.

One can admit that the general tendency in choosing material qualities for gear hobs (and generally for any cutting tool) is oriented to either HSS or carbide, both of them coated with different anti-abrasive thin layers.

2.2.4. The Rake Face and Its Regrinding

The rake face and rake angle are key issues in the geometry of a gear hob. A very important work that deals with this subject is [95]. Because of the specific construction, the gear hob's rake face is—in most of the constructive solutions—not a planar one, but helical. This makes determining the shape of the cutting edge a difficult process. According to the cited work, the gear hobs can be designed to have a 0° rake angle, or a positive rake angle. The 0° rake angle is preferred because it is easier to determine the shape of the cutting edge, but this is not the best solution in terms of cutting conditions. Better cutting conditions, when it comes to the cutting process and general behavior of the gear hob, are given by a positive rake angle. This poses a correction of the cutting edge shape to keep the accuracy of the gear hob determining the correct shape of the cutting edge, which in this case is a difficult task. The study [95] also revealed the errors induced by different rake angles in the shape of the machined gear teeth, as shown in Figure 9 [95].

The errors on the tooth of the machined gear are generated by the low precision of the gear hob profile. A 0° rake angle does not produce profile errors at the machined gear. On the contrary, a non-zero rake angle, a concave or convex rake face, and the unevenness of angles induced by regrinding are all factors that alter the correct profile of the gear. The type of error on the gear tooth profile is graphically illustrated for each factor of influence in Figure 9 [95].

A non-zero rake angle causes tilting of the side cutting edges and this almost compromises the possibility of determining the correct shape of the cutting edge, even using advanced means.

Because of specific geometry and technological restrictions, gear hobs are reground exclusively on the rake face. This is why the rake face and regrinding (resharpening, according to some authors) are approached together. Regrinding the gear hob modifies its outer diameter, and thus the helix angle of the tooth, and the helix angle of the rake face, both defined on the pitch cylinder, present contradictory evolutions: while the first increases, the second decreases, and thus, the initial perpendicularity between the tangents and the helices is compromised. The real angle decreases with the sum of the variations of the helix angles mentioned before. The direct effect of this is an alteration of the geometry of the cutting tool with every regrinding. Furthermore, it is impossible to keep the shape of the rake face after regrinding. It was proved that the interference of the grinding wheel and the helical rake face causes the alteration of the shape of the gear hob's rake face, and hence, also of the cutting edge profile [96,97].

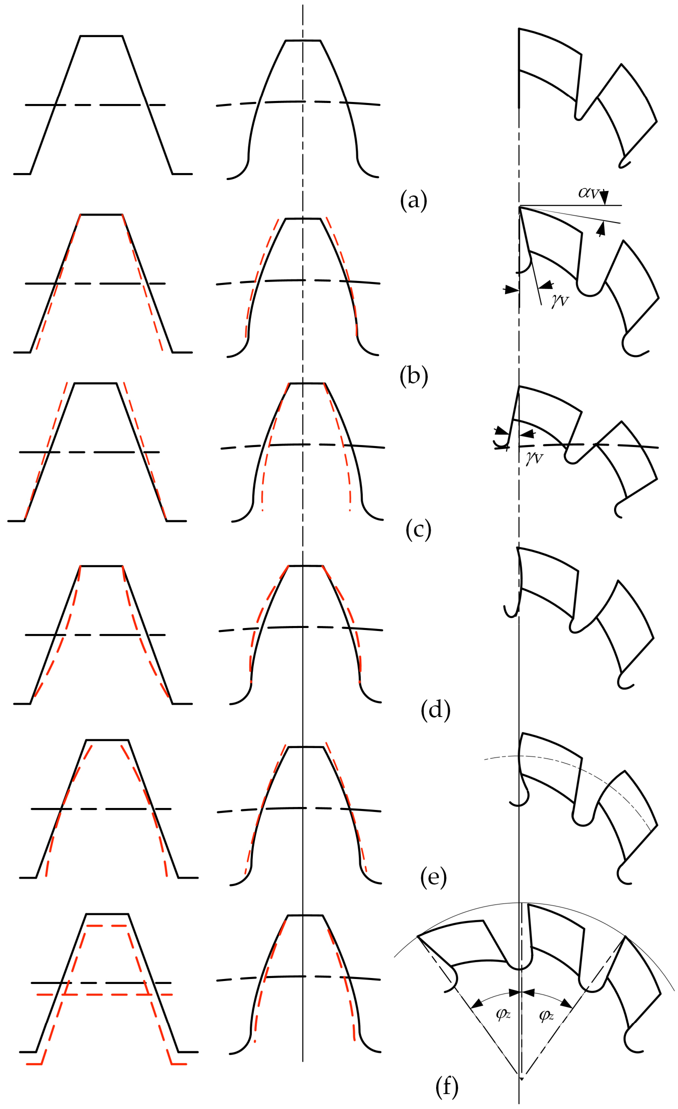

Figure 9. Errors on the tooth of the machined gear due to the lack of accuracy of the gear hob profile. (**a**) 0° rake angle (no errors); (**b**) positive rake angle; (**c**) negative rake angle; (**d**) concave rake face; (**e**) convex rake face; (**f**) unevenness of angles induced by resharpening. The theoretic profile is drawn in a solid line, and the real one in a dashed line [95].

Regrinding is an important concern of the researchers dealing with gear hobs. A study demonstrated that by applying an adjustment to the grinding wheel, the negative effects of regrinding can be minimized [98]. Furthermore, a new circle arc shape is used to replace the theoretical shape of the grinding wheel, so it now can be easily machined on a CNC machine (no need for special interpolations to generate the wheel profile, but only circular interpolation).

Another method to determine the profile of the grinding wheel used to resharpen gear hobs is proposed [99]. A mathematical model was developed to determine the correct profile of the grinding wheel and automatically generate the G code for CNC machining. This method successfully replaces the old-fashioned one, which needs repeated time-wasting adjustments to achieve the desired profile.

The rake face and rake angle with the related subjects—alteration by regrinding, regrinding, the profile of the cutting edges—are generally approached exclusively by geometrical approximations because of the complexity of the surface, and mainly due to the technological restrictions. The conclusion is that there is much room for future research to obtain improved solutions.

2.2.5. Undercuts

The undercut is another issue that generates many problems in gear hobbing. This phenomenon occurs in different situations: when regrinding the rake face of the gear hob, when profiling the clearance face, and when cutting a gear by hobbing. The undercut is never wanted, so special measures have to be taken to avoid it (if this is possible). Once it occurs, the undercut cannot be removed, so the single approach is to prevent its appearance. The undercuts can be prevented mainly by design, but adjustments to the cutting tool can also help the issue. One of the first references to undercuts in the literature dates back to 1983 [90]. Computer-aided modeling and simulation ease the task of revealing the undercut, as a first step to avoiding it. A Visual Basic program is available to create a model of the gear hobbing process. It allows studying how several factors such as the modulus and modification coefficient influence the undercutting phenomena [100].

The minimum number of teeth that can be cut on a gear without undercutting the teeth profile in the specific circumstances of a certain shape of gear hob can be determined by a computer program [101].

An option for new research can aim at new methods of designing and manufacturing the gear hobs able to reduce or even eliminate the undercuts during the machining of the gears. There exist two paths to follow. The first one considers the conical shape of the rake face grinding wheel unchangeable, and thus, the shape of the cutting edges must be computed; then, these edges are rototranslated about the axis of the gear hob, leaning on a conical helix, which results as an effect of the superposition of helical and radial relieving motions. Now, a second relieving grinding wheel profile must be computed. The second solution preserves the ruled shape of the rake face and tries to compute the profile of the rake face grinding wheel. In order to enlarge the setting possibilities, CNC grinding machines may have an emphasized importance here.

2.2.6. Manufacturing of Gear Hobs

The subject of manufacturing can be split into two areas: subjects related to the behavior of the gear hobs during the gear-cutting process, and subjects related to the peculiarities of the gear hob manufacturing technologies. Both domains were already discussed, as reported below:

- Gear hobbing in several aspects, such as chip-forming, temperature in the cutting area and lubrication, cutting forces, cutting parameters, and others;
- Manufacturing (and maintenance—regrinding/sharpening) of the gear hobs.

It can be stated that gear hob manufacturing technology must follow, till a given point, the manufacturing technology of a cylindrical worm. In the case of a monolithic construction (the gear hob is realized from one single blank of raw material), the operations and phases, till the cutting of the flutes, are the same as a worm gear drive's worm cutting.

The flutes are realized by milling using a semi-conical disc mill, where the rake face is meshed with the conical part. The profiling of the teeth is realized by relieving. The first phase is the roughing, which is always performed with a profiled turning tool. After the heat treatment, grinding operations occur. The most sensible is the grinding of the side relief faces. There exist two methods: grinding with a disk or grinding with a shaft. If using a disk-type tool, side relief faces cannot be ground on their whole extent, due to the occurrence of interference (Figure 10, [10]).

The side relief faces containing the cutting edges are ground with the conical side of the grinding disk. As one can see in Figure 10, the helical relieving motion is defined by the rotation of the hob υ, the radial feed of the grinding wheel $k_{th}\upsilon/2\pi$, and the axial feed $p_{ax}\upsilon/2\pi$. The axis of the grinding disk is tilted with the angle of the pitch helix λ_0 to the horizontal plane $(x_a z_a)$. The reference center of the disk is raised over the horizontal plane by h_y. It is obvious that, due to the disk radius value and h_y, there exists mathematically a double infinity of correct solutions for the grinding wheel profile. An optimization for approaching with a circular arc or Bezier curves [100] is the subject of further research.

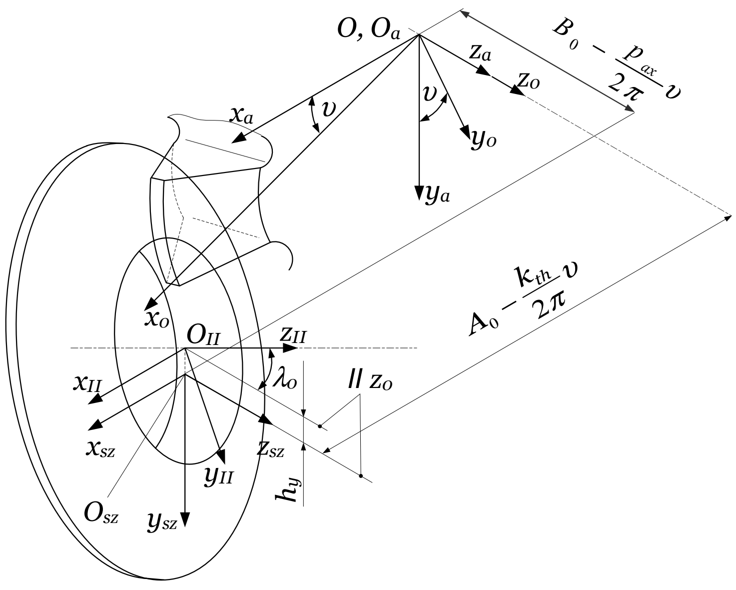

Figure 10. The grinding of relief faces with a disc-type tool [10].

The resharpening of the gear hob geometrically consists of a series of rotations of the helical rake face about the hob's axis, with angles corresponding to the relief face wear. Due to this, the tooth basis width decreases while its height remains almost constant, and this leads to the weakening of the tooth rigidity. Practically, it is recommended to stop the resharpening when the rake face fits half of the angular pitch. In conclusion, grinding on the whole tooth surface is not necessary, thus validating the use of the disk-type tool, which assures the necessary cutting speed even at a relatively lower rotation. The disadvantage of the procedure consists of the modification of the profile at every dressing of the disk because its diameter will decrease.

The part of the tooth that cannot be ground must be sunk, in order to avoid interference with the gear blank during the cutting. This can be avoided by applying, from the half of the angular pitch, a second relieving. This is only a roughing operation, characterized by an increased relieving parameter $k_2 \approx 1.5\, k_{th}$.

Shaft-type grinding wheels can be also used (Figure 11, [10]). In this case, the whole tooth surface can be ground.

Finally, a very sensitive operation is the grinding of the rake face. An undercut of the rake face by grinding is defined as exceeding the theoretical Radzewich rake face [64]. This is considered a reference due to its simplicity: it is drawn by a straight line, perpendicular to the axis of the worm while describing a helical motion [95]. This is always executed on special gear hob sharpening machines, using the conical face of the grinding disk.

The conclusion that can be stated is that the success of the grinding operation is achieved by using a precise machine tool infrastructure and performant and exact mathematical modeling of the reciprocate meshing surfaces. All these affect the shape of the cutting edge and the shape of the generating worm.

In the case of manufacturing gear hobs with inserts or assembled coil-type insert holders [10], the specific technological problems disappear: here, the geometric precision is assured by the precision and the accuracy of driven axes of the CNC machines involved in the manufacturing process. The precision of the hob is also decisively influenced by the precision of the inserts and the accuracy of their positioning on the main body of the gear hob.

The survey of the literature reveals that manufacturing the gear hobs is a subject less approached by researchers than the gear hobbing process. This statement indicates that there is much room for future research. The concrete-focused research subjects in the domain will be identified and discussed in the next section of the literature review.

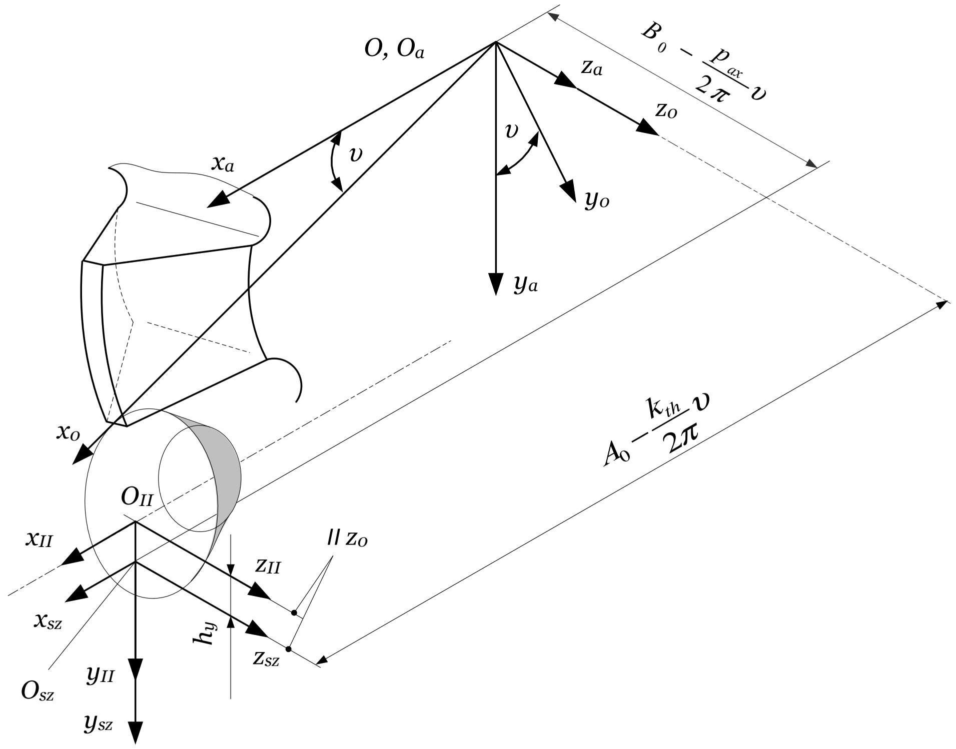

Figure 11. The grinding of relief faces with a disc-type tool [10].

3. Discussion

3.1. A Literature Systematization

Up to this point of the presented research in the current review, the most relevant scientific works were selected. For a clearer bird's-eye view, they were classified into two large categories: the gear hobbing processes and the gear hobs. In each category, some subdomains were identified, without claiming that the list is exhaustive. For gear hobbing processes, the following were considered most relevant subdomains:

- Chip-forming [11–13];
- Cutting forces and torque [14–20];
- Temperature in the cutting area and lubrication [21–32];
- Wear and durability [33–40];
- Other general aspects [41–74];
- Gear hobbing machines [75–77].

As one can see, after the subsection "Other general aspects", the list continues with one more item which apparently is not directly connected to the previous ones, but which is an important component of the cutting process, so it could not be omitted from the list.

The most populated subdomain is, as expected, the subsection "Other general aspects" because it includes narrow subjects that do not fit either of the previous subdomains.

Some very closely related issues, such as temperature lubrication and wear durability, were joined together in the list.

The large category of *Gear hobs* has been split into five subdomains, as follows:

- The constructive solutions [78–80];
- Designing the gear hobs [81–91];
- Cutting materials [92–94];
- The rake face and regrinding [95–99];
- Undercuts [100–102].

Despite the classification applied, there can be found subjects that easily could be included in either of the two categories. This is because the processes are so closely related to the cutting tools that the domains are difficult to strictly delimit. Such subjects are included in the first category.

Some very particular subjects, such as the hypotheses that are used in gear hobs design, or machining the clearance face of the gear hobs, to mention only two of them, have not been approached in the literature. This fact suggests new future research directions.

3.2. Some Gaps and Bottlenecks in the Current Research

Analyzing the literature, the continuous progress of the gear hobs and gear hobbing processes is noticed. Yet, the specialists can observe that some aspects are still not sufficiently studied, and others are not approached at all. Among these can be stated the following issues:

- Still assuming simplifying hypotheses in determining the gear hobs geometry, with bad consequences on the gear hobs' geometrical precision;
- The CAD/CAM systems facilities are not exploited enough for their entire potential in simulating the cutting processes and designing the gear hobs, observing interferences between the cutting tool and workpiece, and hence undercuts;
- The gear hobs used for finishing are designed and produced exclusively with a 0° rake angle, with bad implications for the cutting conditions—unjustified big cutting forces;
- The gear hobs lose their precision after regrinding because of the decrease in diameter and alteration of the cutting angles and the edge line shape;
- Undercuts do not allow the correct regrinding of the gear hob;
- A gear hob having a planar rake face would be free of some problems related to determining the cutting edge profile and regrinding;
- The problem of low geometrical precision of the composite gear hob persists, and is not studied enough;
- Despite cooling being a sensible issue at gear hobbing, inner cooling is neither applied, nor studied;
- The clearance faces of the gear hob teeth are turned and ground on the relieving lathe; thus, due to the helical relieving process, the side relief angles result in small values;
- Almost not at all exploited the specific features of CNC machine tools in gear hobs manufacturing.

All the issues mentioned above are worthy of being studied, to provide new solutions for improving the gear hobs and gear hobbing processes. Even if some of the proposed re-flection subjects seem to be unsolvable, involving advanced research means, ingenuity and, why, not? the courage to try might offer unexpected favorable solutions.

3.3. Future Research Directions

One of the goals of this literature survey was to identify some new future research directions. Some gaps in the scientific research have been mentioned above. According to the classification already presented, some subjects worthy of being further studied are listed below.

3.3.1. General Directions for Research on Gearing Cutting Tools and Processes

The chip-forming process is one of the factors that, along with the cutting tool geometry and the machinability of the materials to be machined, determines the size of the cutting forces. Hence, deep research aiming at a better understanding of the mechanism of forming the chips can help decrease the cutting forces and, indirectly, energy savings.

Despite the negative effect of the thermic deformation of the workpiece, for roughing machining, it would be interesting to know whether either overheating or under-cooling the workpiece leads to lower cutting forces or better cutting conditions.

The temperature and heat removal seem to be kept well under control in green conditions by MQL lubrication and dry machining, even under high-speed conditions. However, high-speed gear hobbing is still worthy of being researched.

CNC machine tools are more and more used in the manufacturing of gears and gear hobs due to their versatility and capability to generate complex tool paths. Their main drawback is low productivity, so research on this subject is needed. A future research direction can target the goal of designing and producing new machine tools that combine the versatility of CNC multi-axis machine tools with the high productivity of specialized gear hobbing ones. The new proposed research directions are in fact extensions of the current research. More challenging research with a much higher level of novelty meant to increase the quality of the gear hobs is needed.

3.3.2. Future Research Directions

A very important issue in designing and producing gear hobs and gears is the geometrical profile errors of the gear hobs, which inevitably are transferred to the gears machined. The main sources of the profile errors are the simplifying hypotheses assumed in determining the profile of the gear hobs and the technological restriction that causes undercuts or other problems. To overcome these problems, some future research directions are stated as follows:

- Adopting new, innovative strategies to determine the gear hobs profile, which do not need simplification, so they lead directly to a real profile that matches perfectly the theoretical one;
- New principles of designing, manufacturing technologies, and regrinding technologies that preserve the correctness of the gear hob precision (shape) after regrinding;
- New geometries of the gear hobs that allow regrinding without undercuts; here can be mentioned the possibility of designing and producing gear hobs with a planar rake face;
- New, or improved technologies to determine the theoretical profile of the gear hob on the rake face positively angled. The result would be a two-in-one gear hob that combines the effectiveness of the roughing gear hobs (positive rake angle) with the precision of the finishing gear hobs (zero-angled rake face);
- New but still machinable shape of the clearance face that ensures an adequate clearance angle of the side-cutting edges.

Once (at least) some of these objectives achieved, important progress in gear hob design and production will be noticed.

3.3.3. Main Requirements for Improving the Gear Hobbing Technologies

Based on the literature review, and the needs of industry and society, three main requirements for improving the gear hobbing technologies have been identified:

- Higher productivity (effectiveness), with the following measures to be taken:
- Applying to an extended scale the high-speed machining;
- Cutting processes with increased feed rate;
- Optimized cutting parameters;
- New cutting materials that offer the cutting tool increased durability;
- Use gear hobs with adequate geometry that allow both roughing and finishing gears by the same gear hob.
- Higher geometrical and dimensional precision of the products: gear hobs, and hence the gears machined, with the following measures to be taken:
- Designing and producing gear hobs with a teeth profile free of errors;
- Designing and producing gear hobs able to preserve the profile precision after regrinding;
- Adequate clearance angle along the entire cutting edge of the gear hob teeth;
- Cutting methods that ensure an even wear of all the teeth of the gear hob.
- Eco-friendly technologies with the following measures to be taken:
- Applying the MQL lubricating, and mostly, dry machining;
- Giving up the mineral lubricants, and replacing them with eco-friendly cutting fluids;
- Applying inner cooling;
- Any measure meant to save energy;

- Approaching the cutting tools (design and production) and cutting processes in an integrated manner that takes into account the carbon footprint along the entire life of the product.

A final remark on future research directions states the need to involve Artificial Intelligence (AI) in the domain of gear hobs and gear hobbing processes in as many research processes as possible, either theoretical or experimental.

4. Conclusions

The present work presents an extensive, but not exhaustive, literature review aiming to provide the readers with a bird's-eye view of the generous domain of gear hobs and gear hobbing technologies for spur and helical gears. The main results of the work are as follows:

1. A systematization of the literature, according to two main areas, gear hobs, and gear hobbing processes, with their subdomains;
2. Identifying some gaps in the literature that need to be filled in by new research;
3. Stating some new future research directions.

The systematization of the literature aimed to group the articles targeting the same narrow subject, so the readers can easily focus on certain problems of gear hobs and gear hobbing technologies. The contents of the review offer information based on the map of the large domain of manufacturing gears. The authors' view from a distance allowed them to observe some gaps in the literature, some grey and white islands on the map. The first ones need to be further researched so the knowledge can be extended to offer better solutions for certain problems than the existing ones. The white islands either have not at all been explored, or the efforts of the researchers so far have not shown satisfactory results. Identifying the gaps in the past and current scientific research points to the sensible areas inside the technology of spur gears. Based on these gaps, and taking into account the industry's continuously increasing demands, on the one hand, and the need for sustainable development of the society on the other hand, some possible future directions for research are stated. They target mainly three objectives: increasing the geometrical and dimensional accuracy of the machined gears, higher effectiveness of gear hobbing processes, and an eco-friendly industry of gear hobs and related gears.

In the authors' opinion, one of the hottest points is the design of the gear hobs. New approaches are needed, so the simplifying hypotheses in determining the cutting edges' shape are to be removed. Hence, an accurate geometry, identical or at least very close to the theoretical one of the gear hobs, could be achieved, and this would have a direct and positive influence on the precision of the products machined by the newly designed gear hobs. A possible new geometry of the relief face of the gear hobs—considering the advanced and extended facilities offered by the CAD/CAM systems and CNC machine tools—is meant to ensure the proper values of the clearance angle along the entire cutting edge of the tooth, and is susceptible to preserving the shape accuracy of the gear hobs after repeated regrinding, with beneficial effects on the total life of the cutting tools.

There is a belief that these goals can be achieved, taking into account the new capabilities of surface synthesis and the possible involvement in the design process of Artificial Intelligence.

As one can observe, despite the approached domain being a well-established and developed one, there still is much room for new scientific research.

The intention of the authors was to open, based on the current achievements presented in the literature, and on the continuously increasing requirements of the industry, new perspectives for future scientific research on manufacturing spur gears, without neglecting the protection of the environment.

Author Contributions: Conceptualization, N.H., M.-V.D. and M.M.; methodology, N.H., M.-V.D. and M.M.; validation, N.H., M.M., M.-V.D. and G.O.; writing—original draft preparation, M.-V.D. and

M.M.; writing—review and editing, M.-V.D., M.M. and G.O. All authors have read and agreed to the published version of the manuscript.

Funding: This research received no external funding.

Institutional Review Board Statement: Not applicable.

Informed Consent Statement: Not applicable.

Data Availability Statement: The original contributions presented in the study are included in the article, further inquiries can be directed to the corresponding authors.

Conflicts of Interest: The authors declare no conflict of interest.

References

1. Rominger, G.S. Worm. Gear. Cutting Machine. U.S. Patent 405,030, 24 January 1893.
2. Baerbalck, H.; Hamilton, O.H.; Carr, R.S. Relieving Mechanism for Engine Lathes. U.S. Patent 870,759, 12 November 1907.
3. Fellows, L.E.R. Machine for Grinding Gear Generating Cutters. U.S. Patent 686,599, 12 November 1890. (Application filed 24 June 1899).
4. Verified Market Reports. Available online: https://www.verifiedmarketreports.com/product/gear-manufacturing-market/ (accessed on 1 March 2024).
5. Boral, P.; Gołębski, R.; Kralikova, R. Technological aspects of manufacturing and control of gears—Review. *Materials* **2023**, *16*, 7453. [CrossRef] [PubMed]
6. Xiao, Q.; Li, C.; Tang, Y.; Pan, J.; Yu, J.; Chen, X. Multi-component energy modeling and optimization for sustainable dry gear hobbing. *Energy* **2019**, *187*, 115911. [CrossRef]
7. Web of Science. Available online: https://www.webofscience.com/wos/woscc/full-record/WOS:000245459700171 (accessed on 2 March 2024).
8. Chu, C.T.; Shen, S.H.; Hu, C.Y.; Chen, C.C. A universal hob for corrected circular arc-tooth point-meshing gears. *Sci. Sinica* **1963**, *12*, 723.
9. Litvin, F.L.; Fuentes, A. *Gear Geometry and Applied Theory*; Cambridge University Press: Cambridge, UK, 2009.
10. Máté, M. *Cylindrical Gear Cutting Tools*; Transylvanian Museum Society: Cluj Napoca, Romania, 2016; ISBN 978-606-739-070-4. (In Hungarian)
11. Ueda, Y.; Sakurai, N.; Takagi, T.; Ishizu, K.; Yan, J. Exploratory investigation of chip formation and surface integrity in ultra-high-speed gear hobbing. *CIRP Ann.* **2022**, *71*, 89–92. [CrossRef]
12. Bouzakis, K.D.; Friderikos, O.; Tsiafis, I. FEM-supported simulation of chip formation and flow in gear hobbing of spur and helical gears. *CIRP J. Manuf. Sci. Technol.* **2008**, *1*, 18–26. [CrossRef]
13. Habibi, M.; Chen, Z.C. A semi-analytical approach to un-deformed chip boundary theory and cutting force prediction in face-hobbing of bevel gears. *Comput. Aided Des.* **2016**, *73*, 53–65. [CrossRef]
14. Troß, N.; Brimmers, J.; Bergs, T. Calculation of the maximum chip thickness for a radial-axial infeed in gear hobbing. *Procedia CIRP* **2021**, *99*, 232–236. [CrossRef]
15. Norbert Hodgyai, N.; Tolvaly-Roșca, F.; Máté, M. A Comparison between a Classical and a Modified Root Fillet. *Műszaki Tudományos Közlemények* **2021**, *15*, 25–32. [CrossRef]
16. Mikołajczyk, T.; Latos, H.; Pimenov, D.Y.; Paczkowski, T.; Gupta, M.K.; Krolczyk, G. Influence of the main cutting edge angle value on minimum uncut chip thickness during turning of C45 steel. *J. Manuf. Process.* **2020**, *57*, 354–362. [CrossRef]
17. Kaçal, A.; Gulesin, M.; ULAŞ, H. System design and manufacturing for measurement of cutting forces in gear hobbing process. *J. Fac. Eng. Archit. Gazi Univ.* **2010**, *23*, 795–800.
18. Brecher, C.; Brumm, M.; Krömer, M. Design of gear hobbing processes using simulations and empirical data. *Procedia CIRP* **2015**, *33*, 484–489. [CrossRef]
19. Abe, T.; Fukunaga, K. Gear precision and cutting force at dry hobbing gear cutting for gears made of brass material. *Key Eng. Mater.* **2010**, *447–448*, 297–300. [CrossRef]
20. Stark, S.; Beutner, M.; Lorenz, F.; Lampke, T.; Karpuschewski, B.; Halle, T. Experimental and numerical determination of cutting forces and temperatures in gear hobbing. *Key Eng. Mater.* **2012**, *504–506*, 1275–1280. [CrossRef]
21. Bouzakis, K.D.; Lili, E.; Michailidis, N.; Friderikos, O. Manufacturing of cylindrical gears by generating cutting processes: A critical synthesis of analysis methods. *CIRP Ann.* **2008**, *57*, 676–696. [CrossRef]
22. Frățilă, D.F. Research of environment-friendly techniques influence on gear accuracy in context of sustainable manufacturing. *Proc. Rom. Acad. Ser. A—Math. Phys. Tech. Sci. Inf. Sci.* **2013**, *14*, 56–63.
23. Gupta, K.; Laubscher, R.; Davim, J.P.; Jain, N. Recent developments in sustainable manufacturing of gears: A review. *J. Clean. Prod.* **2016**, *112*, 3320–3330. [CrossRef]
24. Yldiz, Y.; Nalbant, M. A review of cryogenic cooling in machining processes. *Int. J. Mach. Tools Manuf.* **2008**, *48*, 947–964. [CrossRef]

25. Troß, N.; Brimmers, J.; Bergs, T. Tool wear in dry gear hobbing of 20MnCr5 case-hardening steel, 42CrMo4 tempered steel and EN-GJS-700-2 cast iron. *Wear* **2021**, *476*, 203737. [CrossRef]
26. Fratila, D. Evaluation of near-dry machining effects on gear milling process efficiency. *J. Clean. Prod.* **2009**, *17*, 839–845. [CrossRef]
27. Kharka, V.; Jain, N.K.; Gupta, K. Sustainability and performance assessment of gear hobbing under different lubrication environments for manufacturing of 20MnCr5 spur gears. *Sustain. Mater. Technol.* **2022**, *31*, e00388.
28. Kharka, V.; Jain, N.K.; Gupta, K. Influence of MQL and hobbing parameters on microgeometry deviations and flank roughness of spur gears manufactured by MQL assisted hobbing. *J. Mater. Res. Technol.* **2020**, *9*, 9646–9656. [CrossRef]
29. Kharka, V.; Jain, N.K.; Gupta, K. Performance comparison of green lubricants in gear hobbing with minimum quantity lubrication. *Tribol. Int.* **2022**, *173*, 107582. [CrossRef]
30. Zhang, S.; Sun, Z.; Guo, F. Investigation on wear and contact fatigue of involute modified gears under minimum quantity lubrication. *Wear* **2021**, *484*, 204043. [CrossRef]
31. Yuan, S.M.; Yan, L.T.; Liu, V.D.; Liu, O. Effects of cooling air temperature on cryogenic machining of Ti–6Al–4V alloy. *J. Mater. Process. Technol.* **2011**, *211*, 356–362. [CrossRef]
32. Sujan, D.; Moola, M.R.; Qua, S.Y. Environmental friendly cutting fluids and cooling techniques in machining: A review. *J. Clean. Prod.* **2014**, *83*, 33–47. [CrossRef]
33. Dong, X.; Liao, C.; Shin, Y.; Zhang, H. Machinability improvement of gear hobbing via process simulation and tool wear predictions. *Int. J. Adv. Manuf. Technol.* **2016**, *86*, 2771–2779. [CrossRef]
34. Cheng, Y.N.; Ma, C.; Zhang, J.; Zhou, H.; Xin, L.; Wang, X. Simulation and experimental study of tool wear in high-speed dry gear hobbing. *Int. J. Adv. Manuf. Technol.* **2022**, *119*, 3181–3204. [CrossRef]
35. Bouzakis, K.D.; Kombogiannis, S.; Antoniadis, A.; Vidakis, N. Gear hobbing cutting process simulation and tool wear prediction models. *J. Manuf. Sci. Eng.* **2002**, *124*, 42–51. [CrossRef]
36. Karpuschewski, B.; Beutner, M.; Köchig, M.; Härding, C. Influence of the tool profile on the wear behaviour in gear hobbing. *CIRP J. Manuf. Sci. Technol.* **2018**, *18*, 128–134. [CrossRef]
37. Khalilpourazary, S.; Meshkat, S.S. Investigation of the effects of alumina nanoparticles on spur gear surface roughness and hob tool wear in hobbing process. *Int. J. Adv. Manuf. Technol.* **2014**, *71*, 1599–1610. [CrossRef]
38. Stachurski, W.; Kruszynski, B. Influence of cutting speed on the hob wear in hobbing with the minimum quantity lubrication. *The. Vjesn.* **2020**, *27*, 341–345. [CrossRef]
39. Kühn, F.; Löpenhaus, C.; Brimmers, J.; Klocke, F.; Bergs, T. Analysis of the influence of the effective angles on the tool wear in gear hobbing. *Int. J. Adv. Manuf. Technol.* **2020**, *108*, 2621–2632. [CrossRef]
40. Klocke, F.; Gorgels, C.; Weber, G.-T.; Schalaster, R. Prognosis of the local tool wear in gear finish hobbing. *Prod. Eng. Res. Dev.* **2011**, *5*, 651–657. [CrossRef]
41. Balajti, Z.; Ábel, J.; Dudás, I. Examination for post-sharpening adjustment of cutting edge of a worm gear hob with circle arched profile in axial section. *Procedia Manuf.* **2021**, *55*, 260–265. [CrossRef]
42. Balajti, Z.; Ábel, J. Edge geometry test method with correctly positioned CCD cameras for production geometrical development of a worm gear hob with arched profile. *Procedia Manuf.* **2020**, *51*, 365–372. [CrossRef]
43. Claudin, C.; Rech, J. Development of a new rapid characterization method of hob's wear resistance in gear manufacturing—Application to the evaluation of various cutting edge preparations in high speed dry gear hobbing. *J. Mater. Process. Technol.* **2009**, *29*, 5152–5160. [CrossRef]
44. Shih, Y.P. Mathematical model for face-hobbed straight bevel gears. *J. Mech. Des.* **2012**, *134*, 091006. [CrossRef]
45. Shih, Y.P. Manufacture of face-hobbed straight bevel gears using a six-axis CNC bevel gear cutting machine. *Int. J. Adv. Manuf. Technol.* **2013**, *69*, 2499–2515. [CrossRef]
46. Kim, J.H.; Kim, D.H. Evaluation of fatigue life of automotive bevel gear. *Key Eng. Mater.* **2006**, *324–325*, 839–842. [CrossRef]
47. Efstathiou, C.; Tapoglou, N. Simulation of spiral bevel gear manufacturing by face hobbing and prediction of the cutting forces using a novel CAD-based model. *Int. J. Adv. Manuf. Technol.* **2022**, *122*, 3789–3813. [CrossRef]
48. Simon, V.V. Influence of tooth modifications on tooth contact in face-hobbed spiral bevel gears. *Mech. Mach. Theory* **2011**, *46*, 1980–1998. [CrossRef]
49. Simon, V.V. Optimal machine-tool settings for the manufacture of face-hobbed spiral bevel gears. *J. Mech. Des.* **2014**, *136*, 081004. [CrossRef]
50. Yang, J.; Li, H.T. A method to generate the spiral flutes of an hourglass worm gear hob. *J. Mech. Des.* **2018**, *140*, 063301. [CrossRef]
51. Suh, S.H.; Jih, W.; Hong, H.; Chung, D. Sculptured surface machining of spiral bevel gears with CNC milling. *Int. J. Mach. Tools Manuf.* **2001**, *41*, 833–850. [CrossRef]
52. Liu, S.Y.; Song, C.S.; Zhu, C.C.; Liang, C.C.; Bai, H. Investigation on contact and bending stress of face-hobbed and face-milled hypoid gear. *Mech. Mach. Theory* **2020**, *150*, 103873. [CrossRef]
53. Zhang, W.Q.; Cheng, B.; Guo, X.; Zhang, M.; Xing, Y. A motion control method for face hobbing on CNC hypoid generator. *Mech. Mach. Theory* **2015**, *97*, 127–143. [CrossRef]
54. Gonzalez-Perez, I.; Fuentes-Aznar, A. An exact system of generation for face-hobbed hypoid gears: Application to high reduction hypoid gear drives. *Mech. Mach. Theory* **2023**, *179*, 105115. [CrossRef]
55. Huang, K.F.; Yu, J.W.; Luo, H.; Shang, Z.T.; Huang, S.; Fu, L. An efficient vectorization solution to cutting dynamics modeling for face-hobbing of hypoid gears. *Mech. Mach. Theory* **2024**, *191*, 105504. [CrossRef]

56. Fan, Q. Computerized modeling and simulation of spiral bevel and hypoid gears manufactured Gleason face hobbing process. *J. Mech. Des.* **2006**, *128*, 1315–1327. [CrossRef]
57. Hu, Z.Q.; Li, Y.K. Design of 4-axis reconfigurable CNC machine tool for relief grinding sphere gear hob. *Adv. Mater. Res.* **2011**, *201–203*, 561–564. [CrossRef]
58. Dimitriou, V.; Antoniadis, A. CAD-based simulation of the hobbing process for the manufacturing of spur and helical gears. *Int. J. Adv. Manuf. Technol.* **2009**, *41*, 347–357. [CrossRef]
59. Matsuo, K.; Suzuki, Y.; Fujiki, K. Analysis of the effect on gear accuracy of workpiece/tool positioning accuracy in the hobbing process. *J. Adv. Mech. Des. Syst. Manuf.* **2017**, *11*, JAMDSM0071. [CrossRef]
60. Wu, D.Y.; Yan, P.; Guo, Y.; Zhou, H.; Yi, R. Integrated optimization method for helical gear hobbing parameters considering machining efficiency, cost and precision. *Int. J. Adv. Manuf. Technol.* **2001**, *113*, 735–756. [CrossRef]
61. Cao, W.D.; Yan, C.P.; Ding, L.; Ma, Y.F. A continuous optimization decision making of process parameters in high-speed gear hobbing using IBPNN/DE algorithm. *Int. J. Adv. Manuf. Technol.* **2016**, *85*, 2657–2667. [CrossRef]
62. Liu, G.H.; Yan, H.Z.; Zhang, J.J. Optimization of cutting/tool parameters for dry high-speed spiral bevel and hypoid gear cutting with cutting simulation experiment. *Int. J. Adv. Manuf. Technol.* **2012**, *472–475*, 2088–2095. [CrossRef]
63. Ni, H.X.; Yan, C.; Ge, W.; Ni, S.; Sun, H.; Xu, T. Integrated optimization of cutting parameters and hob parameters for energy-conscious gear hobbing. *Int. J. Adv. Manuf. Technol.* **2022**, *118*, 1609–1626. [CrossRef]
64. Cao, W.D.; Yan, C.P.; Wu, D.J.; Tuo, J.B. A novel multi-objective optimization approach of machining parameters with small sample problem in gear hobbing. *Int. J. Adv. Manuf. Technol.* **2017**, *93*, 4099–4110. [CrossRef]
65. Liang, D.; Chen, B.; Gao, Y. Hobbing manufacturing of new type of involute-helix gears for wind turbine gearbox. *Int. J. Precis. Eng. Manuf. Technol.* **2019**, *6*, 305–313. [CrossRef]
66. Radzevich, S.P. A way to improve the accuracy of hobbed involute gears. *J. Mech. Des.* **2007**, *129*, 1076–1085. [CrossRef]
67. Ainoura, M.; Yonekura, M.; Nagano, K. A study on finishing of hardened gears by carbide hob and the accuracy of hobbed gear. *Bull. JSME* **1983**, *26*, 682. [CrossRef]
68. Yonekura, M.; Sugimoto, T.; Sumi, M.; Kumagai, F.; Nagano, K.; Sakuragi, I. A study on finish hobbing with carbide hob: Improvement of gear accuracy using new hobbing machine. *JSME Int. J. Ser. C Mech. Syst. Mach. Elem. Manuf.* **1998**, *41*, 291–298. [CrossRef]
69. Hiroo, Y.; Sakuragi, I.; Kunitake, Y.; Satayotin, K. Gear tooth error caused by hob misalignment. In *Proceedings of the International Conference on Mechanical Transmissions, Vols 1 and 2*; Chongqing University: Chongqing, China, 2006; pp. 862–867.
70. Gao, H.Q.; Wang, S.W.; Chen, Q.G. Analysis and strategy on gear-shape error. *Appl. Mech. Mater.* **2011**, *42*, 347–350. [CrossRef]
71. Wang, Y.Z.; Xu, H.K.; Shen, H.; Wang, G.; Wang, Z.; Vasques, C. A study on the effect of gear hobbing process parameters on the residual stress of the tooth root. *Appl. Sci.* **2024**, *14*, 597. [CrossRef]
72. Yagishita, H. Dynamic rotational accuracy of a middle size gear hobbing machine and the gear cutting performance. Experimental study on the evaluation of generating accuracy of gear teeth in the hobbing machine. *Bull. Jpn. Soc. Precis. Eng.* **1981**, *15*, 7–13.
73. Vasiloni, A.M.; Dragoi, M.V. Smart Adaptive CNC Machining—State of the Art. In Proceedings of the International Conference Innovative Manufacturing Engineering Conference (IManE), Chisinau, Republic of Moldova, 29–30 May 2014.
74. Liu, X.; Zhao, F.; Mei, X.S.; Tao, T.; Shen, J.G. High-efficiency gear hobbing technics based on fuzzy adaptive control of spindle torque. *J. Mech. Eng. Sci.* **2019**, *233*, 3331–3345. [CrossRef]
75. Kosarev, O. An automated-system for checking the accuracy of the kinematic chains on gear hobbing machines. *Sov. Eng. Res.* **1985**, *5*, 60–62.
76. Azvar, M.; Katz, A.; Van Dorp, J.; Erkorkmaz, K. Chip geometry and cutting force prediction in gear hobbing. *CIRP Ann.* **2021**, *70*, 95–98. [CrossRef]
77. Zhao, W.H.; Liu, Z.; Yang, Y.; Zou, Z.; Shu, R.Z.; Lei, S.C.; Gao, X. Improving the transmission error source tracing method for gear hobbing machines. *Adv. Mech. Eng.* **2022**, *14*, 1–11. [CrossRef]
78. Piotrowski, A.; Golebski, R.; Boral, P. Geometric analysis of composite hobs. *Trans. Famena* **2020**, *44*, 43–54. [CrossRef]
79. Nieszporek, T.; Piotrowski, A. Enhancing the Accuracy of Composite Hobs. In Proceedings of the XXI PolishSslovak Scientific Conference Machine Modeling and Simulations, Hucisko, Poland, 17 May 2007.
80. Hu, Y.; Xiang, M.J.; Qiu, X.; Song, P.F.; Song, J.A.; Peng, F.H. An improved design of inserted tooth finishing hob for involute gears. *J. Mech. Sci. Technol.* **2014**, *28*, 3203–3208. [CrossRef]
81. Hsieh, J.K.; Tseng, H.C.; Chang, S.L. A novel hob cutter design for the manufacture of spur-typed cutters. *J. Mater. Process. Technol.* **2009**, *209*, 847–855. [CrossRef]
82. Huang, C.L.; Lee, G.S.; Chang, L.S. A new solution for sharpening helical flute hobs. *Mech. Mach. Theory* **2021**, *164*, 104419. [CrossRef]
83. Moderow, R. The Right and Wrong of Modern Hob Sharpening. In Proceedings of the 19th Annual Gear Manufacturing Simposyum, Chicago, IL, USA, 7–9 April 1991.
84. Kolesov, N.V.; Domnin, P.V.; Zav'yalov, S.S. Disk tool for machining helical surfaces. *Russ. Eng. Res.* **2015**, *35*, 290–291. [CrossRef]
85. Yoshino, H.; Ishibashi, A. A method for calculating grinding wheel-profile for hob finishing—Design and manufacture of gear cutting tools and gears with an arbitrary profile. *JSME Int. J. Ser. III Vib. Control. Eng. Eng. Ind.* **1989**, *32*, 124–130. [CrossRef]
86. Sambhav, K.; Tandon, P.; Dhande, S.G. A generic mathematical model of single point cutting tools in terms of grinding parameters. *Appl. Math. Model.* **2011**, *35*, 5143–5164. [CrossRef]

87. Jiang, H.; Han, J.; Tian, X.; Lu, Y.; Li, G.; Xia, L. Research on generating gear grinding machining error based on mapping relationship between grinding wheel surface and tooth flank. *Machines* **2022**, *10*, 1202. [CrossRef]
88. Zhao, X.F.; Lin, Y.; Liu, H.Q.; Zhang, J. Research on increasing hob tip fillet radius to decrease addendum modification coefficient. *Appl. Mech. Mater.* **2013**, *271–272*, 1105–1109. [CrossRef]
89. Gherghina, G.; Tutunea, D.; Popa, D.; Bogdan, M.L.; Lambrache, N. The method of design and manufacturing of the gear hobbing cutter with bulges. *Appl. Mech. Mater.* **2014**, *657*, 13–17. [CrossRef]
90. Mitchiner, R.G.; Mabie, H.H.; Moosavi-Rad, H. The undercutting of hobbed spur gear teeth. *J. Mech. Des.* **1983**, *105*, 22–128. [CrossRef]
91. Tseng, J.T.; Tsay, C.B. Undercutting and contact characteristics of cylindrical gears with curvilinear shaped teeth generated by hobbing. *J. Mech. Des.* **2006**, *128*, 634–643. [CrossRef]
92. Karpuschewski, B.; Knoche, H.-J.; Hipke, M.; Beutner, M. High performance gear hobbing with powder-metallurgical High-Speed-Steel. *Procedia CIRP* **2013**, *1*, 196–201. [CrossRef]
93. Kobialka, C. Contemporary gear hobbing—Tools and process strategies. *VDI BERICHT* **2002**, *1665*, 241–253.
94. Gerth, J.; Larsson, M.; Wiklund, U.; Riddar, F.; Hogmark, S. On the wear of PVD-coated HSS hobs in dry gear cutting. *Wear* **2009**, *266*, 444–452. [CrossRef]
95. Radzevich, S.P. *Gear Cutting Tools: Fundamentals of Design and Computation*, 1st ed.; CRC Press: Boca Raton, FL, USA, 2010.
96. Máté, M.; Tolvaly-Roșca, F.; Hodgyai, N.; Drăgoi, M.V. A New Approach of Defining the Grinding Wheel Profile of the Gear Hob's Rake Face. In Proceedings of the 2022 IEEE 22nd International Symposium on Computational Intelligence and Anformatics and 8th IEEE International Conference on Recent Achievements in Mechatronics, Automation, Computer Science and Robotics (CINTI-MACRO), Budapest, Hungary, 21–22 November 2022.
97. Hodgyai, N.; Máté, M.; Tolvaly-Roşca, F.; Drăgoi, M.V. Peculiarities of the grinding process of a gear hob helical rake face. *Acta Univ. Sapientiae Electr. Mech. Eng.* **2021**, *13*, 39–51. [CrossRef]
98. Yoshino, H.; Ohshima, F. Sharpening of Hob Cutting Edges with Helical Flutes. In Proceedings of the International Conference on Mechanical Transmissions, Chongqing, China, 5–9 April 2001.
99. Chen, X.D.; Wang, H.X.; Lao, Q.C. Development of Calculating Grinding Wheel-profile Software Applied to the Sharping Grinder Machine. *Adv. Mater. Res.* **2012**, *411*, 135–139. [CrossRef]
100. He, J.N.; Gao, Y.; Bin Zhang, H.; Zhang, C.; Deng, X.L. Simulation research on undercutting properties of involute gears based on VB. *Adv. Mater. Res.* **2013**, *655–657*, 408–411. [CrossRef]
101. Qin, D.T.; Chen, X.O.; Chen, B.K.; Lin, C. The Undercutting and Pointing of Hobbed Double Involute Gear Teeth. In Proceedings of the International Conference on Mechanical Transmissions, Chongqing, China, 1 January 2002.
102. Balajti, Z. Determination of Undercutting Avoidance for Designing the Production Technology of Worm Gear Drives with a Curved Profile. *Machines* **2023**, *11*, 56. [CrossRef]

MDPI AG
Grosspeteranlage 5
4052 Basel
Switzerland
Tel.: +41 61 683 77 34

Materials Editorial Office
E-mail: materials@mdpi.com
www.mdpi.com/journal/materials

Academic Open
Access Publishing

mdpi.com

ISBN 978-3-7258-4077-9